NANOMANUFACTURING HANDBOOK

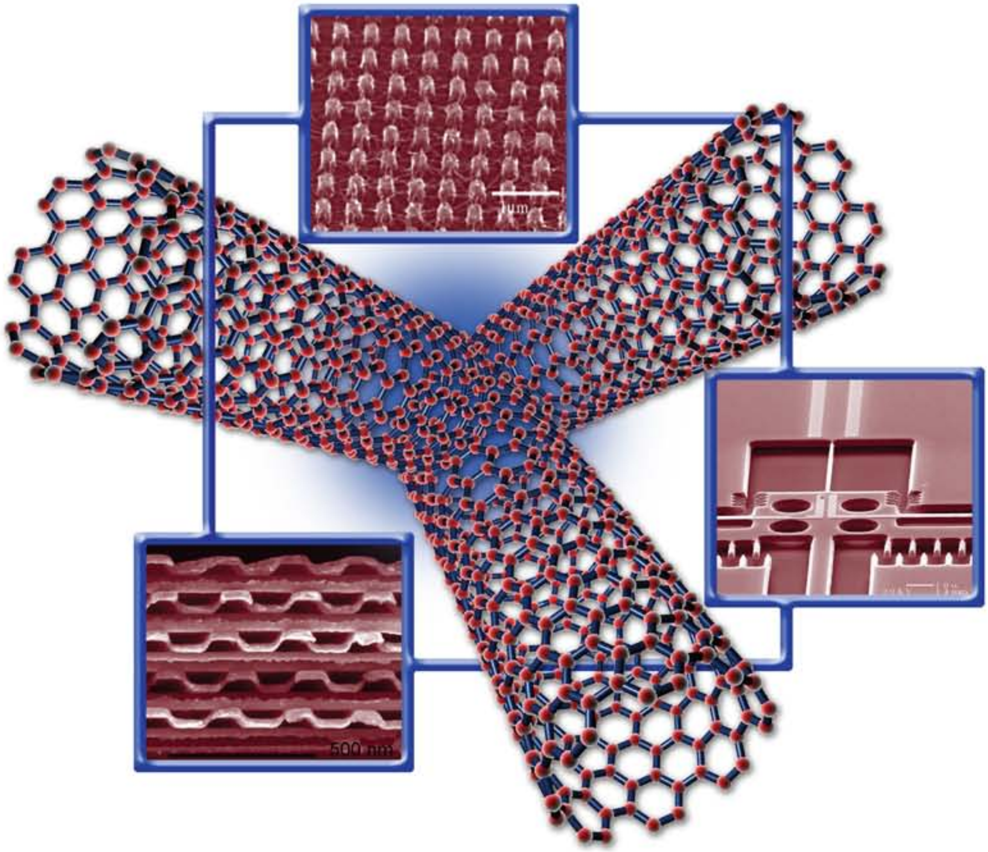

AHMED BUSNAINA

CRC Press
Taylor & Francis Group

Nanomanufacturing Handbook

NANOMANUFACTURING HANDBOOK

AHMED BUSNAINA
NORTHEASTERN UNIVERSITY,
BOSTON, MASSACHUSETTS, USA

CRC Press
Taylor & Francis Group
Boca Raton London New York

CRC Press is an imprint of the
Taylor & Francis Group, an informa business

CRC Press
Taylor & Francis Group
6000 Broken Sound Parkway NW, Suite 300
Boca Raton, FL 33487-2742

© 2007 by Taylor & Francis Group, LLC
CRC Press is an imprint of Taylor & Francis Group, an Informa business

No claim to original U.S. Government works
Printed in the United States of America on acid-free paper
10 9 8 7 6 5 4 3 2 1

International Standard Book Number-10: 0-8493-3326-1 (Hardcover)
International Standard Book Number-13: 978-0-8493-3326-2 (Hardcover)

This book contains information obtained from authentic and highly regarded sources. Reprinted material is quoted with permission, and sources are indicated. A wide variety of references are listed. Reasonable efforts have been made to publish reliable data and information, but the author and the publisher cannot assume responsibility for the validity of all materials or for the consequences of their use.

No part of this book may be reprinted, reproduced, transmitted, or utilized in any form by any electronic, mechanical, or other means, now known or hereafter invented, including photocopying, microfilming, and recording, or in any information storage or retrieval system, without written permission from the publishers.

For permission to photocopy or use material electronically from this work, please access www.copyright.com (http://www.copyright.com/) or contact the Copyright Clearance Center, Inc. (CCC) 222 Rosewood Drive, Danvers, MA 01923, 978-750-8400. CCC is a not-for-profit organization that provides licenses and registration for a variety of users. For organizations that have been granted a photocopy license by the CCC, a separate system of payment has been arranged.

Trademark Notice: Product or corporate names may be trademarks or registered trademarks, and are used only for identification and explanation without intent to infringe.

Library of Congress Cataloging-in-Publication Data

Busnaina, A. A.
Nanomanufacturing handbook / Ahmed Busnaina.
p. cm.
ISBN-13: 978-0-8493-3326-2 (alk. paper)
ISBN-10: 0-8493-3326-1
1. Nanotechnology. 2. Nanostructured materials. I. Title.

T174.7.B87 2006
620'.5--dc22 2006009680

Visit the Taylor & Francis Web site at
http://www.taylorandfrancis.com

and the CRC Press Web site at
http://www.crcpress.com

Dedication

For my wife Zainab, for her support, love and patience,
and for my children, Wedad, Ibrahim, and Ali.

Foreword: New Frontiers for Nanomanufacturing

In the first decade of the 21st century, nanoscale science and engineering has become a driving force for discovery and innovation. Advances at the nanoscale are leading to new understanding of nature and manmade things, and an increased ability to restructure matter at the atomic and molecular levels. In due course, nanomanufacturing promises to arrive at the top of the wave of productive processes. In the second decade, the next major manufacturing leap won't be found on the typical factory floor. It will take shape in biofactories, programmed chemical reactors, and automated selfassembling lines; it will be more tailored and integrated with each application, and the production may be distributed in technology clusters. Scientists are learning how to harness the basic forces of physics and chemistry to create a mix of atoms that hierarchically "self-assemble" in a predictable and efficient sequence. With public and corporate funding mounting, nanotechnology is now on an accelerated path. With over a $5 billion nanotechnology R&D annual investment worldwide, industry has exceeded government funding of over $4 billion in 2005. We estimate the global market for products that incorporate nanotechnology to be about $110 billion, with an annual rate of increase of about 25 percent per year. Where now, the majority are product improvements made possible by nanotechnology components (estimated to about $80 billion for catalysts, transistors, improved materials, etc.; large companies dominate this domain) and the remaining include the development of new products (about $30 billion worldwide according to Lux Research; small and medium size companies are important here).

Nanomanufacturing has been defined as an approach to design, produce, control, modify, manipulate, and assemble nanometer-scale elements or features for the purpose of realizing a product or system that exploits properties seen at the nanoscale. Nanomanufacturing R&D has as its goal enabling the mass production of reliable and economical nanoscale materials, structures, devices, and systems. It includes bottom-up directed assembling of nanostructure building blocks (from the atomic, molecular, supramolecular levels); top-down, high-resolution processing (ultraprecision engineering, fragmentation methods); physico-chemical engineering of molecules and supramolecular systems (molecules as devices “by design”, nanoscale

machines, etc.); and, hierarchical integration with larger scale systems. This requires a high degree of process control in sensing and actuation of matter at the nanoscale, as well as capabilities for scaling-up. A key goal is minimizing use of materials and energy, reduction of waste and environmental impact, and enabling high-rate, cost-effective production suitable for industrial implementation.

One has to place nanotechnology developments in the long-term where it comes to creating commercial prototypes. Most of what has already made it into the marketplace is in the form of First Generation products (passive nanostructures with steady behavior). Many small and large companies have Second (active nanostructures with changing behavior during use) and embryonic Third Generation (nanosystems) products in the pipeline. Concepts for the Fourth Generation products, including molecular nanosystems, are only in research. The *First Generation* (after 2000) of passive nanostructures is illustrated by nanostructured coatings, nanoparticles, nanowires, and bulk nanostructured materials. The *Second Generation* (after 2005) of active nanostructures is illustrated by transistors, amplifiers, targeted drugs and chemicals, sensors, actuators, and adaptive structures. The *Third Generation* (after 2010) includes three-dimensional nanosystems and systems of nanosystems using various synthesis and assembling techniques such as bioassembling; nanoscale robotics; networking at the nanoscale and multiscale architectures. The *Fourth Generation* (after 2015-2020) includes heterogeneous molecular nanosystems, where each molecule in the nanosystem has a specific structure and plays a different role. Molecules will be used as devices, and fundamentally new functions will emerge from their engineered structures and architectures. The rudimentary capabilities of nanotechnology today for systematic control and manufacture at the nanoscale are envisioned to evolve in these four overlapping generations of new nanotechnology products with different areas of R&D focus. Each generation of new products is expected to include, at least partially as components, products from previous generation.

This volume covers a selection of the nanomanufacturing methods for particularly the "First" generation of nanotechnology products and ideas for the following generations. Several chapters deal with carbon nanotube synthesis and their use in composites, nano-imprint on surfaces, polymeric nanostructures, and production of fibers. Next generations manufacturing methods and products are addressed in another group of contributions on guided assembling of patterns on surfaces, building connectors and processing methods at the nanoscale. The last group of contributions in this volume is dedicated to the role of patenting, regulatory and societal implications. An example of a national program focused on nanoscale manufacturing is presented for Korea.

Convergence with modern biology, digital revolution and cognitive sciences is expected to accelerate the nanotechnology development and its applications. In the first decade, we saw manufactured only nanocomponents and improvement of products and processes. After 2010 we expect to see a broad

introduction of revolutionary products based on the fundamental discoveries made in the first years of the 21st century. While expectations from nanotechnology may be overestimated in short term, the long term implications on healthcare, productivity, and the environment appear to be underestimated.

The readers are encouraged to look at the presented contributions as they relate to each other in creating a growing nanomanufacturing capability. Few nanomanufacturing methods are effectively used in production, more methods are in the design-development phase, but most ideas are still in research. The production capabilities will advance rapidly as the basic understanding, and particularly the tools for measurement and nanomanufacturing, progress. This book will open the interest and provide several basic approaches for the significant developments in nanomanufacturing's promise for the future.

Dr. M.C. Roco
National Science Foundation
and National Nanotechnology Initiative
www.nsf.gov/nano and www.nano.gov

Preface

Nanoscience has been making great strides over the past few years with breakthroughs coming at a surprisingly rapid rate. However, the transfer of nanoscience accomplishments into commercial products is severely hindered by a lack of understanding of barriers to nanomanufacturing. While nanotechnology hold the promise of significant technological and economic advances, commercial products cannot be realized without first answering the question of how one can assemble and wire millions and billions of nanoscale nanoelements such as nanotubes, particles, nanofibers, rods, proteins and many other nanobuilding blocks. Most nanotechnology research focuses on manipulating several to several hundred particles or molecules to assemble a useful device. Commercial scale-up and the promised economic windfall, however, will not be realized unless one can perform fast massive directed (high-rate/high-volume) assembly of nanoelements. To move scientific discoveries from the laboratory to commercial products, many fundamental research issues must be addressed regarding scale-up of processes at high rates and high volume, robustness, defects, reliability, and integration of nanoscale structures into micro-, meso-, and macroscale devices.

Richard Feynman's vision; which predicted many of the breakthroughs we see today, addressed nanomanufacturing in 1959 when he suggested that by manipulating matter at the atomic level, we can build tiny machines that could construct even tinier ones. This analogous (on a much larger scale) to robotics and automation used today to assembly and manufacture electronics, automotives, etc. However, much of the research that goes on in nanotechnology and nanomanufacturing today does not go that far and instead focuses on directing nanoelements (nanobuilding blocks) to self-assemble into structures to make devices and other applications.

Successful nanomanufacturing could give rise to countless applications that will be of a broad significance. For example, consider the following: a daily-wear biosensor capable of monitoring insulin levels for a diabetic, high blood pressure, increased white cell counts, and early detection of cancer, along with options for contacting emergency medical personnel; a personal computer that is small and flexible enough to be worn as a tie or lapel pin; flexible nanotube-based high-efficiency solar cell shingles that coat the outside of buildings to provide home and office energy needs; or sub-millimeter-thick

electronic wall paper that displays movies, video-conference participants, photos, paintings, dynamic designs, etc. on entire walls in your home or office. It could also provide solutions to renewable energy and resources such energy generation, storage, solutions for pollution and environmental problems and water. These exciting applications and solutions could become a reality within the next decade, if nanomanufacturing processes and tools are developed to enable large-scale molecular assembly. There is a need to leverage current and future efforts in nanoscience and technology by bridging the gap between scientific research and the creation of commercial products by established and emerging industries, such as electronic, medical, and automotive. Long-standing ties with industry will also facilitate technology transfer.

The impact of nanotechnology has been projected by the National Science Foundation to be on the order of more than $1 trillion/year by 2015 in new technologies and products. This has been divided by area: $900 billions/year in electronics, $340 billions/year in materials, $180 billions/year in healthcare & pharmaceuticals, $100 billions/year in chemicals (catalysts. etc.), $100 billions/year in sustainability: agriculture, water, energy. It is also projected to add 2 million jobs in nanotechnology. This could lead to a new industrial revolution.

This Handbook covers diverse topics in nanomanufacturing including top-down and bottom-up approaches and addresses reliability and defects and many important issues that touch on how to conduct nanomanufacturing today and how to address many of the technical barriers to nanomanufacturing. It is intended for researchers in industry and academia, practicing engineers and scientists as well as graduate students in science and engineering. It could also be used as a graduate text for a one semester course on nanomanufacturing for science and engineering students.

This book contributions are based on topics and issues presented at the annual International New England Nanomanufacturing Workshops (2003-2006). All authors have participated at the workshop. I would like to thank the authors for their contribution, the CRC/Taylor & Francis staff and the NSF Nanoscale Science and Engineering Center for High-rate Nanomanufacturing staff and associate directors for their help. I also would like to thank the scientists who provided critical reviews of the book chapters.

Editor

Ahmed A. Busnaina is the William Lincoln Smith Chair Professor and Director of National Science Foundation's Nanoscale Science and Engineering Center (NSEC) for High-rate Nanomanufacturing and the NSF Center for Nano and Microcontamination Control at Northeastern University, Boston, Massachusetts. He is internationally recognized for his work on nano and micro scale defects mitigation and removal in semiconductor fabrication. He is also involved in the fabrication of nanoscale wires, structures and interconnects. He specializes in directed assembly of nanoelements and in the fabrication of micro and nanoscale structures. He served as a consultant on micro contamination and particle adhesion issues to the semiconductor industry. He authored more than 300 papers in journals, proceedings and conferences. He organized more than 80 conferences, workshops, symposia and programs for many professional societies, chaired and organized more than 90 sessions and panels. He also serves on many advisory boards including Samsung Electronics; Chemical Industry Nanomaterials Roadmap, International Technology Roadmap for Semiconductors, Journal of Particulate Science and Technology, Journal of Environmental Sciences, Semiconductor International, Journal of Advanced Applications in Contamination Control. He is a fellow of the American Society of Mechanical Engineers, and the Adhesion Society, a Fulbright Senior Scholar and listed in Who's Who in the World.

Contributors

George G. Adams
Mechanical and Industrial Engineering Department
Northeastern University
Boston, Massachusetts

Kaveh Bakhtari
Northeastern University
Boston, Massachusetts

Carol Barry
Department of Plastics Engineering
University of Massachusetts Lowell
Lowell, Massachusetts

Claude Bertin
Nantero, Inc.
Woburn, Massachusetts

Christopher J. Bosso
Northeastern University
Boston, Massachusetts

Darren K. Brock
Nantero, Inc.
Woburn, Massachusetts

Ahmed Busnaina
NSF Nanoscale Science and Engineering Center for High-rate Nanomanufacturing
Northeastern University
Boston, Massachusetts

Kyung-Eun Byun
Physics and NANO Systems Institute
Seoul National University
Seoul, Korea

Nam-Goo Cha
Micro Biochip Center
Division of Materials and Chemical Engineering
Hanyang University
Ansan, Korea

Won-Seok Chang
Ministry of Science & Technology Center for Nanoscale Mechatronics & Manufacturing
Daejeon, Korea

Julie Chen
Department of Mechanical Engineering
University of Massachusetts Lowell
Lowell, Massachusetts

Du-Sun Choi
Ministry of Science & Technology Center for Nanoscale Mechatronics & Manufacturing
Daejeon, Korea

Jun-Hyuk Choi
Center for Nanoscale Mechatronics and Manufacturing
21st Century Frontier R&D Program
Ministry of Sciences and Technology
Daejeon, Korea

Dietrich Dehlinger
University California San Diego
La Jolla, California

Sadik Esener
University California San Diego
La Jolla, California

Phil Gibson
Materials Science Team
AMSSB-RSS-MS
U.S. Army Soldier Systems Center
Natick, Massachusetts

Chang-Soo Han
Center for Nanoscale Mechatronics and Manufacturing
21st Century Frontier R&D Program
Ministry of Sciences and Technology
Daejeon, Korea

Michael J. Heller
University California San Diego
La Jolla, California

Rouget F. (Ric) Henschel
Foley & Lardner LLP
Washington, D.C.

Kwang Heo
Physics and NANO Systems Institute
Seoul National University
Seoul, Korea

Dalibor Hodko
Nanogen
San Diego, California

Seunghun Hong
Physics and NANO Systems Institut
Seoul National University
Seoul, Korea

Jacqueline A. Isaacs
Northeastern University
Boston, Massachusetts

Jun-Ho Jeong
Ministry of Science & Technology
Center for Nanoscale Mechatronics & Manufacturing
Daejeon, Korea

Yung Joon Jung
Department of Mechanical and Industrial Engineering
Northeastern University
Boston, Massachusetts

Juwan Kang
Physics and NANO Systems Institute
Seoul National University
Seoul, Korea

William D. Kay
Northeastern University
Boston, Massachusetts

Tae-Kyeong Kim
Physics and NANO Systems Institute
Seoul National University
Seoul, Korea

Juntae Koh
Physics and NANO Systems Institute
Seoul National University
Seoul, Korea

Dong Joon Lee
Physics and NANO Systems Institute
Seoul National University
Seoul, Korea

Eung-Sug Lee
Center for Nanoscale Mechatronics and Manufacturing
21st Century Frontier R&D Program
Ministry of Sciences and Technology
Daejeon, Korea

Jae-Jong Lee
Ministry of Science & Technology
Center for Nanoscale Mechatronics & Manufacturing
Daejeon, Korea

Sang-Rok Lee
Center for Nanoscale Mechatronics and Manufacturing
21st Century Frontier R&D Program
Ministry of Sciences and Technology
Daejeon, Korea

Patrick Lemoine
Nanotechnology Research Institute
University of Ulster
Newtownabbey
Co. Antrim, Northern Ireland

Stephen B. Maebius
Foley & Lardner LLP
Washington, D.C.

Paul Maguire
Nanotechnology Research Institute
University of Ulster
Newtownabbey
Co. Antrim, Northern Ireland

Shinji Matsui
University of Hyogo Graduate School of Science
Hyogo, Japan

Nicol E. McGruer
Electrical and Computer Engineering Department
Northeastern University
Boston, Massachusetts

James McLaughlin
Nanotechnology Research Institute
University of Ulster
Newtownabbey
Co. Antrim, Northern Ireland

Joey Mead
Department of Plastics Engineering
University of Massachusetts Lowell
Lowell, Massachusetts

Manish Mehta
Industry Forums and Technologies Research Corp.
National Center for Manufacturing Sciences
Ann Arbor, Michigan

Etienne Menard
University of Illinois at Urbana/Champaign
Urbana, Illinois

Ken-ichiro Nakamatsu
University of Hyogo
Graduate School of Science
Hyogo, Japan

Seon Namgung
Physics and NANO Systems Institute
Seoul National University
Seoul, Korea

Pagona Papakonstantinou
Nanotechnology Research Institute
University of Ulster
Newtownabbey
Co. Antrim, Northern Ireland

Jin-Goo Park
Micro Biochip Center
Division of Materials and Chemical Engineering
Hanyang University
Ansan, Korea

Sung Young Park
Physics and NANO Systems Institute
Seoul National University
Seoul, Korea

John Paul Quinn
Nanotechnology Research Institute
University of Ulster
Newtownabbey
Co. Antrim, Northern Ireland

John Rogers
University of Illinois at
Urbana/Champaign
Urbana, Illinois

Thomas Rueckes
Nantero, Inc.
Woburn, Massachusetts

Ronald L. Sandler
Northeastern University
Boston, Massachusetts

Heidi Schreuder-Gibson
Materials Science Team
AMSSB-RSS-MS
U.S. Army Soldier Systems Center
Natick, Massachusetts

Brent M. Segal
Nantero, Inc.
Woburn, Massachusetts

Benjamin Sullivan
University California San Diego
La Jolla, California

Paul Swanson
Nanogen
San Diego, California

Loucas Tsakalakos
General Electric-Global Research
Center
Niskayuna, New York

Jonathan W. Ward
Nantero, Inc.
Woburn, Massachusetts

Kyung-Hyun Whang
Center for Nanoscale Mechatronics
and Manufacturing
21st Century Frontier R&D Program
Ministry of Sciences and Technology
Daejeon, Korea

Contents

Chapter 1 Introduction to Nanomanufacturing 1
Ahmed Busnaina and Manish Mehta

Chapter 2 Surface-Programmed Assembly for Nanomanufacturing 33
Seunghun Hong, Sung Young Park, Juwan Kang, Tae-Kyeong Kim, Juntae Koh, Kwang Heo, Kyung-Eun Byun, Dong Joon Lee, and Seon Namgung

Chapter 3 Fabrication and Applications of Single-Walled Carbon Nanotube (SWNT) Fabrics 55
Darren K. Brock, Jonathan W. Ward, Claude Bertin, Brent M. Segal, and Thomas Rueckes

Chapter 4 Controlled Synthesis of Carbon Nanotubes Using Chemical Vapor Deposition Methods 79
Yung Joon Jung

Chapter 5 Reconfigurable CMOS Electronic Microarray System for the Assisted Self-Assembly of Higher-Order Nanostructures 107
Dietrich Dehlinger, Benjamin Sullivan, Sadik Esener, Paul Swanson, Dalibor Hodko, and Michael J. Heller

Chapter 6 Manufacturing Electrical Contacts to Nanostructures 127
Loucas Tsakalakos

Chapter 7 Nanofabrication Techniques with High-Resolution Molded Rubber Stamps 147
Etienne Menard and John Rogers

Chapter 8 Room-Temperature Nanoimprint and Nanocontact Technologies 161
Ken-ichiro Nakamatsu and Shinji Matsui

Chapter 9 Antistiction Layers for Nano Imprinting Lithography 183
Nam-Goo Cha and Jin-Goo Park

Chapter 10 Nanocontacts and Switch Reliability 217
George G. Adams and Nicol E. McGruer

Chapter 11 Nanoscale Defects and Surface Preparation in Nanomanufacturing 251
Ahmed Busnaina and Kaveh Bakhtari

Chapter 12 Improved Carbon Materials for Nanomanufacturing Applications 281
Patrick Lemoine, John Paul Quinn, Pagona Papakonstantinou, Paul Maguire, and James McLaughlin

Chapter 13 Nanomanufacturing Processes Using Polymeric Materials 313
Carol Barry, Julie Chen, and Joey Mead

Chapter 14 Patterned Electrospray Fiber Structures 351
Phil Gibson and Heidi Schreuder-Gibson

Chapter 15 Patenting Nanotechnology 367
Rouget F. (Ric) Henschel and Stephen B. Maebius

Chapter 16 Leaving the Laboratory: Regulatory and Societal Issues Confronting Nanotechnology Commercialization 377
Christopher J. Bosso, Jacqueline A. Isaacs, William D. Kay, and Ronald L. Sandler

Chapter 17 R&D Activities for Nanoscale Manufacturing Processes and Enabling Equipment in Korea 389
Chang-Soo Han, Jun-Hyuk Choi, Hak-Joo Lee, Jae-Jong Lee, Doo-Sun Choi, Won-Seok Chang, Jun-Ho Jeong, Eung-Sug Lee, Kyung-Hyun Whang, and Sang-Rok Lee

Index 397

Chapter 1

Introduction to Nanoscale Manufacturing and the State of the Nanomanufacturing Industry in the United States

Ahmed Busnaina and Manish Mehta

Contents

1.1 Nanomanufacturing Challenges ... 3
1.2 Top-Down Approach ... 4
1.2.1 Nanoimprint Lithography for Nanoscale Devices ... 5
1.3 Bottom-Up Approach ... 5
1.4 Combined Top-Down and Bottom-Up Nanomanufacturing Approaches ... 7
1.4.1 Nanoscale Patterning ... 7
1.4.2 Possible Approaches for Directed Self-Assembly of Nanoelements ... 9
1.4.2.1 Directed Assembly ... 9
1.4.3 Directed Self-Assembly of Nanoelements Using Nanotemplates ... 10
1.4.3.1 Nanotemplates for Guided Self-Assembly of Polymer Melts ... 11
1.4.4 Nanoscale Patterning Using Block Copolymers ... 12
1.4.5 Directed Self-Assembly of Conductive Polymers Using Nanoscale Templates ... 13
1.5 Registration and Alignment ... 14
1.6 Reliability and Defect Control ... 15
1.6.1 Reliability and Characterization Tools ... 15
1.6.2 Removal of Defects Due to Micro and Nanoscale Contamination ... 16

1.7 Nanomanufacturing Industry Survey 16
1.7.1 Background 16
1.7.2 Aggregate Observations 16
1.7.2.1 Diverse Nanotechnology Products in Development 18
1.7.2.2 Increased Corporate and Public Awareness 19
1.7.3 Key Industry Barriers 19
1.8 Recommended National Priorities for the Near Term 20
1.8.1 Accelerating Nanotechnology Developments 20
1.8.2 Government-Led Public-Private Collaborations 21
1.9 Strategic U.S. Industry Indicators and Summary Trends 23
1.9.1 Geographical Profile 23
1.9.2 Major Players in Nanomanufacturing 23
1.9.3 Nanotechnology Products 24
1.9.4 Nanomanufacturing Application Markets 24
1.9.5 Corporate Urgency 24
1.9.6 Change Management 24
1.9.7 Organization Capacity 25
1.9.8 Internal Infrastructure 25
1.9.9 Collaborative Development 26
1.9.10 Drivers for Partnering 26
1.9.11 Staffing for Nanomanufacturing 26
1.9.12 Commercialization Timelines 26
1.9.13 Government's Role in Nanomanufacturing 27
1.9.14 Nanomanufacturing Industry Challenges 27
1.9.15 Technology Transfer Preferences 28
Acknowledgment 28
References 28

Scientific breakthroughs in nanoscience have come at a surprisingly rapid rate over the past few years. The transfer of nanoscience accomplishments into technology, however, is severely hindered by a lack of understanding of barriers to manufacturing in the nanoscale dimension. For example, while shrinking dimensions hold the promise of exponential increases in data storage densities, realistic commercial products cannot be realized without first answering the question of how one can wire millions and billions of nanoscale devices together, or how one can prevent failures and avoid defects. Most nanotechnology research focuses on surface modification, manipulating several to several hundred particles or molecules to be assembled into desirable configurations. There is a need to conduct fast massive directed assembly of nanoscale elements at high rates and over large areas. To move scientific discoveries from the laboratory to commercial products, a completely different set of fundamental research issues must be addressed — primarily those related to viable commercial scale-up of production volumes, process robustness and

reliability, and integration of nanoscale structures and devices into micro-, meso-, and macroscale products. The field of nanomanufacturing is incredibly broad, cutting across all industries and scientific realms.

The first part of this chapter (Section 1.1 through Section 1.6) gives an overview of nanomanufacturing challenges, top-down and bottom-up approaches, combined top-down and bottom-up approaches, nanoscale registration and alignment and reliability and defect control. The second part (Section 1.7 through Section 1.9) covers the current state of nanomanufacturing in the United States through the recently finished 2005 NCMS Survey of Nanotechnology in the U.S. Manufacturing Industry. The study is sponsored by the National Science Foundation. The survey covers the nanomanufacturing Industry, and recommended national priorities for the near term and strategic U.S. industry indicators and summary trends.

Many workshops were organized by the Nanoscale Science, Engineering, and Technology (NSET) Subcommittee of the National Science and Technology Council's Committee on Technology to address challenges facing the National Nanotechnology Initiative (NNI). The NNI goal is to accelerate the research, development, and deployment of nanotechnology to address national needs, enhance the economy, and improve the quality of life in the United States and around the world. NNI seeks to do this through coordination of activities and programs across the federal government. The workshops also help to identify funding priorities and long-term goals toward commercializing nanotechnology. The "grand challenges" identified by the NNI are directly related to applications of nanotechnology and have the potential of having a significant economic and societal impact. The nine grand challenge areas are as follows:

- Nanostructured materials by design
- Manufacturing at the nanoscale
- Chemical-biological-radiological-explosive detection and protection
- Nanoscale instrumentation and metrology
- Nano-electronics, -photonics, and -magnetics
- Healthcare, therapeutics, and diagnostics
- Nanoscience research for energy needs
- Microcraft and robotics
- Nanoscale processes for environmental improvement

1.1 Nanomanufacturing Challenges

The NNI Grand Challenges and the NSF Workshop on Three Dimensional Nanomanufacturing[1,2] held in Birmingham, Alabama, in January 2003, identified three critical and fundamental technical barriers to nanomanufacturing:

1. How can we control the assembly of 3D heterogeneous systems, including the alignment, registration, and interconnection at three dimensions and with multiple functionalities?

2. How can we handle and process nanoscale structures in a high-rate/high-volume manner, without compromising the beneficial nanoscale properties?
3. How can we test the long-term reliability of nano components, and detect, remove, or prevent defects and contamination?

The first and the second joint workshop by the National Nanotechnology Initiative (NNI) and the Semiconductor Research Corp. (SRC) for "Silicon Nanoelectronics and Beyond (SNB): Challenges and Research Directions" held in December 2004 and 2005 identified the need for new research to develop new non charge based switches but also stressed the need to develop new nanomanufacturing technologies among them:

Fabricating nanobuilding blocks and nanostructures to assemble nanodevices with precise orientation and location, size and shape control; new structures to enable ballistic transport; contacts and contact engineering, interconnects and structures to manage heat removal. Research is needed to develop nanoscale materials by design, self-assembly for functionality; nanoscale materials characterization and metrology; and properties of materials at nanoscale, as well as biomimetic concepts, predictive modeling of directed self-assembly, and assembly of components at a variety of scales by self-assembly. Some of the research gaps that need to be addressed are:

Have a complete assessment of emerging devices in terms of functionality, performance followed by the reliability and eventual manufacturability. Maintain initial focus on hybridization with CMOS along with parallel options that may not involve CMOS.

New research directions need to be addressed in addition to current research efforts going on in many industry, universities and government research centers and laboratories. First, heterogeneous process integration such as combination of hierarchical directed assembly techniques with other processing techniques. The second is nanoscale metrology tools, such as in-line or in-situ monitoring and feedback. The third is high-throughput hierarchical directed assembly; the fourth is nanoscale components and interconnect reliability. The fifth is nanoscale defect mitigation and removal and defect tolerant materials, structures and processes, e.g. self-healing. The sixth is probabilistic design for manufacturing that addresses variability and noise at the atomic scale.

1.2 Top-Down Approach

Top-down approaches using many relatively new techniques such as ion beam assisted deposition (IBAD), FIB, EUV lithography, e-beam lithography, AFM (DIP Pen or AFM field evaporation) lithography, plasmonic imaging lithography and nanoimprint lithography and many others have been pursued for many years. The work published in this area includes all the work that is done in semiconductor manufacturing which is published in thousands of articles per year. This is very broad and diverse to be covered here.

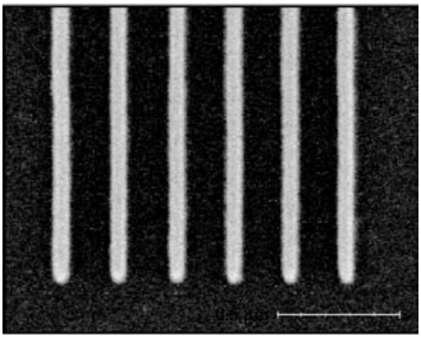

Figure 1.1 30-nm lines on semi-isolated pitch made using UV-NIL process (step and flash imprint lithography variant)[3].

The development work has been incremental and no significant breakthrough has been reported in the last year. One notable development, HP and UCLA (Y. Chen group) have made progress in making molds for nanoimprint lithography that have nanoscale features smaller than 10 nm, using thin film deposition techniques to produce a mold.

1.2.1 Nanoimprint Lithography for Nanoscale Devices

Nanoimprint lithography is a promising economic nanoscale patterning technique, Figure 1.1, that made much progress in the past few years on tool designs and processing techniques.[3] Recent research and development efforts have focused on developing new materials for specific nanoimprint applications. Material proposed for nanoimprint includes imprintable dielectrics, conducting polymers, biocompatible materials, and materials for microfluidic devices.

Enabling UV-NIL for nanoscale device manufacturing will require the development of new photocurable precursors. Photocuring adds another constraint on materials design, but offers the advantages of using a low-viscosity imprint resist especially in high-throughput and multilevel device fabrication. The development of a photocurable interlayer dielectric may have a significant impact on the semiconductor industry by simplifying the fabrication processes.

1.3 Bottom-Up Approach

Patterning, templating, and surface functionalization are commonly used for directed assembly. Geometrical shaping and structuring processes at the nanoscale are used in many applications to produce functional devices, templates or integrated multi-element systems. For example, many lithography techniques could be combined with focused ion beam, two-photon lithography, or probe-based methods including AFM, STM, near-field optical and mechanical tip scribing, as well as soft lithography techniques. These could

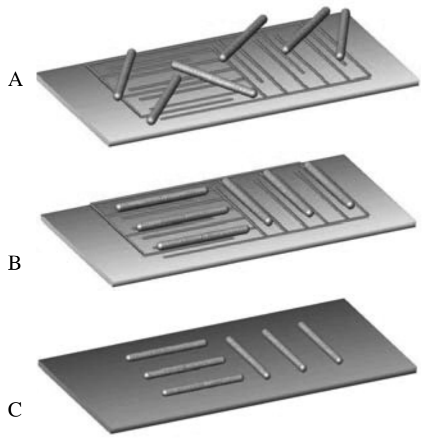

Figure 1.2 Nanotubes deposited (A), assembled (B) on a nanotemplate, then transferred to a second substrates (C).[4]

also be extended to 3-dimensional patterning by processes such as stereolithographic layering. These approaches lead to many different barriers, but what is consistent is that all will need repeatable, scalable, and controllable processes. The above mentioned patterned substrates could be used as nanotemplates to enable precise assembly of various nanoelements. However, in order to extend these tools to a true nanomanufacturing a process, the assembly needs to be conducted in a continuous or high-rate/high-volume processes (for example multi-step or reel-to-reel processes). This way, nano building blocks and block copolymers can be guided to assemble in prescribed patterns (2-D or 3-D) over large areas in high-rate, scaleable, commercially relevant processes such injection molding or extrusion.

Figure 1.2 shows how a large-scale directed assembly process could work, the electrostatically (or chemically) addressable nanotemplate which controls the placement and positioning of carbon nanotubes, nanoparticles, or other nanoelements.[4] The nanotubes align on the charged wires of the nanotemplate (step B); the assembled (patterned) nanoelements can then be transferred onto another substrate as shown in step C. This will be covered in more detail with examples in this chapter in more details in Section 1.4.

Biologically-inspired assembly/molecular manufacturing is one of the most challenging nanomanufacturing techniques. It is ideal to think of utilizing the many directed self-assembly techniques inherent in nature to make a wide range of hierarchical structures. There are many barriers to mimicking nature including precision synthesis or the ability to obtain the same building blocks repeatedly and reliably (sequence, composition, block and chain lengths, etc.). To go beyond self-assembly (uniform structures) and have the

possibility to fabricate super molecular structures, we need to utilize the same interaction potentials (e.g., shape, electrostatics, hydrophobicity, metal coordination, controlled arrangement of functional sites).[5] The modification of viruses and proteins to serve as assemblers of newly designed materials[6] has shown a promising potential for using them in nanomanufacturing. Most of the directed bottom bottom-up approaches use templating. This is especially true if the desired patterns are non-uniform. The next section discusses different approaches for the use of templates in assembling block copolymers, nanoparticles and nanotubes.

1.4 Combined Top-Down and Bottom-Up Nanomanufacturing Approaches

Current nanotechnology research focuses on surface modification, matching molecules and "sockets" at the level of manipulating few to several-hundred particles or molecules to be assembled into desirable configurations. Commercial scale-up will not be realized unless one can perform high-rate/high-volume assembly of nanoelements economically and using environmentally benign processes. High-rate/high-volume directed self-assembly will accelerate the creation of highly anticipated commercial products and enable the creation of an entirely new generation of applications yet to be imagined, because they are developed with scalability and integration as a requirement. This includes understanding what is essential for a rapid multi-step or reel-to-reel process, as well as for accelerated-life testing of nanoelements and defect-tolerance. For example, a fundamental understanding of the interfacial behavior and forces required assembling, detaching, and transfer nanoelements, required for guided self-assembly at high-rates and over large areas is needed.

1.4.1 Nanoscale Patterning

Nanoscale patterns can be created using e-beam, dip pen, or nanoimprint lithography (Figure 1.3). In many ways, dip pen nanolithography represents a bridge between top-down and bottom-up approaches. It is a tool for the direct or manual deposition of organic molecules onto solid substrates.[7–9] Because the organic molecules interact with both the substrate as well as other organic molecules, DPN has a self-assembly component. The e-beam and DPN lithography are not suitable for high-rate manufacturing, but they are suitable for making the above nanotemplates.

For smaller patterns, self-ordering growth of nanoarrays on strained interfaces is an attractive option for preparing highly ordered nanotemplates with specific feature sizes and densities.[10–12] Reconstructed surfaces, e.g. Au(111) or Pt(111), and monolayer thick strained films, e.g. Ag or Cu on Ru(0001) and $Si_{0.25}Ge_{0.75}$ on Si(001), exhibit well-ordered networks of misfit

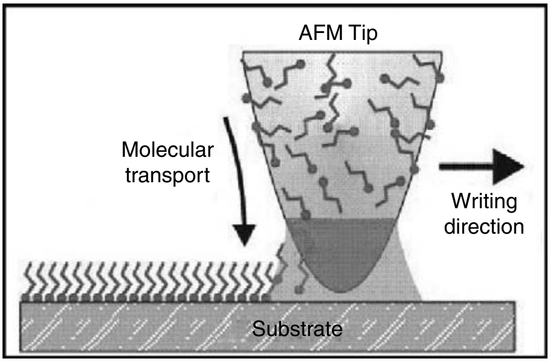

Figure 1.3 Diagram depicting the basic concepts of DPN.[7–9]

dislocations that can be engineered to create nanotemplates with specific feature size, density, and structure.[13–20] As shown in Figure 1.4a, a perfectly ordered lattice of sulfur vacancy islands, each about 2 nm across and 5 nm apart is formed when a single monolayer of Ag on Ru(0001) is exposed to sulfur.

Using self-assembly, these patterns can be even smaller and more compact such as the case when we form nanowires using functionalized fullerene as shown in Figure 1.5. The fields of supramolecular chemistry and self-assembled monolayers (SAMs) are well established, however, using supramolecular chemistry to pattern surfaces (bottom-up self-assembly) is new. The challenges are to use functionalized fullerenes to pattern surfaces and synthesize suitably functionalized fullerenes for self-assembly on substrate surfaces. Fullerene molecules are ideal building blocks for the bottom-up self-assembly of nanotemplates because they are soluble in a host of solvents, can be functionalized using selective chemistries, have a relatively high cohesive energy,[21] and bind well to a variety of substrates.[22] Functionalized [60] fullerenes with multiple supramolecular synthons can form spontaneous self organization into [60] fullerene nanowires with spacing: 1 to 10 nm,

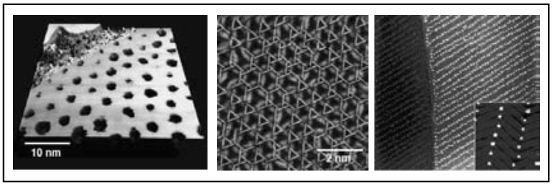

a **b** **c**

Figure 1.4 Nanoscale self-assembly at strained interfaces forms ordered patterns suitable for use as nanotemplates[4].

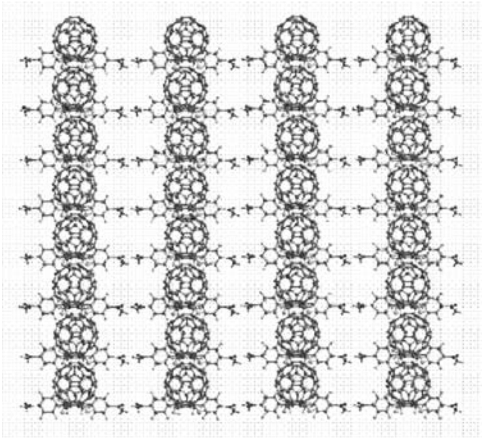

Figure 1.5 Fullerene nanowires with 1–10 nm spacing[4].

controlled by functional groups as shown in Figure 1.5. These nanowires can be used for high resolution patterns for nanotemplates that can be used for directed self-assembly.

1.4.2 Possible Approaches for Directed Self-Assembly of Nanoelements

Assembly techniques such microchannnels[23,24] and electric fields,[25] have been explored for local assembly of carbon nanotubes for interconnects and electromechanical probe.[26,27] These techniques, however, do not provide precise large-scale assembly at high-rates and high-volumes. The electrostatically addressable nanotemplate offers a simple means for controlling the placement and positioning of nanoelements for transfer using conductive nanowires. Gold nanowires have been used initially, and other conductors will be developed for use in templates.

1.4.2.1 Directed Assembly

To demonstrate how the large-scale assembly process will work, the electrostatically addressable nanotem plate which controls the placement and positioning of carbon nanotubes, nanoparticles, or other nanoelements is shown in Figure 1.6. The nanotubes align on the charged wires of the nanotemplate. The nanotemplate and nanoelements (Step 2) can form a device or can function as a template to transfer patterned arrays of nanoelements onto another substrate as shown in Steps 3 and 4. When the nanotemplates are moved with nano-precision accuracy and alignment, they can be used to deposit a wide variety of nanoelements into very closely

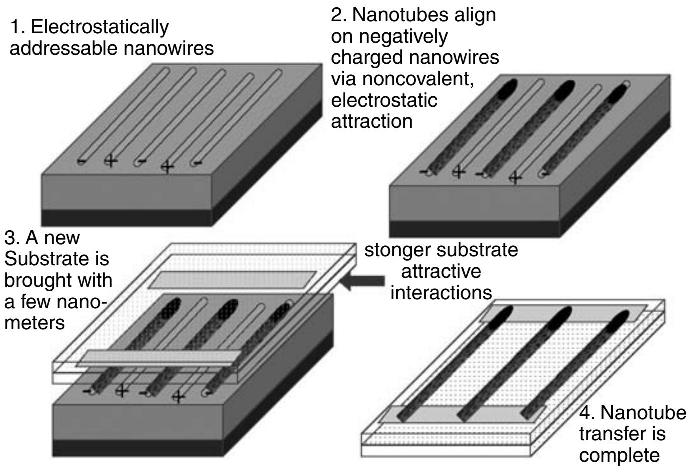

Figure 1.6 Steps of 2-D molecular assembly.[4]

packed columns or rows with a very narrow pitch. Figure 1.7 shows red fluorescent negatively charged PSL particles assembled on positively charged wires only.

1.4.3 Directed Self-Assembly of Nanoelements Using Nanotemplates

Nanotemplates can be used to enable precise assembly and orientation of various nanoelements such as nanoparticles and nanotubes. The directed assembly of colloidal nanoparticles into nonuniform 2D nanoscale features

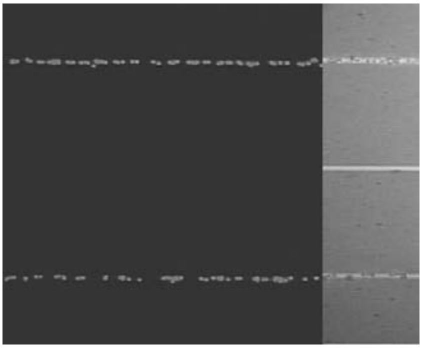

Figure 1.7 Self assembly of particles onto Au wires.[4]

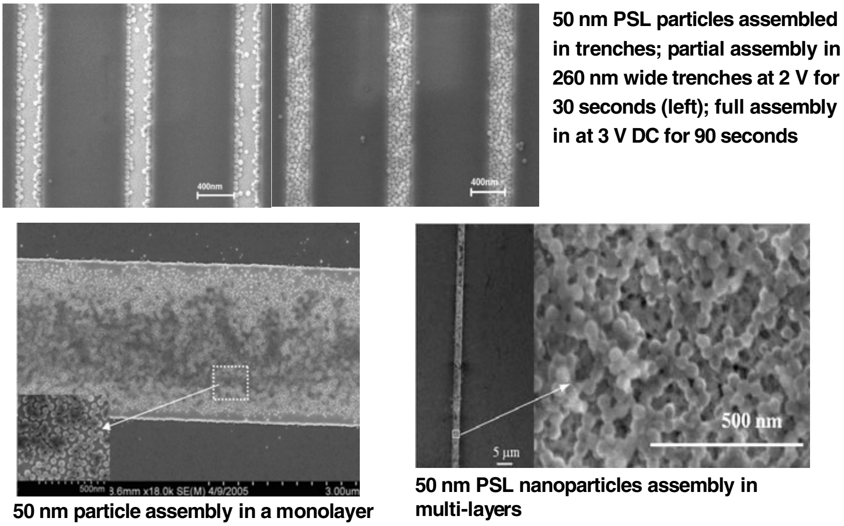

Figure 1.8 Directed of assembly of nanoparticles in nanoscale trenches.[4]

has been demonstrated via template-assisted electrophoretic deposition. The assembly process is controlled by adjusting the applied voltage, assembly time, or the geometric design of templates. Assembly of PSL particles in trenches is shown in Figure 1.8. The figure shows the control of the assembly process to produce monolayers or multilayers as well as full or partial assembly of nanoparticles. Polystyrene latex (PSL) and silica nanoparticles as small as 10 nm were used and assembled into nanoscale features. This approach offers a simple, fast means of nanoscale directed self-assembly of nanoparticles and other nanoelements over a large scale.

Electrostatically addressable nanotemplate could also be used to directly assemble carbon nanotubes. The nanotubes align on the charged trenches of the nanotemplate as shown in Figure 1.9. The figure shows that trench sizes varying from 80–300 nm were used for the assembly. The voltage was varied from 3 V to 5 V. The density of SWNTs assembled inside the trenches was dependent on the trench size and the voltage applied. In all cases the nanotubes assembled inside the trenches oriented along the direction of the PMMA trench. When the PMMA was dissolved, the nanotubes remained at the location of assembly. At voltages lower than 5 V, no nanotubes assembled inside trenches with widths smaller than or equal to 100 nm. At a higher voltage (5 V) the SWNTs assembled inside trenches with width less than 100 nm.

1.4.3.1 Nanotemplates for Guided Self-Assembly of Polymer Melts

Block copolymers are of considerable interest because of their ability to self-assemble into a variety of interesting and useful morphologies.[28]

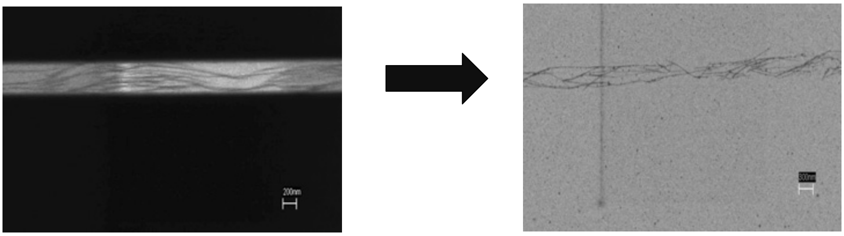

SWNTs Assembled within polymer trenches **SWNT on gold after dissolving polymer**

Figure 1.9 Assembly of aligned nanotubes in nanotrenches based templates.[4]

These morphologies can be used as flexible templates for assembly of nanodevices,[29] etc. that are appropriately modified to "mate" with the block copolymer.[30,31] They have already been used to prepare ordered structures[32] incorporating nanorods,[33] nanoparticles[34–37] and also as nanoreactors.[38] Unguided, the type of morphology depends on polymer type, composition, and processing conditions, and results in structures that are not defect free over large areas. Several approaches for morphology control of block copolymers include nanopatterned surfaces[39,40] and electric fields.[41,42] Recently, Kim et al.[43] used a chemically modified surface to prepare defect free nanopatterns over large areas. Nanotemplates use for the control of nanoscale morphology in high-rate/high-volume manufacturing methods would open the door to commercial production of nanoscale morphology in polymeric materials and would also allow for the manufacturing of 3-D structures with controlled surface morphology via injection molding.

1.4.4 Nanoscale Patterning Using Block Copolymers

Nanoscale patterning using block copolymers involves combining "Bottom-up" and "Top-down" processes. The block copolymers are two polymer chains that are covalently linked together at one end. Immiscible block copolymers in a thin film self-assemble into highly ordered morphologies where the size scale of the features is only limited by the size of the polymer chains. For advanced nanoelectronics, self-assembly is insufficient and there is a need for directed self-assembly processes to produce complex patterns. This may require the synthesis of polymers that have well-defined characteristics to enable fine control over the morphology and interfacial properties.

When considering nanoscale features, sharp angles present severe curvature constraints on the copolymer such that the microdomains of the copolymer cannot follow these features. One way to overcome this is to use templates to pattern block copolymers and a homopolymer has been introduced by Nealey and co-workers.[44]

They used small amounts of homopolymer added to the copolymer as shown in Figure 1.10. The homopolymer segregated to the areas of high

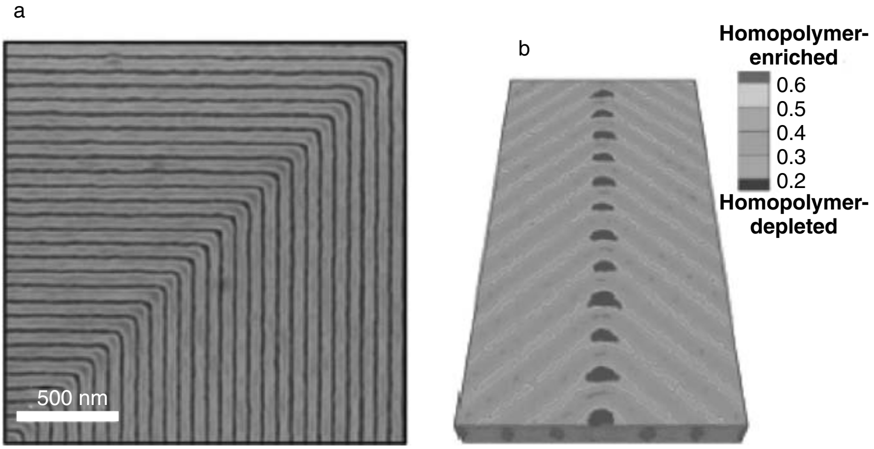

Figure 1.10 (a) FMSEM Image of a spin-coated thin film of a blend of PS-b-PMMA, having a lamellar microdomain morphology, with PS and PMMA. The film was prepared on a patterned heterogeneous surface with right angles in the pattern. The mixture is seen to relicate the underlying pattern with high. (b) Redistribution of homopolymer facilitates assembly: concentration map of the homopolymers on the surface, where it is seen that the homopolymer is concentrated at the sharp edges to alleviate the curvature constraints arising from the patterning.[44]

curvature, alleviating the strain on the copolymer, and as a consequence, the template features could be reproduced with high fidelity. This suggests that the copolymer microdomains can correct small defects in the patterning from the lithographic step and possibly improve the aspect ratio of the features for subsequent etching processes.

1.4.5 *Directed Self-Assembly of Conductive Polymers Using Nanoscale Templates*

The approach presented here utilizes the "rigid" nanotemplates as the assembly or the mold surface as in an injection molding process (or as a die in an extrusion process). This approach would allow the preparation of unique patterns, and the ability to pattern much smaller feature sizes. Nanotemplates, suitably patterned are used to control the block copolymer or blend morphology under high-rate processes from the melt as shown in Figure 1.11. The assembly of conductive polymer (Polyaniline; PANI) using a template with micro features (1-2 micron line width) is shown in Figure 1.12. The figure shows successful assembly of PANI on the template. It also shows successful transfer of the assembled PANI to polystyrene and polyurethane substrates.

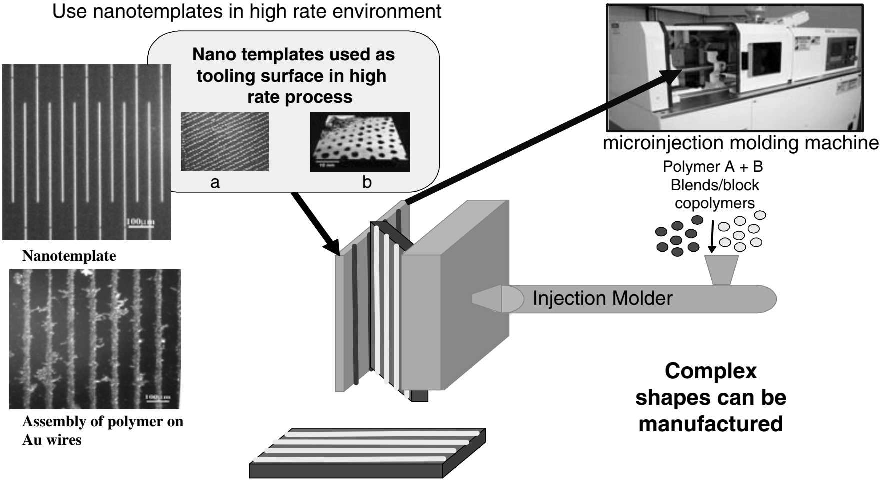

Figure 1.11 Guided self-assembly of polymer melts at high-rates.[4]

1.5 Registration and Alignment

The high-rate transfer of nanoelements from a nanotemplate to another substrate is needed for directed assembly. However, several technologies are needed to enable uniform contact or a very small uniform gap, and nanoscale registration over the length scale of the substrate for multiple layers. Although, no method currently exists to meet these requirements, techniques used in bump bonding of chips to circuit boards and in wafer bonding offer suggestions for a feasible approach. One approach could be that the two complimentary

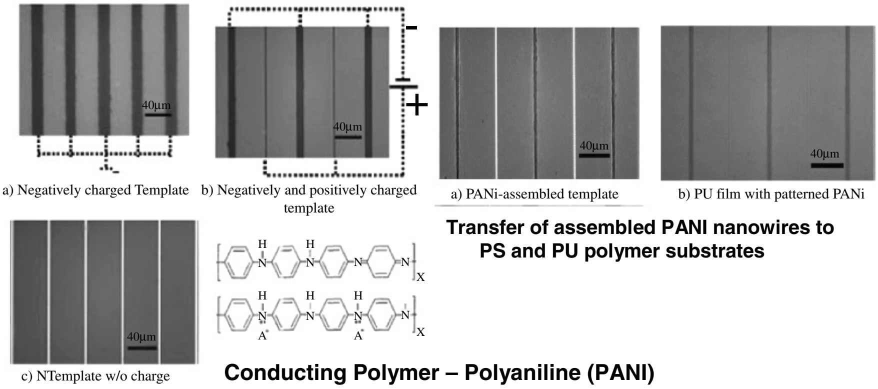

Figure 1.12 Assembly of polymer using electrostatically addressable templates.[4]

surfaces are brought into contact at one edge using a pre-alignment procedure. Next, chemical forces take over and very slightly distort the substrate and template as the contact area propagates forward to bring matching features together and completes the physical registration. One of the manufacturing challenges will be to understand the interaction between the forces involved in the alignment process and the mechanics of the substrate and template.

1.6 Reliability and Defect Control

As the assembled devices are manufactured, there is a need to address reliability and failure. Since the functionality of manufactured devices becomes dependent on nanoscale structures, reliability becomes a critical issue. Establishing a robust process and system can be broken down into 3 distinct, but interrelated functions: 1) prevention through a better understanding of failure mechanisms, 2) removal of defects, and 3) development of fault tolerance and self repair.

1.6.1 Reliability and Characterization Tools

A critical barrier to the design of nanostructures and devices is the lack of available data on the reliability and properties of nanoscale materials to feed into the modeling efforts. An approach is to use MEMS-based devices to test a range of nanoscale structures such as nanowires, nanotubes or nanofibers. There are relatively few characterization methods for the mechanical properties of the individual nanofibers available.[45,46] The MEMS devices could consist of three classes. One class contains structures for electrical characterization. The second class of devices has moving or suspended parts,[47] and will permit rapid cycling (10^3-10^5 Hz) of temperature, strain, and current flow in (for example) deposited nanowires in order to accelerate the generation of defects. The third class of devices consists of suspended nanostructrues. For example, (Figure 1.13) microscopic defect generation can be

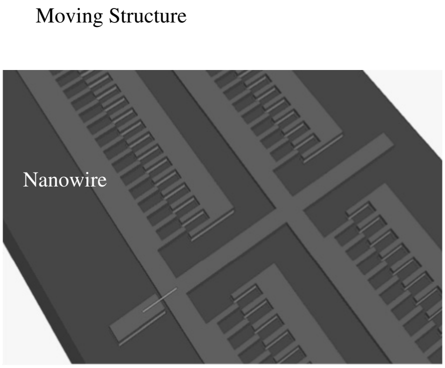

Figure 1.13 MEMS comb drive performing pull test to investigate nanoscale material properties.[4]

tracked during the measurement of the tensile stress-strain curve and yielding of nanowires. Similarly, the reliability of connection between wires and interconnects can be investigated.

1.6.2 Removal of Defects Due to Micro and Nanoscale Contamination

It is expected that controlling contamination and the detection and removal of defects will be critical for nanomanufacturing. Surfaces prepared for nanoscale applications such as deposition of monolayers or self-assembly of nanoelements need to be free of particulate and other contamination on the order of a nanometer or less. Currently in the semiconductor industry, the state of the art only offers non selective removal of contaminants; although it is applied over a large area and relatively quickly. The removal of defects takes about 20-25% of the total manufacturing processes. The upcoming challenges in nanomanufacturing will be greater. There will be a need for selective removal of defects and impurities (e.g., oxygen in carbon nanotubes). Chemistry will play a much larger role than it does now. There will be a greater need to understand the adhesion of surfaces, particles, and nanoelements in a variety of conditions and situations. Also, the removal of defects will have to be accomplished without disturbing or destroying assembled nanoelements and nanostructures.

1.7 Nanomanufacturing Industry Survey

1.7.1 Background

In 2005, the National Science Foundation (NSF) awarded a grant to the National Center for Manufacturing Sciences (NCMS) to poll over 6,000 senior-level executives in leading U.S. organizations with leadership, technology or strategic research and development (R&D) responsibility to assess the outcome of growing private and public investments made in nanotechnology under the National Nanotechnology Initiative (NNI). The overarching objective in conducting this largest known cross-industry benchmark study was to determine whether surveyed organizations treat nanotechnology differently from any other generation of advanced science and technology. The metric established by NSF was 300 survey responses to develop a credible profile–the survey netted 594 completed responses, representing a response rate of 10%.

1.7.2 Aggregate Observations

The NCMS survey of nearly 600 industry executives indicates that the state of the U.S. Nanomanufacturing Industry is generally vital, innovative and competitive for demonstrated passive nanotechnology products with many two-dimensional product applications growing rapidly for end-uses

across diverse industry sectors. The survey confirms that the U.S. has the best-developed and mature research facilities, entrepreneurial culture and governance infrastructure for promoting new nanotechnology-driven economic development.

Besides the numerous entrepreneurial startups and small businesses (often led by researchers with academic or government laboratory connections), many larger manufacturers of conventional industrial materials and products as well as OEMs and end users, have begun to pursue internal research, actively seek new technologies, and partner in order to evaluate the potential for incorporating nanotechnology in differentiating their current product lines. Some of the world's largest manufacturing organizations are actively developing their own pipelines and strategies for future products by adopting the specialized techniques to leverage risks and penetrate new markets with nanotechnology. Corporate partnering is critical for embryonic nanotechnology businesses to attain growth and viability; it begins anywhere from peer relationships to technology co-development and co-marketing, to culmination in merger and acquisition.

The survey found that organizations are proceeding cautiously in the development and commercialization of innovations such as active three-dimensional nanotechnology products that involve more direct human, societal and environmental impact. The nanomanufacturing industry for second generation (potentially disruptive) nanotechnology products is still in its infancy–there are as yet no commercial devices based on true nanotechnology. The challenges facing the industry are not limited to the technology itself–rather, factors such as funding, commercialization strategies, regulation and a variety of socio-business issues will affect the long-term success of organizations entering this domain.

Due to the cross-disciplinary nature and broad societal implications of nanotechnology, few organizations possess the vertical integration needed to rapidly commercialize the envisioned second generation nanoproducts from conception to consumption. While there is much exploratory partnering and co-development within the industry, it will accelerate when the early nanotechnology applications crossing the "valley-of-death" are able to demonstrate unquestionably superior performance of existing macro-scale products and systems at affordable cost, improved margins and higher reliability.

Large-scale, market-driven investments have been somewhat inhibited due to the lack of broader, in-depth understanding of nanotechnology's complex material-process-property phenomena and its interactions with humans and the environment. These issues uphold the perception of uncertainty and long lead times in the industry. Therefore, the near-term impact of nanotechnology is likely to be fragmented, product-specific and evolutionary rather than revolutionary. The distillation of survey trends and executive attitudes indicates that while new applications will grow in the near-term largely by entrepreneurial means (e.g. technology push to seek niche applications), the longer-term growth of a nanomanufacturing venture would depend on the organization's core competency to vertically integrate

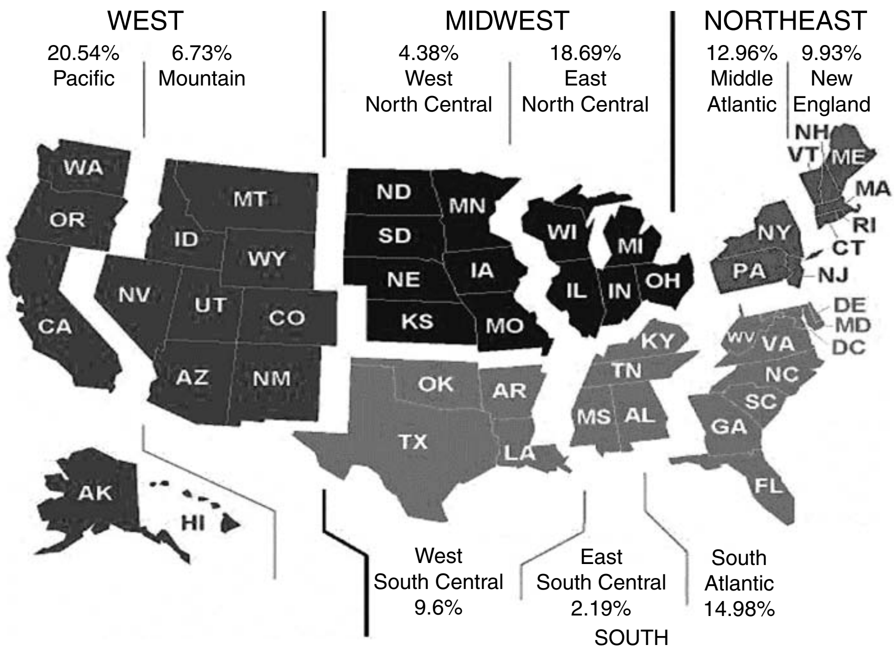

Figure 1.14 Geographical Distribution of 594 Respondents Corresponds Closely with Major Public Investments in Nanotechnology.

and partner with end users on the basis of platform nanotechnologies as well as its ability to meet defined performance objectives (i.e. market pull factors) that help meet the customers' bottom-line.

1.7.2.1 Diverse Nanotechnology Products in Development

Aggregate survey responses indicated that the U.S. Pacific region leads the nation in development of diverse nanotechnology products and application markets that are being pursued for potentially disruptive economic, social, environmental and military advantage (Figure 1.14). The U.S. leads the world in the generation and commercialization of nanoscale materials, manipulation tools and measurement innovations being applied to initially benefit the consumer products, digital storage, photovoltaic and semiconductor manufacturing industries. Myriad new applications of advanced nanocoatings, nanofilms and nanoparticles are being developed for introduction in the near-term (3-5 years) on a broader range of durable goods, consumer electronics and medical products (Figure 1.15). Nanoproduct applications are also being developed for the next generation semiconductor, energy, chemical catalysis and pharmaceutical/biomedical products. These would eventually mature into convergence products with higher sensory complexity, self-assembly and autonomous functionality, offering greater potentials for achieving the envisioned economic and societal impact.

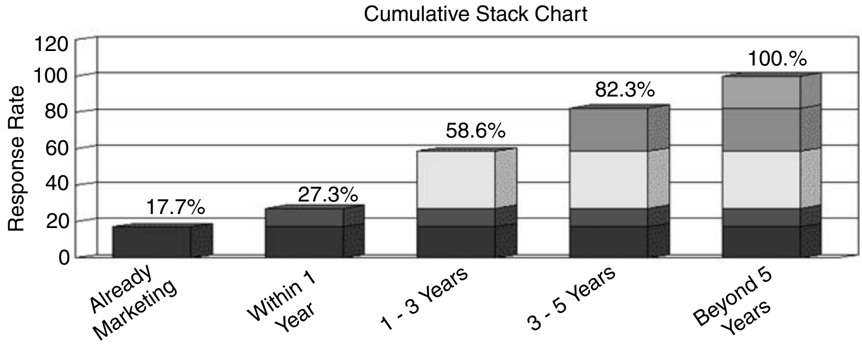

Figure 1.15 Commercialization Timelines Indicate Many New Nanoproducts Introductions in 2007-2011

1.7.2.2 *Increased Corporate and Public Awareness*

Traditional manufacturing organizations, while interested in adopting nanotechnology, tend to be preoccupied with issues of short-term profitability and other approaches that prioritize returns and revenues over long-term growth (such as innovation and skills development). Recent pronouncements of the importance of nanotechnology herald a significant change in corporate and National attitudes. For prepared organizations, these trends represent new opportunity for paradigm shifts in change management to drive innovations for superior product lines, and realize improved investment returns on a global scale.

These positive trends are attributed in large part to the substantial seed investments, leadership and outreach efforts made by the NNI through R&D undertaken across academia, small and large businesses and the National Laboratory infrastructure. Concurrently, the increased branding of leading-edge consumer products and coining of science fiction terms with "nano" have also raised societal awareness, albeit with mixed results. They have the longer-term impact of preparing both, a new generation of knowledge workers and informed consumers.

Survey respondents unanimously indicated that sustained government sponsorship is essential to attract the attention of senior manufacturing industry executives, investors, media and the public. Government support will expedite improved fundamental understanding of nanotechnology and further clarify its potential, while fostering both, early markets and entrepreneurship towards the more advanced generation product applications.

1.7.3 *Key Industry Barriers*

The majority of the surveyed executives indicated their organizations faced considerable difficulty in nanomanufacturing, ranging from emergent technology issues, to raising capital for critical infrastructure investments, attracting

the technical and business talent, connecting with early end-users, and producing competitively to meet new market applications and volumes.

Intellectual property issues and the sharing of knowledge were identified as areas of significant concern, as well as the lack of clear regulatory policy, which could impede industry, and impact the public's reaction to future product developments. The continued education of the public and the key policy makers (State and Federal), government agencies and legislative bodies regarding these issues will result in clearer product approval pathways, robust standards and responsible practices, and thereby help ensure the continued dominance of the U.S.

While the nanomanufacturing industry faces unique challenges, similarities do exist with other recent technology waves such as the Internet and biotechnology, offering many lessons learned for formulation of sound anticipatory approaches. The answers to addressing the top-ranked challenges lie in continuing the aggressive National R&D policies for pursuing targeted investigations in fundamental nanoscale science, engineering and manufacturing technology. NCMS recommends several approaches for addressing the technology and business needs of the U.S. Nanomanufacturing Industry, while responsibly accelerating the benefits of new or enhanced products for societal benefit. NCMS further recommends the reclassification of the conventional definition of "small" business, as many of the largest organizations working with nanotechnologies would be considered small businesses by traditional industry standards. The following three broad re-classifications are suggested in addressing the unique needs of current generation of nanotechnology businesses:

- Small nanotechnology businesses (less than 20 staff)
- Medium nanotechnology businesses (21–100 staff)
- Large nanotechnology businesses (over 100 staff)

Table 1.1 lists several approaches and National strategies for addressing clusters of identified barriers to the nanomanufacturing industry.

1.8 Recommended National Priorities for the Near Term

1.8.1 Accelerating Nanotechnology Developments

Critical investment-, business- and regulation-related issues need to be addressed concurrently and collaboratively by State and Federal policymakers in order to maintain the current high momentum of innovation in nanotechnology advances. Long-term policies for National investment and the stimulation of public-private-academic partnerships are imperative for developing the fundamental science base, facilitating technology transition to applied research, and demonstrating credible nanotechnology-enabled applications that are perceived as meaningful to our quality of life. The potential

Table 1.1 Strategies to Address Critical Identified Barriers Faced by the U.S. Nanomanufacturing Industry

Industry barrier(s)	Recommendation(s)
High cost of processing/ Process scalability issues/ Lack of development tools	Collaborative R&D in value-chains R&D to reduce/combine process steps R&D in new equipment and to improve product yields
Long time-to-market/ Unclear societal benefits	Government incentives for private R&D investments Raise public awareness of benefits via successes Promote supplier-end user partnerships
Insufficient investment capital	Government investment in pre-competitive R&D Stimulate market pull via end users Mentor startups for attracting investment
Intellectual property issues	New business models for nanotech value-chains Legal reform, train legal and judicial professionals Streamline partnering with academia and National Labs Facilitate supplier-end user partnerships
Shortage of qualified manpower/ Multi-disciplinary aspects	Retrain tech workforce in basic science/testing/quality Attract students to science and engineering careers
Regulatory and safety concerns/ Environmental and toxicity issues	Streamline permit/product approvals at agencies Increase government-sponsored R&D Broader dissemination of findings Balanced legislation and regulatory practices

risks and hazards associated with the more revolutionary envisioned nanotechnology applications need to be assessed and disseminated by trusted sources to raise the public's awareness, and thereby gain societal confidence. Strong incentives will help resulting innovations become swiftly translated into industry-led technology demonstrations that enhance the public's awareness and acceptance. This will require dramatic changes in business strategy and unprecedented levels of public-private regulatory collaborations to responsibly commercialize future nanoproduct applications. Such levels of integration do not presently exist.

1.8.2 Government-Led Public-Private Collaborations

It is unlikely that the vast field of nanotechnology would reach the levels of maturity (like other traditional physical science-based industries did) within our lifetimes. This justifies the case for greater government investment in nanotechnology. Private and institutional investments can grow faster when

some of the fundamental technical issues of process scalability and cost of production of new nano-components as well as associated risks have been more comprehensively addressed. Collaborative R&D and targeted technology demonstrations would also help scope the potential economic returns across nanotechnology value-chains.

Government can lead by defining and funding National priorities, and creating meaningful incentives for early industrial adopters of nanotechnology, in order to accelerate the broad-based translation of nanotechnology advances across multiple industry sectors. Public-private collaborations in applied nanotechnology will hasten societal support when targeted towards nearer-term National concerns such as:

- Increasing productivity and profitability in manufacturing
- Improving energy resources and utilization
- Reducing environmental impact
- Enhancing healthcare with better pharmaceuticals
- Improving agriculture and food production
- Expanding the capabilities of computational and information technologies

Areas where government involvement in nanotechnology can have high National impact while leveraging substantially larger private investments include:

1. Incentives favoring longer-term investments (e.g. tax-free bonds for financing, tax credits for capital investments, reduced capital gains tax rates, investment-specific loan guarantees, etc.)
2. Promoting and streamlining strategic alliances for businesses and researchers with larger players or end users
3. Providing mentorship and business planning assistance to small businesses to identify key technology benefits and attract private capital
4. Underwriting and disseminating "good science" research and public education into the long-term issues related to waste disposal, safety and regulations
5. Undertaking tort and legal reform which will provide developers greater immunity and protection once their products are Federally approved

State governments and economic development bodies could assist small and large businesses link up in neutral environments by promoting leverage of nano-incubator and user facilities. By working with university and National Laboratory technology transfer organizations, they could facilitate simpler access to nanotechnology resources and training available in educational institutions, thereby stimulating new partnerships with entrepreneurs. Offering matching funds and other seed incentives to organizations pursuing Federal nanotechnology programs would provide further impetus

for businesses and researchers to partner in commercialization ventures. Several progressive U.S. states have already initiated these next-generation technology partnerships.

1.9 Strategic U.S. Industry Indicators and Summary Trends

1.9.1 Geographical Profile

The geographical distribution of 594 respondents, illustrated by U.S. Census regions, generally correlated well with the U.S. regions receiving the highest infusion of NNI funds[48] and other private investments, and agreed with the Small Times annual ranking[49] of leading U.S. regions reporting the highest levels of commercial activity in nanotechnology (Figure 1.14). Predictably, the Pacific regions represented the largest proportion (20.5%), considering that the electronics and semiconductor industry has been at the cutting edge of nanoscale science and engineering for several years, and the region is the single largest adopter of nanomanufacturing techniques. This was followed by respondents in the East North Central regions (18.7%), South Atlantic (15%), Mid-Atlantic (13%), New England (9.9%) and West South Central (9.6%).

1.9.2 Major Players in Nanomanufacturing

Over half of the 594 respondents indicated their organizations were directly involved in nanomanufacturing developments, either as end-users (OEMs), manufacturer-integrators or component suppliers.

- A high proportion of educational and R&D facilities are involved in the development of nanomanufacturing technologies (Figure 1.16).

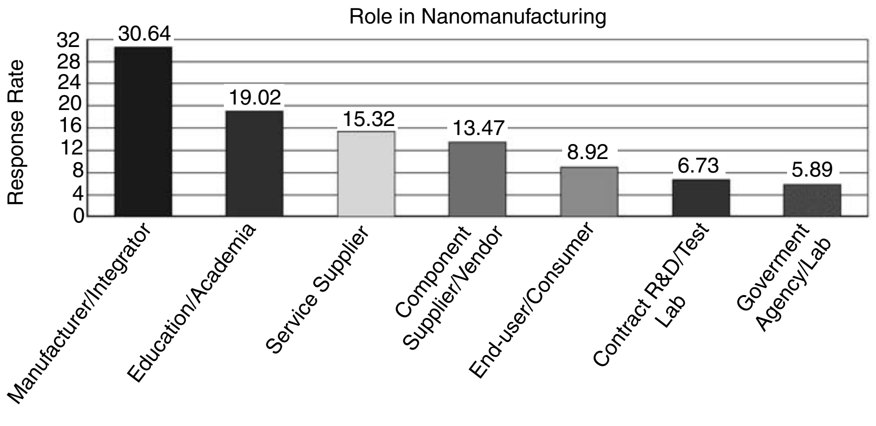

Figure 1.16 Respondents' Roles in the U.S. Nanomanufacturing Value-Chain.

1.9.3 Nanotechnology Products

Diverse products incorporating nanotechnology are in varying stages of development and commercialization.

- The top passive nanotechnology products already commercialized or soon-to-be commercialized in the foreseeable future (up to three years out), comprise higher precision materials, tools and devices for enhanced manufactured goods, equipment, and sub-components such as:
  Semiconductors, nanowires, lithography, and print products
  Nanostructured particulates and nanotubes
  Coatings, paints, thin films, and nanoparticles
  Defense, security, and protection gear
  Telecommunications, displays, and optoelectronics products.
- A greater diversity of nanotechnology products are in development in organizations in the Pacific, New England, Mid-Atlantic, and South Atlantic regions.

1.9.4 Nanomanufacturing Application Markets

Nanotechnology developments are being targeted for use in diverse industry sectors — the top application markets for nanotechnology products are:

- 52% Equipment, Logistics and Distribution
- 46% Electronics and Semiconductors
- 46% Computing, Information Technology, and Telecommunications
- 38% Aerospace
- 34% Automotive
- 33% Chemicals and Process Industries

Figure 1.17 provides a graphic representation.

1.9.5 Corporate Urgency

Management attitudes are changing–medium and large organizations (50 or more staff) place a higher priority on commercialization of nanotechnology.

- 52% of the aggregate respondents stated nanomanufacturing is considered a High priority for development in their organizations, while about 20% indicated Low priority (dominated from East North Central and New England regions).

1.9.6 Change Management

Majority of medium and large nanotechnology organizations (50 staff or higher) were coping relatively well with adopting new commercialization

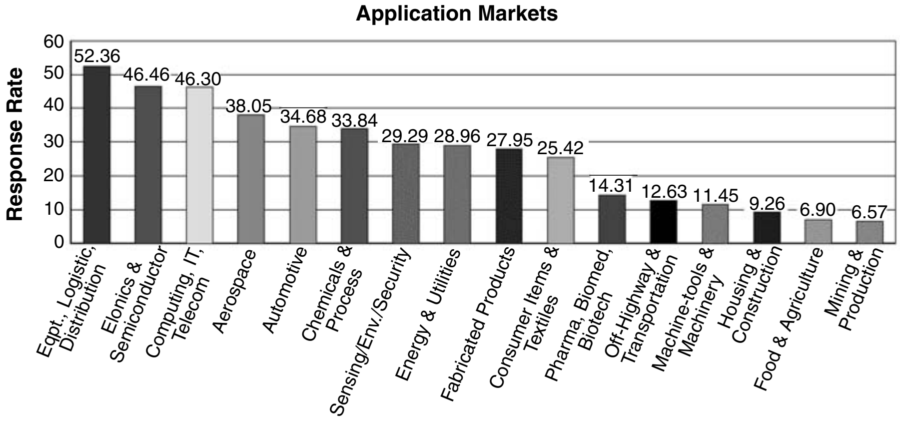

Figure 1.17 Nanotechnology Developments Being Targeted for Use in Diverse Industry Sectors.

strategies and technology management approaches, but smaller organizations reported greater difficulty in coping with market and business changes.

- Nearly one-fifth of the respondents indicated serious concerns. About 25% of the respondents from the East North Central region and 19% from the West North Central region stated their organizations were coping poorly.

1.9.7 Organization Capacity

Increasing numbers of senior executives in the conventional U.S. Manufacturing Industry have begun examining the potential of nanotechnology to take their organizations into new growth phases, product directions and markets, and translating this interest into R&D partnerships, procurement or acquisition of new nanotechnology development resources.

- About 70% of aggregate respondents reported Medium to High levels of organizational capacity to pursue nanomanufacturing.

1.9.8 Internal Infrastructure

Nanotechnology infrastructure is unevenly distributed across the U.S. and in its utilization by various industry sectors–additional specialty tools and targeted facility investments are needed in the private sector.

- Aggregate respondents were equally divided in rating the adequacy of their available infrastructure (ultra-clean rooms, laboratory space and facilities, processing equipment, test and diagnostics capability, etc) for undertaking nanomanufacturing developments–39% selected Plentiful, 30% selected Adequate, and 31% selected Inadequate (with 9% selecting Significantly Lacking).

1.9.9 Collaborative Development

Collaborative developments, while on an increasing trend, are highly product specific in the U.S. Nanotechnology Industry.

- Over three-quarters of aggregate survey respondents indicated their organizations are involved in collaborative arrangements with external organizations, while about 20% were working largely internally on nanotechnology developments–the highest percentages of these respondents are in the Mountain (34%), West South Central (29%), and Pacific (26%) regions.

1.9.10 Drivers for Partnering

Nanotechnology organizations were motivated to partner and collaborate for three main goals: to gain access to new markets and/or distribution channels; to better assess end users' needs in order to co-develop focused products and solutions incorporating nanotechnology advances; or (in the case of longer-term nanotechnology research) to leverage resources and reduce development risks.

- Respondents expressed nearly equal preferences on what motivated their organizations to collaborate in nanotechnology. Smaller nanotech organizations were more likely to partner for gaining access to capital equipment, while larger organizations were driven to pursue global markets with their nanoproducts.

1.9.11 Staffing for Nanomanufacturing

Over 80% of nanotechnology businesses are smaller (< 20 staff), entrepreneurial, technology-heavy entities comprised of startups and spin-off organizations; only 5% employ over 100 staff a rational re-categorization of business entities by size is recommended to better address the unique needs of the nanotechnology industry.

- Many organizations involved with first generation (passive) nanotechnology developments are poised to profit through licensing of patents. They have limited potential for large-scale growth of jobs and the commoditization of raw materials that occurred in traditional manufacturing.

1.9.12 Commercialization Timelines

60% of the respondents expected to market nanotechnology products by 2009. Organizations in the Pacific region appear to have a steady stream of new product introductions across all timeline categories. Medium-sized (21-100 staff) nanotechnology organizations are best poised for growth, partnering or acquisition.

- The proportion of respondents indicating market entry within one year with nanotechnology products was the highest in the Mountain (25%) and the East North Central (17%) regions. Regions indicating the highest proportions of product introductions within three years were West North Central (42%), New England (40%), and Mid-Atlantic (36%) regions.

1.9.13 Government's Role in Nanomanufacturing

Nearly 95% respondents favored government involvement in the commercialization of nanomanufacturing, most preferring strong and meaningful incentives for industrial adopters of nanotechnology.

- These aggregate trends towards incentives were driven by two main issues:
  1. The belief the U.S. could lose its competitive advantage in future nanotechnology innovations, and needs to counter the offshore growth of traditional manufacturing and research operations.
  2. Industry wants more government-led R&D collaborations in programs focused on regulation, nanotoxicity, and environmental impact.

1.9.14 Nanomanufacturing Industry Challenges

The aggregate respondents indicated overwhelming consensus around the key barriers affecting the commercialization of nanotechnology. Industry perceives similar challenges and threats at three distinct levels (Figure 1.18).

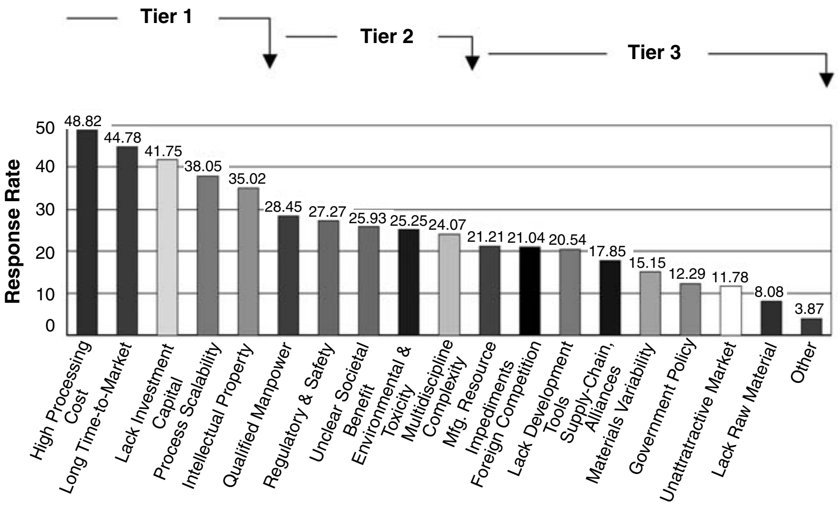

Figure 1.18 U.S. Nanomanufacturing Industry Faces Three Distinct Tiers of Barriers.

1.9.15 Technology Transfer Preferences

Respondents expressed differing preferences for accelerating "nanoknowledge" transfer mechanisms across the manufacturing value-chain.

- The top three nearly equal selections depended on whether an organization's goal was to pursue partnerships, seek investors, technology scouting (technology pull), or dissemination (technology push) activities–they were:
  1. Industry trade shows and conferences
  2. Technology demonstrations
  3. Industry online media.

Acknowledgment

The directed assembly and reliability work reported here is supported by the National Science Foundation Nanoscale Science and Engineering Center (NSEC) for High-rate Nanomanufacturing (NSF grant-0425826). The 2005 NCMS Survey of Nanotechnology in the U.S. Manufacturing Industry was sponsored by the National Science Foundation (Award # DMI-0450666). Our thanks are also due to Ascendus Technologies for survey design, Small Times Media LLC, and all organizations associated with dissemination of the survey, as well as to the nearly 600 survey respondents and interviewees for their time and valuable insights.

References

1. Busnaina, A., Barry, C., Mead, J. and Miller, G., "NSF Workshop on 3-D Nanomanufacturing: Partnering with Industry; Conclusions and Report," Proceedings, MANCEF-COMS 2003, Amsterdam, The Netherlands, September 8-11, 2003. pp. 263–268.
2. www.nano.neu.edu/nsf_workshop_agendaII.html
3. Stewart, M. D. and Willson, C. G., "Imprint Materials for Nanoscale Devices," Stewart, M. D. and Wilson, C. G. MRS Bulletin, Volume 30, December 2005, pp.947–951.
4. Courtesy of the NSF Nanoscale Science and Engineering Center for High-rate Nanomanufacturing, Northeastern University, Boston, MA.
5. Tirrell, M., "New Molecular Systems (In Research): Directed Self-Assembling", NNI workshop on Manufacturing at the Nanoscale, Washington, D.C., March 31, 2004.
6. Belcher, A., "New Molecular Systems (In Research): Biologically-Inspired Assembly," NNI workshop on Manufacturing at the Nanoscale, Washington, D.C., March 31, 2004.
7. Piner, R.D., Zhu, J., Xu, F.; Hong, S., and Mirkin C.A. "Dip-pen" nanolithography," *Science* 1999 , 283, 661–663.

8. Hong S., Zhu, J., and Mirkin C.A., "Multiple ink nanolithography: Toward a multiple-pen nano-plotter," *Science* 1999 , 286, 523–525.
9. Hong, S. and Mirkin C. A., "A Nanoplotter with Both Parallel and Serial Writing Capabilities," *Science* 288, 1808 (2000).
10. H. Brune et al., "Self-organized growth of nanostructure arrays," *Nature*, 394, 451 (1998).
11. T. Yokoyama et al., "Selective assembly on a surface of supramolecular aggregates with controlled size and shape," *Nature*, 413, 619 (2001).
12. F. Rosei et al, "Organic molecules acting as templates on metal surfaces," *Science*, 296, 328 (2002).
13. A. R. Sandy et al., "Structure and phases of the Au(111) surface: X-ray-scattering measurements," *Physics Review B*, 43, 4667 (1991).
14. M. Bott et al., "Pt(111) reconstruction induced by enhanced Pt gas-phase chemical potential," *Physics Review Letters*, 70, 1489–1492 (1993).
15. R. Q. Hwang et al., "Near-Surface Buckling in Strained Metal Overlayer Systems," *Physics Review Letters*, 75, 4242 (1995).
16. J. Tersoff et al., "Self-organization in growth of quantum dot superlattices," *Physics Review Letters*, 76, 1675 (1996).
17. K. Pohl et al., "Identifying the forces responsible for self-organization of nanostructures at crystal surface," *Nature*, 397, 238 (1999).
18. J. Hrbek et al., "A Prelude to Surface Chemical Reaction: Imaging the Induction Period of Sulfur Interaction with a Strained Cu Layer," *J. Phys. Chem. B*, 103 (cover), 10557 (1999).
19. O. L. Alerhand et al, "Spontaneous Formation of Stress Domains on Crystal Surfaces," *Physics Review Letters*, 61, 1973 (1988).
20. K. Pohl et al., "Thermal Vibrations of a Two-Dimensional Vacancy Island Crystal in a Strained Metal Film," *Surface Science*, 433–435, 506 (1999).
21. Girifalco, L.A. and Hodak, M. Van der Waals binding energies in graphitic structures. *Physical Rev. B* 2002, *65*, 125404.
22. Girard, C., Lambin, P., Dereux, A., and Lucas, A.A. Van der Waals attraction between two C_{60} fullerene molecules and physical adsorption of C_{60} on graphite and other substrates. *Physical Rev. B* 1994, *49*, 425.
23. Messer, B., Song, J. H., and Yang, P. "Microchannel Networks for Nanowire Patterning," *Journal of the American Chemical Society*, 122, 10232 (2000).
24. Huang, Y., Duan, X., Wei, Q., and Lieber, C. M., "Directed Assembly of One Dimensional Nanostructures into Functional Networks," *Science* 291, 630 (2001).
25. Duan, X., Huang, Y., Cui, Y., Wang, J., and Lieber, C. M., "Indium phosphide nanowires as building blocks for nanoscale electronic and optoelectronic devices," *Nature* 409, 66 (2001).
26. Guillorn, M. A., McKnight, T. E., Melechko, V. I., Britt, P. F., Austin, D. W., Lowndes, D. H., and Simpson, M. L., "Individually addressable vertically aligned carbon nanofiber-based electrochemical probes," *Journal of Applied Physics*, 91(6), 3824 (2002).
27. Li, J., Ye, Q., Cassell, A., Ng, H. T., Stevens, R., Han, J., and Meyyappan, M., "Bottom-up approach for carbon nanotube interconnects," *Applied Physics Letters*, 82(15), 2491 (2003).
28. Hadjichristidis, N., Pispas, S., and Floudas, G., Block Copolymers : Synthetic Strategies, Physical Properties, and Applications, John Wiley and Sons, Hoboken, NJ, 2003.

29. McClelland, G.M., Hart, M.W., Rettner, C.T., Best, M.E., Carter, K.R., and Terris, B.D., "Nanoscale patterning of magnetic islands by imprint lithography using a flexible mold," *Applied Physics Letters*, 81, 1483 (2002).
30. Kim, D.H., Lin, Z., Kim, H.-C., Jeong, U., and Russell, T.P., "On the replication of block copolymer templates by poly(dimethylsiloxane) elastomers," *Advanced Materials,* 15, 811 (2003).
31. Kim,Y.S., Lee, H.H., and Hammond, P.T., "High density nanostructure transfer in soft molding using polyurethane acrylate molds and polyelectrolyte multilayers," *Nanotechnology,* 14, 1140 (2003).
32. Maldovan, M., Carter, W.C., and Thomas, E.L., "Three-dimensional dielectric network structures with large photonic band gaps," *Applied Physics Letters*, 83, 5172 (2003).
33. Chen K. and Ma, Y., "Ordering Stripe Structures of Nanoscale Rods in Diblock Copolymer Scaffolds," *Journal of Chemical Physics*, 116(18), 7783 (2002).
34. Tokuhisa H. and Hammond, P.T., "Nonlithographic Micro- and Nanopatterning of TiO_2 Using Polymer Stamped Molecular Templates," Langmuir, 20, 1436 (2004).
35. Ali, H. A., Iliadis, A. A., Mulligan, R.F., Cresce, A.V.W., Kofinas, P., and Lee, U., "Properies of self-assembled ZnO nanostructures," *Solid-State Electronics*, 46, 1639 (2002).
36. Clay R. T. and Cohen, R. E., "Synthesis of Metal Nanoclusters within Microphase-separated Diblock Copolymers: ICP-AES Analysis of Metal Ion Uptake," *Supramolecular Science*, 4, 113 (1997).
37. Sohn B. H. and Cohen, R. E., "Electrical Properties of Block Copolymers Containing Silver Nanoclusters within Oriented Lamellar Microdomains," *Journal of Applied Polymer Science*, 65, 723 (1997).
38. Liu, T., Burger, C., and Chu, B., "Nanofabrication in Polymer Matrices," *Progress in Polymer Science*, 28, 5 (2003).
39. Rockford, L., J., Mochrie, S.G., and Russell, T. P., "Propagation of Nanopatterned Sustrate Templated Ordering of Block Copolymers in Thick Films," *Macromolecules*, 34, 1487 (2001).
40. Yang, X. M., Peters, R. D., Kim, T. K., Nealy, P. F., Brandow, S. L., Chen, M-S., Shirey, L. M., and Dressick, W. J., "Proximity X-ray Lithography Using Self- Assembled Alkylsilixone Films: Resolution and Pattern Transfer," *Langmuir*, 17, 228 (2001).
41. Schaffer, E., Thurn-Albrecht, T., Russell, T. P., and Steiner, U., "Electrically Induced Structure Formation and Pattern Transfer," *Nature*, 403(6772) 874 (2000).
42. Thurn-Albrecht, T., DeRouchy, J., Russell, T. P., and Jaeger, H. M., "Overcoming Interfacial Interactions with Electric Fields," *Macromolecules*, 33, 3250 (2000).
43. Kim, S. O., Solak, H. H., Stoykovich, M. P., Ferrier, N. J., DePablo, J. J., and Nealy, P. F., "Epitaxial Self-Assembly of Block Copolymers on Lithographically Defined Nanopatterned Substrates," *Nature*, 424, 411, (2003).
44. Stokovich, M.P., Muller, M., Kim, S.O., Solak, H.H., Edwards, E.W., de Pablo, J.J., Nealey, P.F., "Directed assembly of block copolymer blends into non-regular device oriented structures," Science, 2005, 308, 1442–1446.
45. Buer, A., Ugbolue, S. C., and Warner, S. B., "Electrospinning and Properties of Some Nanofibers," *Textile Research Journal,* 41(4), 323, (2001).

46. Ko, F.K., Khan, S., Ali, A., Gogotsi, Y., Naguib, N., Yang, G., Li, C., Shimoda, H., Zhou, O., Bronikowski, M., Smalley, R.E., and Willis, P.A. "Structure and Properties of Carbon Nanotube Reinforced Nanocomposites," American Institute of Aeronautics and Astronautics, 1426 (2002).
47. Van Arsdell W. W. and Brown, S. B., Subcritical crack growth in silicon, IEEE Journal of MEMS, 8(3), pp. 319–327, 1999.
48. Roco, M.C., "Nanoscale Science and Engineering at NSF," Proceedings of 2005 NSF Nanoscale Science and Engineering Grantees Conference, December 12–15, 2005, Arlington, VA.
49. Stuart, C., "Annual Ranking of Small Tech: Only One First Place But Many Winners," Small Times, March 14, 2005.

Chapter 2

Surface-Programmed Assembly for Nanomanufacturing

Seunghun Hong, Sung Young Park, Juwan Kang, Tae–Kyeong Kim, Juntae Koh, Kwang Heo, Kyung-Eun Byun, Dong Joon Lee, and Seon Namgung

Contents

2.1 Introduction 34
2.1.1 New Materials and New Paradigm: Bottom-Up vs. Top-Down 34
2.1.2 Nanomanufacturing Issues in Nanotechnology 35
2.1.3 Self-Assembly in Nature: from Nano to Macro 36
2.2 Large-Scale "Surface-Programmed Assembly" 37
2.2.1 Basic Concepts 37
2.2.2 Surface Molecular Patterning 38
2.2.2.1 Dip-Pen Nanolithography 38
2.2.2.2 Microcontact Printing and other Molecular Patterning Methods 42
2.2.3 Assembly and Alignment of Nanostructures 42
2.2.3.1 Nanoparticles 42
2.2.3.2 Carbon Nanotubes and Nanowires 43
2.2.3.3 Biomotors 47
2.3 Conclusions 50
Acknowledgments 50
References 51

2.1 Introduction

2.1.1 New Materials and New Paradigm: Bottom-Up vs. Top-Down

Due to the recent dramatic development of nanotechnology, people have invented many new nanostructures (Figure 2.1), including nanoparticles,[1–3] carbon nanotubes (CNTs),[4,5] and nanowires.[6–8] In addition, people also are beginning to understand new properties of existing nanostructures such as electron transport through individual DNA molecules[9,10] and mechanical force generated by a single protein motor.[11] Some people are now trying to build functional devices using these new nanostructures by combining them with conventional microfabricated devices.[12–14] These devices are often called "hybrid devices" because they are composed of both synthetic nanostructures and conventional microfabricated devices. Examples of hybrid devices include molecular electronic circuits[15,16] and biomotor-based nanomechanical systems.[17] However, because most of the new nanostructures are first synthesized in a solution or powder form, one has to "pick up and assemble" individual nanostrucures onto substrates to build hybrid devices. This new

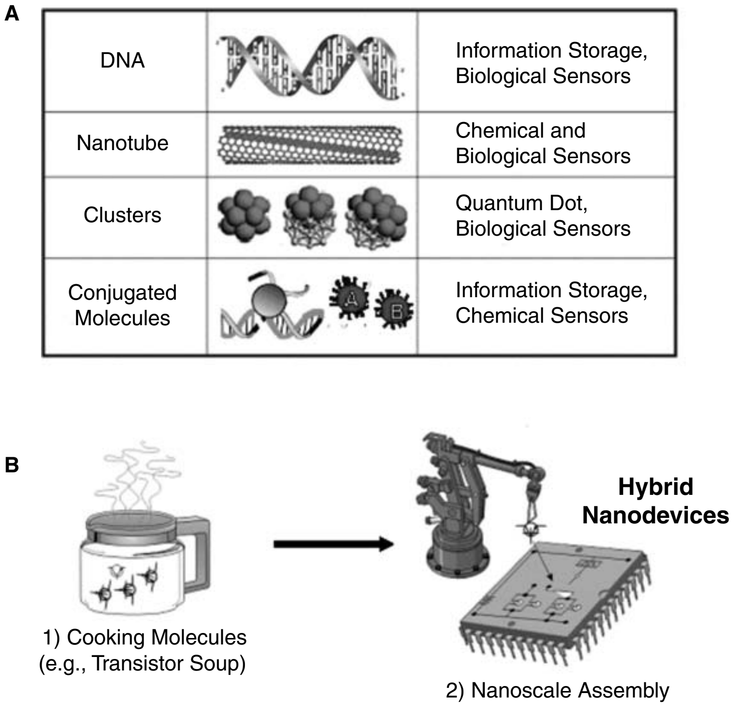

Figure 2.1 (A) Examples of new nanostructures. (B) "Bottom-up" mode strategy for the fabrication of "hybrid devices."

mode of device fabrication is often called the "bottom-up" method in contrast with the "top-down" strategy[18] of the conventional microelectronics industry where a wafer is "cut off" into a desired shape for device fabrication.

2.1.2 Nanomanufacturing Issues in Nanotechnology

A good example of hybrid devices fabricated via the "bottom-up" strategy is the fabrication of nanowire-based devices (Figure 2.2).[19–23] Recently there have been many reports regarding advanced electronic devices based on nanowires and carbon nanotubes. In some applications, nanowire-based devices show capabilities superior to conventional devices. One example is the carbon nanotube-based interconnect, which can hold about a one hundred times larger current density than conventional copper wires.[24] Another is silicon nanowire-based flexible circuits, which are flexible and still can be as fast as conventional silicon-based devices.[25]

However, one major problem is that most of these nanowires and nanotubes are first synthesized in solution or powder forms as shown in Figure 2.2(A).[26] Let us assume it would take about one second to assemble a single nanowire.

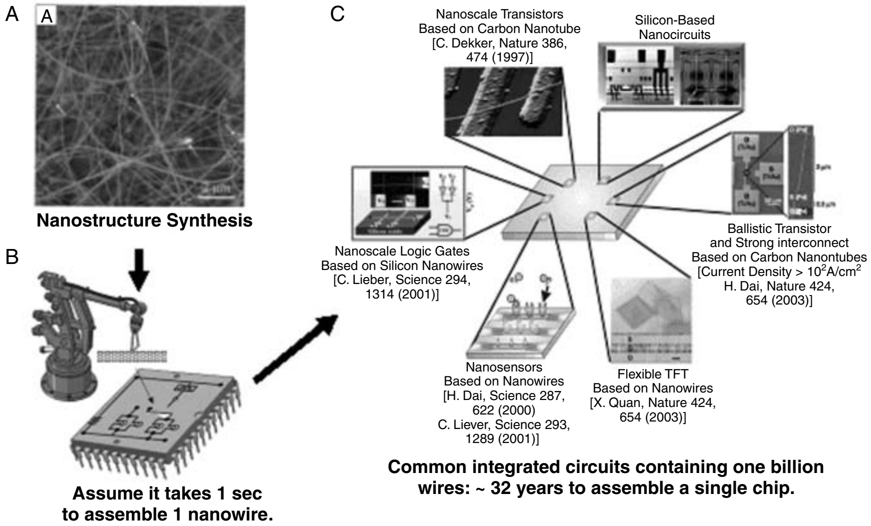

Figure 2.2 Schematic diagram depicting the nanomanufacturing problem in nanowire-based devices. Because nanowires are first synthesized in a solution or powder form, even if it takes just one second to assemble one nanowire onto substrate, it will take over 32 years to build a simple computer chip such as a random access memory (RAM) chip, which usually requires a billion wires. (A) Scanning electron microscopy (SEM) image of ZnO nanobelts. (From Pan, Z.W. et al., *Science*, 291, 1947, 2001. With permission.) (B) Various prototype devices based on nanowires. (From Tans, S.J. et al., *Nature*, 386, 474, 1997; Huang, Y. et al., *Science*, 294, 1313, 2001; Duan, X. et al., *Nature*, 425, 274, 2003; Javey, A. et al., *Nature*, 424, 654, 2003. With permission.)

(As a matter of fact, the fabrication of a single nanowire-based device often takes more than a day, and it requires expertise in advanced nanofabrication.) Because a common integrated circuit chip such as random access memory (RAM) requires more than a billion nanowires, we can estimate that it will take about 32 years to assemble a single RAM chip. This is a completely ridiculous situation, and no one would want to spend 32 years fabricating a single computer chip.

This type of problem is often called the "nanomanufacturing" problem, and it has been holding back any practical applications of nanowire-based devices and many other hybrid devices. This also has been a major issue in the commercialization of nanotechnology. In other words, even though nanotechnology can control individual atoms and molecules in nanoscale resolution, it is not yet clear how one can "scale up" this technology to build macroscale devices for real-life applications.

2.1.3 Self-Assembly in Nature: from Nano to Macro

Our solution for this problem is inspired by the "self-assembly process" in nature (Figure 2.3). Biomolecules are able to recognize other biomolecules. It is often called the "molecular recognition" mechanism.[27] For example, single-strand DNA (ssDNA) molecules can recognize other ssDNA molecules and they combine to form double-strand DNA (dsDNA) molecules.[7,28] Antibodies bind to specific antigens. The self-assembly strategy based on molecular recognition has been used by nature to build complicated biosystems for billions of years. For example, nanoscale biomolecules self-assemble to form microscale individual cells. Again, the microscale cells self-assemble to form much larger macroscale structures such as a human body. In some sense, we can say that each individual human is "living evidence" proving that the self-assembly process can be used to build a large system such as human body from nanoscale structures such as biomolecules.

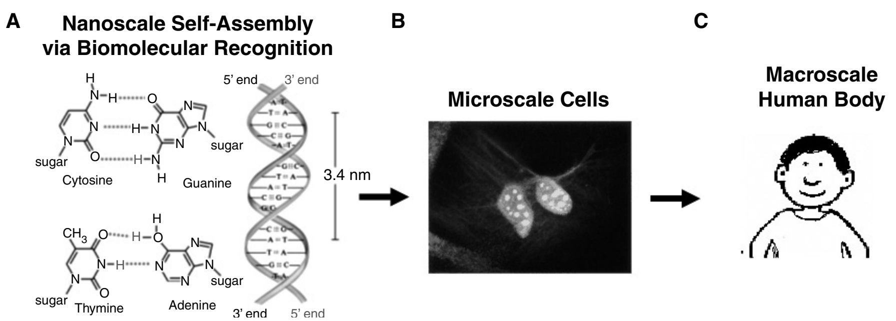

Figure 2.3 Schematic diagram depicting the basic concept of the self-assembly process in biological systems. (A) DNA. (B) Fluorescence image of cells. (From Bruchez, J.M. et al., *Science*, 281, 2013, 1998. With permission.)

2.2 Large-Scale "Surface-Programmed Assembly"

2.2.1 Basic Concepts

One solution for this problem is often called the surface-programmed assembly (SPA) process, and it adapts the self-assembly process of nanostructures inspired by self-assembly in nature.[29] This process can be realized by combining two simple steps with conventional microfabrication processes (Figure 2.4): (1) surface molecular patterning and (2) surface-directed assembly of nanostructures. First, specific regions of solid substrates are functionalized via desired chemical or biological functional groups such as carboxylic acid or amine. The surface functionalization can be done by patterning molecular monolayers using various patterning methods such as dip-pen nanolithography,[30–34] microcontact printing,[35–37] or photolithography.[18,38] By patterning nanoscale regions of the substrate with specific functional groups, we are giving the solid substrate the ability to recognize specific nanostructures in the solution. When the patterned substrate is placed in the solution of nanostructures, the patterned regions have an affinity to specific nanostructures, and the nanostructures are adsorbed onto the regions. Because molecular patterning can be done very quickly via parallel patterning methods (e.g., stamping, photolithography) and millions of nanostructures self-assemble in a parallel fashion in the solution, the entire process can occur in a very short time, usually in a few minutes. Actually, this process may remind us of our experiences in art class when we were in elementary school. When we draw a picture with glue on paper and throw sand particles on it, sand particles adhere only to the regions coated with glue. This phenomenon is often called "selective adsorption" in scientific terminology. The SPA process is somewhat similar to this in nanoscale. However, it also should be noted that the actual SPA process involves mechanisms that are a bit more complicated than simple selective adsorption. In the following we will describe (1) how one can pattern organic molecules on solid substrates and (2) how nanostructures assemble onto the patterned substrate.

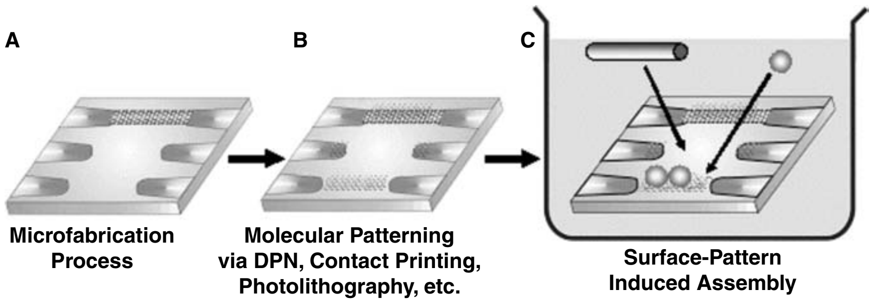

Figure 2.4 Schematic diagram depicting the surface-programmed assembly process.

2.2.2 Surface Molecular Patterning

2.2.2.1 Dip-Pen Nanolithography

One method to pattern organic molecules on solid substrates is dip-pen nanolithography (DPN).[39,40] DPN uses an atomic force microscope (AFM) tip to directly deposit organic molecules onto solid substrate (Figure 2.5A). The basic concept of DPN is pretty simple. When the molecule-coated AFM tip is in contact with the substrate, molecules diffuse out onto the substrate and form molecular layers such as self-assembled monolayer. A key for this process is how to create the exact amount of diffusion of molecular species. DPN allows us to pattern organic molecules with a nanoscale resolution (Figure 2.5B).

Common molecular species that are used for the DPN process form a self-assembled monolayer (SAM) on solid substrate (Figure 2.6).[41–43] These molecules usually comprise three parts: (1) chemisorbing group, (2) spacer, and (3) end group. When these molecules are deposited onto solid substrates, they chemically anchor to the substrate using the chemisorbing group and expose the end group. The spacer is usually an inert part. By coating the surface with a monolayer of these molecules, one can completely change the surface properties to those of end groups. One can choose different chemisorbing groups depending on the substrates. Also, one can choose different end groups so that these groups specifically interact with the desired nanostructures in the solution. One example is alkanethiol molecules. Each alkanethiol molecule binds to three Au atoms and they form well-ordered crystalline structures (Figure 2.6B). Various SAM molecules have been developed for decades. These days, one can easily find SAM molecules for virtually any substrates. Also, one can find molecules with various end groups such as carboxylic acid, amine, and methyl. One can even prepare molecules with biofunctional groups (e.g., DNA, proteins) as end groups so that functionalized substrates can specifically interact with biomolecular nanostructures.

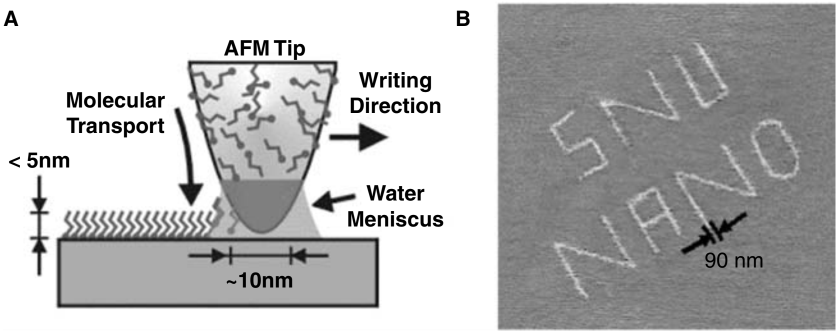

Figure 2.5 (A) Schematic diagram depicting dip-pen nanolithography. (From Piner, R.D. et al., *Science*, 283, 661, 1999. With permission.) (B) Lateral force microscope image of nanoscale letters written via dip-pen nanolithography. The letters are written with 16-mercaptohexadecanoic acid on an amorphous Au surface.

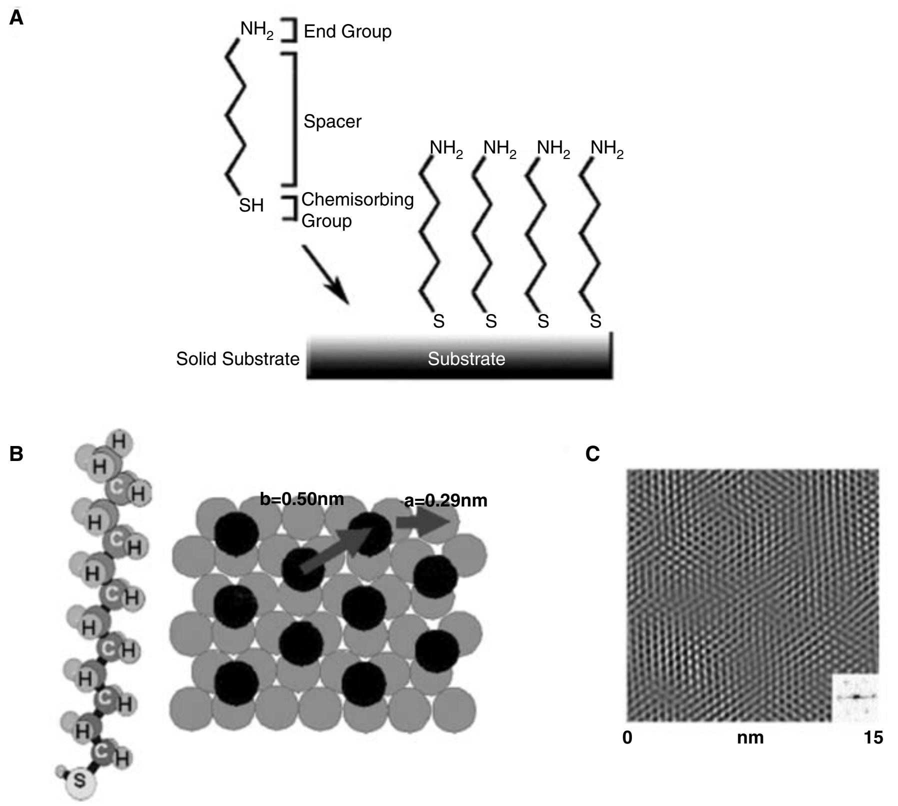

Figure 2.6 (A) Self-assembled monolayer molecules. (B) Alkanethiols on Au(111). (C) Lattice resolved lateral force image of a 1-octadecanethiol self-assembled monolayer deposited onto Au(111) by DPN. The image has been filtered with a Fast Fourier Filter, and the FFT of the raw data is shown in the lower right insert. (From Piner, R.D. et al., *Science*, 283, 661, 1999. With permission.)

The DPN method can be used to pattern various molecular species including biological molecules (Figure 2.7). Wilson et al. demonstrated the deposition of collagen proteins onto Au surfaces.[44] In this case, sulfur at the Cys amino acid anchors to Au surfaces. Demers et al. demonstrated the deposition of DNA molecules. DPN can be used to pattern multiple molecular species with nanoscale resolution (Figure 2.8).[45]

Another important advantage is that because DPN uses an AFM tip to deposit organic molecules, one can take full advantage of the high resolution of AFM for generating multiple-ink nanoscale patterns with perfect registration. Hong et al. developed a method to pattern different SAM molecules with perfect registry (Figure 2.8).[30,46] In this method, a molecule-coated AFM tip is used to image the alignment marks or pre-existing molecular patterns on the substrate, and the molecules are deposited only onto specific locations with perfect registry

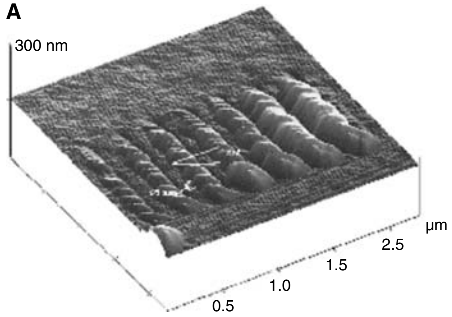

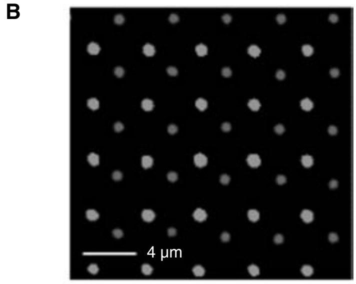

Figure 2.7 (A) AFM topography image of collagen patterns generated via DPN on Au surface. (From Wilson, D.L., *Proc. Natl. Acad. Sci. USA*, 98, 13660, 2001. With permission.) (B) Fluorescence microscope image of DNA patterns generated via DPN on Au surface. (Demers, L.M. et al., *Science*, 296, 1836, 2002. With permission.)

with respect to the pre-existing molecular patterns. This strategy allows one to generate molecular patterns that make up different molecule species.

One drawback of the DPN method is that it is a serial patterning method because molecular patterns are generated one by one using usually a single AFM tip. A possible solution for this problem can be patterning with

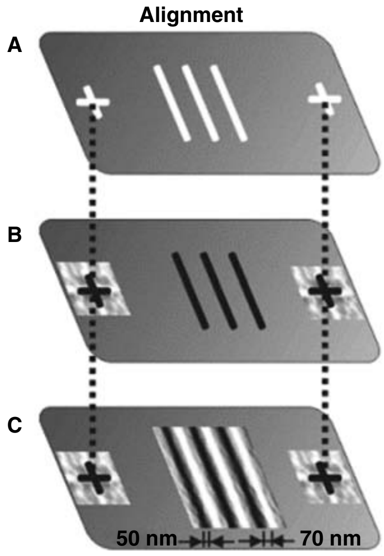

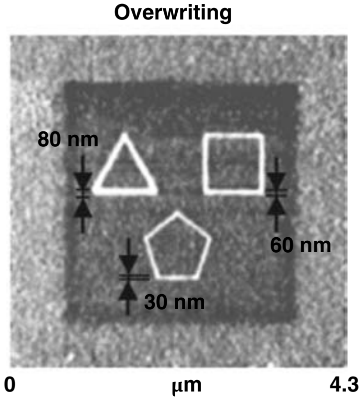

Figure 2.8 (left) Schematic diagram depicting the method for generating aligned soft nanostructures. (right) Lateral force microscope image of SAM patterns in the shapes of polygons drawn by DPN with 16-mercaptohexadecanoic acid on an Au surface. A 1-octadecanethiol (ODT) SAM has been *overwritten* around the polygons. (From Hong, S. and Zhu, J., *Science*, 286, 523, 1999. With permission.)

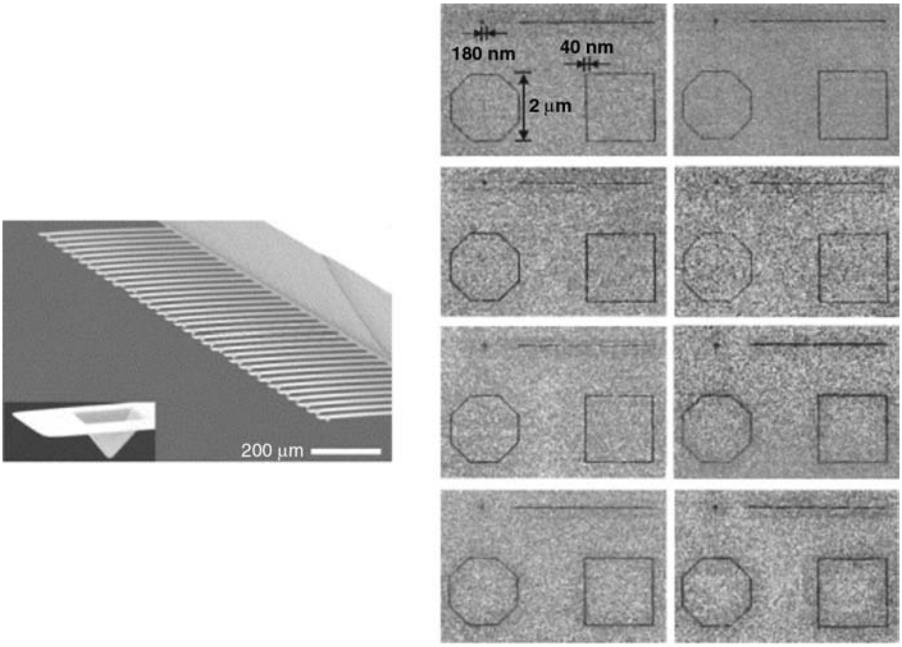

Figure 2.9 (left) SEM image of 32-pen AFM tip system for multiple patterning. (From Zhang, M. et al., *Nanotechnology*, 13, 212, 2002. With permission.) (right) Lateral force microscope images of eight identical patterns generated with one imaging tip and eight writing tips coated with 1-octadecanethiol molecules. (From Hong, S. et al., *Science*, 288, 1808, 2000. With permission.)

multiple AFM tips simultaneously (Figure 2.9). Hong et al. demonstrated the simultaneous generation of multiple patterns using a multiple pen system.[31,47] Significantly, because the DPN process is based on the diffusion of organic molecules, the deposition rate of molecules onto the substrate does not depend much on the contact force between the tip and surface, which is actually very important in building parallel patterning systems. In previous nanolithography methods based on scanning probe microscopes, patterning speeds depend on various scanning parameters such as tunneling current for scanning tunneling microscopes and contact forces for atomic force microscopes. In this case, if one wants to build parallel patterning systems based on multiple tips, each tip should be equipped with separate feedback circuits, sensor, and actuators, which dramatically increase the complexity. On the other hand, because the patterning speed of the DPN method does not depend on the contact forces, one can easily achieve uniform patterning speed from multiple AFM tips without attaching a sophisticated feedback system onto each tip, which dramatically simplifies instrumentation. Actually, such multiple-pen DPN systems are commercially available these days.

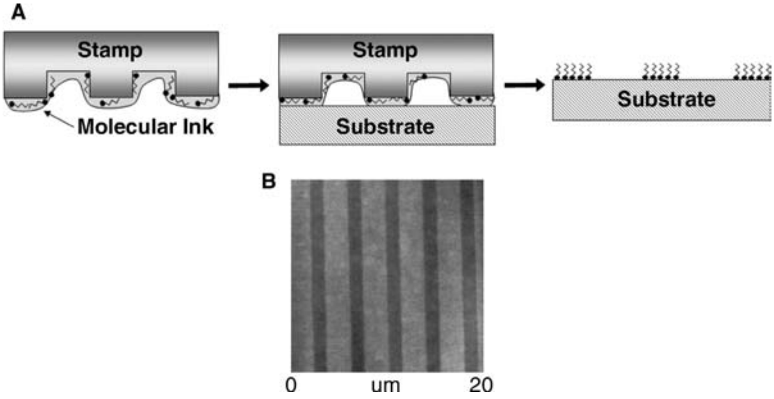

Figure 2.10 (A) Schematic diagram depicting microcontact printing method. (B) AFM image of 1-octadecanethiol patterns generated via the microcontact printing method.

2.2.2.2 Microcontact Printing and other Molecular Patterning Methods

Organic molecules can be patterned using the microcontact printing method (Figure 2.10). This method was first developed by George Whitesides' groups,[35–37,48,49] and it uses a micrometer-scale stamp to directly deposit organic molecules onto solid substrate. Because the stamping is a parallel method, one can pattern a large surface area in a short time. However, because the stamp is usually made with a flexible polymer such as PDMS, its resolution is usually limited to submicro- or micrometer scales.

The organic molecules can also be patterned by various other methods such as photolithography,[18,38] e-beam lithography,[50–52] and ion-beam lithography.[52,53]

2.2.3 Assembly and Alignment of Nanostructures

2.2.3.1 Nanoparticles

When the patterned substrate is placed in the solution of nanostructures, nanostructures are selectively adsorbed onto the regions with specific functional groups. One simple example can be the selective adsorption of Fe_3O_4 nanoparticles (Figure 2.11).[54] In this case, –COOH-terminated 16-mercaptohexadecanoic acid SAM is first patterned on an Au surface using the DPN method. Then the remaining area is backfilled with methyl-terminated 1-octadecanethiol molecules. When the patterned substrate is placed in the solution of nanoparticles, the nanoparticles assemble only onto the –COOH-terminated SAM region and form a magnetic array. Again, this process is somewhat similar to our old practice in art class where sand particles selectively adhere to the glue patterns on paper. We are using organic molecules as "glue" and nanoparticles as "sand particles."

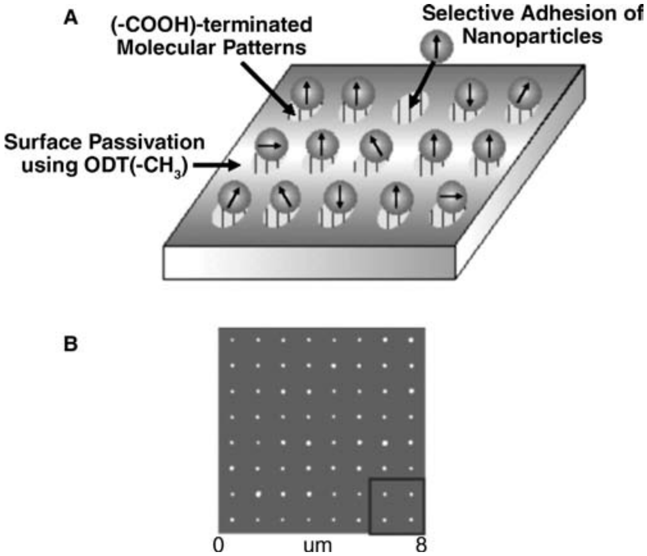

Figure 2.11 (A) Surface-templated assembly process for nanoparticles. (B) AFM topography image of array of iron oxide dots prepared by the surface-templated assembly process. (From Liu, X. et al., *Adv. Mater.*, 14, 231, 2002. With permission.)

2.2.3.2 Carbon Nanotubes and Nanowires

However, when we talk about one-dimensional nanostructures such as carbon nanotubes and nanoparticles, the situation becomes a little more complicated. Recently there has been great interest in advanced devices based on carbon nanotubes and nanowires.[13,23,55–62] These include transistors, interconnect, and sensor. However, a major stumbling block holding back their practical applications can be the lack of a mass production method for such devices. Because most nanowires are first synthesized in a solution or powder form, one has to pick up and assemble individual nanowires onto solid substrate to build functional devices, which is not an easy task.

It should be noted that the assembly of nanowires requires additional complexity beyond simple selective adsorption. Let us think about our experience in art class again. After drawing pictures with glue, if we throw match sticks instead of sand particles onto the paper, the sticks will assemble onto the glue, but with "random orientation." In the case of a one- or multi-dimensional nanostructure assembly, it is critical that one should be able to control the orientations of assembled nanowires as well as their locations.

Dai et al. selectively grew single-wall carbon nanotubes (swCNTs) from catalyst patterns to create a large array of swCNT-based devices (Figure 2.12).[61] This method allows one to fabricate a large-scale array of pristine swCNT devices. However, it requires high-temperature processing steps, which are not compatible with conventional CMOS processing steps. Also, carbon nanotubes tend to grow in random orientations from catalyst patterns, and it is very difficult to control the growth direction of swCNTs.

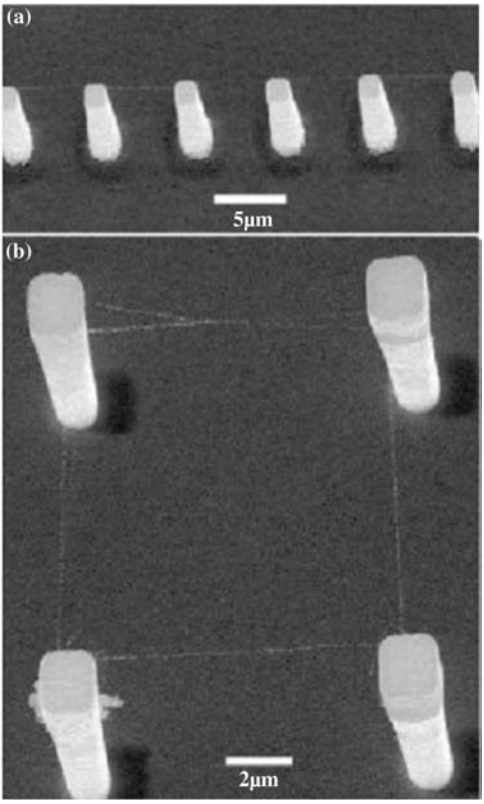

Figure 2.12 SEM image of array of swCNTs grown from catalyst patterns. (From Cassell, A.M. et al., *J. Am. Chem. Soc.*, 121, 7975, 1999. With permission.)

On the other hand, Huang et al. used SAM patterns to selectively assemble nanowires onto the desired location (Figure 2.13).[64] In addition, they applied liquid flow to align assembled nanowires along desired directions. This method allows one to fabricate aligned nanowire structures, which later can be used for complicated device fabrication. However, flow cell is not compatible with the microelectronics industry, and it can be a time-consuming task to fabricate millions of nanowire-based devices with "arbitrary orientations" using this method. Other researchers have aligned nanowires and nanotubes using various external forces such as electric or magnetic field[65–68] and gas flow.[69]

Unlike previous methods that require external forces to align nanowires, in the "surface-programmed assembly" process nanowires are adsorbed onto specific molecular patterns and they even self-align along the patterns. Thus, one can build millions of nanowire-based devices in a parallel fashion.

Rao et al. adapted the "surface-programmed assembly" method to selectively assemble and precisely align swCNTs on solid substrate without relying on any external forces (Figure 2.14).[70] In this strategy, polar and nonpolar regions are first created on solid substrate using SAM patterns. When the

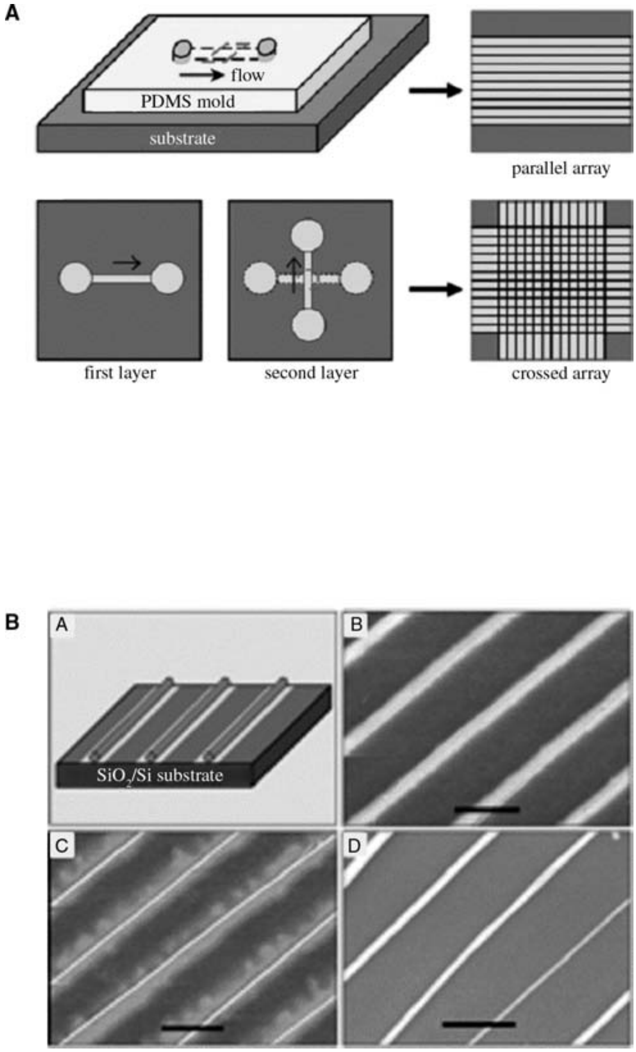

Figure 2.13 (A) Schematic diagram depicting the flow-cell method for nanowire assembly and alignment. (B) SEM image of Si nanowires assembled by the flow cell method. (From Huang, Y. et al., *Science*, 291, 630, 2001. With permission.)

substrate is placed in the solution of carbon nanotubes, CNTs assemble only onto polar regions, and they even “self-align” along the polar patterns. Significantly, Hong et al. used pure CNTs without any functionalization. Figure 2.15A shows swCNTs assembled onto polar amine-functionalized cysteamine SAM patterns. It should be noted that swCNTs do not cross the boundary between polar and nonpolar regions, and they even bend themselves to stay in the polar regions. When the linewidth is reduced, a few (Figure 2.15B) or even a series of individual nanotubes (Figure 2.15C) can

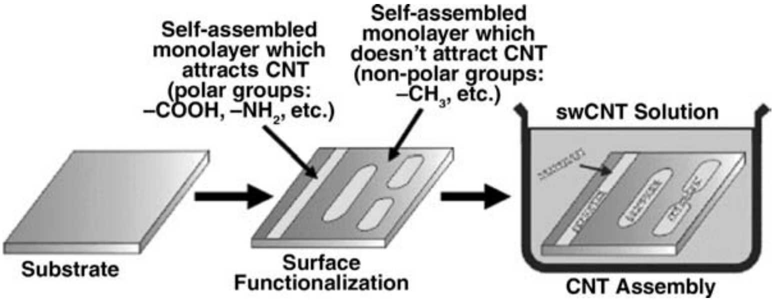

Figure 2.14 Schematic diagram depicting the surface-programmed assembly process of swCNTs.

be assembled along the molecular patterns. Using this method, they were able to assemble individual swCNTs onto desired locations with precise orientations (Figure 2.15D).

The exact mechanism of the swCNT alignment in the SPA process is still under study. However, recent results show some clues about the SPA process. The first question might be whether the swCNTs align "right on" or "away from"

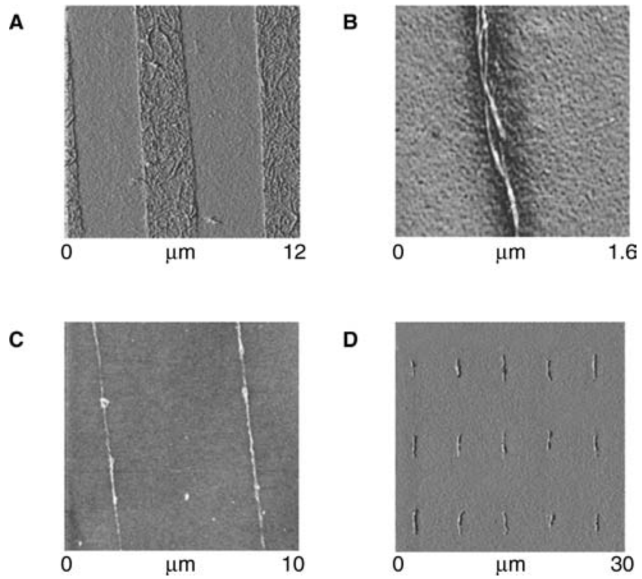

Figure 2.15 (A) AFM topography image of swCNTs assembled onto cysteamine patterns. ODT is used for passivation. (B) Lateral force microscope image of a few swCNTs assembled onto nanometer-scale linewidth patterns. (C) AFM topography image of lines of a series of individual swCNTs on cysteamine patterns. (D) AFM topography image of the array of individual swCNTs assembled onto cysteamine patterns. (From Rao, S.G. et al., *Nature*, 425, 36, 2003. With permission.)

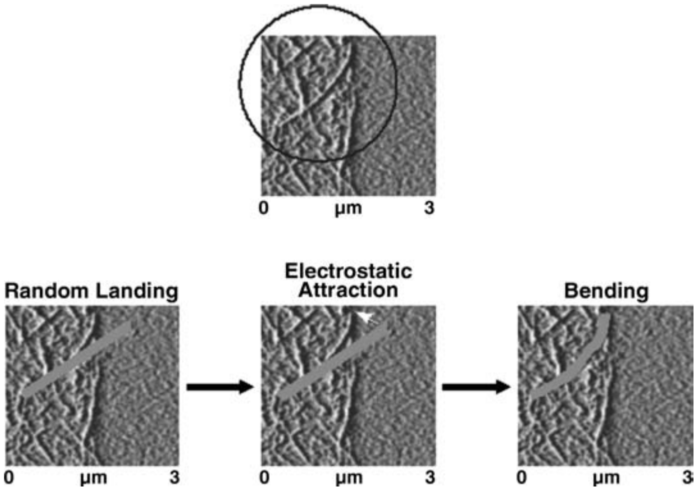

Figure 2.16 (top) AFM contact force image of swCNTs on the boundary between polar and nonpolar regions. (bottom) Schematic diagram depicting the model for swCNT alignment. (From Rao, S.G. et al., *Nature*, 425, 36, 2003. With permission.)

the surface. Figure 2.16 provides a clue. It shows an swCNT near the boundary between polar and nonpolar regions. The swCNT is bent to stay in the polar surface region even though the bending of swCNTs costs a lot of elastic energy. It allows us to come up with some scenario about swCNT assembly. First, swCNTs are adsorbed onto solid substrate, and one end of the swCNT is fixed due to the other adsorbed swCNTs. Then, the lateral force right on the surface drives the swCNTs toward the polar regions. If the swCNTs align along the patterns in the space away from the surface, they should align without bending. The picture implies that there exists a lateral force aligning swCNTs adsorbed right on the surface. This method can be used to assemble an array of millions of individual swCNTs and swCNT junctions over a 1 cm × 1 cm area (Figure 2.17).

The SPA strategy can be applied to pattern nanowire structures. One example is V_2O_5 nanowires (Figure 2.18).[71–74] Myung et al. report that V_2O_5 nanowires can be selectively assembled and aligned on solid substrate using positively charged SAM patterns.[29] Here, methyl-terminated nonpolar SAM is used to avoid nonspecific adsorption. Furthermore, it can continue an additional microfabrication process to fabricate complicated device structures such as nanowire-based transistors.

2.2.3.3 Biomotors

The surface-programmed assembly process can also be applied to functional proteins. One example might be an actomyosin protein motor (Figure 2.19).[17,75–80] Actomyosin comprises two parts: (1) actin and (2) myosin. Actin is like a track and myosin walks on the actin filaments by consuming adenosinetriphosphate (ATP) as a fuel. This is the basic mechanism of muscle

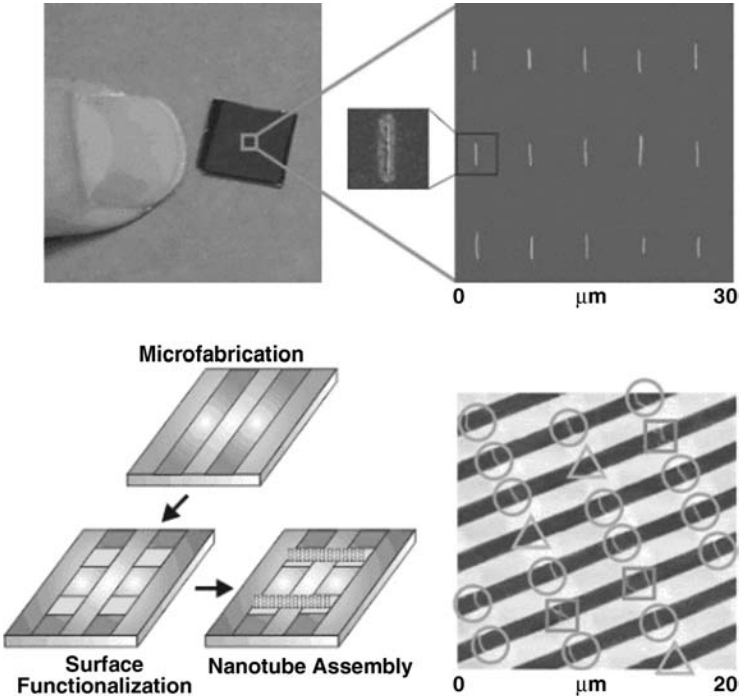

Figure 2.17 (top) AFM topography image of an array of millions of swCNTs assembled onto a large sample surface. (bottom) AFM topography image of array of millions of swCNT junctions. (From Rao, S.G. et al., *Nature*, 425, 36, 2003. With permission.)

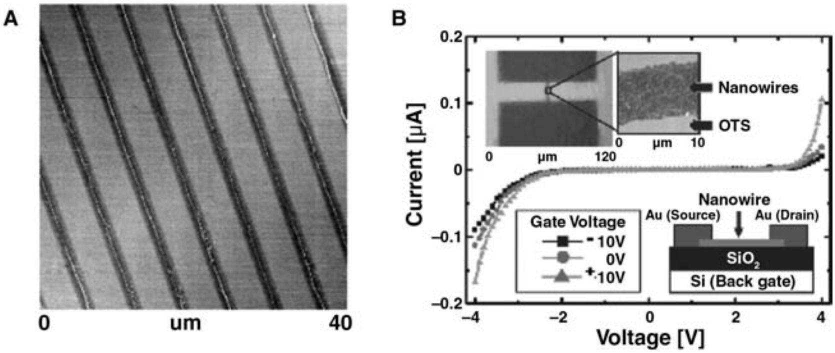

Figure 2.18 (A) AFM topography image of a series of individual V_2O_5 nanowires assembled onto cysteamine patterns. (B) Gating effect of V_2O_5 nanowire-based field effect transistors using the substrate as a back gate. (From Myung, S. et al., *Adv. Mater.*, 17, 2361, 2005. With permission.)

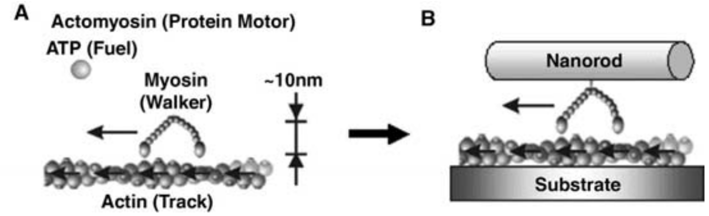

Figure 2.19 (A) Schematic diagram depicting the structure of actomyosin protein motors. (B) Schematic diagram depicting the basic concept of a transport system using protein motors.

contraction in our bodies. It should be mentioned that the protein motors often show an energy conversion efficiency of over 45%, and individual myosins can generate over 10 pN forces that can be measured by macroscopic instruments such as AFM. This is one of the most efficient existing engine structures that have been optimized by evolution over billions of years.

Many researchers are trying to build nanoscale actuators using these protein motors. For example, one can lay down actin tracks on the substrate and attach myosin onto nanowire to build "transport systems." A key technology for this application is a method to selectively assemble biomotors onto specific locations while maintaining their functionality.

Manandhar et al. report a new method to selectively assemble myosin onto the desired location on solid substrates while maintaining their functionality (Figure 2.20).[81] In this strategy, labeled streptavidin is patterned on

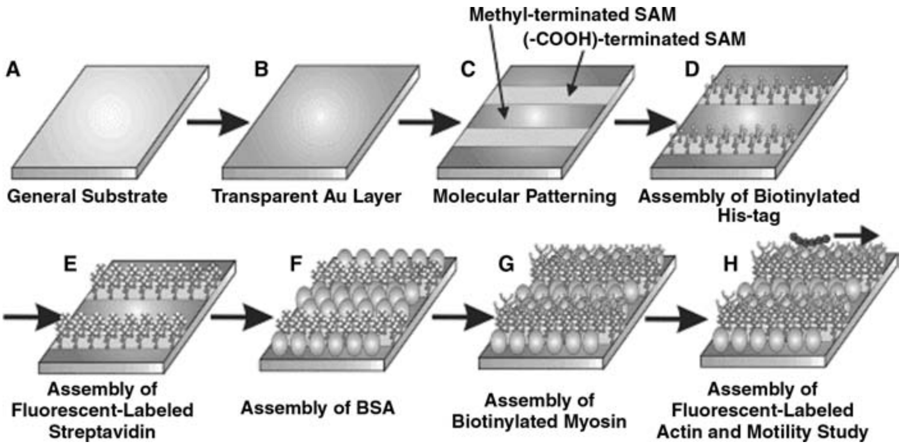

Figure 2.20 Schematic diagram depicting the surface-programmed assembly process of myosin and motility assay.

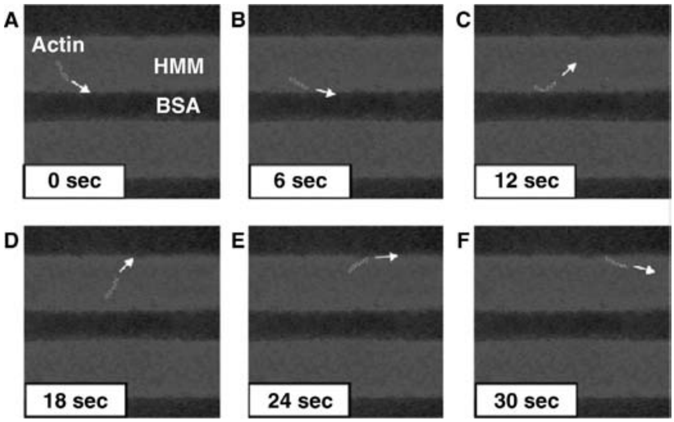

Figure 2.21 A series of movie frames showing the motion of actin filaments on myosin patterns. (From Manandhar, P. et al., *Langmuir*, 21, 3213, 2005. With permission.)

specific regions on the substrate. Then, biotinylated myosin is selectively assembled onto the streptavidin patterns. Figure 2.21 shows a series of movie frames of actin (white line following an arrow) motions on myosin patterns (brighter gray regions). The actin stays in the myosin regions. This result shows that one can selectively assemble biomotors onto specific regions on the substrate while maintaining their functionality. This is a good example showing that the surface-programmed assembly process can be used for various biomolecular nanostructures such as functional proteins.

2.3 Conclusions

The surface-programmed assembly process uses surface molecular patterns to direct the assembly of nanostructures onto desired locations with precise orientations. Based on a simple two-step process, it can be used for the assembly of extremely versatile nanostructures such as nanoparticles, carbon nanotubes, and nanowires. Furthermore, it can also be used to assemble functional proteins such as actomyosin biomotors. Because this process allows us to assemble large-scale integrated devices based on virtually any general nanostructures, it can be one of the ultimate solutions for the “nanomanufacturing” problem of current nanotechnology and may pave the way toward the commercial applications of various nanodevices.

Acknowledgments

This work is supported by the National Research Laboratory Program NANO-Systems Institute National Core Research Center.

References

1. Brust, M. et al., Synthesis of thiol-derivatised gold nanoparticles in a two-phase liquid-liquid system, *J. Chem. Soc. Chem. Commun.*, 801, 1994.
2. Patil, A.N., Andres, R.P., and Otsuka, N., Synthesis and minimum energy structure of novel metal silica clusters, *J. Phys. Chem.*, 98, 9247, 1994.
3. Hyeon, T., Chemical synthesis of magnetic nanoparticles, *Chem. Commun.*, 927, 2003.
4. Iijima, S., Helical microtubules of graphitic carbon, *Nature*, 354, 56, 1991.
5. Guo, T. et al., Catalytic growth of single-walled nanotubes by laser vaporization, *Chem. Phys. Lett.*, 243, 49, 1995.
6. Morales, A.M. and Lieber C.M., A laser ablation method for the synthesis of crystalline semiconductor nanowires, *Science*, 279, 208, 1998.
7. Braun, E. et al., DNA-templated assembly and electrode attachment of a conducting silver wire, *Nature*, 391, 775, 1998.
8. Xia, Y. et al., One-dimensional nanostructures: synthesis, characterization, and applications, *Adv. Mater.*, 15, 353, 2003.
9. Fink, H.W. and Schönenberger, C., Electrical conduction through DNA molecules, *Nature*, 398, 407, 1999.
10. Porath, D. et al., Direct measurement of electrical transport through DNA molecules, *Nature*, 403, 635, 2000.
11. Howard, J., *Mechanics of Motor Proteins and the Cytoskeleton*, Sinauer Associates, Sunderland, MA, 2001.
12. Tans, S.J., Verschueren, A.R.M., and Dekker, C., Room-temperature transistor based on a single carbon nanotube, *Nature*, 393, 49, 1998.
13. Cui, Y. et al., Nanowire nanosensors for highly sensitive and selective detection of biological and chemical species, *Science*, 293, 1289, 2001.
14. Huang, Y. et al., Logic gates and computation from assembled nanowire building blocks, *Science*, 294, 1313, 2001.
15. Reed, M.A. et al., Conductance of a molecular junction, *Science*, 278, 252, 1997.
16. Reed, M.A. et al., Molecular random access memory cell, *Appl. Phys. Lett.*, 78, 3735, 2001.
17. Soong, R.K. et al., Powering an inorganic nanodevice with a biomolecular motor, *Science*, 290, 1555, 2000.
18. Campbell, S.A., *The Science and Engineering of Microelectronic Fabrication*, Oxford University Press, New York, 1996.
19. Tans, S.J. et al., Individual single-wall carbon nanotubes as quantum wires, *Nature*, 386, 474, 1997.
20. Kong, J. et al., Nanotube molecular wires as chemical sensors, *Science*, 287, 622, 2000.
21. Derycke, V. et al., Carbon nanotube inter- and intramolecular logic gates, *Nano Lett.*, 1, 453, 2001.
22. Fuhrer, M.S. et al., Crossed nanotube junctions, *Science*, 288, 494, 2000.
23. Martel, R. et al., Single- and multi-wall carbon nanotube field-effect transistors, *Appl. Phys. Lett.*, 73, 2447, 1998.
24. Javey, A. et al., Ballistic carbon nanotube field-effect transistors, *Nature*, 424, 654, 2003.
25. Duan, X. et al., High-performance thin-film transistors using semiconductor nanowires and nanoribbons, *Nature*, 425, 274, 2003.

26. Pan, Z.W., Dai, Z.R., and Wang, Z.L., Nanobelts of semiconducting oxides, *Science*, 291, 1947, 2001.
27. Skerra, A. et al., Engineered protein scaffolds for molecular recognition, *J. Mol. Recogn.*, 13, 167, 2000.
28. Keren, K. et al., DNA-templated carbon nanotube field-effect transistor, *Science,* 302, 1380, 2003.
29. Myung, S. et al., Large-scale "surface-programmed assembly" of pristine vanadium oxide nanowire-based devices, *Adv. Mater.*, 17, 2361, 2005.
30. Hong, S. and Mirkin, C.A., A nanoplotter with both parallel and serial writing capabilities, *Science*, 288, 1808, 2000.
31. Hong, S. and Zhu, J., Multiple ink nanolithography: toward a multiple-pen nano-plotter, *Science*, 286, 523, 1999.
32. Piner, R.D. et al., "Dip-pen" nanolithography, *Science*, 283, 661, 1999.
33. Li, Y., Maynor, B.W., and Liu, J., Electrochemical AFM "dip-pen" nanolithography, *J. Am. Chem. Soc.*, 29, 2105, 2001.
34. Ivanisevic, A. and Mirkin, C.A., "Dip-pen" nanolithography on semiconductor surfaces, *J. Am. Chem. Soc.*, 123, 7887, 2001.
35. Kumar, A. and Whitesides, G.M., Features of gold having micrometer to centimeter dimensions can be formed through a combination of stamping with an elastomeric stamp and an alkanethiol "ink" followed by chemical etching, *Appl. Phys. Lett.*, 63, 2002, 1993.
36. Xia, Y. and Whitesides, G.M., Replica molding with a polysiloxane mold provides this patterned microstructure, *Angew. Chem. Int. Ed.*, 37, 550, 1998.
37. Xia, Y. et al., Unconventional methods for fabricating and patterning nanostructures, *Chem. Rev.*, 99, 1823, 1999.
38. Jaeger, R.C., *Introduction to Microelectronic Fabrication*, 2nd ed., vol. V, Prentice Hall, New Jersey, 2002, Chapter 2.
39. Haaheim, J. et al., Dip pen nanolithography (DPN): process and instrument performance with NanoInk's Nscriptor System, *Ultramicroscopy*, 103, 117, 2005.
40. Bruinink, C.M. et al., Supramolecular microcontact printing and dip-pen nanolithography on molecular print boards, *Chem. Eur. J.*, 11, 3988, 2005.
41. Hyun, J. et al., Molecular recognition-mediated fabrication of protein nano- structures by dip-pen lithography, *Nano Lett.* 2, 11, 1203, 2002.
42. Zhang, H. et al., Biofunctionalized nanoarrays of inorganic structures prepared by dip-pen nanolithography, *Nanotechnology*, 14, 1113, 2003.
43. Schwartz, P.V., Molecular transport from an atomic force microscope tip: a comparative study of dip-pen nanolithography, *Langmuir*, 18, 4041, 2002.
44. Wilson, D.L. et al., Surface organization and nanopatterning of collagen by dip-pen nanolithography, *Proc. Natl. Acad. Sci. USA*, 98, 13660, 2001.
45. Demers, L.M. et al., Direct patterning of modified oligonucleotides on metals and insulators by dip-pen nanolithography, *Science*, 296, 1836, 2002.
46. Noy, A. et al., Fabrication of luminescent nanostructures and polymer nanowires using dip-pen nanolithography, *Nano Lett.* 2, 109, 2002.
47. Zhang, M. et al., A MEMS nanoplotter with high-density parallel dip-pen nanolithography probe arrays, *Nanotechnology*, 13, 212, 2002.
48. Tantra, R. and Cooper, J., Imaging of protein arrays and gradients using softlithography and biochip technology, *Sensor. Actuator. B Chem.*, 82, 233, 2002.
49. Unger, M.A. et al., Monolithic microfabricated valves and pumps by multilayer softlithography, *Science*, 288, 113, 2000.

50. Utsumi, T., Low-energy e-beam proximity lithography (LEEPL): is the simplest the best?, *Jpn. J. Appl. Phys.*, 38, 7046, 1999.
51. Waskiewicz, W.K. et al., Electron-optical design for the scalpel proof-of-concept tool, *Proc. SPIE*, 2522, 13, 1995.
52. Smith, H.I. et al., A new approach to high fidelity e-beam and ion-beam lithography based on an in situ global-fiducial grid, *J. Vac. Sci. Technol.*, B9, 2992, 1991.
53. van Kan, J.A. et al., Micromachining using focused high energy ion beam: deep ion beam lithography, *Nucl. Instr. Meth. Phys. Res. B*, 148, 1085, 1999.
54. Liu, X. et al., Arrays of magnetic nanoparticles patterned via dip-pen nanolithography, *Adv. Mater.*, 14, 231, 2002.
55. Bachtold, A. et al., Logic circuits with carbon nanotube transistors, *Science*, 294, 1317, 2001.
56. Zheng, G. et al., Synthesis and fabrication of high-performance n-type silicon nanowire transistors, *Adv. Mater.*, 16, 1890, 2004.
57. Heo, Y.W. et al., Depletion-mode ZnO nanowire field-effect transistor, *Appl. Phys. Lett.*, 85, 2274, 2004.
58. Star, A. et al., Nanoelectronic carbon dioxide sensors, *Adv. Mater.*, 16, 2049, 2004.
59. Comini, E. et al., Stable and highly sensitive gas sensors based on semiconducting oxide nanobelts, *Appl. Phys. Lett.*, 81, 1869, 2002.
60. Snow, E.S., et al., Chemical detection with a single-walled carbon nanotube capacitor, *Science*, 307, 1942, 2005.
61. Dai, H.J. et al., Nanotubes as nanoprobes in scanning probe microscopy, *Nature*, 384, 147, 1996.
62. Zhang, Y. et al., Coaxial nanocable: silicon carbide and silicon oxide sheathed with boron nitride and carbon, *Science*, 281, 973, 1998.
63. Cassell, A.M. et al., Directed growth of free-standing single-walled carbon nanotubes, *J. Am. Chem. Soc.*, 121, 7975, 1999.
64. Huang, Y. et al., Directed assembly of one-dimensional nanostructures into functional networks, *Science*, 291, 630, 2001.
65. Zhang, Y. et al., Electric-field-directed growth of aligned single-walled carbon nanotubes, *Appl. Phys. Lett.*, 79, 3155, 2001.
66. Liu, J. et al., Controlled deposition of individual single-walled carbon nanotubes on chemically functionalized templates, *Chem. Phys. Lett.*, 303, 125, 1999.
67. Chen, X.Q. et al., Aligning single-wall carbon nanotubes with an alternating-current electric field, *Appl. Phys. Lett.*, 78, 3714, 2001.
68. Hone, J. et al., Electrical and thermal transport properties of magnetically aligned single wall carbon nanotube films, *Appl. Phys. Lett.*, 77, 666, 2000.
69. Zhang, Y. and Iijima, S., Elastic response of carbon nanotube bundles to visible light, *Phys. Rev. Lett.*, 82, 3472, 1999.
70. Rao, S. et al., Large-scale assembly of carbon nanotubes, *Nature*, 425, 36, 2003.
71. Spahr, M.E. et al., Redox-active nanotubes of vanadium oxide, *Angew. Chem. Int. Ed.*, 37, 1263, 1998.
72. Muhr, H.J. et al., Vanadium oxide nanotubes—a new flexible vanadate nanophase, *Adv. Mater.*, 12, 231, 2000.
73. Kim, G.T. et al., Field-effect transistor made of individual V_2O_5 nanofibers, *Appl. Phys. Lett.* 76, 1875, 2000.
74. Chang, Y.J. et al., Percolation network of growing V_2O_5 nanowires, *Appl. Phys. Lett.*, 84, 5392, 2004.

75. Jia, L. et al., Microscale transport and sorting by kinesin molecular motors, *Biomedical Microdevices*, 6, 67, 2004.
76. Patolsky, F., Weizmann, Y., and Willner, I., Actin-based metallic nanowires as bio-nanotransporters, *Nat. Mater.*, 3, 692, 2004.
77. Hess, H. and Vogel, V., Molecular shuttles based on motor proteins: active transport in synthetic environments, *Rev. Mol. Biotechnol.,* 82, 67, 2001.
78. Vale, R.D. and Milligan, R.A., The way things move: looking under the hood of molecular motor proteins, *Science*, 288, 88, 2000.
79. Veigel, C. et al., The stiffness of rabbit skeletal actomyosin cross-bridges determined with an optical tweezers transducer, *Biophys. J.,* 75, 1424, 1998.
80. Schliwa, M. and Woehlke, G., Molecular motors, *Nature,* 422, 759, 2003.
81. Manandhar, P. et al., Highly selective directed assembly of functional actomyosin on Au surfaces, *Langmuir*, 21, 3213, 2005.

Chapter 3

Fabrication and Applications of Single-Walled Carbon Nanotube (SWNT) Fabrics

Darren K. Brock, Jonathan W. Ward, Claude Bertin, Brent M. Segal, and Thomas Rueckes

Contents

3.1 Introduction 56
3.2 Fabrication of SWNT Fabrics 56
3.2.1 Preparation of SWNT Solutions 58
3.2.1.1 Growth and Deposition of SWNTs 58
3.2.1.2 Physical and Electrical Characteristics of SWNTs 59
3.2.1.3 Preparation of CNT Solutions 60
3.2.2 Wafer Coating of SWNT Fabrics 61
3.2.2.1 Process Equipment 61
3.2.2.2 CNT Spin-Coat Process Steps 62
3.2.2.3 Edge Bead Removal Process Steps 62
3.2.3 Qualification of SWNT Fabrics with CMOS Processing 63
3.2.3.1 Coating Uniformity 64
3.2.3.2 Nanotube Fabric Sheet Resistivity 64
3.2.3.3 Sufficient Edge Bead Removal 65
3.2.3.4 Contamination Removal 68
3.2.3.5 Lot-to-Lot Coating Uniformity 68
3.3 Applications of SWNT Fabrics 69
3.3.1 Molecular Microswitches 70
3.3.1.1 Test Structure Fabrication 70
3.3.1.2 Principles of Operation 72
3.3.2 NRAM™—a CMOS-Compatible Nonvolatile Memory Technology 74

3.3.2.1 Circuit Architecture and Description 74
3.3.2.2 Write/Read Operations 74
3.4 Conclusion 76
Acknowledgments 76
References 77

3.1 Introduction

The manufacturability of electronic devices based on carbon nanotubes (CNTs) has traditionally depended on the ability to manipulate and control individual structures at the molecular level. A novel technique has been developed to overcome this hurdle, allowing CNT-based devices to be fabricated directly in existing production CMOS fabrication lines. The first demonstration of this technique has resulted in a CNT-based nonvolatile memory element—a molecular microswitch (MMS). This unique approach relies on the deposition and lithographic patterning of a 1 to 2 nm-thick fabric of nanotubes that retain their molecular-scale electromechanical characteristics, even when patterned with 150 nm feature sizes or below. The MMS is based on a mesh or "fabric" of single-walled nanotubes (SWNTs), freely suspended over a metal electrode, forming an electromechanical switch. These elements represent binary information by modulation of the resistance between the two stable (open/closed) switch states—typically by a factor $>10^5$. In operation, individual patches of this SWNT fabric are elastically deformed by electrostatic attraction to the metal electrode, thus creating a pair of stable nonvolatile states around the equilibrium of two molecular-level forces: an attractive van der Waals force and the restoring tensile strain within the carbon–carbon bonds of the deformed nanotube fabric. As such, the device does not rely on the storage of charge on capacitors or the manipulation of charge carrier densities in a bulk semiconductor. Moreover, because these nonvolatile devices (memory elements) are created in an all-thin-film room-temperature process, they can be monolithically integrated directly with traditional CMOS circuitry to facilitate addressing and readout.

This chapter gives an overview of the nanotube "fabric" concept. Section 3.2 describes the methods used to fabricate these monolayer nanotube fabrics, with special attention to issues associated with their manufacture in modern CMOS foundries. Section 3.3 gives some specific examples of the design structures based on the resulting nanotube fabrics at both the device and circuit levels. Section 3.4 concludes the chapter with a brief summary.

3.2 Fabrication of SWNT Fabrics

Single-walled nanotubes (SWNTs)—cylindrical molecules of graphite with diameters of 1 to 2 nm—are a new type of material that possesses many unique properties.[1] Generally grouped under the umbrella term *nanotechnology,*

such materials allow circuit designers to access the molecular/quantum/atomic behavior of densely integrated systems. Part of the benefit of operating within this "nano regime" is the ability to exploit performance characteristics that have no dual in the macro domain. There are, however, formidable requirements to reach these desired objectives—namely, in the ability to position, control, and access the resulting physical systems at a molecular level.

The key innovation described in this chapter is the use of an ensemble of nanotubes, in the form of a sparse monolayer, which retain their molecular -level properties, while eliminating the need for nanoscale physical control. (Strictly speaking, this arrangement is a submonolayer, as the areal coverage of the material is but a few percent. Nevertheless, the term *monolayer* is adopted to emphasize the single molecule thickness of the material.) Called "fabrics," these monolayers are created by room-temperature spin coating of a solution of SWNTs in a semiconductor-grade solvent. After evaporation of the solvent, the resulting monolayer fabric is lithographically patterned and etched in an oxygen plasma (see Figure 3.1). It is of particular interest that the spin coating of SWNT solutions can be used to produce monolayer fabric converge of very steep aspect ratios (see Figure 3.2). This conformal coating feature is only one of various possible applications. As will be seen in Section 3.2, use of sacrificial layers around the fabric allows the formation of an open cavity, in which a suspended patch of fabric can be mechanically drawn into electrical contact with an electrode. We call these devices molecular microswitches (MMS). The SWNT fabric approach is a natural extension to the previously reported concept by Rueckes et al.[2]

Another advantage of this approach is that the 1 to 2-nm-thick patterned SWNT fabric can be interconnected monolithically with additional standard semiconductor (e.g., CMOS) circuitry above or below, providing buffering and drive circuitry to address and control the MMS devices. By using this technique, the limit to the scalability of the hybrid nanotube/CMOS system depends only on the available photolithographic node. Hence, the CMOS

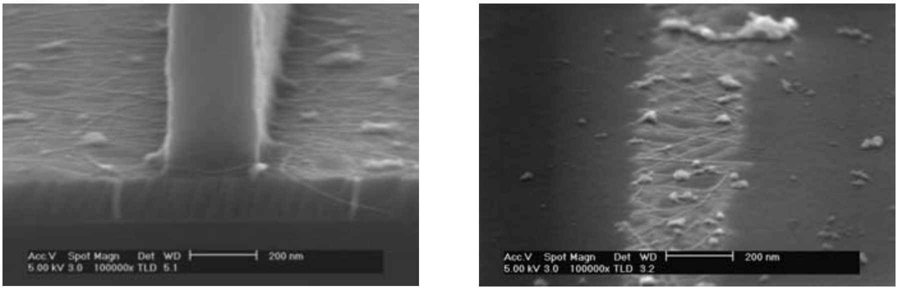

(a) (b)

Figure 3.1 SWNT fabric patterning showing (a) a monolayer fabric with exposed photoresist masking part of the fabric and (b) the resulting transfer of the photoresist pattern to the monolayer fabric after etching the fabric and removing the photoresist.

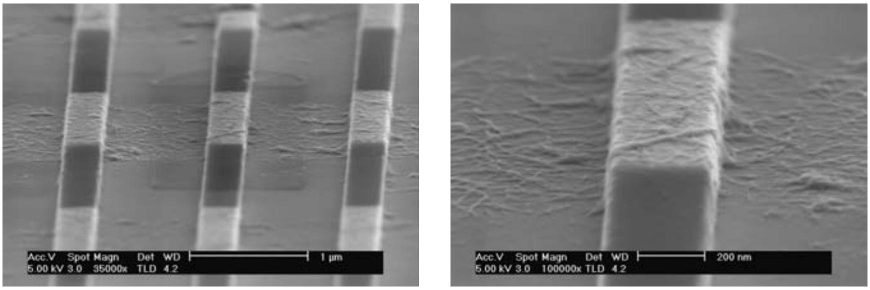

(a) (b)

Figure 3.2 Patterned traces of conducting SWNT fabrics over (a) several 0.3 µm high steps and (b) a close-up view of same.

fabrication, not the inclusion of nanotubes, remains the limiting factor in scaling. Indeed, the ultimate physical limit to the integration density of this approach is the initial concept by Rueckes et al. involving two individual metallic nanotubes and their electromechanical interaction. The following sections describe the creation of nanotube solutions, their deposition by spin coating to form monolayer fabrics, and measurement to verify compatibility with semiconductor foundry requirements.

3.2.1 Preparation of SWNT Solutions

Nantero has developed a procedure to produce semiconductor-electronic-grade SWNT solutions for creating monolayer conductive fabrics. These solutions are compatible with any standard semiconductor fabrication process, including CMOS, silicon-on-insulator (SOI) and III-V compounds. Because the processes involved in producing bulk SWNTs generate impurities in the as-grown carbon nanotube material, raw nanotubes are not compatible with a CMOS process flow. Typical impurities consist of metal particles, amorphous carbon, and other graphitic carbon particles. One issue to be considered during the fabrication of nanoelectronic devices consisting of CNTs is the difficulty in determining whether to deposit the SWNTs by an application method (spinning, spraying, dipping, etc.) or to grow SWNTs at desired locations by a chemical vapor deposition (CVD) method. Figure 3.3 depicts the sequence of steps needed to produce monolayer SWNT fabrics from raw as-grown nanotubes. The following sections examine several of the important issues relating to this sequence.

3.2.1.1 Growth and Deposition of SWNTs

Many CNT device approaches require nanotubes to actually be grown directly on the substrate, using some type of catalytic nanoparticles. CVD of SWNTs directly on active CMOS wafers, however, is not currently feasible because typical CVD temperatures are >800°C for SWNTs. Therefore, Nantero

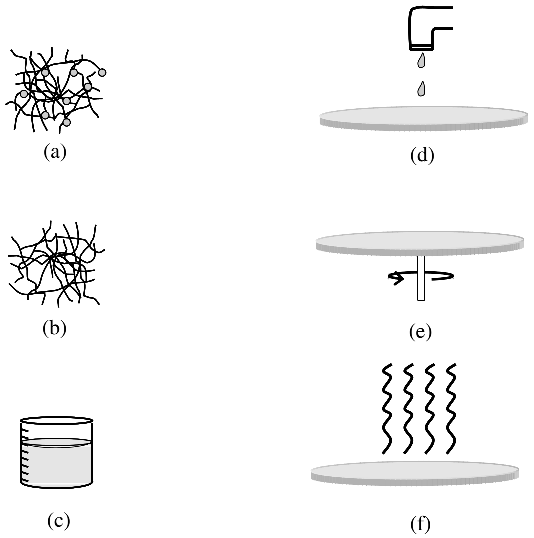

Figure 3.3 Depiction of the SWNT fabric process showing (a) initial as-grown SWNTs with impurities, (b) nanotubes after purification and removal of excess particles, (c) dilution of SWNTs into solution, (d) dispensing solution onto an Si wafer, (e) spin coating to achieve monolayer dispersion, and (f) evaporation of excess solvent to form final nanotube fabric adhered to wafer surface.

has chosen to obtain SWNTs under separate conditions, solubilize them, and then apply them to the active substrate. The solubilization of the nanotubes quickly becomes an important issue because most solvents that readily suspend SWNTs are not permissible in modern CMOS fabs. Moreover, as previously mentioned, as-grown CNTs are inherently dirty, containing metal particles, graphitic particles, amorphous carbon, and other material contaminants (e.g., Group IA and IIA elements).

3.2.1.2 Physical and Electrical Characteristics of SWNTs

(a) Length: When creating SWNT fabrics that will be suspended over a cavity, another issue is the length of the individual nanotubes. Any nanotube that does not sufficiently span the cavity remains cantilevered above the underlying electrode. Although a nanotube is stiff enough to fully support its own weight in such a configuration, its presence could conceivably cause shorting in the structure if the nanotube became bound to the electrode. Fortunately, this can be mediated with particular design techniques in both the configuration of the fabric and electrode(s).

(b) Electrical Conduction: Depending on the chirality of SWNTs, they may exhibit either metallic or semiconducting properties. Generally, the percent fraction of each type can be affected by growth conductions; however, the electrical characteristics of individually placed nanotubes within

devices is typically neither controllable nor selectable on a manufacture-able scale. Fortunately, in the fabric approach presented here, the metallic nanotubes dominate in the electrostatic deflection of the fabric patch and in the van der Waals interaction with the metal device electrodes. The fraction of the nanotubes composing the fabric patch within the device that is semiconducting does not appear to affect the mechanics of the structure.

(c) Orientation: In actual devices the nanotubes are deposited as a randomly oriented monolayer fabric. The random nature of this fabric means that there is a range in threshold voltages from the time the first few nanotubes contact the lower electrodes until the bulk of the tubes are in contact. If devices are set at too low a voltage, just at the point where the device becomes ohmic, there is the possibility that the device can relax and the bit will spontaneously relax to a zero (open) state. The nanotube-to-nanotube bonding maintains the integrity of the fabric, so a bit that has been set at too low a threshold voltage will relax completely, not gradually decay.

3.2.1.3 Preparation of CNT Solutions

To address these issues, Nantero has developed a proprietary process of purification, filtration, and solubilization of SWNTs into a semiconductor-grade solvent. The resulting solution can be readily applied to a substrate in a class-10 or below CMOS fab. This technique has been shown to provide a metallic-free, low-particulate solution that contains SWNTs of sufficient length to span up to a 300 nm wide gap. The solution is dispensed using a standard coat-and-develop wafer track, with a recipe controlling the volume of solution dispensed, duration and speed of spin coat, and finally postbake time and temperature.

The suspension of SWNTs in solvents for application of nanotube "mats" and "Bucky paper" is well known. Preparation of solutions for nanotube fabrics is quite similar. As-grown SWNTs are acquired from any of various commercial sources or, alternatively, may be grown in lab. As illustrated in Figure 3.4, the nanotubes are then treated to a nitric acid (HNO_3) wash. This treatment serves to bind up excess metallics and catalytic nanoparticles that remain after the initial nanotube growth. After separating out this excess material, multiple sonication and filtration steps can be used to "untangle" the remaining nanotube "bundles" and "ropes," providing a batch of evenly dispersed individual nanotubes within the solvent volume. Optical dispersion measurements at 550 nm are used to determine the relative concentration of nanotubes within the solution. Anecdotal evidence suggests that mean nanotube length and statistical distribution of lengths is dependent on the growth mechanism and conditions of the raw nanotubes, as is chirality distribution of the resulting solution. The process of purification may also contribute to the overall distribution in nanotube lengths due to defect-induced cleaving of nanotubes during the nitric acid wash. For creating spin-on nanotube fabrics, a distribution of nanotube lengths between

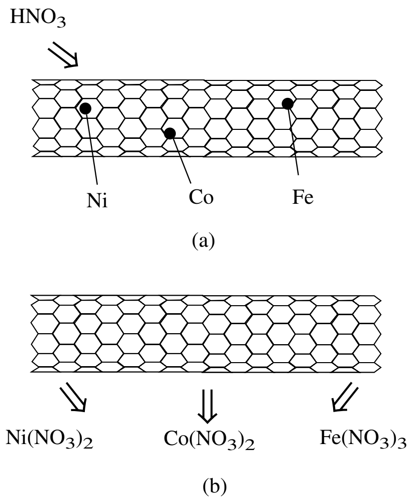

Figure 3.4 Carbon nanotube purification by nitric acid wash showing (a) presence of residual catalytic metal particles and (b) formation of species to bind the unwanted particles into new complexes more easily removed.

1 μm and 2 μm seems to be sufficient. Although the solution preparation conditions differ, SWNTs grown by chemical vapor deposition, laser ablation, and arc discharge can all be prepared in solutions. CVD-grown nanotubes, however, appear to have the greatest potential for high-volume manufacturing due to both good yield and relatively good quality.

3.2.2 Wafer Coating of SWNT Fabrics

One of the major advantages of the CNT fabric approach is that it does not require any new processing equipment or techniques. This section describes the basic methods developed to apply and prepare CNT monolayer fabrics.

3.2.2.1 Process Equipment

Two standard wafer tracks, of the kind generally used to coat photoresist, are used for this process. One track is devoted for use with solvents and is used for the application of the CNT solution to the wafer. The other track system is reserved for use with aqueous solutions only and serves as the platform for edge bead removal and backside/bevel clean. As is standard in the microelectronics industry, the tracks contain programmable modules for controlling the dispensing nozzles, a variable-speed spinning wafer chuck, and multiple hot plates for pre- and postbake. Recipes were entered into the track controllers during experimentation, resulting in a final automated process suitable for a high-throughput manufacturing environment, which can produce a fully coated and cleaned 200 mm wafer in under 15 min.

On the CNT track, the amount of CNT solution dispensed onto the wafer is controlled by adjusting the pressure and/or the dispense time. Typically, only a few milliliters of solution is dispensed over a few seconds. This track contains separate hot plates that are used for both evaporating away the solvent from the CNT solution and subsequent recooling of the wafer.

On the edge bead removal (EBR) track, one dispense nozzle is used for spreading and soaking a 0.26 N tetramethylammoniumhydroxide (TMAH) surfactant-free developer solution (AZ MIF 300) onto the edge region of the wafer. The position of the dispense arm is adjusted so that the developer-exposed edge area is minimized and so the developer will sufficiently flow around the bevel and backside region to remove any attached CNTs. A second dispense arm is used to release deionized (DI) water. This arm is also adjusted so that DI water rinses off the remaining developer residue only along the edges, backside, and bevel region of the wafer. Both dispense nozzles are angled to prevent splashing or dripping of developer or DI water onto the wafer surface. An additional backside rinse nozzle is also attached to the EBR track, below the wafer chuck, which is targeted to remove any CNTs still attached to the backside of the wafer.

3.2.2.2 CNT Spin-Coat Process Steps

After an initial wafer dehydration bake and cool-down period, the wafer is moved to the coating module. There, the Nantero CNT solution is applied onto the surface by a reverse-radial dispense, meaning that as the substrate rotates the dispense arm moves to the edge of the wafer, then to an intermediate position several millimeters away from the edge where the CNT solution begins to dispense. Once the intermediate position is reached and the CNT solution begins to dispense, the dispense arm moves to the center position of the wafer as the dispense is completed. After the center position is reached and the CNT dispense halts, the dispense arm moves back to the home position and the wafer continues to rotate for several more seconds to spread the CNT solution evenly over the wafer.

The substrate spin speed is controlled until the CNT solution has completely evaporated and the surface is dry. This process can be repeated to tailor the resistivity profile of the monolayer CNT fabric. At the end, a final high-speed spin is performed to fully dry the substrate, completing the procedure for constructing the conducting monolayer CNT fabric.

3.2.2.3 Edge Bead Removal Process Steps

To achieve edge bead removal (EBR), two main steps are required—a dispense and soak of developer, followed by a DI water rinse. To begin, a dispense arm is moved to an edge position off the wafer where it begins to dispense developer. The arm moves to a "center" position that is set around the edge of the wafer. The developer dispenses for several seconds before the arm moves off the wafer and the dispense halts. The developer beads up along the edge of the wafer, due to the centrifugal force, with

some slight spread toward the center of the wafer. The surface tension associated with the developer prevents the solution from fully spinning off the edge of the wafer at these rotation speeds. Thus, with proper nozzle positioning and rotation speed selection, a desired edge bead width can be tailored. Typically, this width is several millimeters. After the developer has soaked the wafer, it is removed at a higher rpm setting. This process can be repeated several times, if needed.

Next, a rinse procedure is initiated to cleanse the edge region and backside with DI water. To accomplish this, a front-side DI rinse nozzle first moves to a "center" position along the edge of the wafer and soaks the edge region with DI water. The DI rinse must cover the entire region exposed to the developer to ensure all developer residue is removed. A high spin rate and high velocity of the backside DI rinse was found to efficiently remove any CNTs that may have become attached to the backside of the wafer during the CNT spin-coat procedure. The EBR process concludes with a final wafer drying process removing any remaining DI water from the wafer surfaces.

3.2.3 Qualification of SWNT Fabrics with CMOS Processing

Working with various semiconductor manufacturers, a set of criteria has been developed for the "qualification" of SWNT solutions as an acceptable material for use within a CMOS foundry. These criteria include

- Coating uniformity—The solution concentration should be precisely controlled to generate the required monolayer fabrics <5 nm thick (determined by atomic force microscopy (AFM) measurements) and a uniform fabric coating with no accumulation of the CNT fabric within a wafer [determined by field-emission scanning electron microscopy (FESEM)].
- Target sheet resistance—The resulting CNT fabric should possess a sheet resistance of 100 kΩ per square over a 200 mm wafer (determined by 4-point probe measurements), with a sheet resistance across the wafer uniformity of ± 20% (determined by 4-point probe measurements).
- Removal of excess nanotubes—The CNT fabric should be completely removed from the periphery region of the wafer (determined by FESEM and AFM), with >99% removal of CNTs from the bevel, edge, and backside of the wafer.
- Solution Purity—The CMOS grade CNT solution should possess surface metal contaminants numbering $<15 \times 10^{10}$ atoms added per cm^2 to be within the specifications of a commercial CMOS foundry (determined by vapor phase decomposition inductively coupled plasma mass spectroscopy [VPD ICP/MS]).
- Process Reproducibility—The entire process should be reproducible across three different lots of wafers, where each lot contains 10 wafers, with lot-to-lot uniformity <± 20%.

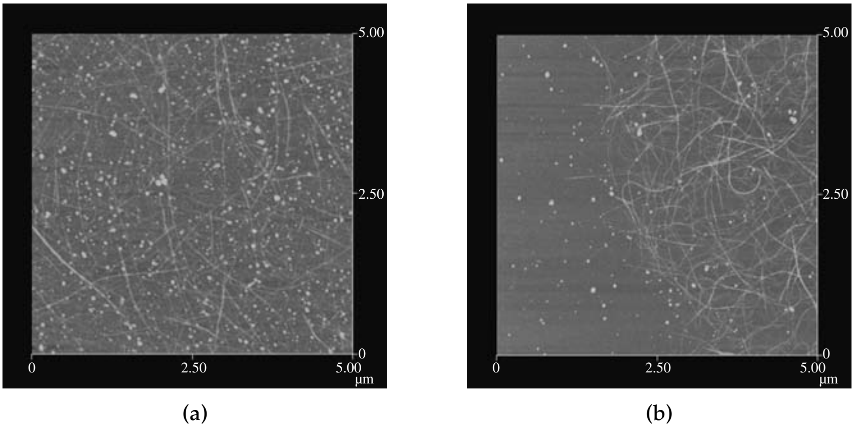

Figure 3.5 AFM images of the dispersed monolayer nanotube fabric after spin coating at (a) the center portion of the wafer and (b) the boundary of the EBR region.

Nantero has demonstrated that all the criteria above can be met. This set of parameters then provides the ability to perform further process integration and engineering of hybrid SWNT fabric/CMOS structures in a semiconductor foundry. The following sections summarize details of the process necessary to achieve this performance.

3.2.3.1 Coating Uniformity

Thickness of the CNT fabric is determined by AFM. The thickness should range between 1 nm and 3 nm for a monolayer-thick fabric. Figure 3.5 contains AFM images of an example monolayer-thick CNT fabric, showing both (a) the center of the wafer and (b) the region from the nanotubes monolayer fabric to the cleaned wafer edge region. A clear transition region between the CNT fabric and the edge region is evident in Figure 3.5(b). Figure 3.6 shows that the monolayer fabric is constructed with a height variation from 2 nm to 4 nm (with the higher values corresponding to overlapping CNTs).

3.2.3.2 Nanotube Fabric Sheet Resistivity

A primary characterization of the process is the measurement of SWNT fabric sheet resistance using a 4-point probe. The 4-point probe method gives a good indication of the quality and uniformity of the CNT fabric over the entire wafer surface. Forty-nine individual measurements are made on a wafer starting from the center point, moving to an inner circle with 8 total measurements, then a middle circle with 16 total measurements, and finally an outer circle with 24 total measurements. An exclusion zone is left just as wide as the required EBR region. Typical voltage values are around 4.99 V, giving typical currents of $I = 0.0028$ mA. Four-point probe measurements of

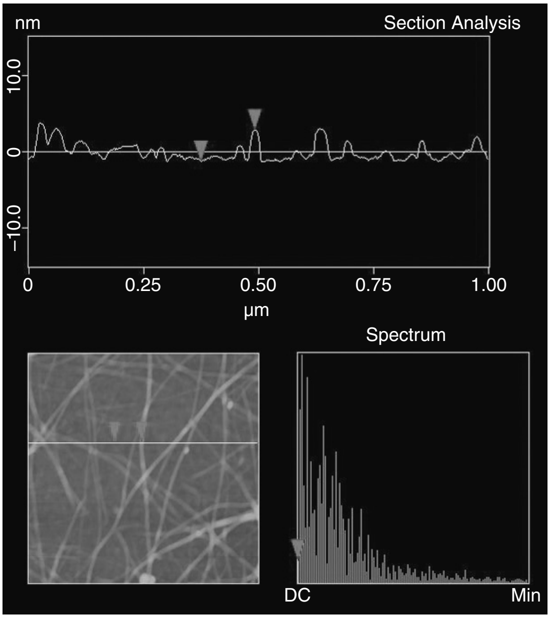

Figure 3.6 AFM measurement of the height of the resulting monolayer nanotube fabric indicating a thickness of 1–4 nm, with the thicker portion corresponding to the crossing of two nanotubes.

a fabric produced from this deposition procedure (the wafer also had an EBR procedure and a final bake procedure performed) contain a mean sheet resistance of 9.44 kΩ/□, a standard deviation of 0.4391 kΩ/□.

3.2.3.3 Sufficient Edge Bead Removal

Field emission scanning electron microscopy (FESEM) measurements are used to examine the surface morphology and characteristics of the CNT fabric both in the center of the wafer, which contains a sparse network of intertwined CNTs, as well as along the transition region from the dense CNT fabric to the cleared EBR region. From previous FESEM knowledge, it is clearly evident that if CNTs were present on the surface, they would be clearly visible at a magnification of 5000 ×. Even small batches of CNTs on the surface should present enough of a charging effect to be observed. After the mid-region, the edge and bevel regions of the wafer are imaged. The effectiveness of the EBR procedure is indicated by the complete lack of any noticeable CNTs along the edge region and bevel region of the wafer. The bevel region is the most likely place for CNT attachment due to the rough surface and the higher surface energies associated with the roughened surface. Thorough scanning of the edge and bevel regions, however, did not detect any stray nanotubes. The final section of the wafer to be scanned for CNTs in the FESEM is the backside of the wafer. Figure 3.7 shows a series of views

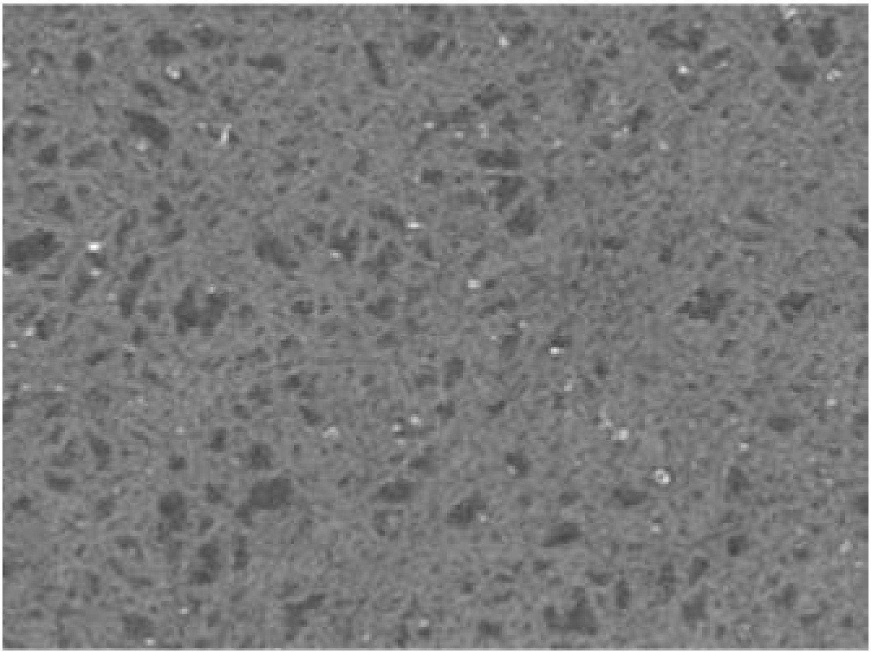

(a)

(b)

Figure 3.7 Inspection of wafer coverage at (a) front-side center, (b) front-side transition, (c) front-side bevel, (d) edge, and (e) back-side bevel, showing the confinement of nanotubes to only the desired portions of the wafer.

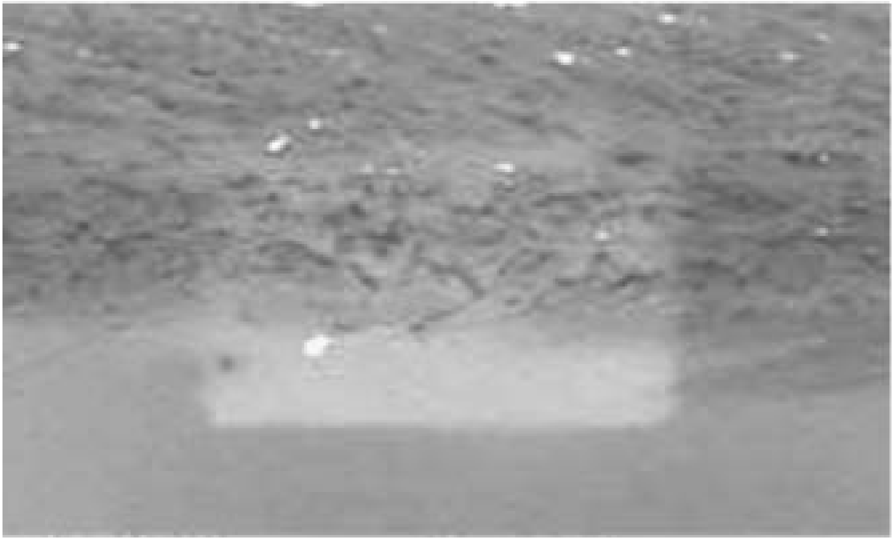

(c)

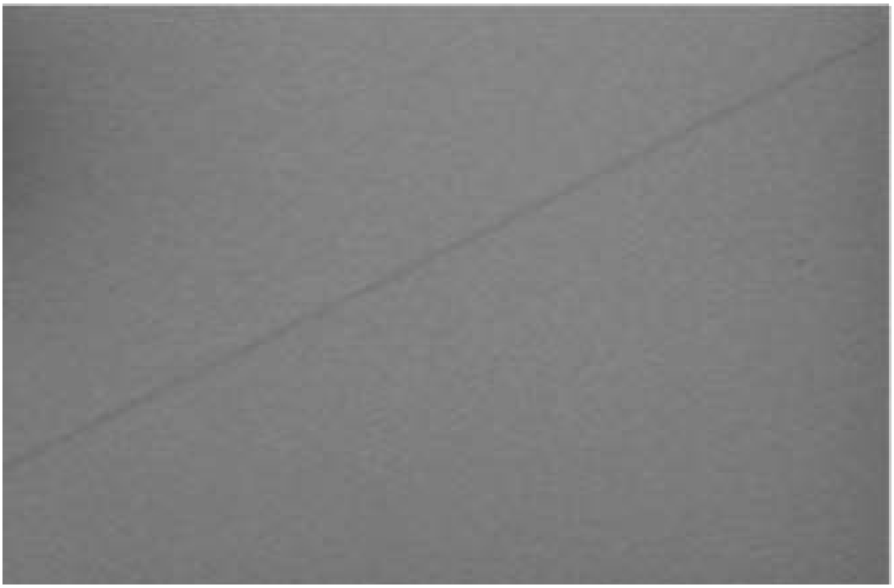

(d)

***Figure* 3.7** (Continued).

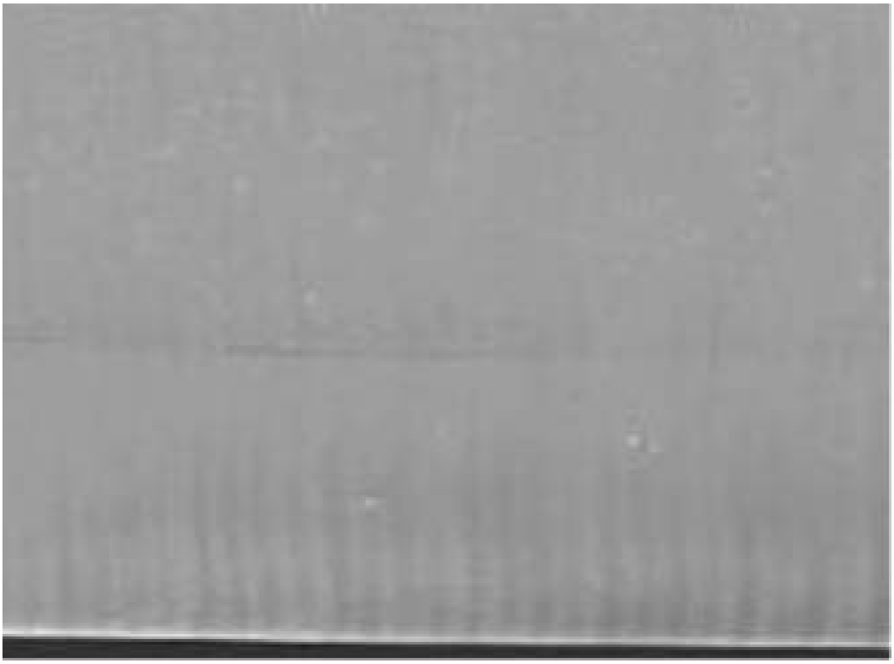

(e)

Figure 3.7 (Continued).

at different points verifying that no CNTs are present along the bevel, edge, or backside of the wafer.

3.2.3.4 Contamination Removal

To verify the absence of any contamination as a result of the CNT coating process, vapor phase decomposition (VPD) measurements were performed on various samples, including wafers coated from a batch of Nantero SWNT solution. To obtain the VPD analysis of the nanotube solution, a bare silicon wafer was used as a control, and a second wafer was processed on both the CNT and EBR tracks for a total of three CNT dispenses and a complete EBR process. Table 3.1 shows an example of VPD analyses on the SWNT solution. Results are presented in 10^{10} atoms/cm^2. As can be seen, amounts of all the trace elements detected on the CNT coated wafer fell well below the required specifications and match closely the elemental analysis from a control bare silicon wafer.

3.2.3.5 Lot-to-Lot Coating Uniformity

Another prerequisite for manufacturability is the ability to repeat the fabrication of a conducting monolayer of CNT fabric on multiple wafers. A mean sheet resistance of $R_S < 100\ \mathrm{k\Omega}/\square \pm 20\%$ is desired for the entire population. The EBR procedure, removing the CNTs from the edge, bevel, and backside regions of the waver, must also be repeatable across multiple lots. For these

Table 3.1 Vapor Phase Decomposition Results[a] Characterizing an SWNT Solution Coated Wafer

	Control wafer	SWNT fabric wafer
Al	1.7	0.50
Sb	<0.003	<0.003
As	<0.03	<0.03
Ba	<0.01	<0.01
Be	0.14	<0.1
Bi	<0.002	<0.002
B	91	11
Cd	<0.005	<0.005
Ca	1.7	1.3
Cr	<0.1	<0.1
Co	<0.02	1.9
Cu	0.18	0.17
Ga	<0.005	<0.005
Ge	<0.01	<0.01
Fe	0.45	0.11
Pb	<0.003	<0.003
Li	0.23	<0.08
Mg	<0.3	0.31
Mn	<0.03	<0.03
Mo	<0.01	<0.01
Ni	0.053	2.7
K	0.22	0.79
Na	1.1	3.1
Sr	0.011	<0.01
Sn	<0.02	<0.02
Ti	<0.1	<0.1
W	<0.005	<0.005
V	<0.03	<0.03
Zn	<0.06	0.13
Zr	0.083	<0.003

[a] Results are presented in # x 10^{10} atoms/cm^2.

measurements, three lots of 10 wafers each (30 total wafers) are coated with the CNT solution as described above. Each individual lot contains a mean sheet resistance of $R_S < 10$ kΩ/□ ± 10%. The mean sheet resistance for the entire population of 30 wafers is $R_S = 9.2$ kΩ/□ ± 6.29%. Both the mean value and process spread are well below the outlined specifications.

3.3 Applications of SWNT Fabrics

The molecular nature of carbon nanotube fabrics allows various CNT physical properties, including electromagnetic, mechanical, chemical, and optical behaviors to be exploited to create integrated electronic devices (including

Table 3.2 Example Applications of Single-Walled Carbon Nanotube Fabrics

Semiconductors	Life sciences	Instrumentation
Nonvolatile and volatile memories	Membranes	Mechanical relays and switches
Global and local interconnect	Valves	Acceleration sensors
Programmable logic devices	Chemical absorption	Thermal sensors and actuators
Transistors	Nano-fluidics devices	Bolometers
Chip-to-chip interconnect	Nano-mixers	Gyroscopes
Telecommunications	Heat exchangers	Membranes
Micro-mirrors	Reaction chambers	Acoustic/pressure sensors
RF components	Nano-channels	Radiation detectors
Inductors	Diagnostic systems	Field emission tips displays

nonvolatile memory devices); chemical, biological, and radiation sensors; passive low-resistance, low-capacitance conformal interconnects; and electromagnetic field emission devices, to name a few. Table 3.2 summarizes a number of proposed applications that could use SWNT fabrics as an enabling component. In the following section, one application—the molecular microswitch—is introduced; and a method for its fabrication is described.

3.3.1 Molecular Microswitches

3.3.1.1 Test Structure Fabrication

The fabrication of SWNT fabric molecular microswitch (MMS) test structures at Nantero employs a sequence of deposition and etching steps that are schematically outlined in Figure 3.8 and described in detail below. To fabricate the nonvolatile nanotube switch, a silicon wafer with a thermally grown oxide (0.5 μm) is employed (Figure 3.8a). Embedded electrodes are constructed by electron beam lithography (EBL) with polymethylmethacrylate (PMMA) as resist. After the electrode pattern is defined in the resist, reactive ion etching (RIE) is performed using CHF_3 gas to construct a trench in the oxide (Figure 3.8b). The embedded electrodes are created by a lift-off process by depositing the electrodes in an electron beam evaporator to fill the trench and then stripping off the resist in N-methyl pyrollidinone (NMP) at 70°C (Shipley 1165) (Figure 3.8c). The electrodes are 0.18 ± 0.02 μm wide and consist of 850 Å of metal (Ti/Pd) and 200 Å of a sacrificial material (Al_2O_3) (Figure 3.8d). The sacrificial material will define the gap height between an unswitched nanotube fabric (not yet deposited) and the lower electrode. The 200 ± 50 Å gap height is theorized to yield an electromechanically switchable bit, corresponding to a tensile strain of $\sigma_{tensile} = 0.9 \pm 0.5\%$ of the nanotubes in the on state, which lies well within the elastic limit of SWNTs.

After the creation of the embedded electrodes, the carbon nanotube fabric is constructed. The nanotube fabric is produced by spin coating the semiconductor-grade SWNT solution on the device wafer. The application

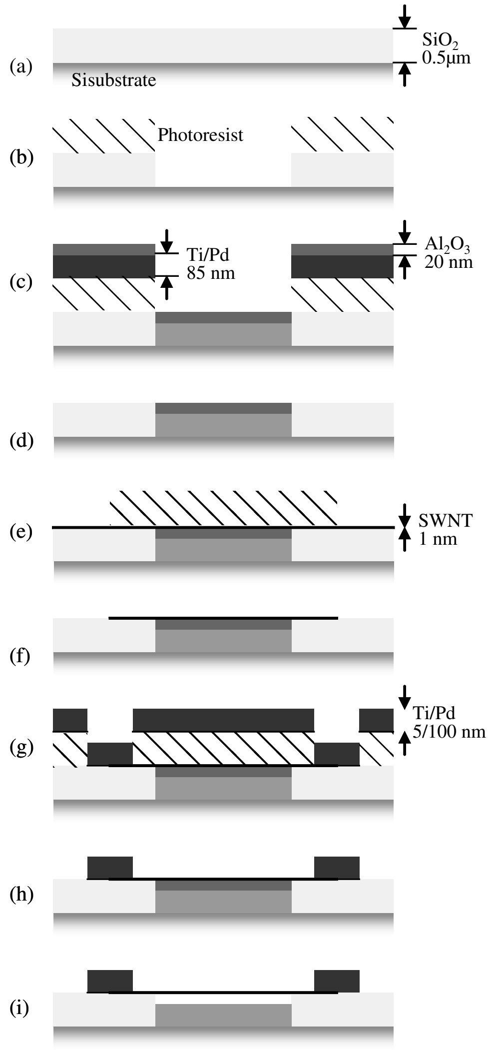

Figure 3.8 Process cross sections for creating a suspended nanotube fabric MMS test device showing (a) starting Si substrate with thermal oxide, (b) trench etched in oxide, (c) deposition of Ti/Pd embedded electrode and Al_2O_3 sacrificial layer, (d) lift-off to create filled trench, (e) spin coat of SWNT solution, (f) pattern of SWNT monolayer, (g) deposition of Ti/Pd clamp lines, (h) lift-off to create leads to bond pads, and (i) wet chemical removal of sacrificial layer to create final device structure.

of the nanotube solution mirrors photoresist spinning techniques. A dehydration bake at 200°C is first performed to remove any residual surface water. After allowing the wafer to cool, the solution is then spun onto the wafer. Multiple spins are required to produce the desired mean sheet resistance of the SWNT fabric of *Rs* 10 kΩ/□ with a standard deviation of approximately

0.4 kΩ/□ and a uniformity of 3.5%. The sheet resistance of the nanotube monolayer can be reliably varied between 10 kΩ/□ and several MΩ/□ by adjusting the concentration of the nanotube solution and the number of spin coating steps.

Once the desired nanotube fabric sheet resistance and density is obtained, positive g-line photoresist (e.g., Shipley 1805) is applied to the wafer (Figure 3.8e). The patterning of the nanotube layer is not limited by the type of photoresist employed; various types of resist have been used successfully. The photoresist-coated wafer is then exposed and developed to form the desired pattern. After development, the exposed carbon nanotubes can be removed cleanly by isotropic ashing in oxygen plasma while the nanotubes underneath the photoresist are protected from oxidation. Typically, an isotropic oxygen plasma of 300 W power is used for removing the exposed SWNTs at a pressure of 270 mTorr and an ashing time of 9 min. The photoresist is subsequently stripped in NMP resulting in a patterned SWNT monolayer fabric (Figure 3.8f).

In this example SWNT stripes are 100 μm long and 3 μm wide, although stripes with widths as small 0.25 μm have also been fabricated using the same process. In a subsequent, aligned EBL step, metal clamp lines (Ti/Pd, 50/1000 Å thick, 0.18 ± 0.02 μm wide) are defined by liftoff in PMMA resist on top of the SWNT stripes, parallel to the embedded electrodes at a distance of 1000 Å (Figure 3.8g,h). These clamps are necessary to prevent uncontrolled adhesion of the SWNTs to the lower electrode upon removal of the sacrificial layer in the following steps. Subsequently, the device electrodes and SWNT stripes are connected to bond pads so that individual junctions on a die can be electrically tested. The distance between SWNT stripe metallization and switching junction is 3 μm. Finally, the patterned SWNTs are suspended by wet chemical removal of the Al_2O_3 sacrificial layer in an aqueous base of TMAH, followed by rinse in DI water and isopropanol (IPA) (Figure 3.8i). Test sites are diced from the wafer and individual dies are wire-bonded into standard TSOP hermetically sealed packages for test and characterization on a corresponding probe socket board.

3.3.1.2 Principles of Operation

Unlike traditional microelectromechanical systems (MEMS) that use flexible membranes, these electromechanical bi-stable switches can be operated as a lumped element at frequencies well into the GHz range. This unique behavior stems from the minute mass of the SWNTs that makes up the throw, resulting in a characteristic frequency for the system in the THz range. The device operation can be considered from the point of view of the classic "ball in a potential well" energy diagram in Figure 3.9. The closing behavior of the MMS test device is illustrated in Figure 3.9a. An applied electrostatic force on the nanotube fabric deforms it, deflecting pulling it in the x-direction, along the potential energy curve. As the fabric is stretched further, the restoring elastostatic force in the fabric increases; hence, the electrostatic force

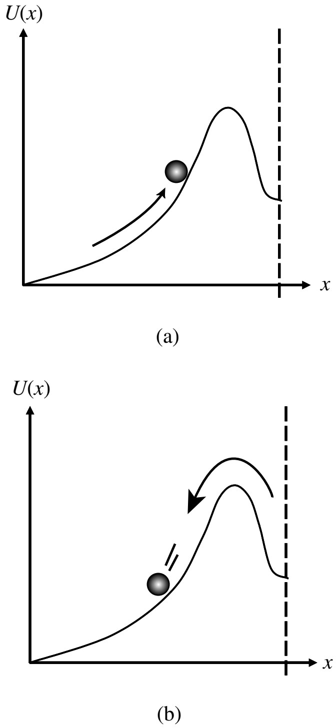

Figure 3.9 Potential energy curves depicting the (a) closing and (b) opening of the MMS.

required to continue the stretching increases. This is reflected by the increasing slope of the curve. When close to the underlying electrode, an attractive van der Waals force opposes the elastostatic force. These two forces balance at the local maximum in the potential energy curve. As soon as the leading edge of the deformed fabric passes this local maximum or "turning point," the attractive van der Waals force dominates and draws the fabric into full contact with the metal electrode. The opening behavior of the MMS test device is illustrated in Figure 3.9b. Without intervention, the ball will remain trapped in this potential well; however, if an oppositely directed electrostatic force is applied, the fabric can be physically moved over this potential barrier, to a location where its own stored elastostatic energy will restore it to the original neutral position. The design is expected to be quite robust due to the conservative nature of the molecular bond stretching. Unlike their macroscopic counterparts, the SWNT fabrics described here are immune to electromigration and defect-induced failure mechanisms.

Test structures similar to those described here have been successfully fabricated and switches between low- and high-resistance states reproducible with no failures. Details of these results have been reported by Ward and Brock and co-workers.[3–5]

3.3.2 NRAM™—a CMOS-Compatible Nonvolatile Memory Technology

By arranging and interconnecting an array of MMS devices, along with monolithically integrated CMOS control circuitry, a complete nonvolatile random access memory (RAM) technology can be created. This section describes one such implementation — the nanotube random access memory (NRAM™) created at Nantero.

3.3.2.1 Circuit Architecture and Description

As seen in Figure 3.10a, the CNT structure forms nonvolatile storage cells when integrated with NFET transistors in a memory array system composed of a matrix of nonvolatile storage cells. The memory array also comprises read and write word lines (WL0, WL1, etc.), release lines (RL0, RL1, etc.), and read, release, and write bit lines (BL0, BL1, etc.). A bit line decoder/driver is used to select bit lines to be activated. The bit lines are selected based on the address inputs and timing inputs. The applied bit line voltage levels are generated by an on-chip voltage generator. Vrd is the read voltage, Vrl is the release voltage, and Vw is the write voltage.

Each nonvolatile cell comprises a select transistor (TS#), a release transistor (TR#), and the nanotube structure itself (NT#), marked with a select node (SN#) and release node (RN#). The gate of TS# is coupled to WL#, the drain of TS# is coupled to BL#, and the source of TS# is coupled to select node SN#. NT# is coupled to REF# (typically ground). The gate of transistor TR# is coupled to RL#, and the drain of transistor TR# is coupled to bit line BL# by a connection that also couples the drain of transistor TR# to the neighboring cell along the WL#. The source of transistor TR# is connected to release node RN#.

3.3.2.2 Write/Read Operations

For a write operation in cell0, first a BL0 release voltage value Vrl is applied through transistor TR0 to node RN0 to ensure that the nanotube structure is in the OFF state. That is, RL0 will activate TR0, and the BL0 voltage is applied through the channel of TR0 to release node RN0. Transistor TR0 is then turned off. Transistor TS0 is activated by WL0, and the voltage Vw of BL0 is applied through transistor TS0 to select node SN0. The applied voltage Vw between nodes SN0 and REF0 (ground) will force the nanotube structure to the ON or logic "1" state. The near-ohmic connection between SN0 and REF0 represents the ON state. If the applied voltage is zero, the cell remains in the OFF state.

For a read operation, BL0 is driven high and allowed to float. WL0 is driven to high voltage and transistor TS0 turns on. BL0 is connected by the conductive channel of transistor TS0 to select node SN0. If the cell is in the ON state, then there will be a conductive path between SN0 and REF0 (ground), and the bit line voltage Vrd will decrease as the bit line is discharged through

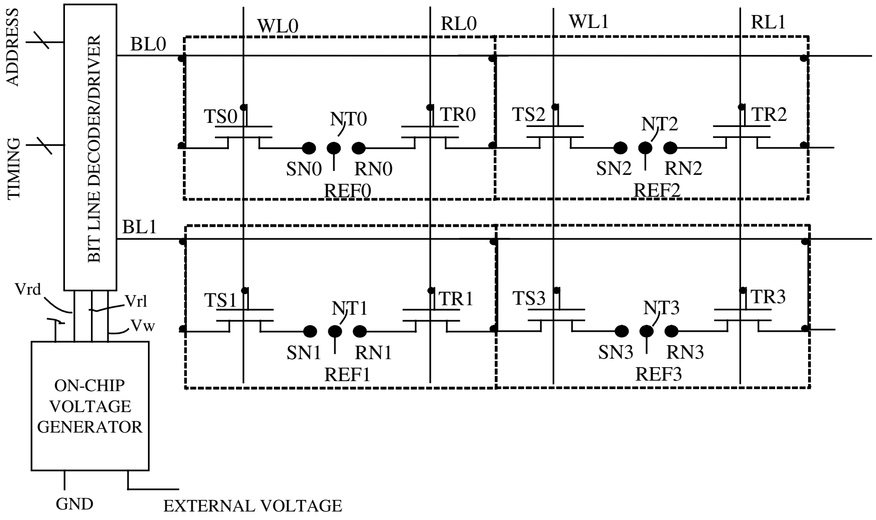

(a)

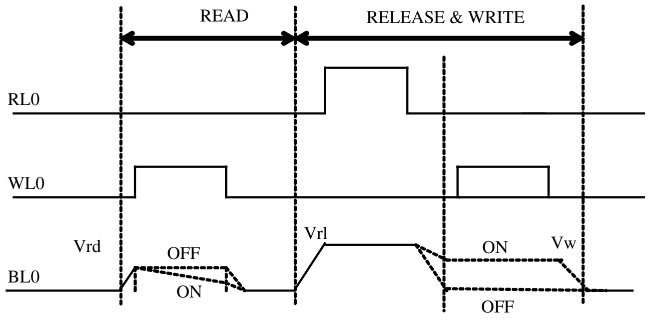

(b)

Figure 3.10 Sample NRAM™ architecture with (a) four MMS devices with two select FETs for each and (b) operation waveforms of the controlling signals in the circuit.

TS0, to SN0, to REF0 (ground). If, however, the cell is in the OFF state, then the path from BL0 through the TS0 channel to SN0 will indicate a high impedance (high mega ohm or giga ohm) relative to REF0 (ground), and bit line voltage Vrd will be unchanged. The sense amplifier/latch circuit (not shown) detects changes in BL0 voltage. If the voltage Vrd on BL0 has decreased, the latch is set to a logic "1" state. If the voltage Vrd is unchanged, then the latch is set to a logic "0" state. The read operation is nondestructive read-out (NDRO) of the cell information. No write-back/regeneration cycle is necessary. Also, if external power is lost, the information in the array is preserved (nonvolatile storage).

The operational waveforms of the device during the read, and release and write operations are shown in Figure 3.10b. During the read operation, cell0, for example, is selected by charging BL0 to a voltage Vrd in the 0.5 to 1 V range and driving WL0 high. If the cell is in the OFF (logic "0") state, Vrd is unchanged. If the cell is in the ON (logic "1") state, then the voltage Vrd decreases. This difference is amplified and latched (circuit not shown).

A write operation is preceded by a release operation. During release, cell0 is selected when BL0 is driven to voltage Vrl, which is typically in the 1 to 5 V range, and RL0 is driven high. BL0 voltage Vrl is applied through transistor TR0 to release node RN0. Cell0 is driven to the OFF state. At the start of the write cycle, cell0 is in the OFF state. Cell0 is selected when BL0 is driven to voltage Vw, which is typically in the 0.5 to 2 V range for writing a logical "1" state (cell is ON) and WL0 is driven to a high state. If BL0 voltage is zero when WL0 is driven to a high state, the cell remains in the OFF or logical "0" state.

3.4 Conclusion

Using monolayer fabrics of single-walled carbon nanotubes (SWNTs) offers a unique method of accessing molecular-scale (e.g., van der Waals) forces for the engineering of novel electronic structures. This chapter has described, in general terms, the methods for producing solutions of SWNTs that can be dispensed by commercial semiconductor coating systems to form monolayers (1 to 2 nm thick) of nanotubes for use as sparse conducting networks. The purity of these solutions has been confirmed, protocols for their use in commercial semiconductor foundries have been developed, and methods for the characterization of the resulting SWNT fabrics have been described.

In concert with the nanotube fabric technology, additional fabrication processing steps have also been developed to create a type of bi-stable device, the molecular microswitch (MMS), which exploits both the electrical and mechanical properties of SWNT fabrics. The MMS process steps are also fully CMOS compatible. As one example, a hybrid SWNT fabric/CMOS architecture has been described for a nonvolatile nanotube random access memory (NRAM™) using MMSs as the data storage element.

Acknowledgments

The authors wish to thank all the staff members at Nantero, without whose dedication and hard work the ongoing development of SWNT fabric and NRAM™ technology would not be possible. Specifically, we wish to thank Steve Buffat, George Ghenciu, Frank Guo, Steve Konsek, Mitch Meinhold, Rahul Sen, Ramesh Sivarajan, and Max Strasburg. We also thank the staff at LSI Logic (Gresham, OR) and BAE Systems (Manassas, VA) for helpful collaborations in transferring the Nantero fabrication process into commercial CMOS foundries.

References

1. Harris, P.J. *Carbon Nanotubes and Related Structures: New Materials for the Twenty-First Century*, Cambridge University Press, Cambridge, UK, 1999.
2. Rueckes, T. et al., Carbon nanotube-based nonvolatile random access memory for molecular computing, *Science*, 298, 94, 2000.
3. Ward, J.W. et al., A non-volatile nanoelectromechanical memory element utilizing a fabric of carbon nanotubes, *Proc. 2004 IEEE Non-volatile Mem. Conf.*, 24, 2004.
4. Brock, D.K. et al., A non-volatile molecular micro-switch for space-based memory applications, *Proc. GOMAC 2005*, April 2005.
5. Brock, D.K. et al., Carbon nanotube memories and fabrics in a radiation hard semiconductor foundry, *Proc. 2005 IEEE Aero. Conf.*, 1, 2005.

Chapter 4

Controlled Synthesis of Carbon Nanotubes Using Chemical Vapor Deposition Methods

Yung Joon Jung

Contents

4.1 Introduction 80
4.2 Carbon Nanotube Synthesis 81
4.2.1 Arc Discharge Method 81
4.2.2 Laser Ablation Method 82
4.2.3 Chemical Vapor Deposition Method 83
4.2.3.1 Carbon Nanotube Growth Using CVD 83
4.2.3.2 General Growth Mechanism of Carbon Nanotubes in CVD 84
4.3 Building Organized MWNT Architectures 85
4.3.1 Vapor Phase Catalyst Delivery CVD 85
4.3.2 Highly Organized Carbon Nanotube Architectures: Design 85
4.3.2.1 Substrate Site Selectivity of MWNTs 85
4.3.2.2 Substrate Preparation by Microfabrication 85
4.3.2.3 Experimental Setup for CVD Growth of Carbon Nanotubes 86
4.3.3 Highly Organized Carbon Nanotube Architectures: Experiment 88
4.3.4 3-Dimensional Carbon Nanotube Architectures 89
4.3.4.1 Multidirectional Carbon Nanotube Architectures 89
4.3.4.2 Multilayered Carbon Nanotube Architectures 89
4.4 Mechanism of Substrate Site Selectivity of Carbon Nanotubes 91

4.4.1 Experimental Procedures for Characterization 91
4.4.2 Morphologies and Elemental Analysis of SiO_2 and Si Surface 91
4.4.2.1 Surface Morphology of Si and SiO_2 Areas after CVD 91
4.4.2 Structural Analysis of Particles Formed on Si and SiO_2 Areas 92
4.5 Building Controlled SWNT Networks on a Large Scale 95
4.5.1 Design of SWNT Networks on Nanoscale Patterned SiO_2 and Si Structures 95
4.5.1.1 Introduction 95
4.5.1.2 Experimental Details 96
4.5.2 Building of SWNT Networks on Nanoscale Patterned SiO_2 and Si Structures 96
4.5.2.1 High-Density SWNT Networks on Nanoscale Patterned Structures 96
4.5.2.2 Roles of CVD Parameters and Catalyst Particle Sizes for High-Density SWNT Growth 98
4.5.3 Effect of Substrate for SWNT Growth 99
4.5.3.1 SWNT Growth on Patterned SiO_2 and Si Substrates 99
4.5.4 Mechanism of SWNT Growth on Si and SiO_2 Substrates 99
4.5.4.1 Role of Catalyst Particles in SWNT Growth on Si and SiO_2 Substrates 99
4.6 Fabrication of Hierarchically Branched Carbon Nanotubes Using Controlled Nanochannels in Templates 101
4.6.1 Introduction 101
4.6.2 Synthesis of Hierarchically Branched Nanotubes 101
4.6.2.1 Designing AAO Nanochannel Templates 101
4.6.2.1 Synthesis of Hierarchically Organized Carbon Nanotubes 102
Acknowledgments 105
References 105

4.1 Introduction

This chapter will discuss the methodologies and mechanisms for the controlled synthesis of carbon nanotubes and building micro- and nanoscale nanotube-based architectures using various chemical vapor deposition (CVD) methods and micro- and nanofabrication techniques. Low-temperature CVD methods are becoming a strong candidate for the large-scale production of carbon nanotubes. Especially, CVD methods enable us to arrange carbon nanotubes into well-defined configurations by controlling catalyst positioning and the CVD process.

Since the first discovery by Sumio Iijima at NEC Co. in 1991,[1] carbon nanotubes have attracted considerable interest due to their unique one-dimensional

nanoscale structures and superior electrical, mechanical, and thermal properties.[2–4] Particularly, carbon nanotubes have fascinating electrical properties such as the ability to withstand high current density (10^9 Amps/cm^2) and ballistic conductance by virtue of their one-dimensional electronic structure.[5,6] These features show significant potential for various applications in the future. The most promising applications of carbon nanotubes are those involving use in electron emission devices[7,8] and nano-electronics such as field effect transistors,[9–12] nanotube-interconnects,[13–15] and nano sensors.[16] To build an integrated nanotube-based system, it is essential to fabricate carbon nanotubes on the designed substrates in a controllable manner. Among several methods for the synthesis of carbon nanotubes, which include arc discharge,[1] laser ablation,[17] and chemical vapor deposition (CVD),[18–21] the CVD method is the most suitable for the controlled synthesis of carbon nanotubes on substrates. In the first part of the chapter, a method to create 1-to-3-D architectures of aligned multi-walled carbon nanotube structures on the patterned SiO_2/Si substrates will be presented. These highly selective and organized carbon nanotube structures are produced by gas-phase delivery of a xylene-ferrocene mixture onto lithographically machined silica surface templates. The level of control provided by this method enables the construction of complex carbon nanotube architectures, which could lead to nanotube-based devices and systems in a scalable fashion. The studies that clearly elucidate the mechanism of carbon nanotube growth selectivity on SiO_2 vs. Si will also be discussed by analyzing the chemistry and the structures of catalyst particles on Si and SiO_2 substrates using several high-resolution characterization techniques.[22–25]

In the second part, template-based controlled synthesis of carbon nanotubes will be described. Especially, a generic synthetic approach to design will be introduced and a large variety of complex carbon nanotube architectures will be built by using the rational design of hierarchically branched nanochannels inside anodic aluminum oxide templates followed by CVD for nanotube growth. These include nanotubes having several generations of Y-branches and a multiplicity of sub-branches.

Finally, a further enhanced method to build high-yield growth of single-walled carbon nanotube architectures in nano-scale forming fully bridged networks between patterned structures will be discussed. By controlling conventional methane CVD parameters and transition metal catalyst deposition and selecting optimal substrate materials, these organized growths are obtained. The role of catalyst particles in carbon nanotube growth on silicon and silicon oxide substrates will be also discussed to understand the mechanism of SWNT growth.[26,27]

4.2 Carbon Nanotube Synthesis

4.2.1 Arc Discharge Method

The arc discharge method has been widely used for the synthesis of both single-walled nanotubes (SWNT) and multiwalled carbon nanotubes (MWNT) in the past ten years (Figures 4.1a). In his first experimental report, Iijima

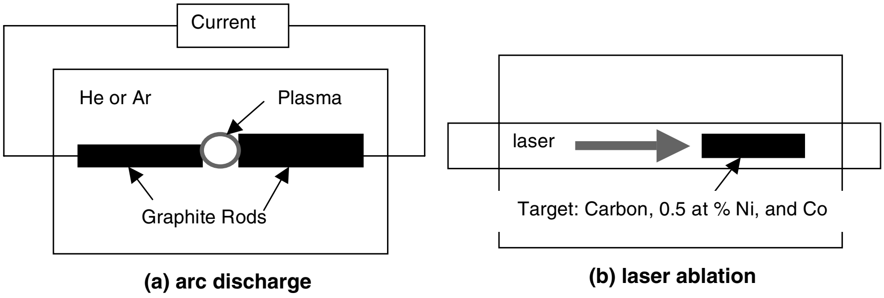

Figure 4.1 Schematics showing experimental setups for (a) arc discharge and (b) laser ablation methods for the synthesis of carbon nanotubes.

showed carbon nanotubes formed on the graphite electrode used in arc-discharge system for fullerene synthesis.[1] After that, Ebbesen and Ajayan developed the large-scale production method of carbon nanotubes (MWNT) by adjusting the growth condition in the arc-discharge process.[28] In this method, two graphite rods (anode and cathode) are generally used as electrodes and He or Ar gas is introduced for inert atmosphere conditions. As the rods are brought close together, a discharge occurs and results in the formation of plasma, where the temperature is close to 3500°C. Thus, the anode is consumed by plasma and ionized carbon atoms are attracted to the graphite cathode. Rod-like deposits are formed on this electrode and MWNTs can be collected in the core of deposits. The deposit also contains other graphitic materials such as fullerenes, amorphous carbon, and polyhedron carbon species. Synthesized MWNTs are usually very straight and have lengths on the order of microns and diameters in the range of 5 to 30 nm. Also by strong van der Waals interactions, nanotubes are usually seen in bundles.

SWNTs are made using a combination of metal catalysts and dense carbon vapor using a similar method for the MWNT growth in the arc-discharge system.[29,30] A hole is drilled in the anode and packed with the mixture of the metal catalysts (Ni and Y) and graphite powder in specific ratios. When plasma is formed between the rods, the rapid growth of SWNTs occurs and results in the formation of weblike networks that contain ropes of SWNTs inside the reaction chamber.

4.2.2 Laser Ablation Method

Using a laser ablation method, high-quality SWNTs at gram scale can be obtained[17] (Figure 4.1b). In this process, a carbon target containing about 0.5% of Ni and Co is placed in a tube furnace heated to 1200°C and intense laser pulses are used to ablate the target under inert conditions. Then, the nanotube material that is generated is collected onto a water-cooled target using inert gas flow. The produced SWNTs are mostly in the form of ropes consisting of tens of individual carbon nanotubes.

4.2.3 Chemical Vapor Deposition Method

4.2.3.1 Carbon Nanotube Growth Using CVD

Although arc discharge and laser ablation have been the primary methods for producing high-quality carbon nanotubes, they have drawbacks. First of all, arc discharge and laser ablation methods are costly due to their high-temperature processes and the limited number of carbon nanotubes that can be produced. Second, both methods grow carbon nanotubes in highly tangled forms with unwanted carbon and metal impurities. Also, controlling carbon nanotubes during growth, such as selectively growing at specific locations and directly building highly organized carbon nanotube structures, is impossible using arc discharge and laser ablation methods. With these considerations in mind, CVD methods are becoming a strong candidate for the large-scale production of carbon nanotubes.

The growth process in CVD involves heating catalyst materials to high temperatures (500 to 1200°C) in a tube furnace and flowing hydrocarbon gases through the tube reactor for a period of time.[18–21,31–33] For MWNT growth, catalytic decomposition of hydrocarbon gases (acetylene, C_2H_2; ethylene, C_2H_4; xylene, C_8H_{10}; or benzene, C_6H_6) on catalytic nanoparticles, such as Ni, Co, and Fe, is required in the growth temperature of 500 to 800°C.[34–37] As shown in Figure 4.2a, highly dense MWNTs grown by CVD methods can be easily aligned with others by van der Waals attraction forces, which allow carbon nanotubes to grow perpendicular to the substrate. Currently, a plasma-assisted CVD method is also being used to grow MWNTs with a further reduced reaction temperature.[38,39]

Also, the growth of SWNTs has been enabled by the use of CVD processes and it is still being actively developed by many researchers in many different ways due to the significant potential for the large-scale synthesis and controlled growth of SWNTs. Initial significant progress was made by Dai et al. and many other researchers in obtaining high-quality SWNTs using the CVD method.[40–44] In their experiments, Dai and co-workers used methane (CH_4) as a carbon source

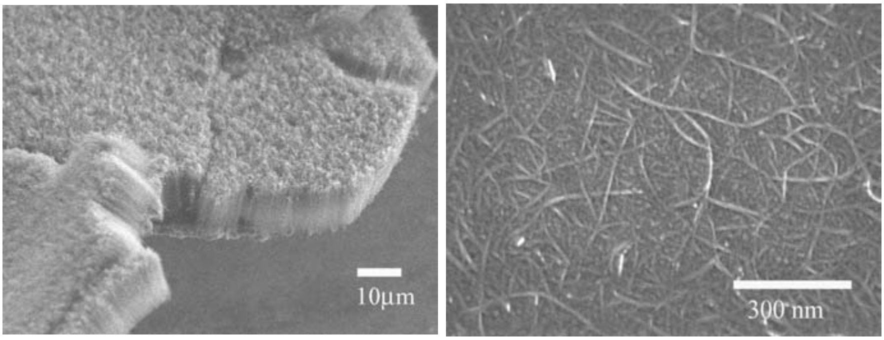

Figure 4.2 Scanning electron microscopy (SEM) images after the growth of (a) MWNTs and (b) SWNTs using thermal CVD methods.

and Fe/Mo bimetallic catalyst supported on a sol-gel derived alumina-silica multicomponent material with reaction temperatures in the range of 850 to 1000°C. Compared with the growth of MWNTs in the CVD method, relatively higher reaction temperatures and smaller catalyst particle size are required to form SWNTs. The choice of CH_4 over other hydrocarbon sources is essential due to its stability at high temperatures, which eliminates self-pyrolysis that may cause the generation of amorphous and graphitic carbon.[3,45] Also, by introducing highly dispersed catalyst materials with strong metal–substrate interactions, good control of SWNT growth can also be achieved.

Figure 4.2b shows the typical SEM image of as-grown SWNTs using the CVD method. The produced SWNTs are mostly in the form of ropes consisting of tens of individual carbon nanotubes. The length of SWNTs can be in the range of a few microns to centimeters, and it can be controlled by the growth time and synthesis methods.[46]

4.2.3.2 General Growth Mechanism of Carbon Nanotubes in CVD

The growth mechanism of carbon nanotubes by the CVD method is still under active investigation. However, the generally accepted model for carbon nanotube growth proposed by several researchers, shown in Figure 4.2, is based on the fact that the high activity of carbon in the gas phase drives carbon to dissolve in the nano-sized catalyst particles (transition metals: Ni, Co, or Fe).[3,47,48] The particles may thus easily become supersaturated or saturated with carbon atoms arising from the decomposition of hydrocarbon gases. The precipitation of carbon from the saturated metal particles leads to the formation of tubular carbon solids in sp^2 structure (graphitic). At the moment, tubule formation is favored because it has no dangling bonds compared with graphite structure and, therefore, can obtain the lowest energy state form. In this model, the metal particles are supported on the substrate material and either strong or weak metal–substrate interaction is assumed. In the first case, Figure 4.3a, carbon nanotubes grow upward from the metal particles that remain attached to the substrate (extrusion or root mechanism). In the case of weak metal–substrate interaction, Figure 4.3b, the particles are detached from the substrate and move up to the head of the nanotubes (tip growth mechanism). A major drawback for

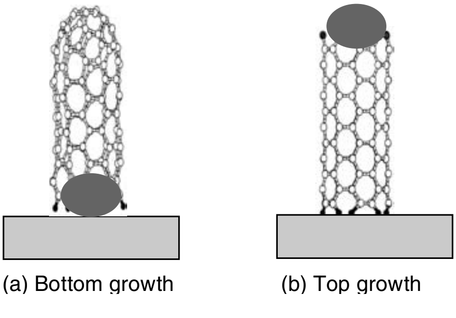

Figure 4.3 Schematic illustrations for two general carbon naotube growth models.

CVD-grown carbon nanotubes is the high density of structural defects compared with carbon nanotubes obtained by arc discharge and laser ablation methods. A low-temperature process for carbon nanotube growth is thought to be one reason for the high density of defects because the CVD process doesn't provide enough thermal energy to anneal carbon nanotubes into perfectly graphitized crystalline structures.[4,45]

4.3 Building Organized MWNT Architectures

4.3.1 Vapor Phase Catalyst Delivery CVD

Rao et al. report the growth of carbon nanotubes through the vapor phase delivery of metal-organic catalyst precursors.[49] In their experiment, various metal-organic catalysts such as ferrocene, cobaltocene, or nickelocene, containing both the transition metals (Fe, Co, and Ni) and hydrocarbon species, were used in a reductive atmosphere to produce carbon nanotubes. Based on the above result, a simple and economic way for producing bulk quantities of carbon nanotubes was developed by Andrews et al. using CVD through the catalytic decomposition of a ferrocene [$Fe(C_5H_5)_2$)–xylene (C_8H_{10})] mixture at 675°C over quartz substrate in a tube reactor.[50]

One of the unique features of this CVD method is that it does not require precatalyst deposition on substrates. Also it can be operated at atmospheric pressure with moderate temperatures, and a process of this nature allows us to scale up the yield of carbon nanotubes easily and can be used for the continuous production of carbon nanotubes.

4.3.2 Highly Organized Carbon Nanotube Architectures: Design

4.3.2.1 Substrate Site Selectivity of MWNTs

Another advantage of the vapor phase catalyst delivery CVD method is the strong substrate site selectivity for carbon nanotube growth. Zhang et al. show the substrate site selective growth of vertically aligned carbon nanotubes using metal-organic precursor (ferrocene/xylene) in the CVD process.[51] In their experimental report, high-density aligned MWNTs were obtained on silicon oxide (SiO_2) substrate surfaces after the CVD process. However, there was no carbon nanotube growth on the silicon (Si) substrate surface (Figure 4.4). Hence, by using a conventional lithography process, they showed the strong possibility of building selectively grown carbon nanotube structures on a patterned SiO_2 area without any precatalyst deposition step in the fabrication process.

4.3.2.2 Substrate Preparation by Microfabrication

Building highly organized micron-scale carbon nanotubes architectures in predetermined orientations and locations starts from designing patterned SiO_2/Si structures using conventional microfabrication techniques.[52,53] Figure 4.5 illustrates the fabrication process to create patterned SiO_2/Si structures for the building of MWNTs structures using a vapor phase catalyst delivery CVD method.

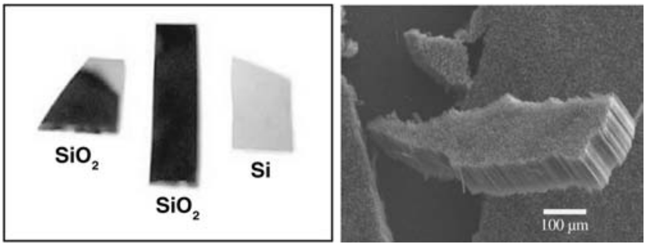

Figure 4.4 Substrate-dependent growth of MWNTs on planar SiO_2 and Si substrates by vapor phase catalyst delivery CVD method (ferrocene/xylene). The SEM image of MWNT film is deposited on Si substrate by vapor phase catalyst delivery CVD method (ferrocene/xylene). For better observation of the thickness of the carbon nanotube film and the degree of alignment, the MWNT array was partially peeled off from the silica substrate using tweezers. (Taken from Zhang et al., *Appl. Phys. Lett.*, 77, 23, 2000. With permission.)

The SiO_2 layers, with a thickness of 80 to 1000 nm, were grown by plasma enhanced CVD (PECVD) or thermal oxidation methods as shown in Figure 4.5b. In some cases thicker SiO_2 layers (up to ~8 μm) were deposited to create a high aspect ratio of patterned SiO_2/Si structures. After that, photoresist (PR1813) was coated on the SiO_2 surface using a spin coater (Figure 4.5c), and the patterns of variously shaped SiO_2/Si structures were generated by photolithography followed by the combination of wet hydrogen fluoride (HF) solution and/or a dry etching process as seen in Figure 4.5d,e. Finally, the photoresist layer on patterned oxide structures was removed and consequently cleaned with DI water. Figure 4.6 shows SEM images of patterned SiO_2/Si structures prepared by the above method before CVD process for carbon nanotube growth.

4.3.2.3 *Experimental Setup for CVD Growth of Carbon Nanotubes*

In our experiment, carbon nanotubes (MWNTs) were produced using the vapor phase catalyst delivery CVD method by exposing a mixture of ferrocene and xylene to prepared substrates. The CVD growth was carried out at an optimized temperature of about 800°C, for 5–30 minutes in a conventional tube furnace. The schematic of the experimental setup is depicted in

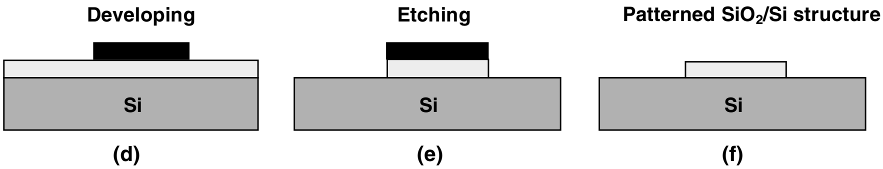

Figure 4.5 Illustration of Si process to create patterned SiO_2 structures: (a) Si (100) wafer, (b) SiO_2 layer deposition, (c) photoresist coating, (d) photolithography, (e) etching SiO_2 layer, and (f) removing photoresist and the completion of processes.

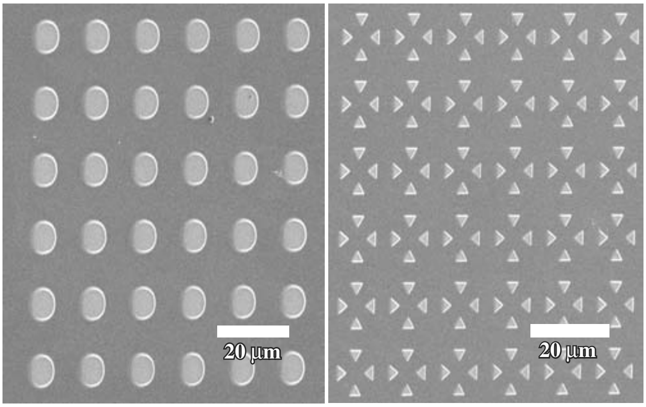

Figure 4.6 SEM images showing patterns of SiO_2/Si of various shapes fabricated by microfabrication techniques described in the text.

Figure.4.7. Prepared SiO_2/Si patterns were first ultrasonically cleaned in acetone and a DI water bath and placed into a tube furnace. In the first experimental step, the CVD chamber was pumped down to a vacuum level on the order of 10^{-2} Torr (50 to 100 mTorr), backfilled with flowing argon to a pressure of about 100 mTorr, and heated up to the desired temperature. After the furnace was heated to the deposition temperature of 700 to 800°C, a solution of ferrocene in xylene at concentrations of ~0.01 g/mL was prevaporized at 150 to 160°C and introduced into the quartz tube. Due to the pressure difference between the cylinder containing the prevaporized ferrocene–xylene

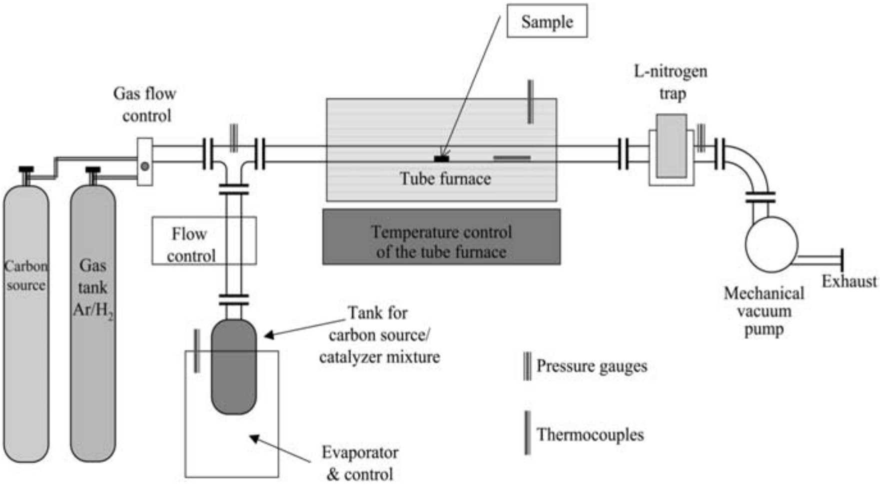

Figure 4.7 Schematic illustration of the CVD system for vapor phase catalyst delivery method for carbon nanotube growth (ferrocene–xylene).

mixture and the CVD system, catalyst and carbon sources were automatically introduced into the CVD chamber to grow carbon nanotubes. Xylene provides the carbon source while Fe from ferrocene serves as the catalyst for the MWNT growth. After the desired reaction time had elapsed, as estimated from the desired nanotube length, the carbon source and catalyst valves were closed and the tube was cooled down in an argon atmosphere.

4.3.3 Highly Organized Carbon Nanotube Architectures: Experiment

Figure 4.8 shows the typical SEM images of organized carbon nanotube architectures formed on preselected substrate sites. It is clearly seen that vertically aligned carbon nanotubes have grown only on the patterned SiO_2 structures (about 100 nm in thickness), while no nanotube growth is observed on pristine Si surfaces or on the native oxide layer. The height of these nanotube pillars is about 50 to 100 μm and can be controlled by changing the time of the CVD process. Blocks of micrometer-sized, cylindrical pillars of vertical, densely organized carbon nanotubes are seen growing from the underlying SiO_2 island patterns, depicted by SEM image and schematically in Figure 4.8. The primary difference between the three cylindrical pillar array sets shown in Figure 4.8a is the separation between individual blocks (2, 5, and 10 μm).

Carbon nanotube structures with different shapes, such as square, triangle, rectangular, and even complex geometry, can be constructed by simply changing the design of SiO_2 patterns, as shown in Figure 4.9. In all cases, the carbon nanotube structures inherit the shapes of the SiO_2 patterns on the

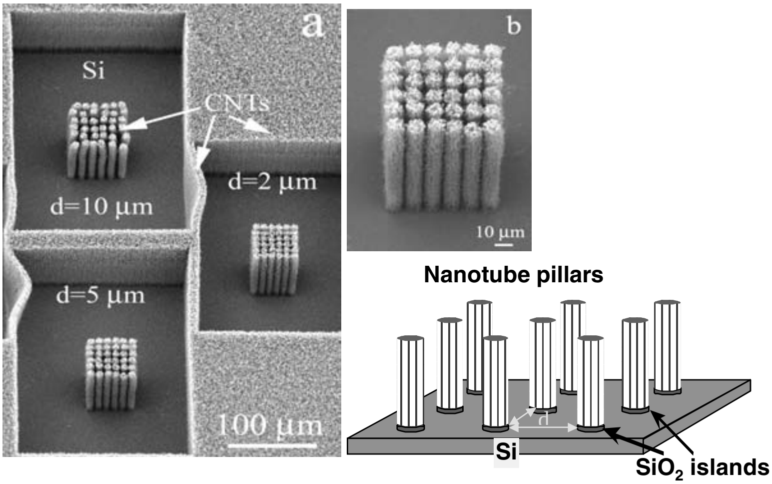

Figure 4.8 Highly ordered nanotube structures grown by chemical vapor deposition from ferrocene–xylene and schematic describing formation of carbon nanotubes on the patterned SiO_2/Si structures. Carbon nanotube pillars grow only on silica parts of the lithographically pretreated silica/silicon substrate, and they keep the perpendicular orientation to the surface for the whole length.

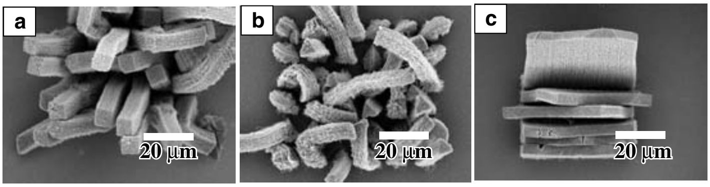

Figure 4.9 Organized aligned carbon nanotube structures from differently shaped silica structures. (a) squares, (b) triangles, and (c) rectangular structures of carbon nanotube architectures.

substrate. We can obtain blocks of ordered carbon nanotubes of predetermined shapes that are as long as 100 μm by merely extending growth time.

Only the in-plane dimensions of silica templates determine the number of carbon nanotubes in each structure (e.g., one pillar). We note that there is no carbon nanotube growth observed from the sidewalls of <100-nm-thick silica islands used in these experiments. However, using thicker silica features results in the in-plane growth (hence, multiple orientations simultaneously) of carbon nanotubes from the sidewalls, as described later. The nanotube blocks remain attached to the substrate even for nanotube lengths >100 μm, indicating reasonable adhesion between the nanotubes and the substrate. We note that the constituent nanotubes within each block respond in a coordinated fashion, such as bending during growth, indicating that the nanotubes are held together within organized structures by coordinated van der Waals–type attraction.

4.3.4 3-Dimensional Carbon Nanotube Architectures

4.3.4.1 Multidirectional Carbon Nanotube Architectures

In the previous section, unidirectional oriented carbon nanotube architectures, which are perpendicular to the substrate surface, were obtained by keeping the thickness of SiO_2 structures below 100 nm. By using thick SiO_2 layers (5 to 10 μm), we were able to create multidirectional growth of carbon nanotubes. For instance, carbon nanotube growth in mutually orthogonal directions is possible by employing templates consisting of deep etched trenches (drilled all the way to the Si substrate) separating several-micrometers-tall SiO_2 towers or lines.

Figure 4.10 shows vertically and horizontally (with respect to the substrate surface) aligned carbon nanotube architectures on various deep-etched SiO_2 structures using the reactive ion etching method, and the schematic models provide excellent examples that demonstrates this concept. Also note that the placement of carbon nanotubes is in two orthogonal directions parallel to the substrate plane itself.

4.3.4.2 Multilayered Carbon Nanotube Architectures

For the multilayered growth of carbon nanotubes, a layer of SiO_2 was patterned and then suspended on Si pillar structures. First, a thermally grown SiO_2 film (2 to 3 μm) was patterned using conventional lithography and etching

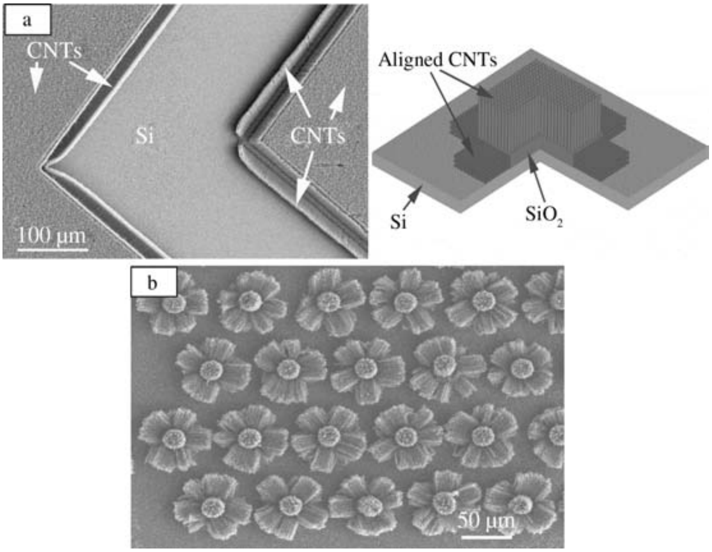

Figure 4.10 (a) Carbon nanotube bundles oriented in horizontal and vertical directions on the deep-etched Si oxide trenches. (b) Repeating carbon nanotube "daisies" arrays produced on cylindrical-shaped tall SiO_2 towers (5 μm).

techniques. Then, the deep etching (40 to 50 μm) of the Si wafer, undercutting the silica layer, was performed using KOH solution at 50°C, and it generated a suspended layer of SiO_2 on Si pillars.

The SEM images in Figure 4.11 show arrays of multilayered carbon nanotube structures that grow in two opposite directions (up and down) from the top and bottom surfaces of a circular SiO_2 layer suspended on an Si base pillar.

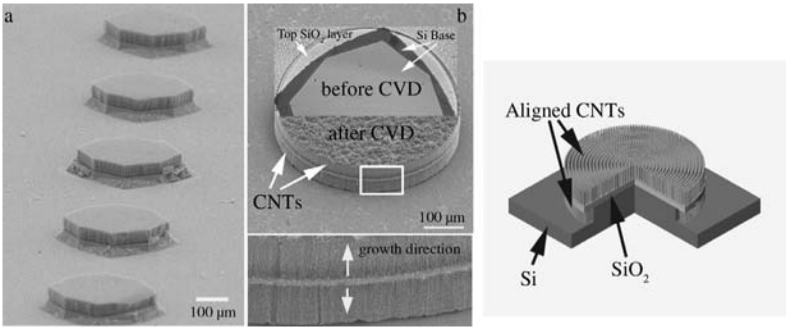

Figure 4.11 (a) A low-magnification SEM image showing arrays of aligned carbon nanotube structures grown at a 180° angle with respect to each other (up and down). (b) An optical micrograph showing the SiO_2 layer (transparent) on the Si base pillar (opaque). The two growth directions from the SiO_2 surfaces (inset) and a schematic illustration of nanotube bilayer growth are also shown.

Transparent patterned SiO_2 films, circularly shaped, on the Si pillar produced by wet etching of Si are observed in optical microscopy images (Figure 4.11b) before CVD. The circle-shaped transparent layer is the silica membrane, and the darker region shows the Si pillar supporting it.

4.4 Mechanism of Substrate Site Selectivity of Carbon Nanotubes

4.4.1 Experimental Procedures for Characterization

As described in the previous section, selectively grown carbon nanotubes were produced using a thermal chemical vapor deposition (CVD) method by exposing a mixture of ferrocene and xylene vapor to the patterned SiO_2/Si substrates at 800°C for 10 to 20 minutes. Pressure was around 100 mTorr and an argon atmosphere was supplied to prevent the patterned SiO_2/Si substrate surface from oxidation. After CVD, aligned carbon nanotubes were grown selectively on the patterned SiO_2 structures but not on the Si surface.

Scanning electron microscopes (SEM) were employed to characterize the growth of carbon nanotubes and surface morphology of the designed substrates after nanotube growth. To examine the morphology of the SiO_2 surface area, the grown carbon nanotube layer was partially removed using tweezers. For the elemental analysis over the substrates after carbon nanotube growth, electron probe micro analyzer (EPMA) with wavelength-dispersive spectroscopy for x-rays and Auger electron spectroscopy were used. A transmission electron microscope (TEM) operated at 300 keV was employed to characterize the structure of catalyst particles and carbon nano- tubes on the substrate. For obtaining the diffraction patterns of particles formed in Si and SiO_2 matrix, an electron beam with 20 to 30 nm diameter was used to minimize contributions from SiO_2 and Si. For the TEM sample preparation for cross-sectional observation, carbon and tungsten films were deposited on the surface of the areas of interest to protect the surface of interest from ion damage. Then, extra materials were removed from both sides of the region of interest using focused ion beam (FIB), until very thin (electron microcopy transparent) specimens (250 nm) were obtained. The thinned part was then removed from the substrate and mounted on a copper mesh using a "microsampling technique."[54]

4.4.2 Morphologies and Elemental Analysis of SiO_2 and Si Surface

4.4.2.1 Surface Morphology of Si and SiO_2 Areas after CVD

The vapor phase catalyst delivery method mentioned here is different from that used in conventional thermal CVD methods in which patterned catalysts on the designed positions need to be deposited on the substrate surfaces before carrying out CVD.[14,21] Therefore, in this method, vapor phase catalyst, Fe, and carbon source are supplied simultaneously all over the substrate at high temperature (800°C).

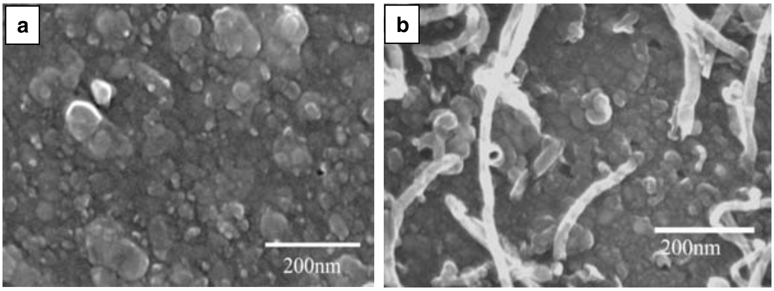

Figure 4.12 High-resolution SEM images on Si and SiO_2 surfaces after carbon nanotube deposition. (a) Close observation on the bared Si surface where no carbon nanotubes have grown. (b) The surface morphology of SiO_2 region after scratching carbon nanotubes. A few nanotubes remained on the SiO_2 surface.

Figure 4.12a,b shows the surface morphology of Si and SiO_2 after CVD. A close view of the Si surface shows that many particles in the range of 20–100 nm are formed on the Si surface, but these apparently do not aid in carbon nanotube growth (Figure 4.12a). A dense film of particles is also observed on the SiO_2 surface where aligned carbon nanotubes grow very well (nanotubes were removed in Figure 4.12b). Particle sizes are observed to be around 20 to 40 nm in the SiO_2 region but larger in the Si region.

4.4.3 Structural Analysis of Particles Formed on Si and SiO_2 Areas

Clear information on these Fe-containing particles after carbon nanotube growth could be obtained by cross-sectional TEM observation of the substrates. TEM images of the cross sections of the substrates after CVD growth of carbon nanotubes are shown in Figure 4.13 and Figure 4.14. On the SiO_2 area, carbon nanotubes as well as Fe-containing particles can be easily identified, even after removing most of the aligned nanotubes (Figure 4.13a,b). Irregularly shaped particles 10 to 40 nm in diameter appear on the top surface of the oxide

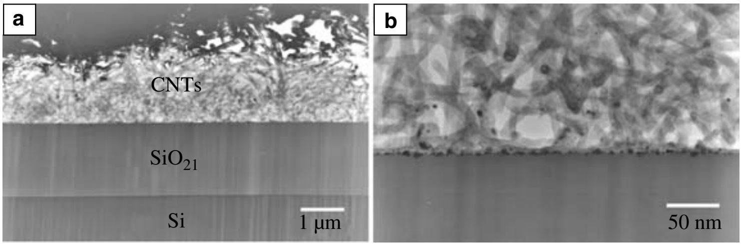

Figure 4.13 TEM images of the cross section of the SiO_2 substrate. (a) SiO_2 area after CVD growth and subsequent removal of carbon nanotubes. (b) Enlarged image from the nanotube/SiO_2 interface in (a) showing the formation of particles on SiO_2 surface and the growth of nanotubes from the particles formed.

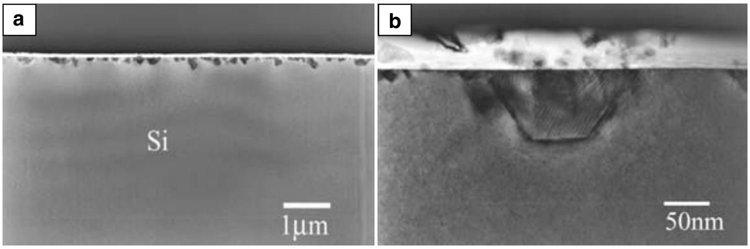

Figure 4.14 TEM images of the cross section of the Si substrate. (a) Si area without any carbon nanotube growth but with precipitates of submicron-sized particles near the surface. (b) Enlarged area from (a) showing the formation of Fe-containing crystals during CVD processing.

area as well as inside the cavities of carbon nanotubes. Nanotubes having diameters of 30 to 40 nm are grown from these dispersed particles, while on the surface of the Si area no trace of nanotubes is found. Instead, larger precipitates of submicron-sized particles are observed beneath the surface, as shown in Figure 4.14a,b.

Selective area electron diffraction was performed to identify the structural information of particles formed on SiO_2 and Si areas. Then patterns were analyzed from fundamental diffraction equations (Bragg equation).

The calculated results from diffraction patterns (DP) in Figure 4.15 indicate that the formed irregularly shaped nano-sized particles on the top of SiO_2 surfaces are pure gamma iron (fcc Fe), which is an active catalyst for carbon nanotube growth. However, on the Si surface, diffraction patterns suggest the formation of iron silicide (tetragonal) and iron silicate (orthorhombic). Therefore, a cross-sectional TEM image of the Si region shows that during CVD processing, nucleation of these new phases occurs from the Si surface and grows into the Si matrix (particle size about 50 to 100 nm; Figure 4.16b).

Compared with gamma Fe particles having irregular shapes on the SiO_2 surface (Figure 4.17a), these crystallized particles inside the Si matrix were formed with well-defined shapes showing stable compound formation through the chemical reaction between Si and vapor/solid phase Fe during the high-temperature CVD process. Electron beam diffraction results on these crystallized particles proved that the particles are mainly iron silicide ($FeSi_2$) and silicate (Fe_2SiO_4), as shown in Figure 4.17b.

From the above results, we draw the conclusion that on the SiO_2 region, the high activity of carbon in the gas phase drives carbon to dissolve into Fe particles formed on the substrate surface during decomposition of ferrocene at high temperature. The Fe particles may thus easily become saturated or supersaturated with carbon atoms and the precipitation of carbon from the surface of the Fe particle leads to the formation of tubular carbon solids in sp^2 structures. Iron particles are chemically stable on the SiO_2 during the full CVD process time. Therefore, the γ-Fe catalysts with small dimensions can effectively catalyze the growth of highly dense carbon nanotubes on the SiO_2 region.

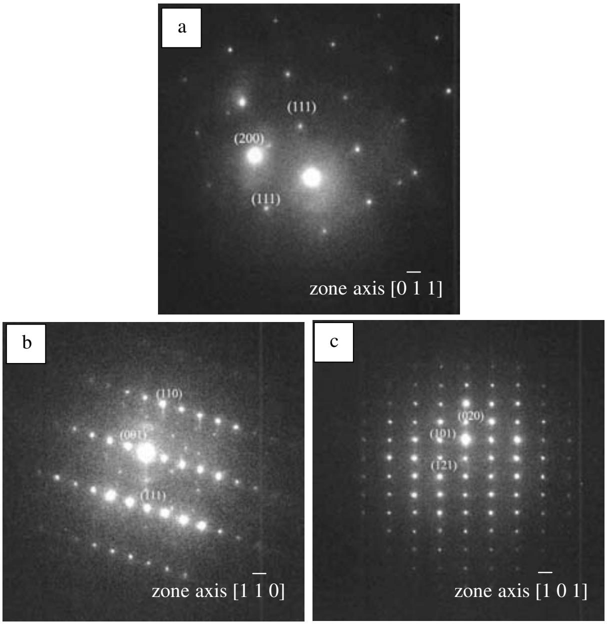

Figure 4.15 Selective area diffraction patterns from the particles on the SiO_2 surface (Figure 4.13) and on the Si surface (Figure 4.14) (a) Gamma iron (fcc Fe) formation on SiO_2 surface. (b) Iron silicide and (c) iron silicate formation during CVD process on Si surface.

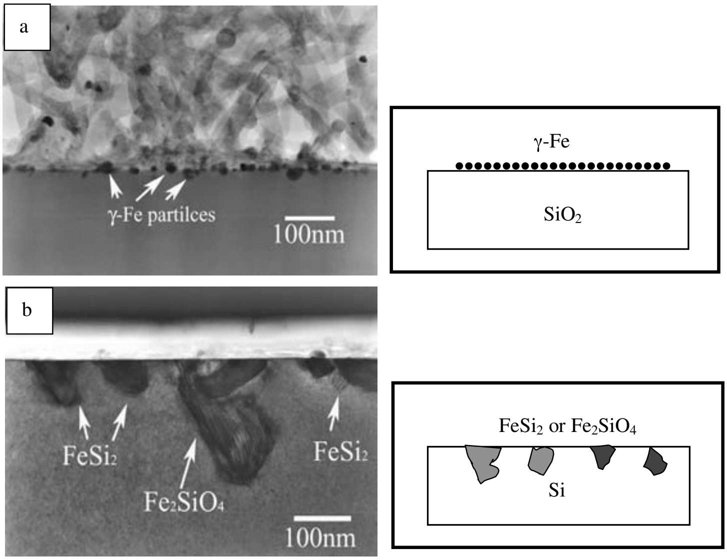

Figure 4.16 TEM images and illustrations show (a) γ-Fe formation on SiO_2 surface and (b) $FeSi_2$ or Fe_2SiO_4 formation on SiO_2 region during CVD of carbon nanotubes.

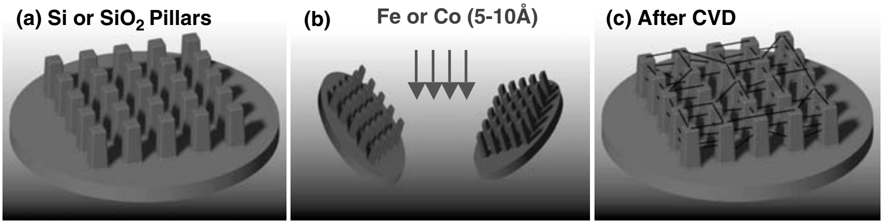

Figure 4.17 Schematic for designing high-density single-walled nanotube networks on patterned substrates using the thermal chemical vapor deposition (CVD) method. (a) Preparing submicron-scale patterned substrates (Si or SiO_2) by x-ray lithography. (b) Thin catalyst (Fe or Co) film deposition on the 45°-tilted patterned substrate uses a two-step process to cover the sides of the pillars. (c) Schematics of SWNT networks bridging the pillars after CVD.

However, on the Si surface, a chemical reaction occurs between the Si, Fe, and oxygen, which exist in small concentrations in our vacuum system. This reaction is dominated by diffusion of Fe through the native SiO_2 layer at high temperature. This results in a complete change of the chemical nature of the deposited Fe particles from an active Fe catalyst to stable compounds such as $FeSi_2$ and Fe_2SiO_4, which are noncatalytic.[55]

4.5 Building Controlled SWNT Networks on a Large Scale

4.5.1 Design of SWNT Networks on Nanoscale Patterned SiO_2 and Si Structures

4.5.1.1 Introduction

The most promising applications of SWNTs are those involving their use in future electronics due to their specific electronic structures and transport properties with their 1 to 2 nm dimensions. However, for building integrated self-assembled SWNT-based systems, it is necessary to controllably produce density-controlled SWNT networks on a large scale. There have been previous reports about the patterned growth of single-walled carbon nanotubes on predesigned substrates using methane (CH_4) as a carbon source.[38,56–58] In particular, Dai et al. and Huang et al. showed the self-directed growth of suspended SWNT networks on 10 μm silicon tower tops having a liquid phase catalyst precursor by chemical vapor deposition (CVD).[59–62] Also recently Homma et al. demonstrated building suspended carbon nanotube networks on 100-nm-scale Si pillar structures by simply depositing a catalyst film on the Si substrate.[63] These are indeed effective ways to control the growth of carbon nanotubes. However, for the actual application of such self-assembled single-walled carbon nanotube networks, additional efforts to build controlled and organized nanotube networks connecting designed locations on a large scale are required.

4.5.1.2 Experimental Details

In these experiments SWNTs are grown on patterned Si and SiO_2 structures by the thermal CVD method using CH_4 as a carbon source.[63] Figure 4.17 shows the schematics for designing and building the SWNT networks in our experiment. For the substrate preparation, Si (100) and SiO_2 (300 nm)/Si (100) were patterned using synchrotron-radiation lithography as shown in Figure 4.17a. Patterned substrates have various shapes in submicron sizes, such as pillars (200 nm diameter and 300 nm height with 250 nm distance between pillars) and lines (500 nm wide and 500 nm distance between line structures).[64]

The prepared substrates were chemically cleaned in H_2O_2/H_2SO_4 (1:4) solution and subsequently rinsed with DI water. Then Fe or Co thin films (5 to 10 Å thickness) were deposited as catalysts for nanotube growth using a conventional vacuum evaporator. During the catalyst film deposition, substrates were tilted twice about +45° and –45° to conformally coat the features with catalysts in order to grow carbon nanotubes on the sidewall of patterned structures as well as on top of the substrate (Figure 4.17c).

For the SWNT growth, prepared substrates were placed on the carbon plate inside a quartz tube above the heater in the CVD furnace. Argon gas was supplied to prevent substrate surface and carbon nanotubes from oxidation while maintaining a pressure of approximately 500 Torr. After the furnace was heated to the deposition temperature of 800 to 950°C, CH_4 was introduced into the quartz tube as a carbon source for the carbon nanotube growth at a flow rate of 300 sccm for 1 to 2 min.

4.5.2 Building of SWNT Networks on Nanoscale Patterned SiO_2 and Si Structures

4.5.2.1 High-Density SWNT Networks on Nanoscale Patterned Structures

Figure 4.18a shows representative SEM images of high-density SWNT networks formed on variously shaped nanoscale SiO_2 patterns using Fe catalyst. First, we clearly observe that the yield of suspended SWNTs is significantly higher than that obtained by any previous method.[63,65] Figure 4.19 is the SEM image of SWNT networks grown on SiO_2 pillars having 200 nm diameter, 300 nm height, and 250 nm distance between neighboring pillars. Both the pillars and substrate were coated with Fe catalyst and reacted in the CVD at 900°C. As shown in our schematic illustration (Figure 4.17b,c), because catalyst films were deposited on the sidewall of pillars as well as top and bottom of patterned structures by tilting the substrates, the nanotubes not only started to grow and connect from the top of silicon oxide pillars but they also made bridges between the sidewalls of the pillars. Therefore, highly dense nanotube networks were formed. Closer observation of the nanotube network structures indicates that many nanotubes are on the bottom of the substrate, and they often grow along the sidewalls of the patterned structures.

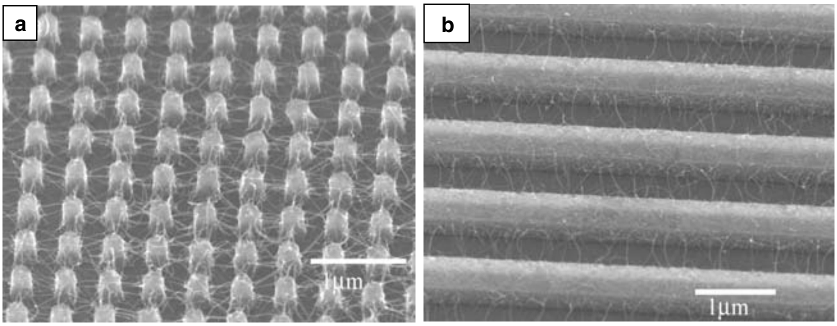

Figure 4.18 (a) SEM image of high-density single-walled carbon nanotubes grown on SiO_2 cylindrical pillars having 200 nm diameter, 400 nm height, and 250 nm distance between pillars. (b) High-density SWNT networks formed on 500–nm-wide SiO_2 line patterns.

Similarly suspended highly dense SWNT growth and network formations are observed when using the same method on different patterns (500 nm wide and distance between lines) as shown in Figure 4.18b. These nanotubes in Figure 4.18 are well directed during growth and form highly organized SWNT architectures following pre-designed geometry of the patterned structures. As previously reported on suspended nanotube growth behavior on Si pillar structures,[60,63] most of carbon nanotubes make a nearest-neighbor connection with the pillars. In the case of line patterns, carbon nanotubes preferentially grow perpendicular to the direction of line shapes regardless of the methane flow direction.

We were also able to create high-density SWNT networks using a Co catalyst film instead of Fe. Compared with Fe catalyst, CVD for nanotube growth using a Co catalyst could be operated at a lower deposition temperature,

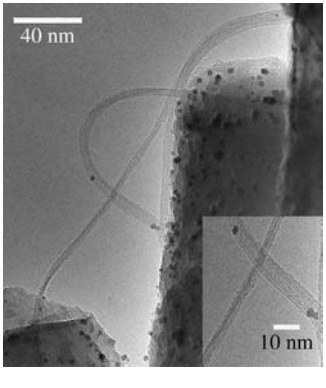

Figure 4.19 TEM images of SWNTs produced by methane CVD on patterned pillar structures and an enlarged (inset) image of the SWNTs indicating formation of SWNT bundles during growth.

800°C, and the morphology of SWNTs is similar to the nanotube networks fabricated by the Fe catalyst at 900°C. However, the probability of building nanotube bridges between patterns spaced at larger distances was observed to be much lower; this might be due to the lower growth temperature, compared with the SWNTs grown by Fe catalyst.

A TEM observation of carbon nanotubes on pillar structures (Figure 4.19) shows that bundles of SWNTs with 1 to 1.3 nm diameters were produced by our method. We could observe that catalyst particles (Fe; 3 to 7 nm diameters) are formed all over the patterned structures. Also the TEM image in Figure 4.19 clearly reveals that SWNT bundles grown from catalyst particles on the patterned pillar structures are connecting to the neighboring pillars forming nanotube bridges.

As briefly mentioned, most of the bridging carbon nanotubes showed nearest-neighbor connections demonstrating a geometrical effect for suspended SWNT formation. The higher possibility of suspended nanotube formation between patterns could be obtained when the aspect ratio of the patterned structure is large and the distance between patterns is smaller. As the pattern (pillar) spacing increased (250 nm, 500 nm), the probability of forming suspended SWNTs decreased. Nanotubes often failed to connect patterns directly, and they fell to the substrate. At the patterned structures with more than 1 μm distance between patterns, the possibility to make SWNTs bridges was very small. The mechanism of suspended SWNT formation has been studied by several researchers.[56,63] However, to better understand the formation mechanism of SWNT networks on patterned nanoscale structures, more detailed investigation is needed.

4.5.2.2 Roles of CVD Parameters and Catalyst Particle Sizes for High-Density SWNT Growth

The general approach for building density-controlled SWNT networks involves selecting optimal substrates and controlling CVD parameters such as the growth temperature, the flow rate of hydrocarbon gases, and the size of catalyst particles. In our CVD process, temperatures in the range of 800 to 900°C and thickness of catalyst (Fe, Co) films in the range 5 to 10 Å are necessary to obtain high-density SWNT growth. When the growth temperature is lower than 800°C, the probability of SWNT growth becomes low. On the other hand, MWNTs are easily produced at this temperature.[65] At around 900°C, highly dense SWNT growth on the Si surface is observed. However, above 950°C, SWNTs are rarely formed. The thickness of catalyst film is also very crucial to produce high-density SWNTs. By changing the thickness of catalyst films (Fe or Co) on nanoscale designed patterns, we could obtain various sizes of catalyst particles directly formed from deposited catalyst films during the high-temperature (800 to 900°C) CVD process for SWNT growth. When the thick catalyst films (>10 Å) were deposited and used for nanotube growth, relatively large catalyst particles were formed during CVD, and consequently the yield of SWNTs was low compared with the thin catalyst film (<10 Å) forming small catalyst particles during CVD.

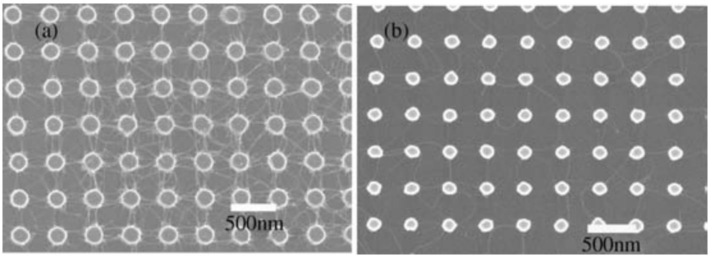

Figure 4.20 Top views of single-walled nanotube networks formed on different substrate materials, with the same CVD parameters showing strong substrate dependence for a high-density single-walled carbon nanotube growth. (a) SiO_2 pillars substrate and (b) Si pillar substrate.

Therefore, by simply depositing thin catalyst film around 5 to 10 Å thickness, we could obtain very small catalyst particles with 3 to 7 nm sizes after CVD for high-density SWNT growth.

4.5.3 Effect of Substrate for SWNT Growth

4.5.3.1 SWNT Growth on Patterned SiO_2 and Si Substrates

Figure 4.20 shows SEM results of highly directional growth of SWNT networks on two different substrate materials. When comparing Si and SiO_2 pillar substrates for nanotube growth, we find that the density of SWNTs on SiO_2 pillar structures shown in Figure 4.20a is much higher than that on Si pillar structures in Figure 4.20b. The observations also show the formation of larger-sized SWNT bundles on the patterned SiO_2 pillar substrate compared with the smaller size of SWNT bundles on the patterned Si substrate.

4.5.4 Mechanism of SWNT Growth on Si and SiO_2 Substrates

4.5.4.1 Role of Catalyst Particles in SWNT Growth on Si and SiO_2 Substrates

Another important result in our experiment is the strong dependence of SWNT growth on substrate materials. Some researchers have already reported the importance of catalyst support materials for nanotube growth.[40,41] In our experiment we note that there is a significant difference in the density of SWNTs between Si and SiO_2 patterned substrates.

To understand the growth mechanism of SWNTs on different substrate materials (Si and SiO_2), we have performed TEM observations of catalyst particles on Si and SiO_2 substrates. Information on these Fe catalyst particles after nanotube growth can be obtained from cross-sectional TEM observation of bare Si and SiO_2 substrates (shown in Figure 4.21 and Figure 4.22). On the SiO_2 area, we can easily observe that the catalyst particles are partially embedded into the SiO_2 matrix (Figure 4.21a). An enlarged TEM image of the SiO_2 area

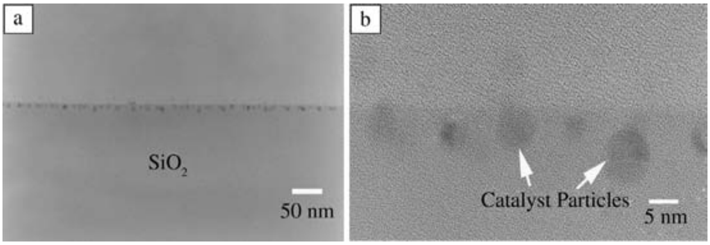

Figure 4.21 Cross-sectional TEM images of the SiO_2 substrate. (a) SiO_2 substrate after CVD. (b) Enlarged picture from (a) showing partially embedded active catalyst particles as indicated with arrows.

(Figure 4.21b) shows irregular-shaped particles with 3 to 7 nm diameter, while on the Si area, we find crystallized precipitates formed with well-defined shapes inside the Si matrix (Figure 4.22a,b) as well as irregular-shaped catalyst particles above the Si surface similar to Figure 4.21b. We do not yet have a clear understanding of the discriminating factors that form small catalyst particles and precipitates. However, these observations seem similar to previous results showing the mechanism of the site selectivity of MWNT growth on SiO_2/Si patterned substrate using the vapor phase catalyst delivery method (ferrocene/xylene).[25] In our previous experiment we found active gamma iron (γ-Fe) catalyst particles effectively promoting MWNT growth on the SiO_2 surface. We also found iron silicide ($FeSi_2$)/iron silicate (Fe_2SiO_4) particles beneath the Si surface during the high-temperature deposition process creating catalytically inactive Fe compounds resulting in no nanotube growth.

Therefore, in our SWNT synthesis process, it is assumed that on the SiO_2 region most of the particles from the thin Co or Fe film exist as a stable catalyst effectively decomposing methane and supplying carbon species for SWNT

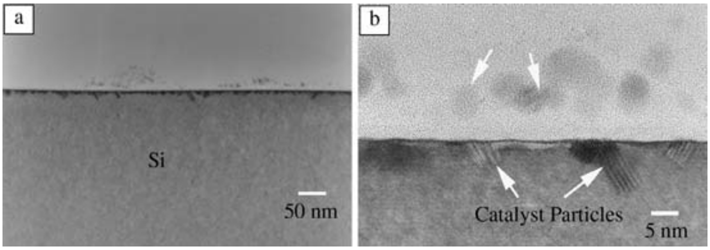

Figure 4.22 Cross-sectional TEM images of the Si substrate. (a) Si substrate after CVD, showing precipitate of submicron-sized particles near the Si surface. (b) Enlarged area from (a) showing both catalyst particles and the formation of compound crystals (arrows) near Si surface during CVD processing.

formation. However, on the Si area there might be a chemical reaction (thereby creating catalytically ineffective compounds) between Si and the catalyst by diffusion of Fe or Co through the native SiO_2 at high temperature.[66–68]

4.6 Fabrication of Hierarchically Branched Carbon Nanotubes Using Controlled nanochannels in Templates

4.6.1 Introduction

Fabrication inside well-ordered nanochannels, such as an anodized aluminum oxide (AAO) template, using CVD is one of popular strategies to produce carbon nanotubes.

AAO membranes have uniform cylindrical pores, which can be controlled by the anodization process of aluminum film or bulk substrate. Using this AAO template, many researchers have created a nanocylinder of desired materials including carbon nanotubes, metallic/semiconducting/polymer nanowires, DNA, and enzyme arrays. This feat (synthesis and electrical characterization of nanotube synthesized inside AAO templates) had been accomplished mainly only for linear and Y-shaped structures. Especially, Y-junction carbon nanotubes have shown interesting electronic properties such as rectification (diode-like behavior) and the abrupt modulation of current from an on to an off state mainly due to the change in band gap across the junction caused by joining different diameter of nanotubes together. The design and controlled synthesis of complex nanowire[69,70–73] and carbon nanotubes[71,74,75] will impact developments in nanoscience and technology.

4.6.2 Synthesis of Hierarchically Branched Nanotubes

4.6.2.1 Designing AAO Nanochannel Templates

The creation of controlled nanochannels, with various levels of complexity, inside these templates provides a powerful way to produce predesigned multiply connected and branched carbon nanotubes. We have developed a rational approach for creating hierarchically branched nanoporous AAO templates and have fabricated a whole new generation of branched carbon nanotubes (MWNTs) inside these using a conventional thermal CVD method without catalyst materials.

A variety of hierarchically organized nanopores inside AAO templates can be fabricated using a modified multistep anodization process. The first-step anodization is the same for all templates: High-purity Al films are anodized in oxalic acid solution under a specific constant voltage for the desired pore size. As the pore diameter is proportional to the anodizing voltage, so the anodizing voltage controls the pore size and pore density during the anodization. A simple calculation shows that the anodizing voltage to form a number (n) of smaller pores from a single stem pore can be

expressed as $(1/\sqrt{n}\ \times V_s$, where V_s is the anodizing voltage for stem pores and n is the number of branched pores from that stem. Therefore, in the second-step anodization, templates with different pore size and architectures undergo a different process of anodization, where the individual channels divide into predetermined multiple numbers of subchannels.

For example, multigenerations of Y-branched nanochannels can be produced by reducing the anodizing voltage multiple times by a factor of $1/\sqrt{2}$ in the second-step anodization until the voltage remains stable during the process. Also, AAO templates with multiply branched pore structure, e.g., one stem is divided into five, can be produced by reducing the anodization voltage by a factor of $1/\sqrt{5}$ to create five branched pores. If the voltage is reduced slowly, the stem pores will divide branched pores gradually (at several depths), but if the voltage is reduced suddenly, the stem pores will be divided abruptly (thereby producing a sharp interface). Using this technique, even several levels of multiply branched pores will be produced by reducing the anodizing voltage by a factor of $1/\sqrt{n}$ to create first-generation multibranched (n) pores, and subsequently reducing the anodizing voltage again by a factor of $1/\sqrt{m}$ to generate the second-generation multibranched pores (m) growing from each of the first-generation multibranched pores.

4.6.2.2 *Synthesis of Hierarchically Organized Carbon Nanotubes*

Multiwalled nanotubes were grown inside the pores of the AAO templates by the pyrolysis of acetylene[74,76,77] at 650°C for 1 to 2 hrs with a flow of gas mixture of Ar (85%) and C_2H_2 (15%), at a rate of 35 ml/min. (No catalyst materials are required to grow carbon nanotubes when AAO nanochannels are used as template.)

Up to four generations of Y-branching have been fabricated onto individual nanotube structures (***1***-< **2**-< **2**-< **2**-< **2**), as shown in Figure 4.23 in the SEM images. The left schematic in Figure 4.23 shows the architecture of each of the nanotubes formed inside the template. Figure 4.23a shows the four parallel interfaces (arrows), seen in a large bundle of nanotubes obtained after template removal, where each of the four generations of Y-branching takes place. The high-magnification image from each of these interfaces (Figure 4.23b–e) clearly reveals the corresponding Y-branches. The diameters of the primary stems and the branches depend on the corresponding anodizing voltages; for any two consecutive branches (at each interface), the ratio of the diameters is approximately $\sqrt{2}$, as seen from the figures. The length of each branch is controlled independently by the corresponding anodization time given for each pore segment generation.[78]

Figure 4.24a–d shows nanotubes where a single stem divides into 2, 3, 4, and 16 (structures ***1***-< ***2***, ***1***-< ***3***, ***1***-< ***4***, and ***1***-< ***16***) branches abruptly. We have been able to controllably produce branching numbers at will, for example, 2, 3, 4, 6, 8, and 16. Also shown in Figure 4.24e,f are the TEM images of the

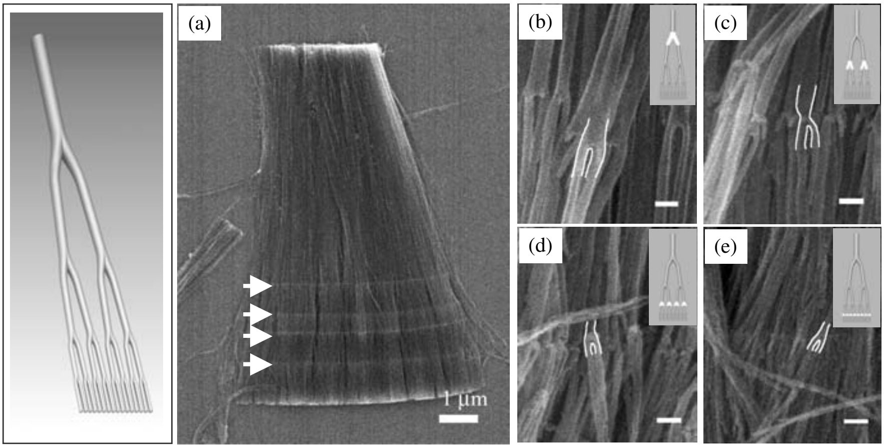

Figure 4.23 Carbon nanotube architectures showing four-generation Y-branching. Drawing on the left shows the structure of the typical four-generation Y-branched nanotube. (a) The four parallel interfaces (marked with white arrows) in the low-magnification SEM image show the locations where the four generations of Y-branching take place. The high-magnification image from each interface clearly reveals the corresponding Y-branches and the decreasing diameters of the branched nanotube segments. (b) The first Y generation, (c) the second Y generation, (d) the third Y generation, and (e) the fourth Y generation. The Y-junction is contoured in white lines for clarity. The insets in (b) through (e) show schematics of the whole architecture with specific junctions highlighted in white. Scale bars are 100 nm.

branched nanotubes, clearly showing the junctions between the larger and smaller nanotubes and the flexibility of the smaller nanotubes (Figure 4.24e).

A combination of Y-shapes and multiple branches can lead to a wealth of new nanoscale architectures. This can be achieved by reducing the anodizing voltages in steps, by factors of $1/\sqrt{2}$ and $1/\sqrt{n}$ sequentially, generating Ys and n-branched pores in the template consecutively. The sequences can be interchangeable (for example, the stem can be split into multiple branches first and each of the branches can subdivide as Ys or vice versa) and recurring (several levels) so that many complicated nanostructures emerge. Continuing this approach, very complicated architectures can be created, for example, a single stem dividing into multiple branches and each of those branches further subdividing into multiples ($[\boldsymbol{1} \prec \boldsymbol{n} \prec \boldsymbol{m}]$ structures, where $\boldsymbol{n}$ and $\boldsymbol{m}$ can be independently varied). Figure 4.25 shows an example of such a complex structure, where two levels of multiple branching are shown (arrows in Figure 4.25a indicate the interfaces at which branching takes place). The primary stem splits first into three branches, each of which further splits into three sub-branches ($\boldsymbol{1} \prec \boldsymbol{3} \prec \boldsymbol{3}$). The high-magnification SEM images of the two interfaces reveal the junctions, showing the branching and the reduction in diameters as the branching occurs.[78]

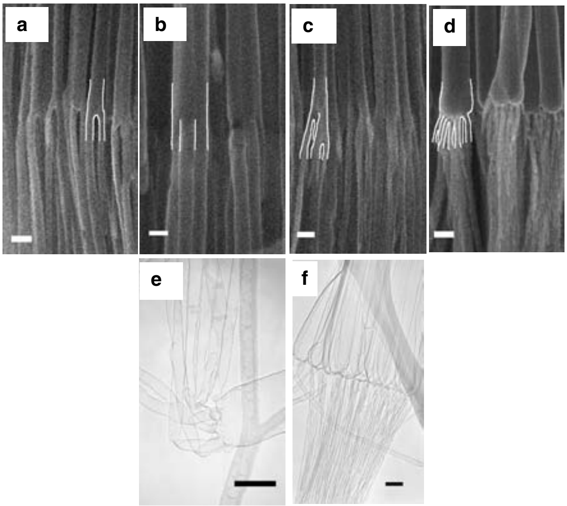

Figure 4.24 Carbon nanotube architectures showing multiple branching. Series of SEM images of multiply branched carbon nanotubes showing the primary stem dividing into (a) 2, (b) 3, (c) 4, and (d) 16 branches abruptly. The junctions are highlighted using white line contours for clarity. In the case of the 16-branched nanotube, only half the branches are visible in the image (due to the three-dimensional structure, the rest of the branches are behind the front visible ones). (e) A TEM image of a nanotube with 8 branches. The smaller branches look more flexible and are seen easily bent. (f) TEM image from an array of multi-branched (16 branches on each) carbon nanotubes. Scale bars are 100 nm.

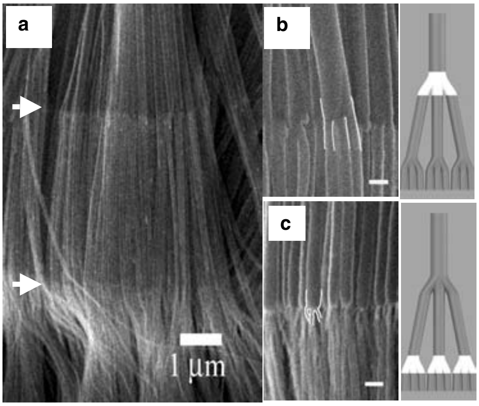

Figure 4.25 Carbon nanotube architectures that have complex hierarchical branching. SEM images show (a) arrays of nanotubes that show two generations of branching (at the locations of the white arrows). At each of the junctions each of the stems splits into three, giving a ***1≺3≺3*** architecture, as discussed in the text. (b), (c) close up of the ***1≺ 3*** junctions (schematic of each of the representative individual nanotube structures is shown on the right). Junctions are highlighted with white line contours for clarity. Scale bars are 100 nm.

Acknowledgments

The work was performed under the guidance of Professor P.M. Ajayan at Rensselaer Polytechnic Institute. YJJ also acknowledges members of Professor P.M. Ajayan's group and NTT Basic Research Laboratories. The work at RPI was supported by IFC-New York.

References

1. Iijima, S., *Nature,* 354, 56, 1991.
2. Dresselhaus, M.S., Dresselhaus, G, and Eklund, P.C., *Science of Fullerenes and Carbon Nanotubes*, Academic Press, New York, 1995.
3. Dresselhaus, M.S., Dresselhaus, G., and Avouris, Ph., *Carbon Nanotubes; Synthesis, Structure, Properties, and Applications*, Springer, Berlin, 2001.
4. Ajayan, P.M., *Chemical Reviews,* 99, 1787, 1999.
5. Wei, B.Q., Vajtai, R., and Ajayan, P.M., *Appl. Phys. Lett.*, 79, 1172, 2001.
6. Frank, S. et al., *Science,* 280, 1744, 1998.
7. Wang, Q.H. et al., *Appl. Phys. Lett.*, 72, 2912, 1998.
8. Choi, W.B. et al., *Appl. Phys. Lett.,* 75, 3129, 1999.
9. Avouris, Ph., *Chem. Phys.,* 281, 429, 2002.
10. Appenzellerr, J. et al., *Phys. Rev. Lett.,* 89, article #126801, 2002.
11. Javey, A., Wang, Q., Ural, A., Li, Y., and Dai, H., *Nano Letters,* 2, 929, 2002.
12. Choi, W.B. et al., *Appl. Phys. Lett.,* 82, 275, 2003.
13. Kreupl, F. et al., *Microelec. Eng.,* 64, 399, 2002.
14. Lee, Y. et al., *J. Appl. Phys.,* 91, 6044, 2002.
15. Wei, B.Q., Zhang, Z.J., Ramanath, G., and Ajayan, P.M., *Appl. Phys. Lett.*, 77, 2985, 2000.
16. Kong, J. et al., *Science,* 287, 622, 2000.
17. Smalley, R.E. et al., *Science,* 273, 483, 1996.
18. Fan, S., Chapline, M.G., Franklin, N.R., Tombler, T.W., Cassell, A.M., and Dai, H., *Science,* 283, 512, 1999.
19. Li, W.Z. et al., *Science,* 274, 1701, 1996.
20. Terrones, M. et al., *Nature,* 388, 52, 1997.
21. Ren, Z.F. et al., *Science,* 282, 1105, 1998.
22. Wei, B.Q. et al., *Nature,* 416, 495, 2002.
23. Y. Jung et al., *Mat. Res. Soc. Symp. Proc.*, 706, Z 3, 2002.
24. Wei, B.Q. et al., *Chem. Mater.,* 15, 1598, 2003.
25. Jung, Y. et al., *Nano Letters,* 3, 561, 2003.
26. Jung, Y. et al., *J. Phys. Chem. B,* 107, 6859, 2003.
27. Homma, Y. et al., *J. Phys. Chem. B,* 107, 12163, 2003.
28. Ebbesen, T.W. and Ajayan, P.M., *Nature,* 358, 220, 1992.
29. Bethune, D.S. et al., *Nature,* 363, 605, 1993.
30. Journet, C. et al., *Nature,* 388, 756, 1997.
31. Jung, I.S. et al., *Appl. Phys. Lett.*, 78, 901, 2001.
32. Lee, C.J. et al., *Chem. Phys. Lett.,* 327, 277, 2000.
33. Xie, S. et al., *Mater. Sci. Eng. A*, 286, 11, 2000.
34. Lee, C.J. et al., *Chem. Phys. Lett.*, 359, 109, 2002.
35. Hernadi, K., *Chem. Phys. Lett.,* 363, 169, 2002.
36. Sinha, A.K. et al., *Chem. Phys. Lett.*, 332, 455, 2000.

37. Han, I.T. et al., *Appl. Phys. Lett.*, 81, 2070, 2002.
38. Ho, G.W. et al., *Thin Solid Films,* 388, 73, 2001.
39. Choi, Y.C. et al., *J. Vac. Sci. Tech. A,* 18, 1864, 2000.
40. Kong, J., Cassell, A.M., and Dai, H., *Chem. Phys. Lett.*, 292, 567, 1998.
41. Cassell, A.M. et al., *J. Phys. Chem. B*, 103, 6484, 1999.
42. Kong, J. et al., *Nature,* 395, 878, 1998.
43. Dai, H. et al., *J. Phys. Chem.*, 103, 11246, 1999.
44. Murakami, Y. et al., *Chem. Phys. Lett.*, 375, 393, 2003.
45. Dai, H., *Surf. Sci.,* 500, 218–241, 2002.
46. Zhu, H.W. et al., *Science,* 296, 884, 2002.
47. Baker, R.T.K. and Harris, P.S., Formation of filamentous carbon, in *Chemistry and Physics of Carbon*, 14, Marcel Dekker, New York, 1978.
48. Sinnott, S.B. et al., *Chem. Phys. Lett.,* 315, 25, 1999.
49. Sen, R., Govindaraj, A., and Rao, C.N.R., *Chem. Phys. Lett.,* 267, 276, 1997.
50. Andrews, R. et al., *Chem. Phys. Lett.,* 303, 467, 1999.
51. Zhang, Z.J. et al., *Appl. Phys. Lett.*, 77, 3764, 2000.
52. Ghandi, S., *VLSI Fabrication,* 2nd edition, Wiley, New York 1994.
53. Thompson, L.F. et al., *Introduction to Microlithography,* 2nd edition, American Chemical Society, Washington, DC, 1994.
54. Ohnishi, T. et al., *Proc. 25th Int. Symp. for Testing and Failure Analysis*, 449, 1999.
55. De los Arcos, T. et al., *Appl. Phys. Lett.,* 80, 2383, 2002.
56. Franklin, N.R. et al., *Appl. Phys. Lett.,* 79, 4571, 2001.
57. Yenilmez, E. et al., *Appl. Phys. Lett.*, 80, 2225, 2002.
58. Cassell, A.M. et al., *Appl. Phys. Lett.*, 82, 817, 2003.
59. Cassell, A.M. et al., *J. Am. Chem. Soc.*, 121, 7975, 1999.
60. Franklin, N.R. and Dai, H., *Adv. Mater.,* 12, 890, 2002.
61. Dai, H. et al., *Appl. Phys. Lett.*, 79, 3155, 2001.
62. Huang, L. et al., *Nano Lett.,* 3, 299, 2003.
63. Homma, Y., *Appl. Phys. Lett.*, 81, 2261, 2002.
64. Campbell, S.A., *The Science and Engineering of Microelectronic Fabrication,* Oxford University Press, Oxford, 1996.
65. Homma, Y. et al., *Jpn. J. Appl. Phys.*, 41, 89, 2002.
66. Ruhrnschopf, K., Borgmann, D., and Wedler, G., *Surf. Sci.,* 374, 269, 1997.
67. Swart, H.C. and Berning, G.L.P., *Appl. Surf. Sci.,* 78, 77, 1994.
68. Chemelli, C. et al., *Appl. Surf. Sci.,* 68, 173, 1993.
69. Milliron, D.J. et al., *Nature,* 430, 190, 2004.
70. Dick, K.A. et al., *Nat. Mater.,* 3, 380, 2004.
71. Wang, D.L. et al., *Nano Lett.*, 4, 871, 2004.
72. Xia, Y. et al., *Adv. Mater.,* 15, 353, 2003.
73. Wang, Z.L., *J. Phys. Condens. Matter,* 16, R829, 2004.
74. Li, J., Papadopoulos, C., and Xu, J., *Nature,* 402, 253, 1999.
75. Papadopoulos, C. et al., *Phys. Rev. Lett.,* 85, 3476, 2000.
76. Davydov, D.N. et al., *J. Appl. Phys.,* 86, 3983, 1999.
77. Sui, Y.C. et al., *Thin Solid Films,* 406, 64, 2002.
78. Meng, G. et al., *PNAS,* 12, 7074, 2005.

Chapter 5

Reconfigurable CMOS Electronic Microarray System for the Assisted Self-Assembly of Higher-Order Nanostructures

Dietrich Dehlinger, Benjamin Sullivan, Sadik Esener, Paul Swanson, Dalibor Hodko, and Michael J. Heller

Contents

5.1 Introduction 107
5.2 CMOS Electronic Microarrays and Controller Systems 109
5.3 Transport and Addressing of Molecules, Nanostructures, and Microstructures 114
5.4 Fabrication of Multiple-Layered Nanoparticle Structures Using CMOS Microarrays 117
5.5 Strategy for Assisted Self-Assembly and Hierarchical Organization 120
5.6 Conclusions and Future Goals 122
References 123

5.1 Introduction

One of the grand challenges in nanotechnology is the development of new nanofabrication methods that will lead to viable cost-effective nanomanufacturing processes. For some top-down manufacturing processes such as photolithography and applications such as silicon/CMOS electronics, the enormous support provided by the microelectronics industry drives the evolutionary improvement of this process. This continued improvement assures silicon/

CMOS-based nanoelectronics for the future. A fabrication area that appears more problematic is the integration of heterogeneous molecular, nanoscale, and microscale components into higher-order three-dimensional macroscopic structures, materials, and devices.

Viable heterogeneous integration processes will be necessary for many applications including nanoelectronic/photonic-based large-area displays and screens, high-resolution imaging detector arrays, optoelectronic multiplexing devices, and nanophotonic crystal band-gap materials. Such processes will also be necessary for making high-efficiency photovoltaic devices that require integrated 3-D nano/microstructures containing multiple band-gap nanostructured layers with maximum charge separation and minimal charge recombination properties.[1–3] In fact, cost-effective manufacturing processes will be absolutely required for making any new photovoltaic material or device that would be used for large-scale solar energy conversion. Other energy conversion–related areas that will require heterogeneous integration include fuel cell devices with 3-D nano/microstructures containing nanostructured intermetallic rare earth (platinum, palladium) catalysts with intervening fluidic channel and electrode structures.[4,5] Novel smart-morphing nanocomposite materials will require a viable integration process for making 3-D nano/micro/macrostructures with intervening sensor network and morphing material substructures.[6] Finally, new nano/micro integration processes will likely be important for making biosensor array devices with nanoscale detection elements, as well as for nano- to micron-sized *in vivo* biosensor and therapeutic delivery systems or "mother ships" for cancer or other disease treatment.[7–11]

In addition to top-down processes for fabrication and integration, so called "bottom-up" processes are being developed for carrying out hierarchical self-assembly of nanostructures into higher-order materials, structures, and devices.[12–17] Considerable efforts have been carried out on layer-by-layer (LBL) self-assembly processes as a way to fabricate three-dimensional layers of nanostructures that have macroscopic x-y dimensions.[18–20] A variety of techniques have been developed to carry out passive LBL self-assembly processes. In general, they involve dipping an activated substrate material (electrostatically charged, chemically reactive, etc.) into a solution that contains a macromolecule, polymer, or nanoparticle with an opposite charge or reactivity to the substrate material. In such LBL processes, the concentration of the binding components is usually relatively high, the binding reaction steps can take from 10 minutes to more than 30 minutes to complete, and the substrate must be washed extensively before the next layering step is carried out. More often, LBL self-assembly layering processes are carried out using oppositely charged materials.[21–24] However, in some cases, LBL self-assembly processes involve the use of similarly charged materials, for example, where chelation chemistry is used to form coordination-based gold nanoparticle layers.[25] Hammond has recently completed a nanofabrication review article with a very good overview of passive electrostatic-based LBL self-assembly techniques.[26] Nanoparticle deposition

has also been carried out by a variety of electrochemical and charged surface approaches.[27–33] However, these processes are most often not parallelizable. When parallelism or some type of x-y feature is required, LBL self-assembly is carried out on prepatterned substrate materials. Most often this involves the use of standard photolithographic techniques to prepattern a substrate material for subsequent nanoparticle layering in defined areas, i.e., separate layer-by-layer stacks.[34] Other patterned substrate work includes the use of a sacrificial mask achieved by using poly(dimethylsiloxane) (PDMS) on an LBL substrate to create a patterned region that is then covered with nanoparticles using standard LBL methods.[35] While a few LBL and other self-assembly processes are showing some promise, they are in general not developing into the viable cost-effective nanomanufacturing processes that allow widespread applications of the technology. Unfortunately, LBL processes are often relatively slow and nonparallel unless the substrate material is first prepatterned using a lithographic process. Such limitations make the LBL-based fabrication of complex x-y multiple-layer 3-D structures from heterogeneous nanocomponents a very time-consuming and cumbersome process.

Because of such intrinsic limitations of the different nanofabrication processes, there is now particular interest in discovering new ways to combine the best aspects of top-down and bottom-up processes to create a unique paradigm change for nanofabrication. This is particularly true for the integration of heterogeneous molecules and nanocomponents into higher-order 3-D structures.[36–37] To this end, electronic microarrays have exhibited considerable promise as just such a technology.[38]

5.2 CMOS Electronic Microarrays and Controller Systems

Over the past decade, sophisticated electronic microarray devices that are produced by top-down photolithography processes have been developed and commercialized by Nanogen (San Diego, CA). While these devices have been used primarily for DNA hybridization diagnostic applications, they may also have promise for nanofabrication and heterogeneous integration. Active electronic microarray devices use DC electric fields to create transport geometries that allow almost any charged entity (DNA, RNA, peptide, protein, antibody, enzyme, biopolymer) to be electrophoretically transported to any microlocation or test site on the array surface. In the case of DNA hybridization, these devices allow negatively charged DNA molecules to be electrophoretically transported to any positively biased site on the microarray surface.[39–47]

The electric field transport and addressing of biomolecules greatly accelerate their binding at the specific test sites to which they are directed. For most entities the bulk transport and binding process can be more than a 1,000 times faster compared with the traditional passive or diffusion-based methods. For example, DNA hybridization (binding) on a standard passive microarray may take up to several hours when low concentrations of analyte target DNA sequences need to be determined. On active electronic microarrays, the hybridization process is usually carried out in less than one minute.

In order to enable electrophoretic transport and addressing with these active microarrays, the bias potential has to be sufficiently high (>1.2 V) to cause water oxidation at the positive electrode and water reduction at the negative electrode (electrolysis). The products of water oxidation are H^+ and oxygen and the reduction products are OH^- and hydrogen (Equations 5.1 and 5.2).

$$\text{Oxidation} \quad 2\,H_2O \rightarrow 4H^+ + O_2 + 4e^- \tag{5.1}$$

$$\text{Reduction} \quad 2e^- + 2H_2O \rightarrow 2OH^- + H_2 \tag{5.2}$$

Because of this, the microelectrodes on the array are overcoated with a thin hydrogel permeation layer that acts like a sponge for the pH gradients and gases released during electrolysis. The main function of the hydrogel permeation layer is to protect the binding entities (DNA, proteins, etc.) from the adverse effects of the electrolysis products (H^+, OH^-, O_2, H_2) produced at the microelectrode surface. The permeation layer also contains immobilized streptavidin within the matrix, which provides the binding sites for biotin-labeled DNA probes. The H^+ ion gradient generated at the positive microelectrode has been capitalized on to produce a unique environment that promotes conditions for efficient DNA hybridization. This "electronic hybridization" process involves the use of histidine, a zwitterionic buffer, which becomes protonated in the vicinity of the positively charged microelectrode. The positively charged histidine is capable of screening the negative phosphate charge on the double-stranded DNA backbone, thereby reducing the charge repulsion and stabilizing the hybridization between the DNA strands. In DNA hybridization assays, biotinylated DNA capture probes can first be electronically addressed and bound onto specific test sites of the microarray. Subsequently, unknown target DNA sequences can be addressed to the different test sites, with hybridization occurring only where the capture probe and target DNA sequences are complementary. By reversing the polarity at the microelectrode (negative activation), the nonspecifically bound DNA molecules can be driven away from the test site. This unique feature of the electronic microarray allows an electronic stringency method for differentiation of DNA binding strength to be performed at each array site. Electronic stringency enables single-base differentiation and determination of single nucleotide polymorphisms (SNPs). Thus, electronic microarray devices, produced by a top-down process, are able to elegantly control and accelerate the specific self-assembly bottom-up process of DNA hybridization.

A variety of active microarray devices have been designed and fabricated, including ones with 100, 400, and 10,000 test sites or microlocations. Earlier 100-test-site devices used external wiring to control the microelectrodes on the array surface. Such external control of the voltage and current on a large number of electrodes can be cumbersome, and thus for higher-density arrays it is advantageous to integrate the microelectrode bias control circuitry on the same microchip. Newer 400- and 10,000-test-site microarrays represent more sophisticated devices that integrate CMOS control elements to regulate currents and voltages to each of the microelectrodes.[48] In addition to voltage and current

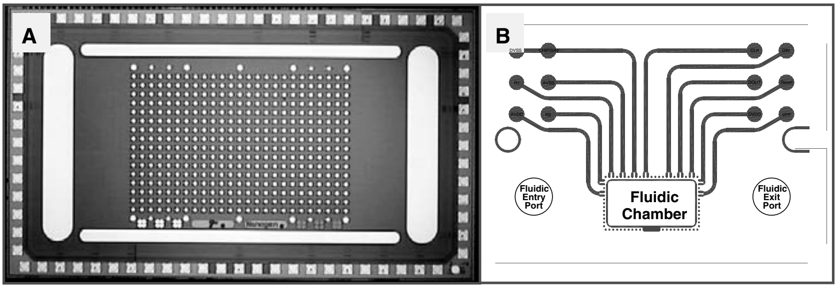

Figure 5.1 (A) photo of a CMOS microarray (5 mm × 7 mm) with 400 50-micron test-site microelectrodes and 4 large perimeter counter electrodes used to produce electric field geometries that encompass the whole microarray surface area (~4 mm × 6 mm). The chip is coated with a polyacrylamide gel permeation layer that is 1 micron thick when dry and about 10 microns thick when hydrated. The permeation layer is impregnated with streptavidin, which then allows biotinylated DNA sequences, proteins, or nanoparticles to be immobilized onto the permeation layer surface. (B) Mounted chip with fluidic chamber and the pin-out pattern for electrical connections.

control, the more recent devices introduced digital communication, memory, temperature sensing, sourcing, and measuring circuits into the microarray.

Nanogen's 400-test-site system consists of a 16 by 25 array with 50-micron-diameter electrodes spaced 150 microns center to center (see Figure 5.1). Thin-film deposition and patterning techniques are used to incorporate the platinum microelectrode array on the surface of the standard CMOS chip. Underneath each of the 400 electrodes is an analog sample and hold circuit that maintains a predefined voltage on the electrode. A digital-to-analog converter sequentially queries the digitally stored bias value for each electrode and refreshes each sample and hold circuit accordingly. A separate loop sequentially measures the voltage and current at each electrode. Microelectrodes can operate at a fixed voltage or current by means of a feedback loop or at a fixed voltage offset from a reference electrode. The 400-test-site CMOS chip also contains a p-n junction-based temperature sensor and erasable programmable read only memory (EPROM) memory to store thermal calibration coefficients, serial numbers, and assay-related data. The chip has only 12 external electrical connections: +5 V and ground for the digital circuits, +5 V and ground for the analog circuits, digital signal in, digital signal out, clock signal, reset, and two terminals for an external current sampling resistor. Seventy-six flip-chip solder bonds connect the chip and package. For structural support, the ceramic substrate doubles as both a fluidic chamber and an electrical contact interface (Figure 5.1). In order to prevent having to compromise on the quality of either the circuitry or the electrode array, the CMOS section of the device is fabricated at one foundry while the platinum microelectrode array is fabricated at a second foundry. Figure 5.2 show a section of the microarray and the 50-μm-diameter microelectrodes. A cross section through one of the microelectrodes shows some of

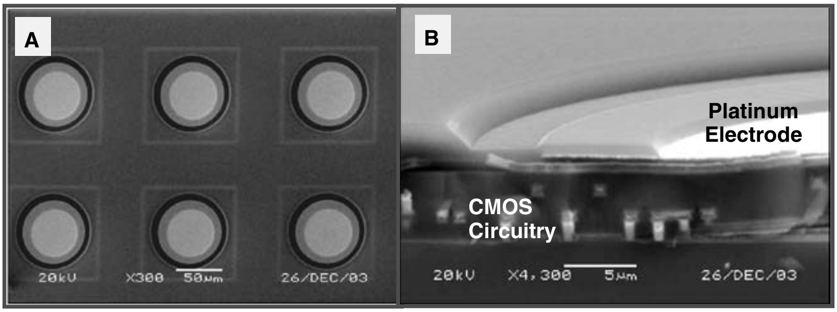

Figure 5.2 (A) A group of the 50-micron electrodes on the 400 test site microarray, and (B) a cross section through the chip at one of the 50-micron sites exposing the underlying Si base, some of the CMOS circuitry, and a portion of the platinum microelectrode structure.

the underlying CMOS structure. The CMOS process requires 18 masking steps followed by an additional 3 masking steps for the platinum microelectrodes. After the finished wafers have been inspected for defects, the wafers are diced into individual chips then flip-chip bonded onto the ceramic substrates. The flip-chip on substrate (FCOS) is next thermally calibrated, and then assembled into the NanoChip 400 plastic cartridge housing.

The concurrent size reduction in the CMOS microarray controller system now provides a relatively inexpensive and compact unit that can be run with a laptop computer (Figure 5.3). The 400-test-site CMOS chip can be mounted directly onto the controller system (as shown in Figure 5.3), which in turn can be placed on a conventional micromanipulator probe station. An epifluorescent microscope with a CCD imaging system is used to observe and record the assisted self-assembly process taking place on the surface of the microarray, as nanostructures are organized into higher-order two- and three-dimensional structures. Additionally, these systems and techniques may also be useful for carrying out the precision functionalization of nanoparticles and nanocomponents with high-fidelity binding molecules such as DNA or proteins. Electric field devices have the intrinsic ability to orient molecular or nanoscale objects that have asymmetry in their charge distribution. This property may be exploited to position DNA or protein ligand molecules around nanospheres and other nanostructures with better precision.[56] These high-precision nanostructures or "molecular legos" would impart higher specificity and geometric order in the subsequent self-assembly process. Overall, high-precision nanostructures or molecular legos will lead to more robust higher-order structures that have better performance properties. Figure 5.4 shows a generalized scheme for the two-step process of using electronic microarrays to first carry out the nanofabrication of precision nanostructures or molecular legos and then to subsequently assist in the self-assembly into higher-order structures, materials, and devices.

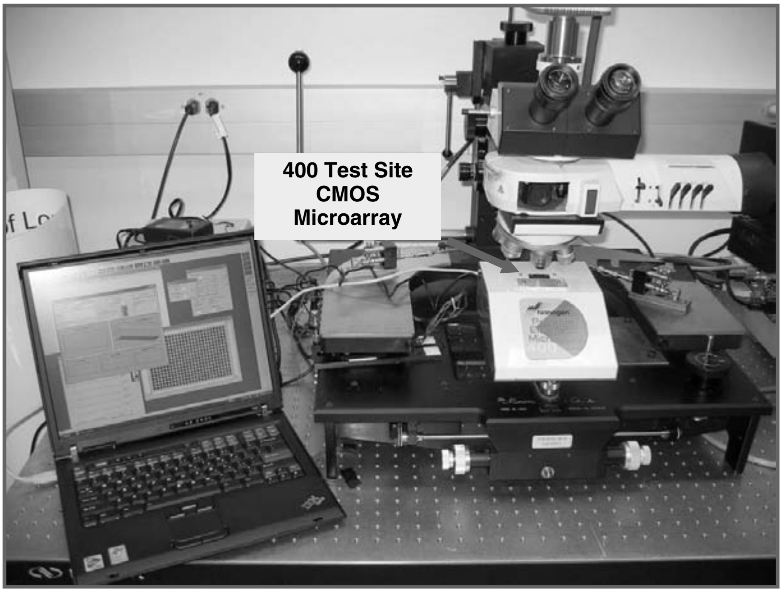

Figure 5.3 The complete electric field nanofabrication system for carrying out heterogeneous integration, nanoparticle layering, and assisted self-assembly on the 400 site CMOS microarray devices. The miniaturized CMOS array controller system (with a 400 site CMOS microarray) is mounted on a standard micro-manipulator probe station with an epifluorescent microscope and CCD imaging systems. A laptop computer is used to control the overall system.

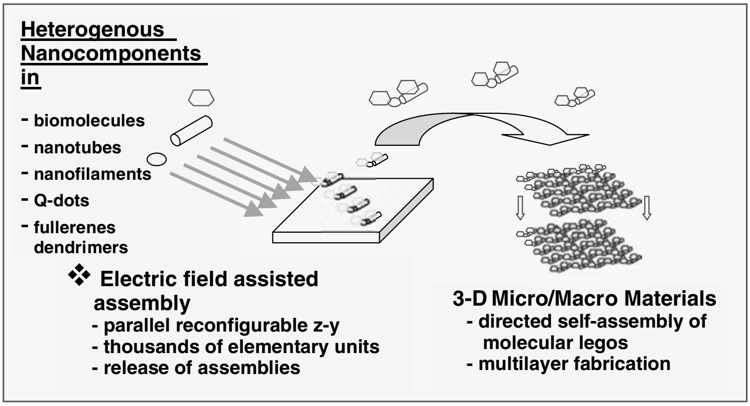

Figure 5.4 A more generalized scheme for using electronic microarrays to carry out a two-step nanofabrication and assisted self-assembly process. In the first step, the electronic microarray is used to carry out the nanofabrication of precision nanostructures or molecular legos. In the second step, the device is used to assist in the self-assembly of the nanostructures into higher-order structures, materials, and devices.

5.3 Transport and Addressing of Molecules, Nanostructures, and Microstructures

In addition to DNA hybridization reactions, electronic microarray devices are also able to rapidly accelerate protein/ligand binding reactions, such as streptavidin/biotin and antibody/antigen, by vastly increasing the local concentration at the test site. While used primarily for DNA hybridization applications, it has also been demonstrated that these microarrays have the intrinsic ability to direct the transport and control the positioning (addressing) of almost any type of charged molecule, nanostructure, or micron-sized object on the microarray surface. This includes most types of polymeric or metallic nanoparticles, quantum dots, cells, and even micron-sized semiconductor components, such as 20-micron-diameter "lift-off" light-emitting diodes or LEDs.[49–57] In addition to electrophoretic transport and addressing of molecular and nanoscale entities, analog microarrays enable dielectrophoretic manipulation of nanoscale and microscale objects such as bacteria, blood, and cancer cells.[58–59] The ability to use both electrophoretic (DC) and dielectrophoretic (AC) manipulation of molecular, nanoscale, and micron-scale entities represents a powerful combination for assisted assembly fabrication. Figure 5.5

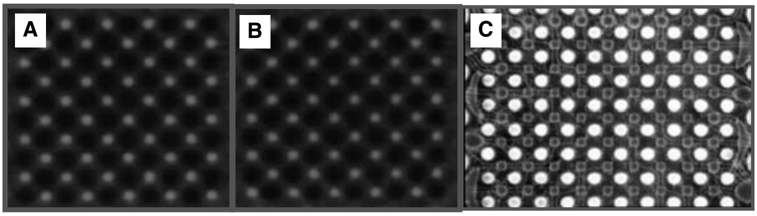

Figure 5.5 Results of using electronic microarrays to carry out the DC electrophoretic transport and positioning of fluorescent DNA molecules into checkerboard patterns (A,B), and the AC dielectrophoretic separation of bacteria cells from red blood cells (C). (A,B) The controlled parallel movement (checkerboarding) of negatively charged fluorescent DNA molecules between alternating positively and negatively biased test sites. The sample solution contains about 50 nM concentration of a 20-mer oligonucleotide sequence that is labeled in the 5′-terminal position with Bodipy Texas Red fluorophore (Ex ~ 590 nm, Em ~ 650 nm), the microelectrodes (beneath test site/microlocations) are biased positive and negative in a checkerboard fashion, and the field is reversed every six seconds. At about 3 V DC, the fluorescent DNA molecules (~7 nm in length) are transported back and forth a distance of 200 microns during the 6-second switching time period. This result clearly demonstrates the ability of microarray devices to control the transport of molecular-sized entities (DNA) in a highly parallel manner. (C) The dielectrophoretic separation of bacteria (*E. coli*) from blood cells. The bacteria are seen as the white covering deposited onto the high-field regions (surface of the 80-micron electrodes), while the blood cells (red spots) are concentrated in the low-field regions between the 80-micron diameter electrodes. (From Cheng, J., Sheldon, E.L., Wu, L., Uribe, A., Gerrue, L.O., Carrino, J., Heller, M., and O'Connell, J., *Nat. Biotechnol.*, 16, 541–546, 1998. With permission.)

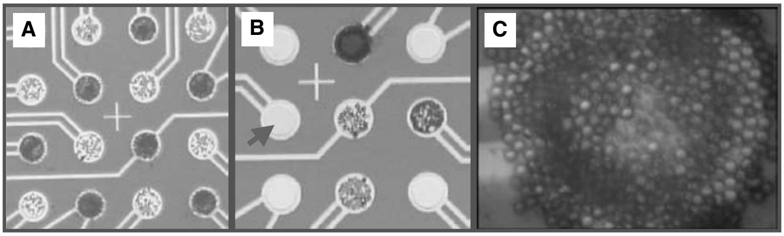

Figure 5.6 (A) The parallel (multiplex) addressing of two differently sized negatively charged polystyrene spheres (1 micron and 5 microns) onto the 80-micron diameter test sites of the microarray. (B) The selective serial addressing of 10-, 5-, 2-, and 1-micron negatively charged microspheres and 100-nanometer nanospheres onto the 80-micron test sites of a microarray device (10-micron spheres at center test site, 5-micron spheres at bottom-center test site, 2-micron spheres at right test site, 1-micron spheres at upper-center test site, 100-nanometer spheres at the left-center test site with the arrow, and the four corner test sites were not addressed). (C) The addressing of negatively charged 1-micron polystyrene microspheres to a selectively activated 80-micron-diameter test site of the electronic microarray, and then the addressing of the larger 5-micron microspheres over the 1-micron microspheres. (The transport and addressing of all microspheres and nanospheres were carried out using DC electric fields at about 3 V for 30 to 60 seconds.)

shows some results of using electronic microarrays to carry out the electrophoretic transport and positioning of fluorescent DNA molecules into checker board patterns (Figure 5.5A,B), and the AC dielectrophoretic separation of bacteria cells from red blood cells between the high-field and low-field regions of the array (Figure 5.5C). This not only is an example of using electronic arrays to carry out different types of electric field manipulation, but also demonstrates the ability of these devices to transport or position biological entities with three orders of magnitude difference in size, i.e., DNA about 10 nm, bacteria about 1 micron, and red blood cells about 10 microns. The ability to use electronic microarrays to transport and address entities other than biological molecules was demonstrated very early in the development of the technology.[39] By way of further example, Figure 5.6 shows the parallel or multiplex addressing of micron-sized polystyrene particles (Figure 5.6A), the serial addressing of micron-sized and nanoscale (100 nm) polystyrene particles (Figure 5.6B), and some early micron-scale particle layering (Figure 5.6C). Such results demonstrate the intrinsic ability of electronic microarrays to carry out the directed transport and addressing of a variety of different sizes and types of molecular, nanoscale, and microscale entities. These results also demonstrated the ability of the microarray devices to carry out a first-order layering of microparticles. Microsphere and nanoparticle transport and add ressing have also been demonstrated (Figure 5.7) with negatively charged 5-micron microspheres being transported, positioned, and then redispersed from the 50-micron-diameter test sites of the 400 test-site CMOS microarray (one minute run time at 3.5 V DC). Figure 5.8 shows an example of negatively charged 250-nanometer fluorescent nanoparticles

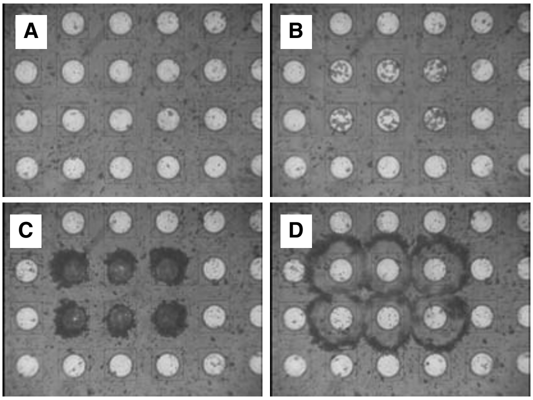

Figure 5.7 The sequence for transport, addressing, and redispersion of 5-micron negatively charged polystyrene spheres using the 400 test site CMOS microarray. (A,B) The negatively charged 5-micron microspheres being selectively transported and concentrated onto six positively charged test sites. (C,D) The microspheres concentrated onto the six test sites and then repulsed by reversing the bias on the electrodes (400 site CMOS microarray with 50-micron microelectrodes, one-minute run time at 3.5 V DC).

being transported, positioned, and then redispersed from the test sites on the microarray (one minute run time at 3.5 V DC). These results demonstrate the intrinsic ability of electronic microarrays to carry out the directed transport, addressing, and removal of a variety of nanoscale and microscale structures from the test sites of the array device.

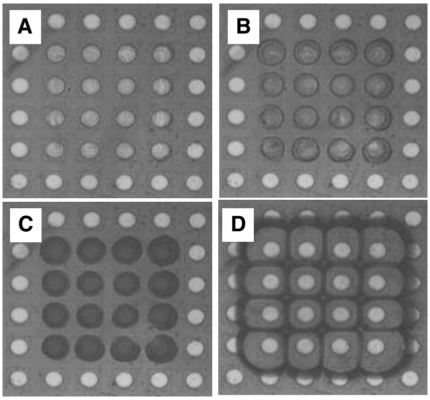

Figure 5.8 The sequence for transport, addressing, and redispersion of 250-nanometer negatively charged polystyrene nanoparticles using the 400 test site CMOS microarray. (A,B) The negatively charged 250-nm nanoparticles being selectively transported and concentrated onto six positively charged test sites. (C,D) The nanoparticles concentrated onto the six test sites and then repulsed by reversing the bias (400 site CMOS microarray with 50-micron microelectrodes, one minute run time at 3.5 V DC).

5.4 Fabrication of Multiple-Layered Nanoparticle Structures Using CMOS Microarrays

Electronic microarrays have clearly demonstrated the ability to be used to carry out the directed self-assembly of DNA molecules. In fact, this is the basis for their commercialization and use in DNA genotypying diagnostic applications. The first step in this directed self-assembly process involves the transport and addressing of a biotinylated DNA sequence to a specific test site, where the DNA sequence becomes bound via the biotin/streptavidin ligand reaction. This binding of the biotinylated DNA molecules to the streptavidin protein molecules within the permeation gel layer of the test site is both rapid and specific. Thus, the protein-ligand binding reaction of streptavidin with biotin itself represents a first-level self-assembly step.

In further electronic microarray directed self-assembly work, a variety of nanoparticles derivatized with either biotin or streptavidin have been assembled into multiple layers via the biotin/streptavidin ligand binding reaction. It now appears that up to 20 layers of alternating biotin/streptavidin derivatized quantum dots can be assembled onto selected microarray test sites in less than one hour. Figure 5.9 shows the results of a 400 test-site CMOS microarray parallel layering experiment with 5, 10, and 20 depositions of quantum dots. Alternating layers of negatively charged 15-nm red fluorescent streptavidin and green fluorescent biotin quantum dots were addressed to microlocations with a total layering time of under one minute per layer. The total time per layer includes washing steps to remove non-specifically bound particles. Figure 5.10 demonstrates the scalability of microarray methods, with the parallel deposition of 25 alternating layers of 40-nm streptavidin/biotin modified nanoparticles collecting atop the microelectrode. It was previously unknown whether sufficient current density could traverse aggregated layers of nanoparticles to allow sequential deposition to continue indefinitely, yet these results indicate that the permeability of nanoparticle aggregates is amenable to repeated layering.

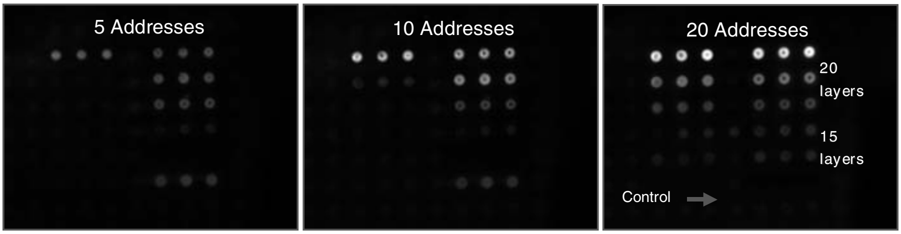

Figure 5.9 Fluorescent microscope analysis results for a series of parallel electric field layering experiments of 5, 10, and 20 addresses of alternate layers of 15-nm red fluorescent streptavidin quantum dots and green fluorescent biotin quantum dots on the 50-micron sites of 400 site CMOS microelectronic array device. The 20-address experiments shows the fluorescent intensity changes for the 20, 15, 10, and 5 quantum dot layers. Layering time was about one minute per layer including washing steps.

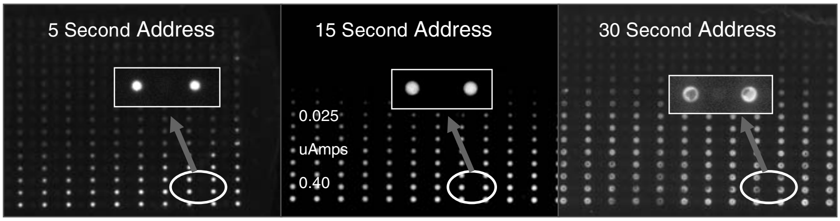

Figure 5.10 Fluorescent analysis results for highly parallel electric field 3-D layering of 25 alternate layers of 40-nm red fluorescent streptavidin nanoparticles and green fluorescent biotin nanoparticles onto the 50-micron-diameter test sites of a CMOS 400 site microarray device. Addressing times were 5 seconds (A), 15 seconds (B), and 30 seconds (C) at DC current levels that ranged from 0.025 μAmp to 0.40 μAmp. Inserts are enlargements of a small section of the microarray each showing the results for 0.375 μAmp on four test sites. Nanoparticle addressing times between 5 and 15 seconds with DC current between 0.35 μAmp and 0.40 μAmp appear to be optimal. The longer 30-second addressing time caused damage to the layered nanostructure. Total layering time is one minute or less per layer, including the washing steps.

It should be noted that the concentrations used within electrophoretic layering are far lower than traditionally used in LBL. One of the main advantages of the microarray technique is that pico- to nanomolar concentrations of bulk reactants can be transported into very high local concentrations above the area of interest and still drive the kinetics of binding. This can be leveraged to reduce the cost of the overall process, as well as to improve the purity of surrounding structures.

In contrast, passive LBL nanofabrication processes are usually at least one order of magnitude slower, are generally carried out in a nonparallel manner (except when used on prepatterned substrates), and do not provide any option for reconfiguring the x-y geometry of the substrate or platform in real time (which may contribute to contamination and lowers the complexity of the achievable hierarchical assembly). These results demonstrate the ability of microarray devices to rapidly perform multiple parallel nanoparticle depositions in a highly parallel manner.

The following provides more detail on some of the experimental procedures and device operations that were used to carry out the assisted assembly of multiple-layered nanoparticle structures. The Nanogen ACV400 control system and 400 test-site CMOS microarrays were used for all the experiments. The controller system is able to supply 0 to 5 V (positive or negative bias) and up to 1 μA of current to each of the microelectrodes on the array. The electronic microarray itself is set within a well capable of holding 30 μl of liquid. The procedure for transporting and addressing the various derivatized nanoparticles for multiple-layer deposition was carried out as follows:

1. The gel is first washed to remove impurities and a protecting layer of arabinose prior to electrophoretic addressing deposition. This is done by placing 30 μL of DI water (all diH_2O was 18.2 mOhms,

Millipore Simplicity 185) in the well to allow the sugar to dissolve and pipetting to assist the removal of the sugar. Afterward the microarray is washed with 6 applications of 25 μL of water to remove any remaining impurities.

2. The streptavidin permeation gel surface is functionalized with biotin dextran (Sigma B-9264, 9.1 mol biotin/mol) to provide adhesion for the streptavidin nanoparticles on the top surface of the gel. Next, 20 μL of 2 μM biotin dextran in water is allowed to sit on the microarray surface for 20 minutes to allow for binding to the gel layer. The microarray is then washed 6 times with 25 μL of water to remove any excess biotin dextran from the array surface. This helps constrain binding to the top of the gel.
3. The microarray is then washed 6 times with 25 μL of 0.2 μm filtered (Nalgene Sterile 0.2 μm) 100 mM aqueous L-histidine (Sigma H-6034) buffer to equilibrate the gel with the L-histidine. Then, 100 mM L-histidine is also used as the electrophoresis buffer.
4. The microarray is electronically configured to have a current ramp from 0.025 μAmp to 0.4 μAmp in 0.025 μAmp increments across alternating columns. This allows one to simultaneously test various current densities to determine parameters for optimal particle deposition, which is another advantage of using a microarray for hierarchical assembly. Activation times per step used in this experiment were 5, 10, 15, 20, and 30 seconds.
5. The first layer of nanoparticles is functionalized with streptavidin, which allows the nanoparticles to be bound to the biotin dextran surface of the microarray. The second layer is the biotin derivatized nanoparticles, which now can be bound to the first layer of streptavidin nanoparticles. The subsequent layers are alternating streptavidin and biotin nanoparticles. The particular experiments being described used either Quantum Dot Corporation Streptavidin and Biotin conjugated quantum dots (Q10301MP, Q10131MP) diluted to 1 nM in 100 mM L-histidine, or Molecular Probes biotin and streptavidin 40 nm fluorescent particles (F8770, F8766) diluted to 50 nM concentration in 100 mM L-histidine. The nanoparticles are placed in diluted solution of 20 μl aliquots into the microarray well structure. The electronic deposition (transport and specific test-site addressing) of the nanoparticles is carried out with an addressing time ranging from 5 to 30 seconds per layer. Because all the derivatized nanoparticles have a net negative charge, the test sites are biased positive for electronic addressing. Between layers, the microarray is washed 6 times with 25 μl of 100 mM L-histidine buffer to remove the nonspecifically bound nanoparticles and those remaining in the solution phase. After washing, a CCD camera image is taken of the nanoparticles viewed through the epifluorescent microscope using either Cy3, Texas Red, or appropriate quantum dot filters. The deposition and washing is repeated with alternating complementary biotinylated nanoparticles

and streptavidin nanoparticles for as many as 40 layering steps, although degradation in transport properties is not observed even after 40 depositions. This indicates that many more layers can be grown before approaching the limits of this technique.

For experiments designed to compare the simultaneous accumulation of nanoparticle layers of various thicknesses, a modified device operation protocol was implemented. This procedure involved (1) preparing the microarrays for deposition as previously described above in steps 1 through 3 of the device operation and nanoparticle deposition parameters and (2) carrying out a total of 20 addressing applications of biotin and streptavidin quantum dot nanoparticles to the microarray. In these experiments, the microarray was programmed for 10 different activation zones. Each zone was for a different total number of addressing applications (5, 10, and 20). Each zone had the same constant current and was on (active) for 15 seconds for each addressing application. The first five zones were all started on the first quantum dot nanoparticle application. The total time they were on during nanoparticle applications was 1, 5, 10, 15, and 20 seconds. The results for these experiments are shown in Figure 5.9. The fluorescent intensity is seen to proportionally increase in relation to the total number of nanoparticle addressings, i.e., highest for the 20-layer addressing. The goal of the second experiment (shown in Figure 5.10) was to try to determine the best addressing time and DC current level for nanoparticle addressing. Addressing times of 5, 15, and 30 seconds were used for a total of 25 nanoparticle depositions. Current levels for the each addressing time (5, 15, 30 seconds) ranged from 0.4 µAmp to 0.025 µAmp, in 0.025 µAmp intervals. Similar procedures as described above were used in these experiments, except 40 nm negatively charged biotin and streptavidin fluorescent nanoparticles were used instead of quantum dots. The results for these experiments appear to show that the 5 to 15 seconds of addressing time in the 0.25 to 0.40 µAmp current range is optimal. The higher addressing time of 30 seconds shows some damage to the nanoparticle layers at the higher current ranges (see Figure 5.10). It is also important to point out that other work with these electronic microarrays has shown that the assembled molecules and nanostructures can be removed from the test sites. This has been demonstrated for DNA sequences that are hybridized to the microarray surface, and now there is preliminary evidence that assembled silica gel structures covering the whole surface can be "lifted off." Such a lift-off process would make the technology even more attractive for future nanomanufacturing applications.

5.5 Strategy for Assisted Self-Assembly and Hierarchical Organization

One of the primary objectives of ongoing research in this area is to demonstrate that electronic microarray devices represent a viable technology for carrying out the assisted self-assembly of functionalized nanostructures into viable

higher-order two- and three-dimensional structures, materials, and devices. Some of the more immediate fabrication goals relate to demonstrating the assisted assembly of quantum dots and other nanoparticles, as well as functionalized carbon nanotubes into higher-order structures using the present electronic microarray devices. Another objective is to develop a newer microelectronic array assembler system to carry out the precision functionalization of nanocomponents and their subsequent assisted organization and assembly into higher-order structures. Future goals will be to use the next generation assembler system to make alternating monolayers of inorganic and semiconductor nanoparticles with DNA sequences as the interstitial biomolecular binding agent, and to produce a variety of different 3-D multilayered nanostructured materials with microscopic dimensions, i.e., x-y-z dimensions for the final layered materials ~1 mm × 1 mm × 1 to 2 micron in thickness.

The overall concept for electric field assisted self-assembly of nanocomponents into complex higher-order 3-D structures including a network of microchannels is shown in Figure 5.11. In this sequence, Figure 5.11A shows a section of the microarray platform with a matrix of square-shaped addressable microelectrodes about 1 to 2 μm², and a set of larger perimeter electrodes about 50 μm in diameter. Figure 5.11B shows the microelectrode matrix coated with a porous hydrogel permeation layer (5 μm in thickness). This is the base construction layer onto which the first layer of nanocomponents would be

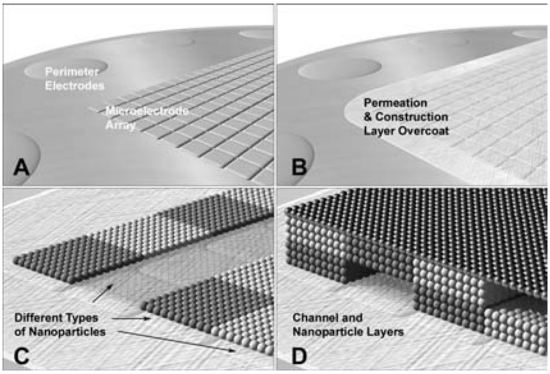

Figure 5.11 Concept for carrying out electric field assisted assembly and 3-D layering of different types of nanoparticles onto a microarray platform device (drawings not to scale). (A) A section of the microarray platform with a matrix of square-shaped addressable microelectrodes about 1 to 2 μm², and set of larger perimeter electrodes about 50 μm in diameter. (B) The microelectrode matrix overcoated with a porous hydrogel permeation layer (5 μm in thickness). This is the base construction layer onto which the first layer of nanocomponents would be bound. (C) Post addressing and binding of the different types of nanospheres (dark, light, and clear) to the base permeation layer. (D) The further 3-D layering of the different nanospheres to the initial layer, and a final, covering one type of nanosphere. The clear bead layers would later be etched out leaving a matrix of microchannels throughout the final structure. The final structure can be released from the microarray platform.

bound. Figure 5.11C shows post addressing and binding of the different types of nanospheres (dark, light, and clear) to the base permeation layer. Figure 5.11D shows the further 3-D layering of the different nanospheres to the initial layer, and a final covering with a capping type of particle. The clear bead layers shown in these images are meant to be etched or dissolved out to create microchannels throughout the final structure. This capability would be extremely important for the production of highly integrated fuel cell devices, as well as for complex biosensor devices that require integrated microfluidic channels. Again, it is important to point out that the final constructs can be easily released from the microarray platform. This capability further adds to the promise that this type of nanofabrication technology may ultimately be used for nanomanufacturing purposes.

5.6 Conclusions and Future Goals

To date, we have developed an electronic microarray platform that enables controlled, solution phase, layer-by-layer deposition of molecular, nanoscale, and micron-scale components. We have also shown that real-time reconfiguration of the {x, y} current densities on the microelectrodes promotes greatly accelerated transport of constituent nanocomponents into the designated patterned areas. More specifically, we have shown that current density-mediated electrophoretic transport across a gel-shielded microelectrode allows for the local concentration or repulsion of nanoparticles (i.e., polystyrene nanoparticles, quantum dots, DNA, and proteins) to be orders of magnitude higher than passive solution-phase deposition, without incurring damage from electrolysis products. As the parallel, controlled integration of diverse constituent materials is a fundamental requirement for the construction of efficient intermetallic nanostructures and high-efficiency photovoltaics, shielded electrophoretic assembly shows great promise toward achieving this goal. However, the transport properties of functionalized nanoparticles across time varying pH and field gradients have not been catalogued, making precise *de novo* assembly difficult. Therefore, there is a need in future studies to characterize the accumulation of nanostructures as a function of bulk solution properties, current density, functionalization, and other electrophoretic parameters, as well as to integrate these empirical results into a rigorous, testable transport model. We have also shown that repeated application of shielded electrophoretic transport to nanoparticle systems with alternating complementarity can be used to create flexible, micron-thick substrates that can be later removed from the underlying electrode. Our evidence indicates that chemical reactions, binding events, and material deposition can be localized and accelerated in a specific, controllable fashion with nanometer-scale vertical resolution. This finding is also very significant, given that little was known about the reduction of ion flux within repeated transport of confluent nanoparticle layers. Based upon our research to date, it seems likely that the material properties, stability, and porosity of these layers can be adjusted by variation of electrophoretic parameters and constituent nanoparticles. Essentially, these microarray devices may lead to the development of a fundamental, scalable

manufacturing process for heterogeneously integrated nanomaterials. In addition, we have shown that shielded electrophoretic deposition is strongly dependent upon the solution-permeation gel interface. It is unknown whether elastic behavior within the gel substrate has deleterious effects on flexible layers. However, the spatial variance as a result of nonlinearities is unacceptable to precision patterns of nanostructures. Future work involving a permeation layer for precise nanostructured materials would promote specific surface adhesion, resist distortion when dried, demonstrate low elasticity, and provide sufficient buffering capacity to protect the upper layers from the electrolysis products.

In summary, electronic microarray devices that produce reconfigurable electric field patterns at the micron-scale level can be used to control the parallel z-dimension self-assembly of nanocomponents within the pattern. In principle, such devices allow the fabrication of highly integrated 3-D layered nanostructures within microscale geometries of electronic or optoelectronic circuitry, fluidic channel networks, or other structural material matrices. Additionally, the finished constructs and materials can be easily released from the assembly platform. Electronic microarray technology represents a unique synergy of combining the best aspects of top-down and bottom-up technologies into a potentially viable nanomanufacturing process. It also represents a bio-inspired logic for self-assembly and hierarchal scaling of nanostructures into integrated macroscopic systems, and it addresses nanostructure integrity and viability issues for maintaining the efficiency of electronic, photonic, catalytic, and dynamic properties as nanocomponents are integrated into higher-order structures. Such a nanofabrication technology will be required for producing highly integrated nano/micro/macrostructures including nanophotonic-based large-scale arrays and displays, high-efficiency multiple-band-gap photovoltaics, fuel cells with nanostructured intermetallic catalysts and integrated fluidic channeling, smart-morphing nanocomposite materials, and *in vivo* biosensor and mother-ship drug delivery devices.

References

1. Svrcek, V., Slaoui, A., and Muller, J.C., Silicon nanocrystals as light converter for solar cells, *Thin Solid Films,* 451, 384, 2004.
2. Mwaura, J.K., Pinto, M.R., Witker, D., Ananthakrishnan, N., Schanze, K.S., and Reynolds, J.R., Photovoltaic cells based on sequentially adsorbed multilayers of conjugated poly(p-phenylene ethynylene)s and a water-soluble fullerene derivative, *Langmuir,* 21, 10119, 2005.
3. Kapur, V.K., Bansal, A., Le, P., and Asensio, O., Non-vacuum processing of CuIn1-xGaxSe2 solar cells on rigid and flexible substrates using nanoparticle precursor inks, *Thin Solid Films,* 431, 53, 2003.
4. Kim, D.W., Choi, H.S., Lee, C., Blumstein, A., and Kang, Y., Investigation on methanol permeability of Nafion modified by self-assembled clay-nanocomposite multilayers, *Electro chem. Acta,* 50, 659, 2004.
5. Hacker, V., Wallnofer, E., Baumgartner, W., Schaffer, T., Besenhard, J.O., Schrottner, H., and Schmied, M., Carbon nanofiber-based active layers for fuel cell cathodes —preparation and characterization, *Electrochem. Comm.,* 7, 377, 2005.

6. Catledge, S.A., Fries, M.D., Vohra, Y.K., Lacefield, W.R., Lemons, J.E., Woodard, S., and Venugopalan, R.J., Nanostructured ceramics for biomedical implants, *Nanosci. Nanotechnol,* 2, 293, 2002.
7. Akerman, M.E., Chan, W.C., Laakkonen, P., Bhatia, S.N., and Ruoslahti, E., Nanocrystal targeting in vivo, *Proc. Natl. Acad. Sci. USA,* 99, 12617, 2002.
8. Gao, J., Gao, T., and Sailor, M.J., A porous silicon vapor sensor based on laser interferometry, *Appl. Phys. Lett.*, 77, 901, 2000.
9. Dancil, K.-P.S., Greiner, D.P., and Sailor, M.J., A porous silicon optical biosensor: detection of reversible binding of IgG to a protein a-modified surface, *J. Am. Chem. Soc.*, 121, 7925, 1999.
10. Chan, S., Fauchet, P.M.,Li, Y., Rothberg, L.J., and Miller, B.L., Porous silicon microcavities for biosensing applications, *Phys. Stat. Sol. A*, 182, 541, 2000.
11. Crommelin, D.J., Strom, G., Jiskoot, W., Stenkes, R., Mastrobattista, E., and Hennick, W.E.J., Nanotechnological approaches for the delivery of macromolecules, *Control Release,* 87, 81, 2003.
12. Prime, K.L. and Whitesides, G.M., Self-assembled organic monolayers: model systems for studying adsorption of proteins at surfaces, *Science,* 252, 1164, 1991.
13. Kim, B., Tripp, S.L., and Wei, A., Self-organization of large gold nanoparticle arrays, *J. Am. Chem. Soc.,* 123, 7955, 2001.
14. Bowden, N., Terfort, A., Carbeck, J., and Whitesides, G.M., Self-assembly of mesoscale objects into ordered two-dimensional arrays, *Science,* 276, 233, 1997.
15. Fink, J., Kiely, C.J., Bethell, D., and Schiffrin, D.J., Self-organization of nanosized gold particles, *Chem. Mater.,* 10, 922, 1998.
16. Lee, S-W., Mao, C., Flynn, C.E., and Belcher, A.M., Ordering of quantum dots using genetically engineered viruses, *Science,* 296, 892, 2002.
17. Mirkin, C.A., Letsinger, R.L., Mucic, R.C., and Storhoff, J.J., A DNA-based method for rationally assembling nanoparticles into macroscopic materials, *Nature,* 382, 607, 1996.
18. Decher, D. and Schlenoff, J.B., *Multilayer Thin Films-Sequential Assembly of Nanocomposite Materials,* Wiley-VCH Verlag, Weinheim, 2003.
19. Hughes, M.P, *Nanoelectromechanics in Engineering and Biology,* CRC Press, Boca Raton, FL, 2003.
20. Brenner, D., Lyshevski, S., Iafrate, G., and Goddard, W.A., *Handbook of Nanoscience, Engineering and Technology,* CRC Press, Boca Raton, FL, 2003.
21. Wanunu, M., Popovitz-Biro, R., Cohen, H., Vaskevich, A., and Rubinstein, I., Coordination-based gold nanoparticle layers, *J. Am. Chem. Soc.,* 127, 9207, 2005.
22. Artyukhin, A.B., Bakajin, O., Stroeve, P., and Noy, A., Layer-by-layer electrostatic self-assembly of polyelectrolyte nanoshells on individual carbon nanotube templates, *Langmuir,* 20, 1442, 2004.
23. Yuan, J.J., Zhou, S.X., You, B., and Wu, L.M., Organic pigment particles coated with colloidal nano-silica particles via layer-by-layer assembly, *Chem. Mater.,* 17, 3587, 2005.
24. Ma, N., Zhang, H.Y., Song, B., Wang, Z.Q., and Zhang, X., Polymer micelles as building blocks for layer-by-layer assembly: an approach for incorporation and controlled release of water-insoluble dyes, *Chem. Mater.,* 17, 5065, 2005.
25. Zapotoczny, S., Golonka, M., and Nowakowska, M., Novel photoactive polymeric multilayer films formed via electrostatic self-assembly, *Macromol. Rapid Comm.,* 26, 1049, 2005.

26. Hammond, P.T., Form and function in multilayer assembly: new applications at the nanoscale, *Adv. Mater.,* 16, 1271, 2004.
27. Jacobs, H.O., Campbell, S.A., and Steward, M.G., Approaching nanoxerography: the use of electrostatic forces to position nanoparticles with 100 nm scale resolution, *Adv. Mater.,* 14, 1553, 2002.
28. Barry, C.R., Gu, J., and Jacobs, H.O., Charging process and coulomb-force-directed printing of nanoparticles with sub-100-nm lateral resolution, *Nano Letters,* 5, 2078, 2005.
29. Mardilovich, P. and Kornilovitch, P., Electrochemical fabrication of nanodimensional multilayer films, *Nano Letters,* 5, 1899, 2005.
30. Allred, D.B., Sarikaya, M., Baneyx, F., and Schwartz, D.T., Electrochemical nanofabrication using crystalline protein masks, *Nano Letters,* 5, 609, 2005.
31. Tsai, D.H., Kim, S.H., Corrigan, T.D., Phaneuf, R.J., and Zachariah, M.R. Electrostatic-directed deposition of nanoparticles on a field generating substrate, *Nanotechnology,* 16, 1856, 2005.
32. Lumsdon, S.O., Kaler, E.W., and Velev, O.D., Two-dimensional crystallization of microspheres by a coplanar AC electric field, *Langmuir,* 20, 2108, 2004.
33. Lin, J.C., Yates, M.Z., Petkoska, A.T., and Jacobs, S., Electric-field-driven assembly of oriented molecular-sieve films, *Adv. Mater.,* 16, 1944, 2004.
34. Hua, F., Shi, J., Lvov, Y., and Cui, T., Patterning of layer-by-layer self-assembled multiple types of nanoparticle thin films by lithographic technique, *Nano Letters,* 2, 1219, 2002.
35. Ko, H.H., Jiang, C.Y., and Tsukruk, V.V., Encapsulating nanoparticle arrays into layer-by-layer multilayers by capillary transfer lithography, *Chem. Mater.,* 17, 5489, 2005.
36. Small Wonders, Endless Frontiers: Review of the National Nanotechnology Initiative, National Research Council, 2002.
37. The National Nanotechnology Initiative—Strategic Plan, National Science and Technology Council, December 2004.
38. Heller, M.J., Tu, E., Martinsons, R., Anderson, R.R., Gurtner, C., Forster, A., and Sosnowski, R., Active microelectronic array systems for DNA hybridization, genotyping, pharmacogenomics and nanofabrication applications, in *Integrated Microfabricated Devices*, 2002, pp. 223–270.
39. Heller, M.J., An active microelectronics device for multiplex DNA analysis, *IEEE Eng. Med. Biol.* 15, 100, 1996.
40. Sosnowski, R.G., Tu, E., Butler, W.F., O'Connell, J.P., and Heller, M.J., Rapid determination of single base mismatch in DNA hybrids by direct electric field control, *Proc. Nat Acad. Sci. USA*, 94, 1119, 1997.
41. Edman, C.F., Raymond, D.E., Wu, D.J., Tu, E., Sosnowski, R.G., Butler, W.F., Nerenberg, M., and Heller, M.J., Electric field directed nucleic acid hybridization on microchips, *Nucleic Acids Res.*, 25, 4907, 1997.
42. Heller, M.J., An integrated microelectronic hybridization system for genomic research and diagnostic applications, in *Micro Total Analysis Systems '98*, Harrison, D.J. and van den Berg, A., Eds., Kluwer Academic Publishers, Dordrecht, 1998, pp. 221–224.
43. Heller, M.J., Tu, E., Holmsen, A., Sosnowski, R.G., and O'Connell, J.P., *Active Microelectronic Arrays for DNA Hybridization Analysis in DNA Microarrays: a Practical Approach*, Oxford University Press, Oxford, 1999, pp. 167–185.
44. Heller, M.J., Forster, A.H., and Tu, E., Active microelectronic chip devices which utilize controlled electrophoretic fields for multiplex DNA hybridization and genomic applications, *Electrophoresis,* 21, 157, 2000.

45. Gurtner, C., Tu, E., Jamshidi, N., Haigis, R., Onofrey, T., Edman, C.F., Sosnowski, R., Wallace, B., and Heller, M.J., Microelectronic array devices and techniques for electric field enhanced DNA hybridization in low-conductance buffers, *Electrophoresis*, 23, 1543, 2002.
46. Kassengne, S.K., Reese, H., Hodko, D., Yang, J.M., Sarkar, K., Swanson, P., Raymond, D.E., Heller, M.J., and Madou, M.J., Numerical modeling of transport and accumulation of DNA on electronically active biochips, *Sensor. Actuator. B*, 94, 81, 2003.
47. Huang, Y., Sunghae, J., Duhon, M., Heller, M.J., Wallace, B., and Xu, X,, Dielectrophoretic separation and gene expression profiling on microelectronic chip arrays, *Anal. Chem.*, 74, 3362, 2002.
48. Swanson, P., Gelbart, R., Atlas, E., Yang, L., Grogan, T., Butler, W.F., Ackley, D.E., and Sheldon, E., A fully multiplexed CMOS biochip for DNA Analysis, *Sensor. Actuator. B*, 64, 22, 2000.
49. Esener, S.C., Hartmann, D., Heller, M.J., and Cable, J.M., DNA assisted micro-assembly: a heterogeneous integration technology for optoelectronics, in *Proc. SPIE Critical Reviews of Optical Science and Technology, Heterogeneous Integration*, Hussain, A., Ed., CR70, Chapter 7, 1998.
50. Gurtner, C., Edman, C.F., Formosa, R.E., and Heller, M.J., Photoelectrophoretic transport and hybridization of DNA on unpatterned silicon substrates. *J. Am. Chem. Soc.*, 122, 8589, 2000.
51. Huang, Y., Ewalt, K.L., Tirado, M., Haigis, R., Forster, A., Ackley, D., Heller, M.J., O'Connell, J.P., and Krihak, M., Electric manipulation of bioparticles and macromolecules on microfabricated electrodes. *Anal. Chem.*, (73) 1549, 2001.
52. Edman, C.F., Gurtner, C., Formosa, R.E., Coleman, J.J., and Heller, M.J., Electric-field-directed pick-and-place assembly, *HDI*, 10, 30, 2000.
53. Edman, C.F., Swint, R.B., Gurthner, C., Formosa, R.E., Roh, S.D., Lee, K.E., Swanson, P.D., Ackley, D.E., Colman, J.J., and Heller, M.J., Electric field directed assembly of an InGaAs LED onto silicon circuitry, *IEEE Photon. Tech. Lett.*, 12, 1198, 2000.
54. Daniel, M., Hartmann, D., Schwartz, G., Tu, M., Heller, S., and Esener, C., Selective DNA attachment of particles to substrates, *J. Mater. Res.*, 17, 473, 2002.
55. US # 6,569,382 "Methods and Apparatus for the Electronic Homogeneous Assembly and Fabrication of Devices," issued May 27, 2003.
56. US #6,652,808 "Methods for the Electronic Assembly and Fabrication of Devices," issued November 25, 2003.
57. US #6,706,473 "Systems and Devices for the Photoelectrophoretic Transport and Hybridization of Oligonucleotides," issued March 16, 2004.
58. Cheng, J., Sheldon, E.L., Wu, L., Uribe, A., Gerrue, L.O., Carrino, J., Heller, M., and O'Connell, J., Electric field controlled preparation and hybridization analysis of DNA/RNA from E. coli on microfabricated bioelectronic chips, *Nat. Biotechnol.*, 16, 541, 1998.
59. Cheng, J., Sheldon, E.L., Wu, L., Heller, M.J., and O'Connell, J., Isolation of cultured cervical carcinoma cells mixed with peripheral blood cells on a bioelectronic chip, *Anal. Chem.*, 70, 2321, 1998.

Chapter 6

Manufacturing Electrical Contacts to Nanostructures

Loucas Tsakalakos

Contents

6.1 Introduction 127
6.2 Direct Synthesis 128
6.3 Post Synthesis 136
6.4 Molecular Electronics 140
6.5 Quantum Dots 143
6.6 Quality of Contacts 143
6.7 Conclusions 144
References 144

6.1 Introduction

In the past 5 to 10 years there has been tremendous progress in the synthesis of novel nanostructures, the literature being too vast to review here. Structures such as nanowires, nanotubes, nanoparticles, quantum dots, functional organic molecules, and synthetic biological nanostructures (proteins, DNA, etc.) have been demonstrated and have been proposed as building blocks in numerous electronic applications, including elements in computing systems,[1–3] flexible display backplanes,[4,5] sensors,[6] light emitting diodes,[7] and solar cells.[8] In order for these novel nanostructures to be effectively used in electronics products, methods for forming electrical contacts to such structures in a manufacturable fashion are required. The term *manufacturable* implies that the contacts can be made at a high rate in a scaleable process (across large substrates), with precise control of the contact area, resistance, density, and yield. Related to the formation of contacts is the notion that a

certain level of control over the position of such structures on a substrate or within layers is required.

While the electronics industry has considerable experience with manufacturing contacts to "top-down" fabricated nanodevices in, for example, Pentium chips, the ability to contact individual nanostructures synthesized by emerging vapor, chemical, and biological techniques at high rates and yields remains to be developed. Nevertheless, various techniques have been developed for contacting nanostructures, primarily for research purposes.

The methods outlined in this chapter represent the state of the art in wiring of nanostructures. The chapter will review the technical features of these approaches and describe their potential for introduction into high-volume manufacturing processes. However, which approach will ultimately be used in a manufacturing process is highly dependent on the requirements of the product, such as tolerance, contact resistance, yield, and cost. It is noted that in general the field of "nanomanufacturing" is in a state of flux with new developments presented in the literature at a high pace. We therefore expect to update this chapter in future versions of the handbook to describe new techniques as well as highlight nanomanufacturing processes that have entered the production phase.

The contents of the chapter are split along two general lines: (1) contacts that are formed during synthesis of the nanostructure and (2) contacts formed after the synthesis has occurred. The latter typically requires assembly and position processes, which will be described as appropriate. Emphasis will be placed on one-dimensional nanostructures such as nanowires and nanotubes, although contacts to nanoparticles and functional molecules will be discussed.

6.2 Direct Synthesis

The ability to fabricate contacts during the synthesis of nanostructures possesses several distinct advantages. It is possible to prefabricate the contacts on a substrate and then simply introduce the substrate into the process tool required for nanostructure synthesis. Furthermore, and perhaps most importantly, it does not require elaborate techniques for precisely positioning the nanostructures on the substrate. Nevertheless, in some cases external fields (electric, magnetic, and stress) may be required. Another potential disadvantage is that severe constraints may be placed on the materials and processes used to form the nanostructures because materials incompatibilities such as thermal expansion mismatch or chemical reactivity may dominate. The thermal budget may also be severely limited as a result. In this section several specific examples of heterogeneous materials integration at the nanoscale for the purpose of making electrical contacts will be described in order to provide the reader with concrete ideas on how a specific problem may be approached. As will be apparent, the technique employed may be highly dependent on the materials systems and synthetic strategies.

Perhaps the prototypical nanostructure is the carbon nanotube (CNT). CNTs were originally synthesized using a vacuum arc technique by Iijima

and Ickihashi[9] and later via pulsed laser ablation (PLA) introduced by Smalley and co-workers[10] techniques that do not readily allow for direct synthesis on substrates. However, it was later shown that it is possible to directly synthesize carbon nanotubes across electrode contacts using thermal chemical vapor deposition (CVD).[11] This is accomplished both with and without the use of an electric field applied across the electrodes during CVD.[12] The nature of these contacts to CNTs is typically the Shottky type, and field effect transistors were demonstrated,[13] including the demonstration of an electrostatically doped p-n junction.[14]

The growth mechanism responsible for the synthesis of the CNTs by CVD is a modification of the so-called vapor-liquid-solid (VLS) technique, originally discovered by Wagner and Ellis for synthesis of single crystal silicon whiskers.[15] The technique requires metal catalyst nanoparticles, which are supersaturated by atoms from a hydrocarbon vapor that subsequently precipitates as a nanotube. The key to making such contacts to CNTs is to deposit the metal catalyst particles (typically an Fe-Ni-Cr mixture) as a thin film in a confined space on top of a larger metal electrode (Figure 6.1). The structure is then simply placed in the CVD furnace and carbon nanotubes are grown using well-known recipes, primarily using gases such as methane, propane, and ethylene.

Inorganic nanowires, another class of emerging nanomaterials, also may be formed using the VLS mechanism. However, growth across electrodes has proven to be quite a challenge for nanowires such as Si, ZnO, GaAs, and GaN. Indeed it is only recently that Decker et al.[16] used CVD in an electric field to grow nickel silicide nanowires directly from electrodes on a substrate (Figure 6.2), the silicide being formed as a result of reaction of the silicon introduced by silane with the nickel present in the electrodes. This author has also demonstrated growth of ZnO nanowires on metal electrodes and bridging of electrodes by the nanowires (Figure 6.3). It is also possible to

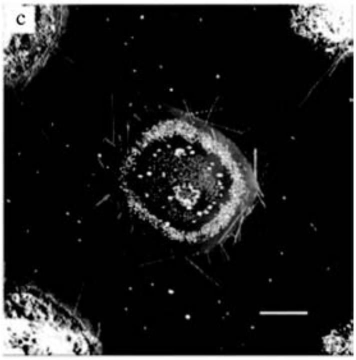

Figure 6.1 Scanning electron microscope (SEM) image of carbon nanotubes grown from the edge of catalyst islands. (From Zhang, Y. et al., *Appl. Phys. Lett.*, 79, 3155, 2001. With permission.)

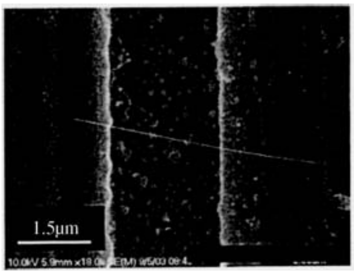

Figure 6.2 SEM image of a NiSi nanowire grown across electrodes. (From Decker, C.A. et al., *Appl. Phys. Lett.*, 84, 1389, 2004. With permission.)

form bilayer metal electrodes in which the catalyst is placed below an inactive layer such that nanowires are formed from the edge of the metal electrode and grow toward an oppositely placed electrode.

A variant of such edge growth was recently demonstrated by Saif Islam et al.[17] In this technique, trenches are wet or dry etched into an Si substrate. The catalyst metal, Au for the case of Si nanowires, is deposited at a glancing angle

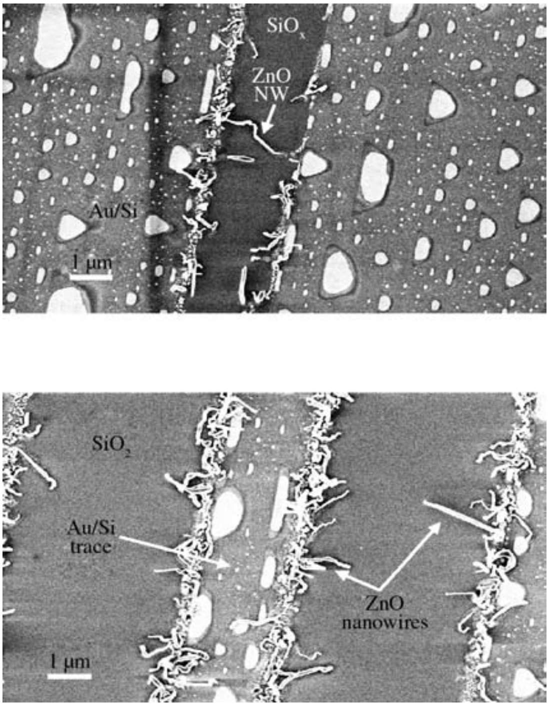

Figure 6.3 SEM images of ZnO nanowires grown across Au metal traces on Si. (L. Tsakalakos, unpublished.)

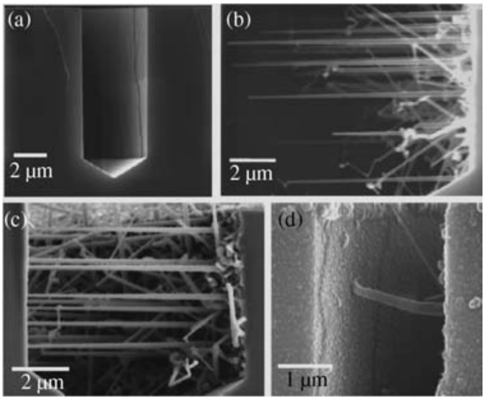

Figure 6.4 SEM images of Si nanowires grown across trenches formed in Si substrates. (From Saif Islam, M. et al., *Nanotechnology,* 15, L5, 2004. With permission.)

such that it coats the top edge of the trench (Figure 6.4). Due to the homoepitaxial growth of the Si nanowire on the Si substrate, the wires grow horizontally from the edge and contact the opposite side of the trench. The metal catalyst at the growing top of the nanowires spreads onto the opposite surface until growth is terminated. A similar approach may be used with silicon-on-insulator substrates to provide electrical isolation of the nanowires from the substrate.

Yet another means of achieving connection to horizontally grown one-dimensional nanostructures is to confine the nanowires/tubes inside the well-defined geometry of a nanofluidic channel.[18] Metal is deposited and patterned on a substrate, and silicon nitride is deposited over the metal lines to define the height and width of the channels (Figure 6.5). Holes are opened into the top of the nitride layer above the metal lines and much of the metal (e.g., Au) is etched back, leaving small slugs of metal to act as the catalyst. CVD is then used to grow the nanowires, which automatically make contact. This approach is particularly promising for large-scale integration of 1-D nanostructures.

The techniques described above primarily rely on CVD growth of 1-D nanostructures. However, there are also electrochemical methods available for the synthesis of nanostructures. This general synthetic approach involves the use of arrays of nano-sized channels in an inorganic or organic matrix to act as templates for the synthesis of nanowires and/or composite structures. The best-known example of this is the use of anodic aluminum oxide (AAO; sometimes referred to as porous anodic aluminum, PAA), in which a bulk or thin film slab of aluminum is oxidized in a solution upon application of a potential.[19] This process leads to the formation of 10- to 100-nm-sized pores in the aluminum oxide layer that can be tens of micrometers long (Figure 6.6). When performed on a substrate, the channels are oriented perpendicular to the plane of the substrate. One then electrodeposits

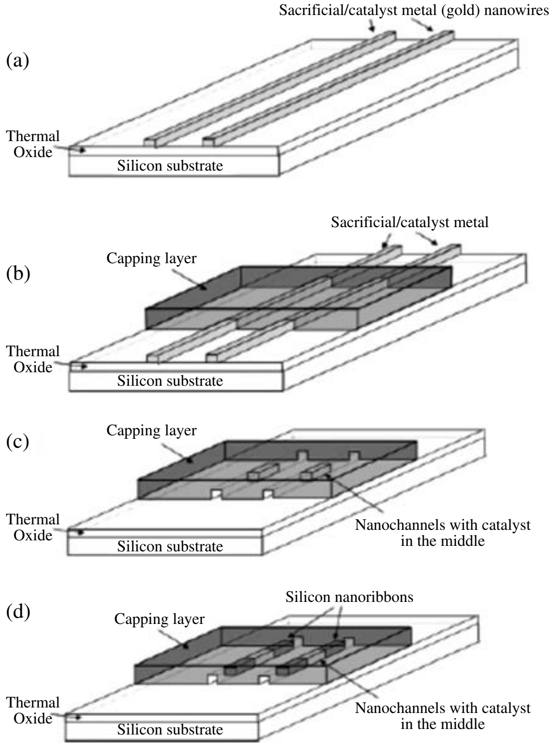

Figure 6.5 Process flow for the fabrication of self-assembling/positioning Si nanowires/nanoribbons using nanochannel templates. (a) Sacrificial/catalyst metal (Au) lines defined by e-beam lithography and lift-off. (b) Deposition and patterning of the capping layer. (c) Partial etching of the sacrificial metal to form the nanochannels with catalyst in the middle. (d) Si nanowire/nanoribbon growth by the VLS mechanism. (From Shan, Y. et al., Nano Letters, 4, 2085, 2004. With permission.)

metal into the nanopores using a suitable precursor solution (see Figure 6.6).[20] Alternatively, nanowires can be grown in the template by VLS growth after electrodeposition of a suitable catalyst in the nanopores (Figure 6.7).[21] This method was used to make electrical contacts to a large number of Si nanowires in a bulk AAO array and measure their collective electrical current-voltage response (Figure 6.8).[22,23]

A method for forming the nanopores such that their length is in the plane of the substrate has been developed by Cojocaru et al.[24] In this manner it is possible to form nanowires aligned in the plane of the substrate and contact them on either end afterwards (Figure 6.9). The number of nanowires that may be formed by this method depends on the initial thickness and width of the aluminum layer, although the exact value remains to be determined. The possibility of forming a single layer of aligned wires remains to be demonstrated, however.

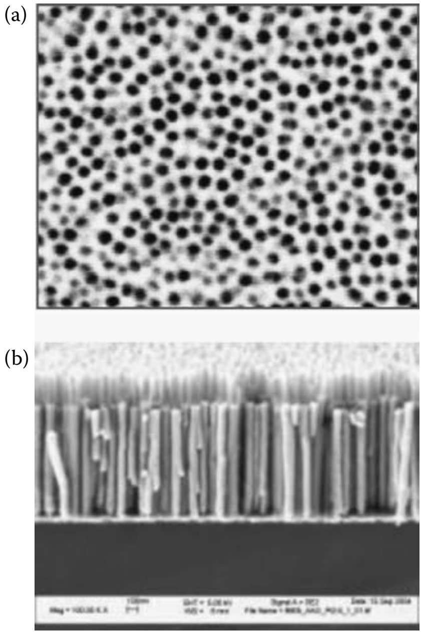

Figure 6.6 (a) Plan view image of AAO film on a silicon substrate and (b) cross-sectional view of Ni nanowires electrodeposited in AAO on a silicon substrate. (Courtesy of Dr. R. Corderman, GE Global Research.)

The use of *in situ* electric and/or magnetic fields to align one-dimensional nanostructures during synthesis is also promising, as noted above. This technique was first shown by Dai and co-workers[25] for CNTs, and useful devices were demonstrated. The field strength used was on the order of 5 V/μm, a field easily achievable with microlithographically patterned electrode structures.

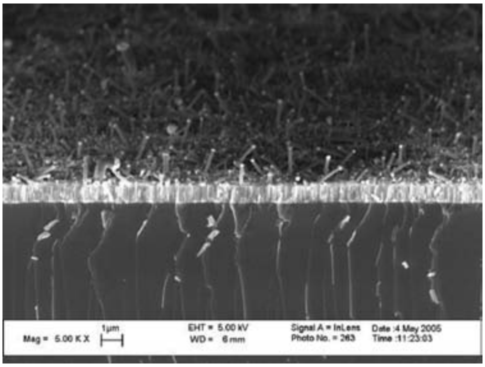

Figure 6.7 Si nanowires grown by VLS in an AAO nanotemplate on a silicon substrate (L. Tsakalakos unpublished). (From Tsakalakos, L. et al., *J. Appl. Phys.*, 98, 4317, 2005. With permission.)

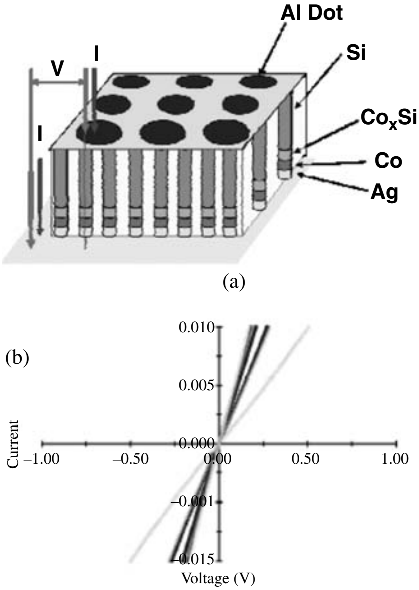

Figure 6.8 (a) Schematic structure used to make contact to Si nanowire array and (b) I-V data collected after annealing the contact. (From Dilts, S.M. et al., *Mater. Res. Soc. Symp. Proc.*, 832, F9.10.1, 2005. With permission.)

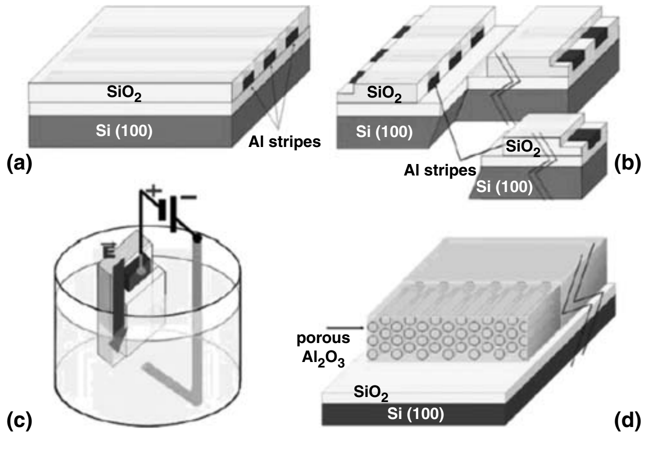

Figure 6.9 Schematic of the method for forming anodized alumina nanotemplates in the plane of a substrate by (a) patterning an Al thin film and capping with a dielectric, (b) patterning the composite structure, (c) placing the substrate in an electrochemical bath to form (d) the final nanoporous alumina structure. (From Cojocaru, C.S., et al., *Nano Letters*, 5, 675, 2005. With permission.)

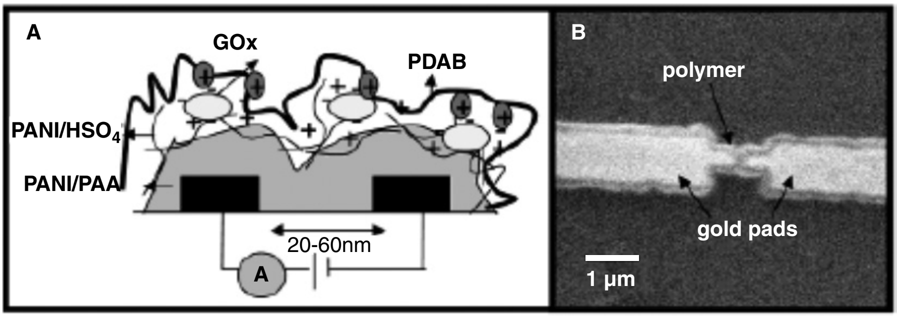

Figure 6.10 Schematic and SEM of a polymer nanojunction glucose sensor formed by direct electrochemical growth across the nano-gap electrodes. (From Forzani, E.S., et al., *Nano Letters,* 4, 1785, 2004. With permission.)

A similar approach was used to form nickel silicide nanowires across electrodes, where the field strength during flow of silane was on the order of 5 V/μm.[26] Silicon nanowires have also been grown across MEMS electrode structures.[27] These general techniques are attractive in that patterned features may be fabricated prior to synthesis of the nanostructures; however, practical issues associated with making electrical contacts to the substrates at high temperature may limit their applicability to high-volume manufacturing.

In addition to inorganic nanowires, it is possible to form organic nanostructures across metal electrodes. The nanowires are formed electrochemically across electrodes when a potential is applied (Figure 6.10).[28] This approach is useful for forming biochemical nanosensors.

A similar method may be used to make contacts to individual molecules for so-called "molecular electronics" applications (see below). The nanostructures in this case are organic molecules that have been designed to have functionality such as switching and memory.[29] This requires the fabrication of electrodes with gaps on the order of 1 to 10 nm such that the functional organic molecules may span the gap and make contact to the metal, typically by a thiol (Au-S) bond. Saifullah et al. described an approach for reliably fabricating such electrodes with sub-5-nm gaps (Figure 6.10).[30]

The approaches described above integrate nanostructures with metal electrodes during synthesis; however, the electrodes are rather large compared with the size of the structures and have been prefabricated. Another option is to synthesize the nanostructures and then directly attach metal wires to the end of the structure. This was recently demonstrated for CdSe nanowires formed by a solution-based process in which metal end caps were attached *in situ* (Figure 6.11).[31] This is powerful in that intimate electrical contact with the nanowire may be made. However, the structures must eventually be aligned and integrated with larger-scale structures. In the next section methods of wiring nanostructures that have already been synthesized will be reviewed.

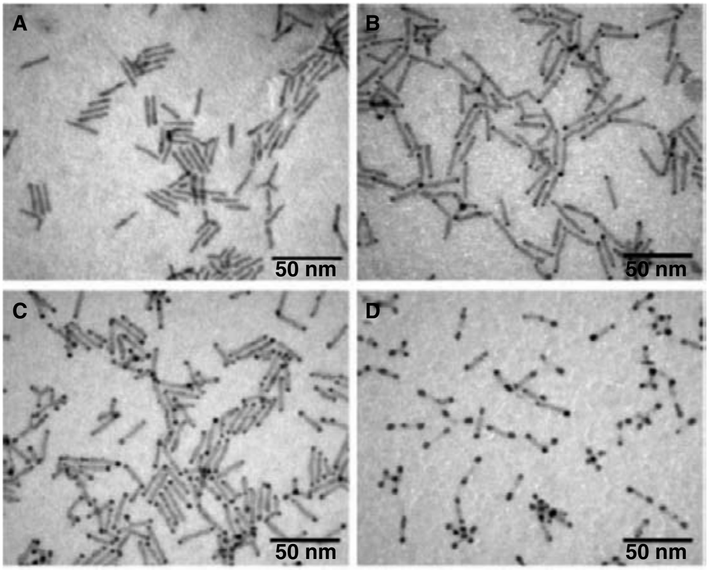

Figure 6.11 CdSe nanorods (a) before and (b–d) after deposition of Au nanoparticles on the tips by increasing concentration of $AuCl_3$ in solution. (From Mokari, T. et al., *Science*, 304, 1787, 2004. With permission.)

6.3 Post Synthesis

The post-synthesis methods generally require the dispersion of the nanostructures of interest in a fluid medium such that they may be deposited on a substrate and electrical contacts subsequently made. The advantage of such methods is that the nanostructures are made separately so the material's compatibility with the contact at high temperature does not impact growth. It is also possible to grow nanostructures of different composition separately and then integrate them on the substrate of interest afterwards.

The easiest approach is to disperse nanowires randomly on a substrate and make contact by standard photolithography, assuming the nanostructures are of high enough aspect ratio to bridge the gap that can be formed by the photolithography tool. While this approach generally produces adequate devices for research purposes (Figure 6.12),[32] it is not suitable for manufacturing because the yield is relatively low (<10%). This is due to the random placement of the nanostructures that have to match well-defined contact features, making the probability of such contact relatively low.

It is also possible to pattern the contacts by the use of electron beam lithography (EBL), which is indeed the standard approach used in research. The technique is rather tedious; prepatterned alignment marks are placed on the substrate to act as reference points for triangulation of the position of the desired nanostructures during a pre-examination of the substrate

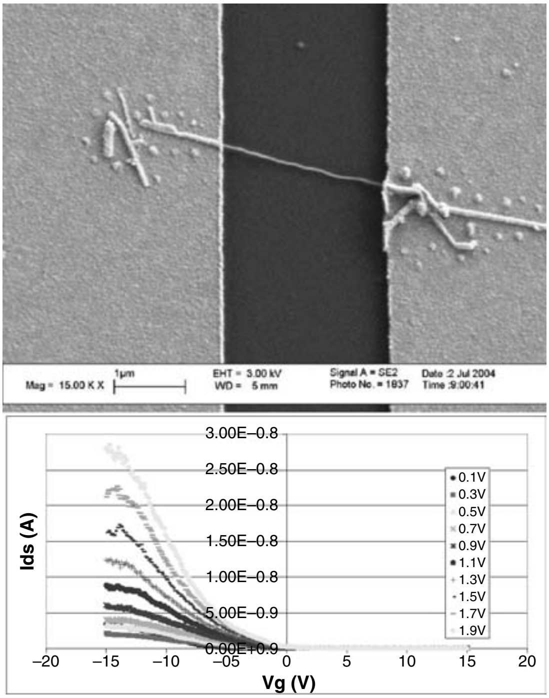

Figure 6.12 SEM image of a silicon nanowire (SiNW) field effect transistor (FET) made by random dispersion and photolithography and transfer characteristics of a p-type doped SiNW FET. (L. Tsakalakos, unpublished)

surface (after deposition of the structures from liquid). The desired pattern is then generated in a CAD file that is then fed into the electron-beam lithography software. Photoresist is deposited on the sample and the nanostructures must again be located in the SEM, taking care to avoid over-exposure of the resist. The pattern is then written after precise alignment of the reference points and synchronization with the software. At present it appears this approach is not conducive to manufacturing.

The yield of devices based on one-dimensional nanostructures may be increased by the use of alignment techniques that provide preferred orientation for high aspect ratio nanostructures. One such approach is to use structured fluid flow fields to align the nanostructures, primarily by the use of microfluidics. Zhong et al[2] have shown that microfluidic techniques may effectively align nanowires onto a substrate and allow for the formation of junctions between nanostructures at random angles to one another. While this technique allows for the demonstration of novel devices, its applicability to large-scale manufacturing remains to be determined. Furthermore, for less stiff nanostructures, such as carbon nanotubes, the forces generated in the microfluidic channels may not be high enough to effectively align them.

Rather, it has been shown that the much higher shear forces generated during spin coating and related processes can align CNTs and related structures.

The well-known Langmuir–Blodgett (L-B) technique, invented at the GE Research Center in the 1930s,[33] has been shown to be an effective means of aligning nanostructures. The L-B process involves the separation of molecules or nanostructures onto the surface of a liquid in a trough. The area of the trough is subsequently reduced, which compresses the material present on the surface and can lead to alignment of molecules/nanostructures due to thermodynamics. Yang and co-workers used the L-B process to align Ag nanowires and then place them on a substrate, demonstrating a surface-enhanced Raman device.[34] Concurrently, Lieber and co-workers were able to align multiple layers of nanowires on a substrate at right angles to one another and in confined spaces after subsequent lithography (Figure 6.13).[35] While no devices using L-B techniques have been demonstrated to date, this approach may prove relevant for nanomanufacturing.

Another fundamentally different method for precise placement of post-synthesized nanostructures is the concept of chemically functionalizing discrete areas of a substrate with a compound that will react with the surface of the nanostructures. The nanostructures themselves may or may not be functionalized, or the contrast between hydrophobic and hydrophilic areas imparts a force on the nanostructure near the interface forcing it to one area. This was first demonstrated with CNTs, which were preferentially attracted to a patterned Au surface containing polar cysteamine molecules relative to nonpolar 1-octadecanethiol (Figure 6.14).[36] A similar technique was used for placement of metal nanowires on a substrate.[37] The problems associated with this class of placement methods are that (1) the chemical patterning requires another high-resolution lithography step in order to have a sufficiently small area; (2) typically, bunches of nanostructures are captured by the chemically functionalized regions on the substrate rather than a single nanostructure; and (3) the presence of organic molecules on the surface of electrically active nanostructures may impact their critical electrical characteristics.

Electric field alignment, described above, may also be used for 1-D nanostructures after synthesis. The fundamental principle is that dipoles generated in the nanostructure during application of an AC electric field will produce a torque on the wires, causing them to align perpendicular to the electrode gap. This method was first demonstrated for Au nanostructures by Smith et al.[38] and also subsequently applied to ZnO and InP nanowires.[39,40] While in principle this is a very useful method with possible applications in manufacturing, the quality of contacts (to be discussed below) is not sufficient after alignment without further application of an aligned top electrode layer or by a thermal annealing step. Magnetic alignment and assembly of ferromagnetic nanowires has also been shown.[41]

In addition to chemical vapor deposition, there are many other synthetic schemes for synthesizing semiconducting 1-D nanostructures, including the solution-based chemical synthesis described above, and the use of wet etching

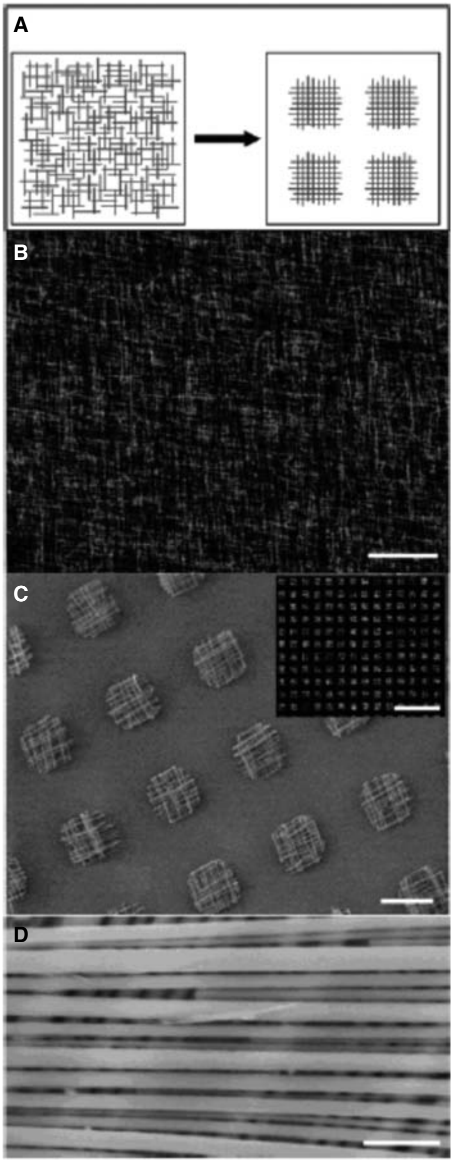

Figure 6.13 Demonstration of a patterned, cross-bar nanowire architecture formed by sequential Langmuir-Blodgett deposition. (From Whang, D. et al., *Nano Letters*, 3, 1255, 2003. With permission.)

of substrates.[43] When combined with microcontact printing, this latter technique may be relevant to large-scale manufacturing of certain devices using semiconducting nanowires such as Si and Ge. A bulk substrate is masked with a metal layer and wet etched anisotropically to yield submicrometer strips of single-crystal material with a triangular cross section. The wires are then lifted

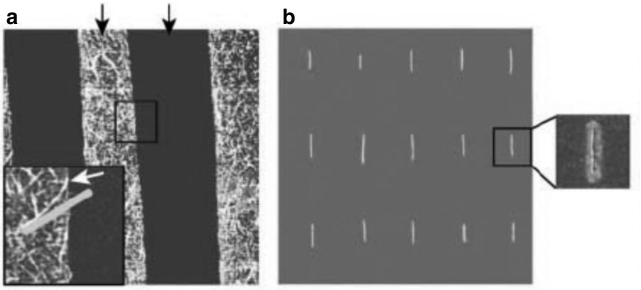

Figure 6.14 Example of selective deposition of carbon nanotubes to a patterned polar region on an otherwise nonpolar chemically functionalized substrate. (From Rao, S.G. et al., *Nature*, 425, 36, 2003. With permission.)

off the substrate by a soft transfer wafer and placed on another substrate as desired. This is of particular interest for flexible electronics applications.

Finally, it is possible to form semiconductor nanowires using a top-down technique developed by Heath and co-workers entitled superlattice nanowire pattern transfer (SNAP).[44] The method uses GaAs/AlGaAs multilayer thin-film structures grown on a substrate in which one of the materials in the superlattice is selectively etched at the substrate edge to form an ultra-high resolution mask for stamping (Pt) metal nanowire traces onto an SOI substrate. The SOI is subsequently dry etched to form free-standing Si nanowire arrays with diameters and pitches as small as 18 nm and 30 nm, respectively (Figure 6.15). The lengths of the wires may be hundreds of microns. The stamp may be used numerous times, making this a promising nanowire manufacturing method. Electrical contacts are formed after nanowire fabrication and require additional steps,[45] although alignment during the contact formation and individual nanowire contacts require further development.

6.4 Molecular Electronics

The nanostructures described above are 1-D organic or inorganic structures with a relatively high aspect ratio. Another class of electrically active structures is the single molecules currently being investigated for so-called molecular electronics, or "moletronics," that in principle could provide the ultimate in high-density, high-speed electronic chips, although being quite far from commercialization.[46] This area of research poses significant technical challenges for making good contacts. Indeed, the nature of the contacts and their impact on measured properties are currently under debate. Some of the leading methods for making contacts to single molecules or groups of molecules are discussed below.

One of the first demonstrations of measuring single molecules was achieved with the so-called "mechanical break junction" (MBJ) by Reed and co-workers.[47] The technique involves fabricating a nanowire on an Si substrate that spans a perforation etched in the substrate. The substrate

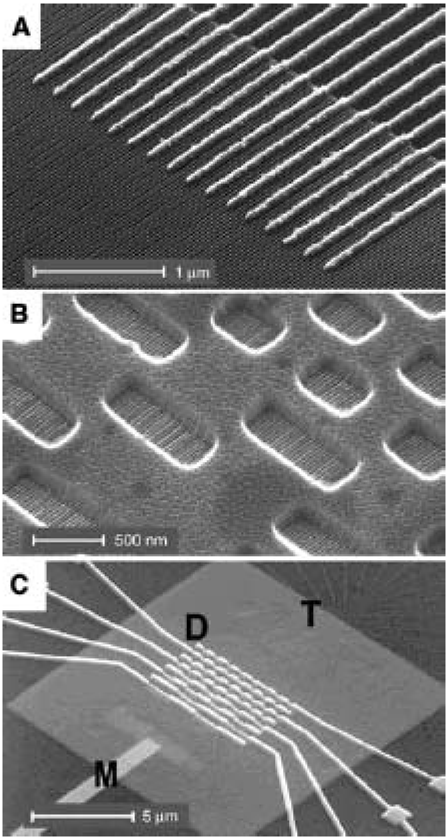

Figure 6.15 SEM images of a Si nanowire demulitplexer circuit fabricated using SNAP with electrical contacts made to 2 or 3 nanowires by electron-beam lithography. (From Beckman, R. et al., *Science*, 310, 465, 2005. With permission.)

is then broken in a controllable fashion such that the separation between the two segments of the wire on the substrate surface may be adjusted with a precision on the order of angstroms. Molecules may be inserted in the gap that attach to the metal with thiol bonds. This technique is clearly not well suited for manufacturing, although it is useful for research purposes.

Another method that is applicable to research is the use of a scanning tunneling microscopy (STM) or conducting atomic form microscope (AFM) to make contacts to single molecules.[48,49] A self-assembled monolayer (SAM) is placed on a Au-coated substrate. SAMs contain a certain density of defects in the form of pinholes. Thiolated functional molecules are then inserted in these pinholes and gold nanoparticles are attached to the top side of the molecules (Figure 6.16). The surface is imaged with the AFM and the probe is then placed in direct contact with the Au nanoparticles.

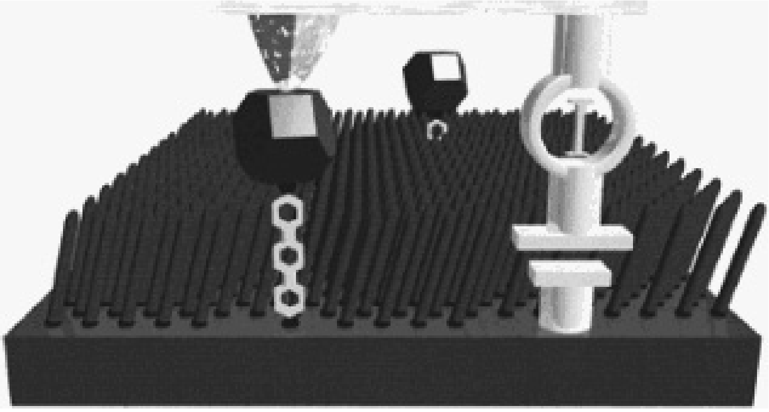

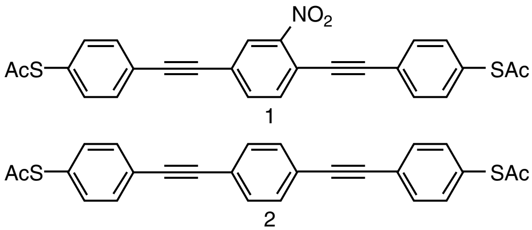

Figure 6.16 Method of making electrical contact to organic molecules in a SAM using AFM. (From Rawlett, A.M. et al., *Appl. Phys. Lett.*, 81, 3043, 2002. With permission.)

Anodic aluminum oxide has also been applied to molecular junctions containing multiple molecules, i.e., on the order of thousands of molecules.[50] This is achieved by electrochemically filling the nanopores of AAO with a metal nanowire that is then capped with Au. Thiolated molecules are then assembled within the pores and a top metal is then electrodeposited. In this manner a large array of molecular junctions is formed, thus requiring statistical analysis in order to yield information on a single junction (containing ~10^3 molecules).

Electron beam patterned electrodes with gaps on the order of 1 to 5 nm are also used for contacting a relatively small number of functional molecules.[51] The gap size pushes the limits of EBL but is possible by adjustment of the parameters for developing the photoresist.

More sophisticated methods for contacting molecules have been developed with greater promise for manufacturing of future products. Williams and co-workers have developed cross-bar architecture in which ~10^3 molecules are sandwiched in the volume between overlapping electrodes.[52] The cross-bar nanoelectrodes are fabricated by nanoimprint lithography,[53] a very promising lithographic technique that is seriously being considered for next-generation lithography of Si-based chips by the electronics industry. This is a more sophisticated design of what was originally proposed by the same group in which the functional rotaxane molecules

were capacitively switched between an Al/Al_2O_3 and Ti/Al electrode structure.[54] Reed et al. have also demonstrated a microfabrication technique that allows one to make contact to assemblies of molecules in a fashion that also hermetically seals them.[55] Nevertheless, the problem of asymmetric contacts, which is a general issue in moletronics, is also present in this design.

6.5 Quantum Dots

Another type of nanostructure is the so-called quantum dot (QD), or zero-dimensional nanostructure. These are inorganic nanoparticles on the order of 1 to 50 nm in diameter that exhibit unique optical and electrical properties due to quantum confinement and surface-related effects.[56] Electrical contact to single QDs is clearly very difficult to achieve although this has been demonstrated.[57] Arrays of QDs can be contacted directly when synthesized by techniques such as molecular beam epitaxy (MBE) or metal organic chemical vapor deposition (MOCVD) if they are confined between two semiconducting layers.[58] Nevertheless, techniques for making contacts to QDs are still under development.

6.6 Quality of Contacts

Above we have described at a high level the numerous methods that have been developed for making contacts to electrically active nanostructures. In this final section, we describe some of the properties of such electrical contacts and the requirements necessary in order for them to allow a device to function properly. In general, electrical contacts may be of an ohmic or Shottky type, the former allowing unimpeded flow of charge across the contact and the latter presenting an energy barrier for transport of carriers.[59] The required carrier type depends on the functionality of the device. For example, it is now known that most CNT-based field effect transistors function because the contacts have Shottky barriers that are modulated by the gate electrodes.[14,60] On the other hand, it is often preferable to have ohmic contacts for inorganic nanowires. The contact resistance itself can be measured by various idealized structures such that it may be used as a parameter in device modeling.[61] Indeed, the choice of materials used for the contacts may significantly impact the performance of devices such as field effect transistors, as has been shown for CNTs[62] and Si nanowires.[63]

Another important factor in nanostructure contacts is that the quality and even apparent behavior of the device may be strongly influenced by the contact geometry. For example, calculations by Lundstrom and co-workers have shown that the area coverage of electrodes on 1-D nanostructures strongly impacts the potential distribution in the device, making devices appear to be of one particular doping type although in fact they may be intrinsic.[64] As the size of the nanostructures begins to approach molecular dimensions, the interaction of metal states with molecular states at the interface may dominate the device behavior.[65,66] These, and other parameters, make manufacturing of electronics devices at the nanoscale an extremely challenging task, yet one rich in scientific and technological content that requires additional research and development.

6.7 Conclusions

In conclusion, various methods for contacting and positioning electrically active nanostructures have been described. The applications of electrically active nanostructures are so numerous that this topic deserves particular attention, especially from the point of view of nanomanufacturing. It was shown that the choice of manufacturing tool for making nanocontacts is highly dependent on the materials and synthetic scheme used. Careful attention must be paid to the contact chemistry and geometry in order to obtain reproducible contacts with reliable characteristics. The exact nanomanufacturing process for making electrical contacts to nanostructures is yet to be determined, and is highly dependent on the particular structure and synthetic scheme employed.

References

1. Huang, Y. et al., Logic gates and computation from assembled nanowire building blocks, *Science*, 294, 1313, 2001.
2. Zhong, Z. et al., Nanowire crossbar arrays as address decoders for integrated nanosystems, *Science*, 302, 1337, 2003.
3. Bachtold, A. et al., Logic gates with carbon nanotube transistors, *Science*, 294, 1317, 2001.
4. Duan, X. et al., High-performance thin-film transistors using semiconductor nanowires and nanoribbons, *Nature*, 425, 274, 2003.
5. Sun, Y. and Rogers, J.A., Fabricating semiconductor nano/microwires and transfer printing ordered arrays of them onto plastic substrates, *Nano Letters*, 4, 1953, 2004.
6. Cui, Y. et al., Nanowire nanosensors for highly sensitive and selective detection of biological and chemical species, *Science*, 293, 1289, 2001.
7. McAlpine, M.C. et al., High-performance nanowire electronics and photonics on glass and plastic substrates, *Nano Letters*, 3, 1531, 2003.
8. Huynh, W.U., Dittmer, J.J., and Alivisatos, A.P., Hybrid nanorod-polymer solar cells, *Science*, 295, 2425, 2002.
9. Iijima, S. and Ichihashi, T., Single-shell carbon nanotubes of 1-nm diameter, *Nature*, 363, 603, 1993.
10. Guo, T. et al., Self-assembly of tubular fullerenes, *J. Phys. Chem.*, 99, 10694, 1995.
11. Kong, J. et al., Synthesis of individual singlewalled carbon nanotubes on patterned silicon wafers, *Nature*, 395, 878, 1998.
12. Zhang, Y. et al., Electric-field-directed growth of aligned single-walled carbon nanotubes, *Appl. Phys. Lett.*, 79, 3155, 2001.
13. Tans, S.J., Verschueren, R.M., and Dekker, C., Room-temperature transistor based on a single carbon nanotube, *Nature*, 393, 49, 1998.
14. Lee, J.U., Gipp, P.P., and Heller, C.M., Carbon nanotube p-n junction diodes, *Appl. Phys. Lett.*, 85, 145, 2004.
15. Wagner, R.S. and Ellis, W.C., Vapor-liquid-solid mechanism of single crystal growth, *Appl. Phys. Lett.*, 4, 89, 1964.
16. Decker, C.A. et al., Directed growth of nickel silicide nanowires, *Appl. Phys. Lett.*, 84, 1389, 2004.

17. Saif Islam, M. et al., Ultrahigh-density silicon nanobridges formed between two vertical silicon surfaces, *Nanotechnology,* 15, L5, 2004.
18. Shan, Y. et al., From Si source gas directly to positioned, electrically contacted Si nanowires: the self-assembling "grow-in-place" approach, *Nano Letters*, 4, 2085, 2004.
19. Behnke, J.F. and Sands, T., Bimodal spatial distribution of pores in anodically oxidized aluminum thin films, *J. Appl. Phys.*, 88, 6875, 2000.
20. Yin, A.J., et al., Fabrication of highly ordered metallic nanowire arrays by electrodeposition, *Appl. Phys. Lett.*, 79, 1039, 2001.
21. Bogart, T.E. et al., Diameter-controlled synthesis of silicon nanowires using nanoporous alumina membranes, *Adv. Mater.*, 17, 114, 2005.
22. Dilts, S.M. et al., Fabrication and characterization of silicon nanowire arrays, *Mater. Res. Soc. Symp. Proc.*, 832, F9.10.1, 2005.
23. Ziegler, K.J. et al., Conductive films of ordered nanowire arrays, *J. Mater. Chem.*, 14, 585, 2004.
24. *Cojocaru*, C.S. et al., Conformal anodic oxidation of aluminum thin films, *Nano Letters,* 5, 675, 2005.
25. Ural, A., Li, Y., and Dai, H., Electric-field-aligned growth of single-walled carbon nanotubes on surfaces, *Appl. Phys. Lett.*, 81, 3464, 2002.
26. Decker, C.A. et al., Directed growth of nickel silicide nanowires, *Appl. Phys. Lett.*, 84, 1389, 2004.
27. Englander, O. et al., Electric-field assisted growth and self-assembly of intrinsic silicon nanowires, *Nano Letters,* 4, 705, 2005.
28. Forzani, E.S. et al., A conducting polymer nanojunction sensor for glucose detection, *Nano Letters,* 4, 1785, 2004.
29. Aviram, A. and Ratner, M.A., Molecular rectifiers, *Chem. Phys. Lett.*, 29, 277, 1974.
30. Saifullah, M.S.M. et al., A reliable scheme for fabricating sub-5 nm co-planar junctions for single molecule electronics, *Nanotechnology,* 13, 659, 2002.
31. Mokari, T. et al., Selective growth of metal tips onto semiconductor quantum rods and tetrapods, *Science*, 304, 1787, 2004.
32. Tsakalakos, L. et al., Mo_2C nanowires and nanoribbons on Si by two-step vapor phase growth, *J. Appl. Phys.*, 98, 4317, 2005.
33. Blodgett, K.B., Films built by depositing successive monomolecular layers on a solid surface, *J. Am. Chem. Soc.*, 57, 1007, 1935.
34. Tao, A. et al., Langmuir Blodgett silver nanowire monolayers for molecular sensing using surface-enhanced raman spectroscopy, *Nano Letters*, 3, 1229, 2003.
35. Whang, D. et al., Large-scale hierarchical organization of nanowire arrays for integrated nanosystems, *Nano Letters*, 3, 1255, 2003.
36. Rao, S.G. et al., Large scale assembly of carbon nanotubes, *Nature*, 425, 36, 2003.
37. Kpvtyukhova, N.I. and Mallouk, T.E., Nanowires as building blocks for self-assembling logic and memory elements, *Chemistry,* 8, 4355, 2002.
38. Smith, P.A. et al., Electric-field assisted assembly and alignment of metallic nanowires, *Appl. Phys. Lett.*, 77, 1399, 2000.
39. Harnack, O. et al., Rectifying behavior of electrically aligned ZnO nanorods, *Nano Letters*, 3, 109, 2003.
40. Duan, X. et al., Indium phosphide nanowires as building blocks for nanoscale electronic and optoelectronic devices, *Nature*, 409, 66, 2001.
41. Salem, A.K. et al., Directed assembly of multi-segment Au/Pt/Au nanowires, *Nano Letters,* 4, 1163, 2004.

42. Milliron, D.J., Colloidal nanocrystal heterostructures with linear and branched topology, *Nature*, 430, 190, 2004.
43. Sun, Y. and Rogers, J., Fabricating semiconductor nano/microwires and transfer printing ordered arrays of them onto plastic substrates, *Nano Letters*, 4, 1953, 2004.
44. Melsoh, N.A., et al., Ultra-high density nanowire lattices and circuits, *Science*, 300, 112, 2003.
45. Beckman, R., et al., Bridging dimension: demultiplexing ultra-high density nanowire circuits, *Science*, 310, 465, 2005.
46. Wada, Y. et al., Prospects and problems of single molecule information devices, *Jpn. J. Appl. Phys.*, 39, 3835, 2000.
47. Reed, M.A. et al., Conductance of a molecular junction, *Science*, 278, 252, 1997.
48. Andres, R.P. et al., "Coulomb staircase" at room temperature in a self-assembled molecular nanostructure, *Science*, 272, 1323, 1996.
49. Rawlett, A.M. et al., Electrical measurements of a dithiolated electronic molecule via conducting atomic force microscopy, *Appl. Phys. Lett.*, 81, 3043, 2002.
50. Kratochvilova, I. et al., Room temperature negative differential resistance in molecular nanowires, *J. Mater. Chem.*, 12, 2927, 2002.
51. Liang, W. et al., Kondo resonance in a single-molecule transistor, *Nature*, 417, 725, 2002.
52. Kuekes, P.J. et al., The crossbar latch: logic value storage, restoration, and inversion in crossbar circuits, *J. Appl. Phys.*, 97, 34301, 2005.
53. Chen, Y. et al., Nanoscale molecular-switch devices fabricated by imprint lithography, *Appl. Phys. Lett.*, 82, 1610, 2003.
54. Collier, C.P. et al., Electronically configurable molecular-based logic gates, *Science*, 285, 391, 1999.
55. Reed, M.A. et al., Prospects for molecular-scale devices, *Proc. IEEE IEDM*, 227, 1999.
56. Alivisatos, A.P., Semiconductor clusters, nanocrystals, and quantum dots, *Science*, 271, 933, 1996.
57. Yuan, Z. et al., Electrically driven single-photon source, *Science*, 295, 102, 2002.
58. Ji, L.-W. et al., InGaN/GaN multi-quantum dot light-emitting diodes, *J. Crystal Growth*, 263, 114, 2004.
59. Sze, S.M., *Physics of Semiconductor Devices*, Wiley-Interscience, New York, 1969, p. 78.
60. Avouris, Ph. and Appenzeller, J., Electronics and optoelectronics with carbon nanotubes, *Indus. Phys.*, 10, 18, 2004.
61. Mohney, S.E. et al., Measuring the specific contact resistance of contacts to semiconductor nanowires, *Sol. State Electron.*, 49, 227, 2005.
62. Javey, A. et al., Ballistic carbon nanotube field effect transistors, *Nature*, 424, 654, 2003.
63. Wu, Y. et al., Single-crystal metallic nanowires and metal/semiconductor nanowires heterostructures, *Nature*, 430, 61, 2004.
64. Guo, J. et al., Electrostatics of nanowire transistors, *IEEE Trans. Nanotech.*, 2, 329, 2003.
65. Landman, U. et al., Metal-semiconductor nanocontacts: silicon nanowires, *Phys. Rev. Lett.*, 85, 1958, 2000.
66. Xu, B. and Nogjian, J.T., Measurement of single-molecule resistance by repeated formation of molecular junctions, *Science*, 301, 1221, 2003.

Chapter 7

Nanofabrication Techniques with High-Resolution Molded Rubber Stamps

Etienne Menard and John Rogers

Contents

7.1 Fabricating Stamps, Molds, Conformable Photomasks, and Dry Transfer Tools....149
7.2 Two- and Three-Dimensional Nanofabrication with Conformable Photomasks....151
7.3 Printing of Polymers and Metal 2-D and 3-D Structures with Rubber Stamps....153
7.4 Dry Transfer Printing of Inorganic Semiconductor Micro/Nanostructures and Carbon Nanotubes....155
7.5 Conclusion and Future Outlook....159
References....159

The development of nanoscience and nanotechnology depends strongly on the capabilities of the fabrication techniques that are used for patterning and chemically modifying materials at the nanoscale. Most of the research and development in this area has, in the past, been driven mainly by the needs of the microelectronics industry. The spectacular progress in this field has been made possible by the successful scaling of lithography techniques down to the 100-nanometer scale. While these techniques are extremely well suited for the patterning of spin-coated photosensitive materials on ultra-flat surfaces, they are incompatible with important classes of organic and chemically or mechanically fragile materials. Significant challenges exist in adapting these methods for unconventional materials found in biology, chemistry and fluidics,

photonics, and plastic electronics. They are also inadequate for patterning on surfaces that are not ultra-flat. Moreover, these techniques are particularly inefficient for generating complex three-dimensional structures in a single patterning step. Recent research seeks to develop new patterning techniques that will enable the efficient fabrication of two- or three-dimensional nanometer-scale structures of unconventional materials, over large areas (i.e., larger than a few square centimeters) and on nonplanar (i.e., rough or curved) surfaces.[1,2]

Some of the simplest types of patterning methods, such as those based on embossing, molding, stamping, writing, etc., are now being re-examined for use in nanofabrication. The development of new materials and chemistries has revealed an impressive potential of these techniques to fabricate structures at the nanoscale level.[3] Some of the efforts in this field began with the development of methods for generating high-resolution molded rubber "stamps."[4] These soft stamps enable the accurate replication of patterns with nanometer-scale dimensions on the surface of a master (i.e., a surface with structured relief).[5,6] These new methods, collectively referred to as "soft lithographic" techniques, now represent a field of research on its own, with active groups worldwide. The first soft lithographic technique relies on the use of a molded stamp that is inked with a chemical ink. Similar to a conventional stamping process, the inked stamps can come into contact with a target substrate in order to transfer patterns of ink in the geometries of the raised area of the stamps. Several low-diffusion chemical inks with an ability to form densely packed self-assembled monolayers on the target substrate surface have been successfully used.[7] These inked patterns typically serve as resists for wet etching of the underlying material (usually metals). The invention of the microcontact printing (μCP) method, led initially by the Whitesides group at Harvard University, has generated considerable interest mainly because of the ability of this technique to generate submicron patterns in a nonclean room environment. The ease with which this patterning technique can be performed, without expensive facilities, also facilitated its fast spread across several scientific research fields. Microcontact printing relies critically on the ability of the rubber stamps to form intimate contact (i.e., without air voids) with a range of surfaces, including those that have some degree of roughness. Some of the fundamental aspects of this "wetting" phenomenon are still not well understood. Recent studies, however, are beginning to yield insights into this process by adapting theories developed for adhesion forces and crack propagation.[8,9]

Since the invention of the μCP method, several related techniques have emerged. For example, soft poly(dimethylsiloxane) (PDMS) rubber stamps have been used for molding and imprinting with resolution down to the single nanometer scale. They have also been used as conformable phase masks, which takes advantage of their low coefficient of absorption in the long (i.e., >300 nm) ultraviolet range. More recently, procedures and surface chemistries have been developed to enable the additive transfer, with PDMS elements, of solid objects such as metal, polymer, or semiconducting materials.[10–12] All of these and other soft lithographic techniques exploit the characteristics (i.e., resolution, modulus, surface chemistry, etc.) of the stamping tool. Several groups have worked to

improve the efficiency of this patterning element.[13–15] Composite stamp structures using high- and low-modulus elastomers have been invented in order to improve the replication fidelity of the stamp.[16] In addition, high-modulus materials such as glass or, more recently, polymers have been used in similar composite designs to reduce the registration distortions (over large areas) down to the micrometer level.

This chapter highlights recent research trends in soft lithography, with some emphasis on our own work.

7.1 Fabricating Stamps, Molds, Conformable Photomasks, and Dry Transfer Tools

Figure 7.1 illustrates the procedure for generating a high-resolution molded rubber stamp. The process begins with a master that is typically produced by conventional ultraviolet photolithography to generate photoresist patterns (preferably low aspect ratio) on the surface of a flat (usually Si) wafer. The Si surface is then treated with an anti-stick self-assembled monolayer before casting and curing the rubber (poly[dimethylsiloxane]—PDMS) material in a conventional convection oven. Finally, the stamp is gently peeled away from the surface of the master (which can be re-used to generate additional stamps). The resolution of this process can be exceedingly high.[17] The ultimate limits

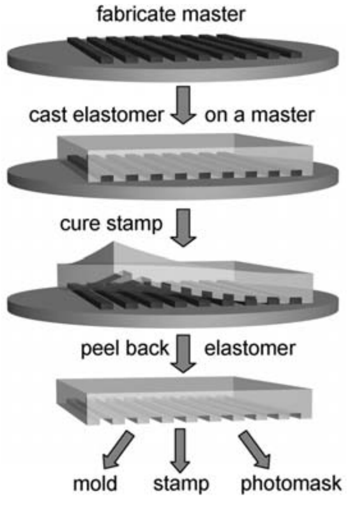

Figure 7.1 Schematic illustration of the casting and curing procedures for building elastomeric rubber stamps, molds, and conformable photomasks out of poly(dimethylsiloxane) (PDMS). PDMS base and curing agent are first mixed, degassed, and then poured over a master treated with an antistick self-assembled monolayer. After curing the polymer in a convection oven, the soft PDMS element is peeled away from the master surface. This molded object can be used as a mold itself, as a high-resolution photomask, or for printing patterns using inks or solid thin films. A single master can be used to produce many such objects.

are difficult to predict, due to substantial uncertainties surrounding the polymer physics and chemistry that dominate in the nanometer regime. Experimentally, however, it has recently been shown that molded structures with dimensions in the single nanometer range (comparable with a few bond lengths in the polymer backbone) are possible. Figure 7.2 shows the results of an experiment with PDMS molds generated by casting against a master that consists of a submonolayer coverage of single-walled carbon nanotubes on a silicon wafer.[18] Such a mold can be used to replicate the relief structure into a variety of photocurable polymers similarly to imprinting techniques.[19–21] A single mold can be used multiple times without significant degradation. These results demonstrate extreme efficiency of these basic soft lithographic procedures for generating and using elastomeric elements.

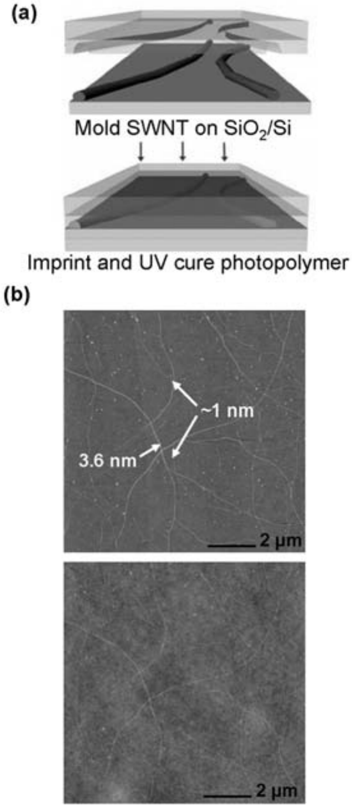

Figure 7.2 (a) Schematic illustration of a process for nanomolding the surface relief of a master on the surface of an ultraviolet curable photopolymer film. (b) Top: atomic force micrographs of a "master" that consists of a submonolayer of single-walled carbon nanotubes (SWNTs; diameter between 0.5 nm and 5 nm) grown on a SiO_2/Si wafer. Bottom: a replicate of the master relief structures in poly(urethane). These results indicate the efficiency of a PDMS stamp for patterning relief structures at the single nanometer scale.

7.2 Two- and Three-Dimensional Nanofabrication with Conformable Photomasks

PDMS rubber stamps can be used as soft photomasks because they are transparent to ultraviolet (UV) light with wavelengths greater than 300 nm. A first method, known as near-field phase-shift lithography involves exposure of a thin (i.e., ~≤micrometer) photoresist layer to UV light that passes through an elastomeric phase mask while the mask is in conformal contact with the resist.[22,23] Figure 7.3a schematically illustrates the method. This approach

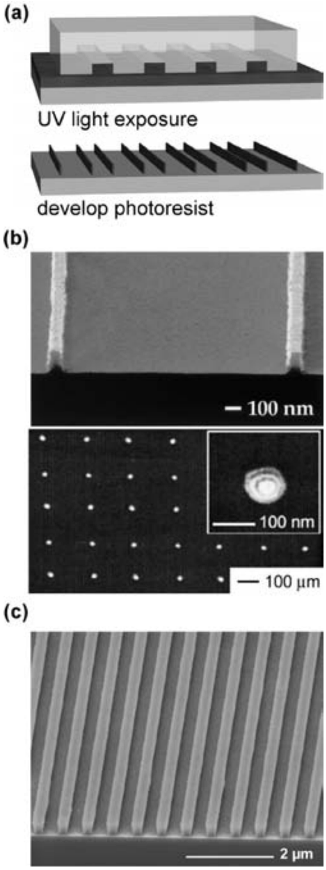

Figure 7.3 (a) Schematic illustration of the procedures for laminating a PDMS stamp on a relatively thin (~≤micrometer) photoresist and generating patterns with nanometer scale after UV exposure. (b) The photoresist lines and dots patterned with one and two exposures, respectively. (c) Dense photoresist lines and spaces formed when the stamp relief structure periodicity is close to the wavelength of the UV light (~365 nm) used for exposure. In this special case, the stamp acts as an amplitude mask and produces a pattern in photoresist that has a one-to-one correspondence with the relief features on the stamp.

requires only a phase mask and a simple handheld UV lamp to generate structures with dimensions as small as 50 nm over large areas (limited by the size of the molded stamp).[24] By carefully choosing the height of the relief features in the master, a sharp minimum appears in the intensity of light at the step edges of relief (when the phase is modulated by π). Developing away the exposed regions of the resist (when a positive resist is used) yields line patterns at the edges of the relief features mask. Figure 7.3b shows high-resolution scanning micrographs of narrow line and dot patterns obtained by one or two exposures in this manner.[25] If the distance between the edges of the stamp relief features is reduced to a value close to the light wavelength, the two nulls in the near-field intensity of the light add together. The transparent stamp then can serve as a subwavelength amplitude-type photomask such that patterns molded in the stamps are reproduced in the photoresist layer in a one-to-one correspondence. Figure 7.3c illustrates this capability with 300 nm lines and spaces in a photoresist layer generated with a stamp that has similar features of relief.

As light propagates away from the surfaces of masks of this type, the intensity varies with position not only in the plane of the mask but also perpendicular to it. In the case of a mask with a grating geometry, this phenomenon is known as the Talbot effect. With thick transparent photoresists, one can exploit this effect to generate complex three-dimensional nanostructures.[26] Figure 7.4 schematically illustrates the method when a coherent

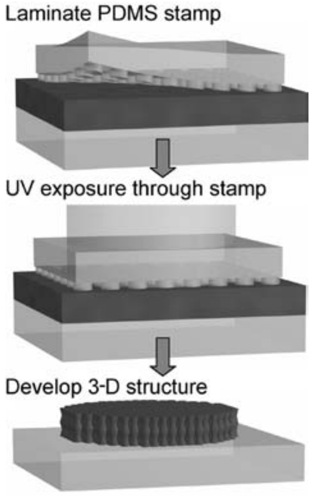

Figure 7.4 Schematic illustration of the process for fabricating 3-D periodic nanostructures using the pattern of intensity formed by passage of light through a PDMS phase mask with subwavelength features of relief. The stamp is first brought into intimate contact with the surface of a substrate coated with a relatively thick (several micrometers) transparent layer of a photopolymer. A laser beam or a regular UV mercury lamp source exposes this polymer through the photomask. The mask is peeled away and the unexposed regions of the photopolymer are removed by a developing step to create 3-D polymer nanostructures.

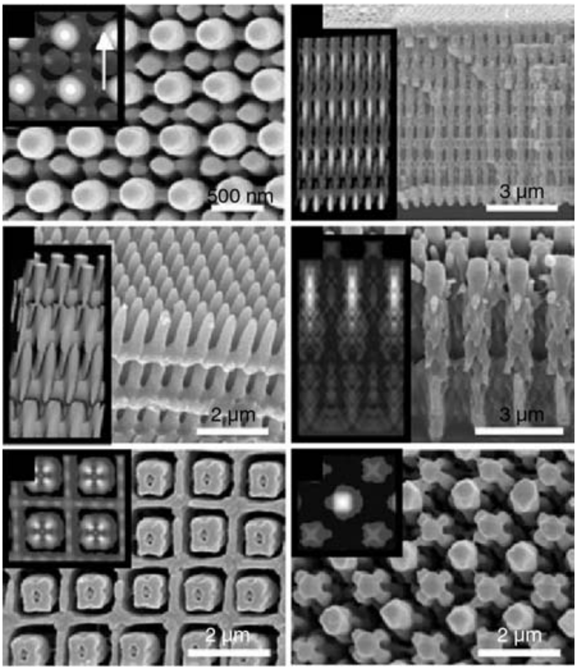

Figure 7.5 Scanning electron micrographs of representative 3-D structures generated using a soft photomask element. The top left inset images show the computed intensity models obtained from the addition of the intensity of the diffracted light beams. The precise fit between the experimental results and the mathematical models is remarkable.

laser beam source is used for exposure. The variation of the intensity can be accurately predicted using a coupled wave or finite element analysis. Figure 7.5 shows various high-resolution scanning electron micrographs of complex three-dimensional periodic structures generated using this method. Supercritical drying during the developing step avoids the destructive effects of surface tension on these fragile structures. These fine 3-D structures have been successfully incorporated into a variety of microfluidic systems for filtering, mixing, and other applications.

7.3 Printing of Polymers and Metal 2-D and 3-D Structures with Rubber Stamps

Lithographic methods and µCP generally pattern resist materials that are then used for etching an underlying layer. As a result, these techniques are considered to be "subtractive" because the layer to be patterned must be etched away in the areas unprotected by the sacrificial resist material (i.e., the photoresist or self-assembled monolayer). Also, µCP techniques are most well developed for patterning of densely packed self-assembled monolayers.

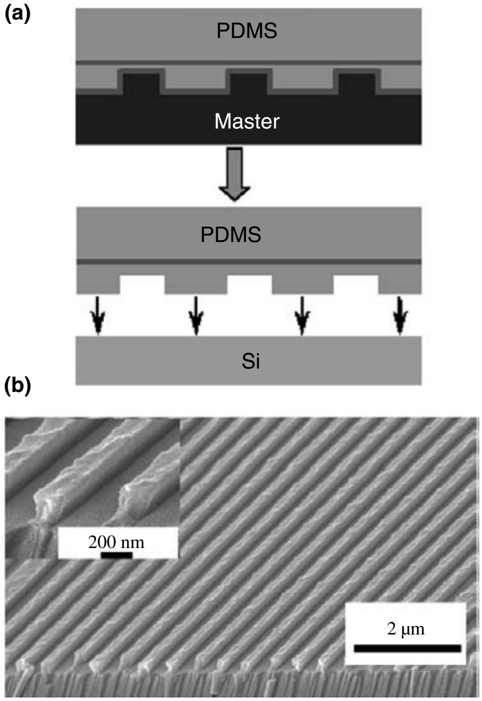

Figure 7.6 (a) Schematic illustration of the decal transfer lithography (DTL) process using a PDMS stamp for transferring PDMS patterns onto the surface of a silicon wafer. (b) Low- and high-magnification scanning electron micrographs of ~300 nm PDMS lines and spaces formed by DTL followed by a short reactive ion etching (RIE) step to remove the top thin layer of PDMS.

To extend the patterning capability to other materials, a new technique called decal transfer lithography has been recently invented by Nuzzo's group at the University of Illinois at Urbana-Champaign.[12] In this technique, the PDMS stamp material itself is transferred onto a target substrate. Figure 7.6a schematically illustrates the method. A nonstick layer is introduced in the stamp structure; it enables the transfer of a micrometer-thin PDMS layer containing the molded relief structures of the master onto the substrate. In order to facilitate the transfer of this PDMS surface layer –OH groups are formed by using an ultraviolet ozone (UVO) light treatment.[27] The closed-form PDMS shapes that are transferred can, if necessary, be opened using a blanket oxygen plasma etch. Figure 7.6b shows low- and high-resolution scanning electron micrographs of 300-nm PDMS lines transferred on the surface of a silicon wafer, after etching away the top thin layer of PDMS. Transistors and other devices have been fabricated with this technique.

In order to avoid the use of sacrificial materials and etching procedures, purely additive soft lithography methods have also been developed. Solid materials such as metal films or polymers can be additively transferred from

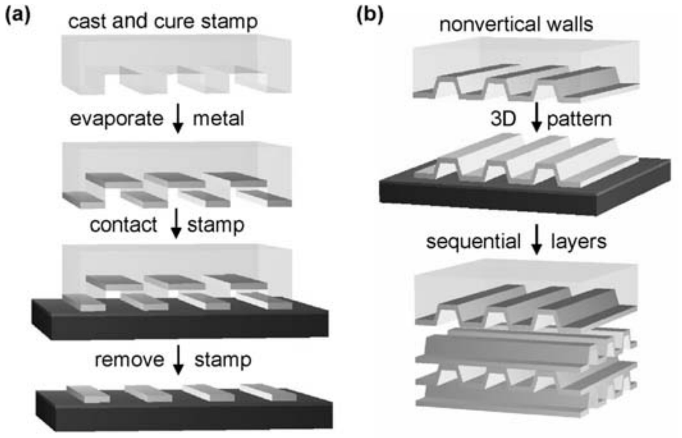

Figure 7.7 Schematic illustration of the nanotransfer printing (nTP) process for fabricating high-resolution 2-D or 3-D patterns of thin metals. (a) Process for generating 2-D metal patterns. A metal coated stamp (formed using a collimated electron beam evaporator) is brought into intimate contact with the surface of a substrate. Chemical bonding or surface energy differences enable the transfer of the metal from the raised area of the stamp to the substrate. (b) Process for generating continuous 3-D structures when the stamp relief side walls are not vertical. Successive cold welding of gold films on top of each other yields complex multilayer structures.

the raised surfaces of a PDMS stamp.[28] These new methods have higher-resolution capabilities than μCP because the solid inks do not diffuse on the substrate surface and because the resolution is not degraded by etching.[29] Metal line patterns having 50-nm widths have been successfully transferred onto the surface of GaAs wafers using this technique, which we refer to as nanotransfer printing (nTP).[30] Figure 7.7 schematically illustrates two different nTP procedures that enable the transfer of discontinuous or continuous 3-D metal patterns (depending on the side wall orientation of the stamp relief patterns).[31,32] High-resolution scanning electron micrographs of submicron resolution nanotransfer printed gold structures are presented on Figure 7.8. The integrity of these free-standing 3-D metal structures is remarkable but depends critically on the careful optimization of the metal evaporation conditions and the stamp and substrate surface chemistries.[31] Similar metal transfer techniques have been developed in other research groups.[33,34]

7.4 Dry Transfer Printing of Inorganic Semiconductor Micro/Nanostructures and Carbon Nanotubes

Soft lithography methods have been developed in part to extend and overcome the inherent limitations of the well-established photolithography techniques. Most of these methods have focused on the patterning or transfer of metal or liquid "ink" materials. It is possible, however, to exploit the soft PDMS stamps to pick up, selectively, individual solid objects from one surface and

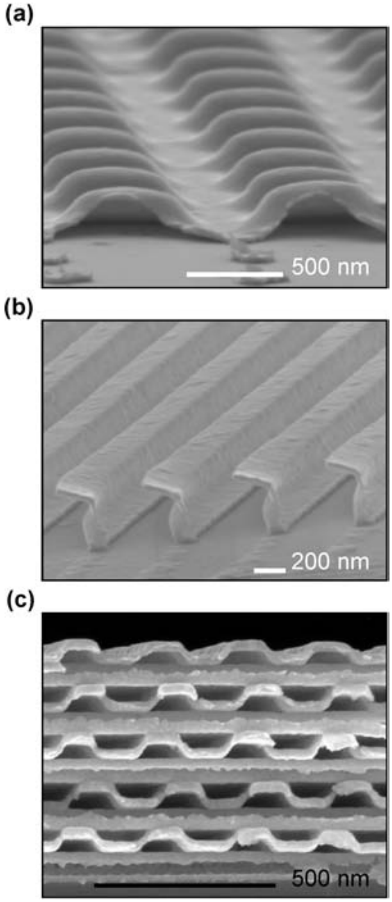

Figure 7.8 Scanning electron micrographs of three-dimensional metal structures obtained by nanotransfer printing gold metal films. (a) Closed gold nanocapsules. (b) Free-standing L structures obtained using a stamp coated with a steeply angled flux of metal. (c) Multilayer 3-D structure obtained by the successive transfer and cold welding of continuous gold nanocorrugated films.

then to transfer those objects onto another target substrate. Figure 7.9 schematically illustrates the transfer printing process of semiconducting elements defined on the surface of a wafer. Figure 7.10a shows, as an example, a high-resolution scanning electron micrograph of indium phosphide (InP) ribbons transferred by dry transfer printing (DTP), from a bulk wafer, onto the surface of a poly(ethylene-terephtalate) (PET) plastic substrate coated with a thin poly(urethane) layer. Figure 7.10b shows similar results for the case of gallium arsenide (GaAs) wires.[35,36] The bottom inset optical images show a cross-patterned array of these elements obtained by successive dry transfer printings. A similar approach can be used for individual single-walled carbon nanotubes (SWNTs). Figure 7.10c shows, for example, an atomic force

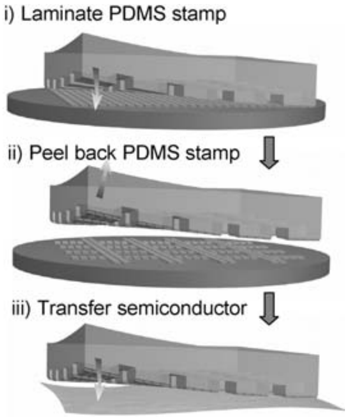

Figure 7.9 Dry transfer printing (DTP) of semiconducting elements from a "mother" wafer to a substrate. A PDMS stamp is brought into intimate contact with the top surface of nanometer-thick semiconducting elements. Surface adhesion forces enable the transfer of these elements from the surface of a substrate to the PDMS stamp. The semiconducting elements are then transferred onto a target substrate coated with an adhesive layer.

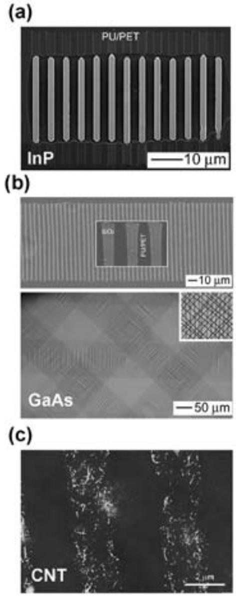

Figure 7.10 Nanoscale semiconducting elements transferred onto poly(urethane) coated poly(ethylene-terephtalate) (PET) plastic substrates. (a) High-resolution scanning micrograph of transferred indium-phosphorus (InP) wires. (b) High-resolution scanning micrographs and optical images of transferred GaAs wires. (c) Single-walled carbon nanotubes (SWNTs) transferred stripes. In this case the PET substrate is coated with poly(methyl-methacrylate) (PMMA).

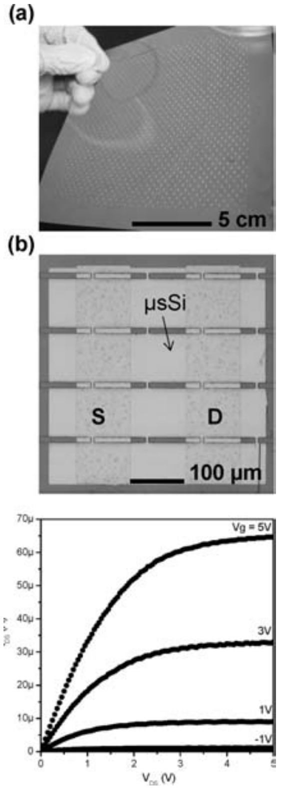

Figure 7.11 (a) Optical picture of a large (~12×12 cm^2) array of μs-Si objects selectively dry transfer printed on a PET substrate. (b) High-magnification optical picture of a completed device on a similar substrate. (c) Current voltage (IV) characteristics of this thin-film transistor device. The average device mobility is ~240 cm^2/Vs.

micrograph (AFM) of the surface of a poly(methyl-methacrylate) (PMMA) coated PET substrate on which SWNTs have been transfer printed. In this case, the stamp was inked by direct spin coating of the SWNTs on the stamp.[37]

The transfer, by dry printing, of high-performance semiconducting elements (such as Si, InP, or GaAs, which are all grown at high temperature) to a low-cost plastic (of the type that would be incompatible with the high-temperature growth procedures for the semiconductors) could be extremely useful for the fabrication of flexible, high-performance electronic devices. This approach has the potential to lead to new consumer electronic systems such as electronic-paper, flexible ultralarge street display panels, and lightweight steerable antenna systems for military applications. It is primarily for these application possibilities that we recently developed a DTP technique. This method was first successfully applied to the fabrication of some of the highest-performance electronic circuit devices on plastic substrates.[38] It can also transfer selectively arrays of elements over large

areas (i.e., several centimeters square) on low-cost substrates with any fill factor. Figure 7.11a shows an optical image of an array of high-performance microstructured silicon (μs-Si) elements (ribbons in this case) transferred onto a PET substrate using the DTP method. Figure 7.11b shows a high-magnification optical picture of a thin-film silicon transistor and its current-voltage (IV) characteristics.[39] The performance of these devices is excellent; they show average device mobilities in the range of ~240 cm^2/Vs. Optimized process and device layout can enable the fabrication of devices with level of performance approaching that of conventional MOS transistor on bulk silicon wafers. Effective mobilities higher than 500 cm^2/Vs have been recently achieved for thin film silicon transistors transfer printed on a thin polyimide substrate[40].

7.5 Conclusion and Future Outlook

The fabrication techniques presented in this chapter have considerable value for applications in nanoscience and nanotechnology, partly because of the simplicity and availability of the materials and equipment on which they rely. They will continue to facilitate research in these areas, particularly for those who do not have access to the more costly conventional lithography patterning systems. We speculate that the dry transfer printing methods will be applicable to solid materials that have dimensions outside the range (smaller and larger) of those illustrated here. Their capability for transferring high-performance semiconducting materials, to virtually any substrate, without compromising their integrity, performance, and alignment has been demonstrated with the fabrication of high-performance thin-film transistors on plastic substrates. Although the use of these techniques has been confined mostly to research laboratories, they are beginning to migrate into prototype industrial lines for the fabrication of large-area display panels. Work in this direction, as well as toward the development of new techniques, will be the focus of future efforts.

References

1. Jeon, S., Menard, E., Park, J., Maria, J., Meitl, M., Zaumseil, J., and Rogers, J.A., *Adv. Mater.*, 16, 1369, 2004.
2. Hur, S.-H., Khang, D.-Y., Kocabas, C., and Rogers, J.A., *Appl. Phys. Lett.*, 85, 5730, 2004.
3. Mirkin, C.A. and Rogers, J.A., *MRS Bull.*, 26, 506, 2001.
4. Xia, Y. and Whitesides, G.M., *Angew. Chem. Int. Ed.*, 37, 550, 1998.
5. Xia, Y., Rogers, J.A., Paul, K.E., and Whitesides, G.M., *Chem. Rev.*, 99, 1823, 1999.
6. Odom, T.W., Thalladi, V.R., Love, J.C., and Whitesides, G.M., *J. Am. Chem. Soc.*, 124, 12112, 2002.
7. Kumar, A. and Whitesides, G.M., *Appl. Phys. Lett.*, 63, 2002, 1993.
8. Huang, Y., Zhou, W., Hsia, K.J., Menard, E., Park, J.-U. and Rogers, J.A., Applied Phy. Lett., 86, (15), 154106, 2005.

9. Huang, Y., Zhou, W., Hsia, K.J., Menard, E., Park, J.-U., Rogers, J.A., and Alleyne, A.G., *Langmuir*, 21, (17), 8058–8068, 2005.
10. Loo, Y.-L., Willett, R.W., Baldwin, K., and Rogers, J.A., *J. Am. Chem. Soc.*, 124, 7654, 2002.
11. Jiang, X., Zheng, H., Gourdin, S., and Hammond, P.T., *Langmuir*, 18, 2607, 2002.
12. Childs, W.R. and Nuzzo, R.G., *J. Amer. Chem. Soc.*, 124, 13583, 2002.
13. Michel, B. et al., *IBM J. Res. Dev.*, 45, 697, 2001.
14. Floch, A. and Schmidt, M.A., *IEEE ASME J. Microelectromechanical. Systems* 8, (1), 85–89, 1999.
15. Burgin, T., Choong, V.-E., and Maracas, G., *Langmuir*, 16, 5371, 2000.
16. Odom, T.W. et al., *Langmuir*, 18, 5314, 2002.
17. Gates, B.D. and Whitesides, G.M., *J. Am. Chem. Soc.*, 125, 14986, 2003.
18. Hua F. et al., *Nano Letters*, 4, 2467, 2004.
19. Aumiller, G.D., Chandross, E.A., Tomlinson, W.J., and Weber, H.P., *J. Appl. Phys.*, 45, 4557, 1974.
20. Xia, Y. et al., *Adv. Mater.*, 9, 147, 1997.
21. Borzenko, T. et al., *Appl. Phys. Lett.*, 79, 2246, 2001.
22. Rogers, J.A., Paul, K.E., Jackman, R.J., and Whitesides, G.M., *Appl. Phys. Lett.*, 70, 2658, 1997.
23. Schmid, H., Biebuyck, H., Michel, B., and Martin, O.J.F., *Appl. Phys. Lett.*, 72, 2379, 1998.
24. Maria, J., Jeon, S., and Rogers, J.A., *J. Photochem. Photobiol. A*, 166, 149, 2004.
25. Rogers, J.A., Paul, K.E., Jackman, R.J., and Whitesides, G.M., *J. Vac. Sci. Techn. B*, 16, 59, 1998.
26. Jeon, S., Park, J.-U., Cirelli, R., Yang, S., Heitzman, C.E., Braun, P.V., Kenis, P.J.A., and Rogers, J.A., *Proc. Nat. Acad. Sci. USA*, 101, 12428, 2004.
27. Childs, W.R. and Nuzzo, R.G., *Adv. Mater.*, 16, 1323, 2004.
28. Felmet, K., Loo, Y.-L., and Sun, Y., *Appl. Phys. Lett.*, 85, 3316, 2004.
29. Loo, Y.-L., Willett, R.W., Baldwin, K., and Rogers, J.A., *Appl. Phys. Lett.*, 81, 562, 2002.
30. Loo, Y.-L., Willett, R.W., Baldwin, K., West, K.W., and Rogers, J.A., *J. Vac. Sci. Techn. B*, 20, 2853, 2002.
31. Menard, E., Bilhaut, L., Zaumseil, J., and Rogers, J.A., *Langmuir*, 20, 6871, 2004.
32. Zaumseil, J., Meitl, M.A., Hsu, J.W.P., Acharya, B., Baldwin, K.W., Loo, Y.-L., and Rogers, J.A., *Nano Letters*, 3, 1223, 2003.
33. Schmid, H., Wolf, H., Allenspach, R., Riel, H., Karg, S., Michel, B., and Delamarche, E., *Adv. Func. Mater.*, 13, 145, 2003.
34. Kim, C., Shtein, M., and Forrest, S.R., *Appl. Phys. Lett.*, 80, 4051, 2002.
35. Sun, Y. and Rogers, J.A., *Nano Letters*, 4, 1953, 2004.
36. Sun, Y., Khang, D.-Y., Hurley, K., Nuzzo, R.G., and Rogers, J.A., *Adv. Funct. Mater.*, 15, 30, 2005.
37. Meitl, M.A., Zhou, Y.X., Gaur, A., Jeon, S., Usrey, M.L., Strano, M.S., and Rogers, J.A., *Nano Letters*, 4, 1643, 2004.
38. Menard, E., Lee, K.J., Khang, D.Y., Nuzzo, R.G., and Rogers, J.A., *Appl. Phys. Lett.*, 84, 5398, 2004.
39. Menard, E., Nuzzo, R.G., and Rogers, J.A., *Appl. Phys. Lett.*, 86, 93507, 2005.
40. Ahn, J.-H.; Kim, H.-S.; Lee, K.J.; Menard, E.; Nuzzo, R. G.; Rogers, J. A., High Speed, Mechanically Flexible Single-Crystal Silicon Thin-Film Transistors on Plastic Substrates. *IEEE Electron Device Letters*, 27, (6), 460–462, 2006.

Chapter 8

Room-Temperature Nanoimprint and Nanocontact Technologies

Ken-ichiro Nakamatsu and Shinji Matsui

Contents

8.1 Introduction 162
8.2 Room-Temperature Nanoimprint Lithography 162
 8.2.1 RT-NIL Using Hydrogen Silsesquioxane 162
 8.2.2 Prebaking-Temperature and Linewidth Dependencies of HSQ-Imprinted Depth 164
 8.2.3 Postbaking Temperature Dependence of HSQ-Replicated Patterns 166
 8.2.4 HSQ Resin Thickness Dependence of HSQ-Imprinted Depth 166
 8.2.5 Bilayer Method for RT-NIL 167
 8.2.6 Water Lift-Off Using HSQ/Poly(Vinyl Alcohol) Bilayer Structures 169
8.3 Room-Temperature Nanocontact Printing 172
 8.3.1 RT-NCP Using SiO_2/Si Mold 172
 8.3.2 RT-NCP Using Poly(Ethylene)/Poly(Methyl Methacrylate) Soft Template 173
 8.3.3 Ag Patterning by RT-NCP 177
 8.3.4 Transfer of an Au Electrode Pattern through Nanocontact Printing 178
8.4 Summary 180
References 180

8.1 Introduction

Nanoimprint lithography (NIL)[1–7] has attracted attention from many industrial fields because of its many capabilities for the fabrication of micro- and nano-applications. NIL, in which resist patterns are fabricated by deforming the physical shape of the resist by embossing it with a mold, is a useful technique for fabricating various nanostructure devices such as quantized magnetic disks.[8–12] This technique has excellent features: patterns less than 10 nm in size can be realized over a large area with high throughput and low cost. However, in the conventional NIL process, the resist must be heated above the glass transition temperature (T_g) to enable deformation of the resist with a mold. Consequently, a resist thermal cycle is required that causes serious problems in replicated pattern accuracy and lowers throughput. To overcome these problems, we have developed room-temperature nanoimprint lithography (RT-NIL) and room-temperature nanocontact printing (RT-NCP). The RT-NIL does not require a resist thermal cycle when pressing a mold onto the resist. The thermal cycle can be eliminated in the RT-NCP, as well as RT-NIL. Therefore, these technologies offer us increased throughput and pattern accuracy in nanostructure fabrication compared with conventional NIL. In this chapter, we demonstrate RT-NIL using hydrogen silsesquioxane (HSQ) (Dow Corning Co. FOX-16) as the replicated materials and replicated 50-nm linewidth.[13–15]

8.2 Room-Temperature Nanoimprint Lithography

8.2.1 RT-NIL Using Hydrogen Silsesquioxane

We used HSQ, which has the structural formula of $H_2(SiO)_3$, as a replicated material. Infrared (IR) spectra confirmed that there was no hydrocarbon in the HSQ material. Therefore, this HSQ resin contains no organic groups, such as, for example, vinyl groups.[16] Figure 8.1 outlines the RT-NIL steps, as follows: (1) HSQ was spin coated onto the substrate. (2) A mold was pressed to the HSQ layer. (3) The mold was removed from the HSQ-coated substrate. (4) CHF_3 reactive-ion-etching was performed to remove the residual layer. To avoid the adhesion of HSQ, the release agent (Daikin Industries Ltd. Optool DSX: Demnamsolvent = 1:1000 by weight) was coated in advance onto the Si mold. The coating method of the release agent is shown in Figure 8.2: (1) The mold was dipped into the release agent for 1 min. (2) The mold was set in the humid atmosphere for 1 h. (3) The mold was rinsed with the solvent perfluorohexane. (4) The mold was dried. Our experiments were performed by using commercially available imprint apparatus (NANOIMPRINTER, Meisyo Co.). Figure 8.3 shows scanning electron microscopy (SEM) micrographs of HSQ replicated patterns after RT-NIL. These HSQ patterns were not baked before imprinting was performed. The HSQ pattern with a small linewidth of 50-nm could be obtained, as shown in Figure 8.3a. As Figure 8.3b shows, the HSQ pattern with 150-nm linewidth and 570-nm height was successfully replicated by RT-NIL.

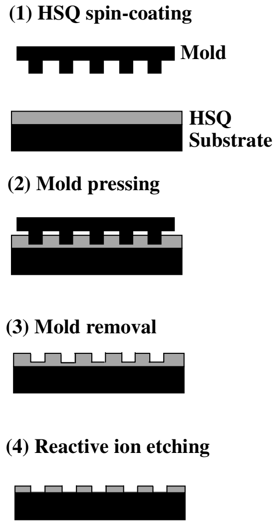

Figure 8.1 Schematic of RT-NIL process using HSQ.

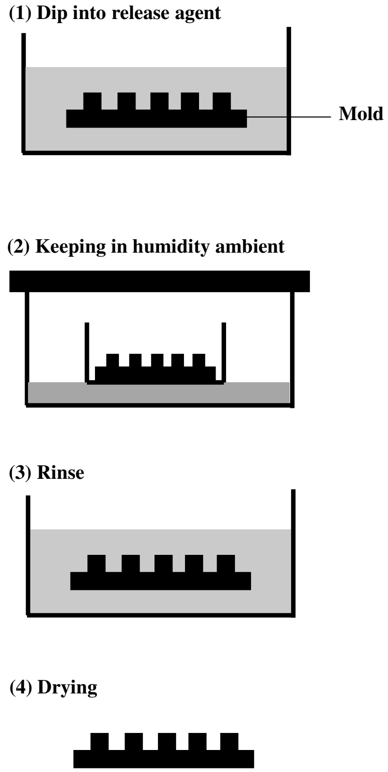

Figure 8.2 Schematic of coating method of the release agent.

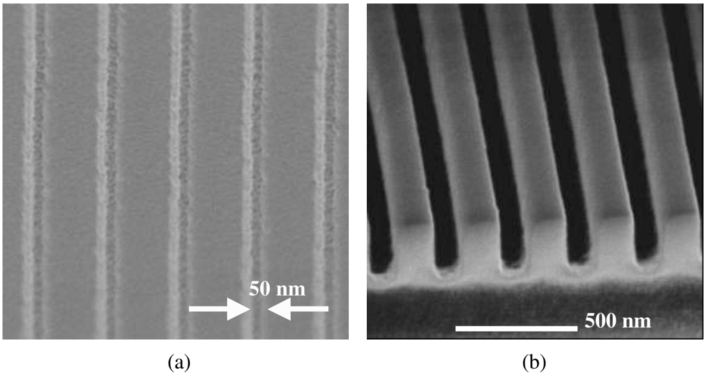

Figure 8.3 HSQ patterns with (a) 50-nm linewidth and 250-nm pitch, and (b) 150-nm linewidth and 300-nm pitch replicated by RT-NIL.

8.2.2 Prebaking-Temperature and Linewidth Dependencies of HSQ-Imprinted Depth

We investigated how prebaking temperature affected the HSQ-imprinted depth. Baking plays two important roles: one is the removal of the solvent containing HSQ resin, and the other is the moderation of the resin's viscosity. A pressure of 22 Mega Pascal was used in the RT-NIL. The HSQ thickness applied on the Si surface by spin coating was 600 nm. A SiO_2/Si mold with 200-nm height and various linewidths was prepared by electron beam (EB) lithography and dry etching for this purpose.

The imprinted depths for 150-nm and 1-μm grating patterns shown in Figure 8.4 were 160 nm and 100 nm, respectively. For a 10 × 9-μm-square HSQ imprinted pattern (Figure 8.6a), the imprinted depth was 30 nm as

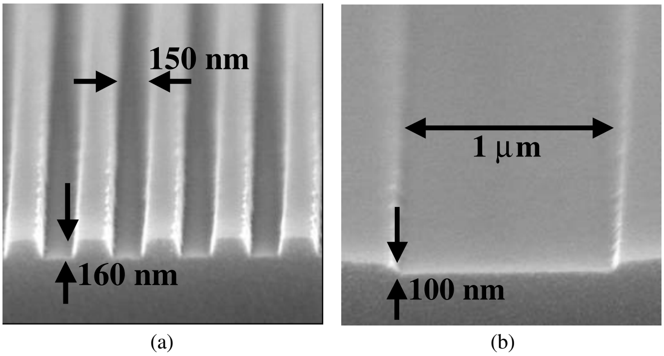

Figure 8.4 Profile of HSQ replicated patterns after RT-NIL.

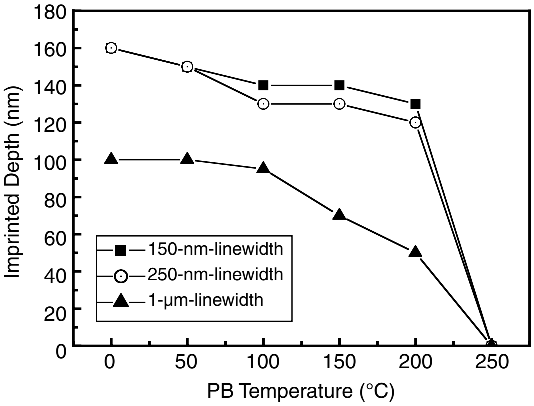

Figure 8.5 Profile of 10 × 9 μm HSQ replicated pattern.

measured by a stylus profiler (Figure 8.6b). We also observed a protrusion of 30 nm at both edges in this imprinted pattern. The excessive pressure to the patternís edge probably caused the protrusion. As Figure 8.6 shows, the HSQ imprinted depth decreased as prebaking temperature increased, and decreased suddenly to zero at the prebaking temperature of 250°C due to the HSQ resin hardening. In addition, the HSQ imprinted depths for a half-pitch of 150 nm, 250 nm, and 1 μm were about 140 nm, 130 nm, and 90 nm, respectively, at the constant prebaking temperature of 100°C. Thus, from the viewpoint of the mold linewidth, the HSQ-imprinted depth tended to decrease as the linewidth of the mold increased when the prebaking temperature was constant. Because the HSQ resin was most deeply imprinted when the prebaking was not performed, we believe that the use of HSQ resin without prebaking is best suited to the replication material in the RT-NILs.

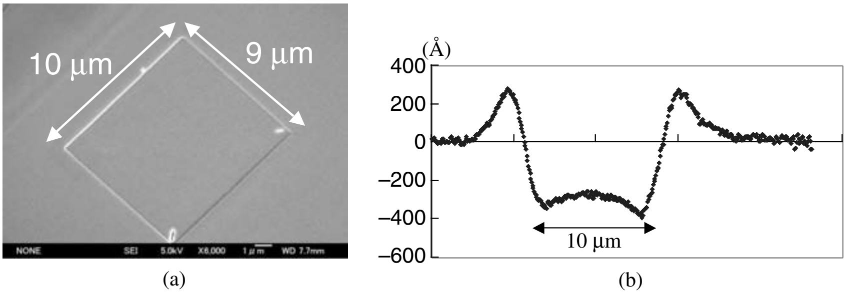

(a)

(b)

Figure 8.6 Prebaking temperature dependence of HSQ imprinted depth on various linewidths.

These results indicate that the imprinted depth in RT-NIL using HSQ depends on the linewidth, probably because of the high viscosity of HSQ, and can be applied for linewidths of less than about 1μm.

8.2.3 Postbaking Temperature Dependence of HSQ-Replicated Patterns

We next investigated the postbaking temperature dependence of 100-nm-linewidth HSQ-replicated patterns after RT-NIL. The key role of the postbaking is to remove the solvent in the HSQ. RT-NIL was applied to 800-nm-thick HSQ on a Si substrate. The HSQ film was not prebaked before imprinting. We used a 44-MPa imprinting pressure and a 5-min imprinting time in this experiment. Figure 8.7 show HSQ-replicated 100-nm-linewidth, 400-nm-pitch patterns with (a) no postbaking and (b) postbaking at 150°C on a hot plate for 10 min. As these SEM observations show, the profiles of the HSQ replicated patterns after postbaking remained the same as the profiles obtained without postbaking, which is a useful characteristic for dry etching.

We also measured the baking-temperature dependence of the dry-etching rate for CHF_3 reactive-ion-etching (RIE) of the HSQ resin. The HSQ film was baked on a hot plate for 10 min, and the gas flow, RF power, and gas pressure were 50 sccm, 100 W, and 2.0 Pa, respectively. The etched depth did not change with the baking temperature up to 150°C; the etching rate of the HSQ was independent of the baking temperature. Therefore, postbaking is not especially necessary before a dry-etching process.

8.2.4 HSQ Resin Thickness Dependence of HSQ-Imprinted Depth

Next, we evaluated the resin thickness dependence of HSQ-imprinted depth. For this investigation, three kinds of HSQ thin films with thickness of 270 nm, 600 nm, and 2 μm, obtained by varying spin-coating conditions, were prepared. An imprinting pressure of 22 MPa was used. Figure 8.8 shows the HSQ resin thickness dependence of the imprinted depth. On the

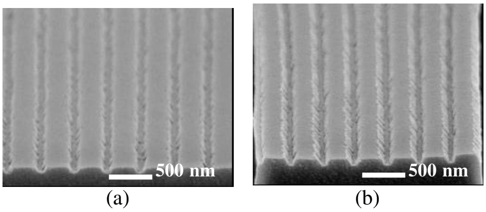

Figure 8.7 HSQ replicated patterns with 100-nm linewidth after postbaking. (a) No postbaking and (b) baking temperature of 150°C.

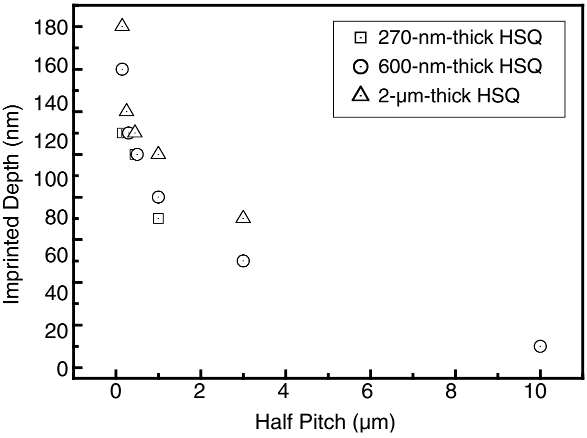

Figure 8.8 Linewidth dependence of HSQ imprinted depth on various HSQ applied thicknesses.

half-pitch of 150 nm, the respective HSQ-imprinted depths for HSQ thickness of 270 nm, 600 nm, and 2 μm were 140 nm, 160 nm, and 180 nm. Hence, this result indicates that the imprinted depth increased with increasing thickness of HSQ film.

8.2.5 Bilayer Method for RT-NIL

Here we describe a bilayer resist method for RT-NIL where HSQ is used as a top layer and AZ photoresist (Shipley Co.) is used as a bottom layer. This method offers two benefits: (1) bilayer structures can be applied to nonflat surfaces, and (2) high-aspect resist patterns can be easily obtained. The HSQ top layer is easily etched using CHF_3 RIE. The etching ratio of AZ photoresist to HSQ is higher than 100 for O_2 RIE. This indicates that little HSQ is etched away by O_2 RIE, and an HSQ top layer has an sufficient etching tolerance for O_2 RIE. We therefore expect, from the viewpoint of etching characteristics, the HSQ/AZ bilayer resist process to be very feasible.

The bilayer resist process we used for RT-NIL is shown in Figure 8.9, and the steps are as follows: (1) A bottom layer of 1-μm-thick AZ photoresist was spin coated onto an Si substrate. This was baked at 250°C on a hot plate for 1 h to increase adhesion between the bottom layer and the substrate. A 0.3-μm-thick HSQ layer was then spin coated onto the AZ photoresist bottom layer. The HSQ top layer was prebaked at 50°C for 2 min to obtain a moderate HSQ for the physical transformation with a mold pattern. (2) An Si mold was fabricated by EB lithography and dry etching, and the HSQ/AZ bilayer substrate was pressed together for 3 min at a set press pressure within a range of 5 to 14 MPa. (3) The mold was removed, and (4) the residual HSQ in the compressed area was etched

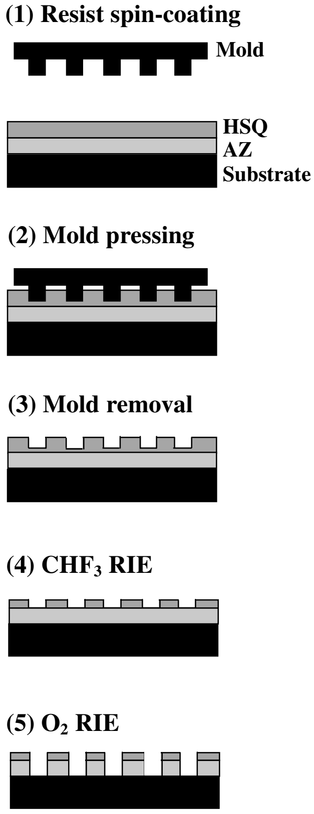

Figure 8.9 Schematic of RT-NIL process where a bilayer of HSQ (top layer) and AZ photoresist (bottom layer) is used.

away by CHF_3 or CF_4 RIE to completely expose the AZ surface. (5) The AZ photoresist bottom-layer was etched by O_2 RIE.

The HSQ top layer was used as a mask for O_2 etching of the AZ photoresist bottom layer because of its extremely low O_2 RIE rate. Because the etch-rate ratio for AZ photoresist to HSQ is higher than 100, HSQ can be applied as a top layer for O_2 RIE. In this way, the HSQ/AZ bilayer resist process is used for RT-NIL.

Figure 8.10a shows an SEM micrograph of the top view of imprinted HSQ patterns with 100-nm linewidth and 200-nm pitch on a 1-μm-thick AZ photoresist bottom layer after O_2 RIE. Figure 8.10b is an enlarged SEM micrograph of Figure 8.10a. These images show that HSQ residual patterns were successfully etched away by CF_4 RIE. Figure 8.11a shows an SEM micrograph of a 100-nm-linewidth and 1-μm-height bilayer structure. As Figure 8.11b shows, an HSQ/AZ bilayer structure with 400-nm linewidth and 800-nm pitch was successfully obtained on a nonflat surface. The respective etching times and gas power were 4 min and 2.0 Pa for CF_4 RIE and 15 min and 1.0 Pa for O_2 RIE.

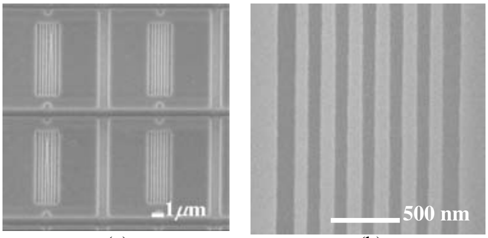

(a) (b)

Figure 8.10 SEM micrographs of replicated patterns with 100-nm linewidth and 200-nm pitch obtained after O_2 RIE.

These results demonstrate that a bilayer resist process for RT-NIL using HSQ as a top layer and AZ photoresist as a bottom layer is feasible and promising for high-aspect nanostructure fabrication.

8.2.6 Water Lift-Off Using HSQ/Poly(Vinyl Alcohol) Bilayer Structures

We also proposed a lift-off process that uses a HSQ/PVA bilayer structure.[17] Poly(vinyl alcohol) (PVA) is a well-known water-soluble polymer. PVA has been proposed as a high-resolution and low-cost nanoimprint template[18] due to its solubility in water. Since PVA cannot be used in patterning by photolithography and EB lithography, a method of NIL is employed. In the conventional lift-off, organic solvents, for example, acetone, are commonly used. On the other hand, the PVA we used in NIL enables the use of water for lift-off. The water lift-off process takes advantage of each capability of PVA and HSQ, is ecological, and provides increased pattern accuracy. The inverse tapered resist structures can be easily fabricated by using HSQ/PVA bilayer structure and are suitable for a metal lift-off. The reason for using HSQ as a transfer material is that room-temperature imprinting can be performed.

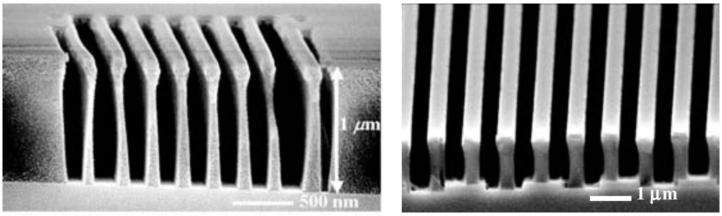

(a) (b)

Figure 8.11 SEM micrographs of (a) a 100-nm linewidth, 1-μm-high bilayer structure, and (b) 400-nm linewidth, 800-nm pitch, and 1-μm-high bilayer structure on a nonflat surface.

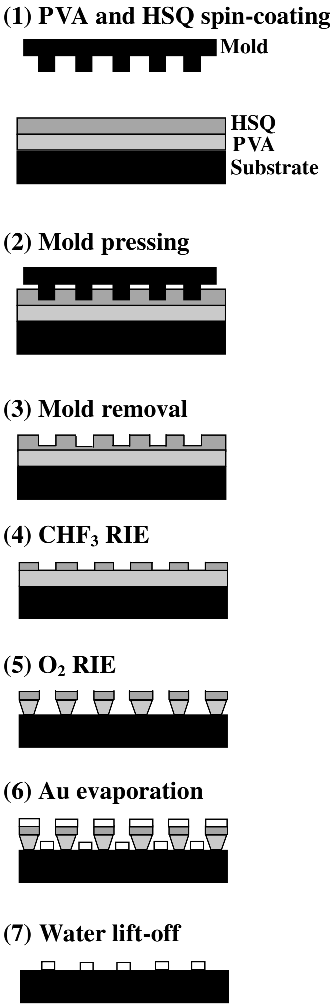

Figure 8.12 Schematic of lift-off process using HSQ/PVA bilayer structure.

The process flow is shown in Figure 8.12. First, PVA solution was spin coated on Si substrate. In our experiment, 4% PVA aqueous solution adjusted by mixing PVA powder and distilled water was used. Then the PVA-coated substrate was baked at 100°C on a hot plate for 10 min to remove water from the PVA resin. The PVA thickness applied on the substrate was 300 nm. Second, an 800-nm-thick HSQ layer was spin coated on the PVA-coated substrate. Third, an SiO_2/Si mold of 570 nm height was pressed onto the HSQ top layer at room temperature at a set press pressure of 15 MPa. The pressure holding time was 1 min. The residual HSQ layer in the compressed area was removed by CHF_3 RIE for 5 min after the mold was separated from the HSQ resin. A pressure of 2.0 Pa and RF power of 100 W were used for CHF_3 RIE.

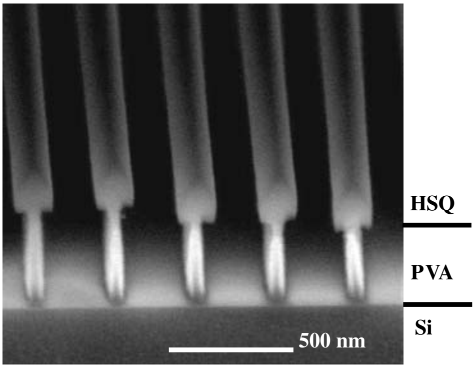

Figure 8.13 SEM micrograph of HSQ/PVA bilayer structure after O_2 RIE.

Subsequently, the PVA bottom layer was removed by O_2 RIE while the HSQ top layer was used as an etching mask. Simultaneously, the PVA bottom layer was intentionally overetched to fabricate an overhang resist structure for the lift-off process. The Si surface of the imprinted area was completely exposed after O_2 RIE. The pressure, RF power, and etching time of O_2 RIE were 1.0 Pa, 100 W, and 3 min, respectively. The measured etching rate of the PVA resin for O_2 RIE was 240 nm/min at gas pressure and RF power of 1.0 Pa and 100 W, respectively. Therefore, the ratio of the etching rate of PVA to that of HSQ exceeds 100 for O_2 RIE. The etching time used for fabricating the overhang structure was sufficient because of the high etching rate of PVA for O_2 RIE. Finally, the lift-off process was performed in water after the vacuum evaporation of gold on the substrate.

Figure 8.13 shows the bilayer structure of 150-nm half-pitch and 560-nm height after O_2 RIE. From this SEM observation, the PVA bottom layer was found to be successfully overetched while the HSQ top layer was used as an etching mask for O_2 RIE. Figure 8.14 shows the Au patterns of 100-nm

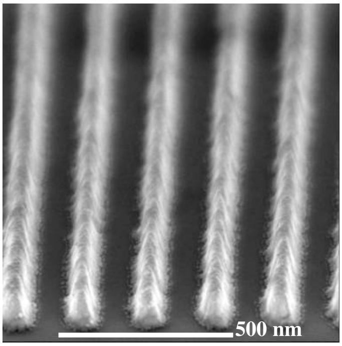

Figure 8.14 Gold patterns of 100-nm linewidth after lift-off process using HSQ/PVA bilayer structure in water.

half-pitch and 170-nm height after the lift-off process in water. These results demonstrate that the lift-off process using PVA as a replicated polymer and the HSQ/PVA bilayer structure is useful and promising in forming the metal patterns in NIL.

8.3 Room-Temperature Nanocontact Printing

8.3.1 RT-NCP Using SiO_2/Si Mold

Direct patterning technologies that allow us to make nanostructure devices by simple processes have been developed. Soft lithography[19–22] is a promising technique for various pattern transfer with a simple process based on contact printing. Contact printing offers the following benefits for obtaining patterns with high accuracy and high throughput: (1) A residual layer does not arise after transferring, (2) the transfer process can be carried out at room temperature, and (3) a low press pressure of less than about 1 MPa can be used. The contact printing technique promises high-throughput fabrication of various microelectronic devices such as field effect transistors.[23] We developed room-temperature nanocontact printing (RT-NCP) that takes advantage of the HSQ adhesion property. The thin HSQ resin containing the solvent has high viscosity that is suitable for the RT-NCP process. The adhesion property is responsible for the ability to be transferred directly onto the substrate. The RT-NCP process we used is shown in Figure 8.15, and the steps are as follows: (1) An HSQ layer was spin coated onto the SiO_2/Si mold. (2) The mold was pressed onto the Si substrate at room temperature with 1 MPa press pressure. (3) The HSQ on the protruding parts of the mold was transferred onto the Si substrate when the mold was separated

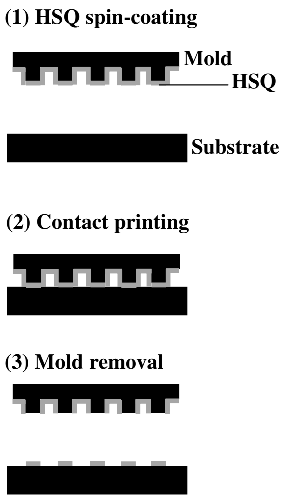

Figure 8.15 Schematic of the RT-NCP process using HSQ as the transfer material.

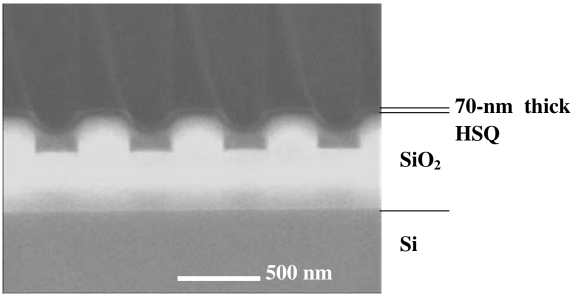

Figure 8.16 SEM micrograph of HSQ-coated mold.

from the substrate. Figure 8.16 shows an HSQ-coated SiO_2/Si mold with 500-nm linewidth, 1-μm pitch, and 300-nm height. The HSQ thickness on the projection part of the mold was 70 nm. This HSQ was transferred from the mold onto the Si substrate at a pressure of 1 MPa. Figure 8.17 shows a 500-nm-linewidth pattern and 1-μm-diameter dot HSQ pattern on an Si substrate after RT-NCP. These patterns were both 50 nm in height. Thus, the linewidth of the transferred HSQ pattern was the same as that of the mold pattern and the 50-nm thickness of HSQ on the projection parts was transferred. The mold was cleaned with acetone immediately after RT-NCP to confirm that the HSQ coated onto a mold could be removed and the mold reused.

8.3.2 RT-NCP Using Poly(Ethylene)/Poly(Methyl Methacrylate) Soft Template

The RT-NCP using a SiO_2/Si mold is presented in Section 8.3.1. However, a uniform contact printing was difficult because of the rigid property of the

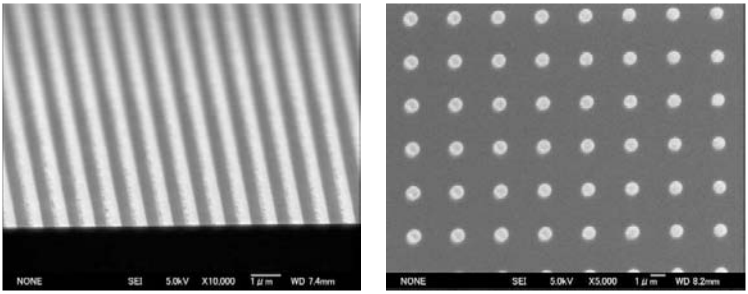

(a) (b)

Figure 8.17 SEM micrographs of (a) 500-nm linewidth and (b) 1-μm dot transferred HSQ patterns after RT-NCP.

SiO_2/Si mold; thus, we found that a flexible template is required to overcome this problem. The best known flexible stamps for contact printing are PDMS stamps. However, in our experiment, HSQ could not be applied on a PDMS stamp because PDMS dissolved in the solvent of HSQ. This means that contact printing using a PDMS stamp is restricted to several transfer materials. To address the restriction, poly(ethylene) (PE) laminated on a poly(methyl meth acnylate (PMMA) sheet is now proposed as the template for RT-NCP as a replacement for the PDMS stamp. The PE sheet has extremely high durability to various solvents without any surface treatment. We were able to cope with the limitation by using the new soft template on which HSQ can be applied, because PE has high tolerance to various solvents. As another benefit, the PE/PMMA sheet is transparent material, which enables us to perform optical alignment that is difficult when using the SiO_2/Si mold. To fabricate the soft template for RT-NCP, the conventional thermal cycle NIL technique[7–11] was used. The fabrication process of the soft template is shown in Figure 8.18. The Si master mold was fabricated by electron beam lithography and dry-etching process for the preparation of PE/PMMA soft templates. (1) The Si master mold 20 mm × 20 mm in size (Figure 8.19a) was pressed onto the PE film. The Si mold has protrusions of 100 nm and various patterns. The release agent was coated beforehand onto the Si mold master to avoid the adhesion of the replication material. The temperature and pressure for the imprinting process

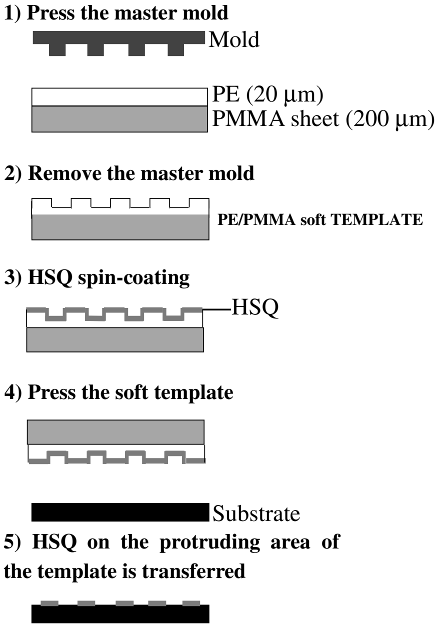

Figure 8.18 Schematic of the fabrication process of PE/PMMA soft template, and RT-NCP process of HSQ using the soft template.

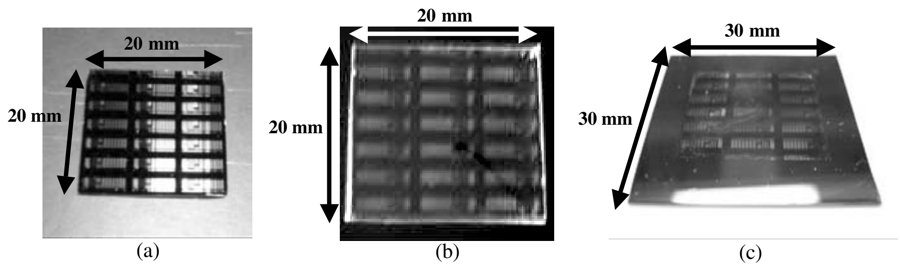

Figure 8.19 Photographs of (a) Si master mold, (b) PE/PMMA soft template, and (c) HSQ transferred patterns onto an AZ photoresist.

were 120°C and 6 MPa, respectively. Because the T_g of the PMMA bottom sheet (110°C) is higher than that of the used PE sheet (55°C), the 200-μm-thick bottom sheet served to prevent the large deformation of the template when the imprinting was performed. (2) The PE/PMMA soft template was completed (Figure 8.19b) when the master mold was removed. (3) HSQ was spin coated onto a mold. (4) The soft template was pressed onto the substrate at room temperature with 0.3 MPa press pressure. This contact printing process was performed within a few minutes of the HSQ coating. (5) The HSQ on the protruding area of the soft template was transferred when the soft template was removed from the substrate. Each PE/PMMA soft template was used only once in our experiment. The measured water contact angle of the PE surface exceeded 90° even if the release agents such as fluorine polymers were not coated onto the soft template. Therefore, the soft template was used without any release agents coating the surface. This is a useful characteristic for transferring nanostructures in contact printing. Figure 8.19c shows a photograph of the HSQ transferred pattern after RT-NCP. Thus, the HSQ patterns containing micro- and nanoscale structures were able to print under the same conditions onto the substrate. Figure 8.20 shows the HSQ transferred pattern

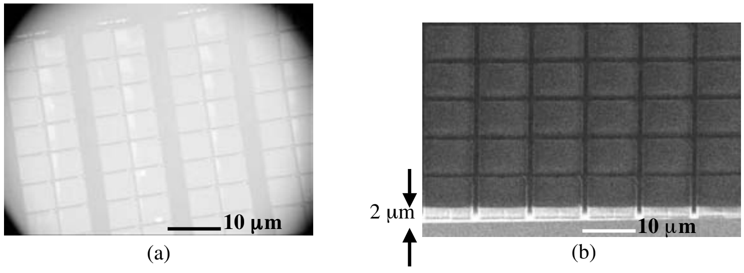

Figure 8.20 HSQ transferred pattern with 8-μm linewidth and 700-nm space after bilayer process using RT-NCP. (a) Optical micrograph and (b) enlarged cross-sectional SEM micrograph.

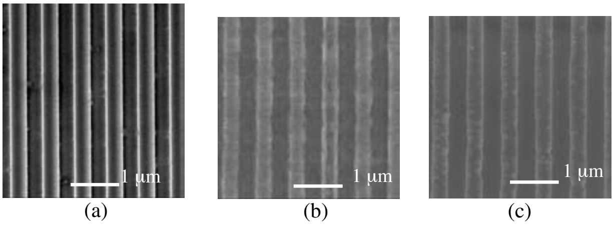

Figure 8.21 SEM micrographs of (a) Si master mold with 350-nm linewidth and 700-nm pitch. (b) PE/PMMA soft template with 350-nm linewidth and 700-nm pitch, fabricated using the Si master mold, and (c) HSQ patterns of 350-nm linewidth and 700-nm pitch transferred using the soft template.

with 8-μm linewidth and 700-nm space after the bilayer process using RT-NCP.[10] The height of the patterns is about 2 μm. HSQ/AZ bilayer microscale structures were successfully obtained with uniformity. Figure 8.21a shows the SEM micrograph of an Si master mold with a 350-nm linewidth. The PE/PMMA soft template fabricated by thermal NIL using the Si master mold is shown in Figure 8.21b. The replicated linewidth was 350 nm, which is the same as that of the Si master mold. Figure 8.21c shows the SEM micrograph of the HSQ pattern with a 350-nm linewidth obtained using the PE/PMMA soft template shown in Figure 8.21b. Thus, from the evidence of these SEM micrographs, precise transfer could be done using the RT-NCP.

Furthermore, the RT-NCP generated HSQ patterns with 100-nm linewidth and 200-nm pitch, and nanoscale patterns of 35-nm linewidth onto the Si substrate, as shown in Figure 8.22. The difficulty of imprinting complex patterns containing both micro- and nanoscale structures can be overcome by using RT-NCP. These results demonstrate that RT-NCP using a PE/PMMA soft template is a useful technology for obtaining various micro- and nano- scale structures, and this technology is widely applicable.

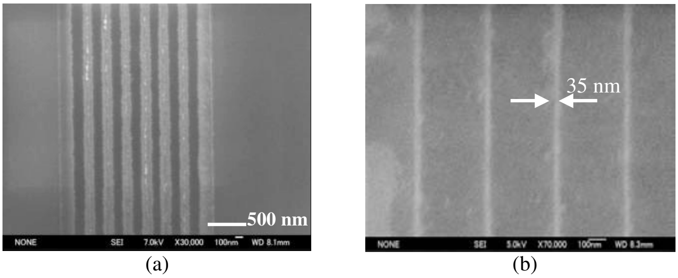

Figure 8.22 HSQ transferred pattern of (a) 100-nm linewidth and (b) 35-nm linewidth obtained after RT-NCP.

8.3.3 Ag Patterning by RT-NCP

Moreover, we proposed a fabrication method for Ag wirings by contact printing, which uses commercially available Ag paste (Harima Chemicals Inc.). This paste is commonly used for ink-jet printing (IJP). The IJP technique is a useful direct patterning technology for obtaining metal patterns. However, obtaining small linewidth patterns of less than 10 μm is difficult using the IJP technique due to, for example, splashing and bleeding ink. On the other hand, in the RT-NCP, these problems can be eliminated. Contact printing has many advantages such as its simple process, low cost, and low load on the environment. The colloid size, percent solids, and viscosity of the Ag paste we used were 5 nm, 57 to 62 wt%, and 5 to 10 MPa·s, respectively. Because this Ag paste had an effective adhesion property as good as that of HSQ resin, we could perform RT-NCP by using it. Our developed patterning process of Ag patterns is as follows. First, Ag paste was spin-coated on a PE/PMMA soft template. Second, the paste-coated soft template was pressed onto SiO_2 substrate at a 0.3 MPa press pressure. The Ag paste on the protrusion parts of the template was then easily transferred onto the substrate. The contact printing was performed within a few minutes of the Ag paste coating. The reason that we can print the Ag paste from the template to the substrate is that this contact printing is based on the high viscosity of the paste containing tetradecane as the alcohol solvent. The printed Ag pattern was baked at 220°C on a hot plate for 1 h to sinter the paste. Figure 8.23 shows enlarged SEM micrographs of the Ag grains of transferred pattern with a 600 μm × 600 μm square after the sintering process. Although the 200-nm-thick Ag grain layer was uniformly connected, as shown in Figure 8.23a, the 80-nm-thick Ag grain layer seemed to be not connected, which can be observed from Figure 8.23b. The thickness of the printed Ag grain layers was measured by a stylus profiler. The thickness difference of the applied layers was caused by spin-coating conditions and the concentration of the Ag paste. We carried out the resistivity measurements by the two-terminal method for the Ag patterns transferred onto the 100-nm SiO_2 layer on Si substrate. The average of measured resistivity of the 200-nm-thick Ag grain layer

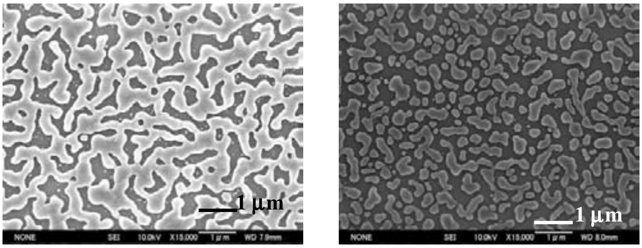

(a) (b)

Figure 8.23 Silver grain layer of transferred pattern with 600 μm × 600 μm square. (a) Thickness of 200 nm and (b) thickness of 80 nm.

Table 8.1 Measurement Results of Resistivity to the Three Kinds of Printed Ag Wirings.

Li (µm)	100	10	1
Res (× 10^{-7}m)	2.5	1.7	1.7

Source: K. Nakamatsu and S. Matsui.

with 600 µm × 600 µm square pattern was 2.5×10^{-7} m. However, current did not flow when the current-voltage characteristic was measured for the 80-nm-thick Ag grain layer. This conduction characteristic was probably caused by whether or not Ag grains were connected. Table 8.1 shows the measurement results of resistivity to the three kinds of printed Ag wirings. These patterns were 200 nm thick. The average amount of measured resistivity for the Ag patterns of 100 µm linewidth, 10 µm linewidth, and 1 µm linewidth were 2.5, 1.7, and 1.7×10^{-7} m, respectively. These values are about ten times higher than that of pure Ag (1.47×10^{-8} m). However, it is likely that the transferred Ag pattern is expected to be sufficient for various applications. Figure 8.24 shows the Ag transferred pattern with 5 × 10-µm square. Figure 8.25 shows the Ag transferred pattern after RT-NCP. The 1-µm-linewidth and 1-µm-space patterns were successfully obtained as shown in Figure 8.25a. The RT-NCP technique also provided an Ag pattern with 200-nm linewidth and 700-nm space, as shown in Figure 8.25b.

These results indicate that Ag direct patterning using RT-NCP is a useful technique for fabricating various metal patterns with simple processes.

8.3.4 Transfer of an Au Electrode Pattern through Nanocontact Printing

We demonstrated nanotransfer printing of a 5-µm-linewidth Au pattern using the adhesion of HSQ.[12] Current (I)-voltage (V) measurements of HSQ resin indicate that it is a good insulator, so the electrical resistivity can be measured for various materials on an HSQ film using a transferred Au electrode pattern.

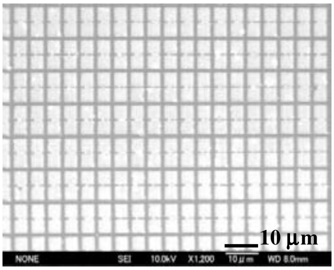

Figure 8.24 SEM micrograph of Ag transferred pattern with 5 × 10-µm square.

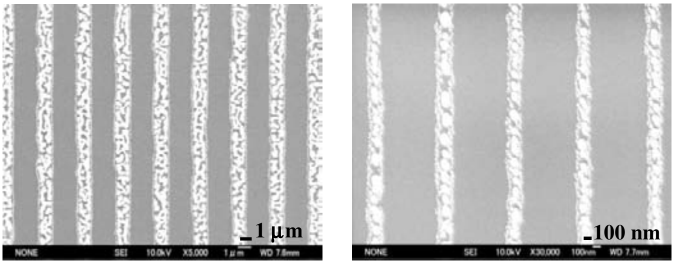

(a) (b)

Figure 8.25 SEM micrographs of Ag transferred pattern. (a) 1-µm linewidth and 1-µm space; (b) 200-nm linewidth and 700-nm space.

This transfer process is as follows. First, a 0.8-µm-thick HSQ resin layer was spin coated onto the 100-nm SiO_2 layer on an Si substrate. Second, a 150-nm-thick Au layer was evaporated onto an SiO_2/Si mold and then pressed onto the HSQ at a 22-MPa press pressure. The Au on the protruding parts of the mold was then transferred onto the HSQ-coated SiO_2 substrate when the mold was separated from the HSQ layer. Figure 8.26 shows an Au electrode pattern on HSQ resin after the transfer process. The electrodes have 300-µm-square pads and 2-µm pitch. This demonstrates that Au patterns can be successfully transferred onto the HSQ resin. To evaluate the transferred Au electrode, we carried out resistivity measurements using a two-terminal method for a 24-µm-long W wire deposited by focused-ion-beam chemical-vapor deposition (FIB-CVD) using a $W(CO)_6$ source gas. The measured resistivity of the deposited W wire was 0.03 cm.

Thus, Au electrodes transferred by RT-NCP onto an HSQ film can be used to measure the electrical characteristics of various materials.

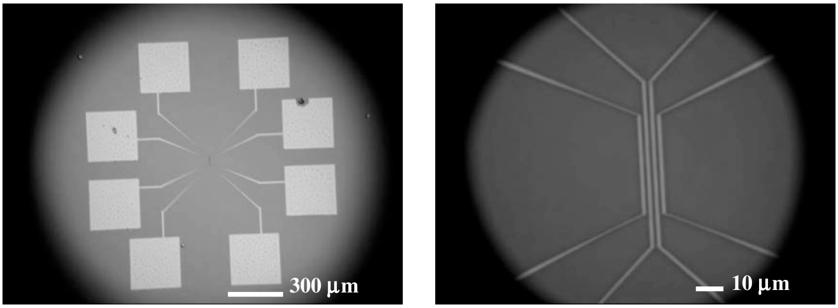

(a) (b)

Figure 8.26 Optical micrographs of an Au transferred electrode pattern on HSQ resin.

8.4 Summary

Room-temperature nanoimprint lithography (RT-NIL) and room-temperature nanocontact printing (RT-NCP) are promising technologies for providing various nanoscale structures with a simple procedure, high throughput, and low cost because these technologies can prevent resist thermal cycle. First, we evaluated the HSQ-replicated patterns after RT-NIL. We found that the imprinted depth of HSQ decreased as prebaking temperature increased, and expect that patterns of less than 1 μm were suitable for RT-NIL. In addition, an increasing HSQ thickness applied on Si substrate affected the imprinted depth increase in the RT-NIL. Second, we described a bilayer resist method for RT-NIL where HSQ was used as a top layer and AZ photoresist was used as a bottom layer. The HSQ/AZ bilayer structure of 100-nm linewidth, 200-nm pitch, and 1-μm height could be obtained by this bilayer method. We presented an ecological lift-off process using a bilayer structure of HSQ/PVA in order to obtain Au patterns, which needed water as the solvent because PVA is a water-soluble polymer. The line and space grating of 150-nm linewidth could be demonstrated by the lift-off in water. Furthermore, HSQ patterns of 20 mm × 20 mm in size were demonstrated through the advanced contact printing using a PE/PMMA soft template. The Ag wiring of 1-μm linewidth obtained by the RT-NCP showed us good resistivity of 1.7×10^{-7} m, suitable for electrical applications. Finally, we described nanotransfer printing of an Au electrode pattern from a mold onto HSQ resin that takes advantage of the resin's adhesion properties, and we considered that the Au electrode transferred onto the HSQ resin is expected to be used sufficiently for resistivity measurements. We therefore expect that the RT-NIL and RT-NCP we developed can be widely applied for various micro- and nanostructure fabrications.

References

1. Chou, S.Y., Krauss, P.R., and Renstrom, P.J., "Imprint of Sub-25 nm Vias and Trenches in Polymers," *Appl. Phys. Lett.*, 67, 3114, 1995.
2. Chou, S.Y., Krauss, P.R., and Renstrom, P.J., "Nanoimprint Lithography," *Science*, 272, 85, 1996.
3. Chou, S.Y., Krauss, P.R., Zhang, W., Guo, L., and Zhuang, L., "Sub-10 nm Imprint Lithography and Applications," *J. Vac. Sci. Tech.*, B15, 2897, 1997.
4. Sun, X., Zhuang, L., Zhang, W., and Chou, S.Y., "Multilayer Resist Methods for Nanoimprint lithography on Nonflat Surfaces," *J. Vac. Sci. Tech.*, B16, 3922, 1998.
5. Heidari, B., Maximov, I., and Montelius, L., "Nanoimprint Lithography at the 6 in. Wafer Scale," *J. Vac. Sci. Tech.*, B18, 3557, 2000.
6 Schift, H., Jaszewski, R.W., David, C., and Gobrecht, J., "Nanostructuring of Polymers and Fabrication of Interdigitated Electrodes by Hot Embossing Lithography," *Microelectronic Eng.*, 46, 121, 1999.
7. Bailey, T., Choi, B.J., Colburn, M., Meissl, M., Shaya, S., Ekerdt, J.G., Sreenivasan, S.V., and Willson, C.G., "Step and Flash Imprint Lithography: Template Surface Treatment and Defect Analysis," *J. Vac. Sci. Tech.*, B18, 3572, 2000.

8. Wu, W., Sun, B.C.X., Zhang, W., Zhuang, L., Kong, L., and Chou, S.Y., "Large Area High Density Quantized Magnetic Disks Fabricated Using Nanoimprint Lithography," *J. Vac. Sci. Tech.*, B16, 3825, 1998.
9. Zhuang, L., Guo, L., and Chou, S.Y., "Silicon Single-Electron Quantum Dot Transistor Switch Operating at Room-Temperature," *Appl. Phys. Lett.*, 72, 1205, 1998.
10. Wang, J., Schablitsky, A., Yu, Z., Wu, W., and Chou, S.Y., "Fabrication of a New Broadband Waveguide polarizer with a Double-Layer 100 nm Period Metal-Gratings Using Nanoimprint Lithography," *J. Vac. Sci. Tech.*, B17, 2957, 1999.
11. Martini, I., Kuhn, S., Kamp, M., Worschech, L., Forchel, A., Eisert, D., Koeth, J., and Sijbesma, R., "Fabrication of Quantum point Contacts by Imprint Lithography and Transport Studies," *J. Vac. Sci. Tech.*, B18, 3561, 2000.
12. Matsui, S., Igaku, Y., Ishigaki, H., Fujita, J., Ishida, M., Ochiai, Y., Namatsu, H., Komuro, M., and Hiroshima, H., "Room-Temperature Nanoimprint and Nanotransfer Printing Using Hydrogen Silsequioxane," *J. Vac. Sci. Tech.*, B21, 688, 2003.
13. Nakamatsu, K., Watanabe, K., Tone, K., Katase, T., Hattori, W., Ochiai, Y., Matsuo, T., Sasago, M., Namatsu, H., Komuro, M., and Matsui, S., "Bi-Layer Resist Method for Room-Temperature Nanoimprint Lithography," *Jpn. J. Appl. Phys.*, 43, 4050, 2004.
14. Nakamatsu, K., Watanabe, K., Tone, K., Namatsu, H., and Matsui, S., "Room-Temperature Nanoimprint and Nanocontact Technologies Using Hydrogen Silsesquioxane," *J. Vac. Sci.Tech.*, B23, 507, 2005.
15. Komuro, M., Taniguchi, J., Inoue, S., Kimura, N., Tokano, Y., Hiroshima, H., and Matsui, S., "Imprint Characteristics by Photo-Induced Solidification of Liquid Polymer," *Jpn. J. Appl. Phys.*, 39, 7075, 2000.
16. Namatsu, H., Takahashi, Y., Yamazaki, K., Yamaguchi, T., Nagase, M., and Kurihara, K., "Three-Dimensional Siloxane Resist for the Formation of Nanopatterns with Minimum Linewidth Fluctuations," *J. Vac. Sci. Tech.*, B16, 69, 1997.
17. Nakamatsu, K., Tone, K., and Matsui, S., "Nanoimprint and Lift-off Process Using Poly(vinyl alcohol)," *Jpn. J. Appl. Phys.*, 44, 8186, 2005.
18. Schaper, C.D., "MxL: Pseudo-Maskless High-Throughput Nanolithography," *Proceedings of SPIE Conference on Emerging Lithographic Technologies VII*, Vol. 5037, 2003.
19. Wilbur, J.L., Kumar, A., Kim, E., and Whitesides, G., "Microfabrication by Microcontact Printing of Self-Assembled Monolayers," *Adv. Mater.*, 6, 600, 1994.
20. Kim, E., Xia, Y., and Whitesides, G.M., "Polymeric Microstructures Formed by Moulding in Capillaries," *Nature (London)*, 376, 581, 1995.
21. Zhao, X.-M., Xia Y., and Whitesides, G.M., "Fabrication of Three-Dimensional Microstructures: Microtransfer Molding," *Adv. Mater.*, 8, 837, 1996.
22. Xia, Y., Kim, E., Zhao, X.-M., Rogers, J.A., Prentiss, M., and Whitesides, G.M., "Formation of Complex Optical Surfaces by Molding Against Elastomeric Masters," *Science*, 273, 347, 1996.
23. Hu, J., Beck, R.G., Deng, T., Westervelt, R.W., Maranowski, K.D., Gossard, A.C., and Whitesides, G.M., "Using Soft Lithography to Fabricate GaAs/AIGaAs Heterostructure Field Effect Transistors," *Appl. Phys. Lett.*, 71, 2020, 1997.

Chapter 9

Antistiction Layers for Nano Imprinting Lithography

Nam-Goo Cha and Jin-Goo Park

Contents

9.1 Introduction 183
9.2 Antistiction Layer for NIL 185
9.2.1 History of Antistiction Layer 185
9.2.2 Need for Successful NIL 186
9.3 Fabrication Methods of Antistiction Layers 188
9.3.1 Spin Coating 189
9.3.2 Liquid SAM (Self Assembly Monolayer) 191
9.3.3 Vapor SAM Method 194
9.3.4 Plasma Polymerization 196
9.4 Characterizations of Antistiction Films 198
9.4.1 Wettability 198
9.4.2 Film Thickness 201
9.4.3 Chemical Analysis of Monolayer Films 203
9.4.4 Surface Morphology and Nanoscale Adhesion 205
9.4.5 Thermal, Chemical, and Tribological Tests 207
9.5 Conclusions and Prospects 210
Acknowledgment 210
References 210

9.1 Introduction

Progress in nanotechnology depends on the ability to fabricate nanostructures in materials with accuracy on a nanometer scale. In order to fabricate nanometer structures, we must understand the underlying science and engineering on a nanometer scale. For nearly two decades, all previously developed

techniques for nanostructures are cost-intensive or limited-access fabrication methods. Recently, several new techniques using a mold are emerging to fabricate nanoscale structures. These mold techniques are called nanoimprint lithography (NIL). It has been developed as an alternative nanofabrication method.[1]

The main technique of NIL is relatively simple when compared with the conventional photolithography method. To nanoimprint a surface, three components are required: molds with suitable feature size, materials to be printed, and equipment for printing with adequate control of temperature, pressure, etc. NIL has the advantage over conventional nanofabrication methods because it is simple, low-cost, and applicable to plastic substrates.[2]

NIL could be classified by hot and cold embossing lithography depending on applied temperatures as described in Table 9.1.[3,4] Hot embossing is the thermal imprinting technique that applies high pressure and temperature. However, cold embossing operates at room temperature with negligible pressure because it uses UV irradiation on UV curable polymer.[5]

Alternative nanofabrication techniques have been actively studied in micro electro mechanical systems (MEMS) and bio-MEMS areas for both general and specific application due to differences in their substrates, processes, and cost of ownership (COO).[6]

For the nano- and micromanufacturing point of view, NIL still needs tremendous input from equipment suppliers; consumables, such as photo and thermal polymers; and mold fabrication. In order to realize the commercial application of NIL techniques, efforts need to be made toward automation and alignment down to 10-nm and over 200-mm wafers.[7] In

Table 9.1 Classification of Nanoimprint Techniques by Their Applied Temperatures

Class		Hot (heat)	Cold (UV)
Wafer scale		Hot embossing lithography (HEL)	UV embossing lithography (UEL)
Step & repeat		Step and stamp imprinting lithography (SSIL)	Step and flash imprinting lithography (SFIL)
Mold		Non-UV transparent, Si, Ni, High temperature plastics	UV transparent Quartz, Glass, PDMS
Process	Pressure	Up to 100 bar	Negligible (<1 bar)
	Temperature	Up to 300°C	Room temperature
Polymer materials		Thermo plastics (PMMA, PC, etc.) and Thermo set materials (Epoxy, etc.)	UV resin

addition, the thermal polymer and UV curable polymer should be thoroughly studied and developed commercially. When NIL is applied to mass production, issues related to defects also should be understood. These defects could be related to mold designs, process conditions, intrinsic problems of tools, the physical and chemical properties of polymer materials, etc.[8]

One of the most commonly observed defect generation sources is the stiction properties of a very thin polymer layer with a mold during and after the embossing process. In both hot and UV embossing, the patterns with low aspect ratio do not cause a serious stiction problem during the embossing process. Patterns with a certain aspect ratio have been known to generate a serious stiction problem.[9] In this chapter, the issues related to stiction are reviewed with characterization methods of their antistiction layers related to nano- and microimprint.

9.2 Antistiction Layer for NIL

9.2.1 History of Antistiction Layer

Attempts to reduce the stiction problem can be traced back to proximity lithography in an effort to reduce the defect level. Surface treatments for masks need to improve their scratch resistance. Some polymer coatings have been applied to the masks to keep their surfaces clean. However, they are too thick to permit the level of high-resolution lithography. They do not have an antisticking property so that may create defects when they contact with resist polymer. Conventional coating using fluorinated silane-based monomers have been applied to masks to alter their high surface energy.[10–12]

Approaches to reduce stiction have been sought in both physical and chemical modifications of surfaces. Stiction has been a serious problem for microelectromechanical systems (MEMS). Hence, a variety of solutions to this problem have been developed.

Engineering solutions use techniques such as using supercritical fluid,[13] freeze sublimation drying,[14] making a spring tip,[15] vapor phase etching of surface layers,[16] or roughening the surface to reduce the contact area.[17] The above techniques can be quite effective in eliminating stiction in certain applications. These physical methods, however, cannot be applied to NIL mold application. Another effective way is surface chemical modification for the prevention of stiction.[18]

Chemical modification uses a molecular film deposited on the surface. It is an effective way to provide a hydrophobic and low-energy surface that greatly reduces stiction. Teflon™ or Teflon-like fluorocarbon (FC) coating could be good examples of chemical modification. They have a low dielectric constant, a low friction coefficient, and an excellent antistiction property

due to their hydrophobicity.[19] If the mold surface has high surface energy, polymer residue easily remains on the top of the mold surface. These defects propagate through the next imprinting process. Moreover, it will result in a catastrophic device failure and yield loss. An antistiction layer, which has a low surface energy, will prevent these defects from imprinting, improve the mask lifetime, and result in higher cleaning efficiency and yield.[20]

9.2.2 Need for Successful NIL

NIL is primarily a physical deformation process of polymeric resist and is fundamentally different from conventional lithography (Figure 9.1). Such simple and unique principles could generate high-resolution patterns at low cost. NIL consists of two steps: imprint and pattern transfer. In the imprinting, a mold could deform a thin resist polymer film deposited on a substrate. After pattern transfer, an anisotropic etching process such as reactive ion etching (RIE) is used to remove the residual resist layer in the compressed area. This residual layer thickness is an important factor for the imprinting process. To optimize the process, the residual layer thickness

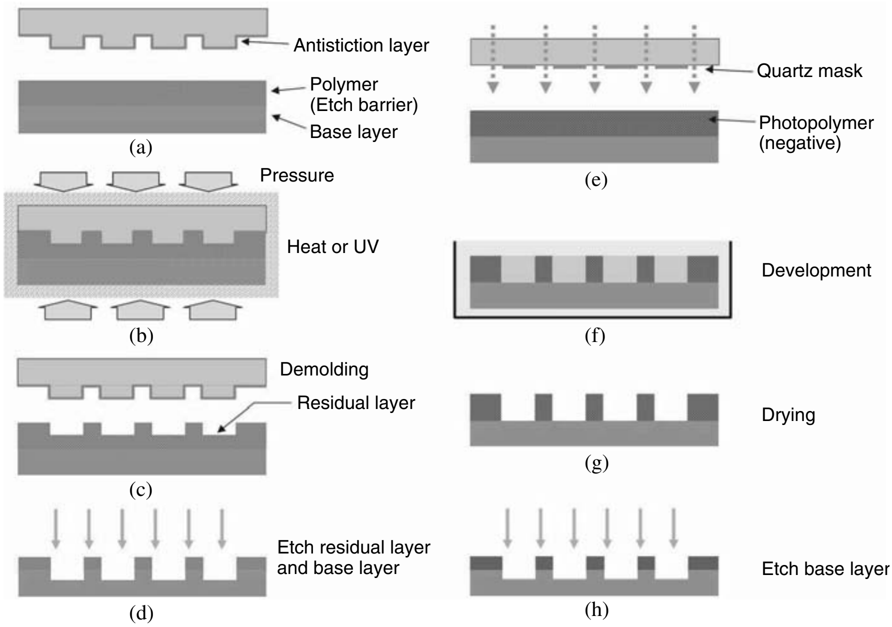

Figure 9.1 Schematic comparison drawings of nanoimprint (a–d) and conventional lithography (e–h).

should be decreased as much as possible. The resist can be either a thermal plastic or a UV curable polymer, or another deformable material. For the thermal plastic resist, it is heated above its glass transition temperature (T_g) during imprinting. For a UV curable polymer, the resist has lower viscosity and is easily deformed at low pressure then cured by UV light radiation. As the structures become smaller and stamp geometries more complex, the understanding of the thin polymer film during the process will be essential. In developing imprinting lithography, it is important to identify the relationship between the polymer properties and other imprint variables such as pressure and imprint time.[21]

Polymer properties such as viscosity, molecular weight, chain dimensions, T_g, shrinkage, adhesion property against substrate and mold material, etch behavior in dry and wet processes, and other material conditions are all very important for the optimization of the imprinting process. The polymer used in NIL has fundamentally different requirements from the polymers used in conventional lithography. The critical properties of the polymer used in NIL are mechanical, whereas in conventional lithography, chemical properties such as radiation sensitivity and the reaction with solvent during the development, are important.[22] The ideal polymer used in NIL has low viscosity above its glass transition temperature. The glass transition temperature is the temperature needed to overcome the chemical forces holding the chain segment of an amorphous polymer together. Above this temperature, the viscosity is many orders of magnitude lower.[23]

One of the key issues of successful NIL technology is to avoid adhesion of the polymer to the mold especially in manufacturing environments. As the feature size decreases and the aspect ratio increases on the mold, the stiction related issues would be more and more pronounced. Adhesion of polymer to the mold during the demolding process can cause such damage to the replica as tear-out patterns, pattern distortion, residual polymer contamination, and mechanical damage of the mold.[24]

Figure 9.2 shows that various kinds of failure can happen such as insufficient wetting, particles, and tear-out of patterns during the hot embossing. The insufficient pattern fillings were affected by the initial film thickness and process temperature. Particles were affected by dirt and dust contamination from the environment. Tear-out patterns were affected by the stamp geometry and stiction problems. To prevent a failure due to unwanted particles, all processes must be conducted in a clean room. During the demolding process, the stiction of polymer to the mold usually occurs on the mold surface.

Stiction-related issues could be significantly reduced by covering the mold surface with an antistiction layer. It is important to have a clear understanding about the mold surface and process target before developing an antistiction layer.

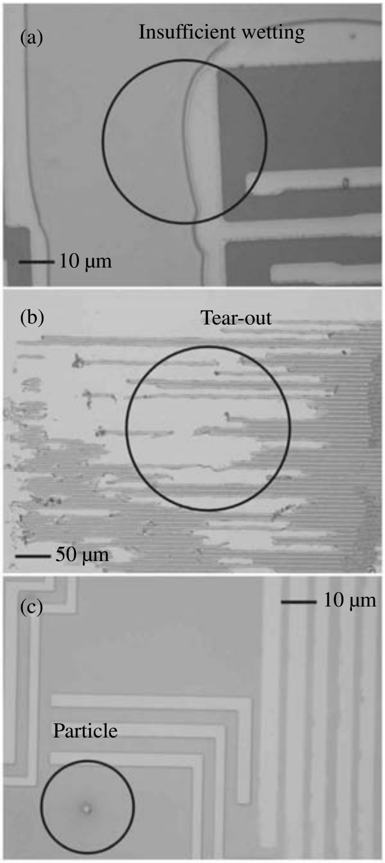

Figure 9.2 Induced defects during hot embossing: (a) insufficient wetting, (b) tear-out, and (c) particles on patterns.

9.3 Fabrication Methods of Antistiction Layers

The technology for hydrophobic coatings has been important for suppressing chemical reactions and bonding formation between polymer (or liquid) and solid surface. The coating has been adopted for various industrial uses such as antistiction, anti-wetting, anti-snow (or ice) adherence, anti-rusting, and reduced friction resistance. If the effects of surface strains or the adsorption of molecular substances can be ignored, the wettablity of the surface on a flat solid substrate is governed by its surface energy. The hydrophobicity of a solid surface is known to be enhanced as the surface energy lowers. Over the past few decades, there has been a considerable number of studies on low-surface-energy coatings. The most common and successful strategies for lowering the surface energy of a solid are to apply the coatings with FC polymers such as PTFE (polytetrafluoroethylene).[25]

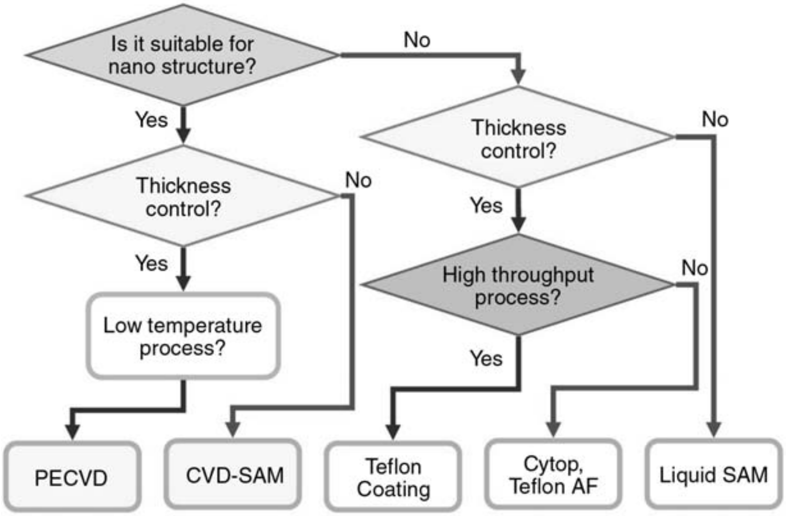

Figure 9.3 Fabrication flow chart for forming the antistiction layer.

Commonly used mold surfaces such as oxide, nitride, and silicon are usually covered with hydroxyl groups (OH^-). Because hydroxyl groups are polar in nature, the surface is said to be polar or hydrophilic (high-energy surface). However, the polymer surface is in nature nonpolar and hydrophobic (low-energy surface). The energy state of the high-energy surface can be lowered by covering it with polymer materials. The high-energy mold surfaces are in general very vulnerable to stiction if polymer materials contact with molds during the imprinting process. The modification of mold surfaces with hydrophobic and lower-energy surfaces can greatly reduce possible stiction problems. There are various ways to make the hydrophobic antistiction layers. Liquid, vapor, and plasma polymerization methods can be used depending on the application.[26] Figure 9.3 shows a schematic diagram for forming an antistiction layer based on its application. Table 9.2 shows the comparison of advantages and disadvantages of these different deposition methods.

9.3.1 Spin Coating

Spin coating is a well-known and traditional method for fabrication of thin films on a rotating flat substrate by dropping a liquid. It is very simple but highly reliable and reproducible.[27] Spin coating involves the acceleration of a liquid puddle on a rotating substrate. The coating materials are usually supplied to the center of the substrate either manually or by a robotic arm. The physics behind spin coating involves a balance between centrifugal forces controlled by spin speed and viscous forces that are determined by solvent

Table 9.2 Comparison of Advantages and Disadvantages of Antistiction Layers Prepared by Different Methods

Method	Advantage	Disadvantage
Spin coating	Easy to fabricate Thick film formation High reproducibility and reliability Well-known and traditional method	Hard to make below a 100 nm thickness Hard to make a uniform coating on patterned surfaces. Can waste up to 98% of process materials
Liquid SAM	Relatively cheap process Strong chemical bonding	Insufficient wetting for nano-structures Low reproducibility and reliability in a large area Waste of organic chemicals Substrates dependant
Vapor SAM	Easier to fabricate than liquid process High reproducibility, high reliability	Relatively higher temperature No control of film thicknesses Substrates dependant
Plasma polymerization	Low temperature process Thickness control from nanometer to micrometer at any substrate High reproducibility and reliability Substrates independent Semiconductor process compatible	Relatively expensive Relatively weak physical bonding

viscosity of polymer. The spin-coating technique consists of six basic stages: dispensing, low-speed spreading, high-speed coating, and baking, as shown in Figure 9.4. Some variable process parameters are involved in spin coating such as solution viscosity, solid content, angular speed, and spinning time. The film-forming process is primarily driven by two independent parameters, viscosity and spin speed. For thicker films, high material viscosity, low spin speed, and a short spin time are needed. Sometimes multiple coatings are preferred for a thicker film. However, it is hard to make a uniform coating on patterned surfaces with spin coating and up to 98% of process materials could be wasted. In addition, it is hard to fabricate a film thickness below 100 nm.[28,29]

Amorphous fluorocarbon polymers can easily make Teflon-like films using the spin coating method. Teflon AF is a fluoropolymer (DuPont, USA)

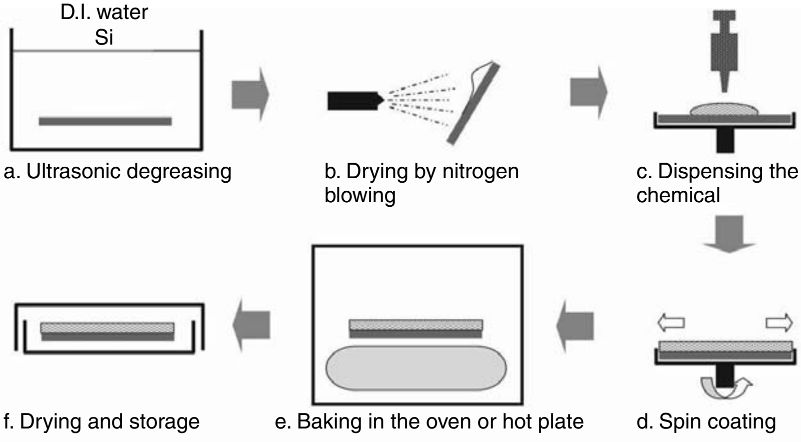

Figure 9.4 Schematic diagram for spin coating procedure.

that is made by the copolymerization of 2,2-bistrifluoromethyl- 4,5-difluoro-1, 3-dioxole (BDD) with other fluorine-containing monomers.[30,31] It has good thermal stability and chemical resistance along with a very low surface energy. However, unlike other fluoropolymers such as PTFE, Teflon AF is amorphous. This characteristic offers many additional properties that make it particularly useful as a mask coating. Because it has none of the crystallites found in semicrystalline materials such as PTFE, coatings (<200 μm) of Teflon AF are virtually transparent to light with wavelengths greater than 200 nm. In addition, Teflon AF is soluble at room temperature in several fluorocarbon-based solvents, allowing it to be easily spin coated onto a photomask. It can also be easily removed using the same solvent.

Cytop (Asahi Glass, Japan) is another family of amorphous fluoropolymer materials that has a cycle ring structure that prevents crystalline in a manner similar to Teflon AF.[32,33] Several grades of Cytop are available with various synthetic modifications incorporated into their structures. These modifications include chain-terminating groups, which are added to improve the adhesion to materials such as metals and glass. Coupling agent pretreatments also designed to improve substrate adhesion are available for both Teflon AF and Cytop. The Teflon AF structure and the Cytop structure are shown in Figure 9.5.

9.3.2 Liquid SAM (Self Assembly Monolayer)

For the application of any chlorosilane-based SAM precursor molecule to a SAM, the first step in the reaction sequence is the hydrolysis of one or more Si-Cl bonds as shown in Figure 9.6.[34] The hydrolysis domino effect results in the formation of one HCl for each Si-Cl bond. If the silicon surfaces are

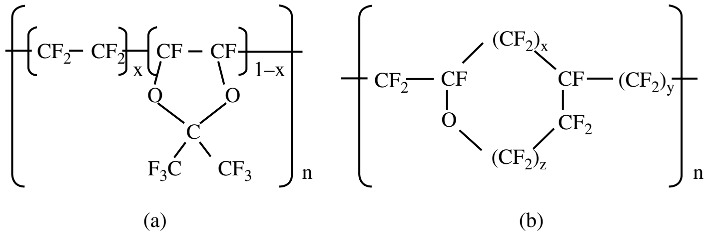

Figure 9.5 The structure of (a) Teflon AF and (b) Cytop.

used as a substrate, they should be first oxidized in order to form a chlorosilane SAM.[35] Chemical systems of adsorbates and substrates that form SAMs are listed in Table 9.3.

Silicon wafers are coated with a thin layer of native oxide (about 1 or 2 nm thickness). One of the primary advantages of silicon substrate is its planarity, flatness, and smoothness. Before the deposition of a SAM film, the surface must be carefully cleaned. The SAM deposition process is shown in Figure 9.7. The wafers are immersed for at least 10 minutes into an acid bath mixture of sulfuric acid and hydrogen peroxide (in the ratio of 80:20%, the mixing of these chemicals gives an exothermic reaction that reaches over 100°C instantly) to remove heavy organic contaminants. Just before the deposition of SAMs, samples are exposed to UV radiation in an oxygen atmosphere that produces ozone and removes light residual organic impurities that might remain on the surface. A trichlorosilane group reacts chemically with the silanols on the surface and leaves a hydrophobic chain on the substrate. If a Teflon-like surface is formed, the contact angle is equal to or higher than 105°C and surface energy is equal to or lower than 18 mN/m. When the coating is partial or heterogeneous, the contact angle is lower and irregular

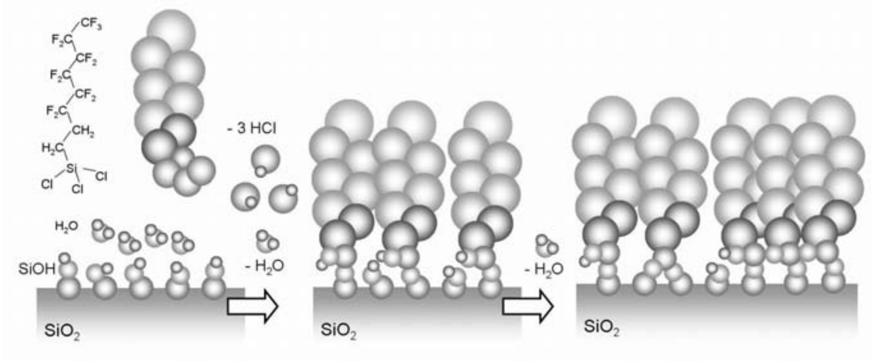

Figure 9.6 Formation of FOTS monolayer on SiO_2 substrate.

Table 9.3 Chemical Systems of Adsorbates and Substrates that form SAMs

Surface	Substrate	Adsorbate(s)
Metal	Au	R-SH, R-SS-R, R-S-R, $R\text{-}NH_2$, R-NC, R-Se, R-Te
	Ag	R-COOH, R-SH
	Pt	R-NC, R-SH
	Pd	R-SH
	Cu	R-SH
	Hg	R-SH
Semiconductor	GaAs (III-V)	R-SH
	InP (III-V)	R-SH
	CdSe (II-VI)	R-SH
	ZnSe (II-VI)	R-SH
Oxide	Al_2O_3	R-COOH
	TiO_2	R-COOH, R-PO3H
	YBa_2Cu_3O7-	$R\text{-}NH_2$
	Ti-Ba-Ca-Cu-O	R-SH
	ITO	R-COOH, R-SH, $R\text{-}Si(x)_3$
	SiO_2	$R\text{-}Si(x)_3$

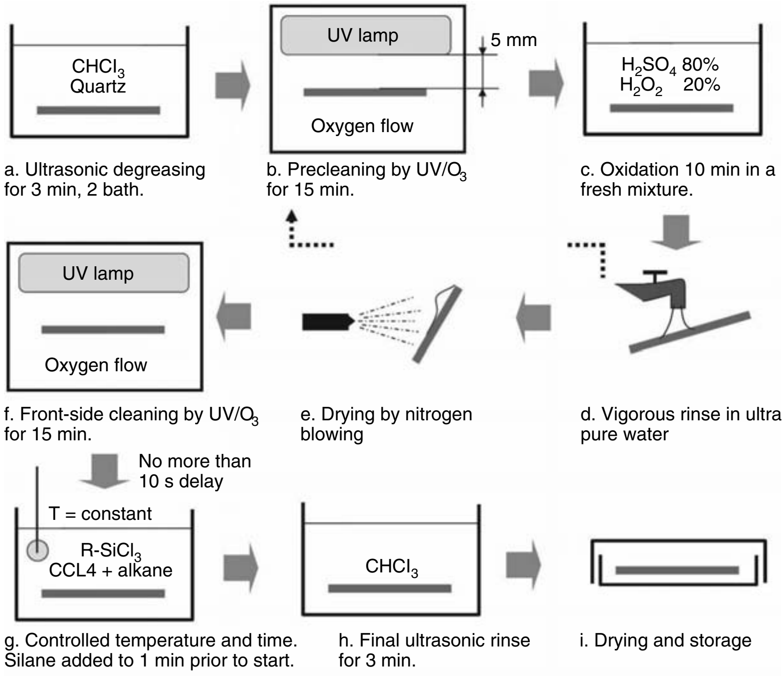

Figure 9.7 A schematic flow diagram of the silanization process for liquid SAM on mold.

and surface energy is greater. Contact angle hysteresis, especially, would be much higher than that on homogeneous film.[36]

Liquid SAM coating by wet process is a cheap and easy way to place the antistiction layer on surfaces. However, because its chemical reaction is limited by substrates, the process has been widely used in research rather than in industry. The actual coating process could be very complex and difficult because the SAM solution must be freshly made and appropriately conditioned immediately before and after each process sequence. This is due to the sensitivity of the SAM solution to ambient humidity and the relatively long time for SAM precursors to be polymerized. Consequently, great care and control are needed for the formation of the SAM. If the SAM is applied to nanostructured molds as an antistiction film, insufficient wetting on these structures may occur due to the capillary action on these patterns (Figure 9.8).[9] The challenges of liquid SAMs are the lack of repeatability and reliability (R&R) and the difficulty in applying it on larger area substrates. Typical precursors for SAMs are listed in Table 9.4.

9.3.3 Vapor SAM Method

The thermal chemical-vapor deposition (CVD) of antistiction film is carried out by the thermal dissociation of chemical compounds on the heated substrate in a controlled environment. Once vaporized, chemical compound molecules reach the heated surface, are dissociated, and form a film. Among species reaching the surface, only molecules with a high sticking coefficient are to be deposited to form films. In order to make the film thickness uniformly on a large area of a three-dimensional surface, the precursor vapor delivery system should be well designed.[37–39]

Recent developments in chlorosilane-based monolayer technology deal with performing the coating process in the vapor phase. Wetting-related defects might occur during liquid phase SAM deposition of the antistiction layer on the nanometer-scale mold coating. As one of cholorosilane precursors, FOTS (perfluorocyltrichlorosilane) is coated after dissolving it in hydrophobic solvents such as hexane. This solvent does not have enough wetting

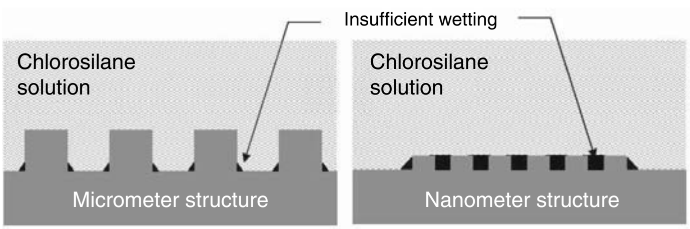

Figure 9.8 Possible wetting defects on nanometer structure during liquid SAM deposition.

Table 9.4 General Chemicals for Formation of SAMs

Name	Chemical composition	Boiling point (pressure)
Dichlorodimethylsilane (DDMS)	$C_2H_6Cl_2Si$	70°C (760 Torr)
Octadecylmercaptan (ODT)	$C_{18}H_{38}S$	210°C (11 mTorr)
Trichlorooctadecylsilane (OTS)	$C_{18}H_{37}Cl_3Si$	220°C (10 mTorr)
Undecyltrichlorosilane (DTS)	$C_{11}H_{23}Cl_3Si$	155°C (15 Torr)
10-Undecenyltrichlorosilane (UTCS)	$C_{11}H_{21}Cl_3Si$	100°C (0.8 Torr)
Perfluorodecyltrichlorosilane (FDTS)	$C_{10}H_4Cl_3F_{17}Si$	216°C (760 Torr)
Perfluoroctyltrichlorosilane (FOTS)	$C_8H_4Cl_3F_{13}Si$	192°C (760 Torr)
Perfluorodecanoic Acid (PFDA)	$CF_3(CF_2)_8COOH$	218°C (740 Torr)

properties on a nanostructure, as shown in Figure 9.8. It could not penetrate to the nanometer structure so that the mold might result in a very poor coating. The vapor phase process has its advantage when the mold features are nanometer scale. In addition, the vapor phase process eliminates the use of organic solvents and greatly simplifies handling of the sample. Moreover, the stoichiometry of the precursor molecules can be more precisely controlled.[38]

A chlorosilane-based chemical such as FOTS has also been used for the vapor phase deposition of SAMs. The principle of gas phase deposition is also very simple. Vapor SAM was deposited in a low-pressure CVD style reactor with in situ plasma cleaning capability of the sample as well as in situ measurement of the film growth that provided excellent process uniformity and reproducibility. The basic diagram of a vapor SAM deposition system is shown in Figure 9.9.

Oxygen plasma cleaning of substrate in the chamber was performed to have typical chlorosilane-based process of vapor SAM before injecting H_2O vapor for the surface oxidation. One or two vaporized SAM chemicals

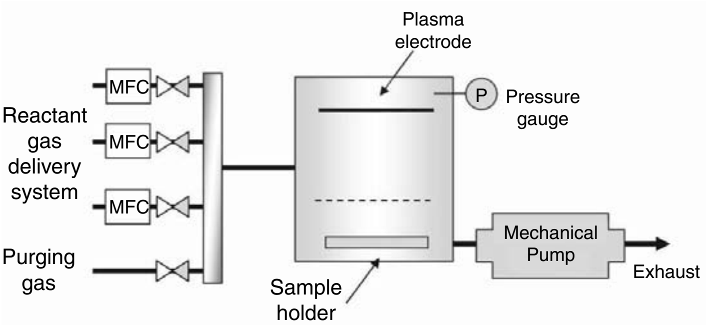

Figure 9.9 A schematic diagram of vapor phase antistiction layer deposition system. Plasma electrode allows in situ cleaning of mold.

are then injected into the chamber to form a monolayer. The process chamber is able to control the temperature and pressure during film formation.[40] This process is a relatively high-temperature process, cannot control the deposited film thickness, and is limited by substrates as well as the liquid SAM process.

9.3.4 Plasma Polymerization

In the case of plasma CVD, the dissociation of chemical compounds does not occur as much on the surface, because the substrate temperature is lower than thermal CVD. The chemical compound molecules are dissociated easily in plasma when chemicals are introduced into the chamber. They are broken by electron bombardment in the plasma, not by thermal dissociation. The precursor gas is introduced to one point in the vacuum chamber using a gas delivery system.[41–43] The basic diagram of the inductive coupled plasma (ICP) polymerization system is shown in Figure 9.10.

Fluorocarbon plasma is an indispensable state for SiO_2 etching in ultra large-scale integration (ULSI) manufacturing.[44] In the selective etching of SiO_2, fluorocarbon plasma plays a key role in the formation of protective fluorocarbon polymer films on the sidewall of Si and Si_3N_4 surfaces. On the other hand, fluorocarbon film prepared by plasma enhanced chemical vapor deposition (PECVD) has attracted interest as one of the most promising materials for low *k* dielectric interlayer. These plasma process technologies with fluorocarbon gases have been studied in terms of plasma-surface interactions. This semiconductor-based vacuum technology is well established, reliable, and reproducible. In this view, plasma polymerization has an advantage in mass production. The plasma polymerization method can control the thickness of the antistiction layer, which can grow from the nanometer to micrometer thickness at any substrate. Figure 9.11 shows that the film thickness increases as a function of deposition time. Figure 9.12 shows the deposited 32-nm-thick FC film on a quartz substrate made by PECVD.

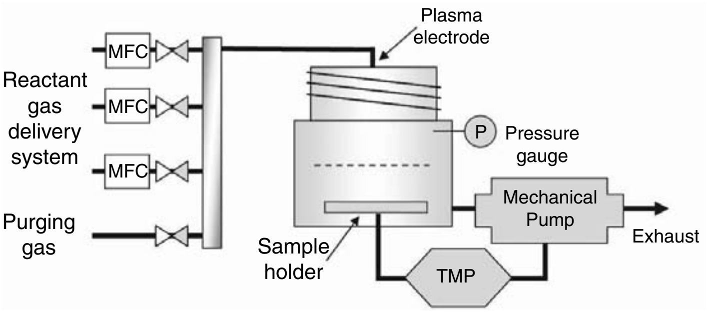

Figure 9.10 A schematic diagram of inductive coupled plasma plasma polymerization system.

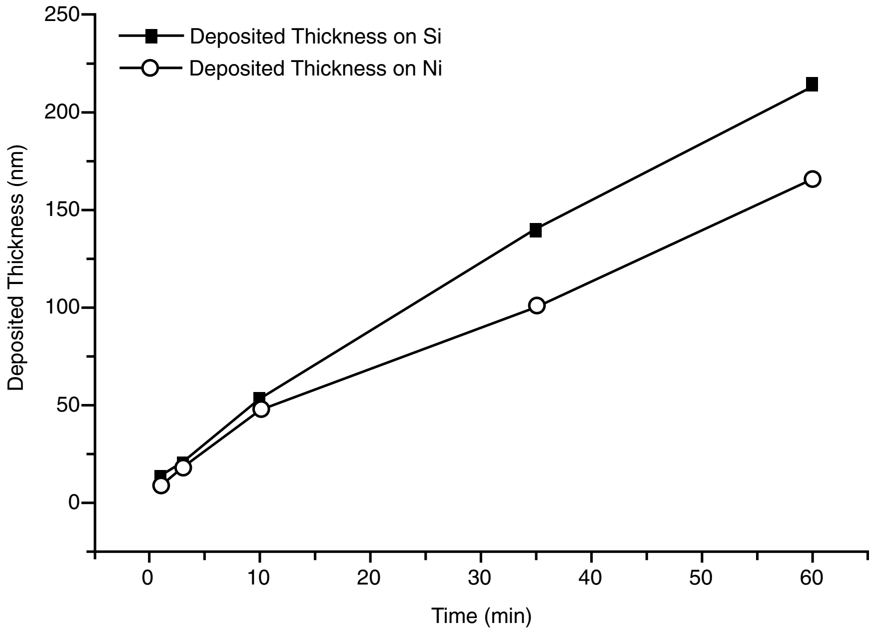

Figure 9.11 The change of the film thickness and deposition rate as a function of deposition time. Deposition condition: 5 sccm C_4F_8, 50 mTorr working pressure, 140°C substrate temperature, and 70 W plasma power.

Some kinds of mold materials such as plastics cannot form the antistiction layer by the liquid SAM method. In addition, some hot embossing processes require a thicker and more stable antistiction layer than monolayer SAM coatings. The fluorocarbon gases such as CF_4, C_2F_6, and C_4F_8 have been widely used for the deposition of fluorocarbon films. However, they have high global warming potential (GWP) values so they have been gradually replaced by low GWP alternative gases such as C_3F_6 and C_5F_8.[46]

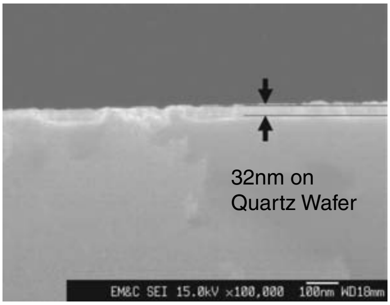

Figure 9.12 Fluorocarbon films on quartz substrate. Deposition condition was C_4F_8 of 2 sccm, working pressure of 50 mTorr, substrate temperature of 200°C, and plasma power of 100 W, and process time was 10 min.

9.4 Characterizations of Antistiction Films

9.4.1 Wettability

Contact angles of liquids on a polymer surface are widely used to predict wetting and adhesion properties of these solid surfaces by calculating their solid-vapor surface energy.[47,48] Using goniometry is a simple and fast way to measure the hydrophilicity or hydrophobicity of surface.[49,50] The reason for contact angle phenomena is very complicated but it is a powerful tool for making distinctions among coating properties, especially of polymer surfaces.

When a liquid drop is in contact with an ideally smooth, undeformable, and homogeneous solid (Figure 9.13), it exhibits an equilibrium contact angle that can be expressed by Young's equation:

$$\gamma_{LV} \cos\theta = \gamma_{SV} - \gamma_{SL} - \pi_e \tag{9.1}$$

where γ_{LV} is surface tension of the solid in equilibrium with its own vapor, γ_{SL} is interfacial tension of the solid in equilibrium with the saturated liquid vapor and θ the contact angle, and $\pi_e = (\gamma_S - \gamma_{SV})$ is equilibrium pressure.

It is generally believed that, if the contact angle is greater than zero, π_e is negligible. Therefore, Equation (9.1) can be rewritten as

$$\gamma_{LV} \cos\theta = \gamma_S - \gamma_{SL} \tag{9.2}$$

In most cases, the static contact angles are often observed on various surfaces (Figure 9.14). The hydrophilic surface has a high surface energy and the hydrophobic surface has a low surface energy. Figure 9.15 shows the captive drop method for measuring dynamic contact angles. The advancing angle is measured when the equilibrium liquid-solid-vapor phase boundary just moves outward as liquid injects into the equilibrium state of a droplet.

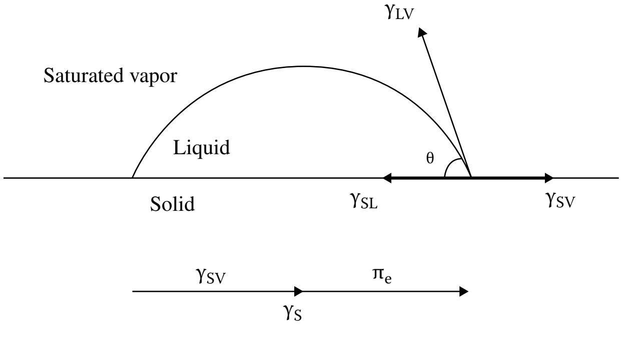

Figure 9.13 A sessile drop of liquid on a solid showing a three-phase force line.

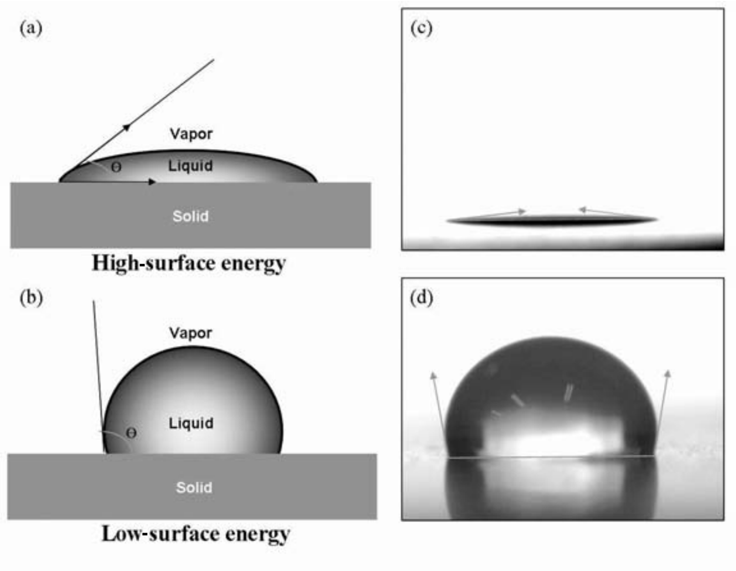

Figure 9.14 Schematic diagram of (a) high-surface energy and (b) low-surface energy. Photograph of (c) low contact angle (~5°) and (d) high contact angle (~108°).

The receding angles are measured when the phase boundary moves inward as the liquid extracts from a droplet, which is known as the captive drop method. The measurements of dynamic contact angles usually provide much richer information on the surface state. The difference of advancing and receding contact angles is known as contact angle hysteresis. Hysteresis of contact angles contains surface information such as surface roughness, chemical heterogeneity, sorption layers, molecular orientation, and swelling effect in the polymer material.

The most common and successful strategy for lowering the surface energy of a solid is to apply coatings with fluorine-based materials such as PTFE,[51] poly-vinylidene fluoride,[52] poly-perfluoroalkylacrylate,[53] fluorocarbon wax,[54] fluorinated monoalkyl phosphates,[55] or fluoroalkylsilane.[56] In fact, the surface energy of polymer solids cannot be measured directly.

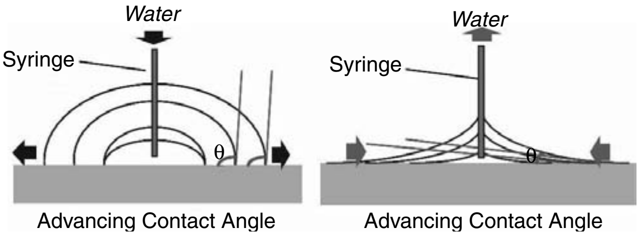

Figure 9.15 Captive drop method to measure advancing and receding contact angles.

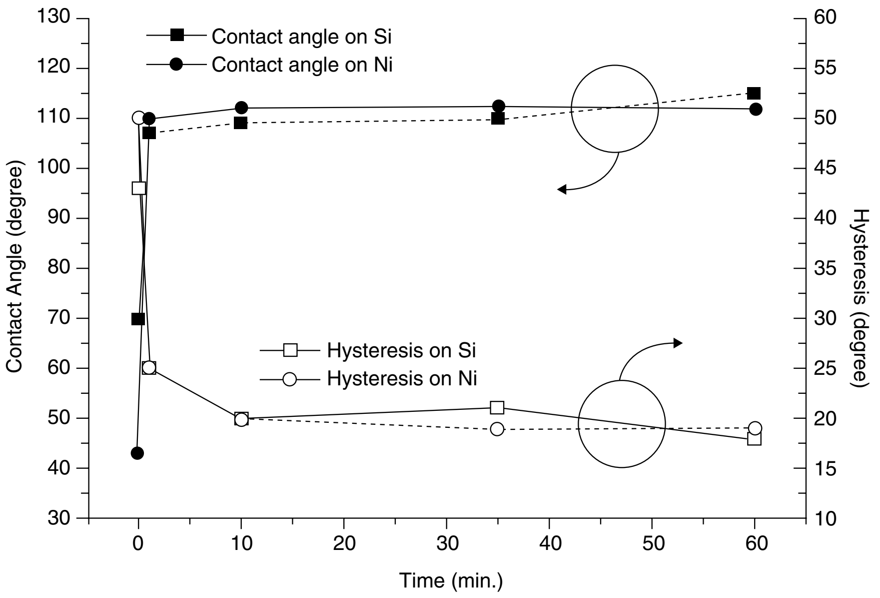

Figure 9.16 Contact angle and contact angle hysteresis of FC films on Si and Ni surface as a function of deposition time. Deposited condition was C_4F_8 of 5 sccm, working pressure of 50 mTorr, substrate temperature of 140°C, and plasma power of 100 W.

This surface energy calculation method consists of contact angle measurements of various liquids on a solid polymer surface and the use of an appropriate theory to estimate the solid surface energy.[47,48] Figure 9.16 shows contact angles of FC films on Si and Ni surfaces as a function of deposition time. Contact angle changes can easily find the film formation. Useful contact angle data for antistiction layers are listed in Table 9.5.

Table 9.5 Contact Angles of Various Substrates

Liquid (surface tension, mN/m)	Solid	Contact angle (deg)	Liquid (surface tension, mN/m)	Solid	Contact angle (deg)
Mercury (484)	PTFE	150	CH_2I_2 (50.8)	PTFE	80
	Glass	128–148		Polyethylene	46–51
DI Water (72)	PTFE	108–112	Formamide (58)	PTFE	86
	PMMA	60		Polyethylene	75
	Glass	< 20	Benzene (28)	PTFE	46
	Gold	0	n-Propanol (23)	PTFE	43
	Platinum	40	n-Decane (23)	PTFE	40
	Polyethylene	93–103	n-Octane (21.6)	PTFE	30

9.4.2 Film Thickness

Cross-sectional scanning electron microscopy (SEM) can directly measure film thickness. However, this method is destructive and time consuming, and it is difficult to prepare the sample. After the deposition of nanometer-thick fluorocarbon films, it is important to measure the polymer film thickness. Without knowing the deposited thickness, it is hard to develop and qualify the antistiction film for nanoimprinting.

Spectroscopic ellipsometry is a nondestructive and very sensitive measurement technique that uses polarized light to characterize thin films, surfaces, and material microstructure. It derives its sensitivity from the determination of the relative phase change in a beam of reflected polarized light.[57–62]

Figure 9.17 illustrates the basic principle behind ellipsometry. First, the polarization state of incoming light is known. This incident light interacts with the sample and reflects from the surface. The interaction of the light with the sample causes a polarization change in the light from linear to elliptical polarization. The polarization change, or a change in the shape of the polarization, is then measured by analyzing the light reflected from the sample.

Ellipsometry measures two values, psi (ψ) and delta (Δ), that describe this polarization change. These values are related to the ratio of Fresnel reflection coefficients, R_p and R_s for p- and s-polarized light, respectively, as shown in the equation below:

$$\rho = \tan(\psi)e^{i\Delta} = \frac{R_p}{R_s} \tag{9.3}$$

Because ellipsometry measures the ratio of two values, it is highly accurate and very reproducible. The ratio is a complex number, thus it contains "phase" information, delta, which makes the measurement very sensitive.

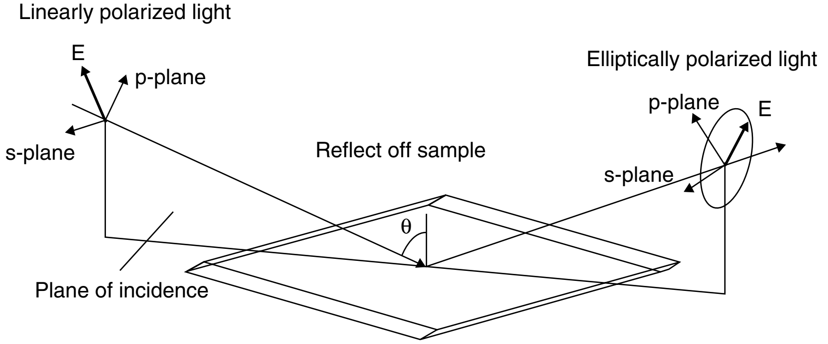

Figure 9.17 Geometry of an ellipsometry measurement.

Ellipsometry does not directly measure optical constants or film thickness but psi and delta are functions of these characteristics. These two values by themselves are not very useful in characterizing a film. What we really want to know are properties such as film thickness, optical constants, refractive index, and other useful data. These characteristics are found in various equations and algorithms to produce a model that describes the interaction of light with the sample. These optical parameters are then matched to computer models to determine the structure and composition of the sample.[63,64] Figure 9.18

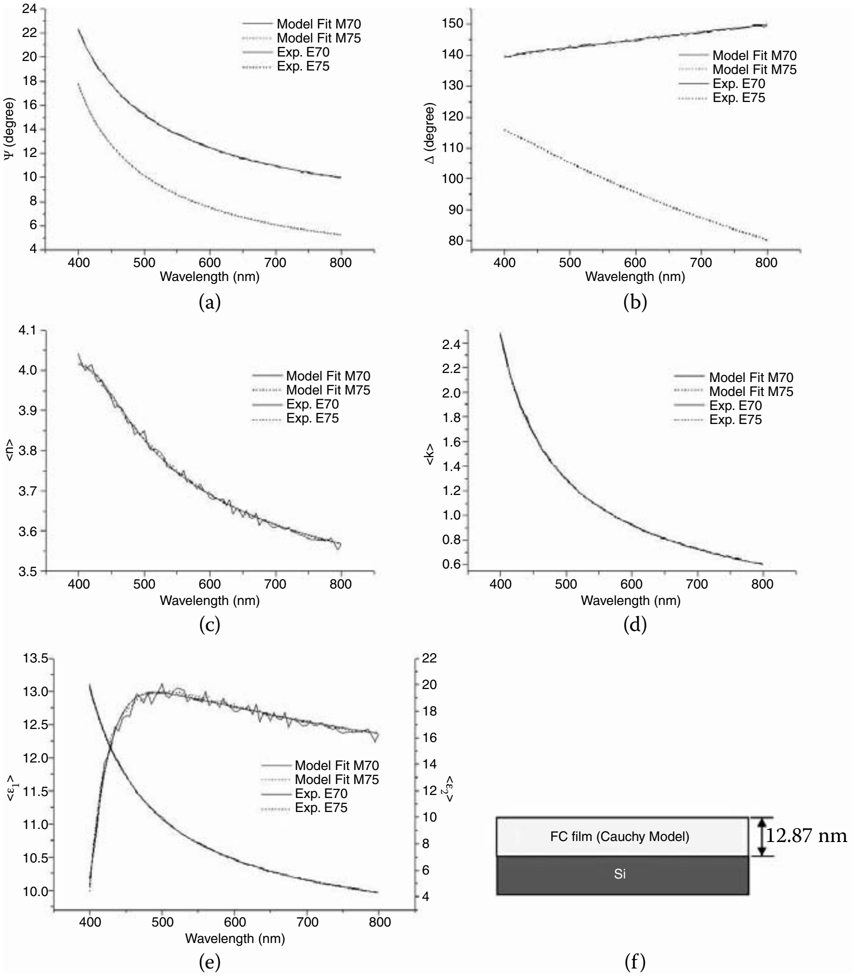

Figure 9.18 The ellipsometry results and model fittings of a FC film on Si such as (a) psi (ψ), (b) delta (Δ), (c) reflective index (*n*), (d) extinction coefficient (*k*), (e) relative dielectric constant (ε_1, ε_2) at 70° and 75° incident angles, and (f) schematic Cauchy model of FC film. Calculated FC film thickness was about 12.87 nm.

shows the measured spectrum of FC film on silicon substrate at 70° and 75° incident angles. These results show psi (ψ) and delta (Δ), refractive index (n), extinction coefficient (k), and relative dielectric constants (ε_1, ε_2). Calculated thickness of a FC film by Cauchy model was calculated to be 12.87 nm.

9.4.3 Chemical Analysis of Monolayer Films

The chemical entity of deposited organic films in a monolayer could be analyzed after the film deposition. Due to its monolayer level thickness, it is not easy to analyze the chemical property of thin film. The representative chemical analysis of the film can be done with attenuated total reflection Fourier transform infrared spectroscopy (ATR-FTIR)[65] and x-ray photoelectron spectroscopy (XPS).[69]

Vibrational motions within chemically bonded constituents of a material have frequencies in the infrared energy range. These motions or oscillations, which are induced by certain vibrational modes within the material, can interact with a beam of infrared radiation directed onto the material. Energy is exchanged between the beam and material when the frequencies are synchronous or in resonance. With FTIR, the intensity of the infrared beam is measured before and after it interacts with the sample, as a function of the light's frequency. In monolayer films, the weak signals due to low concentrations of active species require the utilization of an internal reflection element (IRE) to attenuate and intensify the signals to the detection level. In the ATR-FTIR spectrometry, light enters the IRE and reflects down the length of the crystal. At each internal reflection, the IR radiation actually penetrates a short distance (~1μm) from the surface of the IRE into the polymer. Internal reflection spectrometry provides information related to the presence or absence of specific functional groups, as well as the chemical structure of polymer as shown in Figure 9.19.[66–68] Figure 9.20 shows the ATR-FTIR spectra of the FC films on a Ni substrate.

Photoelectron spectroscopy is based on a single photon-in/electron-out process. In x-ray photoelectron spectroscopy (XPS), which is sometimes known by the alternative acronym ESCA (electron spectroscopy for chemical analysis), the photon is absorbed by an atom in a molecule or solid, leading to ionization and the emission of a core (inner shell) electron (Figure 9.21). The kinetic energy distribution of the emitted photoelectrons (i.e., the number of emitted photoelectrons as a function of their kinetic energy) can be measured using an electron energy analyzer and a photoelectron spectrum can thus be recorded.

The principle of the conservation of energy allows us to write the energy balance equation, valid for the absorption of a photon carrying energy of *h*

$$h = E_{\text{Kinetic}} + E_{\text{Binding}} + \varnothing_{\text{Work function}} \qquad (9.4)$$

where *h* is x-ray beam incident energy, E_{Kinetic} is electron kinetic energy when leaving the specimen, and E_{Binding} is electron binding energy inside the atom.

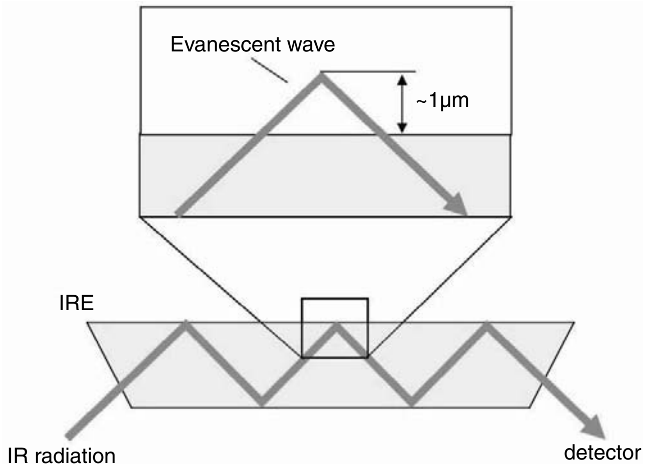

Figure 9.19 Schematic principle of operating ATR-FTIR. It shows the total internal reflection at the interface of an IRE.

For each and every element, there will be a characteristic binding energy associated with each core atomic orbital; i.e., each element will give rise to a characteristic set of peaks in the photoelectron spectrum at kinetic energies determined by the photon energy and the respective binding energies. The presence of peaks at particular energies therefore indicates the presence of

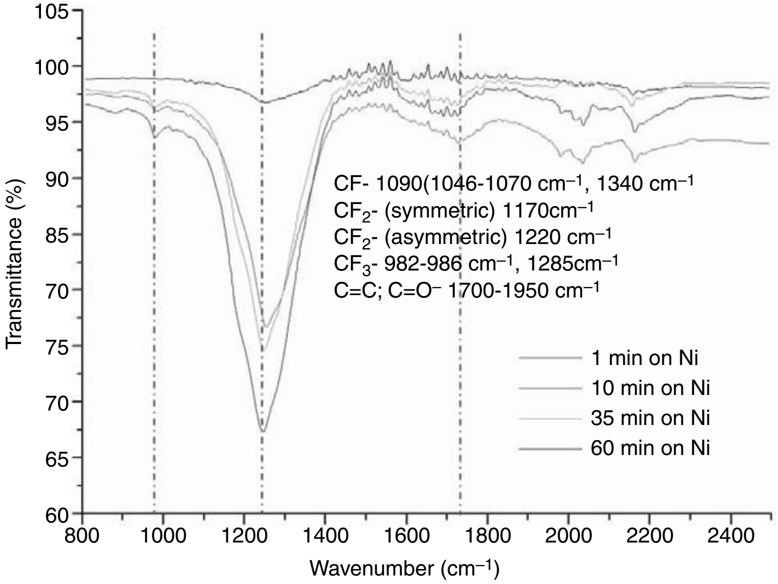

Figure 9.20 ATR-FTIR spectra of the deposited films on Ni surface as a function of time.

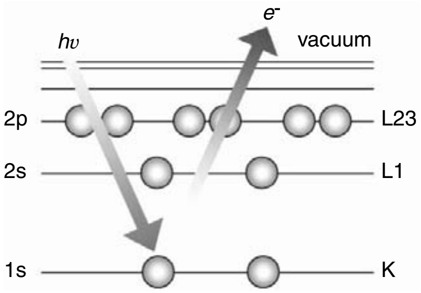

Figure 9.21 Schematic diagram of the process of photoelectron emission.

a specific element in the sample surface. Furthermore, the intensity of the peaks is related to the concentration of the element of sample surface. Thus, the technique also provides a quantitative analysis of the surface composition. The most interesting thing with this technique is its ability to measure binding energy variations resulting from their chemical environment.[70–74] Figure 9.22 shows XPS spectra of PFDA deposited on Al substrate.

9.4.4 Surface Morphology and Nanoscale Adhesion

Atomic probe microscopy (APM) is a technique to observe the surface structure of a sample by measuring the interaction forces between probe tip and surface atoms (Figure 9.23). Atomic force microscopy (AFM) and lateral force microscopy (LFM) are widely used APM modes to study the various tribological phenomena that include surface roughness, adhesion, friction, scratching, wear, indentation, and boundary lubrication.[75,76] In contact mode AFM, the sample's topography can be measured by analyzing the repulsive

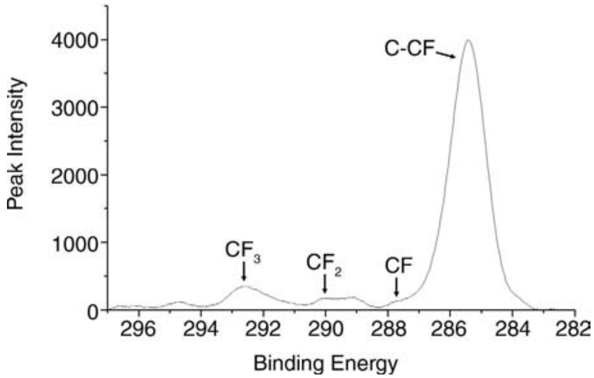

Figure 9.22 XPS spectra obtained on the PFDA deposited samples on Al made by thermal CVD.

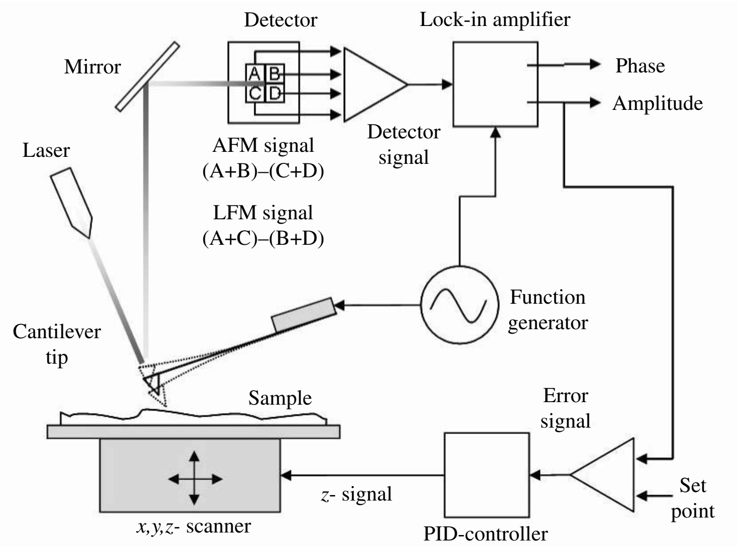

Figure 9.23 Schematic operating principle of AFM/LFM.

force that is exerted vertically between the sample and the probe tip. The principle of LFM is very similar to that of contact mode AFM. In contact mode, AFM measures the deflection of the cantilever in the vertical direction and LFM measures the deflection of the cantilever in the horizontal direction. The magnitude of lateral deflection is determined by the frictional coefficient, the topography of the sample surface, the direction of the cantilever movement, and the cantilever's lateral spring constant. AFM can measure the adhesion force (or pull-off force) between surface and tip. A force–distance curve displays the vertical cantilever deflection vs. tip-sample displacement. This displacement is measured between the sample and the back end of the cantilever. As the lever–sample distance is reduced, the force becomes negative. Adhesion between the tip and sample maintains the contact, although there is now a net negative load. Eventually the tip passes through the point of maximum adhesion. Finally, an unstable point is reached at which the cantilever stiffness exceeds the force gradient of the tip–sample interaction, and the tip snaps out of contact with the sample. The resulting force relaxation is usually called the pull-off force (Figure 9.24). The force-displacement curve can be measured at a single point, or a series of measurements can be carried out over an area of interest. The APM techniques allow for measurements to be correlated with other sample properties such as friction, chemical termination, other types of material heterogeneity,[77–88] SAM films,[89–92] perfluoroalkylpolyethers (PFPE) lubricant on diamond-like carbon (DLC) costing,[93] organic–inorganic composite,[94] protective coating,[95,96] and force mapping.[97] Figure 9.25 shows adhesion force changes as a function of film deposition time.

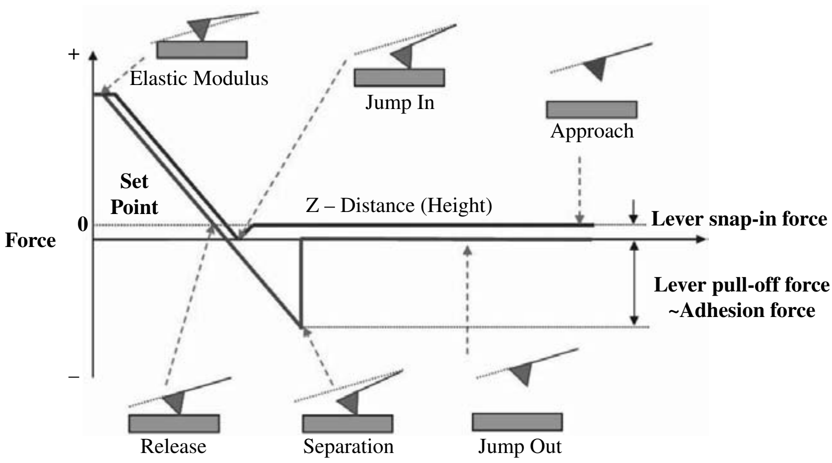

Figure 9.24 Schematic illustration of the force-distance graph to measure adhesion force.

9.4.5 *Thermal, Chemical, and Tribological Tests*

To characterize the prepared films, various test methods can be applied depending on the film's application. Any fabricated layer must satisfy the thermal budget requirements of the imprinting process step. The thermal stability of the antistiction layer is determined by the annealing of the

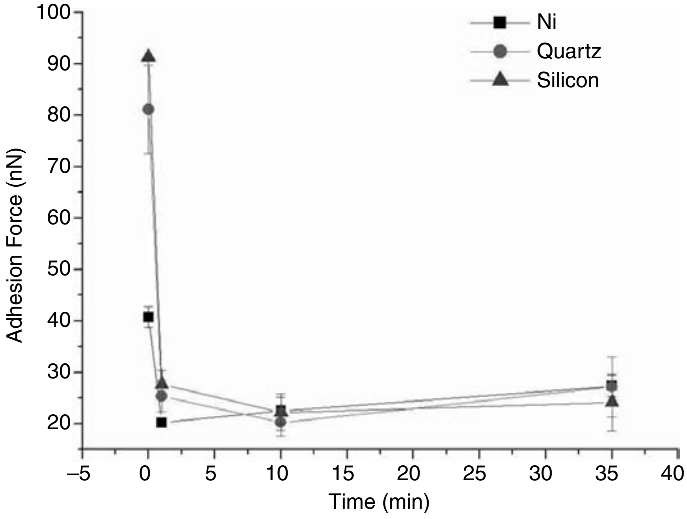

Figure 9.25 Adhesion force changes on a various samples as a function of deposited time. Deposited condition was C_4F_8 of 5 sccm, working pressure of 50 mTorr, substrate temperature of 140°C, and plasma power of 100 W.

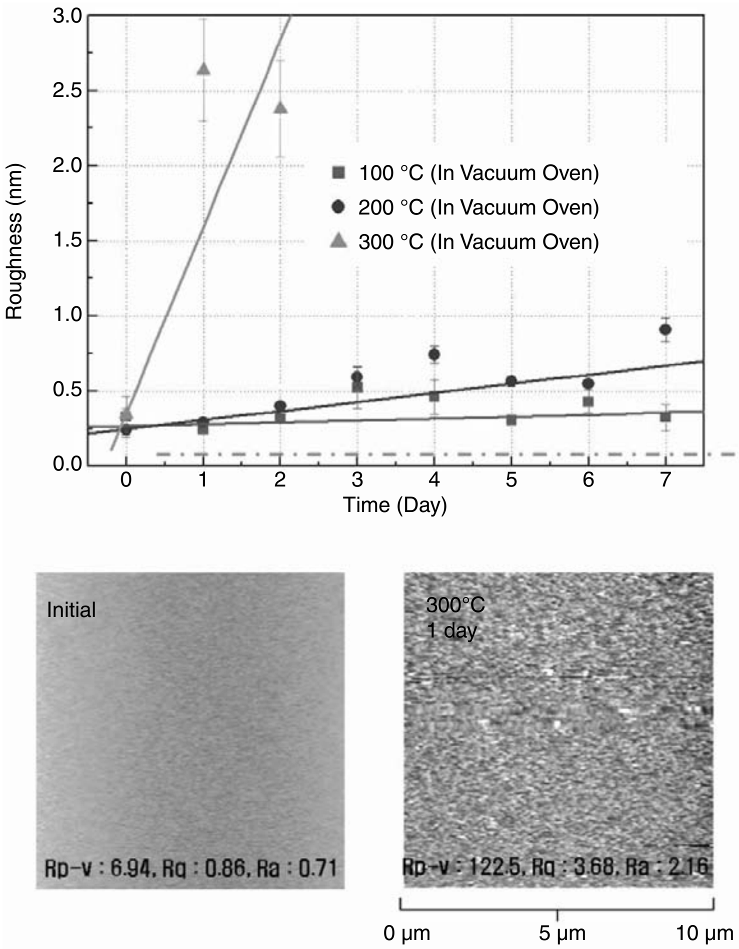

Figure 9.26 Thermal test result of 10-nm-thick FC films made by PECVD. (Rp-v: peak to valley, Rq: root mean square, Ra: average).

samples at various temperatures in atmosphere as a function of time.[98–100] Teflon-like FC films can be used below 260°C and are to be decomposed at higher temperatures as shown in Figure 9.26.

A polymer resist may contain organic solvents, or antistiction layers may also be used in acidic or alkaline environments.[101–103] The chemical resistance of films should be evaluated in these solvents and in acid and alkaline chemicals. A well-prepared antistiction layer should show a good chemical resistance that it is neither dissolved nor changed in either organic solvent or acidic/basic solutions (Figure 9.27).

Usually an antistiction layer reduces the friction when it contacts with other surfaces and acts like a lubricant. Nanotribological tests can be done

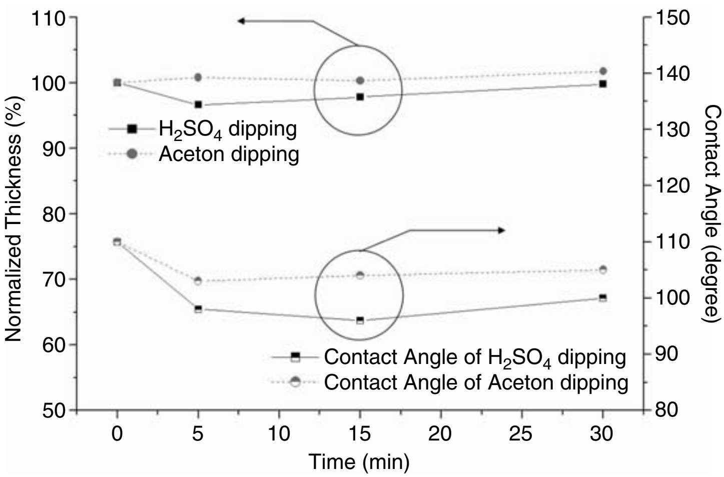

Figure 9.27 Chemical resistance of 50-nm-thick FC film made by PECVD on Ni. Thicknesses and contact angles are slightly changed in acetone, and H_2SO_4 for 30 minutes.

by AFM and a microscale test can be done by a ball test.[104,105] A macroscopic tribological test over full wafer scale can be done by a simple rubbing test.[106,107] The observation of contact angle, film thickness, friction force, and transmittance[108] changes during the rubbing test tells how well the film is prepared (Figure 9.28).

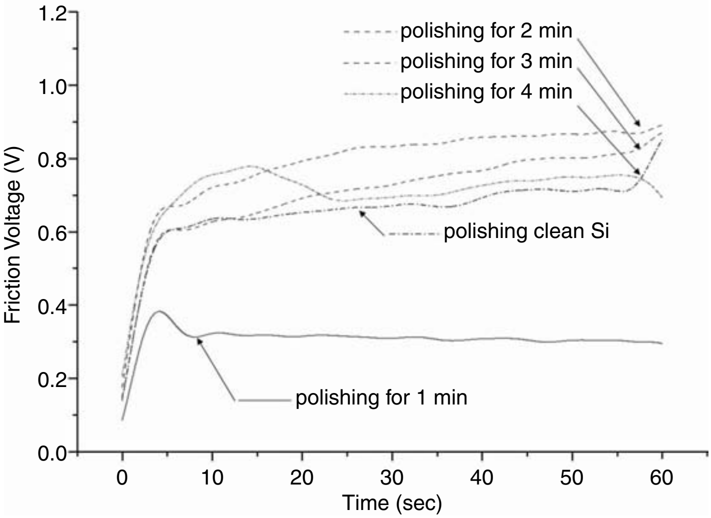

Figure 9.28 Friction voltages of clean and 10-nm-thick FC film coated silicon wafers as a function of polishing time. Polishing condition was pressure of 4 psi, rubbing speeds of 50 rpm, and DI water flow rate of 200 ml/min.

9.5 Conclusions and Prospects

In this chapter, we have reviewed the issues related to stiction during imprinting and discussed its solution, fabrication, and characterization methods for nano- and microimprinting. In order to achieve the commercial application of NIL techniques, defect issues related to stiction between the mold and polymer substrates should be understood, which has been known as one of the most commonly observed defect sources. Antistiction layers, which have a low surface energy composed of amorphous fluorocarbon-polymers, have been shown to provide dramatic improvements in both mold life and mask defect generation in imprinting lithography. The fabricated antistiction layers made by different methods could be evaluated by the various characterization methods.

For patterning of structures down to a few nanometers, both electron beam lithography and nanoimprint lithography are well suited. Due to their differences in technology, application, and cost of ownership, nanoimprinting would be better off to find niche applications such as patterning of functionalized polymers, transparent materials, and low-cost patterning. These applications need to form an assembly of relatively flexible lithography tools for the different requirements from those developed for the major semiconductor industry. In addition, it is clear that a successful antistiction layer technology is required to control defects and enable the potential of imprint lithography to be achieved.

Acknowledgment

This research was financially supported by *the Center for Nanoscale Mechatronics and Manufacturing (CNMM)* under the 21st Century Frontier R&D Programs of *the Korean Ministry of Science and Technology (MOST)* and *the Ministry of Education and Human Resources Development (MOE), the Ministry of Commerce, Industry and Energy (MOCIE), and the Ministry of Labor (MOLAB)* through the fostering project of the laboratory of Excellence.

References

1. Sotomayer Torres, C.M., *Alternative Lithography,* 1st ed, Springer, 2003, Chap. 1.
2. Chou, S.Y., Krauss, P.R., and Renstrom, P.J., Nanoimprint lithography, *J. Vac. Sci. Tech. B*, 14, 4129, 1996.
3. Chou, S.Y. et al., Sub-10 nm imprint lithography and applications, *J. Vac. Sci. Tech., B*15, 2897, 1997.
4. Behl, M. et al., Towards plastic electronics: patterning semiconducting polymers by nanoimprint lithography, *Adv. Mater.*, 14, 588, 2002.
5. Hand, A., A closer look at nanoimprinting, *Semicond. Int.*, 27, 40, 2004.
6. Fan, X. et al., NIL—a low-cost and high-throughput MEMS fabrication method compatible with IC manufacturing technology, *Microelectronics*, In Press, 2005.
7. Li, M., Chen, L., Zhang, W., and Chou, S. Y., "Pattern Transfer Fidelity of Nanoimprint Lithography on Six-Inch Wafers," *Nanotechnology* 14, Institute of Physics Publishing, pp. 33–36, 2003.

8. Park, S. et al., Nanostructuring of anti-adhesive layers by hot embossing lithography, *Microelectronic Eng.*, 67, 252, 2003.
9. Beck, M. et al., Improving stamps for 10 nm level wafer scale nanoimprint lithography, *Microelectronic Eng.*, 61, 441, 2002.
10. Bruning, J.H., Optical lithography–thirty years and three orders of magnitude: the evolution of optical lithography tools, *Proc. SPIE Int. Soc. Opt. Eng.*, 3049, 14, 1997.
11. Resnick, D.J. et al., Release layers for contact and imprint lithography, *Semicond. Internat.*, 25, 71, 2002.
12. Pamidighantam, S. et al., A wet release process for fabricating slender and compliant suspended micro-mechanical structures, *Sensor Actuator Phys.*, 103, 202, 2003.
13. Mulhern, G.T., Soane, D.S., and Howe, R.T., Supercritical carbon dioxide drying of microstructures, *Proceeding of the 7*th *International Conference on Solid-State Sensors and Actuators, Tech. Digest*, 296, 1993.
14. Guckel, H. et al., The application of fine-grained polisilicon to mechanically resonant transducers, *Sensor. Actuator. A*, 21, 346, 1990.
15. Douglass, M.R. and Kozuch, D.M., DMD reliability assessment for large-area displays, *Society for Information Display International Symposium Digest of Technical Papers*, 26, 49, 1995.
16. Anguita, J. and Briones, F., HF/H_2O vapor etching of SiO_2 sacrificial layer for large-area surface-micromachined membranes, *Sensor. Actuator. A*, 64, 247, 1998.
17. Alley, R.L. et al., Surface roughness modification of interfacial contacts in polysilicon microstructures, *Transducers '93*, 288, 1993.
18. Ashurst, W.R. et al., Alkene based monolayer films as anti-stiction coatings for polysilicon MEMS, *Sensor Actuator Phys.*, 91, 239, 2001.
19. Lee, K.K. et al., Chemical, optical and tribological characterization of perfluoropolymer films as an anti-stiction layer in micro-mirror arrays, *Thin Solid Films*, 377, 727, 2000.
20. Ashurst, W.R. et al., Wafer level anti-stiction coatings for MEMS, *Sensor Actuator phys*. 104, 213, 2003.
21. Pfeiffer, K. et al., A comparison of thermally and photochemically cross-linked polymers for nanoimprinting, *Microelec. Eng.*, 67, 266, 2003.
22. Pfeiffer, K. et al., Novel linear and crosslinking polymers for nanoimprinting with high etch resistance, *Microelec. Eng.*, 53, 411, 2000.
23. Ferry, J.D., *Viscoelastic Properties of Polymers*, 2nd ed., John Wiley & Sons, New York, 1970.
24. Gottschalch, F. et al., Polymer issues in nanoimprinting technique, *Solid State Electron.*, 43, 1079, 1999.
25. Adamson, A.W., *Physical Chemistry of Surfaces*, 6th ed, John Wiley & Sons, New York, 1997, Chap. 10.
26. Smith, R.K. et al., Review-patterning self-assembled monolayers, *Prog. Surf. Sci.*, 75, 1, 2004.
27. Yang, J.P., White light emission from a single layer organic light emitting diode fabricated by spincoating, *Chem. Phys. Lett.*, 325, 251, 2000.
28. Xiao, H., *Introduction to Semiconductor Manufacturing Technology*, Prentice-Hall, Upper Saddle River, NJ, 2001, Chap. 6.
29. Haas, D.E. et al., Effect of solvent evaporation rate on skin formation during spin coating of complex solutions, *Proc. SPIE Int. Soc. Opt. Eng.*, 3943, 280, 2000.
30. Zhao, H. et al., Transport of organic solutes through amorphous teflon AF films, *J. Am. Chem. Soc.*, Article, 2005.

31. Alentiev, A.Y. et al., Gas and vapor sorption, permeation, and diffusion in glassy amorphous Teflon AF1600, *Macromolecules*, 38, 7043, 2005.
32. Shinohara, T. et al., Development of an optical device for thermal neutrons by amorphous perfluoropolymer, *Nuclear Instr. Meth. Phys. Res. Sect. A*, 529, 134, 2004.
33. Liu, H.Y., Peng, G.D., and Chu, P.L., Thermal stability of gratings in PMMA and CYTOP polymer fibers, *Optic. Comm.*, 204, 151, 2002.
34. Fadeev, A.Y. and McCarthy, T.J., Self-assembly is not the only reaction possible between alkyltrichlorosilanes and surfaces: monomolecular and oligomeric covalently attached layers of dichloro- and trichloroalkylsilanes on silicon, *Langmuir*, 16, 7268, 2000.
35. Maboudian, R., Ashurst, W.R., and Carraro, C., Self-assembled monolayers as anti-stiction coating for MEMS: characteristics and recent developments, *Sensor Actuator*, 82, 219, 2000.
36. Gennes, P.G. (translated by Reisinger, A.), *Capillarity and Wetting Phenomena: Drops, Bubbles, Pearls, Waves*, Springer-Verlag, New York, 2003, Chap. 1.
37. Schreiber, F., Structure and growth of self-assembling monolayers, *Prog. Surf. Sci.*, 65, 151, 2000.
38. Wanebo, M. et al., Molecular vapor deposition (MVDTM)—a new method of applying moisture barriers for packaging applications, *Journal of Advanced Packaging Materials: Processes, Properties and Interfaces*, Proceedings, 2005.
39. Mayer, T.M. et al., Chemical vapor deposition of fluoroalkylsilane monolayer films, *J. Vac. Sci. Tech. B*, 18, 2433, 2000.
40. Nishikawa, T. and Mitani, T., A new approach to molecular devices using SAMs, LSMCD and Cat-CVD, *Sci. Tech. Adv. Mater.*, 4, 81, 2003.
41. Matsumoto, Y. and Ishida, M., The property of plasma-polymerized fluorocarbon film in relation to CH_4/C_4F_8 ratio and substrate temperature, *Sensor Actuator*, 83, 179, 2000.
42. Jiao, C.Q., Garscadden, A., and Haaland, P.D., Ion chemistry in octafluorocyclobutane (c-C4F8), *Chem. Phys. Lett.*, 297, 121, 1998.
43. Vinogradov, I.P., Dinkelmann, A., and Lunk, A., Deposition of fluorocarbon polymer films in a dielectric barrier discharge (DBD), *Surf. Coat. Tech.*, 174, 509, 2003.
44. Jaszewski, R.W. et al., The deposition of anti-adhesive ultra-thin Teflon-like films and their interaction with polymers during hot embossing, *Appl. Surf. Sci.*, 143, 301, 1999.
45. Motomura, H., Imai, S.I., and Tachibana, K., Surface reaction processes in C_4F_8 and C_5F_8 plasmas for selective etching of SiO_2 over photo-resist, *Thin Solid Films*, 390, 134, 2001.
46. Takahashi, K. et al., Radical kinetics for polymer film deposition in fluorocarbon (C_4F_8, C_3F_6 and C_5F_8) plasmas, *Thin Solid Films*, 374, 303, 2000.
47. Mittal, K.L., *Contact Angle, Wettablity and Adhesion*, Vol. 1, VSP BV, the Netherlands, 1993, Chap. 1.
48. Mittal, K.L., *Contact Angle, Wettablity and Adhesion*, Vol. 2, VSP BV, the Netherlands, 2002, Chap. 2.
49. Quintella, C.M. et al., Observation of wall wettability under imposed flow by fluorescence depolarization: dependence on surface oxygen content and degree of polymer branching, *J. Colloid. Interface Sci.*, 281, 201, 2005.
50. Chen, J. et al., Preparation of sulfonated crosslinked PTFE-graft-poly(alkyl vinyl ether) membranes for polymer electrolyte membrane fuel cells by radiation processing, *J. Membr. Sci.*, 256, 38, 2005.

51. Morra, A., Occhiello, E., and Garbassi, F., Wettability and surface chemistry of irradiated PTFE, *Angewandte Makromolekulare Chemie*, 180, 191, 1990.
52. Yan, L., Shui, Y., and Xiang, C.B., Preparation of poly(vinylidene fluoride)(pvdf) ultrafiltration membrane modified by nano-sized alumina (Al_2O_3) and its antifouling research, *Polymer*, 46, 7701, 2005.
53. Graham, P. et al., Fluoropolymers with very low surface energy characteristics, *J. Fluor. Chem.*, 104, 29, 2000.
54. Bierwagen, G., Shedlosky, T.J., and Stanek, K., Developing and testing a new generation of protective coatings for outdoor bronze sculpture, *Progr. Org. Coating.*, 48, 289, 2003.
55. Shibuichi, S. et al., Super water- and oil-repellent surfaces resulting from fractal structure, *J. Colloid Interface Sci.*, 208, 287, 1998.
56. Mostefaï, M. et al., Fluoroalkylsilanes as non-stick coatings: adhesion of glucose and its thermal byproducts, *Internat. J. Adhesion and Adhesives*, 18, 273, 1998.
57. Woollam, J.A., Snyder, P.G., and Rost, M.C., Variable angle spectroscopic ellipsometry: a non-destructive characterization technique for ultrathin and multilayer materials, *Thin Solid Films*, 166, 317, 1988.
58. Woollam, J.A. et al., VUV and IR spectroellipsometric studies of polymer surfaces, *Nuclear Instruments and Methods in Physics Research Section B: Beam Interactions with Materials and Atoms*, 208, 35, 2003.
59. Kirkpatrick, S.R. et al., Process monitoring and control of low temperature reactively sputtered AlN, *Thin Solid Films*, 332, 16, 1998.
60. Bungay, C.L. et al., IR ellipsometry studies of polymers and oxygen plasma-treated polymers, *Thin Solid Films*, 313, 713, 1998.
61. Woollam, J.A., McGaham, W.A., and Johs, B., Spectroscopic ellipsometry studies of indium tin oxide and other flat panel display multilayer materials, *Thin Solid Films*, 241, 44, 1994.
62. Li,W. et al., Spectroscopic ellipsometry chraracterization of the interfacial roughness in simox wafers, *Thin Solid Films*, 459, 63, 2004.
63. Tompkins, H.G., *A User's Guide to Ellipsometry*, Academic Press, New York, 1993.
64. Tompkins, H.G. and McGahan, W.A., *Spectroscopic Ellipsometry and Reflectometry*, John Wiley & Sons, New York, 1999.
65. Puskas, J.E., *In-Situ Spectroscopy of Monomer and Polymer Synthesis*, Kluwer Academic/Plenum Publishers, New York, 2003, Chap. 4.
66. Yang, W., Cui, F.Z., and Qing, X., Behavior of phosphatidylcholine adsorption on CNx coated PTFE films, *Curr. Appl. Phys.*, in press, 2005.
67. Kano, Y., Inoue, M., Akiba, I., Akiyama, S., Sano, H., and Fujita, Y., "Effect of Substrate on Gradient Domain Morphology Formed in Acrylate Copolymer/Fluoro-Copolymer Blends," *Polymer* Volume 39, Issue 26, pp. 6747–6754, Science Direct, December 1998.
68. Caro, J.C., Lappan, U., and Lunkwitz, K., Insertion of sulfur-containing functional groups into polytetrafluoroethylene (PTFE) by low pressure plasma treatment, *Surf. Coat. Tech.*, 116, 792, 1999.
69. Watts, J.F., *An Introduction to Surface Analysis by XPS and AES*, John Wiley & Sons, New York, 2003.
70. Schulze, M. and Christenn, C., XPS investigation of the PTFE induced hydrophobic properties of electrodes for low temperature fuel cells, *Appl. Surf. Sci.*, 252, 148, 2005.
71. Bodas, D.S., Mandale, A.B., and Gangal, S.A., Deposition of PTFE thin films by RF plasma sputtering on <100> silicon substrates, *Appl. Surf. Sci.*, 245, 202, 2005.

72. Stelmashuk, V. et al., Plasma polymer films rf sputtered from PTFE under various argon pressures, *Vacuum*, 77, 131, 2005.
73. He, J.L. et al., Deposition of PTFE thin films by ion beam sputtering and a study of the ion bombardment effect, *Nuclear Instruments and Methods in Physics Research Section B: Beam Interactions with Materials and Atoms*, 135, 512, 1998.
74. Jaszewski, R.W. et al., Properties of thin anti-adhesive films used for the replication of microstructures in polymers, *Microelect. Eng.*, 35, 381, 1997.
75. Castner, D.G. and Grainger, D.W., *Fluorinated Surfaces, Coatings, and Films*, American Chemical Society, Oxford University Press, Oxford, 2001.
76. Bhushan, B, *Springer Handbook of Nanotechnology*, Springer, Berlin, 2004, Part C.
77. Kajiyama, T. et al., Morphology and mechanical properties of polymer surfaces via scanning force microscopy, *Progr. Surf. Sci.*, 52, 1, 1996.
78. Jones, R. et al., Frictional forces between cohesive powder particles studied by AFM, *Ultramicroscopy*, 100, 59, 2004.
79. Theander, K., Pugh, R.J., and Rutland, M.W., Friction force measurements relevant to de-inking by means of atomic force microscope, *J. Colloid. Interface Sci.* 291, 361, 2005.
80. Song, W. et al., An atomic force microscopic investigation of electro-sensitive polymer surface, *Talanta*, 67, 543, 2005.
81. Zhang, S.W., Feng, D., and Wang, D., Tribological behaviors of composite molecular deposition films, *Tribol. Int.*, in press, 2005.
82. Andersson, K. M., and Lennart B., "Friction and Adhesion of Single Spray-Dried Granules Containing a Hygroscopic Polymer Binder," *Powder Technology*, Volume 155, Issue 2, pp. 101–107, July 20, 2005.
83. Lubarsky, G.V., Davidson, M.R., and Bradley, R.H., Elastic modulus, oxidation depth and adhesion force of surface modified polystyrene studied by AFM and XPS, *Surf. Sci.*, 558, 135, 2004.
84. Liu, D.P. et al., Surface roughness, scratch resistance and tribological properties of hydrogenated amorphous carbon coatings prepared by low-pressure dielectric barrier discharge, *Surf. Coating. Tech.*, 174, 310, 2003.
85. Paige, M.F., A comparison of atomic force microscope friction and phase imaging for the characterization of an immiscible polystyrene/poly(methyl methacrylate) blend film, *Polymer*, 44, 6345, 2003.
86. Cyganik, P. et al., AFM/LFM surface studies of a ternary polymer blend cast on substrates covered by a self-assembled monolayer, *Surf. Sci.*, 507, 700, 2002.
87. Kim, S.H., Marmo, C., and Somorjai, G.A., Friction studies of hydrogel contact lenses using AFM: non-crosslinked polymers of low friction at the surface, *Biomaterials*, 22, 3285, 2001.
88. Beake, B.D. et al., Friction force microscopy study of diamond films modified by a glow discharge treatment, *Diam. Relat. Mater.*, 9, 1421, 2000.
89. Bhushan, B. et al., AFM study of perfluoroalkylsilane and alkylsilane self-assembled monolayers for anti-stiction in MEMS/NEMS, *Ultramicroscopy*, in press, 2005.
90. Graupe, M., Koini, T., Kim, H. I., Garg, N., Miura, Y. F., Takenaga, M., Perry, S. S., Lee, T. R., "Self-Assembled Monolayers of CF_3 Terminated Alkanethiols on Gold," *Colloids and Surfaces A: Physicochemical and Engineering Aspects*, Volume 154, Issues 1–2, pp. 239–244, August 1999.

91. Okabe, Y. et al., Chemical force microscopy of microcontact-printed self-assembled monolayers by pulsed-force-mode atomic force microscopy, *Ultramicroscopy*, 82, 203, 2000.
92. Graupe, M. et al., Wettability and friction of CF_3-terminated monolayer films on gold, *Mater. Res. Bull.*, 34, 447, 1999.
93. Wang, M., Miyake, S., and Matsunuma, S., Nanowear studies of PFPE lubricant on magnetic perpendicular recording DLC-film-coated disk by lateral oscillation test, *Wear*, 259, 1332, 2005.
94. Gu, G., Zhang Z., and Dang, H., Preparation and characterization of hydrophobic organic–inorganic composite thin films of PMMA/SiO_2/TiO_2 with low friction coefficient, *Appl. Surf. Sci.*, 221, 129, 2004.
95. Chung, K.H. et al., Effect of substrate and protective coating on the tribological characteristics of optical recording media, *Wear*, 255, 1306, 2003.
96. Wang, J. et al., Structure and microtribological behavior of Teflon and Teflon/Si_3N_4 micro-assembling film, *Thin Solid Films*, 342, 291, 1999.
97. Suzuki, H. and Mashiko, S., Measurements of adhesive forces on a polytetrafluoroethylene (PTFE) film and glass surface by mapping force curve, *Thin Solid Films*, 331, 176, 1998.
98. Yan, X. et al., Microstructure and mechanical properties of hard carbon films prepared by heat treatment of a polymer on steel substrate, *Surf. Coat. Tech.*, 190, 206, 2005.
99. Theiler, G. et al., Friction and wear of PTFE composites at cryogenic temperatures, *Tribol. Int.*, 35, 449, 2002.
100. Kuutti, L. et al., AFM in studies of thermoplastic starches during ageing, *Carbohydr. Polymer*, 37, 7, 1998.
101. Ahmad, S. et al., A polyesteramide from Pongamia glabra oil for biologically safe anticorrosive coating, *Progr. Org. Coat.*, 47, 95, 2003.
102. Zhao, Q., Liu, Y., and Wang, C., Development and evaluation of electroless Ag-PTFE composite coatings with anti-microbial and anti-corrosion properties, *Appl. Surf. Sci.*, in press, 2005.
103. Zhao, Q., Liu, Y., and Abel, E.W., "Effect of Cu content in Electroless Ni–Cu–P–PTFE Composite Coatings on their Anti-Corrosion Properties," *Materials. Chemistry and Physics*, 87, 2-3, pp. 332–335, October 15, 2004.
104. Ding, J.N., Wong, P.L., and Yang, J.C., Friction and fracture properties of polysilicon coated with self-assembled monolayers, *Wear*, 260, 209, 2006.
105. Zhou, F., Adachi, K., and Kato, K., Friction and wear property of a-CNx coatings sliding against ceramic and steel balls in water, *Diam. Relat. Mater.*, 14, 1711, 2005.
106. Benabdallah, H., Friction and wear of blended polyoxymethylene sliding against coated steel plates, *Wear*, 254, 1239, 2003.
107. Joyce, T.J., Thompson, P., and Unsworth, A., The wear of PTFE against stainless steel in a multi-directional pin-on-plate wear device, *Wear*, 255, 1030, 2003.
108. Ueng, H.Y. and Guo, C.T., Deposition of diamond-like carbon film on phase-change optical disk by PECVD, *J. Vac. Sci. Tech. B*, 23, 24, 2005.

Chapter 10

Nanocontacts and Switch Reliability

George G. Adams and Nicol E. McGruer

Contents

10.1 Introduction 217
10.2 Hertz Contact 218
10.3 Physical Basis of Adhesion 220
10.4 Nano-Contact with Adhesion 223
10.4.1 Elastic Layers 230
10.5 Elastoplastic and Plastic Contacts 231
10.5.1 Scale-Dependent Plasticity 233
10.5.2 Adhesion in Elastoplastic Contacts 233
10.5.3 Finite Element Elastic-Plastic Simulations 235
10.6 Rough Surface Nanocontacts 238
10.7 Micromechanical Switches 240
10.8 Recommendations for Future Research 244
References 245

10.1 Introduction

When an electromechanical switch closes, contact is made between two metallic surfaces, the circuit is completed, and current is allowed to flow across the interface. Although this process may at first appear to be simple, there are many interesting and important phenomena at play during this event. First, the metal surfaces are not atomically flat. In macroscale switches intimate contact occurs at the peaks of these rough surfaces (i.e., at asperity peaks), whereas in microscale switches the contact occurs at the peaks of nanoscale asperities. The combined area of these contacts is called the real

contact area, which is typically orders of magnitude smaller than the nominal contact area. In microswitches the area of each nanocontact is affected by both the applied normal force as well as the force of adhesion. Furthermore, the force is applied to the entire contact; its distribution among the many contacts depends on various roughness parameters as well as the mechanical properties of the materials. These phenomena are reasonably well understood for microscale contacts, but are less well described for nanoscale contacts. Fortunately modern measurement equipment allows for nanoscale surface roughness to be characterized by instruments such as the scanning electron microscope (SEM), the atomic force microscope (AFM), or the scanning tunneling microscope (STM). Mechanical properties, such as elastic modulus and hardness, are usually determined by nanoindentation.

There are a number of models that are applicable for mechanical contacts and also for electrical contacts; these will be discussed in detail later in this chapter. However, the mechanical and electrical problems are tightly coupled. As contact is made, current flows through the contact area. Joule heating causes changes in the real contact area due to thermal expansion and material softening. The role and nature of contaminant films is less well characterized. Repeated contacts and the associated cyclic heating can affect the evolution of the contacts including these contaminants. Contaminants typically increase the contact resistance and decrease the adhesion. Although ultraclean contacts exhibit a desirable very low resistance, the adhesion force can be sufficient to keep the switch permanently closed.

The monographs by Holm and by Slade are invaluable resources for the understanding of electrical contacts.[1,2] In this chapter, we review the state of knowledge of nanoscale contacts and their effect on reliability in micromechanical switches. In Section 10.2, the well-known theory of Hertz elastic contact is presented. The physical basis of adhesion is explained in Section 10.3, followed by a description of the various theories of adhesive elastic contact in Section 10.4. Elastoplastic and fully plastic contacts are discussed in Section 10.5. In Section 10.6 the effect of surface roughness is presented. A presentation specifically devoted to micromechanical switches is the subject of Section 10.7, with suggestions for future research in Section 10.8.

10.2 Hertz Contact

In 1882 Heinrich Hertz presented his now well-known theory of contact between nonconforming elastic bodies, which became known as Hertz contact.[3] Hertz developed this theory as a graduate student during his 1880 Christmas vacation when he was trying to account for the effect of elastic deformation on the interference fringes of two glass lenses pressed together. The assumptions of Hertz contact are (1) the dimensions of the contact area are much less than the radii of curvature of the contacting bodies; (2) the strains are sufficiently small for linear elasticity to be valid; (3) each body can be considered to be an elastic half-space; and (4) the surfaces are frictionless so that only normal tractions (compressive) are transmitted.[4]

Assumption 3 may be viewed as valid for two spherical bodies (such as Hertz's lenses) in contact in which the contact radius is such that Assumption 1 holds. However, Hertz theory can also be applied to individual asperity contacts on a rough surface. In that case the radius of the individual asperity contacts must be much less than the radius of curvature of the asperity. These points will be discussed in detail later. Although Hertz contact applies for ellipsoidal bodies (see Greenwood for a discussion and some simplified equations[5]), in this review we focus on the simpler case of spherical bodies, which are more applicable to contacts in microswitches.

The equations for Hertz contact can be obtained from the elasticity result that the axisymmetric pressure distribution

$$p(r) = \begin{cases} p_0(1 - r^2/a^2)^{1/2}, & r \le a \\ 0, & r > a \end{cases} \tag{10.1}$$

acting on an elastic half-space produces a surface displacement in the normal direction[4] of

$$u(r) = \frac{1-\nu^2}{E}\frac{\pi p_0}{4a}(2a^2 - r^2), \quad r \le a \tag{10.2}$$

The significance of Equation (10.2) is that the pressure distribution given by Equation (10.1) produces a parabolic deformation of the elastic half-space. Hence, for small displacements, the curvature produced by Equation (10.2) is constant and consistent with the deformation produced by a spherical indenter with radius R, provided

$$\frac{d^2u}{dr^2} = -\frac{(1-\nu^2)}{E}\frac{\pi p_0}{2a} = -\frac{1}{R} \tag{10.3}$$

Thus, for two elastic bodies of different radii in contact, both of which are locally spherical at their peaks, the changes in curvature of the two bodies add together resulting in

$$\frac{\pi p_0}{2aE_C} = \frac{1}{R} \tag{10.4}$$

where

$$\frac{1}{R} = \frac{1}{R_1} + \frac{1}{R_2}, \quad \frac{1}{E_C} = \frac{1-\nu_1^2}{E_1} + \frac{1-\nu_2^2}{E_2} \tag{10.5}$$

In Equation (10.5), R_1 and R_2 are the radii of curvatures of the two spherical bodies, E_1 and E_2 are the elastic Young's moduli, and γ_1 and γ_2 are the Poisson's ratios of the contacting bodies. Furthermore, R and E_C are called the composite radius of curvature and the composite elastic Young's modulus, respectively.

A simple integration of the pressure over the contact region gives the applied force P as

$$P = \int_0^a 2\pi r\, p(r)\, dr = \frac{2}{3}\pi p_0 a^2 \tag{10.6}$$

and by combining Equation (10.4) and Equation (10.6)

$$a = \left(\frac{3PR}{4E_C}\right)^{1/3} \tag{10.7}$$

The relative approach of distant points (δ) can be found by summing the displacements at $r = 0$ for the two bodies, resulting in

$$\delta = \frac{\pi p_0 a}{E_C} \tag{10.8}$$

which, along with Equation (10.4) and Equation(10.6) gives

$$\delta = \frac{a^2}{R} \text{ and } \delta = \left(\frac{9P^2}{16RE_C^2}\right)^{1/3} \tag{10.9}$$

In summary, for a given applied force, Hertz contact gives the contact radius from Equation (10.7) and the approach from Equation (10.9), with the composite radius and elastic modulus defined by Equation (10.5).

In the contact of conforming bodies, a small increase in load can lead to a large increase in the contact area. A detailed discussion of these contacts is given by Johnson,[4] which includes a summary of the results of Stuermann[6] for axisymmetric conforming contacts.

10.3 Physical Basis of Adhesion

Nanoscale contacts, such as those occurring in a micromechanical switch, typically are at a scale large enough that continuum theory applies (i.e., contact radii greater than several nanometers), but small enough that the force of adhesion is significant. The monographs by Israelachvili and by

Maugis are invaluable resources, especially for a comprehensive presentation of the physical basis of adhesion and for a thorough description of the mathematical theory of adhesion.[7,8] In this section we present a brief summary of the physical phenomena that lead to the adhesive force between contacting solids.

When a new surface is created in a solid, energy is required in the breaking of bonds as well as in the reorganizing of atoms near the surface. The work needed to create reversibly and isothermally a unit surface area is called the *surface energy* γ.The surface energies for metals and covalent solids are typically 1 to 3 J/m^2, for ionic solids 0.1 to 0.5 J/m^2, and for molecular solids less than 0.1 J/m^2.[7,8] Because atoms/molecules near the surface are acted upon by a different set of forces from their neighbors than are atoms/molecules in the bulk, a tensile force is created parallel to the surface. This force per unit length is called the *surface tension* and is equal to the surface energy.[7,8] The work per unit area needed to separate two solids reversibly and isothermally is

$$w = \gamma_1 + \gamma_2 - \gamma_{12} \tag{10.10}$$

in which γ_1 and γ_2 are the surface energies of bodies 1 and 2 respectively, γ_{12} is the interfacial energy, and w is the Dupré energy of adhesion. For two identical bodies, $w = 2\gamma$ because the interfacial energy vanishes.

The energy of adhesion describes the work per unit area needed to separate two surfaces. For two surfaces separated by a distance Z, the potential energy varies as a function of Z. In particular, when the separation is equal to the equilibrium separation of the surfaces (Z_0), which typically corresponds to a couple of Angstroms, the potential energy is a minimum.[9] The well-known Lennard-Jones potential gives the potential energy *(U)* per unit area as a function of the separation distance Z according to

$$U(Z) = -\frac{A}{12\pi Z_0^2}\left[\left(\frac{Z_0}{Z}\right)^2 - \frac{1}{4}\left(\frac{Z_0}{Z}\right)^8\right] \tag{10.11}$$

and is plotted in Figure 10.1. This potential can be used for most solids with the exception of clean metal contacts at close range as will be discussed later. The derivative of the potential with respect to the separation distance gives the adhesive stress *(σ)* as a function of separation (Z) for parallel (or nearly parallel) surfaces by

$$\sigma(Z) = \frac{A}{6\pi Z_0^3}\left[\left(\frac{Z_0}{Z}\right)^3 - \left(\frac{Z_0}{Z}\right)^9\right] \tag{10.12}$$

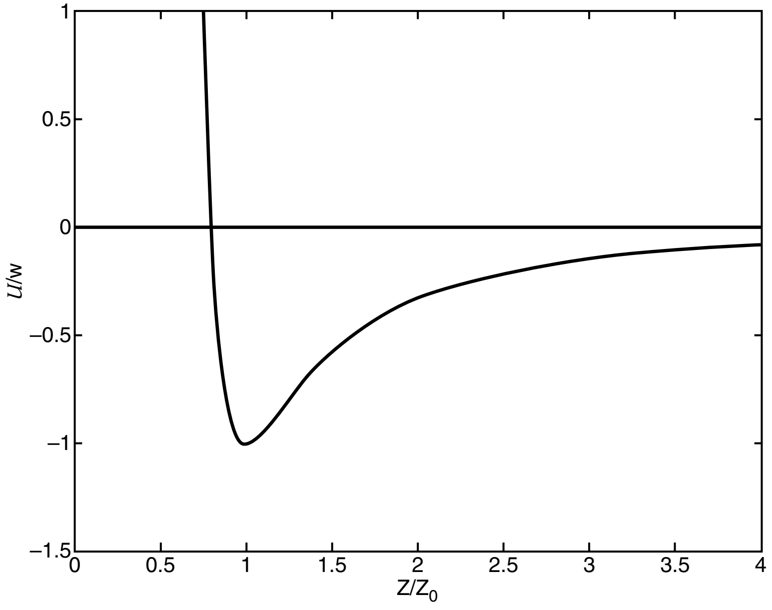

Figure 10.1 Lennard-Jones potential (U) between two half-spaces as a function of separation distance (Z). The work of adhesion is w and the equilibrium spacing is Z_0.

and is shown in Figure 10.2. The constant A in Equation (10.11) and Equation (10.12) is called the Hamaker constant and is related to the surface energy according to

$$A = 32\pi Z_0^2 \gamma \tag{10.13}$$

The maximum value of this adhesive stress is often called the *theoretical stress* (σ_0), which is related to the Hamaker constant by

$$\sigma_0 = \frac{A}{9\pi\sqrt{3}Z_0^3} \tag{10.14}$$

The area under this stress vs. separation curve between the equilibrium separation and infinity is equal to the work of adhesion. Equivalently, the work of adhesion is the negative of the potential evaluated at the equilibrium position.

For clean metals the use of the Lennard-Jones potential, along with a Hamaker constant appropriate for metals, leads to an underestimation of the surface energy. The attractive forces between metals can be accounted for by

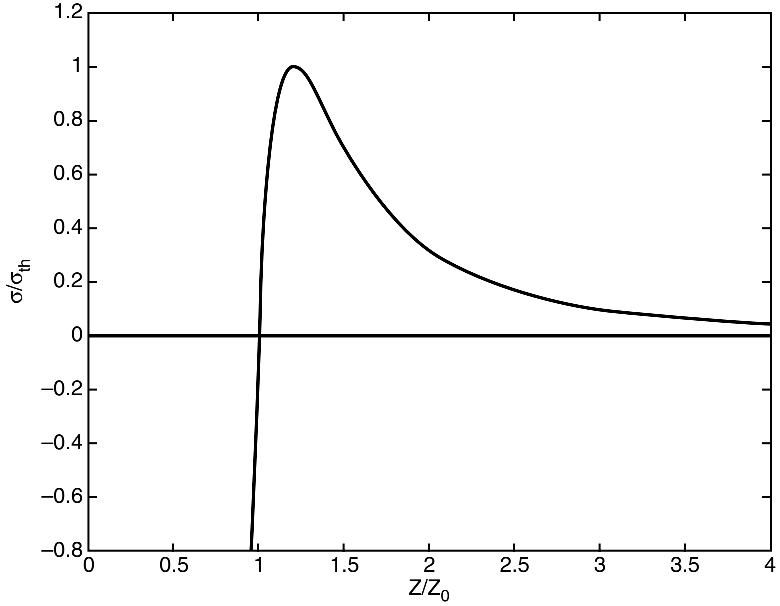

Figure 10.2 Normal stress (σ) between two half-spaces with a Lennard-Jones potential as a function of separation distance (Z). The theoretical stress is σ_{th} and the equilibrium separation is Z_0.

van der Waals forces only at large separations. The strong adhesion is due to short-range forces that can be estimated by the following interaction potential:[7,8]

$$U(Z) = -2\gamma(1+\beta Z^*)\exp(-\beta Z^*), \qquad Z^* = (Z - Z_0)/\lambda$$

$$\sigma = \sigma_0 \beta Z^* \exp(1-\beta Z^*), \qquad \sigma_0 \cong 0.5\sqrt{\frac{E\gamma}{Z_0}} \tag{10.15}$$

where λ is the Thomas-Fermi screening length and $\beta = 0.9$.

10.4 Nano-Contact with Adhesion

For sufficiently small-sized contacts, the force of adhesion between the surfaces of the contacting bodies becomes significant compared with the applied forces. Bradley determined the adhesive interaction between two *rigid* spheres by integrating the intermolecular forces between the bodies.[10] The pull-off force *(P)*, i.e., the force required to separate the spheres, was found to be

$$P = -2\pi w R \tag{10.16}$$

in which the negative sign denotes a tensile force. Experiments were performed on quartz and sodium pyroborate spheres, the results of which were consistent with the theory.

The effect of the elastic deformation of the contacting bodies was included by Johnson, Kendall, and Roberts (JKR).[11] An energy approach was used that accounts for the change in elastic energy, the change in surface energy, and the work done by the applied load. The effect of the adhesive force outside the contact area is neglected. As in linear elastic fracture mechanics, the resulting stress distribution is infinite and tensile at the boundary of the contact region. The attractive intermolecular surface forces cause elastic deformation of the spheres beyond that predicted by the Hertz theory, thereby producing the expected increase of the contact area. The relations among the contact radius *(a)*, the approach *(δ)*, and applied load *(P)*, are given by

$$a^3 = \frac{P_1 R}{K}, \quad \delta = \frac{a^2}{R} - \sqrt{\frac{8\pi a w}{3K}}, \; P_1 = P + 3\pi w R + \sqrt{6\pi w R P + (3\pi w R)^2}, \; K = \frac{4E_C}{3} \tag{10.17}$$

where P_1 is the effective Hertz load due to adhesion, i.e., the Hertz load necessary to produce the same contact radius without adhesion.[8,11] It is clear that Equation (10.17) reduces to Hertz contact when the work of adhesion vanishes (i.e., $w = 0$).

Upon loading in the JKR theory, there is no interaction between the bodies, and hence no deformation, until contact is first made under zero load. At that point the contact region instantly becomes finite due to the sudden inclusion of adhesion. The contact radius and approach under zero applied load are[8]

$$a_0 = \left(\frac{6\pi w R^2}{K}\right)^{1/3}, \qquad \delta_0 = \left(\frac{4\pi^2 w^2 R}{3K^2}\right)^{1/3} \tag{10.18}$$

After continuing to load in compression and subsequent unloading, a tensile force is needed to separate the spheres at a finite contact radius. These quantities are

$$P_{min} = -\frac{3}{2}\pi w R, \quad a_{min} = \left(\frac{3\pi w R^2}{2K}\right)^{1/3} = 0.630 a_0, \quad \delta_{min} = -\frac{a^2}{3R} = -\left(\frac{\pi^2 w^2 R}{12K^2}\right)^{1/3} \tag{10.19}$$

in which the magnitude of the pull-off force is less than that predicted by Bradley for rigid spheres. Also note that the JKR model, which includes

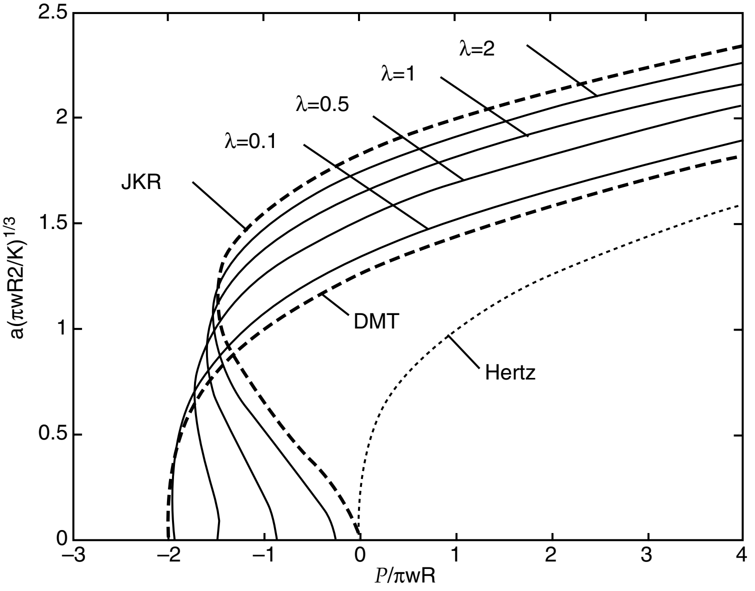

Figure 10.3 Contact radius (a) vs. force (P) for Hertz, DMT, Maugis (various values of λ), and JKR models.

elastic but not plastic deformation, produces hysteresis in the loading/ unloading behavior as shown in Figures 10.3 and 10.4. The JKR theory was supported by experiments on the contact of rubber and gelatin spheres.[11]

Unlike the JKR model, the elastic adhesion model of Derjaguin, Muller, and Toporov (DMT) accounts for the adhesive attraction in the ring-shaped region outside the contact area.[12,13] Thus, the effect of adhesion is to cause the contact force to differ from the externally applied force, i.e.,

$$\frac{Ka^3}{R} = P + 2\pi wR, \qquad \delta = \frac{a^2}{R} \tag{10.20}$$

The DMT model assumes that the deformation outside the contact region and the contact stress profile in the contact region remain the same as in the Hertz theory, but with the load increased by $2\pi wR$. These assumptions result in the DMT curves shown in Figures 10.3 and 10.4. As two spheres approach each other, the DMT theory predicts a pull-on force equal to that obtained by Bradley, which occurs at zero contact radius. That result follows directly from Equation (10.20). Continued loading, followed by subsequent unloading, produces separation at zero contact radius at a pull-off force equal to the pull-on force, i.e., there is no hysteresis. Thus, the pull-off force is given

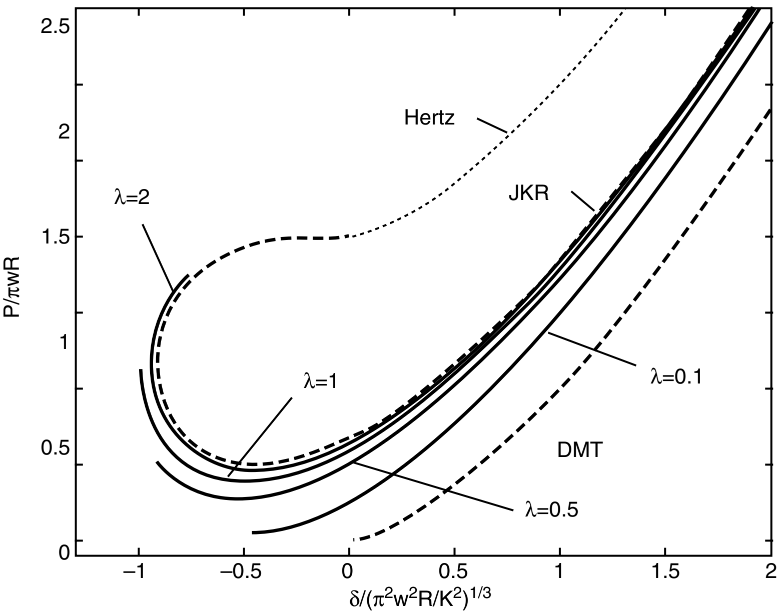

Figure 10.4 Force (P) vs. approach (δ) for Hertz, DMT, Maugis (various values of λ), and JKR models.

by the same expression (Equation [10.16]) as that determined by Bradley.[10] This result is a direct consequence of the neglecting of deformation outside the contact region—at separation both spheres act as rigid bodies.

Note that the magnitude of the adhesive pull-off force decreases as the radius of the contacting bodies decreases. However, this linear decrease in adhesive force is more than compensated for by, for example, the cubic decrease of force due to the weight of an object. Consider a scaling in which the characteristic dimensions change from millimeters to nanometers. Although the pull-off force decreases by a factor of 10^6, the weight decreases by a factor of 10^{18} and the relative importance of adhesion increases by a factor of 10^{12}.

Also note that the JKR and DMT theories give different values of the pull-off force. Due to the assumptions involved, the JKR/DMT models are most suitable when the range of surface forces is small/large compared with the elastic deformations, as pointed out by Tabor.[14] The JKR theory predicts infinite stress at the edge of the contact region, causing the slope of the deformed surface to become infinite immediately outside the contact region. This infinite slope results in the formation of a "necked region" (Figure 10.5). Because the surfaces separate so rapidly with increasing radial position, the effect of the adhesive forces outside the contact region can be readily neglected (JKR theory). In a real deformation the

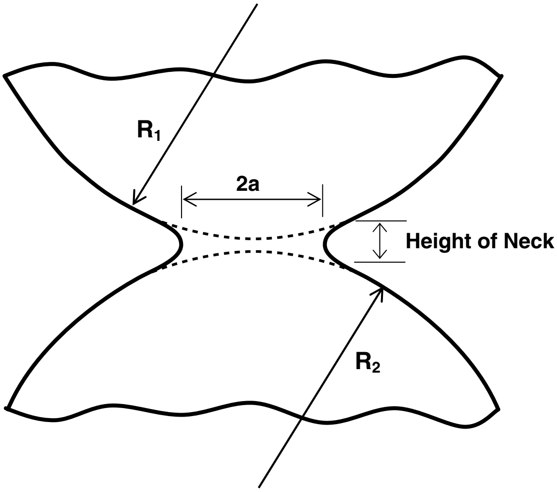

Figure 10.5 Two spherical bodies showing the necked region.

stress, and hence the slope, will both be finite, so that the "neck" will be less pronounced. However, if the range of surface forces is small compared with the elastic deformation, then the portion of the necked region within the range of surface forces is small enough that these adhesive forces can be readily neglected. On the other hand, the DMT model includes these adhesive forces but neglects their effect on deformation outside the contact region. Thus, the DMT theory is expected to be most useful when the *deformation* in the annular portion of the separation region in which adhesion acts is small compared with the range of surface forces. In that case the inclusion of adhesion outside the contact region and the neglecting of the deviation of deformations from the Hertz profile are both justified. The height of the neck is of order $(Rw^2/E_C^2)^{1/3}$ and the Tabor parameter (μ) is given by this neck height divided by the equilibrium spacing (Z_0) or

$$\mu = \left(\frac{Rw^2}{E_C^2 Z_0^3} \right)^{1/3} \tag{10.21}$$

which is a measure of the ratio of elastic deformation to the range of surface forces.[14] The JKR theory is valid for large μ (greater than about 3), whereas the DMT theory is applicable for small μ (less than about 0.1).

Muller, Yushchenko, and Derjaguin evaluated the adhesive force by numerically integrating the stress due to a Lennard-Jones potential.[15] The pull-off force was determined and found to depend upon a single

dimensionless parameter similar to the Tabor parameter. Furthermore, the value of the pull-off force was shown to vary continuously between the DMT and JKR limits. A more comprehensive treatment was given by Greenwood,[16] which confirmed the results of Muller, Yushchenko, and Derjaguin and established the existence of jumps into and out of contact for values of μ greater than unity.

An analytical model, introduced by Maugis, describes a continuous transition between the JKR and DMT models.[17] In the Maugis model the adhesive stress is constant in the portion of the separation region in which the local separation is less than some prescribed value h_0. Separations greater than h_0 involve zero adhesive stress. The adhesive stress is usually taken equal to the theoretical stress (σ_0). Thus, the product $\sigma_0 h_0$ becomes the work of adhesion for the Maugis model, and it is equated to the work of adhesion from the Lennard-Jones potential (Figure 10.6). Thus,

$$h_0 = w/\sigma_0 \cong 0.97 Z_0 \tag{10.22}$$

and the adhesive stress acts in an annular region ($a < r < c$) immediately outside the contact region. The inner radius of the annulus is the contact radius and the outer radius is determined such that the separation at that radius is equal to h_0. This analysis of Maugis[17] gives the nondimensional

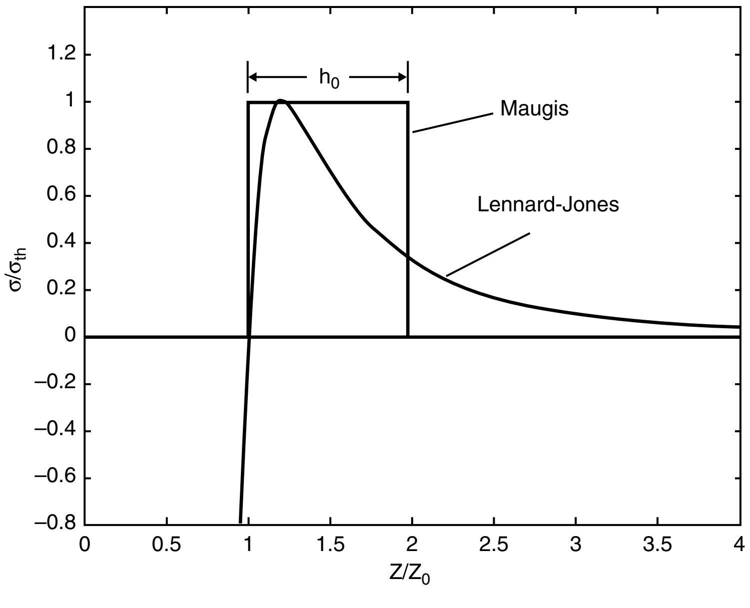

Figure 10.6 Normal stresses due to Lennard-Jones and Maugis potentials. The maximum Maugis stress is equated to the theoretical stress. By equating the areas under these curves, the quantity $h_0 = 0.97\ Z_0$.

relations among the applied load (P_M), contact radius (a_M), and approach (δ_M) as

$$\frac{\lambda a_M^2}{2}\left[\sqrt{m^2-1}+(m^2-2)\tan^{-1}\sqrt{m^2-1}\right]$$
$$+\frac{4\lambda^2 a_M}{3}\left[\sqrt{m^2-1}\tan^{-1}\sqrt{m^2-1}-(m-1)\right]=1$$

$$P_M = a_M^3-\lambda a_M^2\left[\sqrt{m^2-1}+m^2\tan^{-1}\sqrt{m^2-1}\right],\quad \delta_M = a_M^2-\frac{4}{3}a_M\lambda\sqrt{m^2-1} \tag{10.23}$$

where

$$a_M = a\left(\frac{K}{\pi w R^2}\right)^{1/3},\quad \lambda = 2\sigma_0\left(\frac{R}{\pi w K^2}\right)^{1/3}\cong 1.16\mu$$
$$m=\frac{c}{a},\quad P_M=\frac{P}{\pi w R},\quad \delta_M=\delta\left(\frac{K^2}{\pi^2 w^2 R}\right)^{1/3} \tag{10.24}$$

The results are plotted in Figures 10.3 and 10.4, along with the results of the JKR and DMT theories. Because the Maugis formulation is similar to the model of a Dugdale crack,[18] in which the plastic yield zone at the crack tip has a constant tensile stress, it is sometimes referred to as the Maugis–Dugdale model. Shi and Polycarpou extended this model by modifying the Maugis model to more specifically treat noncontacting asperities.[19]

An extremely useful adhesion map for the contact of elastic spheres is provided by Johnson and Greenwood.[20] In a dimensionless load vs. Tabor parameter plane, the regions in which the Hertz, Bradley, DMT, Maugis, and JKR models are applicable are identified (Figure 10.7). Recently elastic adhesion for noncircular contacts has been investigated for an ellipsoidal body and for an elliptical flat-ended punch.[21,22]

A somewhat simpler alternative to the Maugis model is given by Greenwood and Johnson by superimposing two Hertz solutions.[23] One of these Hertz solutions is compressive with a radius equal to the contact radius *(a),* whereas the other is tensile with radius equal to the adhesion radius *(c).* Thus, the adhesive stress decreases with increasing local surface separation. The results are very close to those of Maugis. Due to the simple form of the separation, this model has a potential advantage when used to further develop a viscoelastic model. In fact the measured force required to separate a low-modulus rubber from a smooth hard surface is much greater than predicted by elastic theory.[24] Greenwood and Johnson investigated the adhesion of a viscoelastic sphere

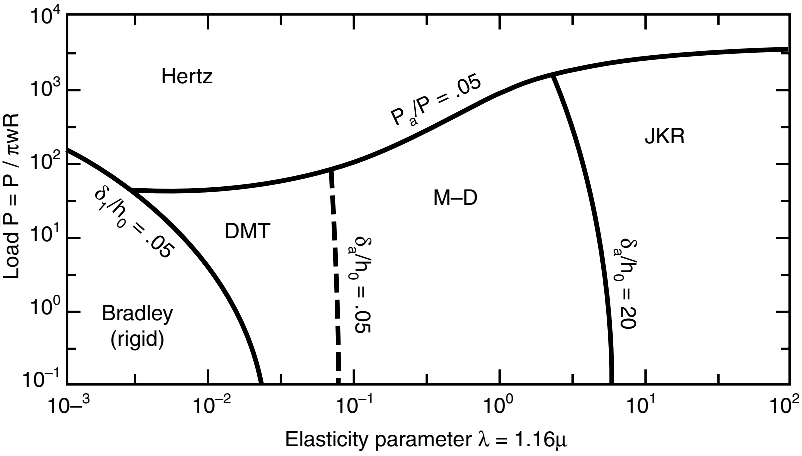

Figure 10.7 An adhesion map. (From Johnson, K.L. and Greenwood, J.A., *J. Coll. Interface Sci.*, 192, 326–333, 1997. With permission.)

and found that the separation force correlates with the viscoelastic properties of the material.[24] Another approximate and simple solution is given by Schwarz, in which the effect of the long-range attractive forces are accounted for separately from the short-range repulsive forces.[25]

10.4.1 Elastic Layers

It is not unusual for one or more of the contacting bodies to have a surface coating. If the radius of the contact is a small fraction of the layer thickness, then the contact can be viewed as occurring with an elastic half-space of the layer material. Otherwise the layered nature of the half-space needs to be treated. Chen and Engel investigated the elastic contact, without adhesion, of a rigid parabolic indenter onto a layered half-space.[26] In nanoscale contacts, however, the relationships among the applied force, the approach, and the contact radius depend on the surface energy of the contacting materials (i.e., the coatings or surface layers) as well as the elastic properties of both the coating and substrate materials, and the coating thickness.

The surface force apparatus (SFA), developed by Tabor and Winkerton and Israelachvili and Tabor, consists of two thin atomically smooth mica sheets each glued to a glass cylinder.[27,28] The cylinders are pressed together with their axes at right angles, thus forming a circular contact. This configuration can be used to measure the adhesive properties of the contacting mica or of a molecularly thin film of intervening fluid. Sridhar, Johnson, and Fleck used a JKR type of adhesion relation to analyze this adhesive contact of the layered SFA structure.[29] The solution was obtained using a finite element analysis with dimensionless variables. The adhesion characteristics

were found to depend upon an adhesion parameter, as well as on the layer thickness ratios and elastic moduli ratios.

Johnson and Sridhar extended their finite element treatment of adhesion in layered systems to the atomic force microscope (AFM) configuration and considered the contact of elastic spherical and flat probes with a compliant elastic coating on a substrate.[30] Results are presented for a range of the adhesion parameters and the elastic moduli ratio. Sridhar and Sivashanker extend the previous analyses of Sridhar, Johnson, and Fleck and Johnson and Sridhar and give more detailed results including empirical relations for the adhesive load, the force vs. contact radius, and the compliance.[31,32] Shull reviewed modeling and experimental research on the mechanics of adhesion in soft elastic and viscoelastic materials.[33]

Sergici, Adams, and Müftü use a Maugis type of adhesion model to investigate the adhesive contact of an elastic sphere with a layered elastic medium.[34] The method of analysis involves integral transform techniques, leading to a singular integral equation that is solved numerically. The use of this model allows the layered contact problem to be applicable for configurations in which the ratio of elastic deformation to the range of surface forces is not necessarily large.

10.5 Elastoplastic and Plastic Contacts

As the applied load in a Hertz contact increases, yielding first occurs below the surface of the body with the lower yield strength. If the Tresca yield criterion is used, then for Poisson's ratio = 0.3, yielding initiates when $p_0 \cong 1.60\,Y$ at a depth of $0.48a$, where Y is the yield strength.[4] This value of the maximum contact pressure for elastic behavior corresponds to a yield load (P_Y) given by

$$P_Y = \frac{\pi^3}{6}\frac{R^2 p_0^3}{E_C^2} \cong 21.2\frac{Y^3 R^2}{E_C^2} \tag{10.25}$$

Results very similar to these are obtained using the von Mises yield criterion.[4]

Consider now the indentation of a deformable body by a rigid sphere. As the load continues to increase above P_Y, the size of the plastically deformed region also grows, but it is surrounded by a reinforcing elastic hinterland during this elastoplastic phase. Eventually, well after the plastic zone breaks to the surface, the *contact* is said to be fully plastic and the mean contact pressure is constant. In both the elastoplastic and fully plastic regimes, the *material* behavior is elastic–perfectly plastic, i.e., the stress–strain curve is elastic–perfectly plastic.

The transition between elastic and fully plastic behavior was investigated by Johnson.[35] Measurements of indentation pressure for a variety of rigid geometry indenters showed that the mean pressure was correlated with

a single parameter given by (E/Y)tanβ, where β is the angle of inclination of the indenter to the surface at the edge of the indentation. For a cone or a wedge, β is constant. However, for spherical indenters, as the load increases, the contact radius increases and so does β. Thus, as was pointed out by Johnson, because the derivation is based on similarity, it is not strictly valid for a spherical indenter because β varies during loading.[35] Thus, the theoretical results give qualitative, rather than quantitative, agreement with experiments. A simple theoretical model based on Hill's expanding cavity model was developed.[36] This model has three zones—a hydrostatic core in which the indenter is embedded, a hemispherical shell in which plastic flow takes place, and an elastic hinterland surrounding the shell.

Subsequently, Studman, Moore, and Jones, and Studman and Field modified Johnson's analysis by allowing the stresses in the core to vary from hydrostatic (under the indenter) to values that satisfy the Von Mises yield criterion at the core boundary.[37,38] Spherical indentations are specifically treated by accounting for the changing geometry of the indentation as the indenter penetrates the material. The resulting equation relating pressure to contact area, which is based on Johnson's work,[35] gives better agreement with experiments.

Tabor[39] showed that for ductile metals, the mean pressure during full plasticity (which is known as the *hardness H*) is related to the yield stress in simple compression according to

$$H = CY \tag{10.26}$$

where C is a constant equal to approximately 2.8. The value of C depends somewhat on the geometry of the indenter. Solutions have been obtained for full plasticity by Ishlinsky, using slip line theory, by assuming that the free surface remains flat.[40] Hill, Storåkers, and Zdunek used deformation theory,[41] and Biwa and Storåkers employed flow theory[42] in order to obtain similarity solutions for full plasticity. The load and contact radius increase substantially from the onset of yielding until fully plastic deformation. Although Equation (10.26) was based on rigid perfectly plastic indentation theory, a modified form can be used for materials that strain-harden. Also, recent finite element modeling suggests that the constant C depends on the ratio of the yield strength to the elastic modulus; this point will be discussed in more detail in Section 10.5.3.

In classical hardness testing, an indenter is pressed against a softer material with a prescribed force. The area of the permanent impression is measured with the aid of a microscope. The ratio of the maximum force to this residual contact area is called the hardness. Its value depends somewhat on the shape of the indenter; in the Brinell hardness test the indenter is spherical. In nanohardness testing, the force and depth of the indentation are monitored during loading and unloading. The hardness and elastic modulus can be calculated from the loading and unloading relations between force and penetration depth. A comprehensive review article on indentation and scaling is given by Cheng and Cheng.[43]

10.5.1 Scale-Dependent Plasticity

Scale dependence has been observed in numerous experimental investigations of indentation hardness.[44–47] In particular, smaller indentation depths typically give greater values of hardness. For sufficiently low values of the indentation depth, the nanohardness can be over an order of magnitude greater than its bulk value. Similarly, experiments with wires in torsion and beams in bending show scale dependence in the yield point (the yield point and hardness are related by Equation [10.26] at the macroscale).[48,49] However, a wire in tension shows considerably less of this scale-dependent phenomenon.[48] For these and other reasons, the scale dependencies of the yield strength and hardness are believed to be associated with geometrically necessary dislocations generated by nonuniform straining.[50,51]

Conventional plasticity theories are incapable of predicting this size effect. Such theories lack a material length scale and hence incorrectly require the hardness and yield strength to be scale independent.[52] Thus strain-gradient plasticity theories, such as the phenomenological theory of Fleck et al.[48] and the mechanism-based theory of Gao et al.[53] have been developed that account for the observed scale-dependent material behavior. Such theories are applicable to scales ranging from hundreds of nanometers up to tens of microns. At these scales there are a sufficiently large number of dislocations for continuum theory to be valid.

Although the mathematics of strain-gradient theories are quite complicated, a finite element model of indentation, with strain-gradient effects, has been developed and implemented.[54] Furthermore, Nix and Gao[51] have shown that the effect of scale-dependent hardness can be accurately represented by

$$\frac{H}{H_0} = \sqrt{1 + \frac{h^*}{h}} \tag{10.27}$$

where H is the scale-dependent hardness, H_0 is the macrohardness, h is the indentation depth, and h^* is the characteristic depth that depends on the shape of the indenter. This simplified form of scale-dependent plasticity is convenient to use in many applications.

For sufficiently small nanoindentations, there is an inadequate number of dislocations for a continuum theory of plasticity to be valid. The recently introduced quasicontinuum method captures the physical effects associated with a small number of dislocations without requiring the huge computational effort of a molecular dynamics simulation.[55] That nanoindentation investigation focused on determining plastic deformation under an indenter.

10.5.2 Adhesion in Elastoplastic Contacts

The effect of adhesion in an elastic–plastic deformation is accounted for by Maugis and Pollock in an approximate manner.[56] This model is applicable

to the JKR regime in which the deformation is large compared with the range of surface forces. In the elastic regime, the applied force *(F)*, the contact radius *(a)*, and the interference *(δ)* are related by the JKR model, i.e., Equation (10.17).[11] The JKR model remains valid until the contact radius reaches the value that would cause plastic yielding to occur without adhesion. A modified version of the Studman model is used by Maugis and Pollock[56] to relate the mean contact pressure p_m to the contact radius, i.e.,

$$p_m = Y\left(1.1 + 0.58\ln\frac{Ea}{2.3YR}\right) \tag{10.28}$$

Although the *magnitude* of the contact stresses are affected by the adhesion force, in both the elastoplastic and plastic regimes the stress distributions and contact radius are assumed to correspond to those without adhesion.

Equation (10.28) was obtained for an elastic–plastic half-space indented by a rigid sphere. However, in some configurations, such as a microswitch, there are two deformable bodies contacting each other. Essentially Equation (10.28) states that a Hertz-like stress distribution of mean contact pressure p_m causes a flat elastic body to deform into a spherical cavity of radius *R*, during elastic–plastic deformation. Thus, an identical stress distribution acting on each of two elastic bodies will produce a *total* change in curvature of *2/R*. For two elastic bodies of the same modulus, Equation (10.28) can be replaced by

$$p_m = Y\left(1.1 + 0.58\ln\frac{Ea}{4.5YR}\right) \tag{10.29}$$

in which *R* is the radius of curvature of the asperity. Because the contact geometry is assumed to be that for a purely plastic contact without adhesion, the applied force *(F)* is related to the mean contact pressure by

$$F = \pi a^2 p_m - 2\pi R w \tag{10.30}$$

After additional loading, the contact pressure becomes equal to the hardness *H*. For the contact of two bodies with identical material properties this fully plastic condition occurs at a critical contact radius $a_p \approx 119YR/E$. Thereafter, the deformation is purely plastic, the contact pressure remains constant, and the force is

$$F = \pi a^2 H - 2\pi R w \tag{10.31}$$

As a consequence of plastic deformation, the effective asperity radius of curvature after elastic–plastic or fully plastic deformation (R_{eff}) is different from its initial value *(R)*. Because the effect of the adhesive forces on the

stress distribution decreases progressively with further loading into the plastic regime, R_{eff} might be assumed to be the same as it would be in the absence of adhesion (see, e.g., Johnson,[4] or recent finite element simulations discussed in the next section). If both deformable bodies have the same yield strength, the changes in the radii of curvature of an asperity and of the corresponding region on the flat body will each be equal to $2R_{eff}$. Thus, due to plastic deformation, the asperity will be partially flattened and the mating region on the originally flat body will acquire a spherical cavity, each extending over a circle of radius equal to the final loading radius.

The effect of adhesion is to cause a finite tensile force (i.e., the adherence force) to be necessary to separate the bodies. If the loading is elastic, the unloading will also be elastic, with separation occurring at the minimum stable JKR contact radius (a_{min}) and with the adherence force determined from Equation (10.16). However, if the loading is elastic–plastic or fully plastic, one of three different unloading modes will occur.[56] When the contact is gradually unloaded from the maximum contact force, the unloading occurs initially with a constant contact radius. This unloading is a consequence of the plastically deformed cavity, which is nearly conformal to the deformed asperity. This initial phase of unloading can be shown to be equivalent to the elastic unloading of a flat punch. Unloading continues until one of the following three conditions is met: (1) ductile separation, in which the average tensile stress is equal to the hardness; (2) brittle separation, in which the applied force reaches the JKR equilibrium value, and separation occurs; or (3) another brittle separation, in which the applied force reaches the JKR equilibrium value, followed by subsequent unloading that causes the contact radius to decrease until the contacts separate. More details can be found in Maugis and Pollock.[56]

10.5.3 Finite Element Elastic-Plastic Simulations

Finite element simulations of contact problems enable the detailed investigation of the elastoplastic regime and its transition into what has been termed full plasticity. Kral, Komvopoulos, and Bogy emphasize the elastic–plastic regime for a half-space indented by a rigid sphere.[57] Both elastic–perfectly plastic and strain-hardening material behavior were used for up to four load/unload cycles. The depth of the residual indentation was found to depend on the strain-hardening material behavior. The pile-up around the periphery of the indentation is greatest for nonhardening materials. The maximum stress during subsequent loading cycles is reduced because of the greater conformity of the contact produced by plastic deformation.

Mesarovic and Fleck treated the elastoplastic spherical indentation and the elastoplastic contact of dissimilar spheres for elastic-perfectly plastic and for strain-hardening materials.[58,59] Contact conditions are classified into four regimes—elastic contact, elastic–plastic deformation, fully plastic similarity regime, and the finite deformation plasticity regime. These regions are shown on the map of Y/E_C vs. a/R in Figure 10.8 in which Y and E_C are replaced by σ_0 and E^* respectively. The similarity regime is characterized

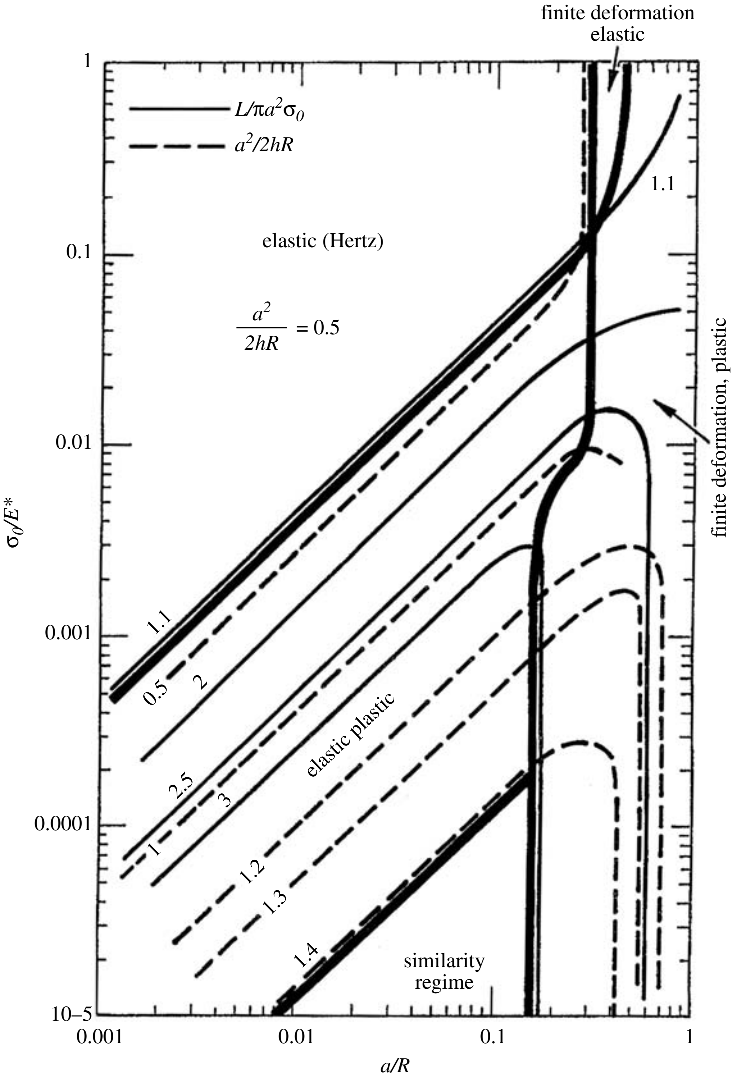

Figure 10.8 Map of frictionless indentation of an elastic–ideally plastic solid, showing regimes of deformation mechanisms. Contours of average pressure (—) and normalized contact area $a^2/(2hR)$ (—) are included. The map is based on the finite-element results for E^*/σ_0 = 3, 10, 30, 100, 250, 500, 1000, and 10,000. L is the applied load, σ_0 is the yield stress, and h is the approach. (From Mesarovic, S.D. and Fleck, N.A., *Proc. Roy. Soc. Lond.*, A455, 2707–2728, 1999. With permission.)

by a constant average pressure equal to the hardness. For large indentations, i.e., the finite deformation plasticity regime, the average pressure decreases to values below the material hardness. For sufficiently high values of the yield strain, the similarity solution is not reached and the maximum average

pressure is less than the hardness, after which point the average pressure decreases into the finite deformation region. Komvopoulos and Ye[60] and Kogut and Komvopoulos[61] also performed finite element analyzes of indentation of an elastic–plastic solid by a rigid sphere during loading and unloading. The mean contact pressure during full plasticity was found to depend on the ratio *E/Y* (i.e., the reciprocal of the yield strain). For large *E/Y* values, full plasticity occurs at a mean pressure of about 2.8*Y*, whereas relatively small values of *E/Y* correspond to a mean pressure of about 2.0*Y*. The relations among the force, approach, and contact radius in Komvopoulos and Ye, and Kogut and Komvopoulos were each fit by empirical relations that facilitate their subsequent use.

For Hertz elastic contact, there is no distinction between a rigid sphere indenting an elastic half-space and an elastic sphere pressed against a flat surface. However, in the plastic regime these configurations do differ. Kogut and Etsion[62] and Jackson and Green[63] performed finite element analyzes of the elastic-plastic contact between a sphere and a rigid flat surface. The contact stresses and the growth of the plastic zone from elastic to elastoplastic and to fully plastic loading were determined. Kogut and Etsion found that the plastic core is surrounded completely by elastic regions for $1 \le \delta/\delta_Y \le 6$ and the entire contact area is elastic.[62] For $6 \le \delta/\delta_Y \le 68$, the contact *area* is elastic–plastic, whereas for $\delta/\delta_Y > 68$, the entire contact *area* is plastic. When $\delta/\delta_Y \ge 110$, the average pressure becomes equal to the hardness value of 2.8*Y*. Jackson and Green found that the hardness depends on the yield strain,[63] which is similar to Mesarovic's findings.[58] Jackson and Green's results compared favorably with limited experimental data. The relations among the force, the approach, and the contact radius in Kogut and Etsion, and Jackson and Green were each fit by empirical relations.

Etsion, Kligerman, and Kadin[64] investigated the residual displacements and residual curvature of the plastically deformed asperity using the model in Kogut and Etsion.[62] The radius of the residual curvature is nearly uniform and agrees closely with Johnson[35] for moderate loading. For greater penetrations, the residual radius of curvature is nonuniform and significantly greater than that in Johnson's work.[35]

The *adhesive* contact of two elastic–plastic spheres was investigated by Mesarovic and Johnson.[65] An analysis of elastoplastic deformation during loading was presented using a fine-grid finite element analysis for elastic–perfectly plastic materials. For unloading from a state of uniform pressure, an analytical model was used. The adhesive behavior was modeled using both JKR and Maugis types of adhesion conditions. A map of decohesion regimes in terms of two dimensionless parameters was presented in Mesarovic and Johnson[65] and is shown in Figure 10.9. Kogut and Etsion extended the finite element model of elastoplastic flattening of a sphere to include the effect of adhesion using a DMT type of model along with elastic–perfectly plastic material behavior.[62,66]

During subsequent load-unload cycles *without adhesion*, most if not all of the plastic deformation occurs only on the first load cycle. A finite element

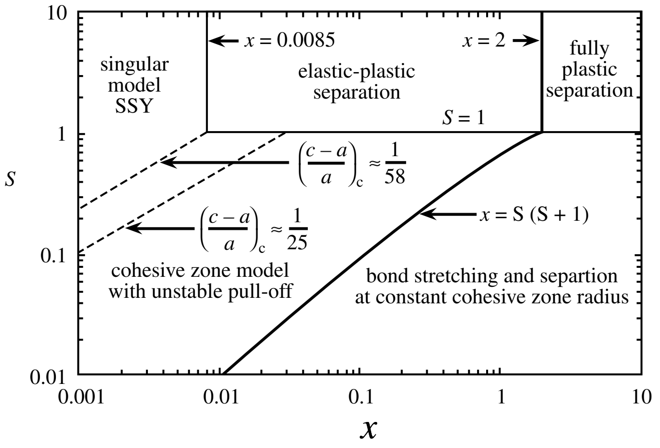

Figure 10.9 Map of decohesion region in (χ,S) space = 1/3, $p_0/\sigma_y = 3$. Line *(c–a)/*a–1/25 corresponds to $\chi^{2/3}$ S^2 1/10. Line *(c–a)/a*–1/58 corresponds to $\chi^{2/3}$ S^2 1/24. $\chi = a/a_0$, where a_0 is the contact radius at the maximum fully plastic loading, and $S = \sigma_0/p_0$, where p_0 is the average contact pressure at the maximum fully plastic loading. (From Mesarovicand, S.D. and Johnson K.L., *J. Mech. Phys. Solid.*, 48, 2009–2033, 2000. With permission.)

analysis of cyclic indentation performed by Yan and Li confirmed that the unloading and reloading are elastic and identical.[67] However, the stresses are not Hertzian. In the elastoplastic/plastic deformation models *with adhesion*, there may be significant plastic deformation on subsequent load cycles. There do not appear to be existing models or simulations of contacts under repeated loading–unloading of asperities in the presence of adhesion. There are potential difficulties in predicting the deformed asperity radius after a load–unload cycle. If the separation of the contacts is ductile, there may be material transfer as the contacts separate.

10.6 Rough Surface Nanocontacts

Multi-asperity contact models may be classified as predominately uncoupled or completely coupled. Uncoupled contact models represent surface roughness as a set of asperities, often with statistically distributed parameters. The effect of each individual asperity is local and considered separately from the other asperities; the cumulative effect is the sum of the actions of individual asperities. On the other hand, coupled contact problems of rough surfaces are more complicated mathematically because the equations of elasticity must be solved for the entire body simultaneously. This procedure often leads to a mixed boundary value problem that can be solved analytically only for simple configurations. The emphasis here is on uncoupled multi-asperity contacts.

A plethora of statistical models of multi-asperity contact has been developed in order to determine how the approach and contact area vary with the applied force. See the review articles by Bhushan or by Adams and Nosonovsky for more details.[68,69] Most of these approaches are related in some way to the pioneering work of Greenwood and Williamson (GW).[70] The GW model, which neglects adhesion, assumes that in the contact between one rough and one smooth surface (1) the rough surface is isotropic, (2) asperities are spherical near their summits, (3) all asperity summits have the same radius of curvature while their heights vary randomly, (4) there is no interaction between neighboring asperities, and (5) there is no bulk deformation. With these assumptions, the Hertz contact theory discussed in Section 10.2 is valid for a spherical asperity on the surface of an otherwise flat elastic body. It is noted that in the elastic contact of a single sphere with an elastic half-space, the contact area varies as the two-thirds power of the applied force. However, when the asperities have a reasonable distribution of heights (e.g., Gaussian) the real area of contact varies approximately linearly with the applied force.

The first three assumptions of the GW theory were relaxed by McCool who treated anisotropic rough surfaces with ellipsoidal asperities.[71] His results were in good agreement with the simpler GW model. Greenwood and Tripp showed that the contact of two rough surfaces can be replaced with the contact of a single rough body with a smooth surface.[72] Greenwood and Tripp investigated the contact of a rough elastic sphere with a rigid flat.[73] For low loads the pressure distribution is broader than it is for Hertz contact. McCool extended the GW model by using an asymmetric distribution of asperity heights and by including the effect of a surface coating.[74] Elastic–plastic models of rough contact were developed by Chang, Etsion, and Bogy who developed a GW type of elastic–plastic contact model based on volume conservation of a plastically deformed asperity control volume.[75] This model was later extended by Yu and Polycarpou to include an asymmetric distribution of asperity heights.[76] Skew was found to significantly affect the relation between the force, contact area, and the number of contacting asperities. Zhao, Maietta, and Chang replaced the Hertz contacts of the GW model with elastic-plastic contacts including the transition between elastic–plastic and fully plastic deformations.[77]

The effect of adhesion in multi-asperity contacts was included by Fuller and Tabor by replacing the Hertz contacts of the GW model with the elastic adhesive contacts from the JKR model.[78] The results depend on an adhesive parameter that represents a statistical average of the competition between the compressive stresses in the higher asperities (which are prying the surfaces apart) and the adhesive forces acting on the lower asperities (which are holding the surfaces together). Maugis combines the DMT model with the GW model resulting in an elastic contact model of a rough surface with adhesion.[79] Adams, Müftü, and Mohd Azhar,[80] as well as Morrow, Lovell, and Ning,[81] combined the Maugis and GW models. These two models span the range of small to large values of the Tabor parameter. The work in Adams

et al. was aimed at both contact and friction, whereas that of Morrow et al. was a contact model that included the effects of noncontacting asperities.[80,81]

Rough surface contact models that include elastoplastic deformation and adhesion have also been developed. Chang et al. included the effect of adhesion in the elastoplastic multi-asperity model by using the DMT model for the contacting asperities.[75,82] Stanley, Etsion, and Bogy extended this model for the adhesion of rough surfaces affected by a very thin layer of lubricant.[83] It was found that a roughness-dependent critical thickness exists marking a dramatic change in adhesive forces. Kogut and Etsion developed a multi-asperity contact model that included the effects of plastic deformation based upon their finite element contact model.[62,84]

Coupled contact problems are complicated mathematically because the equations of elasticity must be solved in the entire body. Instead of a random distribution of asperity heights, only periodic interface profiles (e.g., sinusoidal) are considered. Such problems were treated by Westergaard; Johnson, Greenwood, and Higginson; and Manners without adhesion, and by Hui et al. and Adams with adhesion.[85–89] These solutions allow the limits of applicability of uncoupled models to be evaluated.[90]

Finally, as contacts become smaller, the contact radius can approach the atomic spacings. Recently Cha, Srolovitz, and Vanderlick presented a molecular dynamics simulation of a gold-on-gold contact.[91]

10.7 Micromechanical Switches

Microswitches and microrelays have a number of attractive properties to potentially replace conventional relays or solid-state switches in a number of low-power applications. These switches are smaller in size and faster in switching than existing mechanical relays (reed relays, for example). The product of on-resistance and parasitic capacitance is lower than for transistor switches. Electrostatically actuated MEMS switches consume virtually zero steady-state power, unlike reed relays and p-i-n diode switches. Potential uses of MEMS switches include RF switching in applications such as cell phones, phase shifters, and smart antennas,[92] as well as reed relay replacement in automatic test equipment (ATE) and industrial and medical instrumentation.

There are two actuation mechanisms commonly used—electrostatic and magnetic. Electrostatic switches generally require a higher voltage and consume less power than magnetic switches.[93] Magnetic switches often draw steady-state power in the on-state, and even latching designs draw a relatively high power during the switching operation.[94,95] In either case, the contact force is usually limited by fabrication and cost to several hundred μN. Due to these low contact forces, it is the contact that has proven to be the greatest barrier to obtaining sufficient reliability for commercial applications.

Because part of the available actuation force is needed to close the switch, it is only the remainder of the actuation force that acts on the contact. These forces are generally 2 to 3 orders of magnitude lower than in reed relays. The low contact force makes it difficult to obtain a low and stable contact resistance, often leading to resistances that increase steadily with cycling until the switch is no longer useful. It also encourages the choice of gold as a contact material because it is soft (resulting in a larger real contact area) and inert (resulting in a clean, truly metallic contact surface). However, a large real contact area and a clean-metal contact increase the adhesion force, thereby increasing the possibility of contact stiction causing a "stuck-closed" failure after repeated cycling. If the contact force is increased by reducing the restoring force, the switch also becomes prone to a stiction failure.

Modeling of the constrictive resistance requires knowledge of the size and distribution of contact spots. First consider the constrictive resistance of a single spot of radius a, separating two semi-infinite bodies each of resistivity (ρ). In the case in which the contact radius (a) is small compared with the electron mean free path length (l_e) of the material, the resistance is determined by the Sharvin mechanism,[96] in which electrons travel through the contact spot without scattering, i.e., the constrictive resistance is

$$R_{con} = \frac{4\rho l_e}{3\pi a^2} \tag{10.32}$$

If, on the other hand, the contact radius is much greater than the mean free path length, the resistance is dominated by a diffuse scattering mechanism, as given by the Maxwell spreading resistance (see, e.g., Holm[1]):

$$R_{con} = \frac{\rho}{2a} \tag{10.33}$$

Wexler has given a simple interpolation formula that accounts for the transition between the Maxwell and Sharvin regimes.[97] An analytical solution for this transition region also exists, but is somewhat more difficult to implement.[98]

Investigations of contacts in microswitches (Figure 10.10) without and with adhesion have been presented by Zavracky et al. and Majumder et al.[99–102] The emphasis was on a combination of measurements and multi-asperity modeling (without and with adhesion) in order to predict the contact resistance in electrostatically actuated gold-on-gold switches. The modeling used a finite number of asperities with estimates of the radii of curvature, the distribution of heights, and the number per unit area. Contact modeling used the Chang, Etsion, and Bogy model[75] without adhesion, and the Maugis and Pollock model[56] with adhesion. The constrictive resistance of an isolated contact was found from the contact radius according to the appropriate scale (Maxwell, transition, or Sharvin). Although a method was developed to

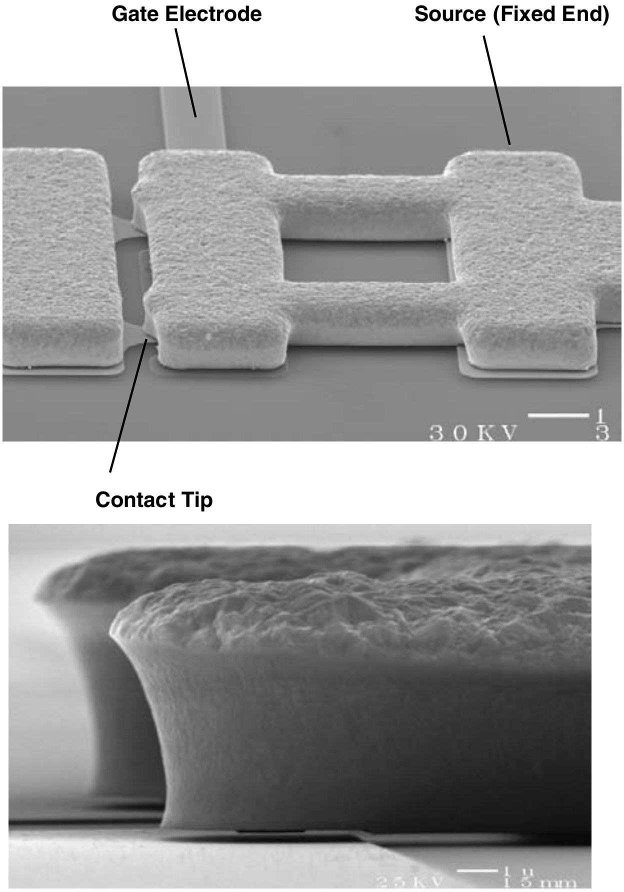

Figure 10.10 SEM micrographs of a microswitch (top) with a close-up of the contact tips (bottom).

estimate the interaction between the constrictions for a known distribution of contacts, the nominal shape of the tip precludes using this method.[103] Instead, an upper bound on the overall contact resistance was found by combining all of the asperity contact areas into a single spot. A lower bound was determined by assuming that the spots conduct independently. The bounds of these models show good qualitative agreement with measurements.

Other authors have used simpler contact models, generally from the viewpoint of device design, e.g., Kruglick and Pister[104] and Lafontan et al.[105] In those cases, the reported contact resistance was high (1 Ω or greater). There has also been some work in looking at contact resistance in the force range applicable to microswitches, using an experimental set-up instead of real devices.[106–108] In these papers, the effect of contact cycling on resistance and adherence was not reported.

Recently Kogut and Komvopoulos presented a contact resistance theory based upon a fractal description of rough surfaces.[109] The model includes elastic–plastic deformation of the asperities and size-dependent constrictive resistance. This method is extended to include a thin insulating film that is treated as an energy barrier that impedes current flow due to tunneling resistance.[110] It was found that the variation of the electrical contact resistance is dominated by tunneling and that its variation with load is less than it is in the absence of the layer. Kogut and Komvopoulos used electrical contact resistance measurements to characterize interfacial adhesion.[111] Tringe et al. used interfacial force microscopy to study the electrical contact between a sputtered-gold-coated tip and an electroplated gold film in a dry nitrogen environment.[112] The contamination layer, consisting mostly of hydrocarbons, is characterized mechanically and electrically. The results show that the contact resistance and adhesion are dominated by the contaminant, which can be broken down with force and voltage. The conductivity of the layer increases significantly after exposure to ozone.

When a switch closes, the contact tip impacts the drain, typically bouncing one or more times before settling down. This dynamic behavior is important for two reasons. First, the switch cannot be used until the bouncing has stopped, effectively increasing the closing time. Second, the impact force can be several times greater than the contact force.[113] The increased magnitude of the impact force, as well as the additional impacts associated with bouncing, may be responsible for reduced switch lifetime. This expected reduced lifetime due to the impact force may be exploited for use in accelerated testing.[114]

As current flows through the microswitch, Joule heating causes the temperature to increase. Due to the temperate-dependent resistivity of materials, this temperature increase results in an increase of the switch resistance. This phenomenon has been studied in microswitches by Hyman and Mehregany,[107] Yan et al.,[115] and Jensen et al.[116] The finite element method was used in the latter two studies and Yan et al. showed SEM images of one side of a failed contact (Figure 10.11) subjected to excessive current.[115]

Another more subtle, yet undesirable, phenomenon occurs due to temperature-dependent resistivity. Consider two RF signals at nearly equal frequencies that lead to the well-known beating phenomena in which the sum of the two signals can be represented by the product of a low-frequency component (at one-half the difference frequency) and a high-frequency term (at the average frequency). The switch responds thermally to the low-frequency component, but because of the thermal response time it responds far less to the high-frequency term. The resistance of the switch then varies at the difference frequency of the two signals. This variation in the resistance modulates the signals applied to the switch, causing distortion. In the frequency domain, this distortion leads to undesirable side bands separated from the original signal components by the difference frequency. This phenomenon is called intermodulation distortion and was investigated by Johnson, Adams, and McGruer for an electrostatically actuated microswitch.[117]

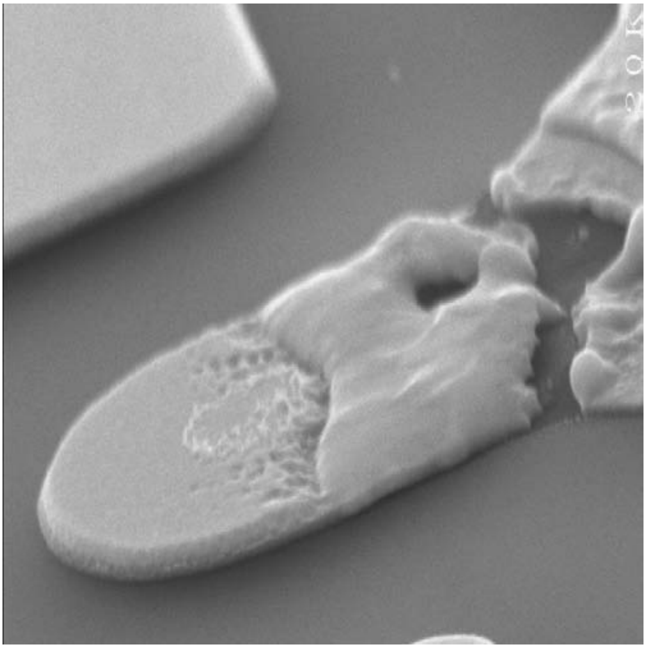

Figure 10.11 SEM micrograph of a failed drain in a microswitch. The switch was subjected to a high current.

Intermodulation distortion can also occur in capacitive microswitches.[118] In this case changes in capacitance, induced by switch vibrations, lead to the distortion. In both contact-type and capacitive microswitches, the intermodulation distortion is typically much less than in semiconductor switches such as the p-i-n diode.

10.8 Recommendations for Future Research

There is much need for continuing research in order to improve microswitch performance and reliability. A reduction in switch bouncing can lead to a reduction in the effective closing time. Switch bounce, along with the related impact force, requires that the contact undergo more contact cycles than switching cycles, along with a greater force (i.e., the impact force) than is necessary to maintain the switch in its closed position. The roles of the impact force, the number of contact cycles, and purely mechanical cycling (without passing current), as well as the role of the impact force in accelerated testing methods, need to be better understood.

Unwanted materials in the contact region affect switch performance and reliability. Thus, the role of contaminants on the surface must also be characterized, and their influence on contact resistance and contact heating needs to be understood. High-power applications require a better understanding

of contacts under elevated temperature. The coupling of thermal, electrical, and mechanical contact analyses in order to account for thermal expansion as well as thermal softening at sufficiently high temperature may provide useful insight. The objective is to predict thermally induced switch failure as well as intermodulation distortion.

It is well known that microswitch performance evolves with the number of switching cycles. In some cases the resistance decreases leading to an adhesive failure, whereas in other situations the resistance increases beyond an acceptable limit.[102] Material transfer between the contacting surfaces has also been measured.[114] The overarching goal is to understand evolution of these nanoscale contacts, as influenced by current flow, contact and impact forces, Joule heating, and the presence of contaminants. The formulation of appropriate models will be synergistic with the development of means of accelerated testing to validate the theory.

References

1. Holm, R., *Electrical Contacts*, 4th edition, Springer-Verlag, Inc., New York, 1967.
2. Slade, P.G., *Electrical Contacts Principles and Applications*, Marcel Dekker, Inc., New York, 1999.
3. Hertz, H., Über die Berührung fester elastischer Körper (On the contact of elastic solids), *J. reine und angewandte Mathematik*, 92, 156, 1882.
4. Johnson, K.L., *Contact Mechanics*, Cambridge University Press, Cambridge, MA, 1985.
5. Greenwood, J.A., Analysis of elliptical hertzian contacts, *Tribol. Int.*, 30, 235, 1997.
6. Stuermann, E. (Shtaerman, I.,Ya), On Hertz theory of local deformation of compressed bodies, *Comptes Rendus (Doklady) de l'Académie des Sciences de l'URSS*, 25, 359, 1939.
7. Israelachvili, J.N., *Intermolecular and Surface Forces*, 2nd edition, Academic Press, London, 1992.
8. Maugis, D., *Contact, Adhesion and Rupture of Elastic Solids*, Springer-Verlag, Berlin, Heidelberg, New York, 2000.
9. Yu, N. and Polycarpou, A.A., Adhesive contact based on the Lennard-Jones potential: a correction to the value of the equilibrium distance as used in the potential, *J. Coll. Interface Sci.*, 278, 428, 2004.
10. Bradley, R.S., The cohesive force between solid surfaces and the surface energy of solids, *Phil. Mag.*, 13, 853, 1932.
11. Johnson, K.L., Kendall, K., and Roberts, A.D., Surface energy and the contact of elastic solids, *Proc. Roy. Soc. Lond.*, A324, 301, 1971.
12. Derjaguin, B.V., Muller, V.M., and Toporov, Y.P., Effect of contact deformations on the adhesion of particles, *J. Coll. Interface Sci.*, 53, 314, 1975.
13. Muller, V.M., Derjaguin, B.V., and Toporov, Y.P., On two methods of calculation of the force of sticking of an elastic sphere to a rigid plane, *Coll. Surface.*, 7, 251, 1983.
14. Tabor, D., Surface forces and surface interactions, *J. Coll. Interface Sci.*, 58, 2, 1976.

15. Muller, V.M., Yushchenko, V.S., and Derjaguin, B.V., On the influence of molecular forces on the deformation of an elastic sphere and its sticking to a rigid plane, *J. Coll. Interface Sci.,* 77, 91, 1980.
16. Greenwood, J.A., Adhesion of elastic spheres, *Proc. Roy. Soc. Lond.,* A453, 1277, 1997.
17. Maugis, D., Adhesion of spheres: the JKR-DMT transition using a Dugdale model, *J. Coll. Interface Sci.,* 150, 243, 1992.
18. Dugdale, D.S., Yielding in steel sheets containing slits, *J. Mech. Phys. Solid.,* 8, 100, 1960.
19. Shi, X. and Polycarpou, A., Adhesive transition from noncontacting to contacting elastic spheres: extension of the Maugis-Dugdale model, *J. Coll. Interface Sci.,* 281, 449, 2005.
20. Johnson, K.L. and Greenwood, J.A., An adhesion map for the contact of elastic spheres, *J. Coll. Interface Sci.,* 192, 326, 1997.
21. Johnson, K.L. and Greenwood, J.A., An approximate JKR theory for elliptical contacts, *J. Phys. Appl. Phys.,* 38, 1042, 2005.
22. Yang, F., Adhesive contact between an elliptical rigid flat-ended punch and an elastic half space, *J. Phys Phys. Appl. Phys.,* 38, 1211, 2005.
23. Greenwood, J.A. and Johnson, K.L., An alternative to the Maugis model of adhesion between elastic spheres, *J. Phys. Appl. Phys.,* 31, 3279, 1998.
24. Greenwood, J.A. and Johnson, K.L., The mechanics of adhesion of viscoelastic materials, *Phil. Mag. A,* 43, 697, 1981.
25. Schwarz, U.D., A generalized analytical model for the elastic deformation of an adhesive contact between a sphere and a sphere and a flat surface, *J. Coll. Surf. Sci.,* 261, 99, 2003.
26. Chen, W.T. and Engel, P.A., Impact and contact stress analysis in multilayer media, *Int. J. Solid. Struct.,* 8, 1257, 1972.
27. Tabor, D. and Winkerton, R.H.S., The direct measurements of normal and retarded van der Waals forces, *Proc. Roy. Soc. Lond.,* A312**,** 435, 1969.
28. Israelachvili, J.N. and Tabor, D., The measurement of van der Waals dispersion forces in the range 1.5 to 130 nm, *Proc. Roy. Soc. Lond.,* A331**,** 19, 1972.
29. Sridhar, I., Johnson, K.L., and Fleck, N.A., Adhesion mechanics of the surface force apparatus, *J. Phys. Appl. Phys.,* 30, 1710, 1997.
30. Johnson, K.L. and Sridhar, I., Adhesion between a spherical indenter and an elastic solid with a compliant elastic coating, *J. Phys. Appl. Phys.,* 34, 683, 2001.
31. Sridhar, I. and Sivashanker, S., On the adhesion mechanics of multi-layer elastic systems, *Surf. Coat. Tech.,* 167, 181, 2003.
32. Sridhar, I., Zheng, Z.W., and Johnson, K.L., A detailed analysis of the adhesion mechanics between a compliant elastic coating and a spherical probe, *J. Phys. Appl. Phys.,* 37, 2886, 2004.
33. Shull, K.R., Contact mechanics and adhesion of soft solids, *Mater. Sci. Eng.,* R 36, 1, 2002.
34. Sergici, A.O., Adams, G.G., and Müftü, S, Adhesion in the contact of a spherical indenter with a layered elastic half-space, *J. Mech. Phys. Solids,* 54, 1843–1861, 2006.
35. Johnson, K.L., The correlation of indentation experiments, *J. Mech. Phys. Solids,* 18, 115, 1970.
36. Hill, R., *The Mathematical Theory of Elasticity,* Clarendon Press, Oxford, 1950.
37. Studman, C.J., Moore, M.A., and Jones, S.E., On the correlation of indentation experiments, *J. Phys. Appl. Phys.,* 10, 949, 1977.

38. Studman, C.J. and Field, J.E., The indentation behaviour of hard metals, *J. Phys. Appl. Phys.*, 9, 857, 1976.
39. Tabor, D., *Hardness of Metals,* Clarendon Press, Oxford, 1951.
40. Ishlinsky, A.J., The axisymmetric problem in plasticity and the Brinell Test, (in Russian), *Prikladnaia Mathematika i Mekhanika,* 8, 201, 1944.
41. Hill, R., Storåkers, B., and Zdunek, A.B., A theoretical study of the Brinell hardness test, *Proc. Roy. Soc. Lond.,* A423, 301, 1989.
42. Biwa, S. and Storåkers, B., An analysis of fully plastic Brinell indentation, *J. Mech. Phys. Solid.,* 43, 1303, 1995.
43. Cheng, Y.-T. and Cheng, C.-M., Scaling, dimensional analysis, and indentation measurements, *Mater. Sci. Eng.,* R 44, 91, 2004.
44. Atkinson, M., Further analysis of the size effect in indentation hardness tests of some metals, *J. Mater. Res.,* 10, 2908, 1995.
45. Bhushan, B., *Handbook of Micro/Nanotribology,* 2nd Edition, CRC Press, Boca Raton, FL, 1999.
46. De Guzman, M.S., Neubauer, G., Flinn, P., and Nix, W.D., The role of indentation depth on the measured hardness of materials, *Mater. Res. Symp. Proc.,* 308, 613, 1993.
47. McElhaney, K.W., Vlassak, J.J., and Nix, W.D., Determination of indenter tip geometry and indentation contact area for depth-sensing indentation experiments, *J. Mater. Res.,* 13, 1300, 1998.
48. Fleck, N.A., Muller, G.M., Ashby, M.F., and Hutchinson, J.W., Strain gradient plasticity: theory and experiment, *Acta Metall. Mater.,* 42, 475, 1994.
49. Stölken, J.S. and Evans, A.G., A microbend test method for measuring the plasticity length scale, *Acta Mater.,* 46, 5109, 1998.
50. Fleck, N.A. and Hutchinson, J.W., Strain gradient plasticity, *Adv. Appl. Mech.,* 33, 295, 1997.
51. Nix, W.D. and Gao, H., Indentation size effects in crystalline materials: a law for strain gradient plasticity, *J. Mech. Phys. Solid.,* 46, 411–425, 1998.
52. Hutchinson, J.W., Plasticity at the micron scale, *Int. J. Solid. Struct.,* 37, 225, 2000.
53. Gao, H., Huang, Y, Nix, W.D., and Hutchinson, J.W., Mechanism-based strain gradient plasticity–I Theory, *J. Mech. Phys. Solid.,* 47, 1239, 1999.
54. Begley, M.R. and Hutchinson, J.W., The mechanics of size-dependent indentation, *J. Mech. Phys. Solid.,* 46, 2049, 1998.
55. Tadmor, E.B., Miller, R., Philips, R., and Ortiz, M., Nanoindentation and incipient plasticity, *J. Mater. Res.,* 14, 2233, 1999.
56. Maugis, D. and Pollock, H.M., Surface forces, deformation and adherence at metal microcontacts, *Acta Metall.,* 32, 1323, 1984.
57. Kral, E.R., Komvopoulos, K., and Bogy, D.B., Elastic-plastic finite element analysis of repeated indentation of a half-space by a rigid sphere, *J. Appl. Mech.,* 60,. 829, 1993.
58. Mesarovic, S.D. and Fleck, N.A., Spherical indentation of elastic-plastic solids, *Proc. Roy. Soc. Lond.,* A455, 2707, 1999.
59. Mesarovic, S.D. and Fleck, N.A., Frictionless indentation of dissimilar elastic-plastic spheres, *Int. J. Solid. Struct.,* 37, 7071, 2000.
60. Komvopoulos, K. and Ye, N., Three-dimensional contact analysis of elastic-plastic layered media with fractal surface topographies, *J. Tribol.,* 123, 632, 2001.
61. Kogut, L. and Komvopoulos, K., Analysis of the spherical indentation cycle for elastic-perfectly plastic solids, *J. Mater. Res.,* 19, 3641, 2004.

62. Kogut, L. and Etsion, I., Elastic-plastic contact analysis of a sphere and a rigid flat, *ASME J. Appl. Mech.*, 69, 657, 2002.
63. Jackson, R.L. and Green, I., A finite element study of elasto-plastic hemispherical contact against a rigid flat, *J. Tribol.*, 127, 343, 2005.
64. Etsion, I., Kligerman, Y., and Kadin, Y., Unloading of an elastic-plastic loaded spherical contact, *Int. J. Solid. Struct.*, 42, 3716, 2005.
65. Mesarovic, S.D. and Johnson, K. L., Adhesive contact of elastic-plastic spheres, *J. Mech. Phys. Solid.*, 48, 2009, 2000.
66. Kogut, L. and Etsion, I., Adhesion in elastic-plastic spherical microcontact, *J. Coll. Interface Sci.*, 261, 372, 2003.
67. Yan, S.L. and Li, L.Y., Finite element analysis of cyclic indentation of an elastic-perfectly plastic half-space by a rigid sphere, *Proc. Inst. Mech. Eng. C Mech. Eng. Sci.*, 217, 505, 2003.
68. Bhushan, B., Contact mechanics of rough surfaces in tribology: multiple asperity contact, *Tribol. Lett.*, 4, 1, 1998.
69. Adams, G.G. and Nosonovsky, M., Contact modeling—forces, *Tribol. Int.*, 33, 431, 2000.
70. Greenwood, J.A. and Williamson, J.B.P., Contact of nominally flat surfaces, *Proc. Roy. Soc. Lond.*, A295, 300, 1966.
71. McCool, J.I., Limits of applicability of elastic contact models of rough surfaces, *Wear*, 86, 105, 1983.
72. Greenwood, J.A. and Tripp, J.H., The contact of two nominally flat rough surfaces, *Proc. Inst. Mech. Eng.*, 185, 625, 1970.
73. Greenwood, J.A. and Tripp, J.H., The elastic contact of rough spheres, *J. Appl. Mech.*, 34, 153, 1967.
74. McCool, J.I., Extending the capability of the Greenwood Williamson microcontact model, *J. Tribol. Trans. ASME*, 122, 496, 2000.
75. Chang, R.W., Etsion, I., and Bogy, D.B., An elastic-plastic model for the contact of rough surfaces, *J. Tribol. Trans. ASME*, 109, 257, 1987.
76. Yu, N. and Polycarpou, A.A., Contact of rough surfaces with asymmetric distribution of asperity heights, *J. Tribol. Trans. ASME*, 124, 367, 2002.
77. Zhao, Y., Maietta, D.M., and Chang, L., An asperity microcontact model incorporating the transition from elastic deformation to fully plastic flow, *J. Tribol.*, 122, 86, 2000.
78. Fuller, K.N.G. and Tabor, D., The effect of surface roughness on the adhesion of elastic solids, *Proc. Roy. Soc. Lond.*, A345, 327, 1975.
79. Maugis, D., On the contact and adhesion of rough surfaces, *J. Adhes. Sci. Tech.*, 10, 161, 1996.
80. Adams, G.G., Müftü, S., and Mohd Azhar, N., A scale-dependent model for multi-asperity model for contact and friction, *J. Tribol. Trans. ASME*, 125, 700, 2003.
81. Morrow, C., Lovell, M., and Ning, X., A JKR-DMT transition solution for adhesive rough surface contact, *J. Phys. Appl. Phys.*, 36, 534, 2003.
82. Chang, R.W., Etsion, I., and Bogy, D.B., Adhesion model for metallic rough surfaces, *J. Tribol. Trans. ASME*, 110, 50, 1988.
83. Stanley, H.M., Etsion, I., and Bogy, D.B., Adhesion of contacting rough surfaces in the presence of sub-boundary lubrication, *J. Tribol. Trans. ASME*, 112, 98, 1990.
84. Kogut, L. and Etsion, I., A finite element based elastic-plastic model for the contact of rough surfaces, *Tribol. Trans.*, 46, 383, 2003.

85. Westergaard, H.M., Bearing pressures and cracks, *ASME J. Appl. Mech.*, 6, A49, 1939.
86. Johnson, K.L., Greenwood, J.A., and Higginson, J.G., The contact of elastic regular wavy surfaces, *Int. J. Mech. Sci.*, 27, 383, 1985.
87. Manners, W., Partial contact between elastic surfaces with periodic profiles, *Proc. Roy. Soc. Lond.*, A454, 3203, 1998.
88. Hui, C.Y., Lin, Y.Y., Baney, J.M., and Kramer, E.J., The mechanics of contact and adhesion of periodically rough surfaces *J. Polymer Sci. B Polymer Phys.*, 39, 1195, 2001.
89. Adams, G.G., Adhesion at the wavy contact interface between two elastic bodies, *J. Appl. Mech.*, 71, 851, 2004.
90. Berthe, D. and Vergne, Ph., An elastic approach to rough contact with asperity interactions, *Wear*, 117, 211, 1987.
91. Cha, P.-R., Srolovitz, D.J., and Vanderlick, T.K., Molecular dynamics simulation of a single asperity contact, *Acta Mater.*, 52, 3983, 2004.
92. Rebeiz, G.M. and Muldavin, J.B., RF MEMS switches and switch circuits, *IEEE Microw. Mag.*, 2, 59, 2001.
93. Zavracky, P.M., Majumder, S., and McGruer, N.E., Micromechanical switches fabricated using nickel surface micromachining, *IEEE ASME J. Microelectromech. Syst.*, 6, 3, 1997.
94. Ruan, M., Shen, J., and Wheeler, C.B., Latching micromagnetic relays *IEEE ASME, J. Microelectromech. Syst.*, 10, 511, 2001.
95. Taylor, W.P., Brand, O., and Allen, M.G., Fully integrated magnetically actuated micromachined relays, *J. Microelectromech. Syst.*, 7, 181, 1998.
96. Jansen, A.G.M., van Gelder, A.P., and Wyder, P., Point-contact spectroscopy in metals, *J. Phys.*, C13, 6073, 1980.
97. Wexler, G., The size effect and the non-local Boltzmann transport equation in orifice and disk geometry, *Proc. Phys. Soc.*, 89, 927, 1980.
98. Mikrajuddin, A., Shi, F.G., Kim, H.K., and Okuyama, K., Size-dependent electrical constriction resistance for contacts of arbitrary size: from Sharvin to Holm limits, *Mater. Sci. Semicond. Process.*, 2, 321, 1999.
99. Majumder, S., McGruer, N.E., and Zavracky, P.M., Electrostatically actuated micromechanical switches, *J. Vac. Sci.Tech.*, A15, 1246, 1997.
100. Majumder, S., McGruer, N.E., Adams, G.G., Zavracky, A.P., Zavracky, P.M., Morrison, R.H., and Krim, J., Study of contacts in an electrostatically actuated microswitch, *Sensor. Actuator.*, A93, 19, 2001.
101. Majumder, S., McGruer, N.E., and Adams, G.G., Adhesion and contact resistance in a MEMS switch, *IEEE ASME J. Microelectromech. Syst.*, under review, 2006.
102. Greenwood, J.A., Constriction resistance and the real area of contact, *Br. J. Appl. Phys.*, 17, 1621, 1966.
103. Kruglick, E.J.J. and Pister, K.S.J., Lateral MEMS microcontact considerations, *IEEE ASME J. Microelectromech. Syst.*, 8, 264, 1999.
104. Lafontan, X., Dufaza, C., Robert, M., Pressecq, F., and Perez, G., Concepts, characterization and modeling of MEMS micro-switches with gold contacts in MUMPS, *Proceedings of SPIE–International Society for Optical Engineering*, 4408, 381, 2001.
105. Beale, J. and Pease, R.F., Limits of high-density, low-force pressure contacts, *IEEE Trans. Comp, Pack. Manufact. Tech*, A17, 257, 1994.
106. Hyman, D. and Mehregany, M., Contact physics of gold microcontacts for MEMS switches, *IEEE Trans. Comp. Pack. Techn*, 22, 357, 1999.

107. Bromley, S.C. and Nelson, B.J., Performance of microcontacts tested with a novel MEMS device, *Electrical Contacts, Proceedings of the Annual Holm Conference on Electrical Contacts*, 2001, p. 122.
108. Kogut, L. and Komvopoulos, K., Electrical contact resistance theory for conductive rough surfaces, *J. Appl. Phys.*, 94, 3153, 2003.
109. Kogut, L. and Komvopoulos, K., Electrical contact resistance theory for conductive rough surfaces separated by a thin insulating film, *J. Appl. Phys.*, 95, 576, 2004.
110. Kogut, L. and Komvopoulos, K., Analysis of interfacial adhesion based on electrical contact resistance measurements, *J. Appl. Phys.*, 94, 6386, 2003.
111. Tringe, J.W., Uhlman, T.A., Oliver, A.C., and Houston, J.E., A single asperity study of au/au electrical contacts, *J. Appl. Phys.*, 93, 4661, 2003.
112. McCarthy, B., Adams, G.G., McGruer, N.E., and Potter, D., A dynamic model, including contact bounce, of an electrostatically actuated microswitch, *IEEE ASME J. Microelectromech. Syst.*, 11, 276, 2002.
113. Chen, L., McGruer, N.E., and Adams, G.G., Contact evolution in a micromechanical switch, *Proceedings of the World Tribology Congress III*, September 12–16, 2005, Washington DC, on CD ROM, WTC2005–63970, 2005.
114. Yan, X., McGruer, N.E., Adams, G.G., and Majumder, S., Finite element analysis of the thermal characteristics of MEMS switches, *The 12th International Conference on Solid State Sensors, Actuators and Microsystems*, Boston, MA, June 8–12, 2003, p. 412.
115. Jensen, B., Wang, Z., Saitou, K., Volakis, J.L., and Kurabayashi, K., Simultaneous electrical and thermal modeling of a contact-type RF MEMS switch, *Proceedings of the IMECE '03*, Washington, D.C., November 15–21, 2003.
116. Johnson, J., Adams, G.G., and McGruer, N.E., Determination of intermodulation distortion in a contact-type MEMS microswitch, *IEEE Trans. Microw. Theor. Tech.*, 53, 3615, 2005.
117. Duppopt, L. and Rebeiz, G.M., Intermodulation distortion and power handling in RF MEMS switches, varactors, and tunable filters, *IEEE Trans. Microw. Theor. Tech.*, 51, 1247, 2003.

Chapter 11

Nanoscale Defects and Surface Preparation in Nanomanufacturing

Ahmed Busnaina and Kaveh Bakhtari

Contents

11.1 Introduction....................251
11.2 Physical Removal Using Acoustic Streaming....................254
11.2.1 Boundary Layer Thickness....................255
11.2.2 Drag Force....................256
11.2.3 Adhesion Force....................258
11.2.4 Electrical Double Layer Force....................259
11.2.5 Rolling Removal Mechanism....................261
11.2.6 Particle Removal....................262
11.3 Experimental and Analytical....................263
11.3.1 Selective Removal of Nanoscale Defects....................265
11.3.2 Removal of Nanoscale Particles....................267
11.3.2.1 Effect of Particle Size....................267
11.3.2.2 Effect of Frequency....................269
11.3.3 Submicron Particle Removal from Deep Trenches....................274
11.4 Summary....................278
References.................... 279

11.1 Introduction

An era of the most challenging cleaning applications in nanomanufacturing is upon us. With the International Technology Roadmap for Semiconductors, which is focused solely on top-down manufacturing techniques, decreasing

particle removal requirements of 25 nm, and a surface concentration of 0.01 to 0.15 per cm^2 in 2011, the most challenging cleaning application requirements in semiconductor manufacturing is essential. The critical particle size (that would cause a defect) is expected to decrease to 18 nm by the year 2014.[1]

The field of particle removal and surface cleaning in general extends far beyond the electronics industry. Many applications in biological, medical (implants and equipment), aerospace, imaging, automotive, pharmaceutical, etc. extensively use surface cleaning as a preparation step for pre-or postpreprocessing. The need for clean substrates in nanoscale self-assembly or fabrication is a need that is well recognized. Similarly, the need for scrupulously clean wafers in the fabrication of microelectronic devices has been well recognized since the dawn of solid-state device technology. Clean substrate surfaces are critical in ULSI fabrication for obtaining maximum device performance, long-term reliability, and high yields. For instance in 0.18 μm CMOS technology about 80 of 400 process steps are surface cleaning.[1] Particles larger than about one-quarter of the minimum linewidth may cause fatal device defects. As semiconductor device geometry continues to shrink (60 nm by the year 2008)[2] and wafer sizes increase, the limitations of existing cleaning methods on device yield will become more critical as the size of "killer" particles also shrinks. In nanoscale manufacturing that need is increased by more than one order of magnitude. Surfaces prepared for nanoscale applications such as deposition of monolayers or directed or self-assembly of nanoelements (nanotubes, nanoparticles, etc.) need to be completely free of any particulate contamination equal or smaller than a nanometer depending on the process tolerance. A physical, substrate-independent, cleaning process is highly desirable because it does have to be modified for different substrates (as in a chemical-based cleaning process) and it does not have a potential for modifying the surface (such as etching or roughening).

Traditionally there are several particle removal techniques used in semiconductor fabrication and other industries affected by surface contamination. They include ultrasonics, megasonics, brush scrubbing, dry Argon ice cleaning, plasma etching, or wet etching. Low-frequency ultrasonic cleaning, at frequencies 25 to 200 KHz, is widely used in a variety of industries for cleaning purposes. However, the lower-frequency (25 to 200 KHz) cleaning is known in the industry as ultrasonic cleaning while the high frequency is known as megasonic cleaning (>400 KHz) due to differences in the cleaning mechanism, which has implications in terms of possible damage. The boundary between the two regimes has not been clearly defined yet but is in the range of 200 to 360 KHz. A typical ultrasonic cleaning system consists of piezoelectric transducers attached to the bottom of a tank that typically vibrate at a single frequency. The transducer vibrations are transmitted to the cleaning solution, creating longitudinal pressure waves. Cavities form in the liquid when its tensile strength is exceeded due to rapid alternation between positive and negative pressure as the sound wave propagates through the liquid. Both transient and stable cavities can be formed. Transient cavities, which occur at low frequency, change size rapidly and can implode to cause surface

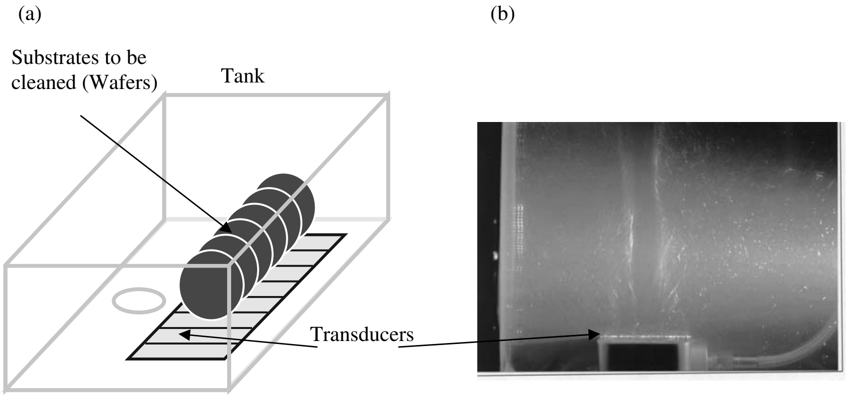

Figure 11.1 (a) Schematic of megasonic cleaning tank. (b) A flow visualization photo showing the bulk acoustic streaming (Eckart streaming) above the transducer.

damage, whereas stable cavities, which occur at high frequency, change very little in size and do not implode.[3–5] The major drawback to ultrasonic cleaning is the surface damage caused by the implosion of these bubbles (called cavitation).

The megasonic cleaning process was introduced for the first time by RCA to the semiconductor industry.[6] Megasonic cleaning, with transducer frequencies typically 360 to 1200 KHz, is widely used in semiconductor (for wafer cleaning) and the hard disk industry. In megasonic cleaning, wafers are immersed above the transducers in a cleaning liquid medium to which sonic energy is applied. A schematic of a typical megasonic tank (used to clean silicon wafers) is shown in Figure 11.1. High-intensity (usually measured in W/cm^2 input to the transducers) sound waves generate pressure fluctuations and acoustic streaming that detach the particles from the surface and remove them.

Busnaina and Gale have shown that cavitation implosion does not occur in megasonic cleaning and that the dominant cleaning mechanism is the acoustic streaming induced by the sound waves.[7] Busnaina et al.[3–5,8,9] studied megasonic particle removal and the effect of acoustic streaming on many cleaning processes especially in postchemical mechanical polishing applications. High particle removal efficiency on Si from megasonics in SC1 and SC2 solutions was also reported by Syverson et al.[10] Again, removal increased with increasing power, up to a maximum tested value of 150 W. Wang and Bell.[11] performed experiments using megasonics for cleaning after Reactive Ion Etch (RIE) planarization. Of the parameters they tested, power had the greatest influence on the results.

The brush scrubbing process uses a soft cylindrical polyvinyl alcohol (PVA) brush that rotates across the surface of a wafer while a water jet is directed at the surface or through the porous brush. It is considered to be the most effective method of removing polishing slurry from the wafer

surface in the post-chemical mechanical polishing (CMP) cleaning process. Reportedly, particles as small as 120 nm have been effectively removed by brush scrubbing. However, the technique is susceptible to particle loading that results in scratching, surface damage, and particle redeposition.

Cryogenic aerosol spray techniques remove particles by bombarding the wafer surface with high-velocity frozen ice particles (cryogenic aerosols) of such inert gases as argon or CO_2. They dislodge particles by transferring kinetic energy from high-velocity aerosols to particles and by transient cooling of the substrate and inducing an expansion difference between particle and substrate.[12] Greater than 99% removal of particles larger than 150 nm has been demonstrated. However, CO_2 has not been shown suitable for semiconductor wafer cleaning because it adds many organic particles condensed by the rapid cooling, and the argon cleaning, although efficient and not adding contaminants, uses a very large amount of gas and, unlike CO_2, cleaning it has to be done in vacuum. Laser-cleaning techniques remove particles by using short-pulsed laser irradiation of a surface. It has been demonstrated to be a promising approach for effective removal of particulate contamination of sizes as small as 100 nm[13,14] and thus may become a yield enabler for 0.18 μm design rules and smaller. However, the extreme thermal shock experienced by the surface is responsible for destroying any film on the wafer, which makes it unsuitable for cleaning patterned wafers with thin films.

11.2 Physical Removal Using Acoustic Streaming

Particles can be removed through the following mechanisms: lifting, sliding, and rolling. The removal process may be a combination of two of these mechanisms. The lifting mechanism is used a great deal in contact cleaning, whereas the rolling mechanism is dominant in noncontact cleaning. Megasonic cleaning is the most widely used noncontact cleaning technique. Particle removal in megasonic cleaning relies heavily on acoustic streaming and the reduction of the boundary layer thickness on the substrates. The mechanics of physical particle removal of nanoscale particles will be explained fully in this section.

Kaskoush et al.[15] found that increasing the frequency above 300 KHz could eliminate the damage on wafer surfaces during wafer cleaning. Gale and Busnaina[16] studied the mechanisms of particle removal in megasonic and ultrasonic cleaning, including the effects of frequency, temperature, and power density.

Acoustic streaming is considered to be the key cleaning mechanism in the removal of submicron particles.[17,18] According to Olim,[19] theoretically it is not possible to remove particles below 100 nm using megasonic cleaning. But in practice, particle sizes down to and less than 100 nm have been effectively removed using megasonics. The reason for the underestimation of Olim's model is that the viscous drag force and the double layer force were not included in the model. Preliminary experiments for the removal of nanoscale

particles (90-, 63-, and 28-nm polystyrene latex (PSL) particles) were conducted using single-wafer megasonic cleaning by Bernard et al.[20] Lin has developed theoretical models to predict removal rates of nanoparticles from silicon wafers.[21]

11.2.1 Boundary Layer Thickness

One of the most important aspects of megasonic cleaning is the size of the acoustic boundary layer, which is very small compared with a typical hydrodynamic boundary layer at the same velocity. The acoustic boundary layer thickness is a function of the acoustic frequency ω ($\omega = 2\pi f$) and the viscosity of the cleaning liquid v:

$$\delta_{ac} = \left(\frac{2v}{\omega}\right)^{\frac{1}{2}} \tag{11.1}$$

By contrast, the hydrodynamic boundary layer is a function of velocity, distance, and viscosity:

$$\delta_H = 0.16\left(\frac{v}{Ux}\right)^{\frac{1}{7}} \cdot x \tag{11.2}$$

where U is the fluid velocity and x is the distance from the leading edge of the wafer.

Figure 11.2 shows that the hydrodynamic boundary layer thickness is larger than 1000 micron (at the center of an 8-inch disk or wafer) in water with $u = 0-4$ m/s. In water, the acoustic boundary layer thickness is 0.61 μm, 0.65 μm, and 0.94 μm for frequencies of 850 KHz, 760 KHz, and 360 KHz, respectively. The acoustic boundary layer exposes submicron particles on the surface to much larger velocities and increases the particle removal efficiency. In a cleaning tank, megasonic waves can be modeled as plane waves traveling between two infinite-length parallel planes. Acoustic streaming velocity at the center of a tank is defined as[22]

$$u = \frac{8\pi^2}{3\rho c^4} \cdot If^2\left(\frac{h^2}{4} - z_1^2\right) \propto If^2 \tag{11.3}$$

where ρ is the density of the cleaning liquid and c is sound speed in liquid. In water, $c = 1481$ *m/s*, I is the intensity of the megasonic wave, f is the frequency of the megasonic wave, h is the distance between the walls, and z_1 is the distance between the plate and the edge of the sound beam.

The effect of acoustic frequency on boundary layer thickness and acoustic streaming velocity is presented in Figure 11.3. As the frequency increases, acoustic streaming velocity also increases but the boundary layer thickness

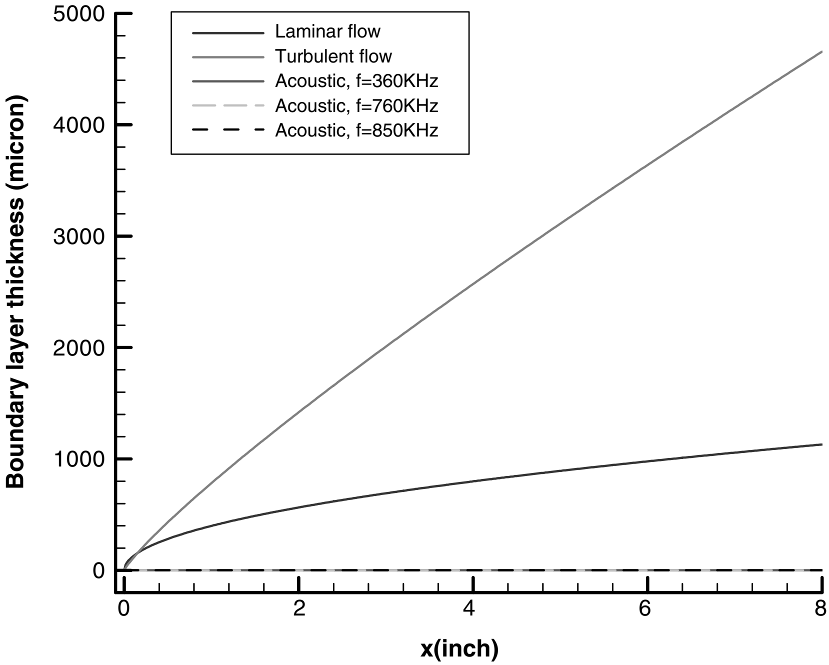

Figure 11.2 Boundary layer thickness vs. distance.

decreases rapidly. The incompressible limitation in water, u = 444.3 m/s (30% of sound speed in water), is reached at a frequency of 8.34 MHz, which induces a 196-nm thick boundary layer.

11.2.2 Drag Force

The acoustic streaming applied to a particle on a surface induces a drag force parallel to the flow direction. The drag force acting on a spherical particle in a Newtonian fluid can be expressed by the following equation:

$$F_D = \frac{C_D}{C_C}\frac{\pi}{8}\rho_f d_p^2 u^2 \tag{11.4}$$

where C_D is drag coefficient.

In linear shear flow boundary layer, distribution of the drag force on a particle is shown in Figure 11.4.

O'Neill[23] showed that when a uniform linear shear flow passes a sphere on a wall, the drag force will be

$$F_D = 1.7 \cdot 6\pi\mu R U_R \approx 32R^2\tau_0 \tag{11.5}$$

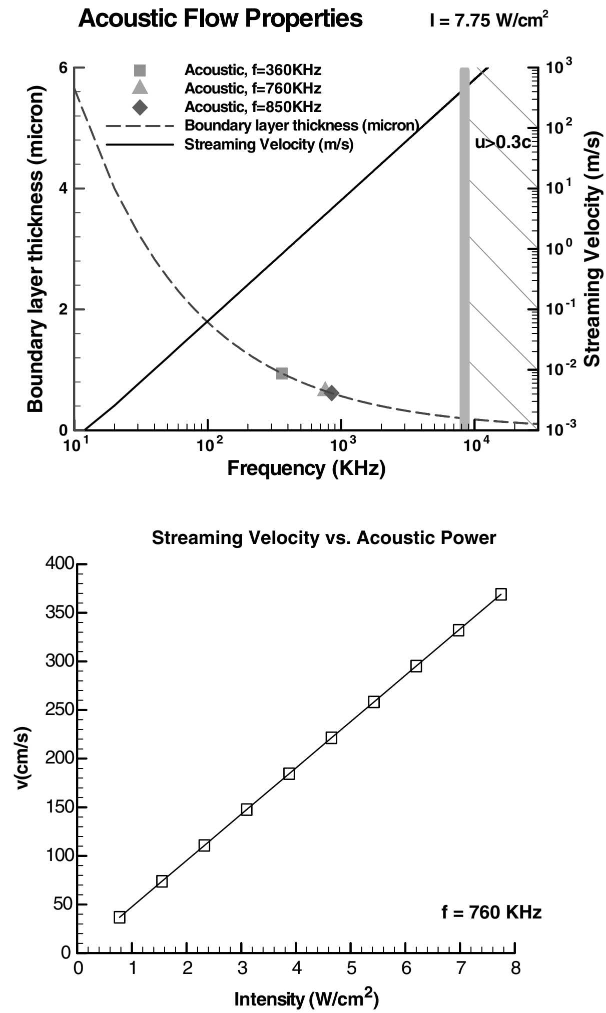

Figure 11.3 Boundary layer thickness and acoustic streaming velocity vs. frequency and intensity (top) and velocity vs. intensity (W/cm^2) (bottom).

where μ is viscosity of the fluid and τ_0 is the wall shear stress.
And the moment about the center of the sphere is given by

$$M_D = 0.944 \cdot 8\pi \mu R^2 U_R \approx 23.7 R^3 \tau_0 \tag{11.6}$$

and the exact solution of the total drag moment about the touching point, shown in Figure 11.4, is given by

$$M_D + F_D R = 55.7 R^3 \tau_0 = 1.74 F_D R \tag{11.7}$$

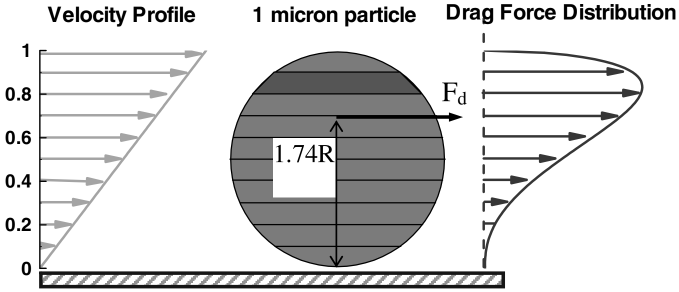

Figure 11.4 Distribution of the drag force on a particle.

where, F_D is the drag force, R is the radius of the particle, and U_R is the velocity of the fluid.

11.2.3 Adhesion Force

In order to predict particle removal efficiency, particle removal and adhesion forces have to be known. Without any external load applied on the particle, its adhesion onto the surface is caused by the omnipresent van der Waals force in the first instance. For all atoms and molecules, even for nonpolar ones, there exist instantaneous dipoles. And the interaction between these dipoles and the induced dipoles in neighboring atoms results in the dispersion forces of atoms/molecules, which is the dominant portion of the van der Waals force.

Hamaker[25] calculated the interaction between macroscopic bodies simply by using the principle of additivity of interactions between all molecules in each body. The adhesion of submicron or nanoparticles is dominated by the van der Waals force, which is given by[26]

$$F_{vdw} = \frac{AR}{6z_0^2} \tag{11.8}$$

The attractive force F_{vdw} deforms the interface and a circular adhesion area is formed between the adherents. The equation above does not take into account the adhesion force component due to deformation. Bowling[27]gave the total adhesion force, including the component due to the deformation, as

$$F_{ad} = F_{vdw} + F_{vdw-deform} = \frac{AR}{6z_0^2}\left(1 + \frac{a^2}{Rz_0}\right) \tag{11.9}$$

where, A is the Hamaker constant, R is the radius of the spherical particle, z_0 is the separation distance between the particle and the substrate (for smooth surfaces it is taken as 4 Å), and a is the contact radius between the deformed particle and the surface.

Present understanding of particle adhesion is dominated by three theories: DMT (Derjaguin–Muller–Toporov), JKR (Johnson–Kendall–Roberts), and MP (Maugis and Pollock) models. The JKR and DMT models are used to describe adhesion of elastically deforming systems. The MP model accounts for tensile interactions and plastic deformations.

Maugis and Pollock expanded the JKR model to the region where the surface force–induced stress exceeds the yield strength of the contacting material,[27] which is the plastic region.

$$a = \sqrt{\frac{2W_a R}{H}} \tag{11.10}$$

where W_a is the work of adhesion between the particles and the surface.

$$W_a = 2\sqrt{\gamma_1 \gamma_2} \tag{11.11}$$

where γ_1 and γ_2 are surface free energies of the particle and the substrate. H is the hardness. Adhesion-induced deformation will occur when the particle is softer than the substrate or vice versa. Busnaina et al.[28–30] show that the adhesion-induced deformation is plastic in the case of polystyrene particles on silicon and that it may take up to 70 hours to reach equilibrium. They also show that if the particles are removed within an hour or less after deposition, the adhesion force and removal is not affected. However, removal is still feasible, but more difficult, after a longer time.

11.2.4 Electrical Double Layer Force

When an uncharged surface is immersed into a liquid, it will attain a surface charge due to preferential adsorption of ions present in the liquid or due to dissociation of surface groups. The final surface charge has to be balanced by an equal but oppositely charged region of counter-ions, some of which are bound to the surface within the so-called Stern layer, while others form the diffuse electric double layer. Both layers are shown in Figure 11.5.

According to the Hogg-Healy-Fuerstenau (HHF) model, the electrical double layer force interacting between a sphere and a plate with constant potential can be expressed[31] as

$$F_{el}^{\Psi} = \pi \varepsilon_r \varepsilon_0 R\left(\Psi_{01}^2 + \Psi_{02}^2\right)\frac{\kappa e^{-\kappa H}}{1 - e^{-2\kappa H}}\left[\frac{2\Psi_{01}\Psi_{02}}{\Psi_{01}^2 + \Psi_{02}^2} - e^{-\kappa H}\right] \tag{11.12}$$

where Ψ_{01} is the zeta potential of the particle of radius R, Ψ_{02} is the zeta potential of the substrate, ε_r is the dielectric constant of the medium, ε_0 is the dielectric permitivity of a vacuum, and κ the Debye–Huckel parameter of the electrolyte solution. High negative zeta potentials are measured at high pH solution for SiO_2, Al_2O_3, W, and PVA,[32] and also for Si and PSL.

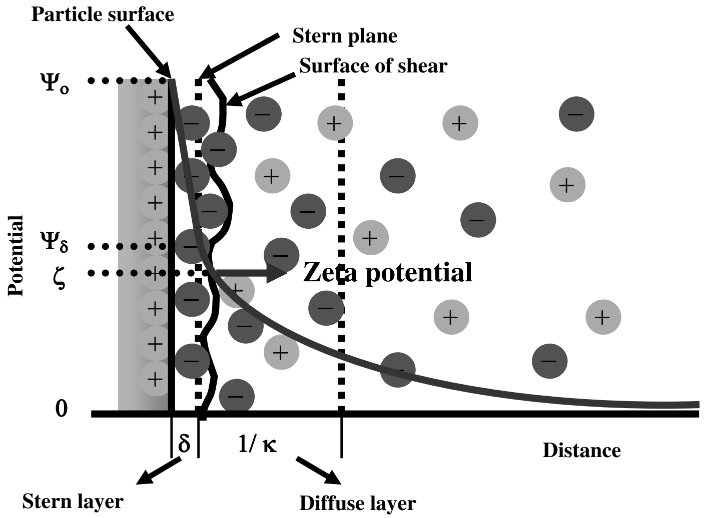

Figure 11.5 Schematic of zeta potential and the double layer.

Using a high-pH cleaning solution, such as SC1 or ammonia, a strong repulsion occurs between the particle and the substrate, reducing the total adhesion force and enhancing the removal of these particles.

The effect of the double layer on particle removal is through the charge (zeta potential) on the particles (as well as the wafer surface). The zeta potential will typically decrease from –40 mv at pH = 7 to –80 mv at pH = 11. This will significantly increase the double layer repulsive force between the particles and the wafer because the repulsion force is a function of the magnitude of the charge (zeta potential) on the particle and the wafer surface. This will decrease the total adhesion force (due to the net Derjaguin, Landau, Verwey and Overbeck (DLVO) potential) between the particle and the wafer, and that makes the needed physical removal force applied by the acoustic streaming through drag and lift force much lower. It has been shown that for particles with a low (less than 1 eV) van der Waals constant, $h\bar{\omega}$ (also known as the Liftshitz–van der Waals constant), and a repulsive double layer, particles may separate upon immersion without applying an external force. Particle detachment by simply changing the pH has also been shown using the packed column technique by Matijevic et al. It is apparent that this may work only for very small particles (less than 20 nm) and with a low van der Waals constant; however, this shows that the van der Waals force may be overcome or greatly reduced by the double layer force when a repulsive double layer is present. The van der Waals constant is related to the Hamaker constant, A, by a factor of $3/4\pi$ ($A = 3/4\pi\, h\bar{\omega}$). The van der Waals constant, $h\bar{\omega}$, for silica on a silicon oxide surface in water is slightly larger than 1 (1.25 eV), which shows that a small physical force (drag) is needed to overcome the total adhesion force.

11.2.5 Rolling Removal Mechanism

There are three different mechanisms for particle removal: sliding, rolling, and lifting. The force required to remove a particle by rolling is less than that required by sliding or lifting.[33–36] Both adhesion and removal forces increase as the particle size increases. The drag force induced by acoustic streaming is larger than that induced by hydrodynamic flow at the same velocity. For acoustic streaming flow with constant megasonic intensity, higher frequency leads to larger drag force because of larger streaming velocity and thinner acoustic boundary layer. The megasonic cleaning creates a tangential drag force on the particle, which results in particle removal by the rolling mechanism.

The force and moment applied on a single particle are shown in Figure 11.6. In this figure Δ is the deformation height of the particle. The ratio of the removal moment to the adhesion resisting moment, MR, is given by

$$\frac{F_d(1.74R-\Delta)+F_{dl}\cdot a}{F_a\cdot a} \tag{11.13}$$

where MR is the moment ratio, Δ is the deformation height of the particle, a is the contact radius between the deformed particle and the surface, F_d is the drag force, F_{dl} is the double layer force, and F_a is the adhesion force.

When the removal moment overcomes the adhesion moment, theoretically the particle is removed by rolling. The drag moment acting on the particle will lead the particle to roll over and detach from the surface.[37]

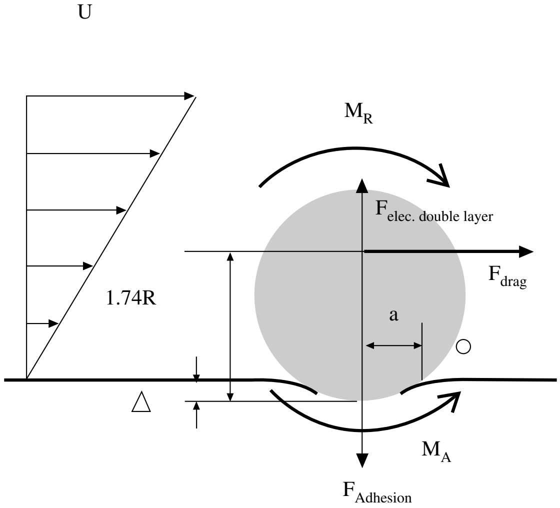

Figure 11.6 Schematic of the force and moment on a particle adhered to a surface. K. Bakhtari, R.O. Guldiken, P. Makaram, A. Busnaina, and J.G. Park, "Experimental and numerical investigation of nanoparticle removal using streaming and the effect of time," J. of Electrochemical Society, Vol. 153, 9, 2006 (in press 041609IES).

11.2.6 Particle Removal

When RM is greater than 1, the particle is rolled away. Figure 11.7 shows the theoretical results of rolling removal of particles in the range of 10 nm to 10 micron. RM increases with particle size. $RM_{SiO_2} >> RM_{PSL}$, namely, harder particles are easier to remove because they are less prone to adhesion-induced deformation. Acoustic flow (at 4 m/s) can remove all silica particles in the shown range and PSL particles larger than 50 nm. Hydrodynamic flow (at 4 m/s) can remove silica particles larger than 10 microns only. The streaming velocity used here (4 m/s) can be obtained by using a megasonic wave with I = 7.75 W/cm^2 and frequency larger than 800 KHz.[5,9] As illustrated in Figure 11.8, higher acoustic frequency leads to larger removal/adhesion moment ratio. The removal of nanosized particles (100 nm) is achievable by using acoustic streaming at frequencies larger than 400 KHz.

In addition to the physical megasonic effect in removing particles, the use of chemistry has shown a big improvement in cleaning efficiency. Using SC1 (Figure 11.9), typical megasonic flow (7.75 W/cm^2, 800 KHz, 4 m/s streaming velocity) can remove all silica particles in the shown

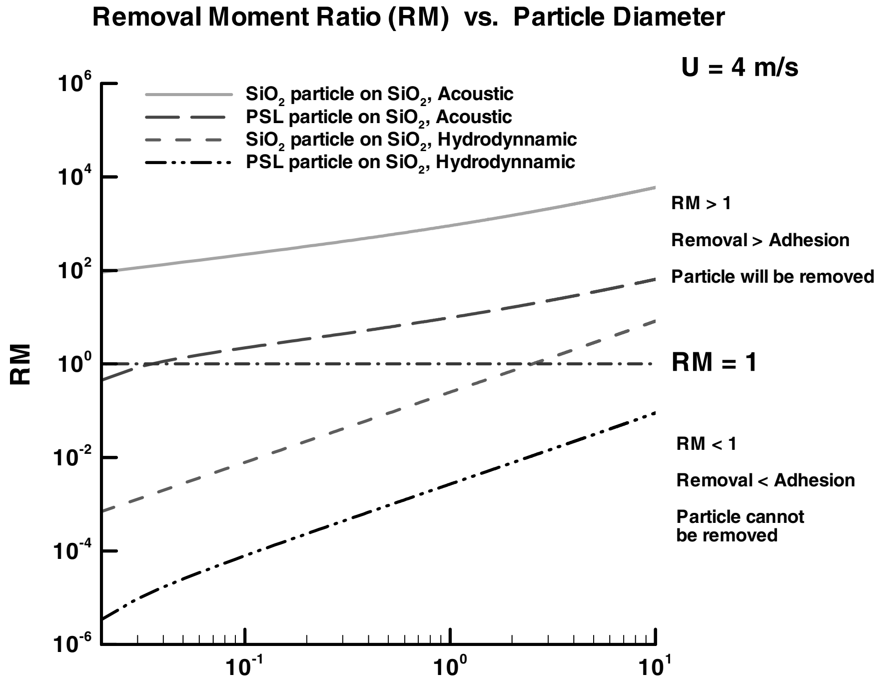

Figure 11.7 Particle removal by acoustic and hydrodynamic flow.

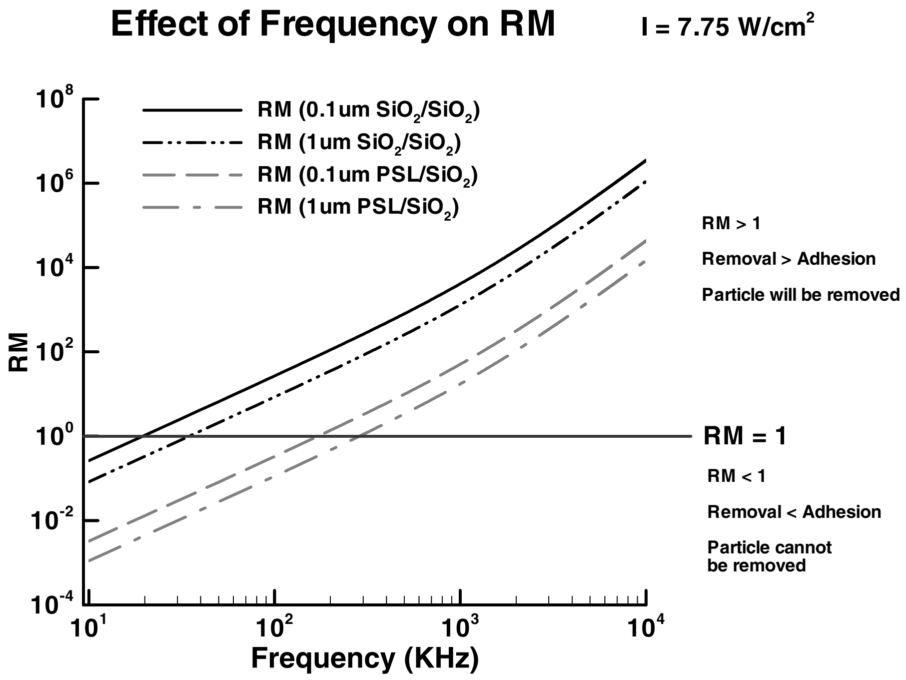

Figure 11.8 Effect of frequency on RM.

range (10 nm to 10 micron) and PSL particles larger than 310 nm. Hydrodynamic flow without megasonics (at 4 m/s) can remove silica particles larger than 0.34 micron and PSL particles larger than 9.07 micron. Figure 11.10 shows the experimental results of silica particle removal. The figure shows that when RM > 1, particle removal percentage is near 80%.

In addition to the physical megasonic effect in removing particles, the use of chemistry has shown a big improvement in cleaning efficiency. The cleaning mechanism in SC1 is based upon the separation of the particles from the substrate by the introduction of an electrostatic repulsion between particles and wafer. The adsorption of the OH^- species on the particles (SiO_2) and wafer, in alkaline pH, is responsible for the creation of a negative zeta potential. The electrostatic repulsion prevents the redeposition of the removed slurry particles. In addition, the ammonium hydroxide acts as a small-scale etchant for the silicon dioxide layers. Thus, particles are undercut by this small-scale etching.

11.3 Experimental and Analytical

Contamination and defects, mainly process generated, are responsible for as much as 75% or more of the yield loss in integrated circuit fabrication[38] and other microfabrication processes. It is expected that controlling contamination

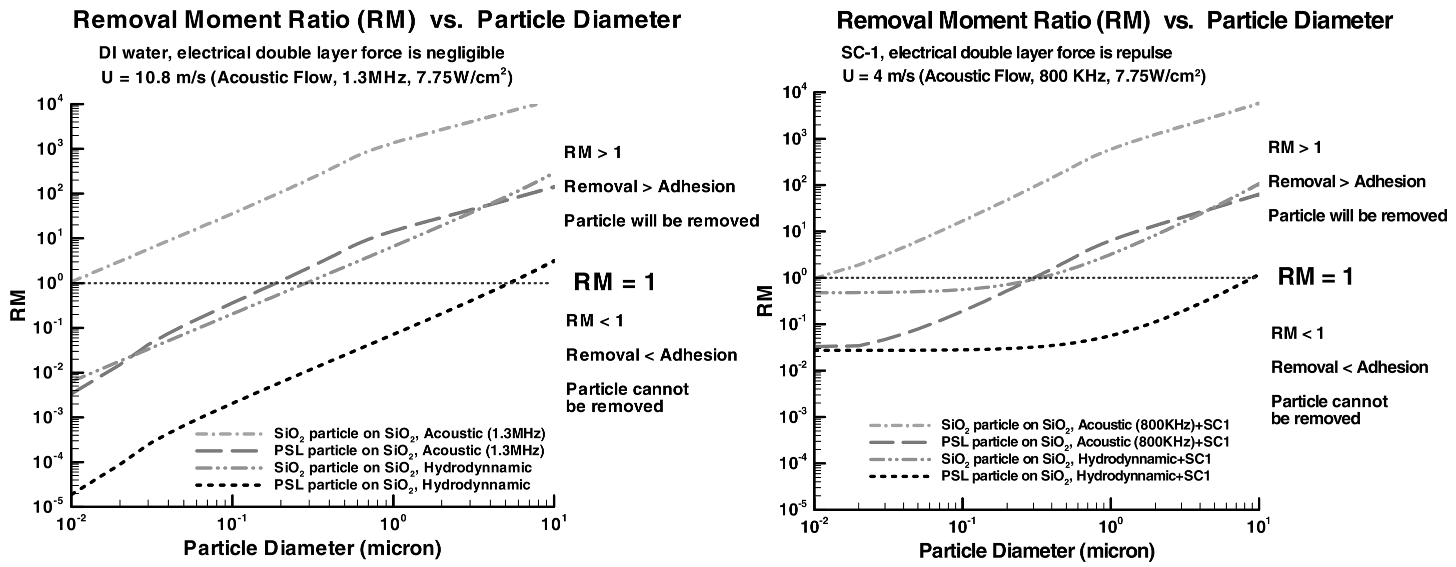

Figure 11.9 Nanoparticle removal in DI water using 1.3 MHz (left) and in SC1 (basic solution) using 800 KHz (right).

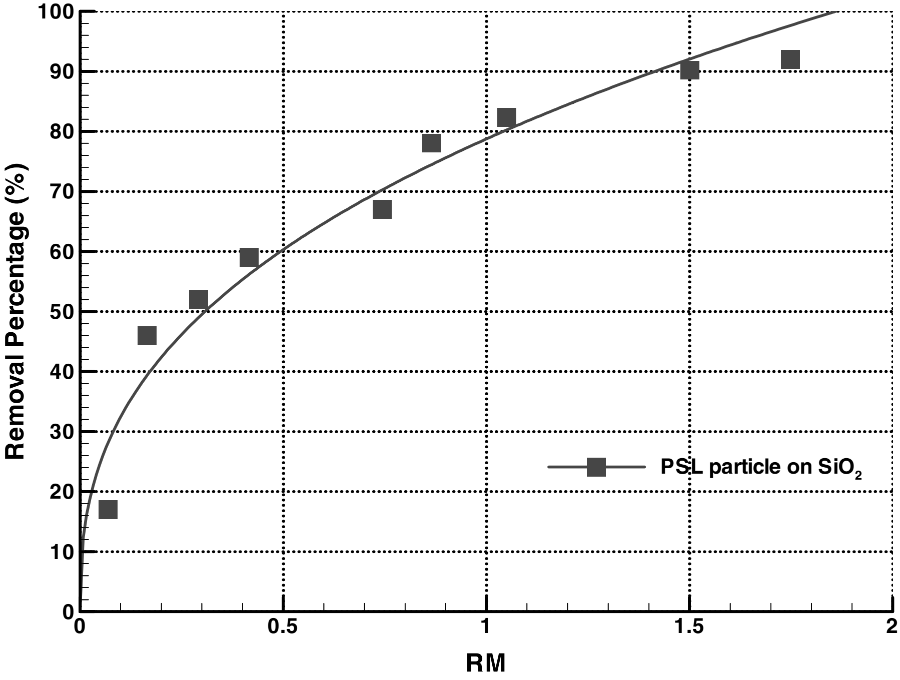

Figure 11.10 Experimental results showing removal percentage vs. the moment ratio (RM) for submicron silica particles.

and the detection and removal of defects will have an adverse impact on nanomanufacturing if these areas are not fundamentally addressed now. Surfaces prepared for nanoscale applications, such as deposition of monolayers or self-assembly of nanoelements, need to be completely free of any particulate contamination on the order of a nanometer or less. This does not necessarily mean a cumbersome and expensive clean room environment. Substrates could be isolated from the manufacturing environment and contaminants can be kept away. It has been shown that the dependence of the adhesion force on time and environmental conditions, especially in nanoscale polymer particles, is significant.[39] Large increases in adhesion force make defect removal extremely difficult. Nanoscale contamination removal from nanostructures has been studied both experimentally and theoretically using numerical modeling. One promising approach is the use of high-frequency pulsating flow (acoustic streaming) to enhance transport from small cavities (e.g., deep trenches and vias) by enhanced convective mixing.[40–42]

11.3.1 Selective Removal of Nanoscale Defects

An example of finding the right parameters in the moment ratio equation in order to selectively remove the particles from a template is shown in Figure 11.11.

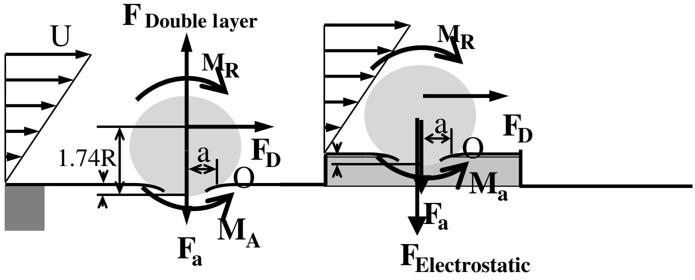

Figure 11.11 Selective removal by precisely controlling the removal parameters.

The gold wire has a higher Hamaker constant than the silicon dioxide surface resulting in a higher adhesion force on the surface and the particle. On the other hand, the double layer force in the case of particle-SiO_2 is in favor of removal but the electrostatic attraction between particle-Au is in favor of adhesion. Therefore, the force required for removing the particle from SiO_2 is less than the force required to remove the particle from Au. That means, if we control the removal force we will be able to keep the particle on the gold substrate while removing the particle on the silicon dioxide surface.

The experimental result for selective cleaning is shown in Figure 11.12. Figure 11.12a shows that fluorescent nanoparticle assembly without cleaning control leaves many particles between the wires that are undesirable. Figure 11.12b shows that when cleaning control is applied, most of the particles are gone. This can be accomplished by understanding the adhesion and removal force of these nanoparticles on the different surfaces and controlling the applied fluid velocity (used for cleaning) on the particles such that only the undesirable particles are removed.

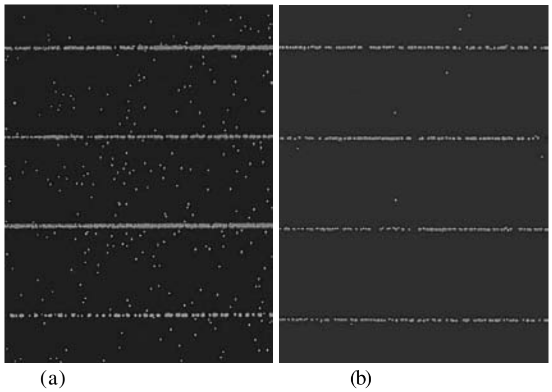

(a) (b)

Figure 11.12 Assembly of fluorescent nanoparticles assembly (a) without cleaning control and (b) with cleaning control.

11.3.2 Removal of Nanoscale Particles

11.3.2.1 Effect of particle size

The removal efficiency of 63-nm polystyrene latex (PSL) particles on bare silicon and 4-nm Si-Cap layer wafers has been investigated. The acoustic streaming velocity in the tank has been used to calculate the drag moment inserted on the particle. The double layer force has also been calculated based on the zeta potential and pH of the cleaning solution. Because PSL is a relatively soft material, the adhesion-induced deformation could be significant. This large deformation leads to higher adhesion force and more difficult removal process. The moment ratio for DI-water and dilute SC1 chemistry (1:2:40 ammonium hydroxide, hydrogen peroxide, and DI water) is:

Bare silicon: RM = 1.2 for DI water and RM = 1.37 for SC1 solution.
4-nm Si-Cap layer: RM = 1.17 for DI water and RM = 1.21 for SC1 solution.

The experimental and theoretical values for removal efficiency after 2 minutes using the megasonic tank are plotted in Figure 11.13.

It should be noted that the removal model used here accounts for only Ekcart streaming, which is considered the dominant mechanism. There are two other streaming mechanisms: Schlichting streaming and microstreaming. Microstreaming, another important mechanism, is very difficult to predict and could contribute 10 to 20% or more to the removal. Thus, the removal force used in the removal moment is not the only removal force on the nanoparticle. So the theoretical values for removal efficiency may be slightly different from the experimental values, but they follow the same trend.

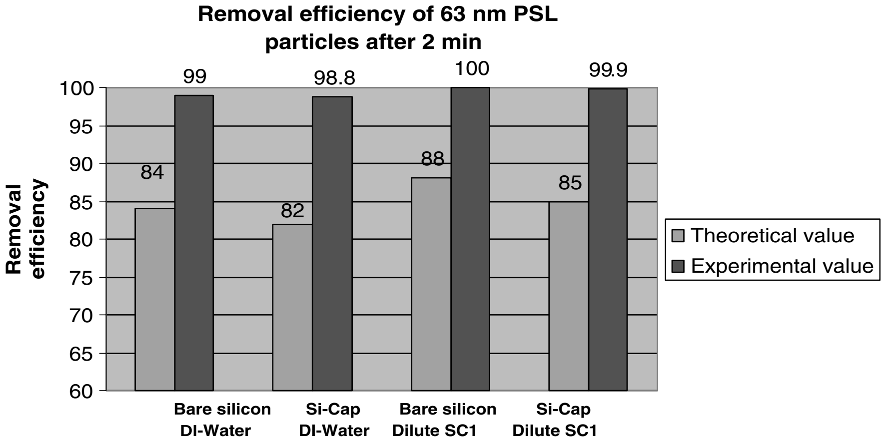

Figure 11.13 Experimental and theoretical removal efficiency values. K. Bakhtari, R.O. Guldiken, P. Makaram, A. Busnaina, and J.G. Park, "Experimental and numerical investigation of nanoparticle removal using streaming and the effect of time," J. of Electrochemical Society, Vol. 153, 9, 2006 (in press 041609IES).

The double layer force, which can be attractive or repulsive, also plays a role in the removal of particles. In SC1 solutions with a high pH the particle is more repulsive compared with DI water, resulting in higher moment ratios.

The experimental procedure was as follows: red fluorescent 63-nm PSL particles were deposited on 8-inch bare silicon wafers using a nebulizer. The wafer was then exposed to sonic energy using a single wafer megasonic tank with a frequency of 760 KHz. An optical autoscanning fluorescent microscope, Nikon Optiphot 200D, was used to scan the particles. Image Pro-plus software was used to count the particles located at a specified location. After 2 minutes, an average removal efficiency of 99% using DI water and complete removal using SC1 was achieved. Due to the stronger adhesion moment between the particles and the 4-nm Si-Cap, the removal efficiency was lower compared with bare silicon. The use of SC1 instead of DI water provided higher removal efficiency in the case of 63-nm PSL particles on both substrates due to the higher repulsive double layer force.

The time effect has also been investigated experimentally as shown in Figure 11.14. A computational fluid dynamic model is developed to investigate the time effect. This model captures the particle behavior within the boundary layer.

The particle detachment from the surface of the wafer is analyzed using the removal moment equations. According to the simulation, removed particles undergo a circulatory and back-and-forth motion as shown in Figure 11.15. The particle trajectory shows the redeposition of particles on the substrate. This redeposition results in longer cleaning time to achieve complete removal.

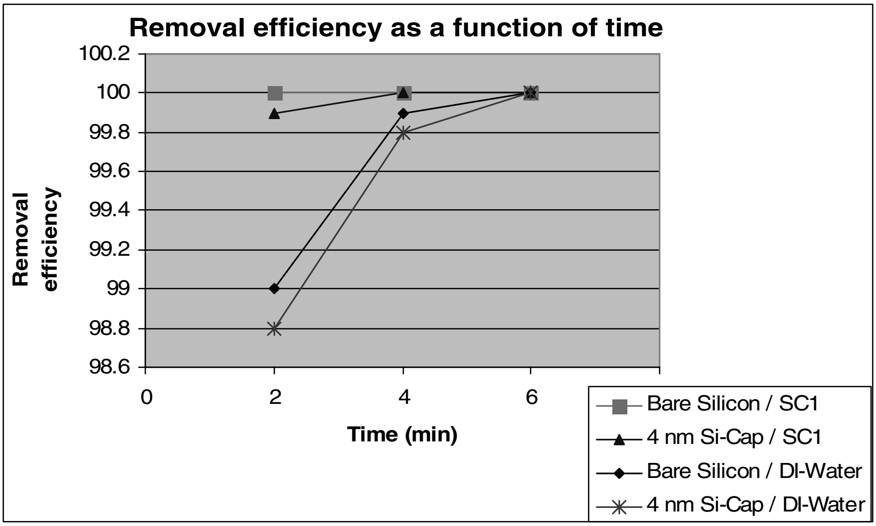

Figure 11.14 Removal efficiency as a function of time. K. Bakhtari, R.O. Guldiken, P. Makaram, A. Busnaina, and J.G. Park, "Experimental and numerical investigation of nanoparticle removal using streaming and the effect of time," J. of Electrochemical Society, Vol. 153, 9, 2006 (in press 041609JES).

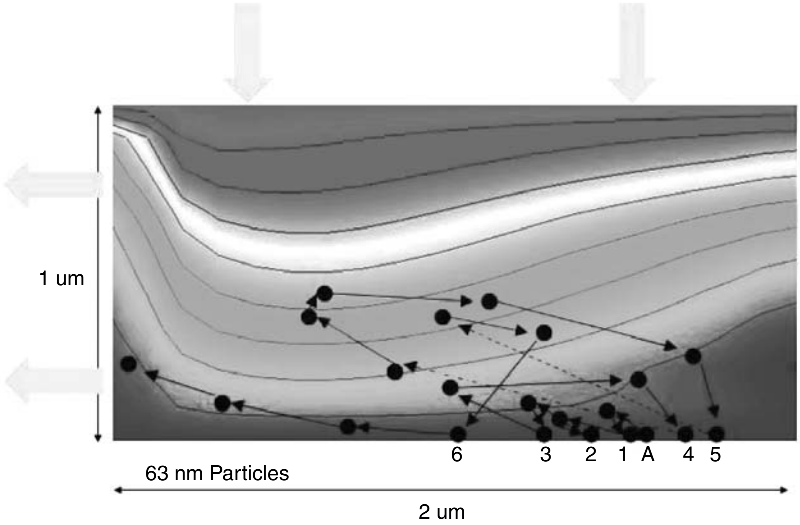

Figure 11.15 Trajectory of 63 nm particle. K. Bakhtari, R.O. Guldiken, P. Makaram, A. Busnaina, and J.G. Park, "Experimental and numerical investigation of nanoparticle removal using streaming and the effect of time," J. of Electrochemical Society, Vol. 153, 9, 2006 (in press 041609JES).

Figure 11.15 shows the trajectory of a 63-nm particle located at the center of the wafer in the megasonic tank. The model is a 2-D model and shows the redeposition of the particle after it travels 2 microns along the wafer. Point A is the original position of the particle. The simulation shows the particle deposits as much as six times on the surface of the wafer before it moves 2 microns toward the outer edge of the wafer. The longer cleaning time was observed for nanoparticles experimentally and numerically. To assess the effect of size on the cleaning time, the trajectory of a larger particle (500 nm) was modeled under the same conditions. The particle trajectory shows that no redeposition occurs and that the particle is being carried away from the surface. This trajectory is shown in Figure 11.16.

11.3.2.2 Effect of Frequency

Complete removal of 63-nm PSL particles was demonstrated on native oxide 8-inch silicon wafers using acoustic streaming in DI water. The acoustic wave generator was a 7-W/cm^2 transducer with a frequency of 760 KHz. Figure 11.17 illustrates the removal efficiency of the 63-nm PSL particles from an Extreme Ultra Violet (EUV) mask (6-inch-square substrate) that has an 11-nm silicon capping layer that has a higher adhesion force than the native oxide silicon wafer. After 2 minutes 95% of the particles were removed. Removal efficiency data were calculated every 2 minutes until complete removal was achieved. Cleaning for 8 minutes was required before complete removal was accomplished. This introduces a time effect that is not well understood and that has not been addressed by researchers.

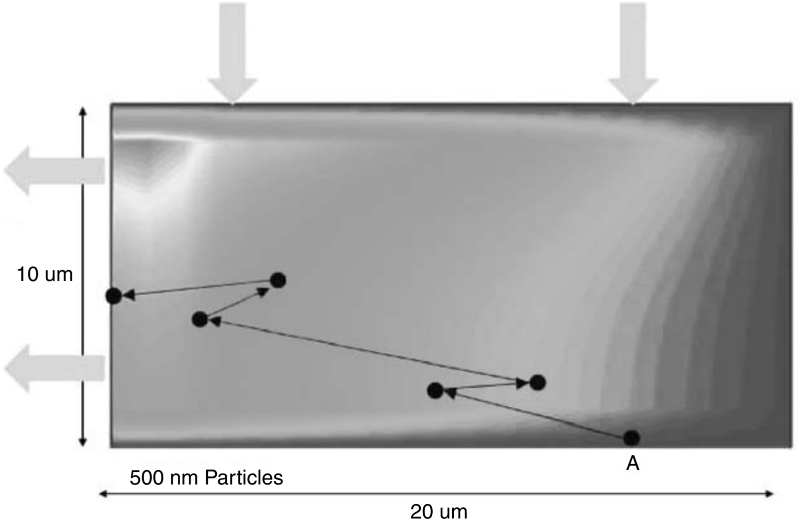

Figure 11.16 Trajectory of 500-nm particles. K. Bakhtari, R.O. Guldiken, P. Makaram, A. Busnaina, and J.G. Park, "Experimental and numerical investigation of nanoparticle removal using streaming and the effect of time," J. of Electrochemical Society, Vol. 153, 9, 2006 (in press 041609JES).

A computational fluid dynamic (CFD) model has been developed to get a better understanding of the detachment mechanism and the particle removal and transport during megasonic cleaning and the effect of time and frequency on cleaning. These simulations have provided a unique approach to compare nanoparticle removal time for different megasonic frequencies. The acoustic streaming and pressure fluctuations are created by transducers that operate

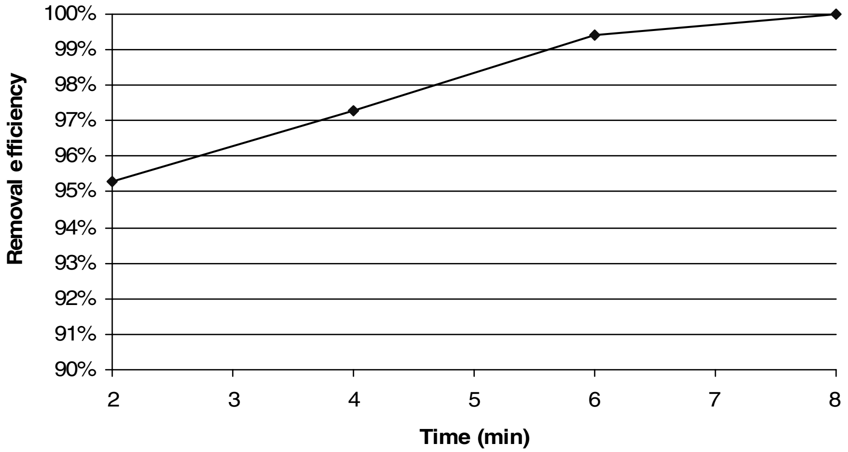

Figure 11.17 Removal efficiency of 63-nm particles from 11-nm silicon capping layer wafer using 760-KHz frequencies.

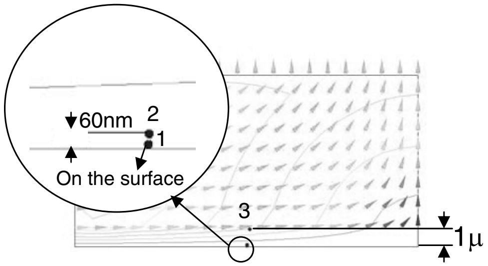

Figure 11.18 Representative velocity vector field at the center of the wafer and three particle locations inside the flow field.

at the same intensity and several frequencies (including 760 KHz). The acoustic streaming velocity is a function of the intensity of the sound wave source and the frequency of vibration. The high frequency results in higher streaming velocity and a thinner boundary layer thickness, which are essential to the removal of nanoparticles. The acoustic boundary layer thickness for a 760-KHz frequency is 630 nm. Figure 11.18 illustrates the velocity vector field close to the wafer for a 20-micron segment at the center of the wafer. Although the particle detachment from the surface is being investigated, particles at two other locations are released into the flow model to get a better understanding of the particle-fluid interaction. These two particles of interest are a particle inside the boundary layer located 60 nm above the surface and a particle outside the boundary layer 1 micron above the surface.

The simulation is time dependent. To compute the time-dependent flow behavior, time steps are chosen based on accuracy and resolution. These time steps have to be different for each frequency to ensure sufficient time resolution within each step.

There were few steps involved in modeling the nanoparticle transport after detachment from the wafer. These steps are as follows:

1. Predict the acoustically induced velocity field near the wafer. This will provide the velocity profile above the wafer surface.
2. Calculate the drag force based on the velocity profile inside the boundary layer acting on the particle.
3. Calculate the moment ratio to show the possibility of particle detachment.
4. Predict the particle trajectory after detachment as the final step if MR > 1. Once the moment ratio model verifies the particle detachment from the wafer surface, the travel time for the particle to move along the wafer and the trajectory are analyzed.

The acoustic streaming in the simulation is induced by the transducer vibrating at the same amplitude and different frequencies (at the tank wall) corresponding to the transducers used in the experiments. The acoustic streaming velocity is used to calculate the removal (drag) force on the particle. The moment ratio value for each frequency is shown in Figure 11.19.

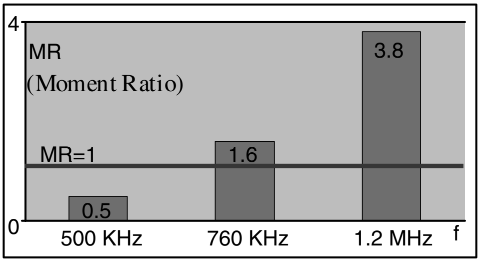

Figure 11.19 Moment ratio for 63-nm PSL particles on a silicon wafer at frequencies of 500 KHz, 760 KHz, and 1.2 MHz.

The MR = 1 line shows the critical value for particle removal. The figure shows that the 500-KHz frequency is not effective for 63-nm PSL particle removal. The 760-KHz frequency results in complete removal that has also been verified experimentally. The moment ratio for 1.2 MHz is more than two times higher than 760 KHz, which also indicates complete removal by a larger removal moment. The time it took to remove the particle in the simulation was monitored to evaluate the effect of frequency on the removal time. Figure 11.20 shows the particle trajectory and the removal time of a single 63-nm particle located at the center of a wafer using two frequencies. After detachment both particles undergo a circulatory and back–and-forth motion. Due to high frequency and velocity, 1.2 MHz results in 4.7 times faster removal time than the lower 760-KHz frequency.

Figure 11.20 shows that it will take less time for 63-nm PSL particle removal using 1.2 MHz. The simulation also shows redeposition of the particle on the surface along its circulatory trajectory.

To get a better understanding of the acoustic streaming interaction with nanoparticles, particles are released into the flow as shown in Figure 11.21 and Figure 11.22. Figure 11.21 shows the simulation of a 63-nm particle

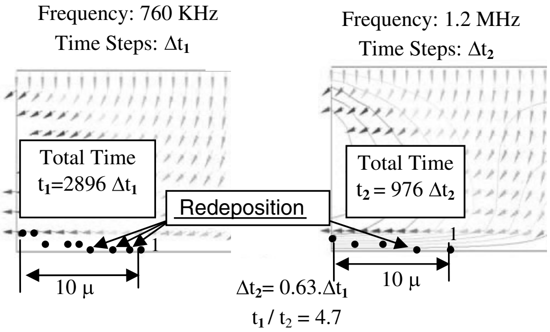

Figure 11.20 Travel time and trajectory for a particle on the surface, for frequency 760 KHz (removal time t_1) and 1.2 MHz (removal time t_2) using CFD simulation.

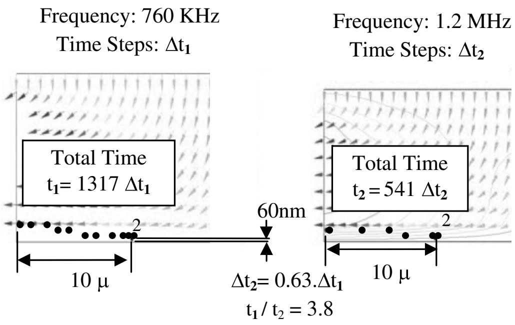

Figure 11.21 Travel time for particle 2, the particle at 60 nm, for frequency 760 KHz (removal time t_1) and 1.2 MHz (removal time t_2).

released into the flow inside the acoustic boundary layer at 60 nm above the surface measured from the surface of the particle.

Figure 11.22 illustrates the trajectory of a 63-nm particle released into the flow outside the boundary layer at 1 μm from the surface (outside the acoustic boundary layer).

Figure 11.20 through Figure 11.22 represent a comparison between the removal time ratio (t_1/t_2) for 760 KHz and 1.2 MHz. As the figures show, the removal time ratio between 760 KHz and 1.2 MHz decreases as the particle location from the surface increases. It takes 4.7 times longer to remove the particle on the surface by 760 KHz instead of 1.2 MHz. If a particle is at roughly one particle diameter distance from the surface (either after detachment or before redeposition), the ratio becomes 3.8. Similarly, if the particle is outside the acoustic boundary layer at 1 μm from the surface, the ratio decreases to 3.2. As the simulation indicates, increasing the frequency from 760 KHz to 1.2 MHz, yields higher streaming velocity and a much different particle trajectory. The number of particle redepositions and particle oscillatory path decreases for 1.2 MHz, mostly inside the boundary layer and close to the wall.

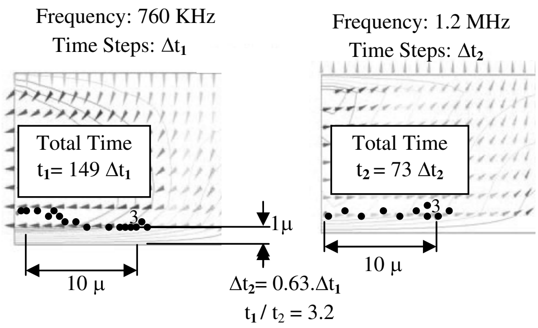

Figure 11.22 Travel time for particle 3, the particle at 1 μm, for frequency 760 KHz (removal time t_1) and 1.2 MHz (removal time t_2).

This results in a higher removal time ratio for particles detaching from the surface compared with particles away from the surface.

Figures 11.21 and 11.22 show that the time required for removal of a 63-nm particle inside the boundary is 8 times longer than that required by the same particle outside the boundary layer. Outside the boundary layer, the results show that the velocity is higher and the oscillatory behavior of the particle is minimal, resulting in a faster removal.

11.3.3 Submicron Particle Removal from Deep Trenches

Complete removal of 300-nm and 800-nm PSL fluorescent particles was demonstrated on 6-inch (150-mm) wafers with six parallel arrays of trenches. The trenches are 112 microns wide and 508 microns deep. Particles were deposited into the trench using a nebulizer. A single wafer megasonic tank 760 KHz, with a maximum power output (640 W), was used. After the megasonic cleaning (using DI water and 87% of maximum power) is done, the wafers are removed and spun dry. A Nikon Optiphot 200D microscope with fluorescent attachment is used to determine the particle count before and after cleaning. Image Pro-plus software was used to count the particles located at specified locations in the trench before and after cleaning.

Fluorescent microscopy at 1000 × magnification and scanning electron microscopy (SEM) at 45,000 × magnification has been used to capture images of the same area on the surface. These SEM pictures (on the wafer surface) verify that all the particles with a diameter of 63 nm and larger are detectable using the fluorescent microscopy metrology.

A computational fluid dynamics model of megasonic cleaning has been developed. This simulation has enabled us to get a better understanding of the particle detachment and removal from a trench and the effect of time on the cleaning. Figure 11.23 illustrates the velocity vector field at two different time steps for the first 100-micron depth of the trench.

Figure 11.24 illustrates the experimental results for removal efficiency at specified depths within the trench as a function of operating time for both 300- and 800-nm particles. The figure shows that after 1 minute cleaning,

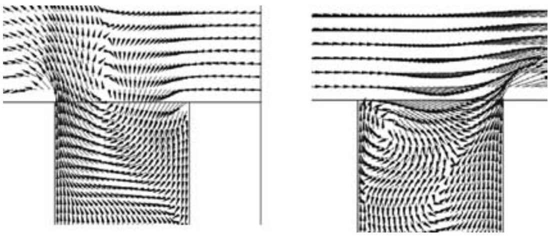

Figure 11.23 The velocity contour and vector field at two different time steps in the CFD model for the trench. K. Bakhtari, R.O. Guldiken, A. Busnaina, and J.G. Park, "Experimental and analytical study of submicrometer particle removal from deep trenches," J. of Electrochemical Society, Vol. 153, 9, 2006 (in press 022609JES).

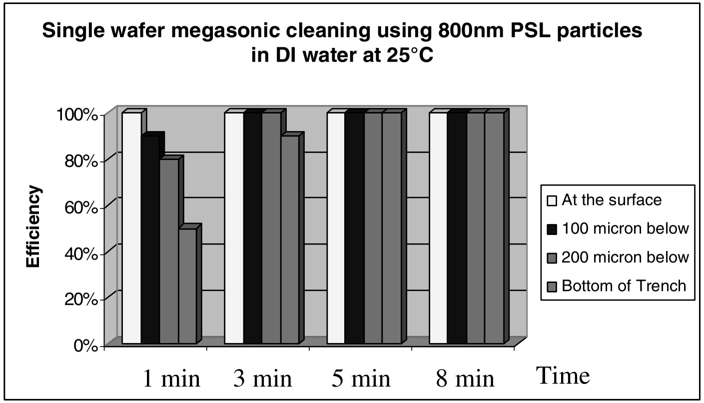

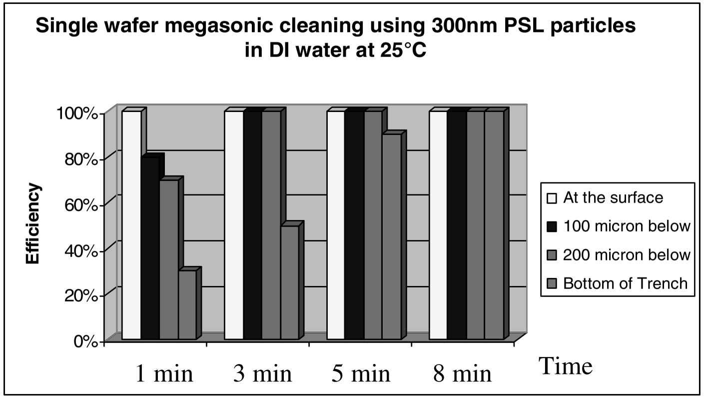

Figure 11.24 Removal of 300- and 800-nm PSL fluorescent particles in DI water at 25°C at different depths and times. K. Bakhtari, R.O. Guldiken, A. Busnaina, and J.G. Park, "Experimental and analytical study of submicrometer particle removal from deep trenches," J. of Electrochemical Society, Vol. 153, 9, 2006 (in press 022609JES).

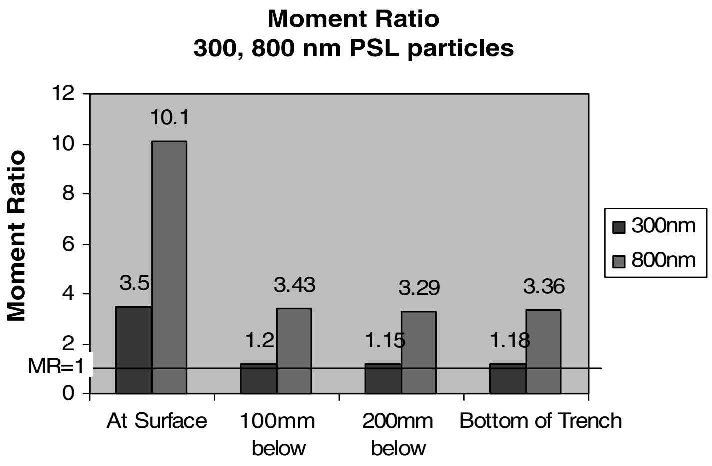

Figure 11.25 Moment ratio values for 300- and 800-nm PSL particle on alumina substrate in DI water. K. Bakhtari, R.O. Guldiken, A. Busnaina, and J.G. Park, "Experimental and analytical study of submicrometer particle removal from deep trenches," J. of Electrochemical Society, Vol. 153, 9, 2006 (in press 022609JES).

complete removal was achieved at the wafer surface near the trench. However, in the trench, the deeper the location, the lower the removal efficiency. At the bottom of the trench only 50% of the 800-nm particles and 30% of the 300-nm particles are removed after 1 minute. Complete removal was achieved after 5 minutes for 800-nm particles and after 8 minutes for 300-nm particles.

To understand the effect of time and depth, a CFD model with a particle removal model based on the rolling mechanism is used. Theoretically, moment ratio greater than 1 indicates particle detachment. Figure 11.25 shows the moment ratio values for the same trench depths used in the experiments. The figure shows that most of the particles could be completely detached from the trench.

The moment ratio model, however, does not explain the long cleaning time observed. The velocity vector field in Figure 11.23 shows that the flow at the particle location is parallel to the sidewalls of the trench. This parallel flow applies a drag force to the particle, attempting to roll the particle from the surface. In addition, the acoustic streaming and pressure fluctuations produce transient vortices inside the trench. Once the particle is detached from the wall these vortices move the particle in an oscillatory motion inside the trench. Particles are released into the trench in the CFD simulation to observe the particle trajectory during the cleaning process. The trajectory of the detached particles at different depths within the trench is monitored during the simulation. The results show that in addition to the particle oscillatory motion normal to the wafer surface, the particles redeposit after detachment. This redeposition of the particles and oscillatory motion are the reasons that a long time is needed to remove the particles from the trench.

Another experimental observation is that the temperature of DI water has a minor effect on the removal efficiency. The effect of temperature on

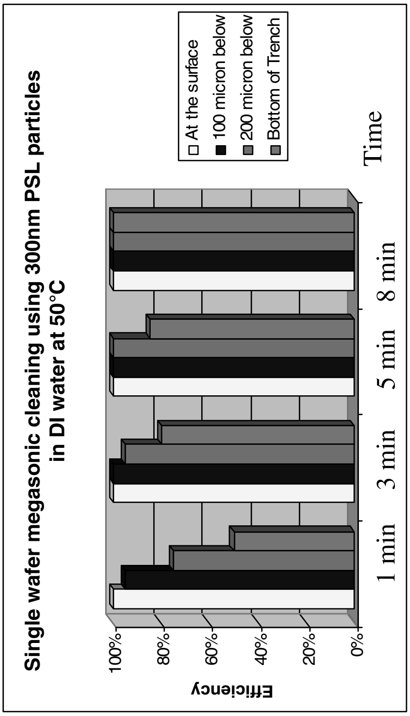

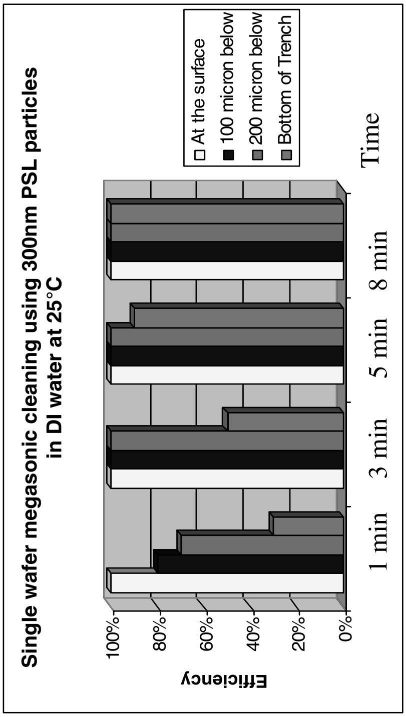

Figure 11.26 Removal of 300-nm PSL fluorescent particles in DI water at different temperatures.

300-nm PSL particle removal is illustrated in Figure 11.26. Although the particle removal at 50°C is faster for the particles closer to the surface compared with particles at 25°C, it takes the same amount of time for both temperatures to get complete removal specifically at the bottom of the trench.

11.4 Summary

The moment ratio model for analyzing nanoscale particles is in good agreement with the experimental results. Results show that dilute SC1 results in higher moment ratio than DI water due to the larger repulsive charge on the particle at a higher pH. The simulation shows that once the nanoparticle is detached from the substrate, it undergoes oscillatory motion and multiple redeposition and removal takes place. The redeposition is the main reason for the longer time required for nanoparticle removal compared with micron- and submicron sized particles. The modeling and experimental results show that 63-nm and larger PSL particles can be completely removed using acoustic streaming from bare silicon and 4-nm Si-Cap layer wafers. When a 7-W/cm^2 transducer input power with 760-KHz frequency is used to clean an 8-inch wafer, complete removal of the 63-nm PSL particles is achieved after 4 minutes in dilute SC1 and after 6 minutes in DI water for both substrates.

The effect of higher-frequency acoustic streaming on 63-nm particle detachment and removal time has been investigated using physical fluid modeling. The acoustic streaming frequency of 760 KHz has been shown to be effective in PSL nanoparticle removal (63 nm) from 11-nm silicon capping layer films using only DI water experimentally and theoretically. Although complete removal is achieved by the 760-KHz frequency, the cleaning time is 8 minutes, which is a relatively long process time. The results show that a lower frequency of 500 KHz is insufficient for effective particle removal. Two higher frequencies (760 KHz and 1.2 MHz) result in complete removal; however, the 1.2-MHz frequency is 4.7 times faster than the 760 KHz.

Complete removal of the 300- and 800-nm PSL particles from a 500-micron deep trench using 760-KHz oscillatory flow has been demonstrated. Complete removal of the considered particles from the bottom of the trench required 8 minutes of cleaning time. The moment ratio model shows that the removal moment was sufficient to detach particles from the wall and the bottom of the trench. The physical model (CFD) simulation results show that once the detachment occurs, the particles undergo oscillatory motion, redeposition, and entrapment inside the circulation zones within the trench. The cleaning time corresponds to the depth of the trench. Particles at the bottom of the trench take longer to remove, but complete removal nonetheless has been shown at the bottom of the trench by experimental and numerical results. The 800-nm particles closer to the surface escape the circulatory zone and eventually leave the trench faster than the 300-nm particles.

References

1. Wolf, S. and Tauber, R.N., *Silicon Processing for the VLSI Era Vol. 1—Process Technology*, 2nd Edition, Lattice Press, Sunset Beach, CA, 2000.
2. Semiconductor Industry Association (SIA), The International Technology Roadmap for Semiconductors (ITRS), 1999.
3. Busnaina, A.A., Kashkoush, I.I., and Gale, G.W., An experimental study of megasonic cleaning of silicon wafers, *J. Electrochem. Soc.*, 142, 2812, 1995.
4. Gale, G.W. and Busnaina, A.A., Removal of particulate contaminants using ultrasonics and megasonics: a review, *Partic. Sci. Tech.*, 13, 197, 1995.
5. Busnaina, A.A. and Gale, G.W, Removal of silica particles from silicon substrates using megasonics cleaning, *Partic. Sci. Techn.*, 15, 1997.
6. Schwartzman, S., Mayer, A., and Kern, W., Megasonic particle removal from soild-state wafers, *RCA Review*, 46, 81, 1985.
7. Busnaina, A.A. and Gale, G.W., Roles of cavitation and acoustic streaming in megasonic cleaning, *Partic. Sci. &Techn.*, 17, 229, 1999.
8. Busnaina, A.A., and Dai, F., The removal of submicron particles in liquid-based cleaning, *J. Adhes.*, 67, 181, 1998.
9. Busnaina, A.A. and Elsawy, T.M., Post-CMP cleaning using acoustic streaming, *J. Electron. Mater.*, 27, 1095, 1998.
10. Syverson, W., Fleming, M., and Schubring, P., *Second International Symposium on Cleaning Technology in Semiconductor Manufacturing*, Electrochemical Society Proceedings PV92-10, 1992, p. 10.
11. Wang, P. and Bell, D., *Third International Symposium on Cleaning Technology in Semiconductor Device Manufacturing*, Electrochemical Society Proceedings PV94–7, 1994, p. 132.
12. Wu, J.J. et al., Wafer cleaning with cryogenic aerosols, *Semicond. Int.*, 113, 1996.
13. Tam, A.C., Leung, W.P., Zapka, W., and Ziemlich, W., Laser-cleaning techniques for removal of surface particulates, *J. Appl. Phys.*, 71, 3515, 1992.
14. Zapka, W., Ziemlich, W., and Tam, A.C., Efficient pulsed laser removal of 0.2μm sized particles from a solid surface, *Appl. Phys. Lett.*, 58, 2217, 1991.
15. Kashkoush, I., Busnaina, A.A., Kern, F.W., and Kunesh, R.F., *Particles on Surfaces,* Mittal, K., Ed., 3,Plenum Press, New York, NY, 1991, p. 217.
16. Gale, G.W. and Busnaina, A.A., Roles of cavitation and acoustic streaming in megasonic cleaning," *J. Particulate Science & Technology,* 17, 3, 229, 1999.
17. A.A. Busnaina, I. I. Kashkoush, and G. W. Gale, *J. Electrochem. Soc.*, 142, 8, 2812, 1995.
18. Busnaina, A.A. and Gale, G.W, Removal of Silica Particles from Silicon Substrates Using Megasonic Cleaning *J. Particulate Science & Technology,* 15, 3/4, 1997, p. 361.
19. Olim, M., *J. Electrochem. Soc.*, 144, 3657, 1997.
20. Bernard, J.M., Guildkin, O., Busnaina, A.A., and Park, J., *Semiconductor Fabtech*, 23rd Edition, 2004, p. 77.
21. Lin, H., Ph.D. Monitoring of Metallic Contamination During Aqueous Semiconductor Wafer Processing, Ph.D. Thesis, Clarkson University, Potsdam, NY, USA, 2001.
22. Nyborg, W.L., Acoustic streaming, in *Physical Acoustics*, Vol. IIB, Mason, W.P., Ed., Academic Press, New York, 1965, p. 265.
23. O'Neill, M.E., *Chem. Eng. Sci.*, 23, 1293, 1968.
24. Hamaker, H.C., *Physica,* 4, 1058, 1937.

25. Rimai, D.S. and Quesnel, D.J., *Fundamentals of Particle Adhesion*, Polymer Surfaces and Interfaces Series, Global Press, Moorhead, MN, 2001.
26. Bowling, R.A., A theoretical review of particle adhesion, *Particles on Surfaces,* Mittal, K., Ed., Plenum Press, New York, 1988, p. 129.
27. Maugis, D. and Pollock, H.M., *Acta Metall.*, 32, 1323, 1984.
28. Krishnan, S., Busnaina, A.A., Rimai, D.S., and DeMejo, D.P., The adhesion-induced deformation and the removal of submicrometer particles, *J. Adhes. Sci. Tech.*, 8, 1357, 1994.
29. Rimai, D.S. and Busnaina, A.A., The adhesion and removal of particles from surfaces, *Parti. Sci. & Tech.*, 13, 249, 1995.
30. Rimai, D.S., Quesnel, D.J., and Busnaina, A.A., The adhesion of dry particles in the nanometer to micrometer-size range, *Int. J. Coll. Surface. A*, 165, 3, 2000.
31. Visser, J., 13, 169, 1995.
32. Steigerwald, J.M., Murarka, S.P., and Gutmann, R.J., *Chemical Mechanical Planarization of Microelectronic Materials*, John Wiley & Sons, New York, 1997.
33. Zhang, F., Busnaina, A.A., and Fury, M., The removal of deformed submicron particles from silicon wafers using spin rinse and megasonics, *J. Electron. Mater.*, 2000.
34. Zhang, F. and Busnaina, A.A., Submicron particle removal in post-oxide chemical-mechanical planarization (CMP) cleaning, *Appl. Phys. A*, 69, 437, 1999.
35. Zhang, F., Busnaina, A., and Ahmadi, G., Particle adhesion and removal in chemical mechanical polishing (CMP) and post-CMP cleaning, *J. Electrochem. Soc.*, 146, 7, pp. 2665–2669, 1999.
36. Soltani, M. and Ahmadi, G., On particle adhesion and removal mechanisms in turbulent flows, *J. Adhes. Sci. Tech.*, 8, 763, 1994.
37. Bakhtari, K., Guldiken, O., Makaram, P., Busnaina, A.A., and Park, J., *The Adhesion Society, Proceedings*, 2005, p. 404.
38. Hattori, T., Contamination control: problems and prospects, *Solid State Tech.*, 33, s1, 1990.
39. Krishnan, S., Busnaina, A.A., Rimai, D.S, and DeMejo, D.P., The adhesion-induced deformation and the removal of submicrometer particles, *J. Adhes. Sci. Tech.*, 8, 1357, 1994.
40. Busnaina, A.A., Lin, H., and Suni, I.I., Cleaning of high aspect ratio submicron trenches, *Proceedings*, *IEEE/SEMI Advanced Semiconductor Manufacturing Conference 2002*, Boston, MA, April 30–May 2, 2002, p. 304.
41. Lin, H., Busnaina, A.A., and Suni, I.I., Physical modeling of rinsing and cleaning of submicron trenches, *Proceedings of the IEEE 2000 International Interconnect Technology Conference*, IEEE Electron Devices Society, San Francisco, CA, June 5–7, 2000, p. 49.
42. Lin, H., Busnaina, A.A., and Suni, I.I., Modeling of rinsing and cleaning of trenches, *International Sematech Wafer Cleaning and Surface Preparation Workshop 2000*, Austin, TX, April 11–12, 2000 (CD).

Chapter 12

Improved Carbon Materials for Nanomanufacturing Applications

Patrick Lemoine, John Paul Quinn, Pagona Papakonstantinou, Paul Maguire, and James McLaughlin

Contents

12.1 Introduction.....281
12.2 Weakness and Strength in Carbon Materials.....282
12.2.1 Single Crystals.....282
12.2.2 Disordered and Nanostuctured Carbon Materials.....283
12.2.3 Existing Comparisons and Van Der Waals Interactions.....287
12.2.4 Van Der Waals Bonds and Viscomechanical Behaviors.....289
12.2.5 Preliminary Results on a-C:H Films and CNT Arrays.....292
12.3 Nanopatterning and Processing of Carbon Materials.....299
12.3.1 Introduction.....299
12.3.2 EBID Formation of a-C:H Films and Structures.....300
12.3.3 FIB Formation of a-C:H Films and Structures.....303
12.4 Conclusions.....308
Acknowledgments.....308
References.....309

12.1 Introduction

As a constituent of many raw materials and manufactured products, carbon has always interested scientists and engineers. Those involved with nanomanufacturing have now specific reasons to re-examine this multifaceted element. First, exotic new forms of carbon, such as carbon nanotubes and fullerenes, have appeared in recent years as crucial building blocks of

nanodevices such as addressable memories and sensor arrays, for example. Second, biological systems often advocated as model systems for nanotechnology are essentially built of carbon backbones. Third, the properties of carbon depend on nanoscale heterogeneity, voids, crystalline defects, secondary bonds, and dangling bonds. Obviously, as the device's dimensions shrink down, the role of these heterogeneities, and their control, becomes of paramount importance.

As this represents a huge field of research activities, this chapter will essentially address two issues. First, we will review the mechanical strength and weakness of carbon materials. We will focus on "real," disordered, or nanostructured carbon materials, the defects being the secondary bonds that can be detected viscomechanically, hence offering a method to conduct comparative investigations not available from other analysis techniques. Second, we will discuss the effect of nanopatterning on carbon materials. As the same energetic beams of ions and electrons are used for either synthesis or etching of carbon materials, we will discuss the possible use of simultaneous synthesis/patterning strategies using electron and ion beam techniques. This could represent a faster, cheaper, and better way for producing carbon devices of nanoscale dimension.

12.2 Weakness and Strength in Carbon Materials

About 30 years ago, Primo Levi described the journey of a carbon atom, from a lump of limestone in the ground to a constitutive element of a nervous cell, acting in his brain. As a novelist, he justified his scenario "The number of atoms is so great that one could always be found whose story coincides with any capriciously invented story."[1] Examining carbon today, with the eye of the scientist, one finds a great variety of materials, a large diversity of experimental studies, and an equally vast assortment of explanations and theories for the observed behaviors. Are those, in some way, capriciously invented stories? It is, after all, a segmented field of research. Comparative studies, which are key to understanding, are remarkably few for carbon. Can we, for instance claim to understand the properties of carbon nanotube materials without explaining what makes them different from carbon fibers? In this section, we will present a range of elemental carbon materials and their mechanical properties, develop comparisons, and reflect on the effect that van der Waals bonds have on the deformations of the carbon network.

12.2.1 Single Crystals

In the past, pure carbon was believed to form in only two crystalline forms, graphite and diamond. Thermodynamically, graphite is the most stable form and therefore the most common. The identification of diamond as another form of carbon was done by Lavoisier in the eighteenth century, an early realization considering the huge disparity between the two materials. Natural diamond forms under large pressure and temperature, through volcanic processes.

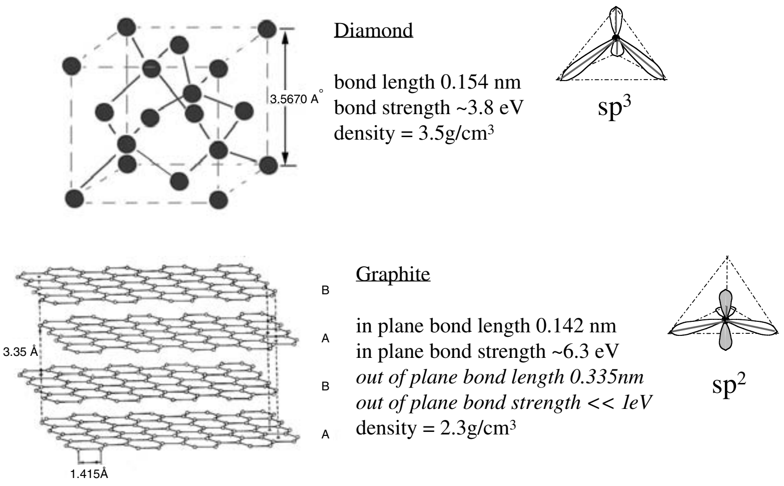

Figure 12.1 Bonding configurations for diamond and graphite.

These extreme conditions can be reproduced in the laboratory with autoclaves;[2] alternatively, synthetic diamond can be prepared under vacuum, for instance, using hydrocarbon gas or fullerene precursors. The contrasting mechanical properties of graphite and diamond are easily explained. In diamond, the carbon atoms are tetrahedrally coordinated to their first nearest neighbour by four sp^3 bonds. This results in a high bond energy per unit volume in all three directions of space. In graphite, the carbon atoms are bound in a planar hexagonal array, the graphene sheet, by trigonal sp^2 bonds. In addition, vertical π orbitals, which overlap along horizontal directions, consolidate these graphene sheets. However, these layers can easily slip past one another as this requires only breaking weak van der Waals bonds (~0.01 eV) (see Figure 12.1) One can add that the outstanding hardness of diamond has triggered a number of theoretical quantum studies on super-diamond crystal phases, cubic carbon nitride, hard metallic carbon phases,[3] and tough carbon foams.[4] These are fascinating and useful efforts; however, they are not sufficient for explaining the many other forms of carbon that are often less ordered. Indeed, in the context of nanomanufacturing, the presence of defects is of paramount importance.

12.2.2 Disordered and Nanostuctured Carbon Materials

These include carbon fibers, diamond-like carbons (DLC), and more exotic forms such as fullerines, carbon nanotubes (CNT), carbon onion rings, and many others. Here, we will focus mostly on CNT, C fibers, and DLC, as these forms are the most relevant to present or emerging nanotechnologies.

Carbon nanotubes: CNTs, first appeared in 1991[5] and, since, have generated much interest and many studies.[6,7] Potential applications include

addressable memories, super-hydrophobic materials, field emitters, nanoscale mechanical reinforcements, molecular hydrogen storage devices, and many more. All CNTs are built around a tubular rolled-up sheet of graphite, often closed at both ends by hemispherical fullerite ends and usually grown from a metal catalyst site. Conceptually, the way in which the graphite sheet is rolled up affects the electronic and optical properties of CNTs. In general, any lattice point in the graphite sheet can be represented as a vector position (n, m) relative to any given origin. The graphite sheet can then be rolled into a tube such that the chosen lattice point is coincident with the origin. Simple rules predict whether a specific (n, m) is conducting or semiconducting: (n, n) tubes ("armchair" chirality) are insulating; (n, m) tubes with $|n-m|=3q$, where q is a nonzero integer, are very small-gap semiconductors; and all other tubes are large-band semiconductors. In addition, CNTs are strong and rigid molecular structures. Here we used macroscopic terms such as the Young modulus and strength to describe the properties of CNTs, which are molecular structures. The Young modulus describes the elasticity of the tube, which can be measured in tension or in bending; the strength represents the limit stress at which the tube deforms in an irreversible manner (yield point) or the ultimate stress, corresponding to rupture of the tube. These characteristics say little of the properties of the CNT materials, made of aligned or entangled tubes, as will be discussed later. Young modulus calculations were made first using thermal vibrations in a transmission electron microscope (TEM).[8] Direct mechanical measurements using atomic force microscopy (AFM) followed for single wall (SWCNT) and multiwall (MWCNT) carbon nanotubes. There is a fairly large scatter of experimental values, depending on the assumption for the tube volume and the chosen experimental protocol; however, the values for the Young modulus and tensile strength are often around 1 TPa and 1 GPa, respectively. Both theory and measurements have shown that the tube chirality has a weak effect on the elastic properties, although no such observations have been made on the tensile strength of CNTs.[9]

The surface of the CNTs can present atomic defects that can trigger chiral variations, changing the tubes' behavior from semiconducting to metallic. They can also represent preferential sites for surface chemistry and useful functionalizations.[10] All these have been investigated much in the way surface defects have been studied on single crystal materials. Because of the difficulty in forming strong assemblies of CNTs, one may also consider the space between CNTs as another type of defect. This arises because CNTs interact only by van der Waals forces. Depending on the catalyst used, the tube bending and packing density may vary, and catalyst engineering has not yet produced cohesive structures of aligned CNTs. Much effort has also been directed at strengthening CNT assemblies by spinning CNT fibers. These coagulation-based spinning techniques use polymer adhesives as intertube lignands.[11,12] However, the process is still too slow for commercialization and the fiber, with 40% polymer content, is not a pure carbon material. One should note that catalytic preparation methods have also produced

nanofibers, where the graphene sheets are oriented perpendicularly (stacked) or at an angle (herringbone) to the fiber axis.[13] Obviously, these materials have poor tensile properties and, like CNTs, they form fragile assemblies but they find applications as molecular energy storage devices.

On the whole, the weak interaction between CNTs has limited their application in technology. For instance, making self-supported films of aligned CNTs would be beneficial to the development of sensors arrays and field emitter devices.[14] Assembling CNTs into ropes or fibers, which can then be weaved into artificial muscles or electronic fabrics, has so far also been a limited success, again, because of the van der Waals interaction. By contrast, the development of CNT composite requires the minimization of CNT–CNT interactions to obtain maximal dispersion; therefore, on the whole, CNTs have appeared in few nanomanufactured devices.

Carbon fibers: Like CNTs, C fibers are sp^2-rich materials. Their tensile strength and Young modulus can be in excess of 3 GPa and 600 GPa, respectively.[15] These high-strength fibers are manufactured from either pitch or polyacetonytrile (PAN) precursors.[16] In both cases, the impressive axial properties of the fibers result from the strong orientation and tight packing of the graphite crystallites, with longitudinal dimensions in the micrometer range. In the transversal directions, a number of crystallite morphologies have been observed: random, radial, concentric, and more complex cross-sectional distributions including some void content. It is in that sense that C fibers may be considered, at least in part, as disordered nanostructured materials. In most cases, C fibers are used as reinforcement agents for composite structures and, therefore, are designed to bear longitudinal mechanical loading. However, studies have shown that the transversal morphology affects the fiber strength.[17] Moreover, they are brittle materials and their low strain at break means that they cannot bear excessive bending. Finally, as C fibers have been used successfully in the industry for the last 20 years, most present research investigations are directed at optimizing the fiber/matrix interface rather than producing stronger fibers.

Diamond-like carbons: DLC describes the mainly amorphous carbon material produced in thin film form by plasma deposition techniques. Historically, this terminology stems from the relatively diamond-like behavior of the material; it is often mechanically hard and electrically insulating. We will conform to this traditional use of the term, for lack of a better one. We note, however, that today DLC covers amorphous carbon (a-C), usually sp^2-rich and prepared by magnetron sputtering; hydrogenated amorphous carbon (a-C:H), of mixed hybridization and prepared by plasma enhanced chemical vapor deposition (PECVD); tetrahedral amorphous carbon (t-aC) and hydrogenated tetrahedral amorphous carbon (t-a:C:H), mostly sp^3-rich, prepared by filtered cathodic vacuum arc (FCVA) deposition or pulsed laser deposition (PLD); and fullerine-like carbon (FLC), usually sp^2-rich and nanostructured, prepared by modified FCVA or PLD techniques. Unlike fullerenes and nanotubes, DLC is easily processable and has already found applications as protective coatings in the tooling, data storage, and biomedical industries.

There is abundant literature devoted to the properties and bonding structure of this material; a fairly extensive review has been compiled by Robertson.[18] Concerning the bonding structure of DLC, the main line of inquiry is to interpret the electronic bands and vibrational density of states of the disordered materials from those of their crystalline counterparts. This approach has been quite successful for other solid-state materials such as Si and Ge. However, as the covalent carbon bond hybridizes into sp^3, sp^2, or sp^1 forms, the case of amorphous carbon has been less successful. Nonetheless, the emerging picture is that

1. sp^2 phases tend to cluster in aromatic or olefinic regions, of varying density and size, depending on the method of preparation, the sp^3 phase constituting the embedding matrix.
2. The hydrogen content makes the films softer but may improve lubricity and hence wear protection.
3. Most of the time, sp^2-rich DLCs are softer than sp^3-rich DLCs, even nonhydrogenated.
4. Constraints in DLC impose distortions in the aromatic domains and hence affect its electronic transport properties.

Finding 3 is one of the most emphatically held beliefs in the DLC community. This is usually justified by the network-forming ability of the tetrahedrally coordinated sp^3 bonds. The constraint counting model, for instance, derives the elasticity of the amorphous network from the bending and stretching of the covalent bonds, emphasizing the crucial role played by the bond coordination number, i.e., highly coordinated networks (i.e., sp^3) show more elastic constraints.[19] In a review study, Robertson, who included the effect of sp^2 clustering in the model, presents this theoretical framework as the main tool of analysis for describing the mechanical properties of amorphous carbon. It fits reasonably well the Young modulus data for tetrahedral amorphous carbon (t-aC), the hardest form of DLC produced so far, but less so for hydrogenated amorphous carbon (a-C:H). Moreover, the model has a number of shortcomings. First, it uses averaged coordination number and bond length, measured from the radial distribution functions of diffraction experiments.[20] As the stiffness of the bonds is derived from interatomic potentials, which are highly nonlinear, the use of average quantities constitutes a fairly inaccurate approximation. Second, it does not include van der Waals interactions, as implicitly recognized by the first proposers. Last, it does not describe plasticity.

Another stumbling block, and notable exemption to Finding 3, is the hard sp^2-carbon network structure prepared by Alexandrou et al.[21] This material appears to be at least 95% sp^2 bonded and displays a hardness of 45 GPa. Alexandrou uses a "squeezed chicken wire" model to explain how the nanoscale curvature of graphene sheets, seen in TEM images, strengthens this FLC material. Others have used similar arguments, invoking the presence of pentagonal and heptagonal rings, and hence curvature, to explain the

relatively high hardness of sp^2-rich carbon and carbon nitride films.[22] Moreover, it may be that the disorder present in most DLCs could bend the sp^2-regions, even for materials with intermediate or low sp^2 content. In these cases, two strengthening effects could be at play, the interlocking of curved graphitic shells and the network-forming ability of the sp^3 regions. The two processes have yet to be incorporated into a single mechanical model and, as yet, the mechanical properties of DLC are not fully understood.

12.2.3 *Existing Comparisons and Van Der Waals Interactions*

Theoretical calculations on CNT are usually based on comparisons with graphite's in-plane properties,[23] hence justifying the high strength and rigidity of these materials. However, it is the comparison to diamond, and its network-forming ability, that is used to justify the superior mechanical properties of t-aC. Therefore, both crystal phases, graphite and diamond, are used to explain strength in carbon materials. This seemingly schizophrenic situation becomes even more confusing when confronting the entire range of carbon materials: t-aC (a hard sp^3-rich thin-film material), FLC (a hard sp^2-rich thin-film material), C fibers (a stiff and strong sp^2-rich fiber of micronic diameter), CNT (a stiff and strong sp^2-rich fiber of nanometric diameter), and carbon nanofibers (a compliant and weak sp^2-rich fiber of nanometric to submicronic diameter). In Table 12.1, we have gathered a variety of elemental carbon materials with a broad range of mechanical properties. Clearly, the data included in this table are not comprehensive. For instance, there are no studies on the hardness of carbon fibers or the tensile properties of free-standing tetrahedral amorphous carbon (t-aC) films. Strikingly, there

Table 12.1 The Mechanical Properties of Various Elemental Carbon Materials

Material	Form	Density (g/cm^3)	Covalent bonds	Young modulus (GPa)	Hardness (GPa)	Tensile strength (GPa)	Ref.
C60	films	~1.7	almost all sp^2	?	~0.2	—	26
C fibers	fibers	1.7–1.9	almost all sp^2	200–600	?	3.8–6.4	soficar
Graphite	bulk	~2	100% sp^2	10	0.2–2	—	26
CNT	fibers	~2	almost all sp^2	1000	?	1	9
CNT arrays	film	<2?	almost all sp^2	0.013	?	—	this work
FLC	films	~2.2	almost all sp^2	480	45	—	21
a-C	films	~2.2	sp^2-rich	100–200	10–20	—	18
a-C:H	films	~2.2	intermediate sp^3	100–300	10–30	—	34,35
t-aC	films	3–3.2	sp^3-rich	300–500	50–80	—	18
Diamond	bulk, films	~3.5	100% sp^3	1000	100	—	26

has been no comparison between MWCNT and concentric carbon fibers. These measurements, not particularly challenging experimentally, have not been carried out to date because, as previously mentioned, the various clusters of investigators have not yet seen the merit of comparative studies. Table 12.1 shows, however, that, whether the material is organized at the micro-scale or nanoscale, whether it forms fibers or thin films, the sp^2 fraction in carbons, high or low, is not the sole prerequisite for superior mechanical properties. Something else is at play. The scarce experimental comparisons available in the literature are insightful in that regard.

One study investigates various grades of graphitic materials, from pyrolithic graphite (highly oriented) to glassy carbon (nanocrystalline).[24] The glassy carbon is harder and stiffer as grain boundaries act as barriers for slip and dislocations. The authors also noticed a reversible elastoplastic hysteresis in their load-displacement curve. This is explained by interlayer slip and friction, again larger for the glassy carbon. However, in a later work,[25] associated with the same authors on the high-temperature treatments of glassy carbons, the hysteresis loop is seen to increase with the nanocrystallite dimensions, as nanoscale graphitic clusters slip past one another. Despite this discrepancy in results, two points are worth noting. First, both studies clearly show a reversible loop in the load displacement curve interpreted with crystalline concepts (as grain boundaries, dislocations, and friction between slip planes). The same trend on an amorphous polymer would have been explained as a viscomechanical effect. We will come back to this later. Second, when discussing mechanical deformations in these graphitic materials of varying disorder and crystallinity, interlayer processes play a prominent role, although the van der Waals force is rarely mentioned.

More recently,[26] nanoindentation has been used to characterize diamond, graphite, and fullerene films. The C60 molecules in these films only link up through weak van der Waals interactions, and hence, the fullerene samples are the more compliant and softer samples, followed by graphite and then diamond. Atomistic simulations that include these van der Waals interactions in graphite and fullerene seem to capture the main experimental features. What is unclear for graphite, however, is (1) how the simulations reproduce the small reversible hysteresis seen in Figure 7a of Field and Swain[24] and (2) what the simulation on graphite would have given without van der Waals forces.

The effect of van der Waals forces on the stacking of graphene layers has been studied for CNT, vapor-grown carbon fibers (VGCF), and single crystal graphite.[27] The d_{002} spacing is about 0.360 nm for some CNTs but is around 0.335 nm for the graphitic single crystals. Lennard-Jones calculations[28] for different contact geometry (graphene–graphene, graphene–C60, C60–C60) show that the repulsion, and therefore the d_{002} distance, increases with the relative curvature of the graphitic surfaces.

Finally, some attempts have been made to include the van der Waals interactions in mechanical calculations on CNTs.[29,30] A number of effects are found. In one study, as the tube diameter and number of shells increase, the

elastic shear modulus decreases and the tensile modulus increases. The authors interpret these results as follows. Under torsion, the covalent bonds and van der Waals stiffness act as springs in series; the low-shear modulus of the van der Waals bonds weaken the assembly. Under tensile loads, the van der Waals and covalent bonds act as springs in parallel; the van der Waals bonds contribute somehow to the tube's stiffness. The same argument can be constructed for shear and tensile yield strength. However, another modeling study has found an increase of buckling strength (combined shear and compressive loading) with number of shells for MWCNTs. These authors claim that the buckled regions of the MWCNTs change hybridization (from sp^2 to sp^3) and the resulting increase in strain energy enhances the buckling load.

12.2.4 Van Der Waals Bonds and Viscomechanical Behaviors

The discussion in the previous paragraph identified van der Waals bonds as defects of the carbon network, weakening both stiffness and strength. In some measure, they may also have a toughening effect. This apparent contradiction will be discussed later. A good starting point is to re-examine what exactly van der Waals (VDW) interactions are, in which materials they are prevalent, how they are detected there, and how feasible it is to use similar methods for carbon-based materials.

van der Waals was a nineteenth-century Dutch scientist who tried to take into account intermolecular interactions to fine tune existing gas laws, hence, the van der Waals equation:[31]

$$\left(P+\frac{a}{V^2}\right)\cdot\left(V-b\right)=R\cdot T \tag{12.1}$$

where P is the pressure, V the molar volume, R the gas constant, and T the temperature. This is a macroscopic law describing combined microscopic effects. Later, these interactions were identified as two antagonistic effects, the electronic cloud repulsion and the attraction due to the interaction between instantaneous dipoles, the two effects being gathered in the Lennard-Jones potential as follows[32]:

$$V\left(r\right)=\frac{c}{r^{12}}-\frac{d}{r^6} \tag{12.2}$$

In some case, the repulsive term is modeled by an exponential ($\sim be^{-ar}$). Although van der Waals introduced Equation 12.1 as only a phenomenological approximation, it does correspond to microscopic mechanisms as the constants a, b, c, and d can be related to one another using simple thermodynamics ($a = \pi.d.\ N_A^2/4a_0^4$ and $b = 0.5.\pi.N_A.a_0^2$, with N_A = Avogadro's number and a_0 the contact diameter of the molecules).[33] Strictly speaking, the

VDW interaction is only represented by the term $-d/r^6$. This dependence on distance can be justified, and the constant d calculated, using classical theory for induced-dipole/induced-dipole interactions, as introduced by London in 1937. A significant feature is that, even for nonpolar atoms, the time-averaged value of this interaction, for all random positions, is nonzero. In this approximate framework, the VDW interaction between two atoms 1 and 2 is

$$V(r) = -\frac{3}{2}\frac{\alpha_{01}.\alpha_{02}}{(4\pi\varepsilon_0)^2}\frac{1}{r^6}\cdot\frac{I_1 \cdot I_2}{(I_1+I_2)} \tag{12.3}$$

α_{01} is the atomic polarizability ($\sim 4.\pi.\varepsilon_{0.}\ a_0^3$, where a_0 is the Bohr radius) and I_1 is the first ionization energy of the atom 1. Quantum treatments may give alternative derivations for the constant d, but the $1/r^6$ dependence remains. Together with dipole–dipole and induced dipole–dipole interactions, which also have the same distance dependence, these interactions are termed long range to differentiate them from chemical binding forces such as covalent, metallic, and ionic interactions. Another difference between chemical forces and long-range interactions is that the latter are usually much weaker, from meV to a fraction of an eV, whereas chemical bonds are usually a few eV. For this reason the adopted terminology is that covalent, metallic, and ionic interactions are called primary bonds. Secondary bonds are represented by VDW and those involving polar molecules or polar groups. The latter include hydrogen bonding, hydrophilic, and hydrophobic interactions. Generally, VDW bonds (~0.01 eV) are weaker than hydrogen bonds (up to 0.4 eV) or hydrophobic interactions (up to 0.1 eV), although for large polarizable entities, such as CCl_4 molecules, the VDW energy can be as high as 0.25 eV.

VDW bonds, and other secondary interactions, are not confined to gaseous systems but are also present in many solid-state materials, mainly in synthetic polymers and biological materials. In commercial thermoplastic and thermosets, secondary bonds are responsible for low density, gas permeability, mechanical compliance, and viscoelasticity. They also have a determining effect on biological systems, influencing the folding and subsequent biological function of proteins and DNA molecules. Polymer scientists and biochemists have designed several strategies to look at secondary bonding processes. First, one can use spectroscopic techniques such as Raman analysis, Fourier transformed infrared spectroscopy (FTIR), or nuclear magnetic resonance spectroscopy (NMR) to detect directly the small bonding energy. The effects correspond to highly resolved low-wave numbers, not easily detected by Raman and FTIR analysis. Second, one can use dielectric relaxation (DR): An AC electric field is cycled (10^2 to 10^7 Hz) across the sample and the complex analysis of the circuit gives its real (ε') and imaginary (ε'') permitivities. These material parameters are representative of the polarization of molecular groups. In particular, the dielectric loss ($\varepsilon''/\varepsilon'$) relates directly to the heat/energy lost during molecular motion.

Polymer scientists see this energy dissipation as representative of secondary bonds. However, DR is not particularly adapted to carbon solids, where the dipoles are very weak (0.1 D for the C-H bond), with trace ketone or hydroxyl impurities possibly giving much stronger signals.

Third, there are a number of mechanical techniques that can detect secondary bonds. These include dynamic mechanical analysis (DMA) and studies of creep, stress relaxation, or the influence of strain rate. Here again, the common denominator to these methods is that they examine processes that are both time dependent and "reversibly dissipative." So let us examine this paradigm more in detail by considering how secondary and primary bonds may affect mechanical deformations. The crucial point is that ionic and covalent bonds are short range (<1 nm) and localized. It is, therefore, highly improbable that a multitude of minute tensile displacements exactly reverse themselves in the compressive part of the loading cycle and have all the molecular groups back at the same coordinates. It could happen for specific situations such as adhesion experiments done with AFM tips or wafer bonding of silicon substrates, but in most cases, the bonds do not reform on compression, and the primary bonds break irreversibly, resulting in plastic deformation or even mechanical failure. This is why materials made of strong primary bonds are not necessarily tough or fatigue resistant. Secondary bonds, on the other hand, are active over a longer range, up to a few 10 nm; they are delocalized. In polymers, secondary interactions do not even correspond to a stable minimal interatomic position because of steric hindrances. These attributes mean that breaking of a secondary "bond" requires a larger displacement than in the case of the primary bond (but not a larger force, generally). Upon compression, "reformation" of that bond is more likely as it can occur over a much larger displacement window than in the case of the primary bond, i.e., it can reform in another place. Therefore, apart from the specific cases mentioned above, reversible damping involves secondary interactions. In theory, the time dependency of the deformation is not the sole attribute of secondary bonds; the speed of sound is finite even in perfect covalent single crystals. However, if we consider a material made of randomly coiled chains under tension, the average bond stretch in the axial direction results from many bond stretches in a number of random directions. The time for completion of these numerous deformation events can be much longer than in the case of the crystal; the material will creep significantly. Although, the time is required to twist and stretch the covalent bonds, it is the coiling, and its modifications, that makes creep significant. This is achieved by "breaking" the secondary bonds (one can picture them as sticky wrapping around the chains) and, hence, with energy losses, i.e., mechanical damping. Therefore, in coiled systems, significant and reversible mechanical damping occurs hand in hand with time-delayed deformation, i.e., viscoelasticity and, more generally, viscomechanical deformations. Furthermore, these two related processes required the presence of secondary bonds. These systems correspond to most polymers but also to some soft metals such as amorphous selenium.[34] Creep in materials that do not contain coiled

chains is conceptually more difficult to interpret, although it is observed in many metals and amorphous materials.

12.2.5 Preliminary Results on a-C:H Films and CNT Arrays

Therefore, studying the influence of VDW bonds on the mechanical properties of carbon solids can be attempted by analyzing their viscomechanical response. The literature survey of section 12.2.3 shows that these studies are feasible. In this section we present recent results on hydrogenated amorphous carbon (a-C:H) films and a CNT array. The former were analyzed with an MTS nanoindenter whereas the latter was characterized using an atomic force microscope equipped with a nanoindenting cantilever. The differences between the two approaches will be discussed when relevant.

The a-C:H films chosen in this study possibly have microscopic regions containing oligomeric fragments and, hence, may display a viscomechanical behavior when deformed at various strain rates. They were deposited onto silicon wafers by plasma-enhanced chemical vapor deposition (PECVD) at low (100 V) and high (500 V) negative self-bias voltage. Details about the deposition conditions, Raman analysis, and nanoindentation protocols are given elsewhere.[35,36] The C-H stretch regions of the FTIR spectra are shown in Figure 12.2. The overall intensity is larger for the 100 V sample as the high bias favors the displacement of hydrogen.[37] The bonded hydrogen content is $n_H = A\int[\alpha d\omega/\omega]$, with $A = 1.35 \times 10^{21}$ cm^{-2}, α the absorption coefficient (cm^{-1}), and ω (cm^{-1}) the wave number.[38] Using densities of d(100 V) = 1.6 g/cm^3 and d(500 V) = 2.3 g/cm^3, calculated from x-ray reflectometry measurements,[39] we find the hydrogen atomic fractions x_H(100 V) = 36.4% and x_H(500 V) = 17.8%, typical values for a-C:H films.[40] For PECVD, non-bonded

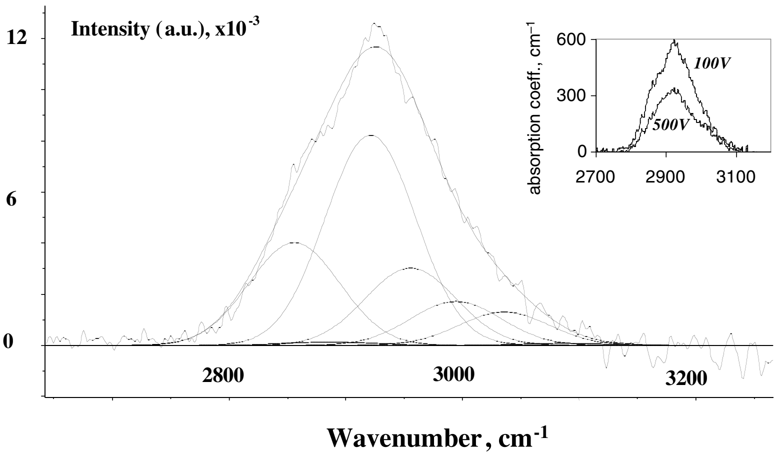

Figure 12.2 C-H stretch region of the FTIR spectrum of the 100 V a-C:H thin film. The insert shows the spectra of the overlapped 100 V and 500 V a-C:H films.

Table 12.2 Results from the Deconvolution of the FTIR C-H Stretch Region for the Two a-C:H Films

Group	Oleo CH_2	Aro CH	Oleo CH	sp^3 CH_3	sp^3 CH_2, CH	sp^3 CH_3	sp^3 CH_2
WN	3085	3035	2995	2955	2920	2885	2855
% 100 V	0.3	4.9	6.4	11.3	61.6	0.5	15
% 500 V	3.5	6.4	10.2	11.8	47.6	15.7	4.9

hydrogen is usually below 10%,[41] therefore, these hydrogenations are significant, even when compared with most hydrocarbon polymers (x_H = 50 to 70%).

The FTIR peaks were deconvoluted using standard peak assignments (see Table 12.2). The H fractions bonded to sp^2 carbon are 11.6% and 20.1% for the 100 V and 500 V, respectively. At 500 V, there are more energetic ions to remove H from hydrocarbon groups, the radicals stabilizing by forming a double bond with their immediate neighbors.[42] For sp^3 carbon, hydrogen bonds to chain-forming entities, CH and CH_2 aliphatic carbons in the 100 V sample, whereas in the 500 V sample, the hydrogen mainly belongs to CH_3 groups. Taking into account the overall peak intensities to estimate the absolute quantities in the films, we find (1) 33% more hydrogenated aromatics in the 100 V sample, (2) 25% less hydrogenated olefinics in the 100 V sample, and (3) 155% more hydrogenated aliphatic chain segments (sp^3-CH and -CH_2) in the 100 V sample. Results (2) and (3) combine to give 120% more polymeric segments in the 100 V sample.

The Raman analysis gives the anticipated broad asymmetric spectra, fitted with the G and D peaks of disordered graphite.[43] The G peak position and intensity ratio increase with bias; G_{pos}(100 V) = 1533 cm^{-1}, G_{pos}(500 V) = 1560 cm^{-1}, I_D/I_G(100 V) = 0.3, and I_D/I_G(500 V) = 0.6, an indication of larger graphitic clusters and larger sp^2 fraction in the 500 V sample. This was reported[44] and is consistent with the hydrogen displacement process described above. Moreover, the spectrum of the 100 V sample has a large luminescence background. Obviously this slope value depends on the illumination conditions but the trend is typical of a-C:H.[45] This is usually associated with hydrogen stabilizing aromatic structures, efficient quenchers of the vibrational decay to the electronic ground state. This is a conceivable explanation [see (1)]; however, in the general case, fluorescence can originate from conjugated olefins[46] (low hydrogen) or graphitic clusters (no hydrogen),[47] giving no correlation to the hydrogen content. This point is rarely considered in the literature.

The hardness (H) and Young modulus (E) were measured at 50-nm elastoplastic total depth with continuous stiffness for various constant strain rates. Figure 12.3 shows higher H and E values for the 500 V, an expected result as hydrogen lowers the average coordination of the carbon network. The 100 V sample exhibits a larger sensitivity to strain rate, conforming to trends observed elsewhere.[48] The Si data on Figure 12.3 show that substrate

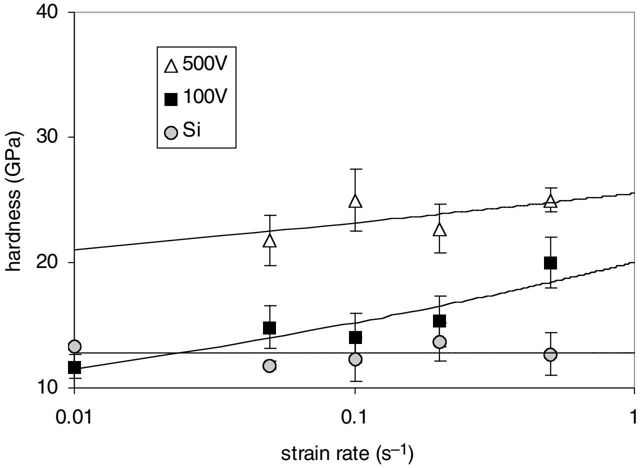

Figure 12.3 Hardness at 50 nm depth versus strain rate for the two a-C:H films and a silicon substrate.

effect and instrumental factors do not affect the measurement This result cannot be explained by a description based on covalent bonds but can, however, be interpreted as due to the time-dependent disentangling and uncoiling of chain segments, in greater number in the 100 V sample, as seen above. The viscoplastic equation $H = A(d\varepsilon/dt)^n$ fits the data with $n = 0.12$ and $n = 0.04$ for the 100 V and 500 V samples, respectively. However, the strain rate does not affect the Young modulus. It is not easy to predict how VDW bonds could affect the network's elasticity. Studies on MWCNT are instructive in that regard. The VDW energy varies with sheet curvature and stacking sequence.[49] Moreover, as more sheets are added, the tensile modulus increases slightly whereas the shear modulus decreases; i.e., under tension, the covalent and VDW stiffnesses act as springs in parallel, whereas under torsion, they are in series.[50] In a-C:H, these various scenarios may concur for VDW interactions between graphitic clusters. Considering the additional VDW bonds between hydrogenated chain segments, the overall effect is hard to forecast. What can be argued, however, is that, as an unzipping path for yield and failure, VDW bonds affect the network's plasticity more than its elasticity, the latter being mainly defined by the covalent coordination of the network, as described by the constraint counting model. Therefore, one cannot estimate H from the measurement of E and the use of the $E/H = 10$ rule, as previously proposed.[51]

To further test these results, we measured the indentation creep following step loading, as described elsewhere for polymers and bulk materials.[52,53] Expecting small creep displacements, the correction for thermal drift (<0.01 nm/s) was done after initial contact (μN load), but before imposing

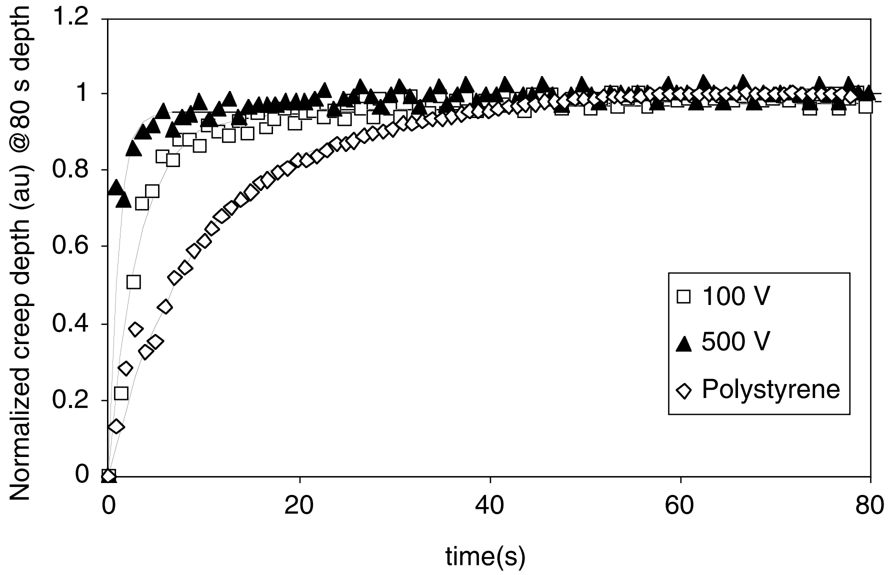

Figure 12.4 Change of depth, normalized to the creep at 80s for two a-C:H films (deposited at 100 V and 500 V bias) and a polystyrene sample.

the creep load, to avoid creep recovery. We used a low creep load L = 2 mN, to have a significant fraction of the creep signal originating from the thin film and to minimize the relative load overshoot during creep. Generally, $\delta L/L$ is 100 times smaller than the relative creep change ($\delta h/h$). Assuming a spherical tip (blunt region of the Berkovitch), h varies as $L^{2/3}$; therefore, the load is considered constant during these creep segments. The change in creep depth, shown in Figure 12.4, is normalized to the depth at 80s, to compare the dynamics of the various samples. The creep is slightly slower for the 100 V sample. The Burgess model used contains a Maxwell (E^*_m and η_m) and a Voigt element (E^*_v and η_v) in series.[54] The total indentation depth is

$$h(t) = [a + b \cdot (1 - e^{-c \cdot t}) + d \cdot t]^{2/3} \qquad (12.4)$$

with $a = 3L/(4E_m{}^*R^{0.5})$, $b = 3L/(4E_v{}^*R^{0.5})$, $c = 1/\tau_v = E^*_v/\eta_v$, and $d = 1/\tau_m = 3L/(4\eta_m R^{0.5})$.

E^*_v, η_v, and τ_v represent the "elastoplastic" stiffness, viscosity, and time constant of the network, whereas E^*_m, η_m, and τ_m represent those of more disentangled, flowing elements. This is clearly a polymeric rheological model although it was successively applied to the low-temperature creep of soda-lime glass. The fit parameters and normalized χ^2 values are reported in Table 12.3 for the two a-C:H films, a polystyrene sample, and the silicon substrate.

Table 12.3 The Burgess Model Was Fitted to the Creep Data of Figure 12.4 for These Three Samples and a Silicon Substrate.

Material	a	b	c	d =1/υ_m	τ_v (a.u.)	τ_m(a.u.)	υ_v (s)	δ^2 (x100)
PS	14251	1331	0.09	1.04	0.009	0.96	11.6	0.07
100 V	668	28	0.21	0.05	0.171	20.83	4.8	0.01
500 V	490	19	0.29	0.02	0.177	41.84	3.4	0.02
Si	0	760	1.02	0.00	0.001	387.60	1.0	8.00

The coefficients a, b, c, and d refer to Equation 12.4.

First, we find that the model does not fit silicon well, for which a logarithmic model (dh = a·log(a·t+1)), representative of crystalline dislocation processes, gives a better fit and, indeed, would be more adapted.[55] Second, going from the 500 V to the 100 V and then to the PS sample, the compliance a and b increases with the interruptions of the covalent scaffold, as expected. The same cross-examination shows that the primary creep occurs over a longer time scale (τ_v increases), but the long-term "flowing" creep is larger (τ_m decreases). This is consistent with more uncoiling and disentangling of the chain segments. Again, examining the 500 V, 100 V, and PS sample, we find a decrease of η_v and η_m. This is also consistent with Equation 12.3, as the hydrogen atom would have a smaller polarizability than the carbon atom. This gives weaker secondary bonding, smaller hardness, and smaller viscosity for the hydrogen-rich 100 V sample. Another contributing factor could be the smaller sp^2 fraction and corresponding decrease in VDW interactions between the aromatic clusters in the 100 V sample. As discussed above, these VDW regions represent interruptions and, therefore, weaknesses in the carbon network. At another level, they also constitute mechanical dampers that may improve the toughness of the materials, much the same way as hydrogen bonding toughens Kevlar fibers and spider silk.

We will now examine viscomechanical measurements carried out on a commercial CNT forest. These are MWCNTs grown by a MWCVD process. SEM micrographs show that most of these MWCNTs are arranged in bundles with diameters varying between 20 nm and 100 nm. The bundle density is approximate 10 bundles/μm^2. The goal is to develop a method to gauge CNT–CNT interactions, as this could be used to optimize functionalization strategies and obtain CNT samples with either a minimal (composite applications) or a maximal (sensor applications) level of interactions. The sample was prepared on a silicon substrate by a microwave PECVD method. Figure 12.5 shows a 5-kV SEM images of the CNT array. This indicates that the film is 10 μm thick and the CNTs are vertically aligned. For a CNT film, it also seems fairly densely packed, although TEM observation would be required to have a more accurate idea about its packing density. One should note, however, that when compared with homogeneous samples such as glassy polymers, DLC, or metals, this sample contains many voids and is obviously of low density.

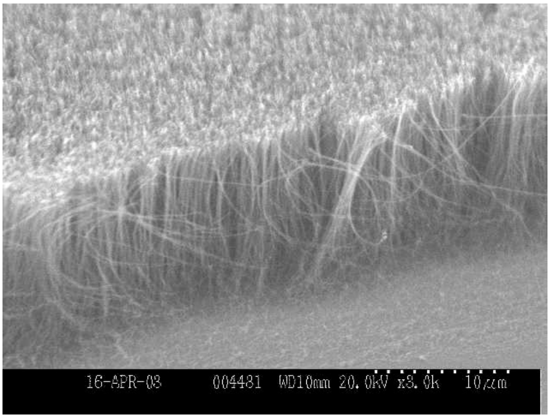

Figure 12.5 SEM micrograph at 5 kV of the CNT array.

The viscomechanical response of this CNT sample was examined with a Dimension 3100 atomic force microscope (AFM). We used a 0.35-mm-long stainless steel cantilever with spring constant k = 195 N/m having a Berkovitch- like diamond tip. As the sample was tested at relatively large depths (a few 100 nm), we took the approximation of a perfectly sharp indenter tip. Its inclination angle β was characterized using SEM imaging and nanoindentation. We also used a blind reconstruction software to analyze AFM images of an array of high-aspect-ratio Si tips. These measurements gave $\beta = 35°$ and, in keeping with the formalism of the nanoindentation Oliver and Pharr model,[56] we have the following relationship between the reduced area A_c and contact depth h_c: $A_c = 9h_c^2/(\tan^2\beta \cdot 3^{1/2}) = 10.6\ h_c^2$. The software permits the variation of the vertical displacement scan rate (in Hz) during indentation, which, considering the stiffness of the cantilever, is more or less equivalent to the indentation displacement rate dh/dt.

We refrained from performing measurements below 1 Hz to avoid creep effects in the piezoelements of the microscope. The force calibration was done on a sapphire sample. We found a constant deflection sensitivity from 1 Hz to 30 Hz of $S_d = 181$ nm/V. We also ensured that (1) the sensitivity did not vary with the load range and (2) no indents were formed on sapphire (no elastic or plastic deformation). The sample was approached in tapping mode with a relatively high, gentle set point (oscillation amplitude $2A_0 = 50$ nm, set point = 80%). We carried out indentations on the CNT sample at several frequencies from 1 Hz to 30 Hz. The software generated indentation force curves (Z of piezoelement versus photodetector voltage V), which were transformed into load-displacement (L-d) curves ($h = Z - (V \cdot S_d)$ versus $L = k \cdot V \cdot S_d$). We found no change in L-d curves from 1 Hz to 30 Hz. We gather in Figure 12.6 the L-d curves for 1 Hz and 30 Hz. The difference between the two curves in the low depth region is due to the nature of the surface contact, which shows statistical variation for a such low density sample. Overall, there is no difference between the two curves; for this frequency range, this CNT

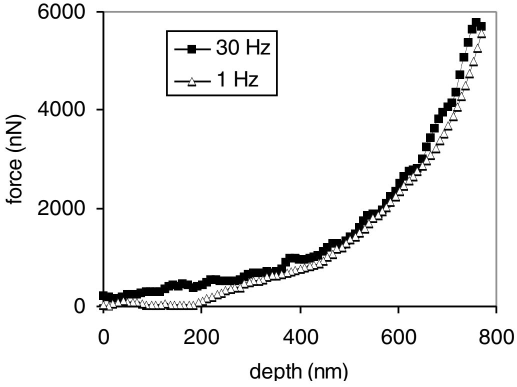

Figure 12.6 Load-displacement curves for the CNT array at 1 Hz and 30 Hz.

sample shows no viscomechanical dependence. Considering the thickness of the CNT film (several microns) and the range of deformation (~800 nm), we believe that most of the deformation is due to buckling of the flexible tubes.

Although AFM nanoindentation has been used on a range of polymeric and inorganic samples and also to measure the deformations of individual CNTs, it has not been used extensively to characterize CNT arrays. One study by Qi et al.,[57] however, presents a comprehensive statistical analysis of mechanical indentations on a range of CNT arrays prepared by a PECVD method. We note a broad qualitative agreement between Figure 12.6 and the results of Qi et al. For instance, a force of several μN gives a few 100 nm displacement into the film. The stiffness, graphically determined from Figure 12.6, is S = 28N/m, which gives $h_c = 570$ nm and $A_c = 3.44$ μm^2, and using $S = 2\,(A/\pi)^{1/2}\,E^*$, we get the reduced modulus $E^* \sim E = 0.013$ GPa. This very low value is essentially due to the low level of interconnection between CNTs. Approximate calculations on single CNTs gives the individual CNT stiffness $k_{cnt} \sim E_{cnt}A/L$. Using the SEM micrograph and an E_{cnt} value of 1 TPa, we get $k_{cnt} \sim 7.8$ N/m. Further simplistic assumptions give the resonant frequency of the CNTs, $f = 1/2.[E/(d \cdot L^2)]^{1/2} \sim 1.1$ GHz. As a forced oscillator, the CNT film will exhibit most mechanical damping around this resonance. Mechanical deformations from 1 to 30 Hz would, therefore, give the same deformation of this sample.

This situation contrasts with that of dense homogeneous solids, such as glasses, DLC, and polymers. In these materials, the individual resonances of the vibrating molecular entities are also in the high-frequency domain although somewhat lower than those of individual CNTs (polymeric chain segments may resonate at frequencies as low as a few KHz). However, compared with these materials, the CNT sample is a more loosely bound network. Although long range, VDW interactions require relatively close contacts (<10 nm), which, according to our SEM micrographs, are relatively few within the film thickness. In this situation, low-frequency

creep effects are difficult to observe and viscomechanical effects would be more adequately characterized using a dynamic technique. This may not be necessarily carried out at GHz frequencies as one study, for instance, used similar CNT arrays as efficient mechanical dampers for piezo beams resonating around 800 Hz.[58] Finally, although kept under careful control, the tapping contact is probably not gentle enough, as it corresponds to an intermittent force of a few μN. Using a more compliant cantilever would help achieve a gentler surface detection. These experiments are currently underway in our laboratory.

12.3 Nanopatterning and Processing of Carbon Materials

12.3.1 Introduction

The structuring and etching of carbon materials is essential for a number of applications. For instance, CNT field emission displays have been fabricated using photolithography.[59] Other applications, including sensors, micromechanical systems, and data storage media, require the definition of patterns of much smaller dimensions. For instance, an area of growing significance is that of using organic templates as precursors for building high-density data storage media[60] or nanocomposites or for designing efficient biomolecular sensors. In many cases, the adsorption of the template is triggered by a shallow patterning or structuring of a carbon substrate with nanoscale dimension. Such high-resolution patterning is usually achieved by using smaller wavelength, more energetic radiation that can be tightly focused down to 10 nm spots, namely, electron and ion beams. The traditional way of making devices for electronic, optical, optoelectronic, or microelectromechanical systems (MEMS) applications is to sequentially deposit and pattern the various components of the device. The difficulty is that energetic ions and electrons are also used to synthesize carbon materials. For instance, DLC, mostly prepared by plasma deposition techniques, is formed by the bombardment of energetic ionic species. CNTs, often prepared by chemical vapor deposition methods, are also growing from an environment of intense ionic bombardment. It seems, therefore, that an optimized deposition process could well result in a pattern of transformed material with inadequate properties. For carbon, the main problem is graphitization, which is known to occur, in DLC for instance, following intense visible[61] or ionic irradiation.[62] Ion beams are also used for doping CNTs and likewise have the potential to create defects on the surface of the CNTs. Another problem with this dual deposition/patterning approach is the complexity and cost of the systems, which cannot always be justified in a commercial context. The alternative strategy discussed here is to use a single-step process to simultaneously deposit and pattern the device. Its added advantage is that tridimensional structures can easily be built by this method and, in theory, process parameters (current density, kV, pressure, etc.) can be tuned more independently than in conventional plasma deposition systems.

The idea behind this technology is that hydrocarbon layers often built up on material surfaces when subjected to electron or ion beam irradiation in the presence of oil vapors from the vacuum system. Electron microscopists have always endeavored to remove these contamination layers and observe the pristine surface below. Over the last 20 years, there has been some effort to use this process as a writing tool for device fabrications.[63] At low magnification and slow scanning speed, the contamination is low and a survey scan of the device can be obtained. The desired pattern is then formed by scanning slowly over a smaller area, eventually with a larger beam current or accelerating voltage. This method produced single electron transistors, hard AFM supertips and tough nanometer-thick resist for the electrochemical formation of porous silicon. [64–66] This contamination resist technology has also been applied to the processing of semiconductor materials such as CdS[67] and GaAs.[68] Focused ion beams (FIB), first introduced for highly specialized tasks such as assisted TEM sample preparation, are also widely used to pattern materials and devices. In the following section we will examine and compare the two approaches, using a conventional scanning electron microscope and a dual FIB-SEM system equipped with a naphthalene gas injector to deposit carbon on silicon substrates. Our interest is twofold. First, having a broad expertise in the deposition and analysis of amorphous carbon, with several deposition systems (PECVD, FCVA, UBMS) and on-site analysis suites (XPS, XRR, AES, FTIR, Raman analysis, and nanoindentation), we would like to explore and compare the carbon material prepared by EBID and FIB techniques, as an alternative to the DLC materials prepared by more conventional plasma deposition techniques. Second, we are interested in carbon nanostructures, to develop nanomechanical probes, to create model surfaces for studying biomolecular adsorption processes, and to engineer templates for nanometrological, sensing, and storage media applications. As this represents a fairly novel activity, we will report only preliminary results and discussion.

12.3.2 EBID Formation of a-C:H Films and Structures

We used a Hitachi S3200N low vacuum scanning electron microscopy (LVSEM) system. The electron current density on the sample was varied by changing the working distance, aperture size, or condensor settings. In addition, our LVSEM system allowed us to change the background pressure from 10^{-4} Pa to 300 Pa. The deposition rate was measured by AFM microscopy. The properties of the deposited films were measured by Raman analysis and nanoindentation. We discuss below the effects of the varying parameters:

- **Time of irradiation:** At 10^{-4} Pa, 5 kV, and 100,000 magnification, we notice from t = 0 s to t = 1000 s a constant deposition rate with time of 12 nm/min. This compares well with growth rates of PECVD (5 to 10 nm/min).
- **Scanning speed:** Figure 12.7 shows a carbon pattern on a silicon substrate acquired at 10^{-4} Pa, 5 kV in TV mode (frame acquisition <<1 s).

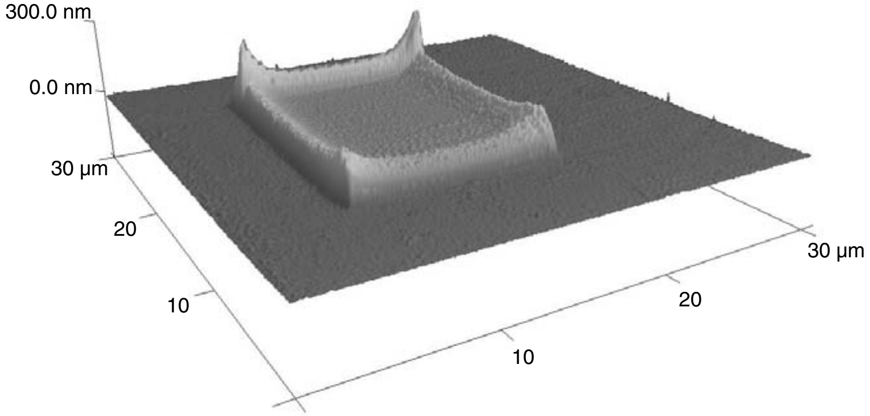

Figure 12.7 Carbon structures grown by EBID, showing tip and edge formation due to the variable residence time during scanning.

The larger residence time at the top left corner and around the edges of the scanned area results in larger carbon thickness, as seen on the figure. Slower scanning speeds give much flatter profiles. This problem is not as pronounced with the electron beam of the dual FIB/SEM FEI system.

- **Working distance:** Again at 10^{-4} Pa, 5 kV, varying the working distance from 5, 8, and 14 mm changes the carbon thickness from 16 nm to 10 nm to 5 nm. This trend, which may be expected as the electron current density increases with WD, may not be valid for all conditions as higher flux could trigger the back-sputtering of the carbon layer. This has been observed in other EBID experiments but also in PECVD.[69]
- **Pressure:** The growth rate is higher at 10^{-4} Pa than at 1 Pa, and this trend remains for higher pressure. Several reasons can be advanced for this result. First, the carbon originates from the oil mist, not from the background air pressure; second, scattering in the ambient gas reduces the electron energy and flux, hence the deposition rate; finally, oxygen is known to etch carbon and, indeed, is used to remove contamination in semiconductor processes.
- **Accelerating voltage:** It is difficult to ascertain its effect, as the electron flux also changes with kV. Nonetheless, using EDX analysis, we found oxygen in the films at both 5 kV and 20 kV. We found that both films had similar Raman spectra and nanohardness. We also noted that below 1 kV, the films are soluble in acetone and, therefore, still probably organic.

Such a Raman spectrum obtained at 514 nm is shown in Figure 12.8. After subtraction of the luminescence background, the spectrum can be fitted

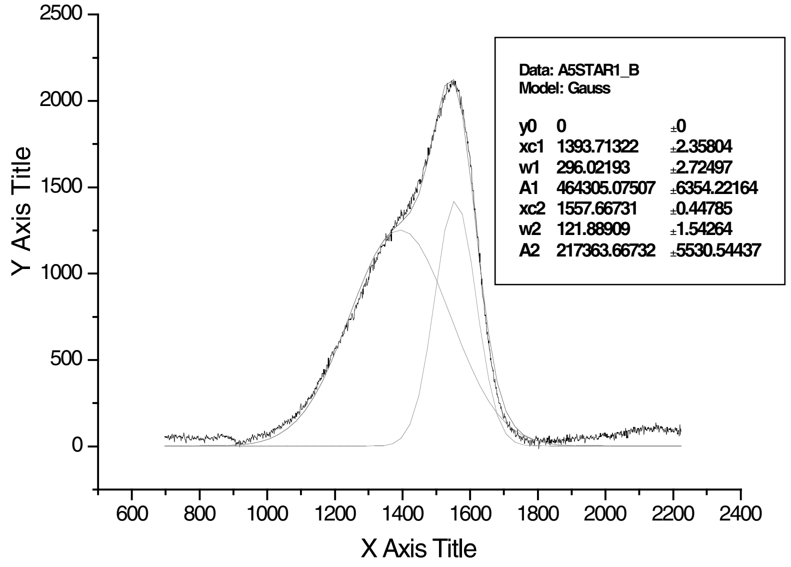

Figure 12.8 Raman spectrum of EBID carbon film.

with the D and G band, usually found in a-C:H spectra. The broad spectral shape is similar to that obtained for a-C:H films grown by PECVD. The I_D/I_G intensity ratio of the EBID sample is much higher (0.86 instead of 0.3 to 0.6) than that of the PECVD sample although both samples have a similar G peak position (~1560 cm^{-1}). Moreover, the width of the D peak is much larger for the EBID sample (FWHM ~ 318 cm^{-1} instead of 200 cm^{-1}). The hardness values measured with the MTS nanoindenter are shown in Table 12.4. Again, these films are somewhat softer than a-C:H grown by PECVD; however, they are much harder than graphite. Overall, these results suggest that EBID carbon is a form of a-C:H. This is also the consensus arising from the literature. Initially, the hydrocarbon molecules adsorbed on the surface are polymerized by the electron beam. At a later stage, this polymeric film is densified and reticulated by preferential displacement of hydrogen, leaving hydrogenated amorphous carbon. Figure 12.9 shows an SEM micrograph of a high-aspect-ratio carbon needle grown by EBID on polycrystalline aluminum.

Table 12.4 Nanohardness Measurements on EBID Carbon films.

Material	H at 50 nm depth	H at 100 nm depth
EBID carbon @ 20 kV	9.6	11.8
EBID carbon @ 5 kV	9.8	11.6
Silicon	12.6	12.3
Graphite	0.2–2	0.2–2

The Depths Represent the Full Elastoplastic Deformation

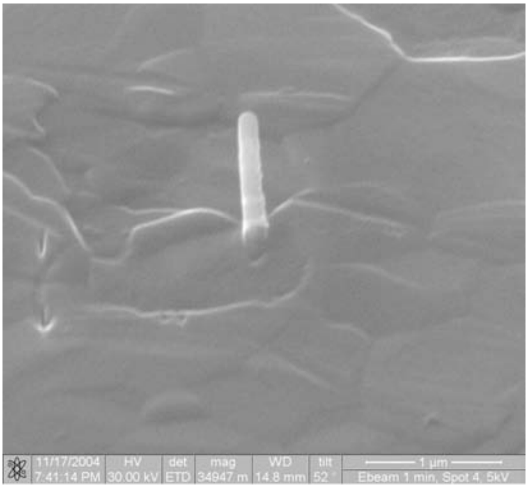

Figure 12.9 SEM micrograph of a high-aspect-ratio carbon needle grown by EBID on polycrystalline aluminum.

12.3.3 FIB Formation of a-C:H Films and Structures

We used a Quanta 3D FEI dual FIB/SEM system. The base pressure was 10^{-6} torr and the carbon was grown from a naphthalene gas injector. The structures were grown by accelerating the ion beam at 30 kV with gallium ion currents varying from 1 pA to 5nA. Some FIB processing examples are shown in Figure 12.10 through Figure 12.13. In Figure 12.10, an FIB carbon supertip

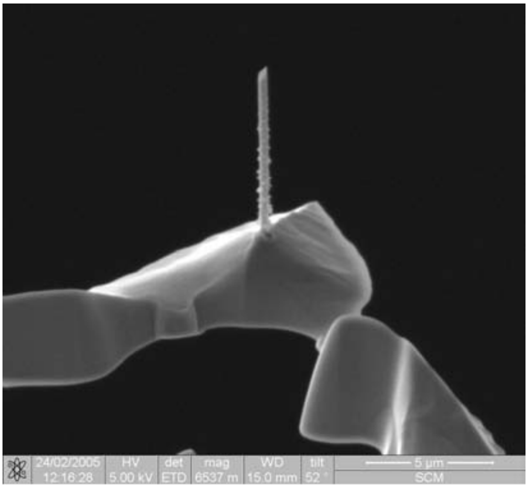

Figure 12.10 FIB carbon supertip grown on a modified AFM cantilever. The Si tip was milled away and the carbon supertip was positioned on the apex of the lever.

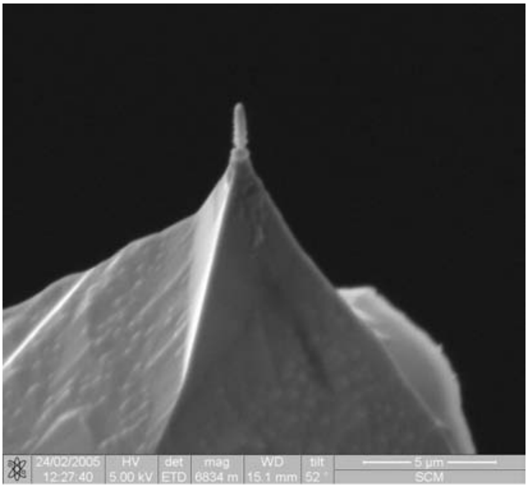

Figure 12.11 FIB carbon supertip grown directly onto an AFM Si tip.

was grown on a modified AFM cantilever. The Si tip was milled away and the carbon supertip was positioned on the apex of the lever. In Figure 12.11, the carbon supertip was grown directly onto an AFM Si tip. However, the structure is possibly fragile, as it is thinner at its base. Therefore, this was then milled and removed using higher ion currents (20 nA). Subsequently, the procedure was repeated with a more attentive astigmatic correction and lower ion current, in a two-stage process, first with 10 pA, then with 1 pA. The resulting supertip, shown in Figure 12.12 and Figure 12.13, grows from

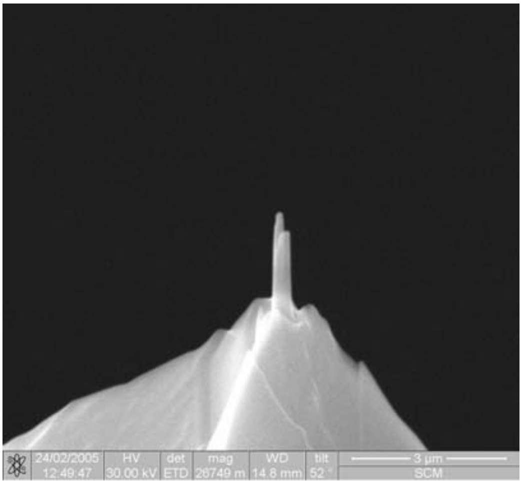

Figure 12.12 FIB carbon supertip grown directly onto an AFM Si tip in a two-stage process, first with 100 pA and then 10 pA.

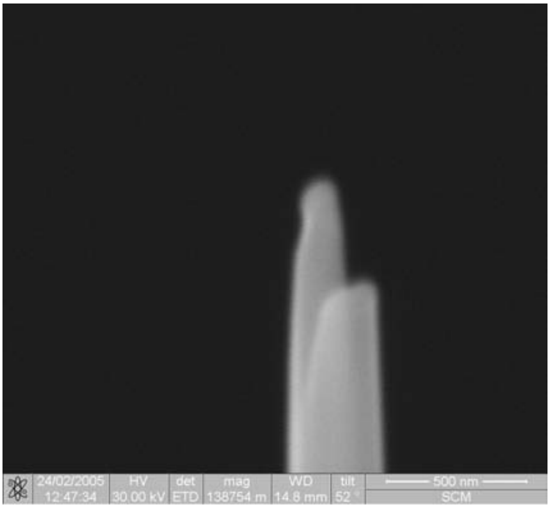

Figure 12.13 A high-magnification view of the supertip shown in Figure 12.11.

a more solid base and its final part, grown at 1 pA, is much sharper, with a sub-100-nm end diameter. In this preliminary study, the carbon supertips were optimized for growth rate and aspect ratio. The use of smaller currents and spot sizes and better astigmatic corrections could give finer tips. However, the resolution is strongly determined by molecular and radical diffusion at the surface and ion and electron scattering within the sample.[70] In this regard, the use of lower kV and denser substrate underlayers (W) may help achieve better resolution.

Nonetheless, these structures, deposited on AFM cantilevers, were successfully used for imaging a sintered ceramic target in tapping mode, as shown in Figure 12.14. Figure 12.15 shows a Raman spectrum of an FIB carbon film prepared at 3 nA. As for EBID, we recognize the spectral features of a-C:H, here with a G peak position at 1539 cm^{-1} and an I_D/I_G intensity ratio of 1.05. We note, however, a satellite peak around 700 cm^{-1}, not observed for EBID carbon. The other FIB carbon films show very similar features. In this case, the nanoindentation measurements were carried out with the AFM microscope, calculating the hardness values from the calibrated load and measured reduced area, imaged in tapping mode. The results are shown in Table 12.5. The values seem higher at the lowest load, shallowest depth. This could be due to gallium incorporation, which indeed would occur for shallow depths.[71] A current of 3 nA seems to give the hardest films. It is difficult to compare these values with those of the EBID carbon films, measured with the MTS nanoindenter. The tip geometries of the two instruments are different, and this will result in differences in shear stress distribution under the diamond tip, hence different hardness values. Looking at the silicon data, it seems that the AFM tip is blunter and gives smaller H values. This considered, we can say that both techniques, EBID and FIB, give carbon films with

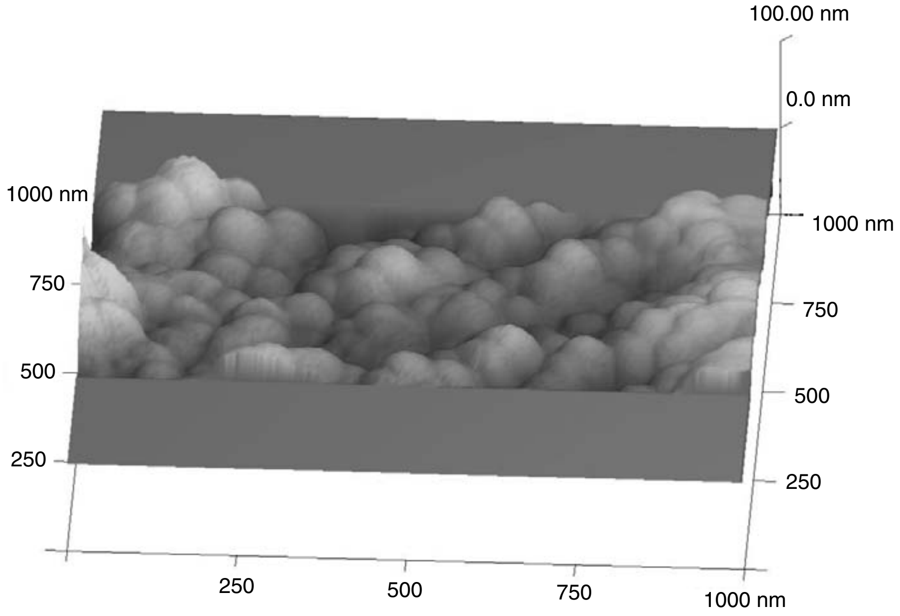

Figure 12.14 Tapping mode AFM image of a sintered ceramic target obtained with the supertip of Figure 12.12.

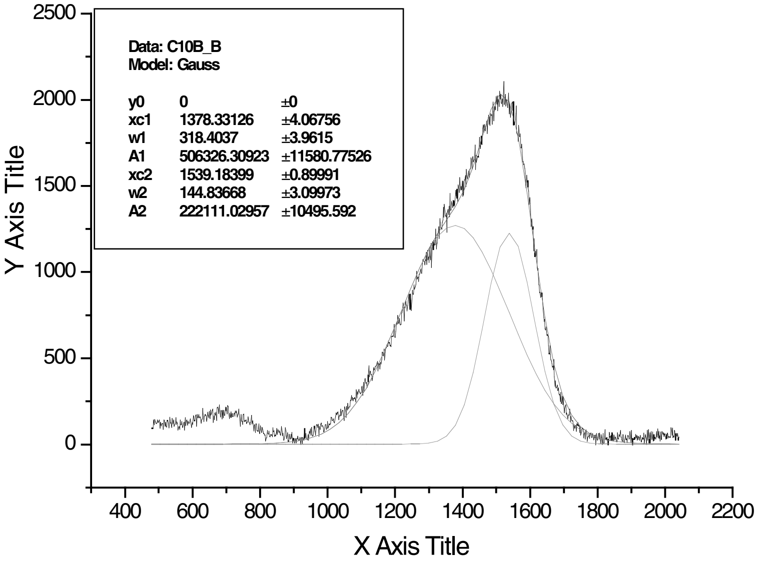

Figure 12.15 Raman spectrum of FIB carbon film.

Table 12.5 Hardness Values of the FIB Carbon Films Measured with the AFM Microscope

Sample	Hardness at 110 vN (GPa)	Hardness at 55 vN (GPa)
FIB carbon @ 0.1 nA	7.9	10.5
FIB carbon @ 0.3 nA	8.1	14.0
FIB carbon @ 0.5 nA	8.6	8.9
FIB carbon @ 3 nA	13.1	22.4
FIB carbon @ 5 nA	9.7	11.7
Silicon	8.0	—
Fused silica	7.0	—

similar hardness values that are in line with those of amorphous carbon films grown by PECVD techniques.

Another observation is that using either energetic electrons or ions and a wide range of hydrocarbon gases, oil mist, naphthalene, or ethylene vapor[72] all seem to result in the formation of hydrogenated amorphous carbon, again as grown by PECVD techniques. Indeed, the current growth model for PECVD considers the growth process as being essentially due to the surface adsorption of hydrocarbon ions and radicals, polymerization, and subsequent densification and reticulation through the preferential displacement of hydrogen, the subplantation of energetic carbon ions into the growing film being less mandatory than in the case of FCVA or PLD depositions. Finally, we noted above the use of EBID to produce ultrathin (~1 nm) insulating layers used for electrochemical patterning/synthesis of porous silicon. By contrast, contamination layers are also used to remove charging artifacts during the e beam processing of diamond tips.[63] Therefore, by the same technique, carbon films with a wide range of electrical conductivity can be produced, and it may be that EBID and FIB processes are able to prepare and pattern a wider range of carbon materials than any single plasma deposition technique. Here lies another precious advantage, as a local and organized control of the surface properties of carbon, work function, sp^3 fraction, hydrogenation, dangling bonds, mechanical compliance, etc., would serve as a powerful tool for engineering the interactions between biomolecules and for building nanodevices based on molecular architectures. This calls for more fundamental surface analysis studies of these carbon films and, more immediately, requires a better control of the current density, which is affected by many factors (kV, gas pressure, focusing, and alignment).

12.4 Conclusions

Carbon's ability to hybridize as single or double bonds is responsible for the formation of not only diamond and graphite; a host of other elemental carbon materials with wide-ranging properties appear in nature or have been synthesized for commercial applications. These materials contain a range of defects such as voids, dislocations, secondary bonds, and dangling bonds. If carbon is to be used as a fundamental building block of nanodevices, as is advocated by many, the influence of these nanoscale heterogeneities must be reassessed within the nanomanufacturing context. This constitutes the first issue examined in this chapter. We focused on diamond-like carbon (DLC), carbon nanotubes (CNT), and carbon fibers, as they are key materials for existing and emerging technologies. Comparing these materials, we concluded that whether the material is organized at the microscale or nanoscale, whether it forms fibers or thin films, the nature of the covalent bonds, sp^2 or sp^3, is not the sole prerequisite for superior mechanical properties. The mechanical behavior of carbon is also influenced by the van der Waals bonds, which may represent the unzipping path of yield and failure. We propose that a distinctive feature of these weak interactions is that they give rise to time-dependent dissipative deformations and, hence, can be detected by measuring the viscomechanical response of the material. Only a few carbon materials have been studied by this method and we presented and discussed recent results on the viscomechanical response of hydrogenated amorphous carbon films and CNT arrays.

The other important topic concerning the nanomanufacturing of carbon devices is the development of an adequate patterning technology. Again, the ability of carbon to hybridize, and its associated metastability, impacts the fabrication process. An optimized coating or material may be altered during patterning, as the same energetic beams of ions and electrons are used for both synthesis and patterning. We suggest that the two tasks may be combined using focused beams of electrons or ions to deposit the material and pattern it at once. Examples of applications include the use of carbon contamination resists for defining electroluminescent porous silicon patterns, hard carbon AFM probes, or single electron transistors. Using Raman spectroscopy and nanoindentation, we showed that both electron and ion beams can be used to synthesize a hydrogenated amorphous carbon that is similar to the material deposited by PECVD techniques. We also showed that the formed nanostructures can be used as high-aspect-ratio tips, for AFM imaging.

Acknowledgments

Many thanks to Dr. Susanta Roy for help with the Raman fitting routine and to Peter O'Hare for providing the ceramic sample.

References

1. Levi, P., *The Periodic Table*, Enaudi, Italy, 1975.
2. Bundy, F.P., Hall, H.T., Strong, H.M., and Wentorf, Jr., R.H., Man-made diamonds, *Nature*, 176, 51, 1955.
3. Scandolo, S. et al., *Phys. Rev. B*, 53, 5051, 1996; Liu, A.Y., et al., *Phys. Rev. B*, 45, 4579, 1992.
4. Tomanek, D, Mesoscopic origami with graphite: scrolls, nanotubes, peapods, *Physica B*, 323, 86, 2002.
5. Iijima, S., Helical microtubules of graphite carbon, *Nature*, 354,56, 1991.
6. Salvetat-Delmotte, J.P. and Rubio, A., Mechanical properties of carbon nanotubes: a fiber digest for beginners, *Carbon*, 40, 1729, 2002.
7. Popov, V.N, Carbon nanotubes: properties and application, *Mater. Sci. Eng. R*, 43, 61, 2004.
8. Treacy, M.M.J, Ebbesen, T.W., and Gilson, J.M., Exceptionally high Young's modulus observed for individual carbon nanotubes, *Nature*, 381, 678, 1996.
9. Salvetat-Delmotte, J.P. and Rubio, A., Mechanical properties of carbon nanotubes: a fibre digest for beginners, *Carbon*, 40, 1729, 2002.
10. Okpalugo, T.I.T., Papakonstantinou, P., Murphy, H., McLaughlin, J., and Brown, N.M.D, High resolution XPS characterization of chemical functionalised MWCNTs and SWCNTs, *Carbon*, 43, 153, 2005.
11. Dalton, A.B., Collins, S., Razal, J., Munoz, E., Ebron, V.H., Kim, B.G., Coleman, J.N, Ferraris, J.P., and Baughman, R.H., Continuous carbon nanotube composite fibers: properties, potential applications, and problems, *J. Mater. Chem.*, 14, 1, 2004.
12. Poulin, P, Vigolo, B., and Launois, P., Films and fibers of oriented single wall nanotubes, *Carbon*, 40, 1741, 2002.
13. Serp, P., Corrias, J.M., and Kalck, P., Carbon nanotubes and nanofibers in catalysis, *Appl. Catal. Gen.*, 253, 337, 2003.
14. Nguyen, C.V., Delzeit, L., Cassell, A.M., Li, J., Han, J., and. Meyyappan, M., Preparation of nucleic acid functionalized carbon nanotube arrays, *Nanoletters*, 2, 1079, 2002.
15. http://www.soficar-carbon.com/uk/pdf/863uk.pdf, May 2004.
16. Walsh, P.J., Carbon fibres, in *The ASM Handbook*, vol. 21, 2001, p. 35.
17. Hashishin, T., Iwanaga, H., Ichihara, M., and Mukai, S.R., Core structure of vapor grown carbon fibres and morphology dependence of tensile strength, *Carbon*, 41, 343, 2003.
18. Robertson, J., Diamond-like amorphous carbon, *Mater. Sci. Eng.*, R37, 129, 2002.
19. He, H. and Thorper, M.F., Elastic properties of glasses, *Phys. Rev. Lett.*, 54, 2107, 1985.
20. Walters, J.K., Algar, C.D., Burke, T.M., Rigden, J.S., Newport, R.J., Bushnell-Wye, G., Howells, W.S., Sattel, S., Weiler, M., and Ehrhardt, H., A neutron and X-ray diffraction study of the influence of deposition conditions on the structure of a-C:H, *J. Non-Cryst. Solids*, 197, 41, 1996.
21. Alexandrou, I., Scheibe, H-J., Kiely, C.J., Papworth, A.J., Amaratunga, G.A.J., and Schultrich, B., Carbon films with an sp^2 network structure, *Phys. Rev. B*, 60, 10903, 1999.

22. Gago, R., Jiménez, I., Albella, J.M., Climent-Font, A., Caceres, D., Vergara, I., Banks, J.C., Doyle, B.L., and Terminello, L.J., Bonding and hardness in non-hydrogenated carbon films with moderate sp^3 content, *J. Appl. Phys.*, 87, 8174, 2000.
23. Robertson, D.W., Brenner, D.W., and Mintmire, J.W., Energetics of nanoscale graphitic tubules, *Phys. Rev. B*, 45, 12592, 1992.
24. Field, J.S. and Swain, M.V., The indentation characterisation of the mechanical properties of various carbon materials: glassy carbon, coke and pyrolytic graphite, *Diam. Rel. Mater.*, 9, 184, 2000.
25. Iwashita, N., Swain, M.V., Field, J.S., Ohta, N., and Bitoh, S., Elasto-plastic deformation of glass-like carbons heat-treated at different temperatures, *Carbon*, 39, 1525, 2001.
26. Richter, A., Ries, R., Smith, R., Henkel, M., and Wolf, B., Nanoindentation of diamond, graphite, Diam. Rel. Mater., 9, 170, 2000.
27. Endo, M., Takeuchi, K., Hiraoka, T., Furuta, T., Kasai, T., Kiang, C-H., and Dresselhauss, M.S., Stacking nature of graphene layers in carbon nanotubes and nanofibres, *J. Phys. Chem. Solid.*, 58, 1707, 1997.
28. Girifalco, L.A., Hodak, M., and Lee, R.S., Carbon nanotubes, buckyballs, ropes, and a universal graphitic potential, *Phys. Rev. B*, 62, 13104, 2000.
29. Li, C. and Chou, T.W., Elastic moduli of multi-walled carbon nanotubes and the effect of van der Waals forces, *Compos. Sci. Tech.*, 63, 1517, 2003.
30. Cumings, J. and Zettl, A., Low-friction nanoscale linear bearing realized from multiwall carbon nanotubes, *Science*, 289, 602, 2000.
31. Van der Waals, J.D., The thermodynamic theory of capillarity under the hypothesis of a continuous variation of density Z.f. *Phys. Chem.*, 13, 657, 1894.
32. Aschcroft, N.W. and Mermin, N.D., *Solid State Physics*, Saunders College Publishing, Forth Worth, TX, 1976, p. 399.
33. Israelachvili, J.N., *Intermolecular and Surface Forces*, Academic Press, London, 1985, chap. 6.
34. Caprion, D. and Schober, H.R., Structure and relaxation in liquid and amorphous selenium, *Phys. Rev. B*, 62, 3709, 2000.
35. Lemoine, P., Zhao, J.F., Quinn, J.P., McLaughlin, J.A., and Maguire, P., Hardness measurements at shallow depths on ultra-thin amorphous carbon films deposited onto silicon and Al_2O_3–TiC substrates, *Thin Solid Films*, 379, 166, 2000.
36. Lemoine, P., Quinn, J.P., Maguire, P., and McLaughlin, J.A., Comparing hardness and wear data for tetrahedral amorphous carbon and hydrogenated amorphous carbon thin films, *Wear*, 257, 509, 2004.
37. Jakob, W., Surface reactions during growth and erosion of hydrocarbon films, *Thin Solid Films*, 326, 1, 1998.
38. Liu, S., Gangopadhyay, S., Sreenivas, G., Ang, S.S., and Naseem, H.A., Infrared studies of hydrogenated amorphous carbon (a-C:H) and its alloys (a-C:H,N,F), *Phys. Rev. B*, 55, 13020, 1997.
39. Abbas, G.A., McLaughlin, J.A., and Harkin-Jones, E., A study of ta-C, a-C:H and Si-a:C:H thin films on polymer substrates as a gas barrier, *Diam. Rel. Mater.*, 13, 1342, 2004.
40. Lejeune, M., Durand-Drouhin, O., Henocque, J., Bouzerar, R., Zeinert, A., and Benlahsen, M., Optical investigations and Raman scattering characterisation of carbon bonding in hard amorphous hydrogenated carbon films, *Thin Solid Films* 389, 233, 2001.

41. Donnet, C., Fontaine, J., Lefebvre, J., Grill, A., Patel, V., and Jahnes, C., Solid state 13C and 1H nuclear magnetic resonance investigations of hydrogenated amorphous carbon, *J. Appl. Phys.*, 85, 3264, 1999.
42. Godet, C., Heitz, T., Bouree, J.E., Bouchet, B., Dixmier, J., and Drevillon, B., Correlation between luminescence properties and microstructure of hydrogenated amorphous carbon films investigated by X-ray diffraction and infrared ellipsometry. *Sol. State Comm.*, 111, 293, 1999.
43. Ferrari, A.C. and Robertson, J., Interpretation of Raman spectra of disordered and amorphous carbon, *Phys. Rev. B*, 61, 14095, 2000.
44. Ogwu, A.A., Lamberton, R.W., Morley, S., Maguire, P., and McLaughlin, J., Characterisation of thermally annealed diamond like carbon (DLC) and silicon modified DLC films by Raman spectroscopy, *Physica B*, 269, 335, 1999.
45. Marchon, B., Gui, J., Grannen, K., Rauch, J.C., Ager, J.W., Silva, S.R.P., and Robertson, J., Photoluminescence and Raman spectroscopy in hydrogenated amorphous carbon films, *IEEE Trans. Mag.*, 33, 3148, 1997.
46. Luzzati, S., Moggio, I., Comoretto, D., Cuniberti, C., and Dellepiane, G., Polarization properties of a novel oriented polydiacetylene, *Synthetic Met.*, 95, 47, 1998.
47. Chang, S.S,. Luminescence properties of spark-processed porous graphite. *Mater. Sci. Eng. B*, 106, 56, 2004.
48. Sanchez-Lopez, J.C., Donnet, C., Loubet, J.L., Belin, M., Grill, A., Patel, V., and Jahnes, C., Tribological and mechanical properties of diamond-like carbon prepared by high-density plasma, *Diam. Rel. Mater.*, 10, 1063, 2001.
49. Hodak, M. and Girifalco, L.A., Fullerenes inside carbon nanotubes and multi-walled carbon nanotubes: optimum and maximum sizes. *Chem. Phys. Lett.*, 350, 405, 2001.
50. Li, C. and Chou, TW., Elastic moduli of multi-walled carbon nanotubes and the effect of van der Waals forces. *Compos. Sci. Tech.*, 63, 1517, 2003.
51. Beghi, M.G., Bottani, C.E., Ossi, P.M., Lafford, T., and Tanner, B.K., Combined surface brillouin scattering and x-ray reflectivity characterization of thin metallic films. *J. Appl. Phys.*, 81, 672, 1997.
52. Yang, S., Zhang, Y.W., and Zeng, K., Analysis of nanoindentation creep for polymeric materials. *J. Appl. Phys.*, 95, 3655, 2004.
53. Fischer-Cripps, A.C., A simple phenomenological approach to nanoindentation creep, *Mater. Sci. Eng. A*, 385, 74, 2004.
54. Shen, J., Green, D.J., Tressler, R.E., and Shelleman, D.L., Stress relaxation of a soda lime silicate glass below the glass transition temperature, *J. Non-Cryst. Solids*, 324, 277, 2003.
55. Nabarro, F.R.N., The time constant of logarithmic creep and relaxation. *Mater. Sci. Eng.*, 309, 227, 2003.
56. Oliver, W.C. and Pharr, G.M., An improved technique for determining hardness and Young modulus using load and displacement sensing indentation experiments, *J. Mater. Res.*, 7, 1564, 1992.
57. Qi, H.J., Teo, K.B.K., Lau, K.K.S., Boyce, M.C., Milne, W.I., Robertson, J., and et al. Gleason, K.K., Determination of mechanical properties of carbon nanotubes and vertically aligned carbon nanotube forests using nanoindentation, *J. Mech. Phys. Sol.*, 51, 2213, 2003.
58. Koratkar, N., Wei, B., and Ajayan, P.M., Carbon nanotube films for damping applications, *Adv. Mater.*, 14, 997, 2002.

59. Young-Rae Cho, Y.R, Lee, J.H., Song, Y.H., Kang, S.Y., Hwang, C.S., Jung, M.Y., Kim, D.H., Lee, S.K., Uhm, H.S., and Cho, K.I., Photolithography-based carbon nanotubes patterning for field emission displays, *Mater. Sci. Eng. B*, 79, 128, 2001.
60. www.nanomagnetics.co.uk.
61. Lamberton, R.W., Morley, S.M., Maguire, P.D., and McLaughlin, J.A., Monitoring laser-induced microstructural changes of thin film hydrogenated amorphous carbon (a-C:H) using Raman spectroscopy, *Thin Solid Films*, 333, 114, 1998.
62. Marks, N.A., Bell, J.M., Pearce, G.K., McKenzie, D.R., and Bilek, M.M.M., Atomistic simulation of energy and temperature effects in the deposition and implantation of amorphous carbon thin films, *Diam. Rel. Mater.*, 12, 2003, 2003.
63. Taniguch, J., Miyamoto, I., Ohno, N., and Honda, S., Utilizing of hydrocarbon contamination for prevention of the surface charge-up at electron-beam assisted chemical etching of a diamond chip, *Nuclear Instruments and Methods in Physics Research Section B: Beam Interactions with Materials and Atoms*, 121, 507, 1997.
64. Komuro, M. and Hiroshima, H., Fabrication and properties of dot array using electron-beam-induced deposition, *Microelec. Eng.*, 35, 273, 1997.
65. Castagne, M., Benfedda, M., Lahimer, S., Falgayrettes, P., and Fillard, J.P., Near field optical behaviour of C supertips, *Ultramicroscopy*, 76, 187, 1999.
66. Djenizian, T., Santinacci, L., Hildebrand, H., and Schmuki, P., Electron beam induced carbon deposition used as a negative resist for selective porous silicon formation, *Surf. Sci.*, 524, 40, 2003.
67. Djenizian, T., Santinacci, L., and Schmuki, P., Electron beam-induced carbon masking for electrodeposition on semiconductor surfaces, *Appl. Phys. Lett.*, 78, 197, 2001.
68. Rehse, S.J., Glueck, A.D., Lee, S.A, Goulakov, A.B., Menoni, C.S., Ralph, D.C, Johnson, K.S., and Prentiss, M., Nanolithography with metastable neon atoms: enhanced rate of contamination resist formation for nanostructure fabrication, *Appl. Phys. Lett.*, 71, 1427, 1997.
69. Lemoine, P., Lamberton, R.W., Ogwu, A.A., Zhao, J.F., Maguire, P., and McLaughlin, J., Complementary analysis techniques for the morphological study of ultra-thin amorphous carbon films, *J. Appl. Phys.*, 86, 6564, 1999.
70. Broers, A.N., Hoole, A.C.F., and Ryan, J.M., Electron beam lithography-resolution limits, *Microelec. Eng.*, 32, 131, 1996.
71. Stanishevsky, A. and Khriachtchev, L., Modification of hydrogen-free amorphous carbon films by focused-ion-beam milling, *J. Appl. Phys.*, 86, 7052, 1999.
72. Guise, O., Marbach, H., Levy, J., Ahner, J., and Yates, Jr., J.T., Electron-beam-induced deposition of carbon .lms on Si(100) using chemisorbed ethylene as a precursor molecule, *Surf. Sci.*, 571, 128, 2004.

Chapter 13

Nanomanufacturing Processes Using Polymeric Materials

Carol Barry, Julie Chen, and Joey Mead

Contents

13.1 Internal (Polymer–Polymer) Interface 314
13.1.1 Interfacial Instability in Nanolayer Melts—Multilayer Extrusion 315
13.1.1.1 Background 315
13.1.1.2 Current Research 316
13.1.2 Controlled Phase Separation in a Polymer blend—Electrospun Nanofibers 320
13.1.2.1 Background 320
13.1.2.2 Current Research 322
13.2 External (Polymer–Tool) Interface 326
13.2.1 Electric Field Effects on Polymer Jets—Controlled Deposition and Orientation of Electrospun Nanofibers 326
13.2.1.1 Background 326
13.2.1.2 Current Research 327
13.2.2 Interfacial Effects in the Formation of Molded Polymer Nanostructures 334
13.2.2.1 Background 334
13.2.2.2 Current Research 335
References 346

Although much of the current nanotechnology research and literature is focused on semiconductor processing and ceramic-based materials, these materials have limitations due to lack of flexibility and relatively high densities,

properties in which polymers excel. Polymers also lend themselves to fabrication using high-rate and continuous processing. As a result, it is expected that polymeric materials will play an important role in the nanotechnology revolution, especially given recent progress in conductive and optical polymers.

Some of the potential new products include extruded multicomponent thin films for conformable, high-density data or energy storage; injection-molded low-cost calibration standards, electrospun nanowires; and nanotextiles for circuits. If these examples of valuable polymer nanomaterials are to become a commercial reality, it is necessary to understand how to create high-volume, low-cost processing solutions.

Nanomanufacturing of polymers is likely to look quite different from current macroscale processes. By making modifications to existing equipment, however, we can economically and efficiently investigate fabrication of continuous fiber, continuous sheet, and nanoscale features. In order to make these processes a commercial reality it is necessary to understand the fundamental science affecting the nanoscale processing of plastics. At these scales, on the order of the molecular size, interfacial behavior becomes a dominant mechanism. The focus of the work is on understanding the effect of polymer properties and process conditions on "internal" interfaces between phases in polymer blends and on the "external" material/tooling interface (see Figure 13.1).

13.1 Internal (Polymer–Polymer) Interface

Interfacial effects in blends and multilayered structures are extremely important to the bulk properties. This interface and the resulting morphology are dependent on a number of factors, both thermodynamic and kinetic. While research has been conducted on macroscale systems[1–3] and nanoscale interfaces,[4–6] limited work has been done to understand and control the interfaces in polymeric materials at the nanoscale under realistic processing conditions.

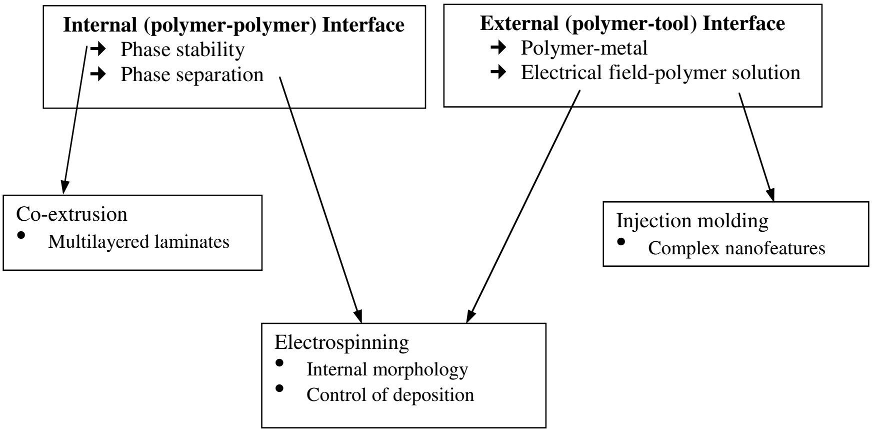

Figure 13.1 Interfacial control.

The interfacial behavior and resulting morphology in blends and multilayer systems depend on a number of factors, including the interfacial tension between the two materials.[7] Generally, the closer in solubility parameter the two materials, the better the quality of the blend, as a result of the smaller domain size of the dispersed phase. For multilayer systems, wide differences in solubility parameter can result in weak adhesion between layers.[8–11] Under realistic nanoprocessing conditions, kinetic effects will assume more importance; thus, the role of viscosity and elasticity in interfacial control must also be understood. Molecular weight of the two polymers is another important factor, both from the aspect of thermodynamics of phase separation, and also as a result of its effect on viscosity and elasticity. The fundamental role of polymer properties (solubility parameter, viscosity, and elasticity ratios) on interfacial development and control between internal polymer–polymer interfaces is the focus of this section.

Two approaches are discussed. First, we will look at bringing two different polymeric streams together and determining the factors that are important in maintaining interfacial control and layer uniformity when the size of the layers approaches the nanoscale. This approach will rely on extrusion methods that bring two or more layers together under controlled conditions. The second approach examines self-assembly techniques, where two polymeric materials initially blended together are designed to separate into nanoscale phases or layers during processing. This approach will use electrospinning techniques to produce nanofibers with controlled morphology within the fiber itself.

13.1.1 Interfacial Instability in Nanolayer Melts—Multilayer Extrusion

13.1.1.1 Background

When application needs cannot be met with the use of a single material, multiple materials are employed to provide the necessary requirements. One advanced method to create multilayered materials employs coextrusion technologies.[12–14] While typical products have two to seven layers, films with up to 2,625 strata have been reported.[15] Baer et al.[12] have created symmetric multilayer materials using a modification of the feedblock technology. Schrenk et al.[16] manufactured multilayer films with up to 4,097 layers, but as the number of layers increased and the thickness of each layer decreased, the individual layers became discontinuous due to flow instabilities. This behavior is an example of the issues unique to maintaining layer identity and uniformity on the nanoscale.

In this work we study the effect of polymer properties on the development of flow instabilities in nanolayered extruded films. Flow instabilities, as shown in Figure 13.2, are an interfacial phenomenon and result in a reduction in properties, for example, mechanical, optical, or barrier. Numerous studies have looked at the influence of polymer properties on

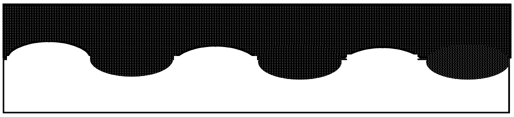

Figure 13.2 Development of interfacial waves for extruded layers.

the development of flow instabilities from a modeling perspective.[17–21] Su and Khomami,[21] Chen and Zhang,[17] and others[18,19] have developed models for stable multilayer extrusion in a number of geometries. While Wilson and Khomami[22] have explored comparison of these models to experimental data for polypropylene and high-density polyethylene, relatively few experimental studies have been performed to support the modeling.[23] Although these efforts have not yet addressed nanoscale issues, a number of factors have been shown to affect flow instabilities, particularly layer thickness, and viscosity and elasticity ratios.[17–21,23] Nonuniform layers can also be found in the absence of viscosity differences as a result of the elasticity of the polymer.[17,18,21,22] Shrenk et al.[24] have suggested that flow instabilities occur when the interfacial shear stress reaches a critical value. Mavridis and Shroff[25] found that instabilities could be reduced by decreasing the interfacial shear stress and reducing the elasticity differences between layers.

Another issue relevant to coextrusion is the phenomenon of viscous encapsulation from the system attempting to achieve minimum energy dissipation. Viscosity differences result in nonuniform layers from "viscous encapsulation" of the higher-viscosity material by the lower-viscosity resin as the higher-viscosity material pushes into the lower-viscosity material.[26,27]

Many of these instabilities are studied in fully developed flow; however, in a real coextrusion process one must also consider the effects of two converging melt streams. These types of studies have important implications in die design. When the two melt streams converge, material at the interface must accelerate from zero to its equilibrium velocity.[27] The length required for the interface to reach equilibrium increases as the viscosity ratios increase and the less viscous material will have a larger shear rate in systems where the two streams have equal flow rates.[27] In these converging streams the higher-viscosity material will push into the lower-viscosity material, moving the interface into the lower-viscosity material. Extensional flows in this merging region are also important.[28]

13.1.1.2 Current Research

This work investigates interfacial instabilities occurring in systems with tens or thousands of micro- or nanoscale layers using a specially designed multilayer extrusion system. Two major interfacial instabilities have been studied in extrusions with fewer than five layers.[29] These are a zigzag (high frequency, low amplitude) instability caused by high interfacial shear stress

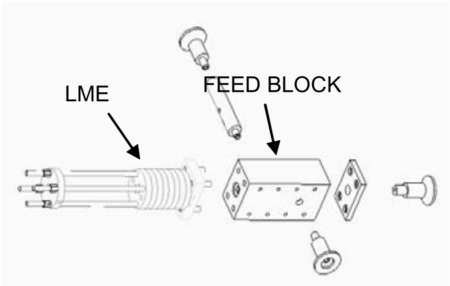

Figure 13.3 Multilayer coextrusion system.

and a wave (low frequency, high amplitude) instability generated by extreme extensional deformation of the minor layer at the merge point.[27,30–35]

Multilayer structures of semicrystalline/amorphous polymers (polycarbonate [PC] and polypropylene ([PP]) have been prepared to study interfacial instabilities and are compared with a composition from two amorphous polymers, PC and a cyclo-olefin polymer.[36] Sheets 25.4 mm wide and 3 mm thick were prepared with three to several thousand alternating layers using a specially designed multilayer coextrusion system as shown in Figure 13.3. Each layer multiplying element (LME) splits the melt stream, divides it, and then brings the two streams together, increasing the number of layers with each LME. With 13 LMEs, the layer size is predicted to be 74 nm.

The extrusion temperature was 280°C for PC/PP compositions in most of the experiments because these two materials showed similar viscosities at this temperature. PC was used as the skin layer as seen in Figure 13.4, which resulted in PC being 80% by volume of the total composition in the samples. For the cyclo-olefin/PC compositions the melt temperature for PC was 274°C and 254°C for the cyclo-olefin. In this case the PC was used as the core layer. Extrudates were quenched in a water bath immediately after processing.

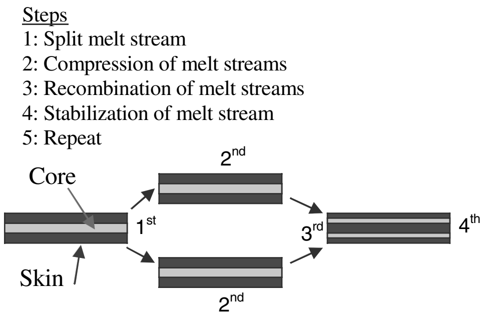

Figure 13.4 Schematic diagram of skin-core structure.

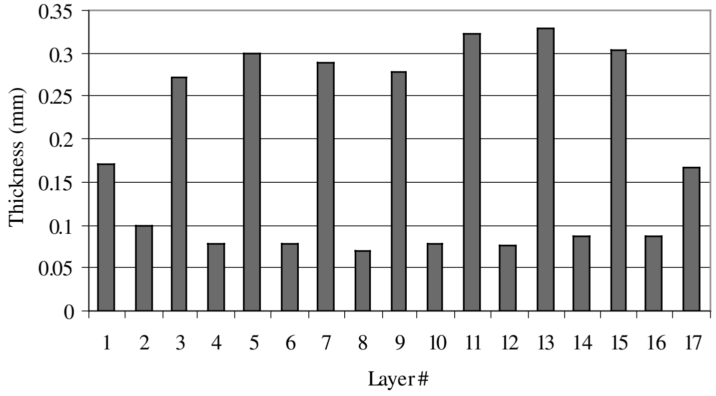

Figure 13.5 Thickness of individual layers. (Odd numbers represent PC; even numbers, PP.)

To eliminate wave-type instabilities, the volumetric flow rates were adjusted to give the same velocities for the two materials at the first merge point in the feedblock. The output ratio of skin-to-core layers from the extruders was set at 4:1 based on the ratio of the cross-sectional areas of the two flow channels in the feedblock. Because the skin layer material was split and placed on either side of the core layer, the actual velocity ratio of skin and core layers in the feedblock was 2:1.

The shear viscosities from the capillary rheometer were used to determine processing temperatures where the viscosities of two materials were similar or where the skin layer material (PC) had lower viscosity than the core material (PP). This was done to avoid viscous encapsulation behavior.[37] As PP and PC are incompatible and no additive to enhance the interfacial strength was included, the multilayer coextrusions delaminated easily, indicating relatively uniform layers during the extrusion process. This is seen in the uniform layer thicknesses from Figure 13.5, taken from samples prepared using three LMEs. Because of the adjusted flow rate to provide the same velocities at the merge point, the thickness of a PC melt flow channel was twice as thick as that of PP, thus the thickness of the PC layers in the extrudate is greater than for the PP.

Until five LMEs, the samples delaminated quite easily, indicating uniform layers. At five LMEs and above, the layers could not be easily delaminated, indicating interfacial instability. In addition, as the number of LMEs increased, deformation of extrudates from the die increased due to the shrinkage of PP layers from crystallization. When six LMEs were used, the deformation was significant.

Two types of instabilities were found. The first type (type I) were wave-type instabilities. Figure 13.6 shows the effect of velocity ratio for three LMEs. As seen in this figure, an increased velocity ratio led to greater wave

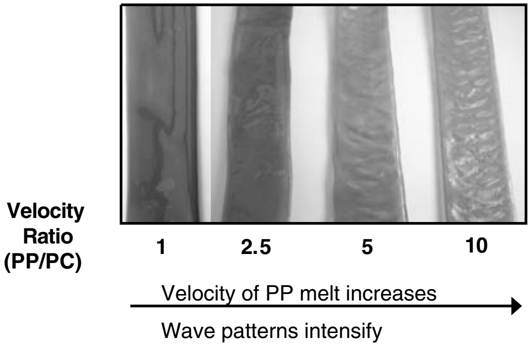

Figure 13.6 Effect of melt velocity ratios on wave patterns.

pattern generation. All samples for three LMEs, regardless of the velocity ratios, could be delaminated. As the number of LMEs increased, the system was more sensitive to differences in velocity ratio. Thus, for multilayer extrusion it is important that the velocities of the two melt streams be matched.

A second type of instability was also found due to breakup of the individual layers (scattering instabilities). This layer breakup is evident as the number of layers increases. Figure 13.7 shows the development of layer instabilities as the number of layers increases. As these melt streams are further split and recombined the instability propagates throughout the extrudate thickness. This creates alternating patterns of stable layers and layers that have been disrupted as shown in Figure 13.8.

To avoid these instabilities, the interfacial shear stresses should be decreased by either increasing the temperature of the LMEs (lowers viscosity) or decreasing the total flow rate of materials, while keeping the flow rate ratio constant. As the temperature of LMEs was increased from 280°C to 302°C, merged layers disappeared.

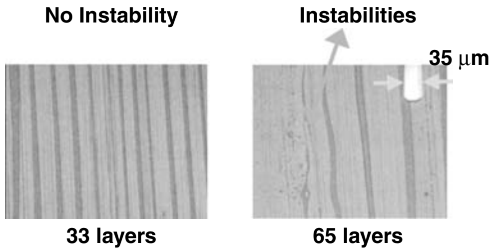

Figure 13.7 Instability (breakup) of layers.

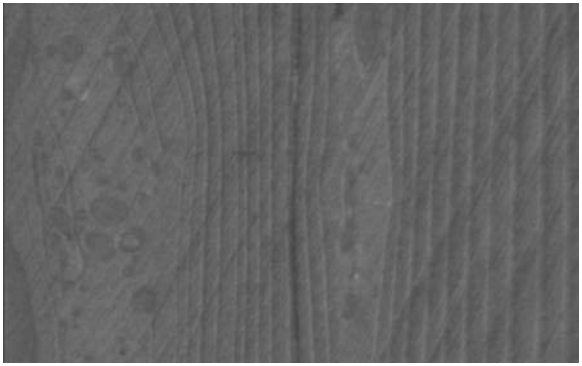

Figure 13.8 Alternating layers of stable and disrupted layers.

13.1.2 Controlled Phase Separation in a Polymer Blend—Electrospun Nanofibers

13.1.2.1 Background

Electrospinning produces submicron-sized fibers through the use of a strong electric field and a polymer solution.[38] Typically, a polymer solution is fed through a pipette. A high-voltage electrode (~10 to 20 kV) placed in the solution charges the polymer. When the repulsion force exceeds the surface tension at the tip of the pipette, a jet of liquid is repelled from the pipette toward the ground plate. Electrospinning has been used in a number of laboratories to produce nonwoven mats of nanofibers for a wide range of polymers.[39–42] Studies of electrospinning have shown the structure of electrospun nanofibers to depend on a variety of factors including molecular weight, concentration, viscosity, and applied field strength.[38,43–45] Characterization of the formation of electrospun nanofibers by scanning electron microscopy (SEM) and transmission electron microscopy (TEM) showed that solution viscosity, net charge density carried by the electrospinning jet, and surface tension of the solution were the main factors.[46–48]

Polymer blends and block copolymers offer significant potential for a variety of applications, but have received more limited investigation, with the focus primarily on the properties of the overall mat, rather than study and control of the molecular architecture within the fiber itself.[49–55] For example, blends of polyaniline and polyethylene oxide (PEO) or sulfonated polystyrene and polyethylene oxide were studied for use in photoresponsive and conductive nanofibers for electronic applications.[56] Styrene-butadiene-styrene triblock copolymers have been electrospun, exhibiting the expected two-phase morphology with domains elongated along the fiber axis.[57] Other researchers have investigated the preparation of co-continuous phase morphologies from electrospinning of polylactide/polyvinylpyrrolidone blend solutions.[58] Selective removal of one of the components generated fine pores on the surface of the fiber.

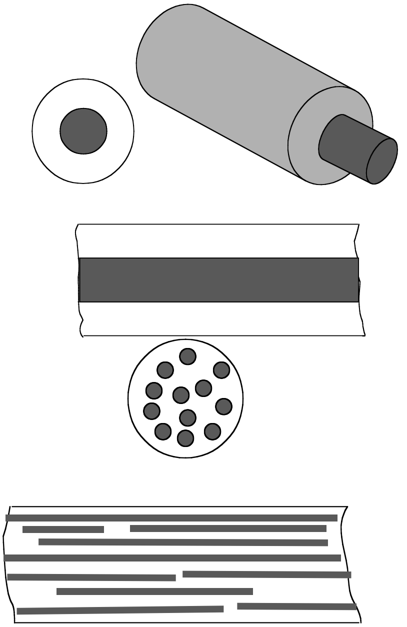

Figure 13.9 Core–sheath- and co-continuous-type structures.

In spite of the plethora of work in electrospinning, there has been relatively little effort toward control of the internal morphology of nanofibers prepared from polymer blends. As depicted in Figure 13.9, the use of block copolymers and blends offers the potential to develop unique fiber architectures, such as core–sheath structures or hollow fibers and co–continuous structures. Possible applications include the development of nanowires from blends of a conducting polymer and an insulating polymer or controlled delivery systems from porous or hollow fibers. These interesting potential applications have led to research in developing techniques to prepare these types of structures. One approach is using nanofibers as a template for depositing other polymers. Dong et al.[59] prepared core–sheath structures via *in situ* polymerization of polyaniline onto electrospun polymethyl methacrylate. Core–sheath fibers have been prepared by chemical vapor deposition of poly(p-xylylene) (PPX) onto electrospun nanofibers of polylactic acid (PLA).[60] Other researchers have studied the potential of spinning two polymer solutions in a co-electrospinning process using two coaxial spinnerts.[61] Core–sheath nanofibers using a number of different polymers, including PEO/polydodecythiophene (PDT), PLA/Pd, and PEO/polysulfone (PSU), have been electrospun by this method.[61–63]

One simple approach is to electrospin these structures directly from a solution of both polymers. Producing the types of molecular architectures depicted in Figure 13.9, using this approach requires better understanding

of what material variables need to be controlled. The phase morphology of polymer blend depends on a number of factors, both thermodynamic and kinetic.[64] Unlike solution cast films, where great care can be taken to obtain equilibrium morphologies, in the electrospinning process, the solvent evaporates within time scales down to the millisecond range[65] so that the kinetics of domain formation may play a larger role in controlling the development of specific morphologies in electrospinning. Solubility parameters, viscosity, and molecular weight are expected to be the most important factors in control of the molecular architecture. While the solution viscosity is known to be an important parameter in overall electrospun fiber geometry, the bulk viscosity is expected to be important as the solvent is evaporated and the solid polymer properties assume more importance during morphology development.

13.1.2.2 Current Research

Electrospinning of polymer blends directly from a single solution was studied for a number of polymer types, composition ratios, and molecular weights.

13.1.2.2.1 Types of fiber structures. As expected, a number of different morphologies can be obtained including core–sheath and co-continuous. Examples of these types of structures are shown in Figure 13.10 and Figure 13.11 for nanofibers prepared from polybutadiene/polycarbonate blends electrospun from a single polymer solution. Both co-continuous and core-sheath structures can be observed.[66,67]

Figure 13.10 presents the TEM image of electrospun PB/PC nanofibers with co-continuous structures using a composition ratio (PB/PC) of 75/25

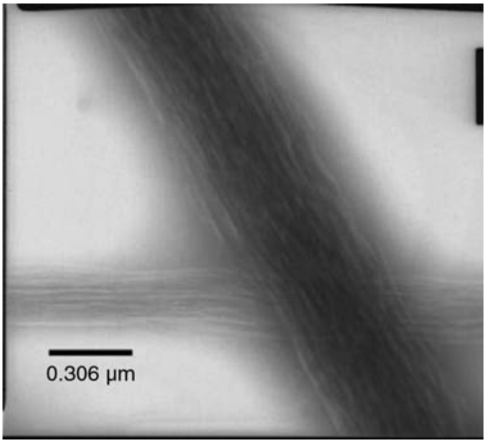

Figure 13.10 Transmission electron microscopy (TEM) of electrospun PB/PC nanofibers (composition ratio of 75/25; stained by OsO_4). (From Wei, M., Sung, C., and Mead, J., *Polymer Preprints*, 79, 2003. With permission.)

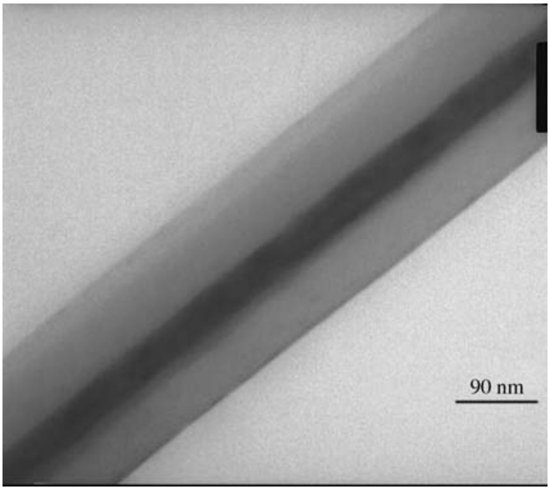

Figure 13.11 TEM images of PB/PC blends with weight ratios of 25/75 after staining by OsO_4.

stained by OsO_4.[66] OsO_4 is known to preferentially stain polybutadiene, resulting in the dark regions in the TEM images for the polybutadiene phase and the light regions as the polycarbonate phase.[68] This structure is typical of a co-continuous morphology with nanolayers or strands of differing phases oriented along the fiber axis.

In addition to co-continuous structures, core–sheath structures were also found. Figure 13.11 presents a core–sheath structure for PB/PC blends with weight ratios of 25/75 after staining by OsO_4. In both cases the phases in the electrospun fibers show elongated structures oriented in the long axis of the fiber as a result of the shearing and elongation occurring during the process.

13.1.2.2.2 Effect of composition ratio. The composition of the two materials in the starting solution also plays a role in the type of morphology developed in the electrospun nanofibers. For polybutadiene and polycarbonate, it was found that when the weight ratio of PB/PC blends was larger than 25/75, co-continuous structures with interconnected PB and PC nanolayers or strands were formed, oriented along the fiber axis. When the weight ratio of PB/PC blends was smaller than 25/75, a change in the morphology occurred, presenting core–sheath structures with PB located in the center of the fiber and PC located on the outside as shown in Table 13.1.

One factor that may play a role in this behavior is the viscosity of the overall blend system. Figure 13.12 presents the Brookfield viscosity of polymer solutions from PC and PB.[67] As seen from this figure the PB shows a large increase in viscosity with increasing solution concentration.

Table 13.1 Effect of Composition Ratio on Fiber Morphology

Composition ratios (PB/PC wt%)	Phase morphology
90/10	
75/25	
65/35	
50/50	
35/65	Co-continuous
25/75	Core sheath
10/90	

At high PB weight fractions, the higher-viscosity PB would lead to greater overall solution viscosity compared with a composition with PC at a similar weight fraction. As the jet travels from the pipette to the target, solvent is evaporated and the polymer molecules begin to phase separate. The rapid solvent evaporation coupled with the higher viscosity of the solution would restrict the ability of the phases to form large domains for systems with high PB content. In systems with higher PC content, the overall solution viscosity is lower providing greater mobility and potential for large domains. This, in part, may explain the change in morphology to core–sheath structures as the PC content reaches 75 wt%. As the content of PC increases, the overall viscosity of the blend system is decreased, providing greater mobility and allowing the domains sufficient mobility to separate into core–sheath structures.

13.1.2.2.3 Effect of molecular weight of components. The molecular weight has a great effect on a polymer's behavior. As molecular weight increases, viscosity tends to increase. The molecular weight of the components in the

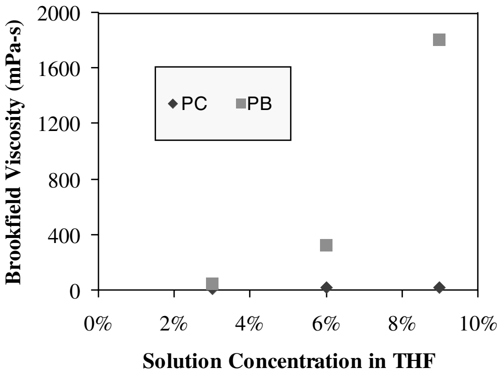

Figure 13.12 Brookfield viscosity of polymer solutions. (Taken from Wei, M., Kang, B., Sung, C., and Mead, J., "Preparation of Nanofibers with Controlled Phase Morphology from Electrospinning of Polybutadiene (PB)/Poly carbonate (PC) Blends" in *Polymeric Nanofibers*, ed. by Reneker & H. Fong ACS Symposium Series 918, American Chemical Society, NY, NY 2006, Ch. 11. *ACS Book Symposium Series*, in press. With permission.)

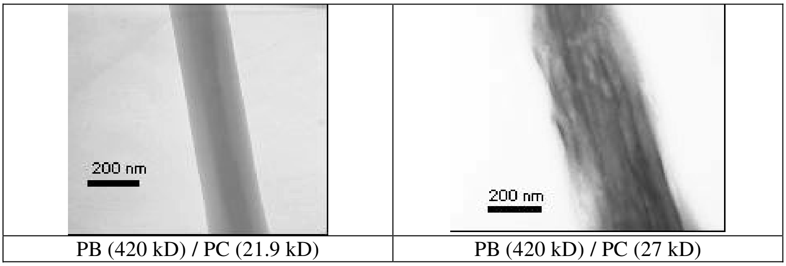

Figure 13.13 Effect of molecular weight on the nanofiber morphology for PB/PC blend ratios of 25/75. (Taken from Wei, M., Kang, B., Sung, C., and Mead, J., *ACS Book Symposium Series*, 918, American Chemical Society, New York, 2006, Ch. 11.)

electrospun solution is expected to influence the morphology of the nanofibers. As the molecular weight of the polymer is increased the viscosity of the blend system increases, leading to potential changes in the morphology of the fiber. The effect of molecular weight on the types of structures seen in the nanofibers is illustrated for 25/75 weight ratio PB/PC blends in Figure 13.13. As the molecular weight was increased from 21.9 kD to 27 kD the morphology changed from core–sheath to co-continuous structures.[67] This behavior clearly illustrates the importance of kinetic behavior in the resultant morphology of the system. Under equilibrium conditions it would be expected that the higher-molecular-weight material would exhibit better phase separation (larger domains).

A similar effect was seen when the molecular weight of PB was increased from 420 to 2500 kD as shown in Figure 13.14.[67] Again, the core–sheath structure was changed to a co-continuous structure. From this behavior we can determine that the viscosity of the system plays a pivotal role in the development of the phase morphology for these electrospun blends.

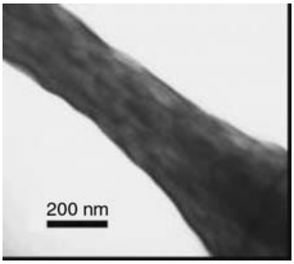

Figure 13.14 Co-continuous structures for PB/PC blend ratios of 25/75. PB (2500 kD)/ PC (21.9 kD). (Taken from Wei, M., Kang, B., Sung, C., and Mead, J., *ACS Book Symposium Series*, 918, American Chemical Society, New York, 2006, Ch. 11.)

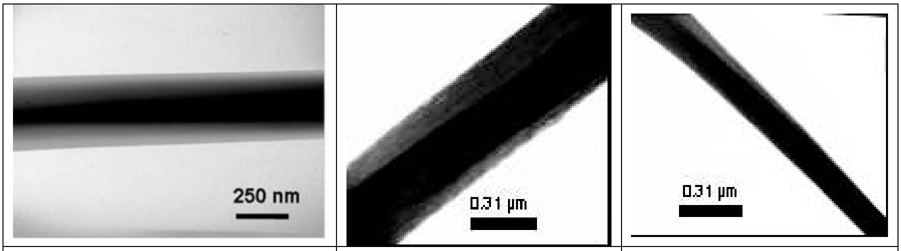

PANI/PS 20/80 wt % (stained by OsO_4)	PS/PC 25/75 wt % (stained by RuO_4)	PMMA/PC –25/75 wt% (stained by RuO_4)

Figure 13.15

13.1.2.2.4 Effect of polymer type. Both core–sheath and continuous structures have been developed in nanofibers from blend solutions. Core–sheath structures have been prepared from blends of polystyrene (PS) and polycarbonate,[69] polymethyl methacrylate (PMMA) and polycarbonate,[69] polyaniline and polycarbonate,[70] and polyaniline and polystyrene[70] as illustrated in Figure 13.15.

Through proper control of the blend composition and process parameters a range of internal fiber morphologies can be fabricated for the desired application.

13.2 External (Polymer–Tool) Interface

Control of geometric features depends on an understanding of the interaction between the polymer material and the tool. Whether the geometries of interest are molded nanofeatures or controlled nanofiber orientation, the "external" interface regions play a dominant role. The work described below includes both rigid (metallic) and noncontacting (electric field) tooling by modifying the injection molding and electrospinning processes. Tooling is typically metallic for extrusion and injection molding. Even at macroscale processing, this polymer–tool interaction is critical for control of heat transfer, surface finish, and defects, such as jetting. With electrospinning, the "tool" is the electric field. This provides a useful method by which to study the effect of surface charge and charge transport in polymer nanofibers.

13.2.1 Electric Field Effects on Polymer Jets—Controlled Deposition and Orientation of Electrospun Nanofibers

13.2.1.1 Background

Section 13.1.2 provided a brief description of the electrospinning process. The electrospinning process, described in a 1934 patent by Formhals,[71] has already been used commercially for well over a decade in the fabrication of filtration membrane.[72] While random fiber mats are often sufficient for 1-D

filtration, many other applications can be envisioned for ultrafine fiber assemblies with controlled two- or three-dimensional textile architectures. Examples of this include tissue engineering scaffold geometries that would promote oriented cell growth, fiber membrane architectures that would allow selective transport of nutrients and waste products to microbioreactors, and 3-D fiber architectures for preferential transport (e.g., of heat on electrons). In addition to specific applications of controlled nanofiber architectures, studies of the interaction between the external electric field and the charged polymer jet provide insight into the fundamental polymer response to non- contacting electric fields.

Despite the significant growth of research activity in electrospinning over the past decade, relatively few efforts have addressed the issue of controlling fiber orientation and distribution.[73,74] The natural path of the electrospun fiber is initially straight from the pipette tip and then conical about the same axis. The conical path is a result of a bending or whipping instability and appears to be responsible for the high draw ratios (e.g., 6×10^4) with axial velocities on the order of 10 m/s. While preliminary experimental results[73–75] suggest that some control of the fiber deposition is possible, a critical component missing from existing predictive models is a suitable representation of the charge transport or electrodynamic behavior.

Many of the current models of the electrospinning process are based on electrohydrodynamics, incorporating conservation of mass and charge, and momentum balance. Spivak et al.[76,77] modeled the convergence in jet radius near the tip of the source orifice. Hohman et al.[78] used a perturbation approach to predict the onset of both axisymmetric and whipping instabilities and used asymptotic approximations to predict changes in jet radius up to this point. Hohman's model correlates reasonably well with their measurements of the jet profiles and the onset of the instability. However, Hohman et al. themselves state that their understanding of the mechanisms for charge transport near the nozzle is inadequate. In fact, in both models the representation of the charge transport is somewhat limited. Thus, while the current models can predict the onset of the instability, they do not appear to address the subsequent divergence of the jet due to electrodynamic effects. Yet, this understanding of the charge and material transport in the space between the onset of instability and the collector is critical for control of the distribution and orientation of fibers. The transport should become more governed by electrodynamics than by hydrodynamics as the solvent evaporates and the charge-to-mass ratio increases. Our objective is to design experiments that will guide the development of models and novel control methods for charged polymer jets and, subsequently, for other nanoscale polymer structures.

13.2.1.2 Current Research

13.2.1.2.1 Charge transport modeling. The ion–jet charge transport in electrospinning can be modeled using the steady-state charge distribution

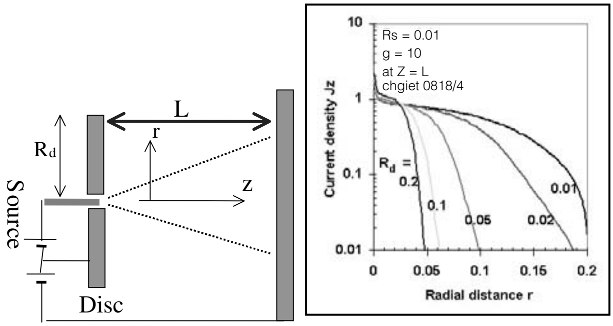

Figure 13.16 Prediction of decrease in the deposition spread at target with an increase in the source radius.

for two parallel plate electrodes (source and target). The diameter of the source electrode was modified to represent a range of electrode configurations from two parallel plates down to a point and plate. The results from the modeling indicate that the spread on the target can be controlled by the radius of the source, Rd, and the injection parameter, g, which represents the strength of the ion source. This parameter is related to material and process parameters such as flow rate, electric field, and polymer and solvent species. An example of the model results is shown in Figure 13.16. The current density (y-axis) corresponds to the amount of fiber deposited at a given radial distance (x-axis) from the center of the target.

Figure 13.16 shows the radial distribution of the current density at the target (z = L). The source radius is fixed at 0.01 L and the injection parameter g, related to the flow rate, is fixed at 10. When the radius of the source electrode is increased from 0.01 L (equal to the size of a point electrode) to 0.2 L, there is a several-order decrease in the spread of the fibers at the target. More details of the model can be found in Bunyan et al.[79,80]

A schematic of the experimental setup with and without a disc electrode is shown in Figure 13.17. A qualitative image of the effect of the point-plate versus the disc-plate (parallel-plate) configuration on the electric field is shown in Figure 13.18 with the point-plate configuration showing diverging field lines, leading to greater fiber spread.

To obtain some initial validation of the charge transport model, measurements of the fiber spread were made for three different disc diameters, with the corresponding normalized values of Rd in parentheses—5 cm ($R_d = 0.15$), 7.5 cm ($R_d = 0.235$), and 10 cm ($R_d = 0.3$). Because the measurement of the injection parameter, g, has not yet been established, the fiber spread value for the 5-cm disc was used to determine the value of g, and this same value was used to predict the fiber spread values for the 7.5-cm and 10-cm discs. As a result, in Figure 13.19 the 5-cm value is an exact match, while the values for the larger discs are close and demonstrate the same trend as the model predictions. Additional studies are underway to further the development of this charge transport model.

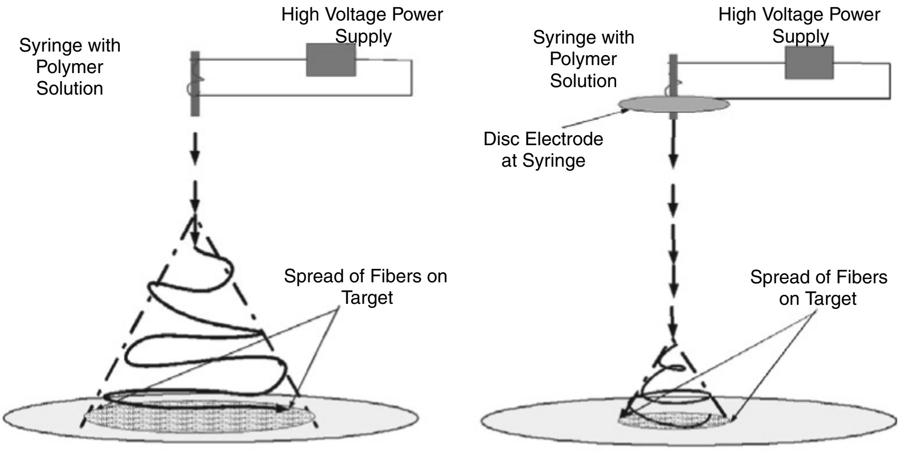

Figure 13.17 Schematic of effect of point-plate and disk-plate electrode configurations on fiber deposition spread.

13.2.1.2.2 Effect of transverse fields on fiber path. Experiments were also carried out to understand the effect of fields along the fiber path. A number of electrostatic applications are based on deflecting the charged particles by creating transverse electric fields. A brief overview of the effect of transverse fields is provided here.

Figure 13.20 shows the experimental setup used for creating the transverse field along the fiber path with a single plate. A rectangular 14 cm × 6 cm

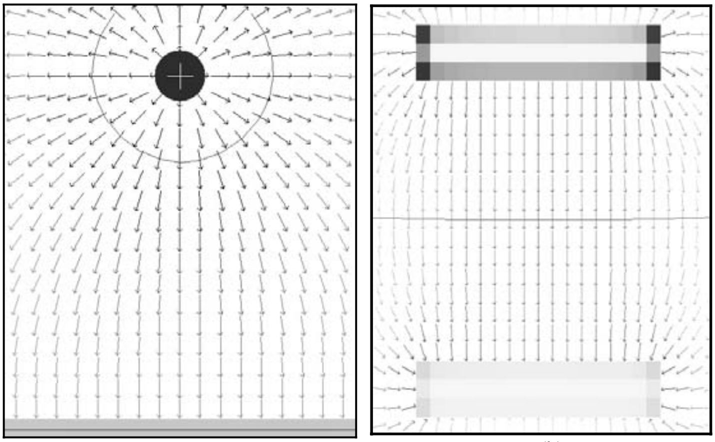

(a) (b)

Figure 13.18 Electrostatic field lines between (a) point source and flat target; (b) two parallel plates.

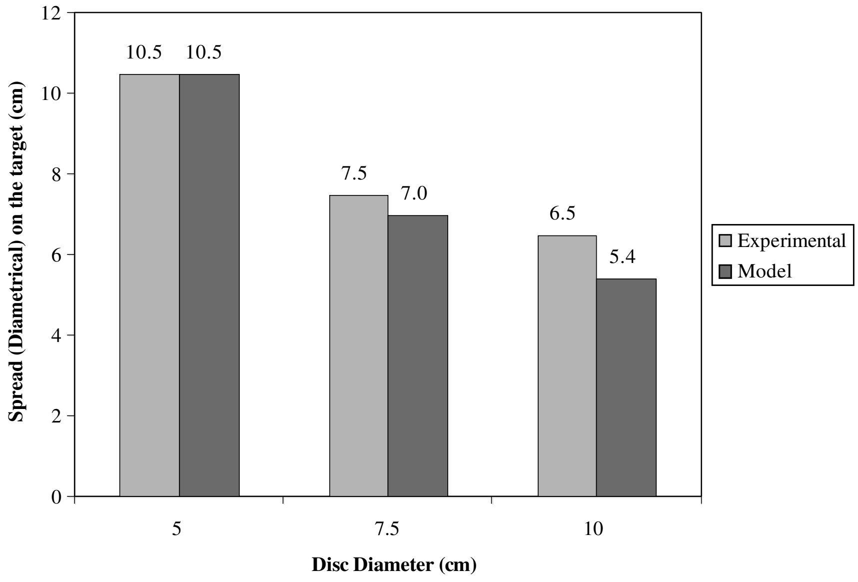

Figure 13.19 Comparison of experimental measurement and model prediction of fiber spread.

aluminum plate was used to create the transverse field. The grounded target was held at a distance of 20 cm from the source. A voltage of 10 kV was applied to the syringe needle and plate with a polymer flow rate of 0.1 ml/min. The plate was held at a distance of 5 cm from the source axis. The positively charged jet coming out of the syringe is repelled by the potential applied to the plate electrode. The deposition of the fibers due to the transverse electric field was studied by measuring the shift in the deposition of the fibers.

The transverse field created by the positively charged plate repelled the electrospinning jet away from it. This resulted in the fibers traveling to the

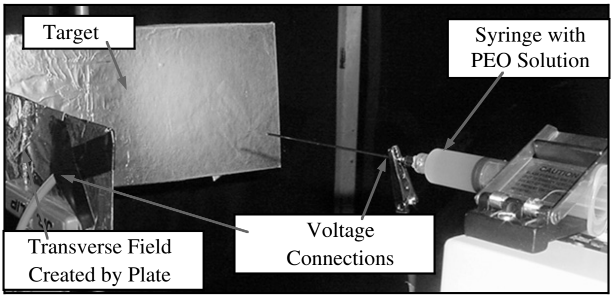

Figure 13.20 Experimental setup for creating the transverse electric field.

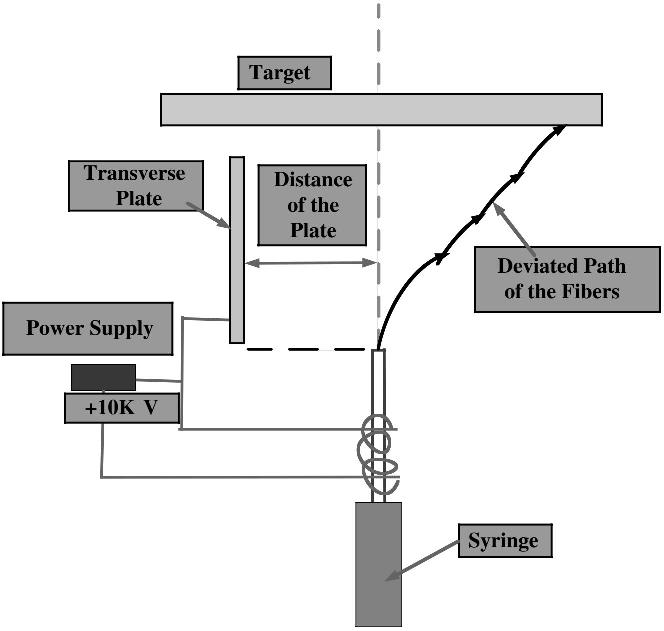

Figure 13.21 Schematic of the effect of the transverse field on the fiber path.

right edge of the target. Figure 13.21 shows the schematic of the setup and the effect on the electrospinning jet. When the transverse plate is added at a distance of 5 cm from the source axis, deposition shifts by approximately 14 cm. The spread of the fibers on the target was significant. Due to the large shift in the fiber deposition, a bigger target was needed to collect the fibers.

The jet was deflected by the field (Figure 13.22), but there was very little control on the final deposition of the fibers. The plate runs parallel to the source axis and the deflected electrospinning jet continues to travel away from the axis due to the field along the length, resulting in large shifts.

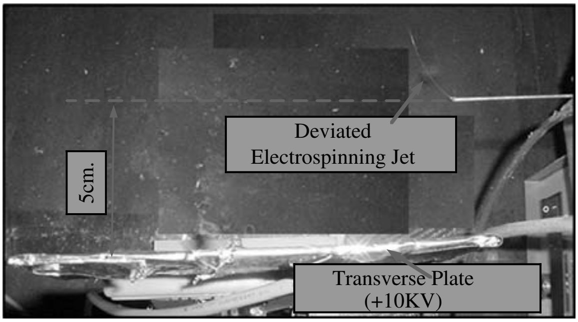

Figure 13.22 Picture showing the electrospinning jet deviating away from the plate.

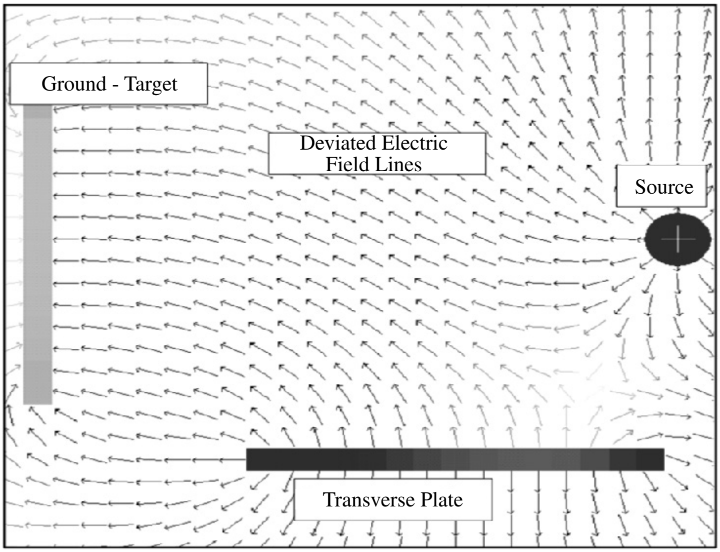

Figure 13.23 Electric field effect due to the transverse field.

The qualitative effect of the transverse plate on the electric field is shown in Figure 13.23. Positive potential is applied to both the source and the plate, and the target is held at zero potential (ground). The field lines from the source take a deviated path to reach the target.

To study this effect further, the field was controlled by using two plates with the same polarity. The distance of the plates from the axis was adjusted to direct the fibers. The schematic is shown in Figure 13.24. Higher voltages were required to initiate the spinning process, but the direction control was better than with a single plate. When the left plate was at a distance of 8 cm and the right at a distance of 14 cm from the axis, the deposition shifted to the right by approximately 4 cm. By varying the magnitude of the deflection field (distance of the plates in this case), the fibers can be directed to different regions on the target. It would be possible to deflect the fibers as in spray printing by electronically controlling the voltage applied to the transverse deflection electrodes.

13.2.1.2.3 Effect of target geometry. Theron et al.[75] designed a rotating disc for aligning the electrospun fibers. Based on the same concept, Figure 13.25 shows a picture of the steel disc mounted on a motor. The 10-cm-diameter disc was cut from a steel plate of 2.5 mm thickness. Rubber sheets of 2 mm thickness were bonded to both sides of the disc to cover the metallic surfaces and expose only the disc edges. The edges of the disc were polished to remove any chips or sharp projections that would create charge concentration. The disc was mounted at a distance of 16 cm from the source. The disc axis was perpendicular to the source axis and the top edge of the disc was held tangential to the syringe axis. The effect of speed of rotation of the disc on the fiber orientation was analyzed.

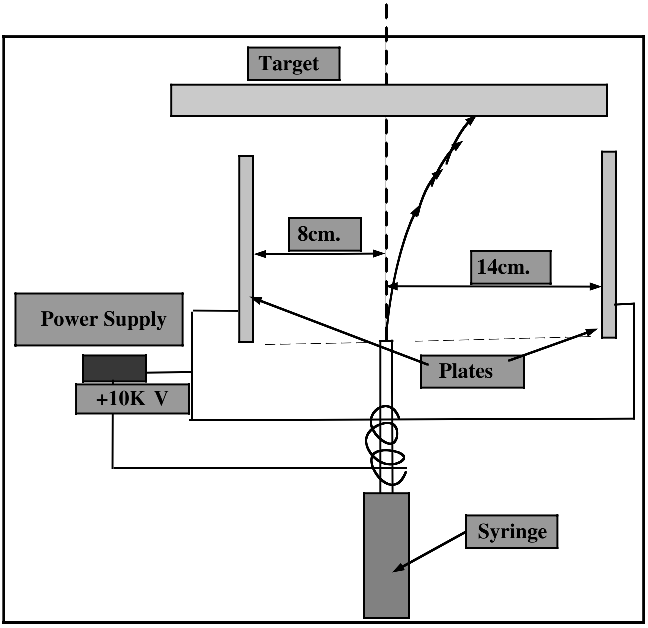

Figure 13.24 Two transverse plates provide better control on the path of the fibers.

With this target, the fibers were attracted to the metal edge due to the converging effect of the thin disc edge on the electrostatic field. The rotational motion of the disc helped to collect and align the fibers. Electrospinning was carried out using a 5-cm disc electrode at the source, which served to decrease the spread. The fibers collected after 5 min of electrospinning with

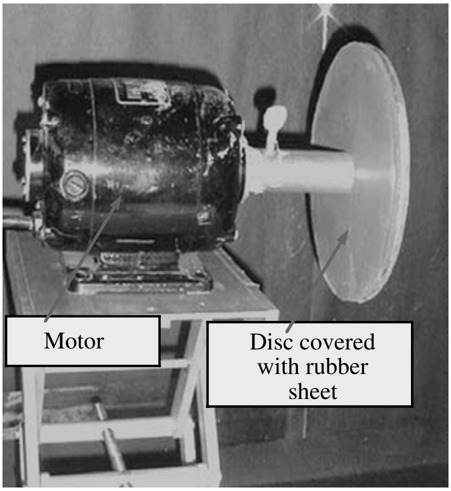

Figure 13.25 Rotating disc target.

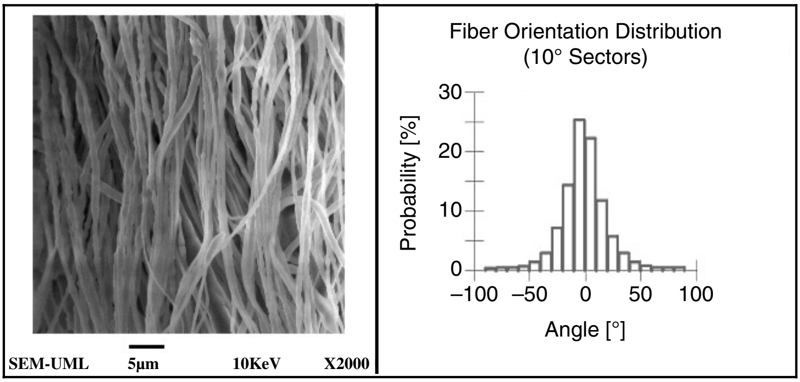

Figure 13.26 SEM image of fibers collected at 500 rpm of disc.

the disc rotating continuously at 500 rpm were carefully separated from the disc edge. The fibers were attached to each other and separated as one long strand from the disc edge.

SEM results of the fibers deposited are shown in Figure 13.26. The deposited fibers show a good directional alignment. Probability results for the fiber alignment are shown next to the SEM images. The alignment was better for the rotating disc than the *cone targets*, with ~60% of the fibers oriented within ±20° of the central angle at −10°.

13.2.2 Interfacial Effects in the Formation of Molded Polymer Nanostructures

13.2.2.1 Background

Injection molding is a versatile process used to produce approximately 30% of all the plastics components manufactured in the United States each year. This process permits high-volume, three-dimensional net shape forming of polymeric components and is generally regarded as the most cost-effective manufacturing technique available for producing large numbers of replicates.

Due to the inherent cost of the tooling, the molding process is routinely computer simulated. Although conventional filling analyses are well established, their predictions sometimes fail for thin-walled parts (thickness <1 mm), sudden changes in geometry, and shrinkage of some materials, particularly semicrystalline polymers. The requirements for molding thin-walled and very small parts (i.e., micromolding) have produced changes in equipment, particularly injection units that permit faster injection rates with short response times and higher pressures;[81,82] more robust machine frames and tooling;[83] and smaller plasticating units to deliver smaller volumes of molten polymer.[84,85] Modeling of such processes is forcing the use of viscoelastic constitutive equations[86–88] and incorporation of pressure sensitivity into

rheological measurements and models;[89–91] increasing the importance of dynamic measurement of the pressure-temperature-volume relationship;[92] and changing the models for cooling[93,94] and shrinkage.[95-98]

Of particular importance to the production of molded nanostructures is isothermal mold filling. When molten polymer contacts the mold walls, it solidifies to form the frozen layer and more molten polymer flows between these layers to fill the part. As parts become thinner, the frozen layer becomes a major component of the part cross section, thereby requiring high fill pressures and increasing residual stresses. Although rapid heating and cooling has long been considered,[99–102] recent advances in thermoelectric devices[103] and the application of preheated thermal coatings[104] have made isothermal mold filling viable. Previous solutions for molding thinner-walled parts have been the use of high mold and melt temperatures, the increase of the filling pressures and speeds, and reduction of material viscosity.[105,106] While isothermal mold filling may not impose such restrictions on the polymeric materials, the surface of the mold wall will probably not be the standard P20 steel. Consequently, the use of isothermal filling introduces two new problems:

- How do material properties affect the filling and shrinkage of nanoscale features?
- How do interactions at the polymer–tool interface influence the molding of these features?

13.2.2.2 Current Research

Tooling materials were selected for their ability to achieve nanoscale features. The resolutions of CNC machining and high-precision (microwire) electro-discharge machining (WEDM) used to cut the traditional tooling materials (steel, aluminum, and beryllium–copper alloys[107]) were about 100 and 1 μm, respectively.[108,109] Of the newer technologies adapted for micromolding tools, laser ablation has a resolution of up to 1 μm for metals and some polymers,[110] whereas Lithographie Galvanoformung Abformung (LIGA), a technique in which x-ray radiation creates features in prepolymer-coated silicon before the cured and cleaned pattern is electroplated (usually with nickel), can provide 0.5 μm or greater features.[111] A similar lithography- plus-electroforming process is used to create tooling for digital versatile disks (DVDs); the flat nickel tooling surface has 140-nm-high projections.[112] Ultraviolet (UV) and electron beam lithography of silicon wafers provide current resolution limits 157 and less than 10 nm, respectively.[113,114] Therefore, the tooling employed in this research included

- Electroformed nickel (DVD) tooling with projections that are 100 nm wide, 440 nm long, and 140 nm deep.
- Etched silicon wafers having features as high as 300 nm and as narrow as 100 nm.
- Etched gallium arsenide (GaAs) wafers having microscale features.
- Silicon and GaAs wafers coated with gold and titanium.

To identify the critical issues in molding—particularly tool cleaning, separation of the solidified melt from the tooling, and tooling robustness—new tooling materials for nanoscale features were initially validated using compression molding of molten polymers. A tool-cleaning procedure was optimized to remove contamination from the tooling prior to molding. In preliminary trials, silicon-based tooling failed to completely release the polymers, whereas electroformed nickel from a DVD master had no residual polymeric material on the tooling surface. Because polypropylene adhered more extensively to silicon, polycarbonate was the primary polymer employed during the silicon and GaAs molding trials. Silicon wafers have been considered inappropriate materials for injection molding tooling[115] because silicon has a fracture toughness, K_{IC}, of 0.95 MPa. $m^{1/2}$ compared with the 15 to 150 MPa. $m^{1/2}$ for metals.[116] The fracture toughness is 0.31 to 0.45 MPa. $m^{1/2}$ for GaAs. This simple comparison of the fracture toughness is misleading because most ceramic materials are vulnerable to tensile stress but tougher when exposed to compressive stress. Compression molding trials showed that silicon tooling did crack under applied pressures of 70 MPa. Careful wafer preparation, insert cavity cleaning, and wafer mounting procedures inhibited crack initiation and therefore were critical to preventing premature fracture during molding. Addition of metallic coatings hindered crack propagation, thereby making the tooling more robust. As a result, silicon wafers could be employed without coatings in compression and injection molding, but uncoated GaAs wafers were so fragile that they usually failed during insertion (rather than molding).

Injection molding of nanoscale features was performed using a commercial micromolding machine (Nissei, model: AU3E) with a 3-g shot size. Tooling containing the nanoscale features was placed as an insert into a standard micro-injection mold. DVD tooling was employed to examine the effects of material type in the molding of nanoscale features. The polymeric materials included optical-grade PC, a cyclic polyolefin (COP), PS, PMMA, PP, and polyamide-6,6 (PA-6,6); selected properties of these materials are listed in Table 13.2.

Table 13.2 Material Properties

Property	Units	COP	PS	PMMA	o-PC	H-PC	PP	PA-6,6
δ	$MPa^{1/2}$	18.4*	17.1	19.4	19.4	19.4	16.0	22.9
T_g	°C	80	97	107	144	148	—	—
T_m	°C	—	—	—	—	—	155	204
η (T)	Pa-s (°C)	47 (250)	18 (238)	18 (288)	35 (316)	20 (316)	12 (260)	71 (249)
n		0.39	0.40	0.45	~1.00	~1.00	0.43	0.71
E_a	kJ/mol	30	39	52	61	40	14	30
α	mm^2/s	0.08	0.07	0.06	0.11	0.11	0.11	0.11
$\Delta\upsilon$	x 10^{-3} cm^3/g	65	53	83	87	87	95	250

* Estimated from apparent polymer structure.

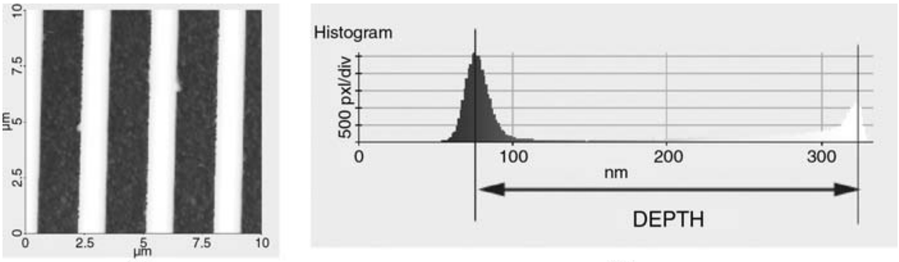

(a) (b)

Figure 13.27 Typical AFM results: (a) 2-D topography of GaAs tooling and (b) the acquisition of the trench depth from an AFM histogram, obtained using AFM image analysis software XEI v.1.2 (PSIA Corp.).

In contrast, the determination of tooling material effects used coated and uncoated silicon and GaAs wafers with the DVD tooling as a control. This molding was performed only with optical-grade PC. For all molding trials, processing parameters were optimized and parts were collected after the process had stabilized (i.e., after 100 parts were molded).

Overall tooling patterns were images using SEM, but the fine features of the tooling and molded surface were characterized by high-precision atomic force microscopy (AFM). With AFM, the features were measured using contact mode and an average scan rate was 0.5 Hz. Force modulation mode (FMM) of the AFM was used to identify the polymer deposition on the tooling. Because the topographies of the experimental tooling were primarily trenches, the surface roughness and trench depths were obtained from AFM scans. The lighter areas in Figure 13.27a are the trenches/projections. In the histogram (Figure 13.27b), the intensity of the AFM signal was plotted as a function of depth. This plot provided two peaks, one associated with the trench bottoms and the other with the plateaus of the tooling or part surface. The average distance between the top of the plateau and the bottom of the trench was defined as the depth, and was calculated from the gap between the mean values for the top and bottom from the histogram. Roughness was determined from the root mean square value of depth by using the AFM image analysis software. Replication from this tooling was assessed using the depth ratio—i.e., the ratio depth of the part features to the depth of the tooling projections—and the surface roughness of the tooling and part.

The DVD tooling, however, lacked uniform trenches (Figure 13.28a). Depth ratio was calculated from average depth of the molded pits and the 140-nm height of the tooling projections. Part surface roughness was evaluated as "feature replication." The scale shown in Figure 13.28b gives a rating of 1 to parts with no replication whereas parts with perfect replication were ranked at 10.

To examine interactions between the DVD tooling and various polymers, processing conditions were using four factor design of experiments (DOE) in which melt temperature, mold temperature, injection velocity, and pack

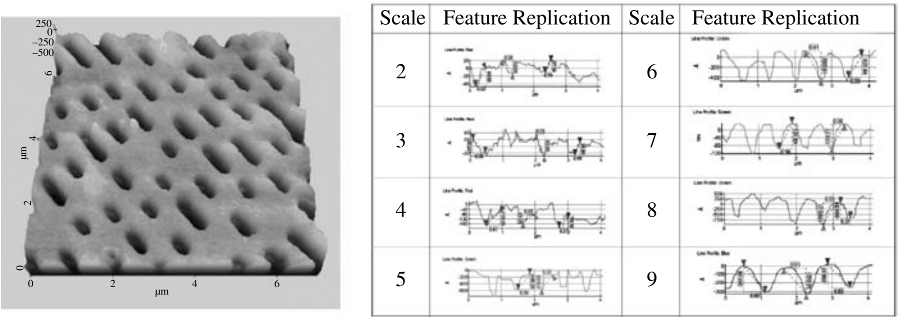

(a) (b)

Figure 13.28 Characterization of DVD-based replication using AFM results: (a) 3-D topography of molded part and (b) rating system for feature replication.

pressure were varied. As shown in Figure 13.29a, depth ratio increased linearly with measured melt temperature. Raising the melt temperature decreases melt viscosity and can be modeled using an Arrhenius equation

$$\eta = \eta_r \exp\left(\frac{E_a}{RT}\right) \tag{13.1}$$

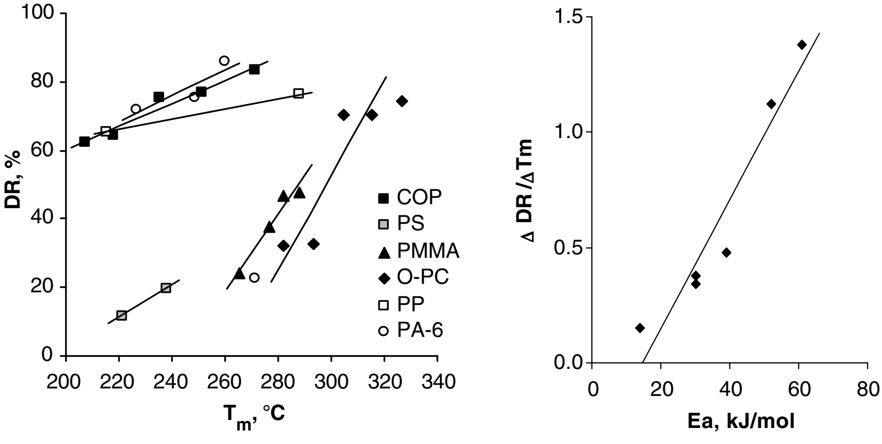

(a) (b)

Figure 13.29 Molding with DVD tooling: (a) the effect of melt temperature on depth ratio and (b) the correlation between the change in depth with respect to changes in melt temperature and the activation energy for flow.

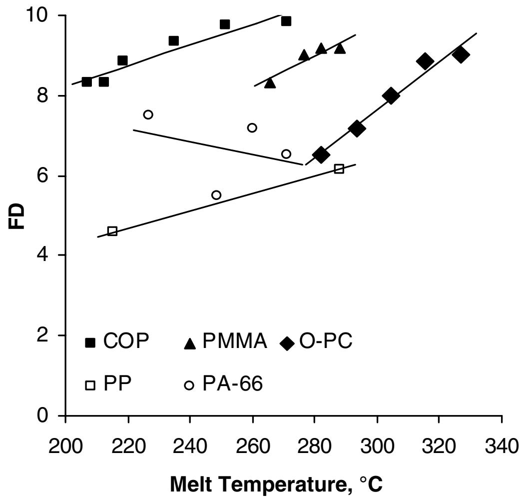

Figure 13.30 The effect of melt temperature on the feature definition (FD) when molding selected polymers using DVD tooling.

where η_r is a reference viscosity, E_a is the activation energy for flow, R is the universal gas constant, and T is the absolute temperature. The exception was polyamide-6,6, which exhibited lower depth ratios at higher melt temperatures. Because the effect of melt temperature on depth ratio increased linearly, with the activation energy for flow, as shown in Figure 13.29b, less-viscous melts were apparently more able to flow into the nanoscale features of the tooling. The apparent viscosities at the optimum melt temperatures, however, were relatively similar (Table 13.2). The exception to this trend occurred with polyamide-6,6. Although the polymer was not degrading the barrel, the polyamide-6,6 melt tended to adhere to the surface of the tooling.

As shown in Figure 13.30, feature definition also improved with melt temperature. This behavior again suggests that more fluid melts were better able to reproduce the tooling pattern. Polyamide-6,6 was again the exception to the trend, with greater melt temperatures producing poorer replication. Measurement of apparent crystallinity using differential scanning calorimetry showed that higher melt temperatures produced a small increase in the degree of crystallization in the nanoscale features. This behavior was not unexpected as hot melts cool more slowly than cooler melts, but the overall cooling time was low. Adhesion to the tooling, however, also increased with melt temperature (Figure 13.31) and seemed to account for the decrease in the quality of the surface replication.

The mold temperature increased with depth ratio (DR) with most polymers (Figure 13.32), but had little effect on the feature definition of the molded parts. This behavior was not unexpected since isothermal or near isothermal mold filling has been promoted for better quality micromolded parts. With the nanoscale features, however, the melt appears to adhere to the tooling

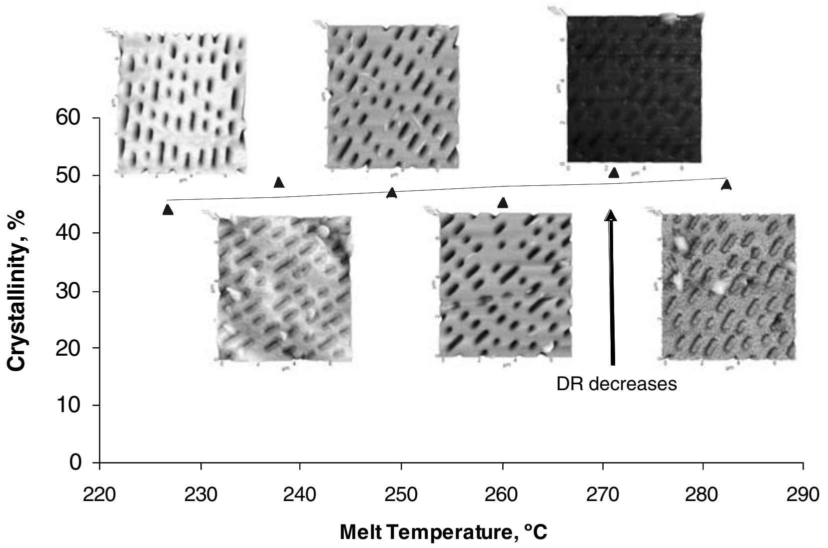

Figure 13.31 The effect of melt temperature on the crystallinity and surface quality of polyamide-6,6 nanoscale features injection molded with DVD tooling.

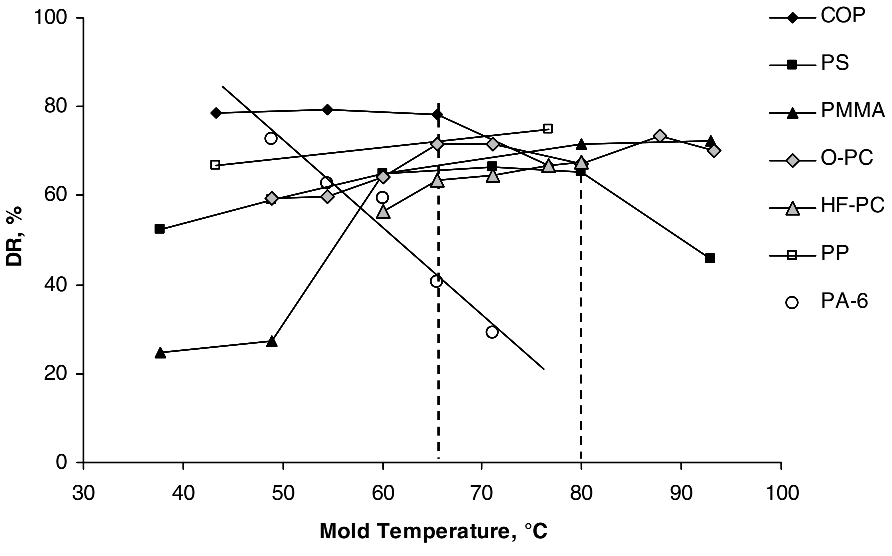

Figure 13.32 The effect of mold temperature on the feature definition when molding polymers using DVD tooling.

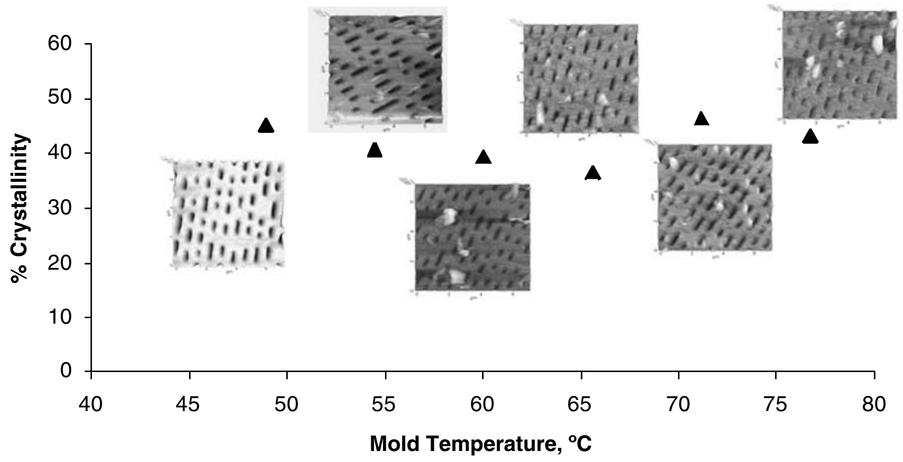

Figure 13.33 The effect of mold temperature on the crystallinity and surface quality of polyamide-6,6 nanoscale features injection molded with DVD tooling.

surface when that surface approaches the measured glass transition temperature, T_g, of the material. Adhesion reduces the depth ratio as shown with COP ($T_g \sim 80°C$) and polystyrene ($T_g \sim 97°C$), but does not impact the feature definition rankings. The relationship between adhesion and the glass transition temperature probably applies only to the amorphous polymers because the glass transition temperature is the critical transition for amorphous materials. Polyamide-6,6 again exhibited a reverse trend with depth ratio decreasing linearly with mold temperature. As shown in Figure 13.33, mold temperature did not produce a significant change in the apparent crystallinity of the nanoscale features, but did increase adhesion to the tooling surface.

Polyamide-6,6 differs from the other polymers used in this study. High levels of hydrogen bonding can occur through the amide linkages in the polymer. Performance with the electroformed nickel DVD tooling suggests that a reaction occurs at the tooling surface. Such behavior is not observed with the steel tooling typically employed for injection molding, but does occur with platinum surfaces.

As expected, packing pressure had little effect on replication although an adequate switchover pressure was required for high-quality parts. Injection velocity also had little effect on overall feature replication. This behavior has also been observed with micromolded parts and is attributed to the short flow lengths in such parts. Part replication, however, was improved with higher pressures in compression molding.

With the electroformed nickel tooling, little correlation was observed between replication and melt viscosity or heat transfer.[117] Differences in the performance of various polymers seem to depend on the slip between the polymer and tooling surface[118] and on reactions occurring at the tooling surface. Heat transfer was far more important for replication when molding with silicon tooling.

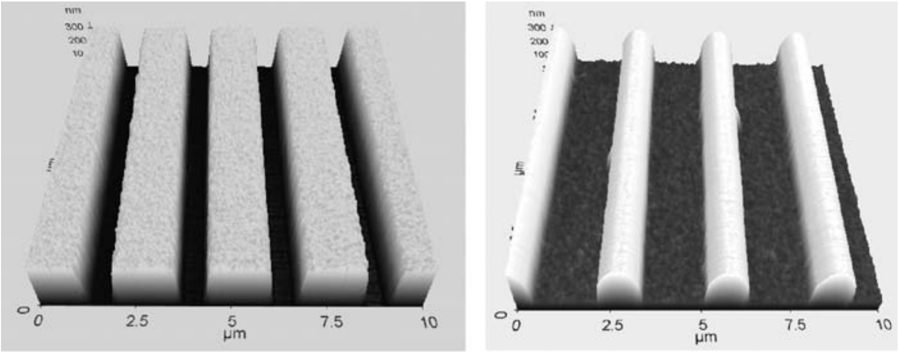

(a) (b)

Figure 13.34 Three-dimensional topography of (a) silicon tooling surface at location 12 before molding and (b) polycarbonate part at location 12 after 3000 molding cycles.

Figure 13.34a shows the three-dimensional view of the silicon tooling before molding, and Figure 13.34b presents the molded optical-grade polycarbonate at the same location after 3000 cycles. Figure 13.35 gives the corresponding line profiles for the silicon wafer and molded polycarbonate, respectively. The silicon tooling showed an average trench depth of about 285 nm, aspect (depth-to-width) ratios that ranged from 0.31 to 1.25, and a trench spacing of 1.3 to 4.6 times the trench width. As illustrated in Figure 13.34a, the walls of the trenches were relatively vertical and there were sharp corners at the bottoms of the trenches. After injection molding, the trenches became projections in the polycarbonate parts. These projections showed fairly steep walls, but were very rounded at the top, indicating a loss in feature resolution during molding. Although the 3000th part molded with the same tooling is shown in Figure 13.34b, the same results were observed with the first molded part.

Aspect ratio seemed to be the defining dimension for replication of all long trenches. As illustrated in Figure 13.36a, the depth ratio decreased with increasing aspect ratio of the tooling, but was similar after 100, 500, 1000, 2000, and 3000 molding cycles. The depth ratio was 75 to 85% for aspect ratios less than 0.65:1, but decreased to less than 15% when the aspect ratio

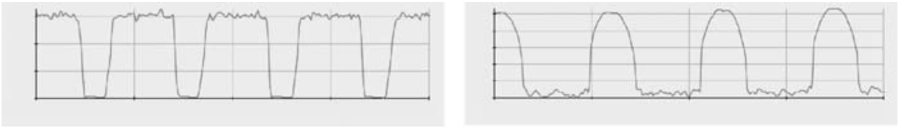

(a) (b)

Figure 13.35 Line profile of (a) silicon tooling surface at location 12 before molding (depth unit: nm) and (b) polycarbonate part at location 12 after 3000 molding cycles (depth unit: nm).

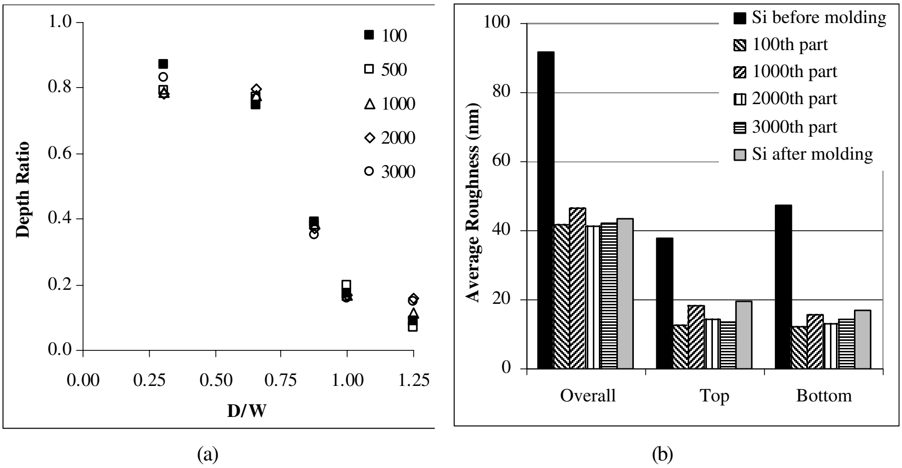

Figure 13.36 Replication using the silicon tooling: (a) effect of aspect ratio of the silicon tooling on the depth ratio in the molded polycarbonate parts and (b) comparison of surface roughness of silicon tooling and molded polycarbonate.

was 1.25:1. All polycarbonate parts injection molded using silicon tooling, compression molded for the preliminary tooling validations, and injection-compression molded from silicon wafers[119] exhibited the same relationship between depth ratio and tooling aspect ratio.

Surface roughness also did not vary with the number of molding cycles (Figure 13.36b). Silicon wafer tooling with an aspect ratio of 0.14 was able to achieve a 96% depth ratio, while the average roughness of 53 nm at the bottom of the tooling trenches resulted in an average roughness of 66 nm for the top of molded polycarbonate projections. Thus, the wide, low- aspect- ratio trench produced almost perfect replication. In contrast, features with a width of 300 nm and aspect ratio of 0.88 originally exhibited an overall surface roughness of 90 nm, with a roughness of 35 nm at the bottom of the trenches and 45 nm at the top of the wafer. Since the trenches became projections in the molded parts, notations top and bottom in Figure 13.36b refer to the projections and trenches, respectively, in the molded parts; the corresponding features in the tooling were grouped under these headings for easier comparison. After molding the surface, roughness of the parts and tooling were similar and showed an overall roughness of about 40 nm. The tops and bottoms of the molded trenches were also smoother, providing surface roughness values of approximately 15 nm.

The low depth ratios and the smoother surfaces obtained from the molded polycarbonate parts suggested that polymer was adhering to the tooling surface. Because polycarbonate has a lower modulus than silicon, any deposited polymer would produce a lower amplitude of cantilever response in FMM than the response to the silicon surface.[120,121] In the FMM results for the unused silicon wafer (Figure 13.37a), the surfaces with the same stiffness (i.e., trench bottom and plateau) exhibited the same color, indicating that the surface of the tooling was homogeneous. The dark thin lines in Figure 13.37a are artifacts

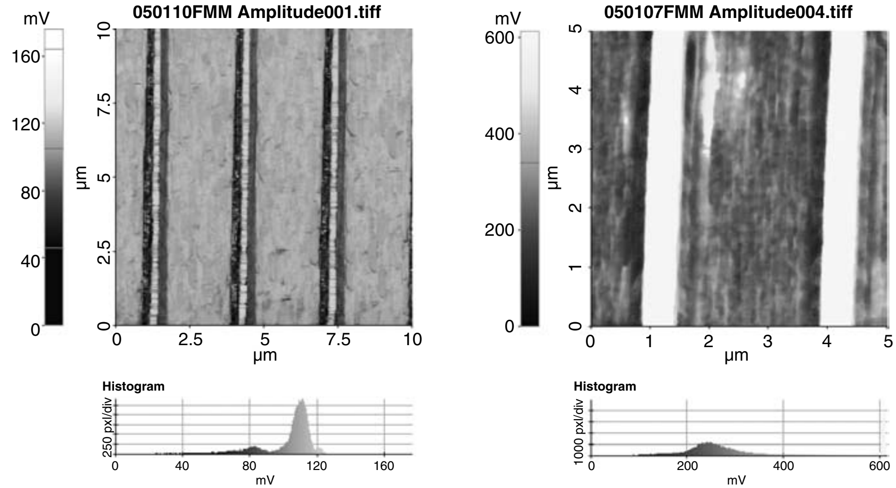

(a) (b)

Figure 13.37 Force modulation analysis of silicon wafer: (a) before molding and (b) after molding.

occurring when the AFM tip scanned the edge of abrupt topographic changes (i.e., the trench walls). In contrast, lighter bands were present in the trench regions of the silicon wafer after 3000 molding cycles (Figure 13.37b). The plateau regions of the used tooling, however, showed the same darker color as the unused tooling. The clear difference in color reflects the modulus difference between silicon and polycarbonate and indicates that polycarbonate adhered to the tooling. When this polycarbonate was removed by soaking the tooling in chloroform, the tooling exhibited its original depth and surface roughness.

Although the electroformed nickel tooling has the same surface temperature as the steel mold, the silicon wafers were insulated from the steel by a polytetrafluoroethylene sheet. This sheet protected the tooling during molding but also retarded heat transfer from the polymer melt. After ejection, the measured surface temperature of the silicon tooling was about 66°C. The tooling temperature, however, was probably much greater just prior to ejection. Thermal models of the molding process suggested that the temperature at the time of ejection was greater than the glass transition temperature of the polycarbonate. Therefore, the polycarbonate nanofeatures probably tore during ejection, leaving polycarbonate in the trenches. Increasing the cooling time for the molded part improved feature replication and left little polycarbonate on the surface of the tooling. Changing the backing material to copper sheeting, however, increased the rate of cooling so much that there was negligible replication of the nanoscale features.

Coating the tooling with metal improved the durability of the tooling, but affected replication. Figure 13.38 presents the three-dimensional views of the titanium-coated GaAs tooling and the molded polycarbonate part.

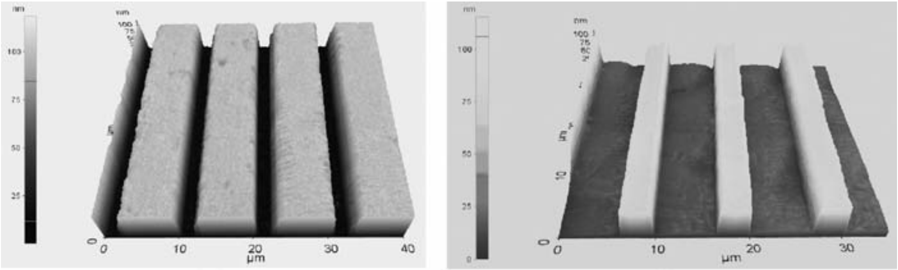

(a) (b)

Figure 13.38 Three-dimensional topography of (a) GaAs wafer with a titanium coating and (b) a polycarbonate part molded with the titanium-coated GaAs tooling.

The corresponding line profiles for the coated GaAs wafer and molded polycarbonate are given in Figure 13.39.

These GaAs wafers had an aspect ratio of about 0.025:1 and the spacing between trenches was 2.4 times the trench width. The trenches of the GaAs tooling were shallower and much wider than those of the silicon tooling. Moreover, the walls of the trenches had a greater taper than those of the silicon wafers and corners at the bottoms of the trenches were more rounded. After injection molding, the trenches became projections in the polycarbonate parts. These projections showed fairly steep walls, but had concave top surfaces. The bottoms of the molded trenches exhibited deep corners and slightly shallow regions in the center of the trench (Figure 13.39b).

As with the silicon tooling, the surface roughness of the GaAs tooling and corresponding polycarbonate parts were measured using AFM. The uncoated GaAs tooling exhibited an overall surface roughness of 39 nm, and the addition of a 20–nm-thick titanium coating did not change that roughness value. At 37 nm, the surfaces of the polycarbonate parts were only slightly smoother than the coated GaAs tooling. Examination of specific surfaces showed that the titanium coating reduced the surface roughness of the plateau surface of the GaAs from 10 to 9 nm, and that this smoothness was reflected in the bottom of the polycarbonate trenches (Figure 13.40). A similar smoothing effect occurred when the bottom GaAs trenches were coated with titanium. The tops of the molded polycarbonate projections, however, exhibited even less

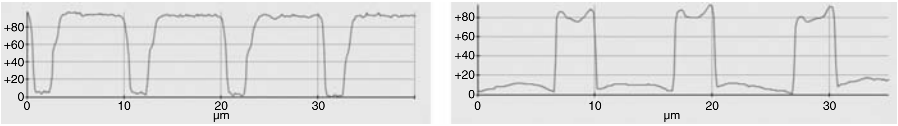

(a) (b)

Figure 13.39 Line profile of (a) GaAs with titanium coating (depth unit: nm) and (b) polycarbonate molded with titanium-coated GaAs tooling (depth unit: nm).

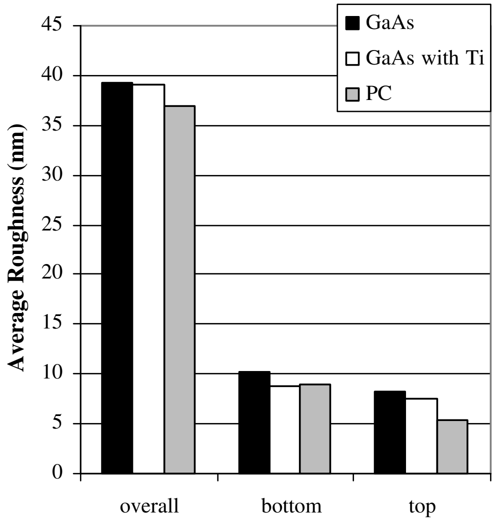

Figure 13.40 Surface roughness for GaAs, titanium coated GaAs, and polycarbonate molded with titanium-coated GaAs.

roughness than the coated tooling surface. Replication was also relatively good. Because the average depth of the tooling was 86 nm, the average projection height (measured at the center of the projection) of 80 nm produced a depth ratio of 93%. While this depth ratio was better than the 75 to 85% exhibited for wide silicon trenches, the aspect ratio (i.e., the ratio of the trench depth to the trench width) was very low (0.025:1) for the GaAs tooling.

While the extremely low aspect ratio and the surface coating may be the reason for the good replication, the wide trench seems to induce volumetric shrinkage in the top of the molded part (as shown in Figure 13.38b and Figure 13.39b). The central deflection (at the top of projection) matches the 10% volumetric shrinkage that occurs as optical polycarbonate cools from 315°C to room temperature. Titanium has a much lower thermal conductivity (21.9 W/m.K) than the 141 W/m.K of silicon. Therefore, this change in thermal conductivity, k, and the design of the mold may be combining to produce a sink mark (i.e., area of greater shrinkage) on the top of the polycarbonate projections. If this mechanism holds true, then the depth ratio for the coated GaAs tooling is close to 100% for the low-aspect-ratio microscale features. The mechanism is currently under investigation as silicon tooling has been coated with aluminum (k = 237 W/m.K) and chromium (k = 593 W/m.K).

References

1. Bonner, J.G. and Hope, P.S., in *Polymer Blends and Alloys*, Folkes, M.J. and Hope, P.S., Eds., Chapman and Hall, Cambridge, UK, 1993, Chap. 3.
2. Lyngaae-Jørgensen, J., in *Polymer Blends and Alloys*, Folkes, M.J. and Hope, P.S., Eds., Chapman and Hall, Cambridge, UK, 1993, Chap. 4.

3. Dooley, J., Jenkins, S., and Naumovitz, J., *SPE Technical Papers*, 47, 386, 2001.
4. Quirk, R.P. and Morton, M., in *Thermoplastic Elastomers,* Holden, G., Legge, N.R., Quirk, R., and Shroeder, H.E., Eds., Hanser/Gardner Publications, New York, 1996, Chap. 4.
5. Jana, S.C. and Jain, S., *SPE Technical Papers*, 47, 2180, 2001.
6. Giannelis, E. P., *Adv. Mater.*, 8, 29, 1996.
7. Coran, A.Y., in *Handbook of Elastomers*, Bhowmick, A.K. and Stephens, H.L., Eds., Marcel Dekker, Inc., New York, 1988, p. 254.
8. Meuller, C., Kerns, J., Ebeling, T., Nazarenko, S., Hiltner, A., and Baer, E., *Polymer Process Engineering '97, Conference Proc.*, London, July 1997, p. 137.
9. Zimmerman, D.A., *Polymers, Laminations and Coatings Conference Proceedings*, Vol. 1, Atlanta, GA, p. 253.
10. Kamykowski, G.W., Goto, S., and Pucci, M.S., *SPE Technical Papers*, 42, 121, 1996.
11. Leclere, I.N., Dinelli, B., and Kuusipalo, J., *TAPPI 1997 Polymers, Laminations, and Coatings Conf. Proc.*, Toronto, Ontario, (1), p. 203, 1997.
12. Nazarenko, S., Hiltner, A., and Baer, E., *J. Mater. Sci.*, 34, 1461, 1999.
13. Nazarenko, S., Dennison, M., Schuman, T., Stepanov, E.V., Hiltner, A., and Baer, E., *J. Appl. Polymer Sci.*, 73, 2877, 1999.
14. Rauwendaal, C., *Polymer Extrusion,* Hanser/Gardner Publications, Cincinnati, OH, 1994.
15. Wheatley, J.A. and Schrenk, W.J., *SPE Technical Papers*, 39, 2864, 1993.
16. Schrenk, W.J., Barger, M.A., Ayres, R.E., and Shastri, R.K., *SPE Technical Papers*, 39, 544, 1993.
17. Chen, K.P. and Zhang, Y., *J. Fluid Mech.,* 247, 489, 1993.
18. Chen, K.P., *J. Non-Newtonian Fluid Mech.,* 40, 155, 1991.
19. Anturkar, N.R., Papanastasiou, T.C., and Wilkes, J.O., *J. Non-Newtonian Fluid Mech.*, 41, 1, 1991.
20. Musarra, S. and Keunings, R., *J. Non-Newtonian Fluid Mech.,* 32, 253, 1989.
21. Su, Y.Y. and Khomami, B., *J. Rheol.*, 36, 357, 1992.
22. Wilson, G.M. and Khomami, B., *J. Non-Newtonian Fluid Mech.*, 45, 355, 1992.
23. Van De Griend, R. and Denn, M.M., *J. Non-Newtonian Fluid Mech.,* 32, 229, 1989.
24. Schrenk, W.J., Bradley, N.L., Alfrey, T., and Maack, H., *Polymer Eng. Sci.,* 18, 620, 1978.
25. Mavridis, H. and Shroff, R.N., Multilayer extrusion: experiments and computer simulation, *Polymer Eng. Sci.,* 34, 559, 1994.
26. Dooley, J., Hyun, K.P., and Hughes, K., *Polymer Eng. Sci.,* 38, 1060, 1998.
27. Khomani, B., Interfacial stability and deformation of two stratified power law fluids I Plane Poiseuille flow, *J. Non-Newtonian Fluid Mech.,* 37, 19, 1990.
28. Khomani, B. and McHugh, A.J., Processing property interactions in poly(vinylidene fluoride). I. An analysis of melt stress history in an extensional flow geometry, *J. Appl. Polymer Sci.,* 36, 859, 1988.
29. Han, C.D. and Shetty, R., *Polymer Eng. Sci.*, 18, 180, 1978.
30. Ramanathan, R. and Schrenk, W.J., *Plast. Eng.*, 6, 73, 1993.
31. Tzoganakis, C. and Perdikoulias, J., *Polymer Eng. Sci.*, 40, 1056, 2000.
32. Zatloukal, M., Martyn, M.T., Coates, P.D., and Saha, P., *SPE ANTEC Tech. Papers,* 295, 2003.
33. Kopytko, W., Zatloukal, M., and Vlcek, J., *SPE ANTEC Tech. Papers,* 7, 2003.
34. Ramanathan, R., Shanker, R., Rehg, T., Jons, S., Headley, D.L., and Schrenk, W.J., *SPE ANTEC Tech. Papers*, 224, 1996.

35. Ranjbaran, M. M. and Khomami, B., *Polymer Eng. Sci.*, 36, 1875, 1996.
36. Ho, K., Lee, J.S., Viriyabanthorn, N., Sung, C., Barry, C.M.F., and Mead J.L., Investigation of interfacial instabilities in nanolayer extrusion, *Proceedings of Society of Plastics Engineers Annual Technical Conference '04*, Chicago, IL, May 16–20, 2004, p. 376.
37. Dooley, J., Hyun, K.S., and Hughes, K., *Polymer Eng. Sci.*, 38, 1061, 1998.
38. Doshi, J., *The Electrospinning Process and Applications of Electrospun Fibers*, Ph.D. Thesis, University of Akron, Akron, OH, 1994.
39. Buer, A., Ugbolue, S.C., and Warner, S., Electrospinning and properties of some nanofibers, *Textil. Res. J.*, 71, 323, 2001.
40. Jaeger R., Schönherr, H., and Vancso, G.J., *Macromolecules*, 29, 7643, 1996.
41. Srinivasan, G. and Reneker, D., *Polymer Int.*, 36, 195, 1996.
42. Reneker, D.H. and Chun, I., *Nanotechology*, 7, 216, 1996.
43. Larrondo, L. and Manley, R., *J. Polymer Sci. B Polymer Phys*, 19, 909, 1981.
44. Doshi, J. and Reneker, D.H., *J. Elec.*, 35, 151, 1995.
45. Baumgaarten, P.K., *J. Coll. Int. Sci.*, 36, 71, 1971.
46. Gibson, P., Schreuder-Gibson, H., and Rivin, D., *Coll. Surf. A*, 187–188, 469–481, 2001.
47. Schreuder-Gibson, H., Sennett, M., Sung, C., Ren, Z., and Huang, Z., Chemistry and physics of fullerenes and carbon nanomaterials, *Fullerenes 2000*, Vol. 10, The Electrochemical Society, 2000, pp. 210–221.
48. Sung, C., Varma, R., and Schreuder-Gibson, H., Electrospinning of PC and their surface characteristics, presented in Fiber Society Meeting, May 23–25, 2001, North Carolina State University, Raleigh, NC.
49. Kim, J.-S. and Lee, D.S., Thermal properties of electrospun polyesters, *Polymer J.*, 32, 616, 2000.
50. Drew, C., Wang, X., Senecal, K., Schreuder-Gibson, H., He, J., Tripathy, S., and Samuelson, L., *SPE Technical Papers*, 46, 1477, 2000.
51. Park, W.H., Jeong, L., Yoo, D.I., and Hudson, S., Effect of chitosan on morphology and conformation of electrospun silk fibroin nanofibers, *Polymer*, 45, 7151, 2004.
52. Kahol, P.K. and Pinto, N.J., An EPR investigation of electrospun polyaniline-polyethylene oxide blends, *Synthetic Met.*, 140, 269, 2004.
53. MacDiarmid, A.G., Jones, Jr., W.E., Norris, I.D., Gao, J., Johnson, Jr., A.T., Pinto, N.J., Hone, J., Han, B., Ko, F.K., Okuzaki, H., and Llaguno, M., Electrostatically-generated nanofibers of electronic polymers, *Synthetic Met.*, 119, 27, 2001.
54. Ohkawa, K., Cha, D., Kim, H., Nishida, A., and Yamamoto, H., Electrospinning of chitosan, *Macromol. Rapid Comm.*, 25, 1600, 2004.
55. Lee, K.H., Kim, H.Y., Ryu, Y.J., Kim, K.W., and Choi, S.W., Mechanical behavior of electrospun fiber mats of poly(vinyl chloride)/polyurethane polyblends, *J. Polymer Sci. B Polymer Phys.*, 41, 1256, 2003.
56. Norris, I.D., Shaker, M.M., Ko, F.K., and MacDiarmid, A.G., *Synthetic Met.*, 114, 109, 2000.
57. Fong, H. and Reneker, D.H., *J. Polymer Sci B Polymer Phys.*, 37, 3488–3493, 1999.
58. Bognitzki, M., Frese, T., Steinhart, M., Greiner, A., and Wendorff, J., *Polymer Eng. Sci.*, 41, 982, 2001.
59. Dong, H., Nyame, V., MacDiarmid, A.G., and Jones, Jr., W.E., *J. Polymer Sci. B Polymer Phys.*, 42, 3934, 2004.
60. Bognitzki, M., Hou, H., Ishaque, M., Frees, T., Hellwig, M., Schwarte, C., Schaper, A., Wendorff, J.H., Greiner, W., *Adv. Mater.*, 12, 637, 2000.

61. Sun, A.C., Zussman, E., Yarin, A.L., Wendorff, J.H., and Greiner, A., *Adv. Mater.*, 15, 1929, 2003.
62. Li, D. and Xia, Y., *Nano Lett.*, 4, 933, 2004.
63. Zhang, Y., Huang, Z., Xu, X., Lim, C.T., and Ramakrishna, S., *Chem. Mater.* 2004, 16, 3406.
64. Paul, D.R., Fibers from polymer blends in *Polymer Blends*, Vol. 2., Paul, D.R., and Newman, S., Eds., Academic Press, New York, NY, 1978, Chap. 16.
65. Fong, H. and Reneker, D.H., *J. Polymer Sci. B Polymer Phys.*, 37, 3488, 1999.
66. Wei, M., Sung, C., and Mead, J., Phase morphology of electrospun nanofibers from polybutadiene (PB)/polycarbonate (PC) blends, *Polymer Preprint.*, 79, 2003.
67. Wei, M., Kang, B., Sung, C., and Mead, J., Preparation of nanofibers with controlled phase morphology from electrospinning of polybutadiene (PB) / polycarbonate (PC) blends, *ACS Book Symposium Series*, in press.
68. Sawyer, L.C. and Grubb, D.T., *Polymer Microscopy,* Chapman and Hall Ltd, New York,, 1978, p. 93.
69. Wei, M., Kang, B., Sung, C., and Mead, J., Phase morphology control of the electrospun nanofibers from the polymer blends, *2004 NSTI Nanotechnology Conference and Trade Show,* Boston, MA, March 2004.
70. Wei, M., Lee, J., Kang, B., and Mead, J., Preparation of core-sheath nanofibers from conducting polymer blends, *Macromol. Rapid Comm.*, (16), 1127, 2005.
71. Formhals, A., Method and apparatus for production of fibers, U.S. Patent No. 1,975,504 (filed 1934).
72. Barris, M.A. and Zelinka, R.L. (assignee: Donaldson Company, Minneapolis, MN), Multi-layered microfiltration medium, U.S. Patent No. 4,650,506 (filed 1986).
73. Dzenis, Y., Spinning continuous fibers for nanotechnology, *Science*, 304, 1917–1919, 2004.
74. Deitzel, J.M., Kleinmeyer, J.D., Hirvonen, J.K., and Beck Tan, N.C., Controlled deposition of electrospun poly(ethylene oxide) fibers, *Polymer*, 42, 8163, 2001.
75. Theron, A., Zussman, E., and Yarin, A.L., Electrostatic field-assisted alignment of electrospun fibers, *Nanotechnology,* 12, 2001.
76. Spivak, A.F., Dzenis, Y.A., and Reneker, D.H., A model of steady state jet in the electrospinning process, *Mech. Res. Comm.*, 27, 37, 2000.
77. Spivak, A.F. and Dzenis, Y.A., Asymptotic decay of radius of a weakly conductive viscous jet in an external electric field, *Appl. Phys. Lett.*, 73, 3067, 1998.
78. Hohman, M.M., Shin, M., Rutledge, G., and Brenner, M.P., Electrospinning and electrically forced jets. I. Stability theory, and II. Applications, *Phys. Fluid.*, 13,:2201–2221, 2001.
79. Bunyan, N., *Control of deposition and orientation of electrospun fibers*, MS Thesis, University of Massachusetts Lowell, 2003.
80. Bunyan, N., Chen, J., Chen, I., and Farboodmanesh, S., Electrostatic effects on electrospun fiber deposition and alignment, *Polymeric Nanofibers,* ACS Symposium Series 918, American Chemical Society, 2006.
81. Tremblay, G., *Plast. Tech.*, 44, 76, 1998.
82. Fassett, J., *SPE Technical Papers*, 41, 430, 1995.
83. Colangelo, A. and Tremblay, G.E., *SPE Technical Papers*, 43, 492, 1997.
84. Neilley, R., *Injection Molding*, 9, 83, 2001.
85. Knights, M., *Plast. Tech.*, 47, 54, 2001.
86. Niarchos, A. and Gogos, C.G., *SPE Technical Papers*, 44, 557, 1998.

87. Brincat, P., Friedl, C., and Talwar, K., *SPE Technical Papers*, 44, 552, 1998.
88. Gupta, M., *SPE Technical Papers*, 47, 794, 2001.
89. Mahishi, M., *SPE Technical Papers*, 44, 547, 1998.
90. Poslinski, A.J. and Oehler, P.R., *SPE Technical Papers*, 42, 470, 1996.
91. Maloney, R.P. and Poslinski, A.J., *SPE Technical Papers*, 44, 543, 1998.
92. Chang, R-Y., Hsieh, Y-C., and Hsu, C-H., *SPE Technical Papers*, 44, 574, 1998.
93. Chang, R-Y., Huang, S-H., Yang, W-L., Chen, I.Y., and Lai, C.C., *SPE Technical Papers*, 46, 449, 2000.
94. Shidhar, L. and Narth, K.A., *SPE Technical Papers*, 45, 496, 1999.
95. Guo, J. and Narh, K.A., *SPE Technical Papers*, 47, 587, 2001.
96. Palluch, K.P. and Isayev, A.I., *SPE Technical Papers*, 46, 528, 2000.
97. Harrell, E.R., Elleithy, R.H., McFarland, C.A., and Summers, J.W., *SPE Technical Papers*, 45, 3558, 1999.
98. Niggemeier, P. and Michaeli, W., *SPE Technical Papers*, 45, 737, 1999.
99. Kang, S., Hieber, C.A., and Wang, K.K., *SPE Technical Papers*, 40, 991, 1995.
100. Kim, B.H. and Suh, N.P., *Polymer Plast. Tech. Eng.*, 25, 73, 1986.
101. Jansen, K.M.B. and Flaman, A.A.M., *Polymer Eng. Sci.*, 34, 894, 1994.
102. Kang, M-H., Kim, D-H., and Chun, Y.H., *SPE Technical Papers*, 46, 3841, 2000.
103. Yao, D., Chen, M., and Kim, B.H., *SPE Technical Papers*, 47, 704, 2001.
104. Ambady, P. and Kazmer, D., *SPE Technical Papers*, 47, 530, 2001.
105. Cosma, L.R., *SPE Technical Papers*, 42, 466, 1996.
106. Mapleston, P., *Mod. Plast. Int.*, 29, 115, 1999.
107. Malloy, R.A., *Plastics Part Design for Injection Molding*, Hanser/Gardner Publications, Cincinnati, OH, 1994.
108. Becker, H. and Heim, U., *Sensor. Actuator*, 83, 130, 2000.
109. Pham, D.T., Dimov, S.S., Bigot, S., Ivanov, A., and Popov, K., *J. Mater. Process. Tech.*, 149, 50, 2004.
110. Kim, J.T., Kim, B.C., Jeong, M.Y., and Lee, M.S., *J. Mater. Process. Tech.*, 146, 163, 2004.
111. Hirata, Y., *Nuclear Instruments and Methods in Physics Research Section B: Beam Interactions with Materials and Atoms*, 208, 21, 2003.
112. http://www.disctronics.co.uk/technology/manuf/rep_master.htm, last accessed 31 January 2004.
113. Fay, B., *Microelec. Eng.*, 61–62, 11, 2002.
114. Lehmann, F., Richter, G., Borzenko, T., Hock, V., Schmidt, G., and Molenkamp, L.W., *Microelec. Eng.*, 65, 327, 2003.
115. Yu, L., Koh, C.G., Koelling, K.W., Lee, L.J., and Madou, M.J., *Proc. Ann. Tech. Conf. Soc. Plast. Eng.*, 47, 785, 2001.
116. Bashir, R., BioMEMS: state-of-the-art in detection, opportunities and prospects, *Adv. Drug Deliv. Rev.* 56, 1565–1586, 2004.
117. Srirojpinyo, C., Yoon, S., Lee, J.S., Mead, J.L., and Barry, C.M.F., Interfacial Effects in Replication of Nano-Scale Features, *Proc. Ann. Tech. Conf. Soc. Plast. Eng.*, 63, 754–758, 2005.
118. Srirojpinyo, C., Yoon, S., Lee, J., Sung, C., Mead, J.L., and Barry, C.M.F., *Proc. Ann. Tech. Conf. Soc. Plast. Eng.*, 50, 743, 2004.
119. D'Amore, A., Gabriel, M., Haese, W., Schift, H., and Kaiser, W., *Concentration of Information*, 2004.
120. Tomasetti, E., Legras, R., Henri-Mazeaud, B., and Nysten, B., *Polymer*, 41, 6597, 2000.
121. Li, F.-B., Thompson, G.E., and Newman, R.C., *Appl. Surf. Sci.*, 126, 21, 1998.

Chapter 14

Patterned Electrospray Fiber Structures

Phil Gibson and Heidi Schreuder-Gibson

Contents

14.1 Introduction 351
14.2 Background 352
14.3 Approach 352
14.4 Pore Size and Air Flow Resistance 358
14.5 Aerosol Particle Filtration 360
14.6 Strength 362
14.7 Conclusions..365
Acknowledgments 365
References..365

14.1 Introduction

Electrospinning is a process for making extremely fine submicron fiber by a process of charging polymer solutions to thousands of volts. This method of manufacturing man-made fibers has been known since 1934, when Formhals filed the first patent on electrospinning.[1] Electrospinning occurs when a polymer solution or melt is charged to high voltage to produce fibers. Voltages of 5 kV to 30 kV are sufficient to overcome surface tension forces of the polymer, and a free surface of charged polymer will produce fine jets of liquid that are rapidly drawn toward a grounded target. The jet splits a few times near the liquid surface, but before it reaches the target, substantial drawing is observed in a series of looping actions of the rapidly solidifying fiber.[2] The fiber is often collected as an interconnected web of small filaments on the surface of a grounded target.

Despite the long history of electrospinning technology, it has never been applied to fabrics as a protective membrane layer. This new application has been under development at the U.S. Army Natick Soldier Center for the purpose of providing protection from extreme weather conditions, enhancing fabric breathability, increasing wind resistance, and improving the chemical resistance of clothing to toxic chemical exposure. Due to the fine fiber size and large expected surface area, electrospun membranes possess the features desirable for catalyst immobilization substrates, absorbent media, and encapsulated active ingredients, such as activated carbon and various biocides.

14.2 Background

The current work is similar to previous studies we have carried out for nanofiber coating on open-cell polyurethane foam loaded with activated carbon particles.[3] Nanofiber spray coatings were applied directly to the foam, and aerosol particle filtration and air flow properties were measured as a function of deposition thickness. The difference in the present work is the use of different substrates, and intentional gradient patterning of the spray. Examples of this past work are shown in Figure 14.1 and Figure 14.2.

An objective of this work is to produce the patterned electrospun fiber layer applied directly to other substrate materials. A good example of patterning is found when fibers are electrospun directly onto an activated carbon sphere filter fabric used in military chemical protective garments. The activated carbon spheres are fairly conductive and provide a good patterning target for the charged fibers. Figure 14.3 shows the natural patterning when spinning directly onto the carbon spheres.

14.3 Approach

The challenge in this current work is to develop a density gradient through the coating thickness, as well as intermingling fibers of different compositions together into the web. A conductive patterned substrate is put behind the target textile, and the pattern can be varied by shifting during the electrospray process to produce the desired gradients through the thickness and across the surface. Deposition density can be controlled by lateral shifting as well as by changing the separation between the conductive pattern and the back of the textile spray target. Shifting of the pattern during the fiber spray deposition will also increase the tortuosity of the interconnected pores formed by the fiber bed. Increase in tortuosity should result in higher filtration efficiency for a given thickness. Patterning may also be a viable way to increase the stand-alone strength of an electrospun

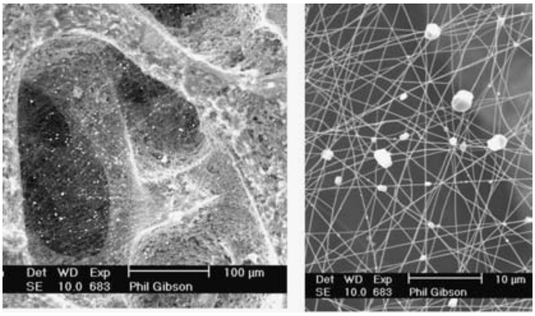

Figure 14.1 Aerosol particles (small white particles) captured in nanofiber web covering large pores in activated carbon loaded polyurethane foam.

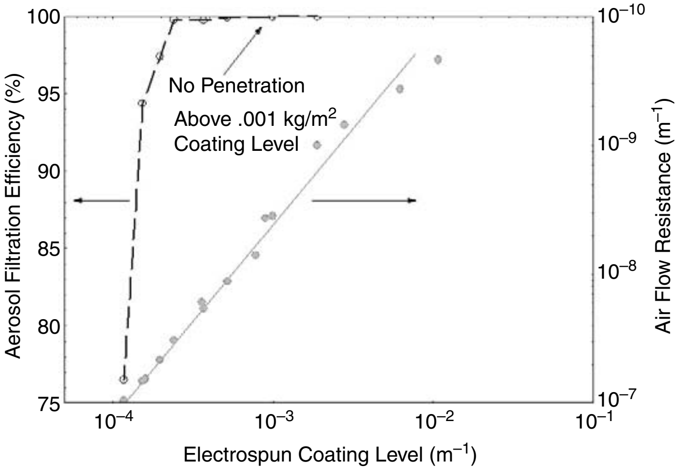

Figure 14.2 Aerosol particle filtration efficiency and air flow properties of electrospun nanofiber coating applied directly to sorptive carbon foam. (From Gibson, P., Schreuder-Gibson, H., and Rivin, D., *AIChE J.*, 45, 190, 1999. With permission.)

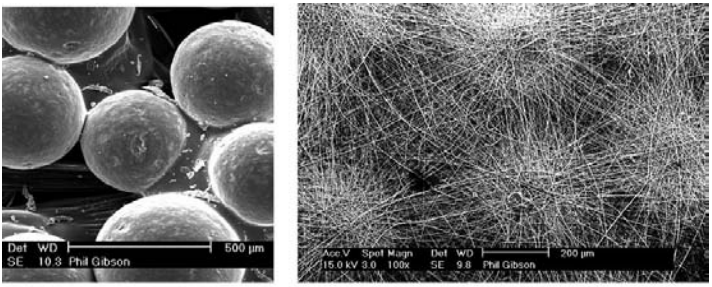

Activated carbon spheres Electrospun fibers coated onto spheres

Figure 14.3 Example of patterning on carbon bead array due to higher electric conductivity of activated carbon spheres.

membrane. A pattern similar to that seen on the surface of a ripstop fabric is formed with a square grid pattern. The thicker pattern laid down on the more conductive grid results in higher mechanical strength, while filtration and air permeability are maintained in the thinner regions between the reinforced areas.

Methods for controlling electrospun fiber patterning have been developed by several groups. Bunyan et al.[4] were able to control fiber deposition patterns by controlling electrode and target configuration. White and coworkers[5] developed several electrospun fiber patterning techniques for "gossamer space structures (solar sails based on Mylar films)" and adhesive layers coated onto textiles. Yarin and coworkers[6,7] showed how to produce aligned fibers and nanofiber structures by manipulating electric fields and targets.

We are building upon these techniques to electrospin directly onto various conductive targets to produce stand-alone fibrous membranes. We are concentrating on three polymers at present. Two of these are elastomeric thermoplastic polyurethanes: Estane from Noveon/B.F. Goodrich, designated as TPU-1, and Pellethane from Dow Chemical, designated as TPU-2. These polymers are tough and highly elastic, have good stress recovery, and are fairly easy to spin. The other polymer is Nylon 6. Nylon produces fibers about 10 times smaller than TPU-1 and TPU-2 (10 nm versus 1 μm), but is not elastic and tends to be brittle and papery in thick applications. We are using nylon because it provides very precise targeting of patterns and will help us determine the limits of resolution of patterning and offsets. The thermoplastic polyurethanes also pattern well but, because of the larger fiber size, will not provide the resolution of patterning possible with nylon.

We have produced electrospun patterned grids with TPU-1, TPU-2, and Nylon 6. Conductive patterns include metal screens, perforated metal grids, and cotton fabrics that are wetted to enhance their conductivity. Electrospun membranes produced with the screens are shown in Figure 14.4 and Figure 14.5.

Patterns can be produced by spinning directly onto a conductive grid, or onto a grid placed beneath a nonconductive substrate. Different patterns through the depth of the membrane layer may be produced by shifting the conductive grid during the spinning process. Figure 14.6 shows the results of rotating and translating the underlying conductive grid.

Figure 14.7 shows the fiber deposition pattern resulting from spinning directly onto a conductive wire grid. The charged fibers are preferentially attracted to the metal wires and are often oriented parallel to the wire axis. Figure 14.8 shows that the smallest electrospun polyurethane fibers are generally larger in size than those produced from Nylon 6 (500 nm versus 100 nm fiber diameter).

One of the advantages of the polyurethane membrane is that it is highly elastic and tough and can stretch along with other materials to which it may be attached. A demonstration of the elastic behavior of a stand-alone electrospun

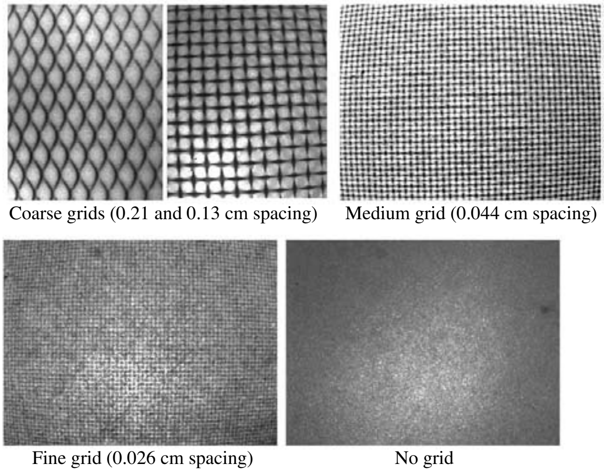

Figure 14.4 Examples of electrostatic patterning using various conductive grids with TPU-1 (thermoplastic elastic polyurethane). Electrospun membrane removed from conductive grid and photographed with back light. Scale: each picture is about 2 cm across. An additional very fine grid with spacing of 0.0078 cm is not shown here.

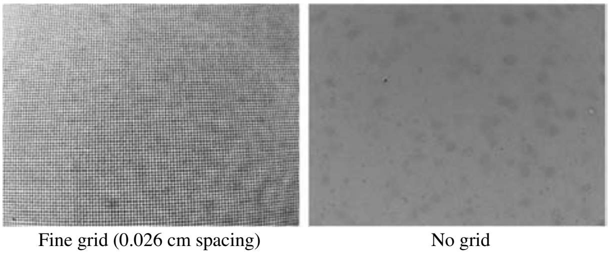

Figure 14.5 Example of electrostatic patterning for Nylon 6. Nylon spun at 15 kV from formic acid. Scale: each picture is about 2 cm across.

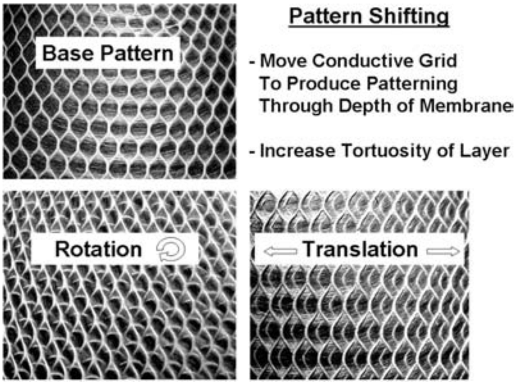

Figure 14.6 Patterning through the depth of an electrospun membrane produced by shifting the underlying conductive grid pattern during fiber deposition.

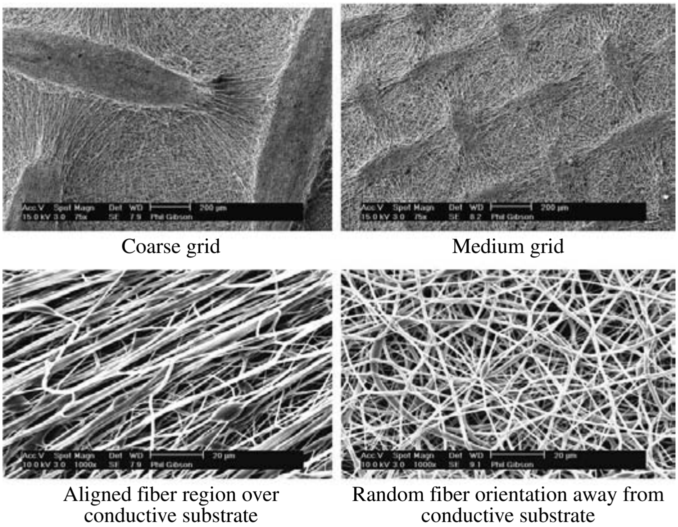

Figure 14.7 Alignment of electrospun fibers over conductive substrate.

polyurethane membrane is shown in Figure 14.9 and Figure 14.10. The ability to stretch under pressure is particularly important in clothing applications. A stretchable membrane may have other applications such as self-cleaning in reverse flow. In the intake phase the membrane filters out particles and experiences minimum deflection if it is against a support backing. In the exhaust phase the membrane expands like a balloon under the pressure of the airflow, the pores open up much wider, aerosol particles are released, and the pores are unclogged.

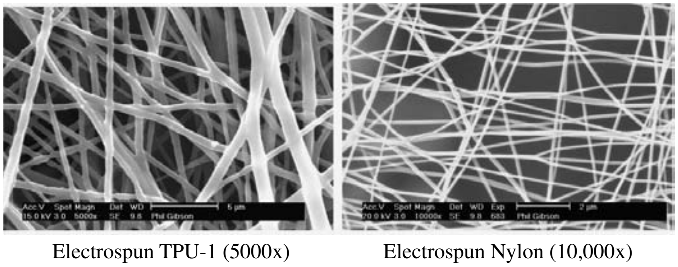

Figure 14.8 Relative fiber sizes for TPU-1 (0.5 to 3 μm) and Nylon (0.1 to 0.5 μm).

Figure 14.9 Illustration of elastic behavior of patterned membrane. Membrane pressurized with gas from below. Electrospun elastomeric polyurethane, large grid pattern.

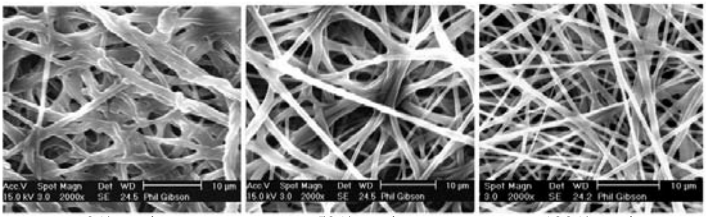

Figure 14.10 Elastic behavior of electrospun thermoplastic polyurethane under biaxial elastic strain.

14.4 Pore Size and Air Flow Resistance

Electrospun fibrous membranes are porous materials. The porosity, pore structure, and pore size determine most of the transport properties we are interested in for these materials (such as air flow resistance and particle filtration). The electrospun porous membranes we make usually have porosities in the range of 60% to 80%, which is comparable to normal nonwoven and woven textiles. The two main variables controlling the transport properties of these membranes are thickness and fiber size. Fiber size is directly related to apparent pore size (the spaces in between the fibers). Thickness is controlled by coating time or deposition rate, while fiber size is influenced

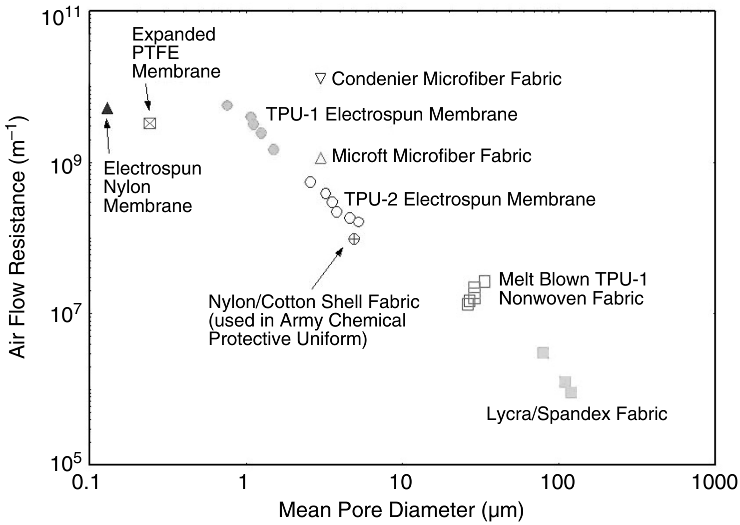

Figure 14.11 Typical pore sizes for electrospun membranes, fabrics, and nonwovens.

by a variety of processing variables including fluid conductivity, fluid viscosity, fluid surface tension, charge density, target distance, and field strength.[8–11]

Pore size and air flow resistance were measured with a liquid capillary expulsion porometer.[12] Smaller mean fiber diameters create smaller mean pore sizes in the electrospun membrane porous structure. Porometry provides a good indication of fiber diameter because the mean pore size is usually of the same magnitude as the mean fiber size. Typical values of air flow resistance and mean pore sizes for electrospun membranes, microfiber fabrics, textiles, and nonwovens are shown in Figure 14.11. Note that air flow resistance (m^{-1}) is essentially the inverse of the more familiar units of air permeability ($ft^3/min/ft^2$) as used in the textile industry.

Air flow resistance (R) is defined by $R(1/m) = \Delta pA/Q\mu$, where Δp = pressure drop (N/m∑); A = sample flow area (m∑); Q = volumetric flow rate (mπ/s); and μ = air viscosity (17.85×10^{-6} kg/m-s at 20°C).

We used porometry to see if patterning affected the mean pore size and air flow resistance of the electrospun membranes. We found that there was no obvious effect of patterning on either mean pore size or air flow resistance of the stand-alone electrospun elastic membranes (Figure 14.12 and Figure 14.13). The differences between patterned samples seem to be due more to random scatter than to any factors having to do with the grid spacing of the patterned samples.

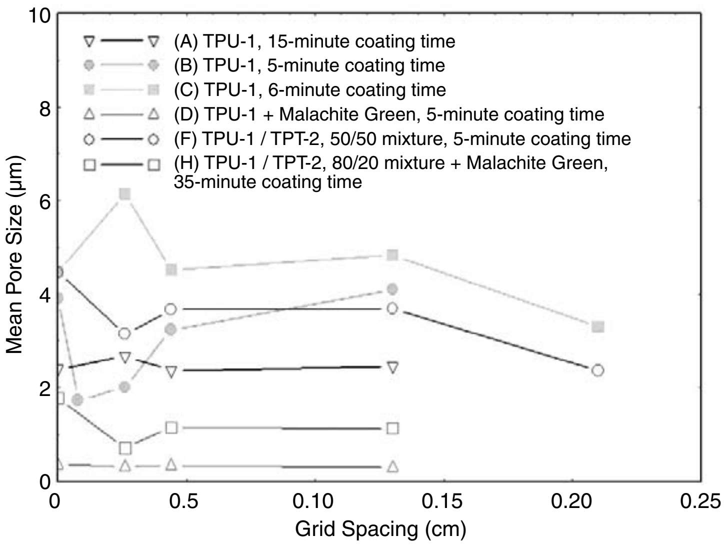

Figure 14.12 Patterning and grid spacing has no clear effect on mean pore size of electrospun elastic membranes.

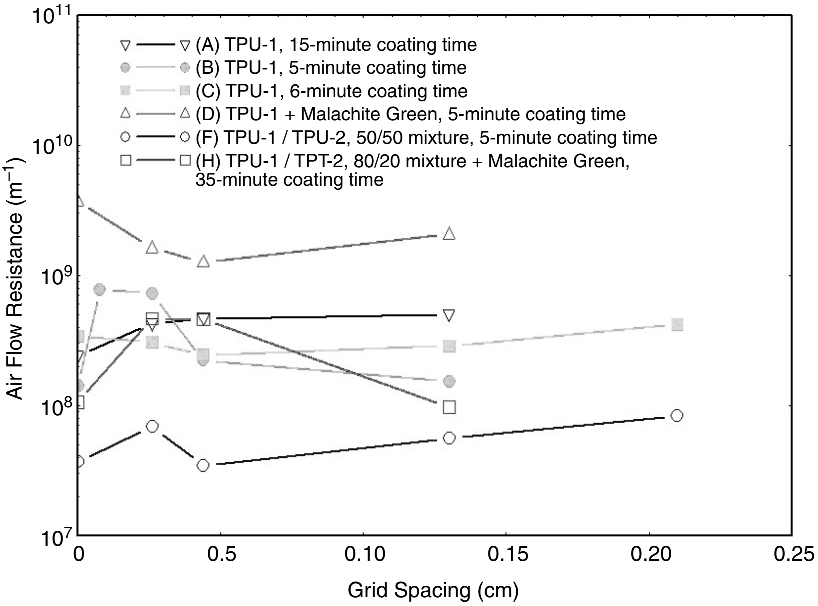

Figure 14.13 Patterning and grid spacing has no clear effect on air flow resistance of electrospun elastic membranes.

14.5 Aerosol Particle Filtration

Electrospun fibers are effective filtration media and are produced commercially for various types of filter products.[13] As mentioned previously, we have been exploring electrospinning as a way to enhance the filtration efficiency of existing clothing materials, particularly by using elastomeric polymers that are able to stretch with and conform to the base fabric without suffering damage.

The patterned electrospun samples were tested for aerosol particle filtration using potassium iodide particles with a mean geometric diameter of 1.8 μm and a fairly narrow distribution between 1 and 3 μm. Further details on the aerosol filtration test system are available in Gibson and Schreuder-Gibson.[14] Figure 14.14 shows the relative sizes of the potassium iodide test aerosol and the fiber sizes in the electrospun membrane samples.

In this phase of the work we are producing fairly thick stand-alone membranes, and nearly all the materials tested are able to completely filter out the test aerosol. However, we would expect that we would see some penetration of aerosols through the electrospun fiber layer when the electrospun fibers are coated in very thin layers onto other substrates, which has been our experience in the past.[15] Because we saw no effect of the fiber patterning on the measured pore size or air permeability, we would also expect to see little effect of patterning on aerosol particle filtration properties.

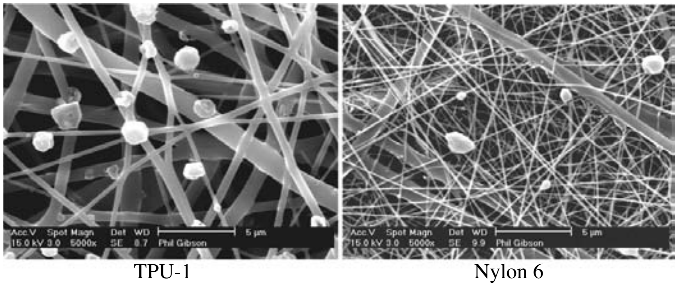

Figure 14.14 Potassium iodide test aerosol particle capture in electrospun TPU-1 and electrospun Nylon 6.

Future work calls for aerosol testing of thin patterned layers sprayed onto woven and nonwoven textile substrates, and we expect to see some aerosol penetration for the very thinnest electrospun layers on such materials.

Figure 14.15 shows aerosol particle penetration for three patterned materials. Two of the materials are a thin layer of electrospun TPU-1 (5-minute coating time) and a mixture of electrospun TPU-1/TPU-2, also coated for 5 minutes. This coating was thin enough to allow some particle penetration. The third material is a much thicker electrospun layer of TPU-1/TPU-2 (35-minute coating time) that allowed very little aerosol particle penetration.

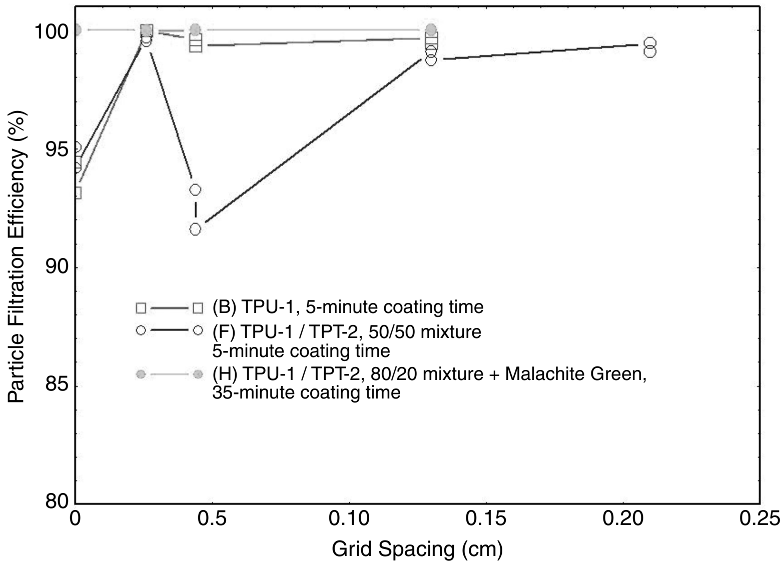

Figure 14.15 Patterning has no clear effect on aerosol filtration properties of elastic electrospun membranes.

One of the reasons we are interested in the patterned electrospun layers is the ability to produce nonuniform densities across the area and through the thickness of the sample. We hope to increase the filtration efficiency of an electrospun layer by forcing air and particles to follow a more tortuous path through the fiber bed, thereby increasing the chance for particle capture. To achieve this, we will be varying the deposition through the thickness of the electrospun layer by shifting the conductive grid so that the high-density regions are discontinuous from one side to the other.

The test system we are using for the aerosol particle penetration measurements is not able to generate or measure particles much below 1 μm. Because the electrospun fibers are highly efficient at capturing particles of this size, it is difficult to see performance differences between different grid spacings if no particles are able to penetrate the layers. Although the pore sizes of some of these membranes are as high as 6 μm, particle diffusion and Brownian motion result in efficient particle capture in the electrospun fiber bed. Aerosol particle penetration through the very thin electrospun layers may be more dependent on small flaws and holes than on actual penetration through a uniform electrospun fiber mat thickness, as reflected in the scattered nature of the data we were able to generate. Aerosol measurements in the future will be extended to include a biological aerosol generated from MS2 virus, which has a diameter near 25 nm. This particle size will be able to more effectively penetrate the small pores of the thicker electrospun membranes and allow us to distinguish the effects of the various grid patterns and offsets much more clearly than we are able to do with aerosol particles of 1.8 μm mean size.

14.6 Strength

Patterning may enhance the strength of electrospun layers. Fibers deposit preferentially over conductive regions and also tend to align themselves with the underlying wire pattern. Patterning may increase the tear resistance of these membranes by the presence of thicker fiber regions that stop tears that begin in the randomly oriented areas of the membrane.

To evaluate strength properties a modified burst test was developed. This test method provided qualitative insight into the elastic capabilities of the electrospun elastomeric membranes, but needs further development to provide reproducible quantitative data.

The electrospun sample was mounted between two metal plates with circular holes. A soft rubber gasket provided sealing and protection from the metal edges of the holes. Gas pressure was slowly increased on one side of the membrane, and a pressure transducer and data acquisition system continuously recorded the gas pressure. The burst pressure is defined as the peak pressure reached before the membrane ruptures (after which the pressure falls nearly to zero).

The burst test was complicated by the fact that the electrospun layers are air permeable. As the air pressure increased, more air flowed through the material. For the elastic membranes, the pore area increased as the sample

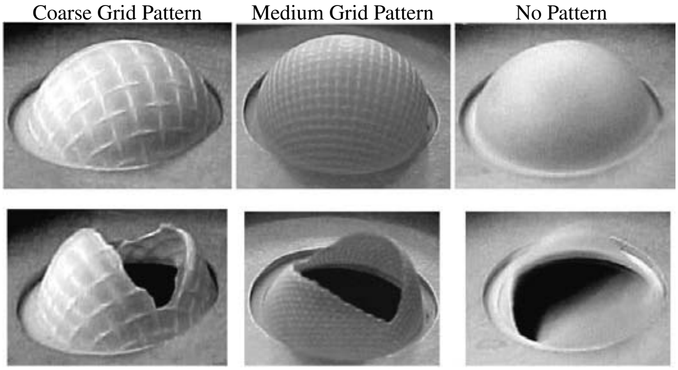

Figure 14.16 Burst testing of fairly thick elastomeric electrospun membranes (electrospun over 15-minute time period). Grid patterns tend to inhibit further tearing of the ruptured membrane.

stretched, increasing the flow rate and further relieving the pressure. For some of the very air-permeable samples, it was impossible to induce rupture or tearing because the material was able to relieve the pressure by its ability to deform and increase total pore area under the imposed pressure. The usefulness of the burst test was also limited by the maximum flow rate from the gas source, and the peak pressure attainable with the data acquisition system and the pressure transducer. Burst pressures above 330 kPa (48 psi) were not recorded, and many samples could not be pressurized to burst because they required higher flow rates than were possible with the gas delivery system used.

Figure 14.16 through Figure 14.18 show typical burst test results for both a thick and a thin electrospun membrane. These particular membranes are

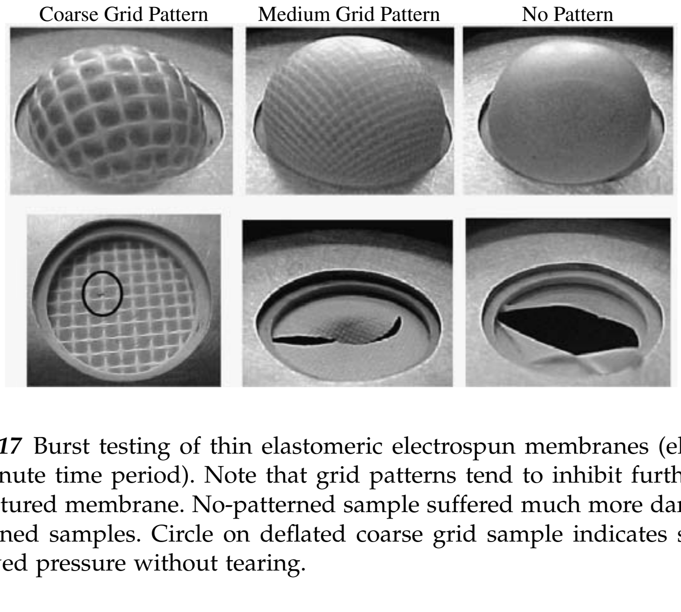

Figure 14.17 Burst testing of thin elastomeric electrospun membranes (electrospun over 5-minute time period). Note that grid patterns tend to inhibit further tearing of the ruptured membrane. No-patterned sample suffered much more damage than the patterned samples. Circle on deflated coarse grid sample indicates small hole that relieved pressure without tearing.

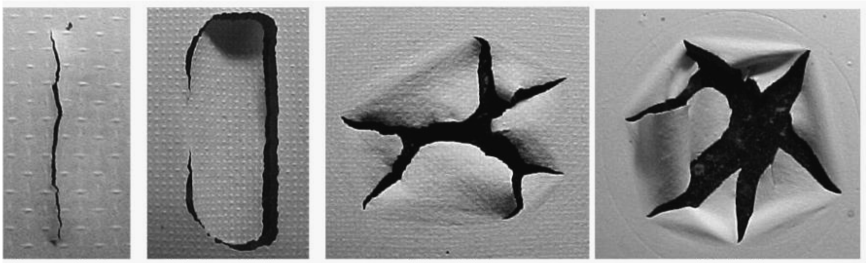

Figure 14.18 Influence of patterning on failure in burst test.

TPU-1 thermoplastic polyurethane. The figures show that the membranes are capable of high strain without rupture. Figure 14.16 through Figure 14.18 show that the grid pattern functions effectively as a ripstop pattern in minimizing damage once the membrane ruptures and begins to tear. Figure 14.16 in particular shows the reinforcing effect of the coarse grid pattern on the inflated highly deformed elastic membrane.

Additional strength testing is planned for these membranes. Simple uniaxial stress–strain curves or uniaxial tear strength may yield more quantifiable results than the simple burst test. An attempt at a simple tear test is shown in Figure 14.19. The elastomeric electrospun membranes are elastic and difficult to restrain and clamp in a tensile tear test. The deformation at the outer edges greatly influences what is happening in the damaged region. The exaggerated opening of the tear before damage begins, and the wrinkling/buckling of the membrane surface also complicates matters. A mechanical biaxial stress–strain test method is a more appropriate test method to evaluate the tear resistance of these highly elastic patterned membranes.

The toughness and strain capability of the elastic patterned electrospun membranes is impressive. Blends of TPU-1 and TPU-2 thermoplastic

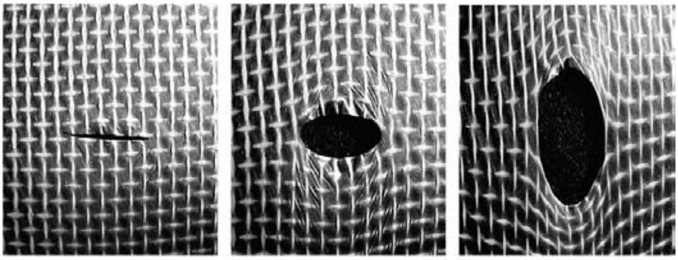

Figure 14.19 Tear testing is difficult due to elastic nature of fibers. Tear/crack begins to propagate at 40% strain. Electrospun 50% TPU-1/50% TPU-2 coarse grid (0.13 cm grid spacing).

polyurethanes seem to have enhanced properties and ease of electrostatic processing over either the TPU-1 or TPU-2 alone. We plan to further investigate commingling/cospinning approaches for elastomeric polymers, including materials such as butyl rubber.[16]

14.7 Conclusions

We investigated the effect of electrostatic patterning on electrospun fibrous membranes. We found that patterning over the range of grid spacings from 0.2 cm to .008 cm produced no significant differences in mean pore size, air flow resistance, or aerosol particle filtration.

We saw qualitative differences in the failure mode and strength of patterned versus unpatterned elastomeric electrospun membranes. Pattern grid size (i.e., coarse, medium, fine) appears to affect tear propagation; patterns resist tear propagation better than unpatterned membranes. The tear resistance is enhanced by the presence of thicker regions of fibers that tend to stop tears. Because there also seems to be some fiber alignment along the metal screen wires that create the grid pattern, the membrane strength may also be enhanced through fiber orientation.

Our future plans are to extend these patterning techniques to optimize thin patterned electrospun layers coated onto other materials, such as stretchable carbon-loaded meltblown webs. We hope to enhance "tortuosity" by shifting the deposition pattern through the thickness of the electrospun layer, and to measure these changes through porometry, aerosol filtration, air flow, and diffusion measurements.

Acknowledgments

The authors are grateful to Ms. Nalini Gupta for preparing some of the intricately patterned electrospun membranes, while working at Natick as an MIT summer student intern.

References

1. Formhals, A., Process and apparatus for preparing artificial threads, U.S. Patent 1,975,504, 1934.
2. Reneker, D., Yarin, A., Fong, H., and Koombhongse, S., Bending instability of electrically charged liquid jets of polymer solutions in electrospinning, *J. Appl. Phys.*, 9, 87, 2000.
3. Gibson, P., Schreuder-Gibson, H., and Rivin, D., Electrospun fiber mats: transport properties, *AIChE J.*, 45, 190, 1999.
4. Bunyan, N., Chen, J., Farboodmanesh, S., and Stevens, K., Control of the morphology and orientation of electrospun nanofibers, *Materials Research Society Symposium Proceedings Series*, 740, Materials Research Society, Pittsburgh, 2002.
5. White, K., Lennhoff, J., Salley, E., and Jayne, K., *Application of electrospinning to the reinforcement and fabrication of gossamer space structures*, The Fiber Society Fall 2002 Annual Technical Conference, Natick, MA, October 16–18, 2002.

6. Theron, A., Zussman, E., and Yarin, A., Electrostatic field-assisted alignment of electrospun nanofibers, *Nanotechnology,* 12, 384, 2001.
7. Zussman, E., Theron, A., and Yarin, A., Formation of nanofiber crossbars in electrospinning, *Appl. Phys. Lett.,* 82, 973, 2003.
8. Fridrikh, S., Yu, J., Brenner, M., and Rutledge, G., Controlling the fiber diameter during electrospinning, *Phys. Rev. Lett.,* 90, 144502, 2003.
9. Shin, M., Hohman, M., Brenner, M., and Rutledge, G., Experimental characterization of electrospinning: the electrically forced jet and instabilities, *Polymer,* 42, 9955–9967, 2001.
10. Hohman, M., Shin, M., Brenner, M., and Rutledge, G., Electrospinning and electrically forced jets: I. Stability theory, *Phys. Fluids,* 13, 2201–2220, 2001.
11. Hohman, M., Shin, M., Brenner, M., and Rutledge, G., Electrospinning and electrically forced jets: II. Applications, *Phys. Fluids,* 13, 2221–2236, 2001.
12. Gibson, P. and Schreuder-Gibson, H., Effect of deformation on the porosity and transport characteristics of elastomeric electrospun nonwoven membranes, *Proceedings of 10th Annual International TANDEC Nonwovens Conference, Nonwovens Development Center (TANDEC)*, University of Tennessee, Knoxville, TN, Nov. 7–10, 2001.
13. Grafe, T., Gogins, M., Barris, M., Schaefer, J., and Canepa, R., Nanofibers in filtration applications in transportation, *Filtration 2001 Conference Proceedings*, International Conference and Exposition of the Association of the Nonwovens Fabric Industry (INDA), Chicago, IL, Dec. 3–5, 2001.
14. Gibson, P. and Schreuder-Gibson, H., Aerosol particle filtration, gas flow, and vapor diffusion properties of electrospun nanofiber coatings, *U.S. Army Natick Research, Development, and Engineering Center Technical Report*, Natick/TR-99/016L, Feb. 1999.
15. Gibson, P., Schreuder-Gibson, H., Wadsworth, L., Zukas, W., Zippel, S., and Mishkin, B., Effect of carbon particulate loading and surface nanofibers on filtration performance of nonwoven media, *American Filtrations and Separations Society 16th Annual Technical Conference and Exposition*, Reno, NV, June 17–20, 2003.
16. Viriyabanthorn, N., Shawon, J., Mead, J., and Stacer, R., Structure and transport properties in electrospun butyl rubber, *Fiber Society Fall 2002 Annual Technical Conference*, Natick, MA, Oct. 16–18, 2002.

Chapter 15

Patenting Nanotechnology

Rouget F. (Ric) Henschel and Stephen B. Maebius

Contents

15.1 Introduction 367
15.2 Federal Support for Nanotechnology..368
15.3 Patent Basics 368
15.3.1 Patents in Perspective..369
15.3.2 Rudiments of Patent Law 369
15.3.3 Foreign Patent Rights 371
15.4 Explosive Growth of Nanotechnology Patents...................................372
15.4.1 Overlapping Patents and Priority Disputes..................................373
15.4.2 Freedom-to-Operate Issues 374
15.5 Conclusion 375
References..375

15.1 Introduction

If anyone doubts how important patents are to the growing field of nanotechnology, pending lawsuits for patent infringement prove the point. For example, Veeco Instruments, Inc. sued Asylum Research, Inc. for infringing Veeco's patents on atomic force microscope technology. And Ultratech, Inc. sued Tamarack Scientific Company for infringing Ultratech's U.S. Patent No. 5,621,813 on a semiconductor lithography system. Ultratech is a supplier of photolithography systems used to manufacture semiconductors and nanotechnology devices.

Patents are not a new concept — they have been around for quite a long time, perhaps dating back to the time of the ancient Greeks, when patent-like rights were awarded for culinary innovation.[1] The first written patent statute appeared in Venice in the 1400s. Soon thereafter, other countries in Europe, including France, Germany, England, and the Netherlands introduced patent laws. Even before the formation of the United States of America, many

colonies including Massachusetts, Virginia, and New York issued patents. All this laid the groundwork for the U.S. Constitution to include a provision giving Congress power to grant exclusive rights to inventors.[2] In 1790, George Washington signed the first federal Patent Act,[3] providing by statute for a federal patenting system to replace the patents of the states with patents issued by the federal government.

15.2 Federal Support for Nanotechnology

In 2003, the President signed into law the 21st Century Nanotechnology Research and Development Act[4] ("Nanotech Act") authorizing $3.7 billion in federal funding for nanotechnology research and development. The act put into law programs and activities supported by the President's high-priority multi-agency National Nanotech Initiative (NNI).[5]

The Nanotech Act emphasizes R&D leading to technology transfer from research laboratories to the commercial sector, e.g., via startup companies. The Nanotech Act provides funding to specific federal agencies for nanotechnology for 2005 through 2008 as follows:

- NSF: Over $385,000,000 per year
- DOE: Over $317,000,000 per year
- NASA: Over $34,000,000 per year
- NIST: Over $68,000,000 per year
- EPA: Over $5,500,000 per year

Given such a massive influx of funds into nanotechnology R&D, it is no surprise that there has been explosive growth in nanotechnology patenting.

15.3 Patent Basics

Learning about patents can be challenging, so the sooner someone new to the field takes the first steps, the better.[6] Patents are a form of intellectual property differing from trademarks, copyrights, and trade secrets. Trademarks identify the source of a product. The value of a trademark lies in the public perception of quality associated with products from a particular company. If a company lacking a good reputation for quality sells products labeled with another more reputable competitor's trademark, the first company benefits unfairly from the competitor's good reputation and could potentially damage that good reputation by selling inferior products. As such, trademarks have essentially no technical content. Copyrights protect the expression of an idea, but do not protect the idea itself.

Trade secrets are most similar to patents in that the same subject matter could be protected either as a trade secret or as a patent. Trade secrets have the advantage of potentially lasting forever, while patents have a limited term (currently 20 years from the filing date). Also, the subject matter must be kept secret to retain trade secret status, while the subject matter must be revealed

in a patent to qualify for patent protection. So an innovator faces a choice between maintaining an invention as a trade secret, which risks that competitors may reverse engineer or independently develop the invention, and filing for a patent, which necessarily involves disclosing the invention to the public.

15.3.1 Patents in Perspective

In a sense, a patent is a form of contract between the inventor and the government. In exchange for revealing the invention to the public, the government grants the inventor an exclusive right to the invention. The public benefits from that disclosure, which otherwise might have been protected as a trade secret undisclosed to the public. The public disclosure aids further innovation, including developments designed around the invention.

In another sense, a patent represents a bundle of rights that the government grants to an inventor. Specifically, the inventor receives exclusive rights to the invention. This "exclusive right" is a right to exclude others from using the invention. The patentee does not necessarily have a right to practice the invention. For example, if an earlier patent covers broadly the field of a later invention, the later patentee could not practice the invention without a license from the earlier patentee.

A patent is also a form of property, i.e., intangible property. As with personal property or real estate, a patent defines what its owner possesses and can be bought or sold. The scope of what the patent owner possesses finds expression in the claims, which a patent presents as a numbered list at the very end of the document.

Finally, a patent is a publication disclosing to anyone interested the details of the invention. That publication contrasts with the secrecy maintained for trade secrets and expands the body of knowledge available to the public. After the patent expires the public is free to use the invention without restriction.

15.3.2 Rudiments of Patent Law

Patent law is the domain of federal, not state, law. A patentee has the right to sue an infringer in a United States federal court.[7] The remedy for infringement may be a monetary award to compensate the inventor by at least a reasonable royalty for use of the invention.[8] The remedy may also include an injunction, or court order, forbidding the infringer from continuing the infringing activity.[9]

Patents are granted by the United States Patent and Trademark Office (USPTO),[10] which is a part of the Department of Commerce, which in turn is part of the executive branch headed by the President of the United States. The USPTO promulgates regulations under which it operates.[11] Patent examiners at the USPTO review patent applications and grant or deny patents, primarily relying on the USPTO Manual of Patent Examining Procedure (MPEP).[12] The only parties to the examination of a patent application are the applicant and the USPTO examiner. Neither the applicant's competitors nor the general public participate. Accordingly, applicants are subjected to a duty of candor

that requires disclosure to the USPTO of any relevant prior art.[13] This duty of disclosure applies to the inventors, patent attorneys, and all others substantively involved in preparing and prosecuting the application before the USPTO. Failure to disclose to the examiner a relevant prior art document could lead to a court ruling that the patent is unenforceable, which means that the patent cannot support a lawsuit for infringement. Due to the heavy penalty for failing to satisfy the duty of disclosure, all persons subject to the duty of disclosure must be made aware of this duty and must diligently comply.

Anyone seeking a patent must satisfy several statutory requirements. Three are typically grouped together: The invention must be new, useful, and not obvious.[14] These requirements are often referred to as novelty, utility, and nonobviousness. The most important of these is often the requirement for nonobviousness, because novelty is generally a simple question of whether the invention is new with respect to the prior art and utility has become a relatively easy requirement to satisfy. The debate thus generally centers on whether a claimed invention would have been obvious over the prior art. Nonobviousness can be a truly difficult question to resolve because it mixes the technical aspects of the field of the invention with a legal framework that laypersons, such as a judge or jury, must navigate.

An inventor can establish nonobviousness by showing that the invention provides results that are unexpected in view of the prior art. In mature fields of technology, this may be difficult to establish because so much information is in the public domain. With new technologies, it can be far easier to establish that the results of the invention are unexpected. This is the case with nanotechnology. "Atoms on a small scale behave like nothing on a large scale, for they satisfy the laws of quantum mechanics," said Richard Feynman in 1959.[15] Because little is known about how materials behave on a nanoscale, the results of new developments in nanotechnology will generally be unexpected. That allows for a broad range of patentable subject matter while nanotechnology matures as a technical field.

Two statutory requirements relate to the depth of the disclosure in the patent application. First, the patent application as filed must provide sufficient information such that a person of ordinary skill in the field of the patent can readily make and use the invention. This requirement completes the bargain between the government and the inventor whereby the inventor receives exclusive rights in exchange for disclosing the invention to the public. That disclosure must be adequate to allow the invention to be used. Second, the patent application as filed must disclose the best mode of carrying out the invention known to the inventor at the time of filing. Again this reflects the need for full disclosure by the inventor in exchange for exclusive rights. The relevant statute, 35 U.S.C. § 112, set forth these requirements in the first paragraph:

> The specification shall contain a written description of the invention, and of the manner and process of making and using it, in such full, clear, concise, and exact terms as to enable any person skilled in the

> art to which it pertains, or with which it is most nearly connected, to make and use the same, and shall set forth the best mode contemplated by the inventor of carrying out his invention.

The enablement requirement is important for new technologies because very little information may exist outside the patent application to enable the invention, and it is thus more likely that the disclosure within the patent application fails to fully explain how to carry out the full scope of the claimed invention. This is less of a problem for mature technologies because much more is known about the field and a patent applicant can more easily point to prior art that explains how to implement various aspects of the invention.

Finally, patent applicants in new technologies can face problems satisfying the requirement that the claims clearly delineate the scope of the invention, so that the public can determine whether proposed devices or processes infringe. This is typically a question of whether terms used in the claims have a clearly discernible meaning. As a technology matures terms of art with commonly understood meanings emerge. However, when a technology is new, terms may not yet be in common use or the same term may have been used in different ways. Even worse, an inventor may have coined a term that appears nowhere but in the patent application. If the application does not define the term clearly, the USPTO may reject a claim containing the term for indefiniteness. The second paragraph of 35 U.S.C. § 112 sets forth this statutory requirement:

> The specification shall conclude with one or more claims particularly pointing out and distinctly claiming the subject matter which the applicant regards as his invention.

The patent application should ideally contain a clear definition of every potentially ambiguous term that appears in the claims, preferably in a separate paragraph for each term beginning with the term set out in quotes.

15.3.3 Foreign Patent Rights

This article emphasizes patents in the United States. However, a patent has force only in the issuing country. A U.S. patent thus has no force outside this country. For protection outside the United States, an inventor must get a patent in each country where the inventor desires to protect the invention.

An inventor faces a large number of foreign countries from which to choose. Consider that currently well over 100 countries issue patents. Rather than file in each foreign country individually, most patent applicants now seek foreign protection through the Patent Cooperation Treaty (PCT),[16] which streamlines international patent filings — but not ultimate examination — through a single administrative process. The PCT currently has 125 member countries. The PCT has no provisions for granting patents, so no "PCT patent" issues, and PCT statements about patentability are advisory only.

The cost of worldwide protection is potentially huge. In each country, the applicant must pay for attorney fees, translations (if the country's language is other than English), and patent office fees for filing, prosecution, issuance (grant), and maintenance fees. While the United States charges periodic maintenance fees only after a patent issues, most foreign patent offices charge such fees (also called annuities or renewal fees) from the date the patent application is filed.

To decide in which countries to seek patent protection an applicant must consider for each country the scope of patentable subject matter, the enforceability of patents in that country,[17] and the market potential for the invention. This decision alone can involve significant cost and resources because it may require input from business people within the company, the company's U.S. patent attorney, and possibly patent attorneys from the foreign countries. One strategy for obtaining patent protection in the world's largest economies, while limiting total cost, would be to pursue patents only in the United States, Japan,[18] and Europe.[19]

15.4 Explosive Growth of Nanotechnology Patents

From a patent perspective, nanotechnology can provide many inventions that are improvements over prior inventions implemented without the benefit of nanotechnology. Consider a patented pharmaceutical with low solubility. The patentee could then develop a nanocrystalline drug formulation with enhanced solubility, thus yielding better performance. This discovery may suffice for a new patent. The enhanced solubility could convert an unmarketable drug to a marketable one. The new patent extends patent protection for the marketed version of the drug beyond the term of the first patent on the original macroscale pharmaceutical. A similar pattern can emerge in other industries.

One can easily confirm the explosive growth of nanotechnology patents using the search engine on the USPTO web site. Since 1988 the number of U.S. patents referring to various nanotechnology terms, e.g., "atomic force microscope," "quantum dot," and "dendrimer," has increased sharply.[20]

The USPTO responded recently to the rapid growth of nanotechnology patent applications by creating a new classification for nanotechnology, Class 977.[21] The U.S. Patent Classification system is meant to serve as a search tool for patent examiners seeking prior art documents in specific technical areas.[22] Establishing a nanotechnology classification is the first step for the USPTO toward a focused approach to examining nanotechnology patent applications. For now, this classification exists only as a simple digest (977/Dig.1 for Nanotechnology) with no subdivisions. The USPTO plans to develop Class 977 to ultimately include definitions, subclasses, and search notes related to classifications in other U.S. classes. For now, the digest 977/Dig.1 applies to patent applications "related to research and technology development at the atomic, molecular or macromolecular levels, in the length of scale of approximately 1–100 nanometer range in at least one dimension."[23,24] The goal is to allow

examiners to use Class 977 and its eventual subclasses for searching prior art, which has been difficult because publications that are relevant to nanotechnology inventions may not have used the term "nanotechnology" and would therefore not be easily found by conventional text searching.

While the USPTO warns that this classification is not comprehensive, the digest is now active and retrieves patents and patent publications on the USPTO web search engine[25] using the search term "CCL/977$."[24] The new Class 977 will also allow the USPTO to track the growth in patent filings in this field to decide whether to create a specialized examining group for nanotechnology. As the number of patent applications classified under Class 977 grows, the PTO may decide to create a special examination group for nanotechnology.

15.4.1 Overlapping Patents and Priority Disputes

Because of the proliferation of nanotechnology patents and ineffective examination by the USPTO, there may arise many overlapping patents. Many areas are crowded already, e.g., nanowires, nanocrystals. For example, one patent may cover silicon nanocrystals having average diameter between 1 and 30 nm. Another patent may cover nanocrystals emitting light in a spectral range no greater than 60 nm. There may be nanocrystals that satisfy both conditions. Such overlap could create mutually blocking rights.

Another source of overlap is where two laboratories simultaneously discover the same invention. To prepare for situations where others file similar patents to yours, carefully preserve your invention records to prepare for a contest to decide who the real or first inventor was. At the USPTO, such a contest is called an "interference."

An interference officially begins when the PTO sends out the declaration of interference, which includes a "standing order" setting forth a number of preliminary due dates and tasks that must be complied with. There are two main phases, the preliminary motions phase and the priority phase. During the preliminary motions phase, the parties may file motions attacking patentability of the claims by the other side (or generally as part of a "suicide" strategy so that the subject matter cannot be patented by either party), as well as motions to deny priority benefit and motions to alter the scope of the counts. It is a critical advantage to be the "senior party" (the one with the earliest effective filing date) because the burden is on the junior party to prove an earlier date of invention than the senior party's filing date. Often, the parties will try to alter the scope of the counts through preliminary motions in order to position themselves as senior party if they do not start out the interference as a senior party. Because one cannot control the motions filed by the other side, it is easy to see why interferences can become costly proceedings where the priority and patentability issues are complex and the other side files motions that must be defended against.

The second phase of an interference is the priority phase. If the board finds that the issue of who invented first must still be decided (i.e., no

case-dispositive preliminary motions have been granted), then the interference proceeds to the priority phase. During this phase, the parties rely on lab notes and other kinds of evidence to prove that they conceived of and/or reduced to practice the claimed subject matter prior to the other party. It is not uncommon for an interference proceeding to cost $500,000 or more if it reaches all the way through the priority phase to a final hearing without a settlement. Furthermore, after an unsuccessful result, the losing party has a right to file an appeal to federal district court (which includes a new discovery process) or appeal directly to the Court of Appeals for the Federal Circuit.

15.4.2 Freedom-to-Operate Issues

A company has limited options when faced with a patent that covers technology the company seeks to use. The company could attack the patent, license the technology from the patent owner, or attempt to design around the patent.

Attacking the patent involves either litigation in federal court or reexamination at the USPTO. Litigation is generally too expensive for nanotechnology companies, which tend to be relatively small startups with limited funds. One can challenge a patent's validity by requesting reexamination at the USPTO, a less expensive option that is useful but limited in scope. The USPTO will only grant a request for reexamination if the USPTO considers that the request presents a "substantial new question of patentability" based on prior art accompanying the request.[26]

Besides challenging a patent's validity in court or at the USPTO, a company can counter-attack with its own patents. Assuming the company has its own portfolio of patents, it can try to identify infringing activity by the competitor and thereby negotiate a cross-license or motivate the competitor not to assert its patents. This tactic can be somewhat unpredictable and risky, and may lead more quickly to an undesirable lawsuit.

In some cases, the easiest option is to license the technology. If a license is available at relatively low cost, the cost of licensing may be considerably less than the cost of litigation. In some cases a license may be available at a cost that competes with the cost in legal fees of evaluating the strength of the asserted patents. This approaches a form of blackmail that has become common practice.[27]

A patent lawyer can help a company faced with patents that a competitor has asserted against it. One approach is to search for prior art to weaken the patent owner's confidence that its patents are valid. A patent attorney can also help design around the patent claims. This would eliminate any need for a license to the patent. Finally, if all else fails, there may be no choice but to draft a license agreement.

A company can use prior art references as a shield because a patent cannot cover what was already known. There are many resources available today for searching the prior art in a particular field of technology. The classic

approach for those with limited resources is to use the USPTO public search facilities, which allow free access by the public to all U.S. patents in hard copy organized by the U.S. classification system. This can be a very time-consuming and inefficient process. The USPTO also makes available on its web site a search engine for searching U.S. patents issued since 1976 and U.S. patent applications published since March 2001.[28] Many commercial electronic databases are available, some with highly sophisticated indexing. For professional help, the Patent Information Users Group is an organization of electronic patent information search specialists.[29]

Designing around patent claims is a creative alternative for avoiding infringement. The USPTO record of proceedings for the application (known as the "file history" or "prosecution history") that led to the patent can provide valuable insight. These USPTO prosecution histories are available to the public as soon as an application publishes or a patent issues.[30] The file history may show that the patent applicant argued the patent does not cover certain subject matter to convince the examiner to allow the case. If so, the patent owner may be precluded from later asserting that the patent covers the same subject matter. A product could be safely designed to avoid infringement by falling within the subject matter disclaimed by the applicant.

15.5 Conclusion

Nanotechnology companies should be wary of the patent landscape. Competitors may obtain patents that limit freedom to operate within a technology space. And they may face difficulty in obtaining adequate patent protection for their own inventions.

A wise strategy would be to learn as much about patents, both domestic and international, as possible and to monitor the patent landscape. This will help guide research efforts and identify entry points before product launch. Use the USPTO web site search engine or other resources to research U.S. patents on nanotechnology. Consider setting up an alerting service to retrieve U.S. patents on nanotechnology as they are issued. A simple approach would be to set up an alerting service to retrieve any new patents issuing under the current nanotechnology classification 977/Dig.1.

In short, use the patent system or risk being its victim.

References

1. Rich, G.S. (Judge, deceased), The "exclusive right" since Aristotle, *Federal Circuit Bar Journal*, 14, 217, 2004–2005.
2. "The Congress shall have the power to promote the progress of science and useful arts by securing for limited times to authors and inventors the exclusive right to their respective writings and discoveries." *U.S. Constitution*, Art. 1, § 8, Clause 8.
3. Now codified as Title 35 of the United States Code. See 35 U.S.C. § 1 et seq. (http://www.uspto.gov/web/offices/pac/mpep/consolidated_laws.pdf).

4. 117 STAT. 1923, P.L. 108–153, 2003.
5. http://www.nano.gov/index.html. See also the web site of the National Nanotech Coordination Office (http://www.nano.gov/html/about/nnco.html).
6. For an introductory manual on patents, see Pressman, D., *Patent It Yourself*, 10th ed., NOLO, Berkeley, CA, 2004.
7. 35 U.S.C. § 281 ("A patentee shall have remedy by civil action for infringement of his patent.").
8. 35 U.S.C. § 284.
9. 35 U.S.C. § 283.
10. The USPTO is located near Washington, D.C., in Alexandria, Virginia (see http://www.uspto.gov).
11. Title 37 of the Code of Federal Regulations. See 37 C.F.R. § 1.1 et seq. (http://www.uspto.gov/web/offices/pac/mpep/consolidated_rules.pdf).
12. See http://www.uspto.gov/web/offices/pac/mpep/index.html.
13. See 37 C.F.R. § 1.56.
14. 35 U.S.C. §§ 101, 102, and 103.
15. Feynman, R., There's plenty of room at the bottom, *Engineering and Science*, California Institute of Technology, February 1960 (reproduced at http://www.zyvex.com/nanotech/feynman.html).
16. The PCT is administered by the World Intellectual Property Organization (WIPO) (http://www.wipo.org). For information on the PCT, see http://www.wipo.int/pct/guide/en.
17. For a concise country-by-country description of patent laws, rights of patentees, and what subject matter is patentable, see Hanellin, E., *Patents Throughout the World*, West Group Eagan, MN (Last updated April 2006).
18. The Japanese Patent Office web site is http://www.jpo.go.jp.
19. See http://www.epo.org for information about the European Patent Office (EPO), which centralizes filing and examination of patents for 30 member states. The EPO is independent of the European Union, which has 25 member states (see http://europa.eu.int).
20. Koppikar, V., et al., Current trends in nanotech patents, *Nanotechnology Law and Business Journal*, Vol. 1, Issue 1, Art. 1, 25–26, April 1, 2004.
21. http://www.uspto.gov/web/patents/biochempharm/crossref.htm.
22. http://www.uspto.gov/web/offices/pac/dapp/sir/co/examhbk/index.html.
23. http://www.uspto.gov/go/classification/uspc977/defs977.htm.
24. The wildcard "$" is necessary because for some reason the classification appears as both "977/Dig.1" and "977/Dig1".
25. http://www.uspto.gov/patft/index.html.
26. 35 U.S.C. §§ 303(a) and 312(a).
27. Andrews, E.L., Rich in the 90s on ideas hatched in the 50s, *The New York Times*, A1, Nov. 13, 1992 ("Increasingly, companies are deciding that it is safer to buy peace for a few million dollars up front than to run the chances of losing 10 times as much in a jury trial.").
28. http://www.uspto.gov/patft/index.html.
29. http://www.piug.org.
30. 37 C.F.R. § 1.14.

Chapter 16

Leaving the Laboratory: Regulatory and Societal Issues Confronting Nanotechnology Commercialization

Christopher J. Bosso, Jacqueline A. Isaacs, William D. Kay, and Ronald L. Sandler

Contents

16.1 Questions about Capacity 377
16.2 Intellectual Property 379
16.3 Regulatory Frameworks and Institutions 380
16.4 Complexity and Public Uncertainty 384
16.5 Why This All Matters 385
16.5.1 Promoting Innovation and Expediting Commercialization 385
16.5.2 Protecting the Public Interest 385
16.5.3 Promoting Public Confidence 386
16.6 Other Sources 387
References 388

16.1 Questions about Capacity

Predictions abound about the commercial potential of nanotechnology, with estimates of a global market ranging anywhere from $1 trillion to $3 trillion in a decade. Moreover, the public and private sectors each are expending

significant effort and money to promote rapid development and effective commercialization of nanotechnology. The U.S. government alone is now spending over $1 billion annually in nanotech research and development, private sector expenditures are estimated to equal if not exceed that figure, and many state governments are funding their own nanotech initiatives to ensure their future economic competitiveness.[1] Similar initiatives are evident in any number of other nations, notably South Korea, Germany, the United Kingdom, and, of course, China. Nanotechnology, everyone agrees, is the Next Big Thing.

The evident, near universal enthusiasm about nanotechnology's future — most famously, perhaps, in Ray Kurzweil's recent book, *The Singularity Is Near*[2]—is rightly tempered by recognition of the potential hurdles along the road to widespread commercialization. Other chapters in this volume lay out a striking array of scientific, technical, design, and process challenges that confront anyone seeking to move nanoscale innovations out of the laboratory. To this list we add a less obvious, but nonetheless pivotal factor: the capacity of government, in the form of appropriate laws, policies, regulations, resources, expertise, and commitment.

Concerns regarding governmental capacity are now emerging, and not only from quarters that some might easily dismiss as alarmist, or even Luddite, in their perspectives about nanotechnology. Even Ray Kurzweil's seemingly unsurpassable faith in the power of technology is muted a bit by his concern that current regulatory processes and frameworks will impede technology innovation and commercialization without necessarily assuring public safety.[2] Yet, to date, relatively little attention has been paid to understanding the current capacity and expected needs of the agencies and officials that researchers, firms, investors, and citizens expect to make critical decisions on a wide range of emerging nanotechnology applications.

In one of a relative handful of targeted studies made so far, an assessment on the applicability of the federal Toxic Substances Control Act (TSCA) to nanoparticles, the Foresight and Governance Project at the Woodrow Wilson Center offered four conclusions with broad relevance to nanotechnology commercialization:

- The unique properties inherent in nanotechnology will pose new challenges to existing regulatory structures and, in the process, create confusion within both industry and government about the nature and scope of regulation.
- Little attention has been paid to the adequacy of the current regulatory system to protect human health and the environment, or about possible alternatives to existing regulatory regimes.
- The absence of any conclusive understanding about the health risks of nanobased substances makes more urgent the need for attention to and a dialog on regulatory adequacy and needed changes.
- Misguided or poorly designed regulatory approaches could have enormous economic consequences.[3]

In sum, there are expressed concerns about existing federal and state government institutional capacity, including (but not limited to) sufficiency in scientific expertise, legal authority, organizational design, and relevant regulatory frameworks, to address the societal and policy challenges posed by nanoscale substances and innovations. As we will discuss, ensuring adequate governmental capacity will be crucial to promoting innovation and expediting commercial production. If it is not clear yet *how* nanotechnology will change the regulatory landscape—and, in turn, be changed by it—there is no doubt these interactions *will* occur, with profound consequences all around. Anyone interested in commercializing nanotechnology, therefore, will have a vested interest in how these as-yet uncertain dynamics play out. Moreover, these concerns bear immediate attention, even if the path to commercialization in some sectors is still years off.

Our basic argument throughout is straightforward and, perhaps, a bit counterintuitive: Rather than acting as stereotypically blunt impediments to technological innovation, appropriately configured and effective regulatory institutions *can* serve to promote the advancement of research and development, to promote smooth and timely commercialization of products containing nanoscale technologies, to protect the public from possible negative effects of these technologies and their use, and, along the way, to be responsive to public concerns regarding those effects. For their part, firms seeking to profit from their current research and development efforts have an obvious vested interest in effective regulatory institutions—even if they do not always publicly admit as much.

This chapter examines just a few of the issues that should concern anyone in the nanotech sector. At this early stage in the trajectory of nanotechnology development, and given the fluidity inherent in both technological innovation and public policymaking, recommendations about specific regulatory frameworks or laws will probably do little but reflect existing ideological orientations about the fundamental role of government. Our purpose here, then, is to draw attention. This chapter focuses primarily on the United States, but the questions raised apply to a wider array of nations and, even, transnational organizations and institutions.

16.2 Intellectual Property

The first potential governmental capacity obstacle to successful commercialization may have nothing to do with the front-line regulatory agencies one usually thinks about, but concerns a relatively low-key agency with a deceptively narrow mandate: the U.S. Patent and Trademark Office (USPTO). Patents, by ensuring the right to enjoy the benefits of one's intellectual property, are the primary means by which society encourages research and innovation. It is the only scientific incentive specifically mentioned in the U. S. Constitution (Article I, Section 8, Clause 8).

Although it does not regulate substances or product uses in the typical understanding of that concept, the USPTO's role as intellectual property

gatekeeper promises to be an early and major factor in the timely, efficient, and responsible commercialization of nanotechnology. The industry in particular has a huge stake in a technologically informed and smoothly functioning intellectual property process and in a gatekeeper whose institutional capacity and scientific competence functioning are up to the task.

As Henschel and Maebius observe in Chapter 15, the USPTO faces significant challenges with nanotechnology. For one thing, the agency already appears to be sagging under the weight of a veritable deluge of patent applications in recent years from sectors widely ranging from software to biotechnology. Indeed, in 2003, USPTO director James Rogan warned Congress of a backlog of over 1 million applications by 2008, with the resulting turnaround time for a clearing a patent stretching to an untenable (for industry) four years.[4] Without a significant transfusion of resources, additional patent examiners in particular, the situation is expected to worsen considerably with the projected influx of patent applications for nanoscale innovations.

Moreover, there are real doubts, even within the agency, about the overall *scientific capacity* of the current roster of patent examiners to assess applications based on nanoscale innovations. The absence of sufficient numbers of scientifically expert examiners will exacerbate the backlog of applications and could lead to instances where patents are granted too easily or approved for similar or identical innovations. Each of these scenarios would be problematic and costly to both applicants and the industry at large.

Such growing concern about the adequacy of the patent system, and the capacity of the USTPO itself, has prompted some in Congress to consider sweeping changes in the U.S. intellectual property system, at this date to no avail. The failure so far of Congress to come to consensus on reform underscores the reality that thinking about patents as a matter of *public policy,* as opposed to the more common and narrower legal perspective, shows it to be exceedingly complex, combining a number of very different public institutions (the USPTO, Congress, and the federal courts) and a wide variety of economic and social actors and organizations. The complexity and challenges are even greater on the global stage, where intellectual property issues lie at the heart of national concerns about economic competitiveness, power, or even national honor.

The capacity of the intellectual property system will have profound effects on research and development investments, the rate of diffusion of technological information, the innovation process, and by extension, the pace of commercialization. Therefore, how the USPTO copes with existing challenges and positions itself for the expected influx of nanoscale innovations and what actions Congress does or does not take in reforming the USPTO and existing patent law are of major consequence to the future commercialization of nanotechnology across the board.

16.3 Regulatory Frameworks and Institutions

At present the federal government is focused on promoting the development and use of new processes and products. At some point soon—perhaps sooner

than many realize—those in Washington will have to confront questions about how to review new products as they move to market, as well as how to respond to possible negative social and environmental effects. Indeed, multiple federal, state, and local agencies are expected to be involved in regulating some of the uses of or effects from these technologies, ranging from product or use approval all the way to more prosaic but not inconsequential issues of zoning approvals for manufacturing facilities and permits for waste disposal. But what is the institutional capacity of federal and state regulatory agencies to deal with an expected influx of new nanoscale technologies, uses, and production processes? What challenges do state and local governments face, and what is being done at those levels? At a minimum, policymakers will be faced with the immense task of rewriting large portions of the already vast and complex set of laws, statutes, and regulations that deal with manufacturing, health and safety, the environment, and other relevant areas.

Some of the potential regulatory capacity problems concern agencies responsible for providing "up front" regulatory approval necessary for new technologies to move to commercial production. The U.S. Food and Drug Administration, for example, is expected to confront a wave of new nanomedical devices and treatments, yet the agency already has trouble managing its present workload and is widely criticized for the length and complexity of its clearance process. Indeed, the agency is widely blamed for slowdowns in the pace of pharmaceutical innovation and commercialization. The FDA currently claims that existing regulations and standards are adequate for most nanotechnology products,[5] but experts outside the agency worry that it currently lacks the regulatory and scientific capacity to fully address nanotechnology needs.[6] Whether the FDA and the Environmental Protection Agency in particular will have the basic institutional capacity to handle the expected regulatory challenge generated by nanotechnology is a matter of serious concern for everyone, not least of all the inventors and companies seeking to gain federal approval for their innovations and products.

Other regulatory capacity challenges concern unintended social and environmental side effects. Some, such as nanoparticle exposure to workers or release into the atmosphere, are of proximate concern. Others are more long term in scope. For example, according to the National Nanotechnology Initiative (NNI) the responsible development of nanotechnology includes a mandate to "increase understanding of the fate, transport, and transformation of nanoscale materials in the environment and their life cycles."[7] Capacity issues thus are not confined to new products. How will we address the inevitable "end of life" issues facing any product, whether in terms of disposal, reuse, or recycling? What expected challenges face government and private sector actors alike in addressing how to deal with nanoparticles once their use comes to an end? Will "end of life" costs be reflected in the pricing of technology, or will they be passed on to the consumers in other ways, such as through tax expenditures?

In addition to posing regulatory challenges, the nanotech revolution represents *opportunities* to reconsider existing regulatory designs and, subsequently,

develop technology-relevant and crosscutting interagency and federal–state modes of regulation. With most previous technological revolutions, governmental regulation and capacity were created only after the need became apparent, often decades after the initial commercial-scale introduction of the technology. To offer but one example, it was not until the enactment of the 1972 Federal Environmental Pesticides Control Act (FEPCA) that Congress begin to align federal regulatory design and capacity to deal directly with the side effects of an entire class of organochlorines (e.g., DDT) that entered the market immediately after World War II.[8] With respect to the promised nanotech revolution, by contrast, institutions and knowledge from previous experience do exist, and those in government are aware of both the significance of the technology and the importance of well-designed and competent regulatory institutions. Thus nanotechnology provides an opportunity for historically informed, government-supported, anticipatory assessment of the regulatory status quo (including, but not limited to, frameworks, models, resource allocation, divisions of responsibility), and the development of alternatives.

It may be possible to build adequate regulatory capacity for nanotechnology through incremental or evolutionary changes in existing regulatory agencies and approaches. Policymaking by analogy is not out of the question. However, substantial, even radical, changes also may be required. Just as nanotechology promises to be a revolution in science and industry, it also might require a revolution (perhaps modest, perhaps radical) in our approaches to regulating emerging technologies and their impacts. In short, the moment is opportune for a serious, crosscutting assessment of federal and state regulatory capacity and design.

D. Kettl, in assessing corporate environmental management systems, suggests that any consideration of alternatives to traditional command and control approaches to environmental regulation poses a "whole new set of interesting policy, political, and ethical questions; this strategy is nothing less than a renegotiation of the basic environmental compact between citizens and government."[9] The same questions, and the same fundamental relationship between citizens and government, adhere to the commercialization of nanoscale devices. Will it be possible, to further echo a point made in that study, "to get the deal right"?

We are at the formative stages of the nanoscale revolution, so for perhaps the first time, the resources (i.e., experience, awareness, foresight) are in place to think proactively and synergistically about aligning government regulatory capacity and approaches with industry and citizen needs. Rather than focus on individual laws, rules, or agencies, now is the time to think in systematic terms about how the federal and state governments should address the expected regulatory challenges posed by nanoscale innovations and social and environmental effects.

For example, it is not clear that the current institutional *design* of the federal regulatory system, one based either on media (e.g., air or water pollution, food pathogens), functional areas (e.g., workplaces), uses (e.g., medical versus food consumption), or target populations (e.g., humans versus animals), is adequate

or desirable to address a new set of technologies with revolutionary properties. But neither is it clear what is to be done. Will or should nanoscale particles, products, devices, or systems be parts of existing agency jurisdictions, or should there be thought given to the creation of a new federal agency that focuses *only* on nanoscale products and issues? This latter question is not posed frivolously. The EPA alone is so burdened by existing mandates often running in different directions that one wonders how the agency will handle even more, and more complex, responsibilities. Its inability to meet a congressionally mandated deadline to assess an entire class of some 600,000 so-called "endochrine disruptors" during the 1990s may have been understandable given the short deadline and magnitude of the task, but the lesson to observers was that radically new ways of thinking are needed if the EPA is to have any hope of operating with any degree of effectiveness, even assuming sufficient budgetary and political support.[10] Similar concerns confront the FDA, elements of the USDA, and other front-line federal regulatory agencies.

It also isn't obvious which *types* of regulatory tools or frameworks will suffice for the challenges posed by the production, use, and disposal of nanoscale products. Will we—or, more to the point, must we—end up with a jumble of tools derived analogously from existing rules and regulations, or is there a novel unified approach that can suit the needs of affected firms and concerned citizens alike? What is the appropriate balance between traditional modes of government enforcement and newer types of performance-based systems? To what extent can the nanotech sector regulate itself, and how?

Moreover, what should states be doing? As B. G. Rabe observes in studying state-level action on climate change, policy making at the state level is often more informal, with fewer entrenched interests and a less densely populated administrative sector. "Consequently," Rabe notes, "many state capitals may offer particularly promising entrepreneurship opportunities, particularly for relatively 'new' issues for which an infrastructure of established policies and interest group positions has not been created."[11] State governments are more likely to openly balance regulation against economic development and are, therefore, less likely to look at environmental regulation (for example) through a zero-sum lens. A useful question, then, is to what degree any emerging nanotechnology regulatory regime should be based on uniform federal rules or allow for state flexibility. This is not a new question, of course, but rarely do we get the opportunity to think about it years in advance and with a rapidly growing understanding of the particular emerging technology at issue.

Finally, we need a better understanding of the extent to which goods and values, besides economic growth and environmental and human health, should be considered in institutional and policy design, as well as whether existing institution and policy designs, or incremental changes from them, are sufficiently responsive to and protective of these values in the context of the challenges posed by the nanotech revolution. For example, what role should the public be afforded in regulatory and policy decisions regarding nanotech at different levels and on different issues, particularly given the

complexity of the scientific information that may be relevant to those decisions? How can responsiveness on the part of regulatory institutions be encouraged, without inappropriately ceding regulatory authority to the public, but still maintaining appropriate standards of public access to process and participatory justice? How can distributive justice be effectively encouraged in the context of what is expected to be a dynamic labor market and economic landscape? How are communal values, esthetic values, and the good of animals and ecosystems, for example, to be afforded consideration? The history of previous technological revolutions shows that economic values and human health are not the only goods at stake with emerging technologies. It is crucial to consider, particularly in the context of a systematic and integrative assessment of U.S. regulatory approaches, whether, to what extent, and how these other values should inform our regulatory institutions and policy designs as we build the requisite capacity for nanotechnology.

The nanoscale revolution offers an extraordinary opportunity to fundamentally rethink the design and institutional organization of a regulatory system that grew by episodic accretion over several decades to address the problems of an industrial economy that is fast giving way to something very new and different. The coming years offer an opportunity to get nanotechnology regulatory policy right, and to get it right in a timely way.

16.4 Complexity and Public Uncertainty

The path from the laboratory to commercial production is also strewn with societal and ethical questions that are independent of and not reducible to either matters of risk assessment or regulatory policy. To what degree does scientific complexity feed into public uncertainty of and potential opposition to the commercialization of some products or applications? How should we proceed under conditions of complexity and uncertainty—with what levels of precaution and assurance, at what pace, in which directions, and with what safeguards?[12]

Recent experiences with genetically modified organisms (GMOs) in agriculture are instructive. The standard story, from the perspective of industry and the scientific community, of what "went wrong" with GMOs is that a lack of disclosure and communication by science and industry led to public ignorance and misconceptions about them, which certain advocacy groups were able to exploit to foster unjustified public opposition to socially beneficial technology. But this account is only partially correct. From the perspective of the concerned public, GMOs were a *novel* technology with potential environmental and human risks, and about which only limited information was available. Moreover, government agencies were not actively investigating these risks nor responding to concerns expressed by the public regarding consumers' being exposed to GMOs involuntarily. Under those conditions, public opposition is reasonable and justified, even if the impacts on technology innovation and dissemination are seen as unfortunate.[13]

A key factor, then, in the opposition to GMOs was public perception that government agencies were not adequately prepared and not adequately

interested in protecting the public good. From their perspective, the EPA was not protecting the environment (nor was any other agency), the FDA was not protecting human health (nor was any other agency), and the public was being marginalized from discussion about safety and regulation, while consumer autonomy was usurped by the absence of labeling. The GMO backlash, and its consequences in terms of slowing innovation, economic costs, and allegedly, human suffering,[14] would not have been as widespread had an adequate and transparent regulatory strategy been in place, one that was seen as ensuring the public interest above all else.

Those promoting the future of nanotechnology should be keen to avoid a GMO-like scenario by identifying the requisite regulatory capacity (including expertise, legal authority, resources, and frameworks) across agencies at both the state and federal level. Public education, outreach, and research on the environmental, health, social, and ethical implications of nanotechnology will not be enough to minimize public opposition.[15]

16.5 Why This All Matters

In short, it is vitally important to those industries and innovators concerned about the future of nanotechnology to pay attention to issues of government capacity and societal impacts. Three major reasons for this stand out.

16.5.1 Promoting Innovation and Expediting Commercialization

Ensuring sufficient governmental capacity is crucial to promoting innovation and expediting commercial production. As noted earlier, scientists, investors, and firms need to be confident that the Patent Office has adequate capacity so that patents will not be backlogged or awarded wrongly. Also, many technology applications, particularly (but not exclusively) in the field of medicine, require FDA regulatory approval prior to entering the marketplace. It is not difficult to imagine a scenario in which a nanoscale-based product, one representing a substantial investment in time and resources, is either forced to make expensive modifications or rejected altogether because of unforeseen changes in the regulatory landscape.[16]

16.5.2 Protecting the Public Interest

On November 17, 2005, David Rajeski of the Wilson Center's Foresight and Governance Project testified before the House Science Committee on concerns about the environmental and safety impacts of nanotechnology. The American public will want to believe that their government will have the capacity to protect them, Rajeski argued, adding, "We need a systemic analysis across agency statutes and programs, across agencies, and across the international landscape, which looks at regulations, voluntary programs, information-based strategies and state and local ordinances and asks the question: 'Will these measures work not just today but in 5 or 10 years?'"[17]

Whatever their broader views about the "proper" role of government, citizens generally expect it to protect them from the potentially harmful effects of technology and its applications. Moreover, citizens expect that government will be open and responsive to their concerns and wants. When regulatory capacity is not in place *as technologies emerge* the public interest can be compromised, with consequent impacts on public faith. The case of toxics is paradigmatic of this. The U.S., at the local, state, and federal levels, continues to address the legacy of unregulated or inadequately regulated release of toxics into the environment beginning with the post-WWII chemical revolution. This legacy involves negative human and environmental health effects, environmental injustice, industry liabilities, and government expenditures for cleanup and remediation. Moreover, the current approaches to toxics regulation and strategies for promoting accountability are largely patchwork and reactionary. They are the product of attempts to respond to environmental degradation, human health risks, and injustices after they were already realized. They are intended to remediate, mitigate, and make restitution for damages done to the public interest, while making future incursions against the public interest less likely.

The lesson for nanotechnology is that governmental agencies must be anticipatory and proactive if they are to protect the public interest from possible risks of emerging technologies. They must attempt to identify the health, safety, and environmental risks and social implications of emerging technologies before they are realized; provide adequate public communication about them to all sectors of society; encourage broad public participation in determining how to avoid, mitigate, or otherwise address them; encourage that the benefits and burdens associated with the technologies are distributed fairly; and prepare their institutions for responding to unanticipated challenges should they arise. Several of these goals are articulated in the NNI strategic plan and five-year assessment. The great hope for nanotechnology, as articulated in the NNI, is that it will promote the welfare of U.S. citizens in a just and sustainable way. Governmental capacity (state, federal, and local) to protect human and environmental health and to encourage participatory democracy and distributive justice is crucial to realizing this vision.[18]

16.5.3 Promoting Public Confidence

Systematic failure by government to demonstrate adequate capacity to respond to public concerns and protect the public with respect to emerging technologies (for reasons of resources, capability, or commitment) eventually undermines public confidence in government.[19] Such a lack of confidence in government can have spillover that results in opposition to those technologies, which, in turn, hampers technological and economic development. While a latent faith in the adequacy in the regulatory system may not assure total public acceptance of novel technologies, its absence will most certainly throw up another obstacle to timely and effective commercialization.

In sum, those who care about the future of nanotechnology, and the path to commercialization in particular, should also care about the capacity of

government to do its job, and no less to the satisfaction of the attentive public. Abstract and often arid ideological debates over the proper "size" of government miss the central point: size will not matter, but competence and transparency most assuredly will.

16.6 Other Sources

Antón, P.S., Silberglitt, R., and Scheider, J., *The Global Tecnology Revolution: Bio/Nano/Materials Trends and Their Synergies with Information Technology by 2015*, RAND, Santa Monica, CA, 2001.

Atkins, P., The future of matter, in *The Next Fifty Years: Science in the First Half of the 21st Century,* Brockman, J., Ed., Vintage 2002, pp. 194–205.

Atkinson, W.I., *Nanocosm: Nanotechnology and the Big Changes Coming from the Inconceivably Small,* American Management Association, 2003.

Cobb, M.D. and Macoubrie, J., *Public Perceptions about Nanotechnology: Risks, Benefits and Trust,* Unpublished paper, 2004.

Colvin, V.L., Testimony before the Committee on Science, U.S. House of Representatives, Nanotechnology Research and Development Act of 2003, 108th Congress, 1st session (9 April 2003).

Eisner, M., *Regulatory Politics in Transition*, 2nd ed., Johns Hopkins University Press, Syracuse, NY, 2000.

ETC Group, *The Big Down: Atomtech: Technologies Converging at the Nanoscale*, 2003, retrieved March 8, 2005, from http://www.etcgroup.org/documents/TheBigDown.pdf.

Gorman, M.E., Groves, I.F., and Catalano, R.K., Societal dimensions of nanotechnology, *Tech. Soc.*, 23, 55–62, 2004.

Joy, B. Why the future doesn't need us, *Wired Magazine,* April 2000, retrieved March 8, 2005, from http://www.wired.com/wired/archive/8.04/joy.html.

Mehta, M.D., From biotechnology to nanotechnology: what can we learn from earlier technologies, *Bull. Sci. Tech. Soc.*, 24, 34–39, 2004.

Roco, M.C., Broader societal issues of nanotechnology, *J. Nanopart. Res.*, 5, 181–189, 2003.

Sanchez, E.M., The expert's role in nanoscience and technology, in *Discovering the Nanoscale,* Baird, D., Nordmann, A., and Schummer, J., Eds., IOS Press, 2004, pp. 257–266.

Service, R., Nanotech forum aims to head off replay of past blunders, *Science*, 306, 955, 2004.

Stuart, C., Our annual ranking of small tech: only one first place but many winners, *Small Times,* 14 March 2005, http://www.smalltimes.com/document_display.c fm?document_id=8922.

Sweeney, A.E., Seal, S., and Vaidyanathan, P., The promises and perils of nanoscience and nanotechnology: exploring emerging social and ethical issues, *Bull. Sci. Tech. Soc.*, 23, 236–245, 2003.

U.S. Executive Office of the President, Office of Science and Technology Policy, National Science and Technology Council, Committee on Technology, Subcommittee on Nanoscale Science, Engineering, and Technology, *The National Nanotechnology Initiative: Strategic Plan*, National Nanotechnology Coordination Office, Arlington, VA, 2004.

Wilsdon, J., The politics of small things: nanotechnology, risk and uncertainty, *Tech. Soc.*, 23, 16–21, 2004.

References

1. U.S. Executive Office of the President, Office of Science and Technology Policy, National Science and Technology Council, Committee on Technology, Interagency Working Group on Nanoscience, Engineering, and Technology, *The National Nanotechnology Initiative: Leading to the Next Industrial Revolution,* OSTP, Washington, D.C., 2003.
2. Kurzweil, R., *The Singularity Is Near: When Humans Transcend Biology,* Viking, New York 2005, pp. 412–424.
3. Wardak, A., *Nanotechnology and Regulation: A Case Study Using the Toxic Substances Control Act*, Foresight and Governance Project, Woodrow Wilson International Center for Scholars, 2, 2003.
4. Statement of James E. Rogan, Under Secretary of Commerce for Intellectual Property and Director of the United States Patent and Trademark Office, before the Subcommittee on Courts, the Internet and Intellectual Property, Committee on the Judiciary, U.S. House of Representatives, 107th Congress, 1st Session, April 3, 2003.
5. Raydos, C., Nanotechnology: the size of things to come, *FDA Consumer Magazine,* 39, 6, 2005; http://www.fda.gov/fdac/features/2005/605_nanotechnology.html._
6. Reynolds, G.H., Nanotechnology and regulatory policy: three futures, *Harv. J. Law Tech., 17,* 180–210, 2003.
7. National Nanotechnology Initiative, *The Initiative and Its Implementation Plan,* National Science and Technology Council, Committee on Technology, Subcommittee on Nanoscale Science, Engineering, and Technology, July 2000, pp. 78–81.
8. Bosso, C.J., *Pesticides and Politics: The Life Cycle of a Public Issue*, University of Pittsburgh Press, Pittsburgh, PA, 1987.
9. Coglianese, C. and Nash, J., *Regulating from the Inside: Can Environmental Management Systems Achieve Policy Goals?* RFF Press, Washington, D.C. 2001, p. ix.
10. Rosenbaum, W., Improving environmental regulation at the EPA: the challenge of balancing politics, policy, and science, in, Environmental Policy: New *Directions for the 21st Century,* Vig, N.J. and Kraft, M.E., CQ Press, Washington, DC, 2006, p. 173.
11. Rabe, B.G., *Statehouse and Greenhouse: The Emerging Politics of American Climate Change Policy,* Brookings, Washington, D.C. 2004, p. 27.
12. See, for example, Bennett, M., Does existing law fail to address nanotechnoscience? *IEEE Tech, Soc. Mag.,* 23, 27–32, 2004.
13. Sandler, R. and Kay, W.D., The GMO-nanotech (dis)analogy? *Bull. Sci. Tech. Soc.* 26, No. 1, 57–6 2006; Moore, J., lessons from the gmo and frankenfood debate: building public trust in new technology and science, Presented at the Woodrow Wilson International Center for Scholars (2002, November 19); retrieved March 8, 2005 from http://www.environmentalfutures.org/nanotech.htm.
14. Kurzweil, *Singularity Is Near,* 414–415.
15. Kulinowski, K.M., Nanotechnology: from 'Wow' to 'Yuck'? *Bull. Sci. Tech. Soc.,* 24, 13–20, 2004.
16. Mnyusiwalla, A., Daar, A.S., and Singer P.A., "Mind the gap": science and ethics in nanotechnology, *Nanotechnology,* 14, R9-R13, at R9, R12, 2003.
17. Rejeski, D., Testimony before the Committee on Science, U. S. House of Representatives, *The Environmental and Safety Impacts of Nanotechnology,* 109th Congress, 1st session, November 17, 2005.
18. Sandler, R. and Kay, W.D., The national nanotechnology initiative and the social good, *J. Law, Med. Ethics* (forthcoming, 2006).
19. Beierle, T.C. and Cayford, J., *Democracy in Practice: Public Participation in Environmental Decisions*. RFF Press, Washington, D.C., 2002.

Chapter 17

R&D Activities for Nanoscale Manufacturing Processes and Enabling Equipment in Korea

Chang-Soo Han, Jun-Hyuk Choi, Hak-Joo Lee, Jae-Jong Lee, Doo-Sun Choi, Won-Seok Chang, Jun-Ho Jeong, Eung-Sug Lee, Kyung-Hyun Whang, and Sang-Rok Lee

Contents

17.1 Introduction 389
17.2 R&D Goals of CNMM 390
17.3 R&D Activities 391
 17.3.1 Research Results of First Phase 392
  17.3.1.1 Nanoimprinting Process and Equipment 392
  17.3.1.2 Nanoinjection Molding 393
  17.3.1.3 Nanomaterials Assembly 394
  17.3.1.3 Nanoprobe Process 394
  17.3.1.4 Nanometrology and Analysis 394
17.4 Conclusion 396
Acknowledgments 396
References 396

17.1 Introduction

The Center for Nanoscale Mechatronics and Manufacturing (CNMM) was established in July 2002 under the 21st Century Frontier R&D Program organized by the Ministry of Science and Technology in South Korea. Nanotechnology,

an emerging area with a vision of revolutionizing the current technology paradigm and creating substantial values for human life in the near future, is in pursuit of developing technological breakthroughs and trends.[1–3] Considering such widely recognized potential significances, almost every advanced country supports R&D activities in nanotechnology through governmental policies and private sectors.[4,5] Nanotechnology is now in the focus of attention in public as well as in the research community.

In 2001, Korea recognized the strategic importance of encouraging government-led nanotechnology and announced general plans for nanotechnology promotion. Since then, several R&D subprograms (or projects) have been launched in the field of nanotechnology. The development of nanomanufacturing and enabling tools, in particular, was emphasized as an infrastructure technology for nanotechnology, which motivated the establishment of CNMM.

Nanoscale mechatronics is an emerging field of fusion technology implementing nanoscience with the traditional approach of mechatronics combined with mechanical and electronic engineering. It essentially covers a wide range of disciplines. In nanoscale mechatronics, CNMM is focused on developing high-productive nanomanufacturing technology and enabling equipment.

17.2 R&D Goals of CNMM

The ultimate goal of CNMM is to develop manufacturing technology with the capability of producing nanocomponents that are smarter, cheaper, and faster, with a minimum feature size in the range of 100 to 10 nm, and to secure the elementary technologies for the enabling tooling. Pattern size in the range of 100 to 10 nm is hard to realize by top-down manufacturing, which has been traditionally in use by the semiconductor industries, and is also difficult to attain through bottom-up methods.[6] Hence, the development of low-cost and highly productive nanomanufacturing and enabling tools is in great demand, particularly in the same scale range, and would make a huge contribution to commercializing of NT if successfully developed.

Because CNMM is in pursuit of commercially valuable technologies rather than academic or scientific interests in nanoscale engineering, it is expected that R&D progress at CNMM would have an immediate impact on related industries. The detailed goals are as follows:

- Fabrication of 2-D/3-D shapes composed of 100 to 10 nm-level dots, lines, and blocks.
- Fully 3-D shape fabrication through the upgraded from existing processes.
- Development of application technologies (Nano MOSFET, Organic Electronics, RF devices, Nano Bio Sensors, etc.).
- Development of 10-nm-level nanopatterning equipment.
- Development of nanoprocess control/analysis/measurement/metrology.

17.3 R&D Activities

As semiconductor industries have grown up, they gradually encountered several technical barriers as follows:

1. Absence of reliable and low-cost nanomanufacturing technologies.
2. Exponentially increasing infrastructure cost.
3. Lack of physical understanding of nanodevice operations.

Optical lithography and its resolution-enhanced technology have continued to be advanced and are still viable in the production line for semiconductors, displays, optical devices, and various microsystems. But the astonishingly increasing cost for fabrication becomes unaffordable, so many current manufacturers get off track except for a few gigantic players in the world. This has spurred the development of next generation lithography (NGL), which promises low-cost, smarter, and mass producible nanoscale patterns. Among those are e-beam projection lithography, maskless lithography, EUV, and immersion lithography by using conventional photons, and nanoimprinting, soft lithography, and probe lithography based on physical contacts. In addition, Si-based technology has intrinsic limitations when applied to nanostructuring of sub-50-nm linewidths, which creates new demands for disruptive technology. Therefore, nanomaterials such as carbon nanotubes and nanowires have been drawing worldwide attention as alternatives. However, it would be quite difficult by either presently known top-down or bottom-up nanomanufacturing approaches to assemble large quantities of such nanomaterials on a large-area substrate with fairly high productivity. Therefore, nanoassembly technology enabling high throughput and high productivity is demanded.

CNMM seeks a nanomanufacturing strategy using nonconventional means. In the case that neither the top-down nor bottom-up method is acceptable, considering hybrid technology coupling two methods would be a breakthrough. With nanomanufacturing at the focus of research, R&D structure in CNMM is divided into three sub-categories: nanomanufacturing, nanofabrication equipment, and nanometrology and analysis as shown in Figure 17.1.

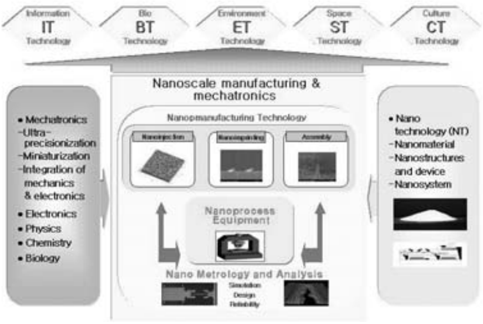

Figure 17.1 R&D structures of CNMM.

Table 17.1 Progress Goals of CNMM

Phase 1	**Fundamental studies and infrastructure construction**
	100-nm-level nanopatterning technology
(2002–2005)	20-nm-level 32 × 32 parallel nanoprobe process technology
	100-nm-level nanofabrication equipment
	100-nm-level nanostructure measurement and analysis technology
Phase 2	**Application technologies**
	50-nm-level nanopatterning technology
(2005–2008)	Sub-50-nm-level nanomaterials assembly process technology
	50-nm-level nanopatterning equipment technology
	50-nm-level nanometrology, analysis, and simulation technology
Phase 3	**Technology commercialization**
	10-nm-level nanopatterning technology
(2008–2012)	Sub-10-nm-level nanomaterials assembly process technology
	10-nm-level nanopatterning equipment technology
	Commercialization of nanometrology and measurement, design of nanoproducts

The technology field of nanometrology, measurement, and analysis focuses on providing the infrastructure technology related to R&D for nanomanufacturing and equipment.

17.3.1 Research Results of First Phase

As shown in Table 17.1, infrastructure establishment and fundamental research are performed mainly in the first phase. Eleven major projects have been in development and are categorized into four subfields in the first phase: nanopatterning, nanoprobe-applied process, nanoequipment, and nanoprocess elementary technology. The details for each individual nanoprocess applied are summarized in Table 17.2. In addition, explorative projects were pursued for the purpose of exploring and verifying creative ideas.

The major representative accomplishments during the first phase (2003–2005) are described below.

17.3.1.1 Nanoimprinting Process and Equipment

Nanoimprint technology, one of the next generation patterning technologies, has been reported to pattern down to 10-nm linewidth in laboratory work. Several problems still exist to shift nanoimprint technology from the laboratory level to the production line for semiconductors and circuits in particular. Among these are fair reliability, productivity, throughput, and large-area process capability. CNMM has fabricated 70-nm-level linewidth on a 4-in wafer using UV nanoimprinting equipment we developed as shown in Figure 17.2

Table 17.2 Explicit Technology List in Thrust for the First Phase

Research field	Core technology
Nanopatterning process	UV large-area imprinting Thermal imprinting for optical devices Sub-μm injection molding Patterning for blood analysis
Nanoprobe process	Scanning probe lithography 32 × 32 multiple scanning probes Assembly of CNT and cell probing
Nanoequipment	Nanoimprinting equipment 6-axis nanomanipulator
Measurement and analysis	Molecular-level analysis Multi-scale Nanoindentation Mechanical tester by MEMS

Meanwhile, CNMM invented the revolutionary design scheme of a stamp, called the element-wise patterned stamp (EPS), for large-area (5 in × 5 in) imprinting on an 8-in wafer by step and repeat (Figure 17.3). Compared with the generally used 1 in × 1 in stamp, productivity improved approximately ten-fold. Technical barriers such as ineffective infiltration into relief when large-area imprinting can be overcome because deep channels in EPS allow excessive resin to flow out of the stamp easily. Hence, uniformly imprinted patterns across the substrate were obtained.

17.3.1.2 Nanoinjection Molding

Nanoinjection molding technology with a metallic nanostamper has been regarded as a suitable mass-production process for replicating nanopatterns because of its low cost and short production cycle time. However, there are two important issues in nanoinjection molding technology. First, based on the fact that the surface quality of the polymer nanoreplica is governed by the interfacial phenomenon such as adhesion between the nanomold and the replicated polymeric patterns, self-assembled monolayer (SAM) was applied to the nanoreplication process as an anti-adhesion layer. Second, because the solidified layer

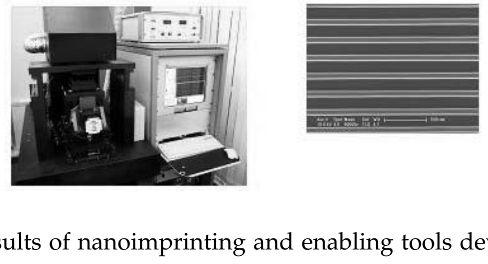

Figure 17.2 The results of nanoimprinting and enabling tools developed.

generated during the polymer filling deteriorates transcribability of nanopatterns by preventing the polymer melt from filling the nanocavities, process conditions such as mold temperature, melt pressure, and injection rate were optimized to injection mold nanopatterned warpage-free substrate. Figure 17.4 shows a nanopattern nickel stamper and injection-molded nanopattern using the nickel stamper. The injection-molded pattern was a circular pillar of which the diameter was about 100 nm and the height was about 100 nm. Finally, nanoinjection molding was applied to the fabrication of ultra-high-density data storage media such as patterned media and blu-ray disc. Figure 17.5 shows a blu-ray disc with 25 GB capacity developed by the same.

17.3.1.3 Nanomaterials Assembly

The assembly technology of carbon nanotubes, a burgeoning active research area in the field of nanotechnology, has been a recent focus of research. We developed the attachment methodology of nanotubes to an AFM probe with the key advantages of lower cost and higher speed than existing methods, enabling mass production of nanocomponents. We fabricated both SWNT and MWNT tips using dielectrophoresis (Figure 17.6). In addition, large-area CNT assembly using Langmuir-Blodgett monolayer has been accomplished.

17.3.1.3 Nanoprobe Process

For the realization of high-speed nanolithography using nanoprobes, CNMM fabricated a 32×32 probe array with sensors and actuators in it (Figure 17.7). In parallel, comprehensive research for dip-pen (DPN), AFM lithography, and NSOM have been performed during the first phase. As the comprehensive research proceeds, it is expected the field of scanning probe lithography would be established as one of useful lithography, even in the limited areas, in the era of nanotechnology (Figure 17.7).

17.3.1.4 Nanometrology and Analysis

The precise characterization of mechanical properties of nanoscale structures needs to be performed simultaneously with the manufacturing process for elements under 100 nm. If the repeatability of patterned structures is not ensured, the nanodevices developed in the laboratory would not be accepted for commercialization. Among the novel devices for measuring mechanical properties of nanostructures, we developed a force-calibrated AFM system for indentation and strip bending tests (Figure 17.8). Furthermore, computational analysis techniques for nanostructures are aiming to solve exciting phenomena occurring in smaller than 10-nm dimension, so molecular-based simulation will be also employed.

In addition, what have been developed are nanomanipulators capable of atomic-level manipulation in six axes, cleaning technology using plasma, and single-cell probe technology by CNT-W probe tip, some of which are being developed for commercialization.

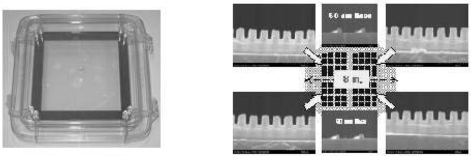

Figure 17.3 5 in × 5 in element-wise patterned stamp (EPS) (left); the imprinted patterns on 8-in wafer by four step and repeats (right).

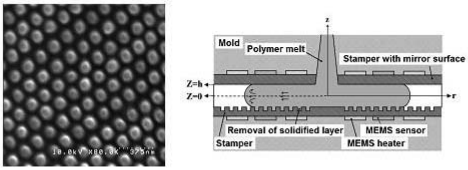

Figure 17.4 Nanopattern nickel stamper (left) and injection-molded nanopatterns with 100 nm diameter and 100 nm height (right).

Figure 17.5 Blu-ray disc replicated by nanoinjection molding process (25 GB capacity).

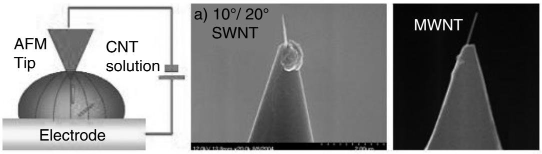

Figure 17.6 Assembly of CNT-AFM probes by dielectrophoresis.

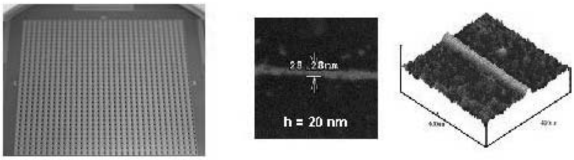

Figure 17.7 32 × 32 Probe array for lithography (left) and 20-nm-level linewidth obtained by DPN (middle and right).

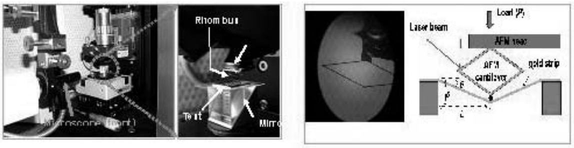

Figure 17.8 Force-calibrated AFM with rhombus-shaped cantilever for strip-bending test.

17.4 Conclusion

The field of nanomanufactuirng appeared around the year 2002 in Korea at the launching of CNMM and has drawn substantial attention so far. Just over four years have passed since then. During the period of CNMM's first phase, the significance for technology development of low-cost and mass-producible nanomanufacturing has been widely recognized. In accordance with increasing technology demands, a national strategy and R&D program have been launched in many countries.

Currently, CNMM shares close interest in the key technologies with other leading-edge research institutes, which get recognized CNMM technologies globally significant and challenging.

CNMM has created many R&D accomplishments so far, some of which have led to commercial and technological breakthroughs, for example, the 150-nm-level Blu-ray disk. We will be steadily progressing for six more years. It is expected that CNMM will contribute to the commercialization of nanotechnology products with affordable prices by providing viable nanomanufacturing tools, which revolutionize the existing microfabrication markets.

Acknowledgments

We thank the Ministry of Science and Technology in Korea as well as all participants of CNMM projects.

References

1. National Nanotechnology Development Plan (www.most.go.kr), Korea.
2. National Nanotechnology Initiative (www.nano.gov), USA.
3. Nanotechnology Researchers Network Center of Japan (http://www.nanonet.go.jp), Japan.
4. Klefenz, H., Nanobiotechnology: from molecules to systems, *Eng. Life Sci.*, 4, 211, 2004.
5. Roco, M.C., Nanoscale science and engineering: unifying and transforming tools, *AlChE J.*, 50, 890, 2004.
6. Compafio, R., Molenkamp, L., and Paul, D.J. *Technology Roadmap for Nanoelectronics*, 6, 1999.

Index

A

a-C, (*see* Amorphous carbon)
Accelerating voltage parameter, 301
a-C:H, (*see* Hydrogenated amorphous carbon)
Acoustic frequency, effects of, in selective particle removal, 269–274
Acoustic streaming, 253
  experimental procedures in, 265–278
  particle removal using, 261–263
  physics of, 254–260
  references on, 279–280
Actinomyosin protein motor, 47–50
Actuation, of micromechanical switches, 240–244
Adhesion
  in elastoplastic contacts, 233–235, 237–238
  nanoscale contact with, 222–230
  in partical removal, 258–259
  physical basis for, 219–223
Aerosol particle filtration, using electrospun nanofiber membranes, 360–362
AFM, (*see* Atomic force microscopy)
Air flow resistance, in electrospun nanofiber membranes, 358–360
Alignment, of nanostructures, 14–15, (*see also* Patterning)
  chemical patterning in, 138
  electrical field in, 133, 138
  Langmuir-Blodgett (L-B) technique in, 138
  microfluidic, 137–138
  self-assembled, 14–15, 42–50
  surface programmed, 42–50
  in swCNT fabrication, 42–47
Amorphous carbon (a-C), 285
  mechanical properties of, 287
Anodic aluminum oxide (AAO)
  in channel templates, 101–104
  in electrical contact synthesis, 131–133
  in molecular electronic junctions, 142
Antibody/antigen binding, 114
Antistiction layer(s), 183, 185–188
  characterization of, 198–210
    chemical, 203–205, 207–209
    film thickness in, 201–203
    nanoscale adhesion in, 205–207
    surface morphology, 205–207
    thermal, 207–209
    tribological, 207–209
    wettability in, 198–200
  fabrication of, 188–198
    liquid SAM (self assembly monolayer), 190–194
    method comparisons in, 190
    plasma polymerization, 196–197
    spin coating, 189–191
    vapor SAM (self assembly monolayer), 194–196
  need for, in nanoimprint lithographic process, 186–188
  references on, 210–215
APM, (*see* Atomic probe microscopy)
Arc discharge method, in carbon nanotube synthesis, 81–82
Aspect ratio
  and depth ratio of molded polymer, 342–343
  stiction and, 185
Assisted assembly fabrication, in CMOS microarrays, 114–116
Atomic force microscopic (AFM) lithography, 4–5, 39–41, 394
Atomic force microscopic probes, 394, 395
Atomic force microscopy (AFM)

in antistiction layer characterization, 205–207
force-calibrated, 394
in molded polymer surface characterization, 337
in molecular electronics, 141
in viscomechanical studies, 297–298
Attenuated total reflection Fourier transform infrared (ATR-FTIR) spectroscopy, 203–205
Awareness, public, 19
AZ photoresist, 167–169

B

Bilayers, in hydrogen silsesquioxane (HSQ) procedure, 167–172
Biochemical nanosensors, 135
Biologically-inspired assembly, 6–7
Biomotors, 47–50
Biotin/streptavidin binding, 114, 117
Blended fibers, (*see* Polymer blend fibers)
Block copolymers, 320–326
in nanoscale patterning, 12–13
Bottom-up approaches, in nanoscale manufacturing, 5–14, 34–36, 108–109
Bouncing, microswitch, 243, 244
Boundary layer thickness, acoustic, 255–256
Branched carbon nanotube synthesis, chemical vapor deposition in, 101–104
Brush scrubbing process, 253–254
Burst testing, of electrospun nanofiber membranes, 362–365

C

Carbon fibers (C fibers), 285
mechanical properties of, 287–289
Carbon materials, 281–287
diamond-like, 285–287
disordered and nanostructured, 283–287
fiber, 285
mechanical properties of, 287–289
nanotube, 283–285 (*see also* Carbon nanotubes)
patterning and processing of, 299–308
references on, 309–312
single crystal, 282–283
van der Waals interactions in, 287–292
viscomechanical analysis of specific, 292–299
viscomechanical behavior of, and van der Waals forces, 289–292
weakness and strength in, 281–287
Carbon nanofibers, mechanical properties of, 287–289
Carbon nanotubes (CNTs), 34, 56
arc discharge synthesis of, 81–82
chemical vapor deposition in controlled synthesis of, 79–106, 129 (*see also* Chemical vapor deposition)
dry transfer printing of, 155–159
interaction between, 284–285
laser ablation synthesis of, 82, 129
mechanical properties of, 287–289
single-wall
chemical vapor deposition in synthesis of, 58–59, 79–107 (*see also* Single-wall carbon nanotubes)
fabric manufacture from, 55–77
physical and electrical characteristics of, 59–60
prepared solutions of, 60–61
self-assembled alignment of, 42–47
structure of, 283–285
van der Waals interactions among, 288–289
viscomechanical analysis of, 296–299
Carbon needle, 300–303
Carbon supertips, 303–308
Center for Nanoscale Mechatronics and Manufacturing (CNMM), 389–396
goals of, 390, 392
references on, 396
research and development results of, 392–395
CFD, (*see* Computational fluid dynamic)
Challenges, in nanoscale manufacturing, 27
Characterization tools, 15–16, 394, (*see also specific process or parameter*)
Charge transport modeling, 327–329
Chemical vapor deposition (CVD), 58, 79–81, 129
of antistiction films, 194–197
in branched carbon nanotube synthesis, 101–104
in carbon nanotube synthesis, 83–84
in electrical contact synthesis, 128–131
growth mechanism of carbon nanotubes in, 99–101
in multi-wall carbon nanotube synthesis, 81–91 (*see also* Multi-wall carbon nanotubes)
references on, 105–106
in single-wall carbon nanotube synthesis, 58–59, 81–85, 95–101 (*see also* Single-wall carbon nanotubes)
substrate characterization in, 91–95
Chlorosilane based monolayer technology, 194–196

Cleaning process, (*see* Surface cleaning/preparation, or specific process)
CMOS microarray system(s), 107–126
  complete, for nanoscale fabrication, 113
  components of 400 test site system in, 111–112
  controller system of, 111–113
  fabrication strategies and goals in, 120–123
  multi-layered nanoscale fabrication using, 117–120
  references on, 123–126
  transport and addressing of structural components in, 114–116
  voltage and current control in, 110–111
CMOS processing, and qualification of single-wall carbon nanotube fabrics, 63–69
CMOS-compatible nonvolatile memory technology, 74–76
CNC machining, 335
CNMM, (*see* Center for Nanoscale Mechatronics and Manufacturing)
CNTs, (*see* Carbon nanotubes)
Coating uniformity, 63, 64
Co-extrusion, 315–316
Collaborative development, 21–23, 26
Combined approaches, in nanoscale manufacturing, 7–14
Commercialization, expediting, 385–386
Commercialization issue(s), in nanotechnology, 377–388, (*see also* Nanotechnology)
  governmental capacity, 377–384
  intellectual property, 367–376, 379–380
  paying attention to, 385–387
  public uncertainty, 384–387
  references on, 387–388
  regulatory frameworks and institutions, 380–384
Commercialization timelines, 26–27
Complementary metal oxide semiconductors (CMOS), (*see CMOS entries*)
Computational fluid dynamic (CFD), 270–274, 276, 278
Conductive grid, electrospun patterns on, 354–355
Conductive polymers, directed self-assembly of, 13–14
Constrictive resistance, modeling, 241–244
Contact resistance theories, 240–244
Contaminants
  in contact resistivity, 243, 244
  micro and nanoscale, 16
  removal of, 251–280 (*see also* Surface cleaning/preparation)
Contamination resist technology, 300
Controlled phase separation, in polymer blend, 320–326
Copyrights, 368
Core-sheath fibers, 321–322, 326
Corporate attitudes, regarding nanoscale manufacturing, 24–25
Coupled contact problems, 238–240
Creep, studies of, 291–292, 294–296
Cross-bar nanoelectrodes, 142–143
Cryogenic aerosol spray cleaning process, 253–254
CVD, (*see* Chemical vapor deposition)
Cyclic polyolefin (COP), properties of, 336
Cytop, 191
  structure of, 192

D

DC electrophoretic transport, in CMOS microarrays, 114–116
DDMS, (*see* Dichlorodimethylsilane)
Decal transfer lithography, 153–155
Defects, micro and nanoscale, 15–16
  in contact resistivity, 243, 244
  removal of, 251–280 (*see also* Surface cleaning/preparation)
  selective removal of, 265–279
Developments, accelerating, 20–23
Diamond, 282–283
  mechanical properties of, 287–289
Diamond-like carbon, 285–287
  bonding and mechanical properties of, 286–287
  covalent bonding hybrids in, 286–287
Dichlorodimethylsilane (DDMS), in vapor phase deposition of SAMs, 195
Dielectrophoresis, 394, 395
Dielectrophoretic manipulation, in CMOS microarrays, 114–116
Digital versatile disks (DVDs), 335
Dip-pen nanolithography (DPN), 7–9, 38–41, 394, 395
Directed assembly process, large-scale, 6
Directed self-assembly, 9–12, (*see also* Self-assembly)
Disc target, rotating, 332–334
DLVO (Derjaguin, Landau, Verwey, Oberbeck) potential, 260
DMT (Derjaguin, Muller, Toporov) elastic adhesion model, 225–230, 259
DNA hybridization, on microarrays, 109–110

DNA molecules, directed self-assembly of, 117–120
DPN, (*see* Dip-pen nanolithography)
Drag force, in partical removal, 256–258
Dry transfer printing (DTP) methods, 155–159
DTS, (*see* Undecyltrichlorosilane)
DVD tooling, and polymer interaction, 335–341
Dynamic mechanical analysis (DMA), 291

E

e-beam lithography, (*see* Electron beam lithography)
EBID, (*see* Electron beam induced deposition)
EBL, (*see* Electron beam lithography)
Edge bead removal process, for single-wall carbon nanotube fabrics, 62–63, 65–68
Elastic and plastic behavior, transition between, 231–233
Elastic layers, 230–231
Elastic-plastic simulations, finite element, 235–238
Elastomeric thermoplastic polyurethanes, in electrospun fiber patterning, 354–358
Elastoplastic contacts, 231–238
  adhesion in, 233–235
Electric field(s), 9
  transverse, effects of, 329–332
Electrical contact(s), 127–146, (*see also* Micromechanical switches)
  direct synthesis of, 128–136
    chemical vapor deposition methods in, 128–131
    electrochemical methods in, 131–136
  molecular, 140–143
  nanowire, 128–140
  post synthesis fabrication of, 136–140
  properties and requirements of, 143
  quantum dot, 143
  references on, 144–146
Electrical double layer force, in particle removal, 259–260
Electrochemical methods, in electrical contact synthesis, 131–136
Electroformed nickel tooling, and polymer melt interaction, 335–346
Electromechanical probe, 9
Electron beam induced deposition (EBID), hydrogenated amorphous carbon films and structures using, 300–303
Electron beam lithography (EBL), 4–5, 42
  in molecular microswitch fabrication, 70–73, 142
  in post synthetic nanowire fabrication, 136–137
Electronic hybridization, 110
Electrospinning process, 320–326, 351–352
Electrospun nanofiber membranes, 354–358
  aerosol particle filtration using, 360–362
  applications of, 355–357
  pore size and air flow resistance in, 358–360
  references on, 365–366
  strength of, 362–365
Electrospun nanofiber patterning, 351–358
  controlling, 354
Electrospun nanofibers, 320–326
  charge transport modeling of, 327–329
  composition ratio effect on, 323–324
  controlled deposition and orientation of, 326–334
  molecular weight of components of, effects of, 324–325
  polybutadiene/polycarbonate, 322–323
  polymer type in, 326
  target geometry and effect on, 332–334
  transverse field effect on fiber path of, 329–332
  viscocity of components of, 323–324, 325
Electrostatically addressable nanotemplates, 11
Element-wise patterned stamp (EPS), 393, 395
Ellipsometry, 201–203
Environmental Protection Agency (EPA), U.S., regulatory capacity of, 381, 383
EPS, (*see* Element-wise patterned stamp)
ESCA, (*see* X-ray photoelectron spectroscopy)
Estane, 354, (*see also* Electrospun nanofiber membranes)
Etching, carbon materials, 299–308
EUV lithography, 4–5

F

FCOS (flip-chip on substrate), 112
FDTS, (*see* Perfluorodecyltrichlorosilane)
Federal government, (*see* Regulatory frameworks, and institutions)
FIB, (*see* Focused ion beam (FIB) technology)
Fiber architectures, polymer, 321–322
  types of, 322–323
Field emission scanning electron microscopy (FESEM), in edge bead removal checks, 65–68
Filtered cathodic vacuum arc (FCVA), 285
Finite element elastic-plastic simulations, 235–238

FLC, (*see* Fullerine-like carbon)
Flow instabilities, in nanolayered extruded films, 315–316
  current research on, 316–320
Fluorinated monoalkyl phosphates, 199
Fluoroalkylsilane, 199
Fluorocarbon wax, 199
Focused ion beam (FIB) technology, 4–5, 300
  carbon structure formation using, 303–308
Food and Drug Administration (FDA), U.S., regulatory capacity of, 381
FOTS, (*see* Perfluorocyltrichlorosilane)
Fourier transform infrared (FTIR) spectroscopy, 290, 293
Freedom-to-operate issues, 374–375
Freeze sublimation drying, 185
Fullerene nanowires, 8–9
Fullerine-like carbon (FLC), 285
  mechanical properties of, 287–289

G

Gallium arsenide tooling, and polymer melt interaction, 335–346
Gold electrode pattern transfer, 178–179
Governmental role/capacity, in nanoscale manufacturing, 21–23, 27, 377–379
Graphite, 282–283
  mechanical properties of, 287–289
Graphitization, 299
Greenwood and Williamson (GW) model, of multi-asperity contact, 239–240
Greenwood-Johnson model, 229–230
Growth mechanisms, for carbon nanotubes, 84–85

H

Hamaker constant, 222, 258–259
Hardness (H), 232
  scale dependent, 233
Hardness measurements
  of EBID carbon films, 301–302
  of FIB carbon films, 305–307
Hertz contact, and equations for spherical bodies, 218–219
HHF (Hogg, Healy, Fuerstenau) model, of electrical double layer force, 259–260
Hierarchically branched nanotube synthesis, 101–104
High resolution molded rubber stamp(s)
  in dry transfer printing methods, 155–159
  making of, 149–150
  printing polymers with, 153–155
  references on, 159–160
  two and three dimensional nanofabrication with, 151–153
  two and three-dimensional metal structure fabrication with, 153–155
High-precision (microwire) electrodischarge machining, 335
Hill's expanding cavity model, 232
Hydrogen silsesquioxane (HSQ) procedure, 162–164
  bilayer method, with AZ photoresist, 167–169
  HSQ/PVA bilayer structure in, 169–172
  imprint depth and resin thickness, 166–167
  line width dependencies, 164–166
  postbaking temperature dependence of patterns, 166
  prebaking temperature, 164–166
  water lift-off in, 169–172
Hydrogenated amorphous carbon (a-C:H), 285
  films and structures of
    using EBID, 300–303
    using focused ion beams (FIB), 303–308
  mechanical properties of, 287
  viscomechanical analysis of, 292–296
Hydrogenated tetrahedral amorphous carbon (t-aC:H), 285

I

in situ electric/magnetic fields, for nanostructure alignment, 133
Industry survey, of nanoscale manufacturing, 16–20
  geographical distribution of respondents in, 18
Infrastructure, for nanoscale manufacturing, 25
Injection micromolding machine, commercial, 336
Injection molding technology, 393–394, 395
Innovation, promoting, 385–386
Intellectual property, 368–372, 379–380
Inventions, (*see* Patent(s))
Ion beam assisted deposition (IBAD), 4–5
Ion beam lithography, 42
Isothermal mold filling, 335, 339–341

J

JKR (Johnson, Kendall, Roberts) elastic adhesion model, 224–230, 259

K

Knowledge base, for nanoscale manufacturing, 28

L

Langmuir-Blodgett (L-B) technique, of nanostructure alignment, 138, 394
Laser ablation method
of carbon nanotube synthesis, 82
for molded polymer structures, 335
Lateral force microscopy (LFM), in antistiction layer characterization, 205–207
Layer multiplying element (LME), in polymer extrusion, 317, 318–319
Layer-by-layer (LBL) self-assembly, 108–109
CMOS controller components in, 109–113
fabrication strategies and goals in, 120–123
of nanoscale structures, 117–120
process of, in CMOS microarray systems, 117–120
references on, 123–126
transport and addressing of structural components in, 114–116
Lennard-Jones potential, 221, 227–228, 289–290
LIGA (Lithographie Galvanoformung Abformung), 335
Low vacuum scanning electron microscopy (LVSEM) system, 300–303

M

Management changes, 24–25
Marketing timelines, 26–27
Maugis and Pollock model, of elastoplastic contact, 233–235, 259
Maugis model, 228–230
Maugis-Dugdale model, 229
Maxwell spreading resistance, 241
Mechanical break junction (MBJ), 140–141
Megasonic cleaning process, 253
particle removal using, 261–263
physics of, 254–260
Memory technology, nonvolatile, 74–76
MEMS-based devices, (*see* Microelectromechanical systems)
Metal organic chemical vapor deposition (MOCVD), 143
Metal structure fabrication, with high resolution molded rubber stamps, 153–155
Microchannels, multi-layered fabrication of, 121–122
Microcontact printing, 42, 148
in nanowire fabrication, 139
Microelectromechanical systems (MEMS), 15–16, 184, (*see also* Micromechanical switches; Molecular microswitches)
Microfluidic alignment, of post synthetic nanowires, 137–138
Micromechanical switches, 127–146, 240–250
actuation of, 240–244
direct synthesis of, 128–136
chemical vapor deposition methods in, 128–131
electrochemical methods in, 131–136
molecular, 140–143
nanowire, 128–140
physical forces affecting, 217–240
post synthesis fabrication of, 136–140
properties and requirements of, 143
quantum dot, 143
references on, 144–146, 245–250
reliability of, 240–250
Micromolding, 334–335
Molded polymer nanostructures
aspect ratio in tooling for, 342–343
melt temperature for, 337–339
metal coating on tooling for, 344–346
mold temperature for, 339–341
packing pressure for, 341
polymer interfacial effects and, 334–335
references on, 346–350
surface depth ratio and tooling aspect ratio for, 342–343
surface roughness and molding cycles for, 343–344
tooling for, 335–337
Molded rubber stamp(s), high resolution
in dry transfer printing methods, 155–159
making of, 149–150
printing polymers with, 153–155
references on, 159–160
two and three-dimensional metal structure fabrication with, 153–155
two and three-dimensional nanofabrication with, 151–153
Molecular beam epitaxy (MBE), 143
Molecular electronics, 140–143
Molecular manufacturing, 6–7
Molecular microswitches (MMS), 56, 57
fabrication of, 70–72, 140–143

in nanotube random access memory creation, 74–76
operation of, 72–73
Molecular patterning, 37–42
Molecular recognition mechanism, 36
MP model, (*see* Maugis and Pollock model)
Multi-asperity contact models, 238–240
Multi-directional carbon nanotube architectures, 89
Multi-layer extrusion, polymer internal interfacial behavior, 314–320
Multi-layered carbon nanotube architectures, 89–90
Multi-layered nanoscale fabrication, using CMOS microarray system, 117–123
Multi-wall carbon nanotubes (MWNT)
arc discharge method synthesis of, 81–82
chemical vapor deposition synthesis of, 83–85
experimental set-up for growth of, 86–88
highly organized design of, 85–88
silicon dioxide pattern changes in creating, 88–89
substrate fabrication for, 85–86
substrate morphology and characterization for, 85, 91–95
three dimensional architecture creation with, 89–91
vapor phase catalyst delivery in building, 85
viscomechanical studies of array of, 296–299

N

Nanochannel templates, controlled, 101–104
Nanocontact printing (NCP)
dry transfer, 155–159
at room temperature, 161–162, 172–179
Nanocontact switch reliability, 217–250
Nanoelements, 9–12
Nanofiber spray coatings, 351–358
Nanofibers, (*see* Carbon nanofibers; Electrospun nanofibers; Nanofiber spray coatings)
Nanofluidic channel, 131
Nanoimprint lithography (NIL), 4–5, 183–185
classification of, by applied temperature, 184
and conventional lithography, comparison, 186
PDMS rubber stamps in, 148–160
process of, and need for antistiction layer, 186–187
at room temperature, 161–172
stiction in, and procedures for reduction, 185–186 (*see also* Antistiction layer(s))
Nanoimprinting process, and development, CNMM, 392–393
Nanolayer melts, (*see* Polymer melts)
Nanoparticles, 12, 34
alignment of, in self-assembly, 42
Nanopore formation, in substrate plane, 132–133
Nanoproduct applications, devel opment of, 18
Nanoreactors, 12
Nanorods, 12
Nanoscale adhesion, in antistiction layer, 205–207
Nanoscale manufacturing, 1–16, 183–185
antistiction layers for nanoimprint lithography in, 183–215
barriers in, 19–20, 391
bottom-up approaches in, 5–7
carbon material improvements for, 281–312
CMOS microarray systems in, 107–126
combined approaches in, 7–14
corporate and public awareness of, 19
defect control and reliability in, 15–16
defect removal in, 251–280
electrical contact fabrication in, 127–146
electrical contact reliability in, 217–250
of electrospun nanofiber membranes, 351–366
geographical profile of, in U.S., 18, 23
with high-resolution rubber stamps, 147–160
industry survey of, 16–20
national priorities in, 20–23
polymeric materials in, 313–350
problems and challenges in, 3–4, 35–36
references on, 28–31
registration and alignment in, 14–15
room-temperature methods in, 161–181
of single-wall carbon nanotube fabrics, 55–77
surface preparation in, 251–280strategic indicators in U. S., 23-28
surface programmed assembly in, 33-54
top-down approaches in, 4-5
trends and summary of, in U.S., 23-28
in United States, 16-28
Nanoscale patterning, (*see* Patterning)
Nanoscale Science, Engineering, and Technology (NSET) Subcommittee, 3
Nanotech act, 368
Nanotechnology
federal regulatory capacity for, 377-384

federal support for, 368
manufacturing processes in (*see* Nanoscale manufacturing)
patenting, 367-376, 379-380
public uncertainty about, 384-385
Nanotemplates, 9-12
Nanotransfer printing, 155
Nanotube(s), (*see* Carbon nanotubes; Multi-wall carbon nanotubes; Single-wall carbon nanotubes)
Nanotube excess, removal of, 63
Nanowires, 34
alignment of, in self-assembly, 42–47
chemical patterning of, 138
direct synthetic methods for, 129–136
inorganic, fabrication methods for, 129–135
organic, fabrication methods for, 135
post synthetic methods for, 136–140
National Center for Manufacturing Sciences (NCMS), survey of, 16–20
National Nanotechnology Initiative (NNI), 3, 4
and regulatory issues, 381, 386
in research and development, 19
National priorities, in nanoscale manufacturing, 20–23
National Science Foundation, 16
NCMS, (*see* National Center for Manufacturing Sciences)
NCP, (*see* Nanocontact printing)
NIL, (*see* Nanoimprint lithography)
NNI, (*see* National Nanotechnology Initiative)
Nonmanufacturing applications, markets for, 24
Nonvolatile memory technology, 74–76
NRAM™, 74–76
circuit architecture and description of, 74
read-write operations of, 74–76
NSET, (*see* Nanoscale Science, Engineering, and Technology (NSET) Subcommittee)
Nuclear magnetic resonance (NMR) spectroscopy, 290
Nylon 6, 354, (*see also* Electrospun nanofiber membranes)

O

Octadecylmercaptan (ODT), in vapor phase deposition of SAMs, 195
Organic films, chemical analysis of, 203–205
Organization capacity, 25
Osmium tetroxide (OsO_4), 321–322
OTS, (*see* Trichlorooctadecylsilane)

P

PAA (porous anodic aluminum), (*see* Anodic aluminum oxide (AAO))
PANI, (*see* Polyaniline)
Particle removal, 251–280
experimental procedures in, 265–279
physics of, 255–261
references on, 279–280
rolling removal mechanism in, 261–263
selective, particle size in, 267–269
Partnering, drivers for, 26
Patent(s), 367–368
adequacy of current system of United States, 379–380
basic knowledge of, 368–372
classification of, 372–373
description of, 369
and foreign patent rights, 371–372
and freedom-to-operate issues, 374–375
law associated with, 369–371
nanotechnology, growth of, 372–373
overlapping, and priority disputes, 373–374
references on, 375–376
Patterning, nanoscale, 5–9
block copolymers in, 12–13
of carbon materials, 299–308
in carbon tube synthesis, 91–101
conductive polymers in, 13–14
dip-pen nanolithography in, 38–41
and directed self-assembly, 9–12
in fiber spray coatings, 351–366
in large scale single-wall carbon tube synthesis, 95–101
microcontact printing and other methods in, 42
in nanowire synthesis, 128–140
in surface programmed assembly, 38–42
PDMS, (*see* Poly(dimethylsiloxane) (PDMS) rubber stamps)
PECVD, (*see* Plasma enhanced chemical vapor deposition)
Pellethane, 354, (*see also* Electrospun nanofiber membranes)
Perfluorocyltrichlorosilane (FOTS), in vapor phase deposition of SAMs, 194–196
Perfluorodecanoic acid (PFDA), in vapor phase deposition of SAMs, 195
Perfluorodecyltrichlorosilane (FDTS), in vapor phase deposition of SAMs, 195
Permeation layer, 110
PFDA, (*see* Perfluorodecanoic acid)
Photolithography, 42
in post synthetic nanowire fabrication, 136

Plasma enhanced chemical vapor deposition (PECVD), 196–197, 285, 292–293, 307
Plasma polymerization, in antistiction film fabrication, 196–197
Plasmonic imaging lithography, 4–5
Plastic contacts, 231–238
Plasticity, scale dependent, 232
PLD, (*see* Pulsed laser deposition)
Poly(p-xylylene)(PPX), and polylactic acid (PLA) core-sheath fibers, 320
Poly(perfluoroalkylacrylate), 199
Poly(vinyl alcohol) (PVA), in room temperature nanolithography, 169–172
Poly(vinyl fluoride), 199
Polyacetonytrile (PAN) precursors, 285
Polyamide-6,6
  melt temperature and DVD tool interaction, 339, 340, 341
  properties of, 336
Polyaniline (PANI)
  directed self-assembly of, 13–14
  and polyethylene oxide, blends of, 320
Polyaniline blends, 326
Polybutadiene/polycarbonate (PB/PC) blend, electrospun, 321–322
  composition ratio effect on, 323–324
  molecular weight of components in, 324–325
Polycarbonate (PC)
  blends of, 326
  extrusion studies of, 317–320
  optical grade, properties of, 336
Polyethylene oxide (PEO)
  blends of, 320
  in core-sheath fibers, 321
Polylactide/polyvinylpyrrolidone blends, 320
Polymer blend(s), controlled phase separation in, 320–326
Polymer blend fibers, electrospun, 320–322
  composition ratio effect on, 323–324
  molecular weight of components of, effects of, 324–325
  polybutadiene/polycarbonate, 322–323
  polymer type in, 326
  viscocity of components of, 323–324, 325
Polymer external interfacial behavior, 326–346
  in molded nanostructure formation, 334–346
  between polymer jets and electrical field, 326–334
Polymer internal interfacial behavior, 313–315
  in controlled phase separation, 320–326
  instability in, 314–320
  in nanolayer melts, 314–320
Polymer jets, and effect of electrical field, 326–334
Polymer melts
  internal interfacial behavior, 314–320
  self-guided assembly, 11–12
Polymer-tool interface, (*see* Polymer external interfacial behavior)
Polymethyl methacrylate (PMMA), properties of, 326
Polymethyl methacrylate (PMMA) blends, 326
Poly(ethylene)/poly(methyl methacrylate) template, 173–176
Polypropylene (PP), 317
  extrusion studies of, 317–320
  properties of, 326
Poly(dimethylsiloxane) (PDMS) rubber stamps, 148–150
  in decal transfer lithography, 153–155
  in dry transfer printing process, 155–159
  as photomasks, 151–153
  references on, 159–160
  two and three-dimensional nanofabrication with, 151–153
Polystyrene (PS), properties of, 336
Polystyrene (PS) blends, 326
Polytetralfluoroethylene (PTFE), 188, 199
Pore size, in electrospun nanofiber membranes, 358–360
Porometry, 359
Pressure parameter, 301
Priorities, national, in nanoscale manufacturing, 20–23
Process reproducibility, 63–64
Products in development, diversity of, 18, 24
Protein motors, 47–50
Protein/ligand binding reactions, 114, 117
PTFE, (*see* Polytetralfluoroethylene)
Public interest/confidence, protecting and promoting, 384–387
Public-private collaboration, in nanoscale manufacturing, 21–23
Pulsed laser deposition (PLD), 285
PVA, (*see* Poly(vinyl alcohol))

Q

Quantum dot(s) (QD), 143

R

Raman analysis, 290, 293, 301–302, 305–307
Reactive ion etching (RIE), in molecular microswitch manufacturing, 70–73

Registration, and alignment, in nanoscale manufacturing, 14–15
Regulatory frameworks, and institutions, United States, 380–384
  capacities of, 380–382
  incremental changes in current, 382–383
Reliability, in nanoscale manufacturing, 15–16
Removal moment (RM), 261
Research and development
  collaboration between public and private, 21–23
  in Korea, 389–396
  legislation and federal government support for, 368
RIE, (*see* Reactive ion etching)
RM, (*see* Removal moment)
Rolling removal mechanism, 261–263
Room-temperature methods, 161–181
  in nanocontact printing, 172–179 (*see also* Gold electrode pattern transfer; Poly(ethylene)/poly(methyl methacrylate) template; Silicon dioxide/silicon mold; Silver patterning)
  in nanoimprint lithography, 161–172 (*see also* Hydrogen silsesquioxane (HSQ) procedure)
  references on, 180–181
Rotating disc target, 332–334
Rough surfaces
  fractal description of, 243
  nanoscale contact between, 238–240
Roughening surface, to reduce contact area, 185
Rubber stamp techniques, 147–160

S

Scale dependent plasticity, 232
Scanning electron microscopy (SEM), in film thickness measurement, 201–203
Scanning speed parameter, 300–301
Scanning tunneling microscopy (STM), in molecular electronics, 141
Secondary bonding processes, detection of, 290–292
Selective adsorption, 37
Self-assembled monolayer(s) (SAMs), 8–9, 38–41, (*see also* Antistiction layer(s))
  in alignment of swCNTs, 44–47
  liquid, as antistiction layer, 191–194
  vapor, as antistiction layer, 194–196
Self-assembly, directed, 9–12, (*see also* Surface programmed assembly)
  in CMOS microarray systems, 117–120
  of conductive copolymers, 13–14
  in nature, 36
  of polymer melts, 11–12
  registration and alignment in, 14–15
SEM, (*see* Scanning electron microscopy)
Semiconductor elements, dry transfer printing of, 155–159
Semiconductor Research Corp. (SRC), 4
Silicon dioxide/silicon mold, in room temperature nanocontact printing, 172–173
Silicon dioxide/silicon substrate fabrication
  morphologic and surface characterization in, 91–92
  for multi-wall carbon nanotubes, 85–86, 91–95
Silicon dioxide/silicon substrate surface area
  mechanism of single-wall carbon tube growth on, 99–101
  morphology and characterization, 91–95
  patterned, in large-scale single-wall carbon nanotube synthesis, 95–101
Silicon wafer tooling, and polymer melt interaction, 335–346
Silver patterning, in room temperature nanolithography, 177–178
Single-wall carbon nanotube fabric(s), 55–77
  applications of, 69–76
  manufacturing process for, 56–69
  in molecular memory switches, 70–72
  in nonvolatile random access memory, 74–76
  qualification of, with CMOS processing, 63–69
  references on, 77
  resistivity of, 63, 64–65
  solution preparation for, 58–61
  wafer coating in manufacture of, 61–63
Single-wall carbon nanotubes (swCNTs)
  alignment of, in self-assembly, 43–47
  arc discharge method synthesis of, 81–82
  chemical vapor deposition synthesis of, 58–59, 83–85, 95–101
  dry transfer printing of, 155–159
  high density growth of, CVD parameters and catalyst particle sizes, 98–99
  large-scale synthesized networks of, 95–101, 394
  laser ablation synthesis of, 82
  physical and electrical characteristics of, 59–60
  silicon dioxide and silicon substrate patterning for, 95–101

solutions preparation for, 60–61
Skin-core structure, 317
Solution purity, 63
SPA process, (*see* Surface programmed assembly)
Spin coating process, 189–191
for single-wall carbon nanotube fabrics, 62
Spring tip, 185
Staffing, for nanoscale manufacturing, 26
Start-up issues, in nanoscale manufacturing, 16–18
State regulatory capacities, 383
Stiction
and aspect ratio, 185
chemical modification of, 185–186
reduction of, historical progression, 185–186
Stiction failure, in micromechanical switches, 240–244
STM, (*see* Scanning tunneling microscopy)
Strain rate, studies of, 291–292
Streptavidin patterns, 49–50
Streptaviding/biotin binding reaction, 114, 117
Stress relaxation, studies of, 291–292
Structuring, carbon materials, 299–308
Styrene-butadiene-styrene triblock, 320
Submicron particle removal, from deep trenches, 274–278
Substrate, (*see Silicon and silicon dioxide substrate entries*)
Substrate selectivity, of carbon nanotubes, 85, 91–95
Supercritical fluid, 185
Superlattice nanowire pattern transfer (SNAP), 140
Supramolecular chemistry, 8–9
Surface cleaning/preparation, 251–254
acousting streaming in, 254–263
chemical processes in, 263
experimental techniques in, 263–278
references on, 279–280
selective, 265–279
Surface energy, methods of lowering, 199
Surface energy gamma, 221
Surface force apparatus, 230–231
Surface functionalization, 5–7
Surface morphology
of antistiction layer, 205–207
of substrate, characterization of, 91–95
Surface programmed assembly, 33, 37–54, 394
alignment of nanostructures in, 42–50
concepts of, 37
and protein motors, 47–50
references on, 51–54
Survey, industry, 16–20
swCNTs, (*see* Single-wall carbon nanotubes)
SWNT (single walled nanotube), (*see* Single-wall carbon nanotubes)

T

Tabor parameter, 227
t-aC, (*see* Tetrahedral amorphous carbon)
t-aC:H, (*see* Hydrogenated tetrahedral amorphous carbon)
Target geometry, and effect on electrospun nanofibers, 332–334
Target sheet resistance, 63, 64
Teflon AF, 190–191
structure of, 192
Temperature dependent resistivity, 243–244
Templates, nanoscale, 5–7, 9–12, (*see also* Nanotemplates)
directed self-assembly of conductive polymers using, 13–14
Tetrahedral amorphous carbon (t-aC), 285
mechanical properties of, 286, 287–289
Theoretical stress, 222
Thermal characterization, of antistiction layer, 207–209
Thiolated functional molecules, 141
Three-dimensional architecture, of multi-wall carbon nanotubes, 89–91
Time of irradiation parameter, 300
Tip growth mechanism, 84–85
Tool cleaning procedure, 336
Top-down approaches, in nanoscale manufacturing, 4–5, 7–14, 34–36, 108–109
Trade secrets, 368–369
Trademark, 368
Transverse electric field, effects of, 329–332
Trescal yield criterion, 231
Tribological characterization, of antistiction layer, 207–209
Trichlorooctadecylsilane (OTS), in vapor phase deposition of SAMs, 195
Twenty-first Century Nanotechnology Research and Development Act, 368

U

Ultrasonic cleaning process, 252–253
10-Undecenyltrichlorosilane (UTCS), in vapor phase deposition of SAMs, 195

Undecyltrichlorosilane (DTS), in vapor phase deposition of SAMs, 195
United States Patent and Trademark Office (USPTO), 369–371, 379–380
United States Patent Classification System, 372–373

V

van der Waals equation, 289
van der Waals force(s), 258
  and viscomechanical behavior, 289–292
van der Waals interactions, in carbon materials, 287–289
  formula describing, 290
Vapor phase catalyst delivery, 85
Vapor phase etching, 185
Vapor-liquid-solid (VLS) technique, 129
Viscocity, of components of electrospun polymer fibers, 323–324, 325
Viscoelastic constitutive equations, 334–335
Viscomechanical analysis, of hydrogenated amorphous carbon films and carbon nanotube arrays, 292–299
Viscomechanical behavior, and van der Waals forces, 289–292
Viscous encapsulation, 316
Von Mises yield criterion, 232

W

Wafer coating, of single-wall carbon nanotube fabrics, 61–63
Wave instability, 317–320
WEDM, 335
Wettability, of antistiction layers, 198–200
Wiring, nanostructural, (*see* Electrical contact(s))
Working distance parameter, 301

X

X-ray photoelectron spectroscopy (XPS), 203–205

Y

Young modulus calculations, 284, 293–294

Z

Zero-dimensional nanostructure, 143
Zeta potential, 260
Zigzag instability, 316–320

Electrical Engineering

Nanomanufacturing Handbook

Breakthroughs in nanotechnology have been coming at a rapid pace over the past few years. This was fueled by significant worldwide investments by governments and industry. But if these promising young technologies cannot begin to show commercial viability soon, that funding is in danger of disappearing as investors lose their appetites and the economic and scientific promise of nanotechnology may not be realized. Scrutinizing the barriers to commercial scale-up of nanotechnologies, the **Nanomanufacturing Handbook** presents a broad survey of the research being done to bring nanotechnology out of the laboratory and into the factory.

Current research into nanotechnology focuses on the underlying science, but as this forward-looking handbook points out, the immediate need is for research into scale-up, process robustness, and system integration issues. Taking that message to heart, this book collects cutting-edge research from top experts who examine such topics as surface-programmed assembly, fabrication and applications of single-walled carbon nanotubes (SWNTs) including nanoelectronics, manufacturing nanoelectrical contacts, room-temperature nanoimprint and nanocontact technologies, nanocontacts and switch reliability, defects and surface preparation, and other innovative, application-driven initiatives. In addition to these technical issues, the author provides a survey of the current state of nanomanufacturing in the United States—the first of its kind—and coverage also reaches into patenting nanotechnologies as well as regulatory and societal issues.

Supplying innovative tools and effective strategies for nano commercialization, this book...

- Takes a critical, no-holds-barred look at the current state of nanotechnology and the barriers to commercialization
- Surveys cutting-edge research into technologies for enabling industrial-scale fabrication, reliability, and integration
- Outlines various fabrication tools and technologies, including high-resolution molded rubber stamps, nanoimprinting lithography, and patterned electrospraying
- Includes abundant references to the current literature
- Addresses reliability, intellectual property, regulatory, and societal issues associated with commercialization

With timely, authoritative coverage accompanied by numerous illustrations, the **Nanomanufacturing Handbook** clarifies the current challenges facing industrial-scale nanotechnologies and outlines advanced tools and strategies that will help overcome them.

CRC Press
Taylor & Francis Group
an informa business
www.taylorandfrancisgroup.com

6000 Broken Sound Parkway, NW
Suite 300, Boca Raton, FL 33487
270 Madison Avenue
New York, NY 10016
2 Park Square, Milton Park
Abingdon, Oxon OX14 4RN, UK

3326
ISBN 0-8493-3326-1
90000
9780849333262
www.crcpress.com